Energy Technology 2018

Carbon Dioxide Management and Other Technologies

Edited by

Ziqi Sun

Cong Wang

Donna Post Guillen

Neale R. Neelameggham

Lei Zhang

John A. Howarter

Tao Wang

Elsa Olivetti

Mingming Zhang

Dirk Verhulst

Xiaofei Guan

Allie Anderson

Shadia Ikhmayies

York R. Smith

Amit Pandey

Sarma Pisupati

Huimin Lu

TMS

Springer

The Minerals, Metals & Materials Series

Ziqi Sun · Cong Wang · Donna Post Guillen
Neale R. Neelameggham
Lei Zhang · John A. Howarter
Tao Wang · Elsa Olivetti
Mingming Zhang · Dirk Verhulst
Xiaofei Guan · Allie Anderson
Shadia Ikhmayies · York R. Smith
Amit Pandey · Sarma Pisupati
Huimin Lu
Editors

Energy Technology 2018

Carbon Dioxide Management and Other Technologies

TMS

Springer

Editors

See next page

ISSN 2367-1181 ISSN 2367-1696 (electronic)
The Minerals, Metals & Materials Series
ISBN 978-3-319-72361-7 ISBN 978-3-319-72362-4 (eBook)
https://doi.org/10.1007/978-3-319-72362-4

Library of Congress Control Number: 2017960927

Printed on acid-free paper

This Springer imprint is published by the registered company Springer International Publishing AG part of Springer Nature
The registered company address is: Gewerbestrasse 11, 6330 Cham, Switzerland

Ziqi Sun
Queensland University of Technology
Brisbane, QLD
Australia

Cong Wang
Northeastern University
Shenyamg
China

Donna Post Guillen
Idaho National Laboratory
Idaho Falls, ID
USA

Neale R. Neelameggham
IND LLC
South Jordan, UT
USA

Lei Zhang
University of Alaska Fairbanks
Fairbanks, AK
USA

John A. Howarter
Purdue University
West Lafayette, IN
USA

Tao Wang
Nucor Steel
Blytheville, AR
USA

Elsa Olivetti
Massachusetts Institute of Technology
Cambridge, MA
USA

Mingming Zhang
ArcelorMittal Global R&D
East Chicago, IN
USA

Dirk Verhulst
Reno, NV
USA

Xiaofei Guan
Watertown, MA
USA

Allie Anderson
Gopher Resource
Tampa, FL
USA

Shadia Ikhmayies
Al Isra University
Amman
Jordan

York R. Smith
University of Utah
Salt Lake City, UT
USA

Amit Pandey
LG Fuel Cell Systems
North Canton, OH
USA

Sarma Pisupati
The Pennsylvania State University
University Park, PA
USA

Huimin Lu
Beihang University
Beijing
China

Preface

This volume contains selected papers presented at the Energy Technologies Symposium organized in conjunction with the TMS 2018 Annual Meeting & Exhibition in Phoenix, Arizona, USA, and organized by the TMS Energy Committee. The papers in this volume intend to address the issues, intricacies, and the challenges relating to energy and environmental science. This volume also contains selected papers from the following symposia: Deriving Value from Challenging Waste Streams: Recycling and Sustainability Joint Session, Materials for Energy Conversion and Storage, Solar Cell Silicon, and Stored Renewable Energy in Coal.

The Energy Technologies Symposium was open to participants from both industry and academia and focused on energy efficient technologies including innovative ore beneficiation, smelting technologies, recycling, and waste heat recovery. The volume also covers various technological aspects of sustainable energy ecosystems, processes that improve energy efficiency, reduce thermal emissions, and reduce carbon dioxide and other greenhouse emissions. Papers addressing renewable energy resources for metals and materials production, waste heat recovery and other industrial energy efficient technologies, new concepts or devices for energy generation and conversion, energy efficiency improvement in process engineering, sustainability and life cycle assessment of energy systems, as well as the thermodynamics and modeling for sustainable metallurgical processes are included. This volume also includes topics on CO_2 sequestration and reduction in greenhouse gas emissions from process engineering, sustainable technologies in extractive metallurgy, as well as the materials processing and manufacturing industries with reduced energy consumption and CO_2 emission. Contributions from all areas of nonnuclear and nontraditional energy sources, such as solar, wind, and biomass are also included in this volume.

We hope this volume will provide a reference for the materials scientists and engineers as well as metallurgists for exploring innovative energy technologies and novel energy materials processing.

We would like to acknowledge the contributions from the authors of the papers in this volume, the efforts of the reviewers dedicated to the manuscripts review

process, and the help received from the publisher. We appreciate the efforts of Energy Committee members for enhancing this proceedings volume. We also acknowledge the organizers of the four other symposia that contributed papers.

Energy Technologies Symposium Organizers

Ziqi Sun, Queensland University of Technology, Australia
Cong Wang, Northeastern University, China
Donna Post Guillen, Idaho National Laboratory, USA
Lei Zhang, University of Alaska Fairbanks, USA
Neale R. Neelameggham, IND LLC, USA
Tao Wang, Nucor Steel, USA
John A. Howarter, Purdue University, USA

Contents

About the Editors

Ziqi Sun is a senior lecturer at the School of Chemistry, Physics and Mechanical Engineering, Queensland University of Technology, Australia. He received his Ph.D. degree in 2009 from Institute of Metal Research, Chinese Academy of Sciences and his B.Eng. degree in 1999 from Central South University China. He was awarded with some prestigious awards and fellowships including the TMS Young Leaders Development Award from The Minerals, Metals & Materials Society (TMS, 2015), Discovery Early Career Research Award from Australian Research Council (DECRA, 2014), Alexander von Humboldt Fellowship from AvH Foundation Germany (2009), Australian Postdoctoral Fellowship from Australian Research Council (APD, 2010), the Vice-Chancellor's Research Fellowship from University of Wollongong (2013), etc. He is also serving as Vice-Chair of the Energy Committee within TMS, Associate Editor of *Surface Innovations* (ICE Science), Editorial Board Member of *Scientific Reports* (Nature Publishing Group), Editorial Board Member of *Journal of Materials Science and Technology* (Elsevier), Guest Professor at Shenzhen Institute, Peking University, and Honorary Fellow at University of Wollongong. Ziqi is the program leader for two ongoing Australian Research Council Projects. He held the roles as symposium organizer and session chair in some prestigious conferences such as TMS conferences and ACerS annual conferences. His major research interest is the rational design of bio-inspired metal oxide

nanomaterials for sustainable energy harvesting, conversion, and storage.

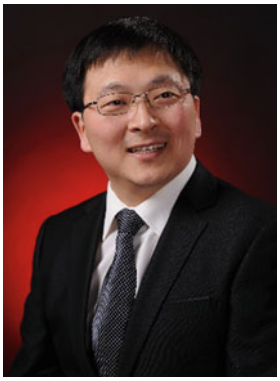

Cong Wang is currently Professor of the School of Metallurgy, Northeastern University. Prior to joining the faculty of his alma mater, Dr. Wang had worked with Alcoa, Saint-Gobain, and Northwestern University, respectively. His expertise includes high-temperature metallurgical processing with a focus on steels. He is the incumbent TMS Energy Committee Chair. He serves on the editorial boards of several journals, including *Metallurgical and Materials Transactions A* and *B*, *International Journal of Refractory Metals and Hard Materials*, *Journal of Materials Science and Technology*, and *Journal of Iron and Steel Research International*. He is also a Corresponding Expert of Engineering, the flagship journal recently launched by Chinese Academy of Engineering. He receives Invitational Fellowship by JSPS (2017), Excellent Young Scientist Award by NSFC (2016), Outstanding Young Manufacturing Award by SME (2014) and Young Leader Professional Award by TMS (2011). He is also the finalist of the prestigious 1000 Talents Program by Chinese Government (2014). As an active member of the global metallurgy community, Dr. Wang serves as the inaugural founder of the International Metallurgical Processes Workshop for Young Scholars (IMPROWYS), and acted as organizers/advisors for various international symposia/workshop of technical significance.

Donna Post Guillen holds the position of distinguished research engineer in the Materials Science and Engineering Department at the Idaho National Laboratory. Dr. Guillen earned a B.S. in mechanical engineering from Rutgers University, an M.S. in aeronautics from Caltech, and a Ph.D. in engineering and applied science from Idaho State University. She has more than 30 years of research experience and has served as principal investigator for numerous multidisciplinary research projects on the topics of waste heat recovery, synthetic fuels production, nuclear reactor fuels and materials experiments, and waste

glass vitrification. The focus of her research is on multiphase computational fluid dynamics and thermal hydraulics for sustainable energy technologies. She applies numerical modeling techniques to provide understanding of a wide variety of complex systems such as, greenhouse gas generation/sequestration for dairies, working with industry (General Electric) to develop a direct evaporator for an organic Rankine cycle, and modeling the waste vitrification process for the Hanford Waste Treatment Plant and the fluidized bed for the Idaho Waste Treatment Unit. She is experienced with irradiation testing and thermal hydraulic analysis for nuclear reactor experiments and serves as Principal Investigator/Technical Lead for the Nuclear Science User Facility Program. She is the lead inventor on two patents related to the development of a new composite material to produce a fast reactor environment within a pressurized water reactor. She actively mentors students, routinely chairs and organizes technical meetings for professional societies, serves in leadership capacity for the American Nuclear Society (Thermal Hydraulics Executive and Program committees), The Minerals, Metals & Materials Society (TMS—Energy Committee Past-Chair) and the American Society of Mechanical Engineers (Thermal Hydraulics and Computational Fluid Dynamic Studies Track Co-Chair), provides subject matter reviews for proposals and technical manuscripts, has published more than 100 conference papers, reports and journal articles, and written/edited three books.

Neale R. Neelameggham is "The Guru" at IND LLC, involved in international consulting in the field of metals and associated chemicals (boron, magnesium, titanium, and lithium and rare earth elements), thiometallurgy, energy technologies, soil biochemical reactor design, etc. He was a visiting expert at Beihang University of Aeronautics and Astronautics, Beijing, China. He was a plenary speaker at the Light Metal Symposium in South Africa—on low carbon dioxide emission processes for magnesium. Dr. Neelameggham has more than 38 years of expertise in magnesium production and was involved in process development of

its start-up company NL Magnesium through to the present US Magnesium LLC, UT until 2011. Neelameggham and Brian Davis authored the ICE-JNME award-winning (2016) paper "21st Century Global Anthropogenic Warming Convective Model," which notes that constrained air mass warming is independent of the energy conversion source—fossil or renewable energy. He is presently developing Agricoal™ and agricoalture to improve arid soils. Dr. Neelameggham holds 16 patents and patent applications, and has published several technical papers. He has served in the Magnesium Committee of the Light Metals Division (LMD) of TMS since its inception in 2000, chaired it in 2005, and in 2007 he was made a permanent co-organizer for the Magnesium Symposium. He has been a member of the Reactive Metals Committee, Recycling Committee, Titanium Committee, and Program Committee Representative of LMD and LMD council. Dr. Neelameggham was the inaugural chair, when in 2008, LMD and EPD (Extraction & Processing Division) created the Energy Committee, and has been a coeditor of the energy technology symposium proceedings through the present. He received the LMD Distinguished Service Award in 2010. While he was the chair of Hydro- and Electrometallurgy Committee he initiated the rare metal technology symposium in 2014. He is coeditor for the 2018 proceedings for the symposia on Magnesium Technology, Energy Technology, Rare Metal Technology, and Solar Cell Silicon.

Lei Zhang is an assistant professor in the Department of Mechanical Engineering at the University of Alaska Fairbanks (UAF). Prior to joining the UAF, Dr. Zhang worked as a postdoctoral associate in the Department of Chemical and Biomolecular Engineering at the University of Pennsylvania. Dr. Zhang obtained her Ph.D. degree in materials science and engineering from Michigan Technological University in 2011, and her M.S. and B.E. degrees in materials science and engineering from China University of Mining and Technology, Beijing, China, in 2008 and 2005, respectively. Her research interest focuses on the design and investigation of the properties of porous

materials and nanostructure-based films for energy and environmental applications. Her current research focuses mainly on the synthesis of metal-organic frameworks (MOFs) and MOF-based nanocomposites, and the manipulation of their properties and applications in gas storage, separation, and water treatment. She is also working on the development and characterization of anticorrosion coatings on metallic alloys for aerospace and biomedical applications.

Dr. Zhang has been actively involved in the activities at The Minerals, Metals & Materials Society (TMS) annual meetings. She has served on the TMS Energy Committee since 2014, and also has served on the Best Paper Award Subcommittee of the TMS Energy Committee. She has served as a frequent organizer and session chair of the symposia at TMS Annual Meetings (2015, 2016, and 2017). She was the recipient of 2015 TMS Young Leaders Professional Development Award.

John A. Howarter is an assistant professor in Materials Engineering at Purdue University with a joint appointment in Environmental & Ecological Engineering. His research interests are centered on synthesis, processing, and characterization of sustainable polymers and nanocomposites. His research impacts water treatment, thermal management in electronic devices, and material design for recycling and value recovery. John has been involved in the Public and Government Affairs (P&GA) Committee of The Minerals, Metals & Materials Society (TMS), where he currently serves as incoming Chair. In addition to working with P&GA, Prof. Howarter is a regular contributor to the technical programming for both TMS and Materials Science & Technology (MS&T) conferences in areas of energy, recycling, and materials sustainability. John earned a B.Sc. from The Ohio State University in 2003 and Ph.D. from Purdue University in 2008, both in materials engineering. From 2009 to 2011, he was a National Research Council postdoctoral scholar in the Polymers Division of the National Institute of Standards and Technology in Gaithersburg, Maryland.

Tao Wang is currently Castrip Research Lab Supervisor at Nucor Steel. He is also the lead engineer in the process and product research and development areas. Dr. Wang's current focus is to develop and modify a novel thin strip casting technology which uses up to 90% less energy to process liquid steel into hot rolled steel sheets than conventional casting methods. Dr. Wang has rich experience in metallurgical thermodynamics, thermal energy storage and transfer, steelmaking, metal solidification and casting, and metal corrosion. Dr. Wang obtained his Ph.D. and M.S. from the University of Alabama; and he received his B.S. from Xi'an Jiao Tong University in China. In his areas of research, Dr. Wang has published multiple papers and patents which led to breakthroughs in thermodynamic modeling, high-efficiency thermal energy transfer medium development, and thin strip metal casting technology.

Dr. Wang received the 2013 Light Metals Division (LMD) Best Energy Paper Award from TMS and is a 2016 TMS Young Leaders Award winner. Also, he was selected to become a member of TMS Emerging Leader Alliance (ELA) in 2015. Dr. Wang serves the technical committees, including the Energy Committee and Pyrometallurgy Committee, within TMS; and Metallurgy-Steelmaking & Casting Technology Committee, Continuous Casting Technology Committee, Southeast Chapter within Association for Iron & Steel Technology (AIST).

Elsa Olivetti is the Thomas Lord Assistant Professor in the Department of Materials Science and Engineering at Massachusetts Institute of Technology (MIT). She received her B.S. in engineering science from the University of Virginia and her Ph.D. in materials science from MIT working on development of nanocomposite electrodes for lithium-ion rechargeable batteries. Olivetti joined MIT's faculty in 2014 where her current research focuses on improving the environmental and economic sustainability of materials in the context of rapid-expanding global demand. Olivetti leverages machine learning as well as data mining coupled with engineering and macroeconomic models to determine the scaled impact of novel materials and processes.

Mingming Zhang is currently a lead research engineer at ArcelorMittal Global R&D at East Chicago, Indiana. His main responsibilities include raw material characterization and process efficiency improvement in mineral processing and ironmaking areas. He also leads a technical relationship and research consortium with university and independent laboratory members and manages pilot pot-grate sintering test facility at ArcelorMittal Global R&D East Chicago.

Dr. Zhang has over 15 years of research experience in the field of mineral processing, metallurgical and materials engineering. He obtained his Ph.D. degree in Metallurgical Engineering from The University of Alabama and his Master degree in Mineral Processing from General Research Institute for Non-ferrous Metals in China. Prior to joining ArcelorMittal, he worked with Nucor Steel Tuscaloosa, Alabama where he was metallurgical engineer leading the development of models for simulating slab solidification and secondary cooling process.

Dr. Zhang has conducted a number of research projects involving mineral beneficiation, thermodynamics and kinetics of metallurgical reactions, electrochemical processing of light metals, energy efficient and environmental cleaner technologies. He has published over 50 peer-reviewed research papers and is the recipient of several U.S. patents. Dr. Zhang also serves as editor and reviewer for a number of prestigious journals including *Metallurgical & Materials Transactions A* and *B*, *JOM*, *Journal of Phase Equilibria and Diffusion*, and *Mineral Processing and Extractive Metallurgy Review*.

Dr. Zhang has made more than 20 research presentations at national and international conferences including more than 10 keynote presentations. He is the recipient of 2015 TMS Young Leaders Professional Development Award. He has been invited by a number of international professional associations to serve as conference organizer and technical committee member. These associations include The Minerals, Metals & Materials Society (TMS) and the Association for Iron & Steel Technology (AIST).

Dirk Verhulst spent the last 40 years in practical process metallurgy research on both sides of the Atlantic, bringing a number of projects from the laboratory to the pilot scale, and a few to industrial implementation. He is presently an independent consultant in process metallurgy and energy efficiency.

Until the end of 2008, he was Director of Research at Altairnano in Reno, Nevada. He participated in the development of the Altair Lithium-ion Battery, and was involved in the design and procurement of the manufacturing plant for the ceramic materials.

Over the period 2003–2008, he worked extensively on the Altair Hydrochloride TiO_2 Pigment Process and the operation of its pilot plant. The complex flow sheet included both hydrometallurgical and pyrometallurgical steps. Optimization of energy use was a key factor to make this new approach competitive.

From 1995 to 2000, he was Senior Development Engineer in BHP's Center for Minerals Technology at the same location in Reno. It is at BHP that the development of the hydrochloride TiO_2 pigment process was initiated. Other BHP projects included novel processes for nickel, cobalt, zinc, and copper.

Prior to 1995, he worked for 17 years in the research department of Umicore in Hoboken, Belgium. He was active in lead refining and in the hydrometallurgy of minor metals (indium, tellurium, selenium), but was mostly involved in the introduction of electric furnaces in lead smelting and slag cleaning. He tackled mathematical models and lab-scale experiments, ran pilot plants and participated in the start-up of industrial operations.

Dr. Verhulst has a doctor of engineering science degree in extractive metallurgy from Columbia University, and a chemical engineering degree from the Free University of Brussels. He wrote and presented publications in the areas of hydrometallurgy, pyrometallurgy, nanomaterials, and environmental science. He holds several patents and patent applications.

Xiaofei Guan is an Assistant Professor in School of Physical Science and Technology at ShanghaiTech University. His primary research interest is in understanding chemical and electrochemical processes for materials synthesis and energy conversion with the goal of improving efficiency and reducing environmental impact. He received his B.S. degree in Applied Physics from Nankai University in 2009, and Ph.D. degree in Materials Science and Engineering from Boston University in 2013. His Ph.D. research was on magnesium recycling, and electrolytic production of energy-intensive metals from oxides. In 2014, he joined Harvard University as a Postdoctoral Fellow and led research on energy conversion and storage devices including solid oxide fuel cells, protonic ceramic fuel cells, and hydride–air batteries, and later worked on synthesis of iron sulfides particularly for solar energy application, which is a joint project between materials, microbiology, and electrochemistry.

Dr. Guan received the Outstanding Ph.D. Dissertation Award in Materials Science and Engineering from Boston University in 2014, and the Young Leaders Professional Development Award from the TMS Extraction and Processing Division in 2015. He also serves as an advisor and guest editor in the Recycling and Environmental Technologies Committee for *JOM*.

Allie Anderson is a research and development engineer at Gopher Resource in Tampa, Florida. She completed her Ph.D. and Master's degrees in Metallurgical and Materials Engineering at the Colorado School of Mines. She received her Bachelor's of Science in Mechanical Engineering from Gonzaga University. Her Ph.D. research focused on the CFD modeling of reverberatory furnaces used for the recycling of lead-acid battery scrap. Allie first became a member of TMS during her undergraduate studies when she started a Material Advantage chapter at her university and has been involved with the organization ever since. In 2015 and 2017, she received the Henry DeWitt Smith scholarship through TMS and has given oral and poster presentations at the annual meetings.

Shadia Ikhmayies received a B.Sc. from the physics department in the University of Jordan in 1983, a M. Sc. in molecular physics from the same university in 1987, and a Ph.D. in producing CdS/CdTe thin film solar cells from the same university in 2002. Now she works in Al Isra University in Jordan as an associate professor. Her research is focused on producing and characterizing semiconductor thin films and thin film CdS/CdTe solar cells. Dr. Ikhmayies also works in characterizing quartz in Jordan for the extraction of silicon for solar cells and characterizing different materials by computation. She published 44 research papers in international scientific journals, three chapters in books, and 73 research papers in conference proceedings. She is the author of two books for Springer *Silicon for Solar Cell Applications*, and *Performance Optimization of CdS/CdTe Solar Cells*, which are in production, the editor-in-chief of the book *Advances in Silicon Solar Cells* for Springer, and the eBook series *Material Science: Current and Future Developments* for Bentham Science Publishers, where these two books are in production.

Shadia is a member of The Minerals, Metals & Materials Society (TMS) and the World Renewable Energy Network (WREN). She is a member of the International Organizing Committee and the International Scientific Committee in the European Conference on Renewable Energy Systems (ECRES2015-ECRES2017). She is a member of the editorial board of the *International Journal of Materials and Chemistry* for Scientific & Academic Publishing, the editor-in-chief of a book for the Research Signpost. She was a technical advisor/subject editor for *JOM*. She is a guest editor for two topical collections published in the *Journal of Electronic Materials*: European Conference on Renewable Energy Systems (2015 and 2016). Shadia is a reviewer in 24 international journals and she is Chair of the TMS Materials Characterization Committee (2016–2017).

York R. Smith received his B.S. and M.S. degrees in chemical engineering from the University of Nevada, Reno. He then moved to the University of Utah where he obtained his Ph.D. in metallurgical engineering. After a postdoctoral research award from the U.S. Department of Energy, Office of Energy Efficiency and Renewable Energy, York then joined the University of Utah faculty in July 2016 as an Assistant Professor of metallurgical engineering. He specializes in chemical metallurgy with current research interests in nonferrous metal recycling, electrochemistry, interfacial phenomena, and sustainable/green metallurgical engineering.

Amit Pandey is currently working as a Development Lead (Material Engineering) at LG Fuel Cell Systems (LGFCS) in North Canton, Ohio. Previously, he was employed at the Johns Hopkins University (JHU) and the Oak Ridge National Laboratory (ORNL). He is primarily interested in structural and functional materials for energy conversion and storage.

Dr. Pandey received his B.S. (2003) in Mining Engineering from Indian Institute of Technology (IIT–BHU) Varanasi, India. Later, he received his M.S. (2005) in Civil Engineering from University of Arizona and Ph.D. (2010) in Mechanical Engineering from University of Maryland. Pandey has a Google scholar citation ~700 and has received young leader awards from various materials societies (ACeRs, TMS, ASM). In 2017, he was selected to attend the U.S. Frontiers of Engineering Symposium, National Academy of Engineering, USA.

Sarma Pisupati is Professor and Chair of the Energy Engineering Program, and Director of Online Education in the John and Willie Leone Family Department of Energy and Mineral Engineering at Pennsylvania State University (Penn State). He also codirects the Coal Science and Technology Program of the EMS Energy Institute. He earned B.S. and M.S. degrees in Chemical Engineering and a Ph.D. degree in Fuel Science. He has been studying and teaching the issues related to the energy and environment for the past 36 years. He has worked in industry for 5 years before joining the faculty at Penn State.

Huimin Lu is currently a professor in School of Materials Science & Engineering at Beihang University. He earned his Ph.D. degree in metallurgical engineering from Northeastern University in 1997. His research mainly focuses on liquid metal storage and light metal fuel cells, light metal metallurgy, and light metal materials processing and characterization. His research results were mainly on material purification technology and complete sets of equipment development and industrialization, and short process low-cost materials preparation science and technology.

Dr. Lu developed the large-capacity solid aluminum electrode three-layer electrolysis refining-oriented crystallization-ionic liquid electro-deposition combined technology, 4N, 5N, and 6N or higher than 6N high-purity aluminum could be produced and applied in integrated circuits, semiconductor, and aerospace fields. Extraction of aluminum–silicon alloy and production of solar high-purity silicon from high-alumina minerals had been applied in the industry. His new process of extracting magnesium by the aluminum–silicon alloy heat-reducing from serpentine is also applied in industry. He developed a high-strength and high-toughness graphene lithium aluminum alloy with high-pressure torsion deformation technology. High-specific energy aluminum–air batteries, magnesium–air batteries, and lithium–air batteries have made a breakthrough; especially aluminum–air batteries will soon be applied. He is studying the new wind energy utilization technology on using non-grid-connected wind power for molten aluminum energy storage, and using aluminum–air batteries for distributed power generation. In addition to teaching several courses on characterization and processing of materials, he has edited three books, published nearly 200 technical papers, and holds 24 patents.

Dr. Lu is a lifelong TMS member, participating in several TMS annual meetings. He is an editor of the TMS2018 symposium on Stored Renewable Energy in Coal.

Part I
Energy Technologies and CO_2 Management Symposium

Gas Hydrate-Based CO_2 Separation Process: Quantitative Assessment of the Effectiveness of Various Chemical Additives Involved in the Process

Hossein Dashti and Xia Lou

Abstract Gas hydrates technology has been considered as an alternative method for carbon dioxide (CO_2) separation. A wide range of studies have been reported in the past decade on the improvement of the separation efficiency by using chemical additives. While most of these studies have shown improved kinetics, thermodynamics and/or separation efficiency at the laboratory scale, there has been no quantitative analysis of the energy consumption for viable industrial applications. Comparison of the effectiveness of the chemical additives from separate studies or groups also is impossible. The present work is focused on the modelling of the hydrate-based CO_2 separation process and provides a quantitative approach that is new in its analysis of the effectiveness of chemical additives in relation to the energy required and the kinetic parameters involved in the process.

Keywords CO_2 capture · CO_2 hydrates · Chemical additives

Introduction

Carbon dioxide (CO_2) separation and capture is one of the most challenging issues to investigate in order to alleviate the problem of CO_2 emissions worldwide. Gas hydrate-based CO_2 capture/separation (HBCC) is a relatively new separation method for CO_2 and has attracted increasing attention in the past decade. The technology employs a unique separation mechanism that is easy to regenerate and is capable of separating various gas mixtures, which might not be achievable via conventional methods. The feasibility study of the process was first reported by Spencer [1], and later supported by Tam et al. [2] According to the authors, the cost of HBCC technology in an integrated gasification combined cycle plant was US$ 8.75 per ton of CO_2 captured. It was reportedly comparable to that of US$ 57 per

H. Dashti · X. Lou (✉)
Department of Chemical Engineering, Curtin University, Kent Street, Bentley, WA 6102, Australia
e-mail: x.lou@curtin.edu.au

Z. Sun et al. (eds.), *Energy Technology 2018*, The Minerals, Metals & Materials Series, https://doi.org/10.1007/978-3-319-72362-4_1

ton of CO_2 captured through the pressure swing adsorption (PSA) method, and that of US$ 49 per ton of CO_2 captured using the monoethanolamine (MEA) chemical absorption method [3].

CO_2 form hydrates between 1.1–4.3 MPa and 273–283 K respectively. Separating CO_2 from the other gases such as oxygen and nitrogen can be achieved by first forming a solid hydrate phase that is enriched with CO_2, followed by separation of the hydrate phase from the gaseous phase and dissociation of the hydrates, leading to the recovery of CO_2 that is much higher in concentration than in the original gas mixture. Upon dissociation, one volume of CO_2 hydrates can release 175 volumes of CO_2 gas at standard conditions [4]. However, the high operation pressures required in the HBCC process lead to the high compression costs and energy consumption. This has limited the viable industrial application of the HBCC [5]. The relatively low separation efficiency also is a challenge [6, 7]. Many chemical additives have been investigated in an attempt to lower the operation pressure, and to increase the formation rate, of CO_2 gas hydrates. Among the most commonly studied chemical additives, tetrahydrofuran (THF) and cyclopentane (CP) have been found to be useful in reducing the operating pressure and increasing the CO_2 recovery rate. Other additives, like tetra-n-butyl ammonium bromide (TBAB), dodecyl-trimethyl-ammonium chloride (DTAC) and $TBANO_3$, have been found to be useful in increasing the gas storage capacity and reducing the operating pressure. Surfactants, such as sodium dodecyl sulphate (SDS), only enhance the hydration rate of the process. Mixed chemical additives also have been studied to enhance their effects in HBCC.

Studies on chemical additives have been mostly focused on the effect of the chemical additives upon the kinetics, the operational conditions and the separation efficacy. Details of the progress in chemical additives improved HBCC can be found in a few recent review papers [6–8]. Other work on chemical additives associated HBCC includes thermodynamic modelling of the CO_2 fluid and hydrate phase behaviour. For instance, Herslund et al. [5, 9, 10] modelled the fluid phase and hydrate phase in the presence of THF, CP and the mixture of both. Verrett et al. [11] developed a thermodynamic model to simulate the HBCC process in the presence of TBAB. Another study by Shi and Liang [12] proposed a thermodynamic model to investigate the effects of TBAB, tetrabutyl ammonium fluoride (TBAF) and tetrabutyl ammonium chloride (TBAC) in HBCC process. Kinetic studies on gas hydrate formation are mostly based on the model established by Englezos et al. [13] that considers both mass transfer and crystallisation processes at the gas-liquid interface. The driving force in this model is the difference between the fugacity of the dissolved gas and the fugacity at equilibrium. However, the report on kinetic models for chemical additives enhanced HBCC process is limited. A recent study by ZareNezhad et al. [14] reported a single component gas (CO_2) hydrates kinetics in the absence and presence of SDS. In this model, the crystallization theory was coupled with the mass transfer phenomena but the gas composition difference between the liquid phase and the solid-liquid interface was considered as the driving force. Sun and Kang [15] also proposed a two-parameter kinetic model to predict the CO_2 hydrate formation rate in presence of THF. In this

work, the Gibbs free energy difference was considered as the driving force. In terms of quantitative analysis of the energy consumption associated with the HBCC, Tajima et al. [16] reported the energy consumption by a designed HBCC process for separating CO_2 from the emitted flue gases, using the thermodynamic approach. There was no chemical additive used in the design. A later report by Duc et al. [17] used the process simulator PRO II, to estimate the energy consumption involved in a multi-staged HBCC process in the presence of TBAB.

The present work is focused on the development and validation of a quantitative approach for the energy estimation of the HBCC process using the production scale reported by Tajima et al. [16]. The proposed approach will then be applied to the reported HBCC processes in the presence of THF [18, 19], TBAB [20, 21], and a mixture of TBAB with DATC [22]. The impact of the chemical additive on the energy consumption in relation to the formation pressure and temperature, and the kinetics of the CO_2 hydrates will be discussed.

Methodology

A schematic flow diagram (Fig. 1) is first established based on the reported HBCC process by Tajima et al. [16]. Two compressors and three heat exchangers are used before the flue gas enters the reactor where the flue gas mixes with water with or without chemical additives. Gas hydrates form in the reactor. The hydrates slurry is separated from the gas phase and sent to a hydrates dissociation reactor from which purified CO_2 is collected.

According to the authors: (1) the process was applied to the treatment of total emission from a 1,000 MW power plant; (2) the total flow rate of the input flue gas was $1.0 \times 10^6 \mathrm{N\,m^3.h^{-1}}$; (3) the volume of the reactor was about 7,000 m^3; (4) the pressurisation was performed using adiabatic compressors with 80% efficiency; (5) the inlet and outlet temperatures of coolant were 253 K and 263 K, respectively; (6) the coefficient of performance (COP) in heat exchangers is assumed to be 3 and (7) the composition of CO_2 in the hydrates stream is 100%. Based on these

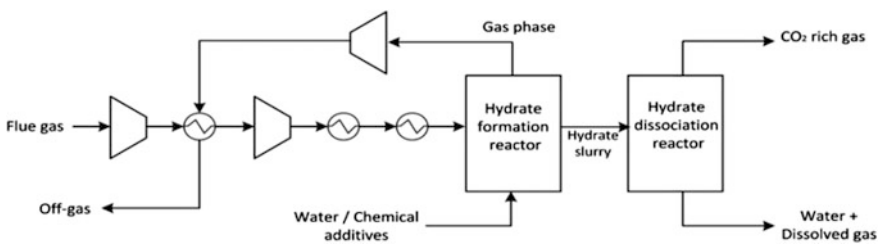

Fig. 1 A schematic flow diagram of the gas hydrate-based CO_2 separation process

assumptions, the total energy consumption involved in this process was calculated using Eq. 1:

$$E_{total} = E_{compression} + E_{cooling} + E_{hydrates} \quad (1)$$

in which $E_{compression}$ and $E_{cooling}$ represent the energy consumption during the compression and cooling stages and $E_{hydrates}$ is the energy consumption associated with hydrate formation and dissociation.

Estimation of $E_{compression}$ and $E_{cooling}$

The energy consumption values in the pressurising and cooling processes were simulated using Aspen HYSYS (V.8.6). The temperature and pressure of the input flue gas were, reportedly, 298 K and 0.1 MPa [16].

Estimation of $E_{hydrates}$

For the estimation of $E_{hydrates}$, an energy balance around the formation and dissociation reactor (Fig. 2) was first established (Eq. 2).

$$E_{hydrates} = \sum_{i=1}^{5} F_i H_i - r_f \Delta H_f + r_d \Delta H_d \quad (2)$$

where F_i is the flow rate of stream i, H_i is the enthalpy of stream i, r_f and r_d are the rates of hydrate formation and dissociation, respectively, and ΔH_f and ΔH_d are the enthalpies of hydrate formation and dissociation, respectively. Below are the details of the modelling of each of the parameters.

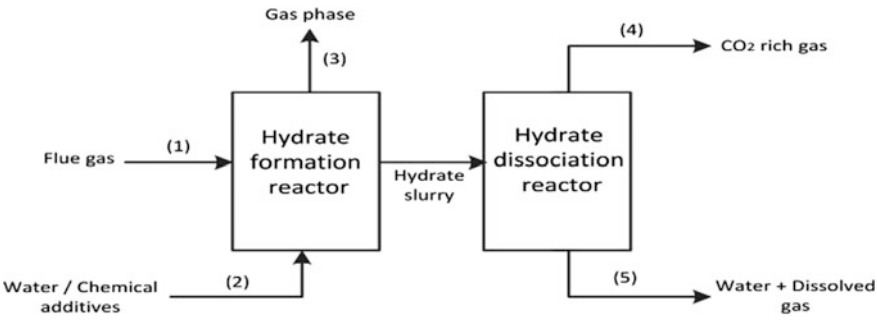

Fig. 2 CO_2 hydrates formation and dissociation unit

Enthalpy of Different Streams

The enthalpy of different streams was calculated using Eq. 3:

$$H_i = \int_0^{T_i} C_{p(mixture),i} dT_i \quad i = 1, 2, 3, 4, 5 \tag{3}$$

where i denotes a specific stream, T_i is the temperature of the stream i and $C_{p(mixture),i}$ is the specific heat capacity of the gas mixture of the stream i at pressure p, given by Eq. 4:

$$C_{p(mixture)} = \sum x_{j,i} C_{P,j} \quad \begin{matrix} j = CO_2, N_2, H_2O, O_2 \\ i = 1, 2, 3, 4, 5 \end{matrix} \tag{4}$$

in which $x_{j,i}$ is the mole fraction of component j in stream i and $C_{P,j}$ is the specific heat capacity of component j at pressure, p, which was determined using Eqs. 5–9 [23]:

$$C_{p,CO_2} = 36.11 + \left(4.23 \times 10^{-2}\right)T - \left(2.88 \times 10^{-5}\right)T^2 + \left(7.46 \times 10^{-9}\right)T^3 \tag{5}$$

$$C_{p,N_2} = 29 + \left(0.21 \times 10^{-2}\right)T + (0.57 \times 10^{-5})T^2 - \left(2.87 \times 10^{-9}\right)T^3 \tag{6}$$

$$C_{p,O_2} = 29.10 + \left(1.15 \times 10^{-2}\right)T + (0.60 \times 10^{-5})T^2 - \left(1.31 \times 10^{-9}\right)T^3 \tag{7}$$

$$C_{p,H_2O(g)} = 33.46 + \left(0.69 \times 10^{-2}\right)T + (0.80 \times 10^{-5})T^2 - \left(3.60 \times 10^{-9}\right)T^3 \tag{8}$$

$$C_{p,H_2O(L)} = 75.4 \tag{9}$$

Enthalpy of Hydrate Formation

The formation of hydrates in the form of a reaction is illustrated by Eq. 10,

$$CO_2(Vapor) + nH_2O\,(Liquid) \rightarrow CO_2 hydrates(Solid) \tag{10}$$

where n is the hydration number, which is reportedly between 5.75 and 7.66 for CO_2 [4, 24]. The enthalpy of hydrate formation is calculated using Eq. 11, taken from Kamath [25],

$$\Delta H_f = C_1 + C_2 T \tag{11}$$

where ΔH_f is in cal/gmol gas and T is the temperature at which hydrates form with $C_1 = 9.290 \times 10^3$ and $C_2 = -12.93$ at-25 < T < 0 °C, and $C_1 = 19.199 \times 10^3$ and $C_2 = -14.95$ at 0 < T < 11 °C.

Enthalpy of Hydrate Dissociation

The amount of heat required to dissociate hydrate crystals is a key thermodynamic property in the hydrate formation and dissociation process. Obtaining this parameter from the numerical equations or experiments is a challenging area of research [26]. While the high-pressure differential scanning calorimeter (DSC) has been found to be useful for the measurement of the dissociation heat in the laboratory setting [27], the application of the Clausius-Clapeyron Eq. 12 has been widely used for simple hydrates systems and it has proven to be thermodynamically correct, as long as the system is univariant [4]. Recent studies by Kang et al. [28], Delahaye et al. [29], and Sabil [30] have further demonstrated the suitability of the Clausius–Clapeyron equation for the calculation of the dissociation enthalpy of single and mixed CO_2 hydrates. The equation is expressed as,

$$\frac{dlnP_{eq}}{d\left(\frac{1}{T_{eq}}\right)} = -\frac{\Delta H_d}{ZR} \tag{12}$$

where T_{eq} and P_{eq} are the absolute temperatures and pressures that were obtained from literature data, [18, 20, 22] R is the gas constant, and Z is the gas compressibility. Note that the equation was derived from the Clapeyron equation assuming that the volume of solid hydrates approximates that of water in the hydrates formation reaction therefore the changes of volume equals to the volume of gases (see Eq. 10). The value of Z was calculated using the Peng-Robinson equation of state [31] by solving Eq. 13:

$$Z^3 - (1 - B)Z^2 + \left(A - 2B - 3B^2\right)Z - \left(AB - B^2 - B^3\right) = 0 \tag{13}$$

where A and B are determined by Eqs. 14–16,

$$A = 0.45724\left[1 + \kappa\left(1 - \sqrt{\frac{T}{T_c}}\right)\right]^2 \frac{P/P_c}{(T/T_c)^2} \tag{14}$$

$$B = 0.07780\frac{PT_c}{TP_c} \tag{15}$$

$$\kappa = 0.37464 + 1.54226\omega - 0.26992\omega^2 \tag{16}$$

Taking T_c = 304.2 K, P_c = 7.38 MPa and ω = 0.228 for CO_2 [23] and plotting ln P_{eq} against $\frac{1}{T_{eq}}$ results in a slope which equals $-\frac{\Delta H_d}{ZR}$.

Hydrate Formation Rate

Research into gas hydrates kinetic models has not been as prevalent as that for thermodynamic models. A recent paper by Ribeiro and Lage [32] has reviewed the kinetic models for hydrates formation. Among all models, the work by Englezos et al. [13] is most commonly quoted and applied. [33] In their model, the hydrates formation rate is expressed as a function of the fugacity difference between the operating condition and equilibrium condition, based on Eq. 17:

$$r_f = aK^*\left(f_g - f_{eq}\right) \tag{17}$$

where a is the interfacial area, f_g and f_{eq} represent the fugacity of the dissolved gas and fugacity at equilibrium, respectively, and K^* is the overall kinetic constant that is determined by Eq. 18,

$$\frac{1}{K^*} = \frac{1}{k_f} - \frac{1}{k_L} \tag{18}$$

where k_f is the crystal growth constant and k_L is the mass transfer coefficient in the liquid phase. For vigorous mixing systems, Fan et al. [21] further developed the model as described by Eq. 19:

$$r_f = \frac{V_g}{RT}\frac{\left(P - P_{eq}\right)}{\Delta t} \tag{19}$$

in which P is the operating pressure and P_{eq} is equilibrium pressure, V_g is the volume of the gas phase and Δt is the time to reach equilibrium. The term P_{eq} is calculated based on the hydrate formation condition inside the reactor, for which Chen-Guo's model [34] was used. It assumes that the fugacity in vapour, f_i^v, equals that in the hydrate phase, f_i^H, at equilibrium condition. Using the equations displayed in Table 1, in which θ is the fraction of linked cavities occupied by gas molecules, c is the Langmuir constant, f_T^0 is an Antoine-like function, f^0 is a function of pressure and temperature, α_w is the activity of water and α is the value dependant on the type of hydrate structure, the value of P_{eq} was computed iteratively via the contracting Newton method until it satisfied $f_i^v = f_i^H$.

Hydrate Dissociation Rate

For hydrates dissociation, a published work on methane hydrates [35] was adapted by this study. The rate of hydrate dissociation, r_d, is calculated using Eq. 20:

Table 1 Governing equations and constants for the determination of P_{eq} [34]

Equations	Constants for CO_2 gas species
$f_i^v = 10^{(Z-1)-\ln(Z-B)-\frac{A}{2\sqrt{2}B}\ln\left(\frac{Z+(\sqrt{2}+1)B}{Z-(\sqrt{2}+1)B}\right)+P_{eq}}$	Z, A and B are calculated by Eqs. 13–15
$\theta = \frac{cf_i^v}{1+cf_i^v}$	
$c = X\,exp\left(\frac{Y}{T-z}\right)$	$X = 1.6464 \times 10^{-17} MPa,\ Y = 2799.66\,K,\ z = 15.90\,K$
$f_T^0 = A\,exp(\frac{B}{T-C})$	$A = 963.72 \times 10^9 MPa,\ B = -6444.50\,K,\ C = 36.67\,K$
$f^0 = f_T^0 exp\left(\frac{\beta P_{eq}}{T}\right)\alpha_w^{-1/\lambda}$	$\beta = 4.242\frac{K}{MPa},\ \lambda = 3/23,\ \alpha_w = 1$
$f_i^H = f^0(1-\theta)^{\alpha}$	$\alpha = 1/3$

$$r_d = k_d A_s\left(f_{eq} - f_g\right) \tag{20}$$

where K_d is the dissociation rate constant and is determined using Eq. 21,

$$k_d = k_d^0 e^{-\Delta E/RT} \tag{21}$$

where $k_d^0 = 1.83 \times 10^{14} \frac{mol}{m^2 MPas}$ is the intrinsic rate constant of CO_2 hydrates dissociation, and $\Delta E = 102.88 \frac{\text{kJ}}{\text{mol}}$ is CO_2 activation energy [36]. A_s in Eq. 22 is determined using:

$$A_s = \left[\frac{6}{\psi \rho_H D_0}\right] n_0^{1/3} n_H^{1/3} \tag{22}$$

where ψ is the sphericity factor and the shape of the CO_2 hydrates is assumed to be spherical, $\psi = 1$, ρ_H is the superficial density of CO_2 (25,431.42 mol/m^3) [37], D_0 is the CO_2 hydrate diameter (5.12×10^{-10} m) and n_0 and n_H are the numbers of moles at t = 0 and time of hydrate formation, respectively. Assuming that the pressure difference is the driving force, the rate of dissociation can be obtained by Eq. 23, as a result of substituting k_d and A_s into Eq. 20.

$$r_d = \left[\frac{1.09 \times 10^9}{\varphi \rho_H D_0}\right] e^{-102880/RT}\left(P_{eq} - P\right) n_0^{1/3} n_H^{2/3} \tag{23}$$

Energy Consumption Calculations

The above model was first applied to the process reported by Tajima et al. [16], assuming that both N_2 and CO_2 form hydrates at the operating conditions. The model was further applied to three cases, assuming the same production scale, in which the chemical additives THF, TBAB, and TBAB + DTAC were used,

Table 2 Operational parameters for energy consumption calculations

Case	Chemical additives	Operating Conditions: (T [K], P [MPa])/(x_{CO_2}, x_{N_2})/Molar flow rate × 10^7 mol/h			References
		Stream 1	Stream 3	Stream 4	
I	None	(274, 14)/(0.10, 0.79)[a]/4.46	(274, 14)/(0.005, 0.87)[b]/4.03	(274, 0.10)/(1, 0)/42.3	[16]
II	THF (1 mol%)	(274, 0.35)/(0.17, 0.83)/4.46	(274, 0.35)/(0.10, 0.90)/3.32	(274, 0.10)/(0.37, 0.63)/1.13	[18, 19]
III	TBAB (5 wt%)	(283, 3.16)/(0.17, 0.83)/4.46	(283, 3.16)/(0.05, 0.95)/2.48	(283, 0.10)/(0.32, 0.68)/1.98	[20, 21]
IV	TBAB (0.29 mol %) + DTAC (0.028 mol%)	(275, 1.66)/(0.17, 0.83)/4.46	(275, 1.66)/(0.05, 0.95)/3.57	(275, 0.10)/(0.65, 0.35)/0.9	[22]

[a]The remaining fraction is 0.04 of O_2 and 0.07 of H_2O [b]The remaining fraction is 0.04 of O_2 and 0.08 of H_2O

respectively. It is noteworthy that only the optimal chemical loadings that have produced the maximum CO_2 separation efficiency have been selected for this study. More details are given in Table 2.

Results and Discussion

For Case I, the computed energy consumption by the compressors and heat exchangers, as well as that associated with the hydrates formation and dissociation, are listed in Table 3. The reported data [16] also are tabulated for comparison. It can be seen that the computed values of $E_{compression}$ and $E_{hydrates}$ are in good agreement with the reported data. It should be noted that the $E_{hydrates}$ reported by Tajima is a sum of the energies associated with the removal of the heat of hydrates formation (29.5 MW), the supply of the sea water for hydrates dissociation

Table 3 Computed energy consumption for Case I. Data in brackets are taken from Tajima's work [16]

Item	Energy consumption, MW
$E_{compression}$	234.5(240.1)
$E_{cooling}$	36.4(15.3)
$E_{hydrates} = \sum_{i=1}^{5} F_i H_i - r_f \Delta H_f + r_d \Delta H_d$	−16.5(29.5 + 0.85 + 0.40)
$E_{recovery}$	−113.7(−127.7)
E_{total}	140.8(158.4)

(0.85 MW) and the water supply for hydrates formation (0.40 MW). There is no provision of the computational details by the authors. The reported recovery energy ($E_{recovery}$) was −127.7 MW from the off-gas stream which was used to cool the feed gas. Our estimation is −113.7 MW, which is slightly lower than the reported data. However, the energy involved in the precooling stage was estimated to be 36.4 MW, which is higher than that of the reported data, 15.3 MW. Taking the differences in the recovered energy from the off-gas stream into consideration, this result also is acceptable. It should be noted that, while Tajima et al. [16] have reported the inclusion of a brine stream to maintain the temperature of the hydrate formation reactor at 274 K, there was no indication of how this has contributed to the cooling energy. Regardless, the computed total energy consumption, using Eq. 1, is 136.4 MW, while the reported value was 158.4 MW, indicating an effective approach for the energy estimation of other cases.

Using the same model, energy consumption values in the presence of different chemical additives also were calculated. The results are summarised in Table 4. In this table, E_m is energy per unit mass of captured CO_2 and $E_{Recovery}$ is recovery energy. In comparison with Case I, reduced compression energy was seen in all cases where chemical additives were used in the HBCC process, mostly due to the reduced operating pressures in the presence of chemical additives [7]. The lowest $E_{compression}$ was seen in Case II, when THF was used due to the significant pressure reduction from 14 to 0.35 MPa. The presence of TBAB also reduced the hydrates-forming pressure, but by a lesser degree. That is, the compression energy

Table 4 Energy consumption involved in four different case studies

Energy value (MW)			Case I	Case II	Case III	Case IV
$E_{compression}$			**234.5**	**52.5**	**195.4**	**139.1**
$E_{cooling}$			**36.4**	**10.8**	**8.7**	**6.8**
$E_{hydrates}$	Hydrate formation	$r_f \times 10^6$(mol/h)	1.2	0.8	1.4	0.8
		$\Delta H_f \times 10^4$ (J/mol)	6.3[a] (5.0)[b]	6.3[a] (12.0)[b]	6.3[a] (16.0)[**]	6.3[a] (12.0)[b]
	Hydrate dissociation	$r_d \times 10^4$ (mol/h)	6.9	1.7	55.0	5.9
		$\Delta H_d \times 10^4$ (J/mol)	5.0	12.0	16.0	12.0
	Energy of streams, $\sum_{i=1}^{5} F_i H_i$		−0.3	2.3	2.4	1.8
	$\sum_{i=1}^{5} F_i H_i - r_f \Delta H_f + r_d \Delta H_d$		**−16.5**	**−23.1**	**−33.7**	**−22.5**
$E_{recovery}$			**−113.7**	**−28.6**	**−89.7**	**−47.6**
E_{total}			**140.8**	**11.6**	**80.7**	**75.9**
E_m (MJ/Kg CO_2)			**2.7**	**0.2**	**1**	**1.1**

[a] and [b] denoting that data were obtained from Eqs. (11) and (12) respectively. The latter was used for $E_{hydrates}$ calculation

was reduced in comparison with Case I, however, the reduction was not as much as that seen in Case II. Using mixed chemical additives (TBAB + DTAC), a more effective reduction in compression energy was observed, due to the resultant lower hydrates formation pressure than when TBAB alone was used [22]. Similarly, the cooling energy was lowered when chemical additives were added to the HBCC process. A greater than 70% reduction was seen in all cases. The results indicate that the influence upon the cooling energy by chemical additives is strongest in the presence of TBAB + DTAC, followed by TBAB alone then THF, in comparison with Case I.

The calculated enthalpy of hydrate formation, ΔH_f, is of a similar value in all cases by using Eq. 11. This is understandable because ΔH_f is a rather weak function of the temperature in this equation. The addition of chemical additives has resulted in some changes in the rate of hydrates formation, as shown in Table 4. The slightly lower rates in Cases II and IV are probably due to the lower operating pressures and, therefore, the lower driving forces for hydrates to form. The enthalpy value of hydrate dissociation,ΔH_d, obtained from the Clausius-Clapeyron Eq. 12, indicated more significant changes upon the addition of chemicals. This is due to the more sensitive nature of the approach, being a function of both the temperature and the pressure. The computed values of ΔH_d for Cases I and II are 5×10^4 J/mol and 12×10^4 J/mol, respectively, which are in agreement with the reported values of 5.7×10^4 J/mol by Yoon et al. [38], and 10.9×10^4 J/mol by Kang et al. [28]. For Cases III and IV, the calculated dissociation enthalpies are 16×10^4 J/mol and 12×10^4 J/mol, respectively, and, to the best of our knowledge, no reported data is available in the open literature. The values of ΔH_d in Cases II, III and IV are greater than that of Case I. Pure CO_2 forms Structure I hydrates. However, in the presence of chemical additives, it forms Structure II and/or semi-clathrate hydrates, which are more stable or contain higher numbers of CO_2 molecules in the cavities, resulting in higher values for the enthalpy of dissociation [30]. There also was a significant increase in the hydrates dissociation rate,r_d, when TBAB was used. This is likely to be due to the higher operating temperature. The lowest dissociation rate was found when THF was used, resulting from the lowest operating temperature. The higher rate and enthalpy of hydrates formation/dissociation in the presence of TBAB has led to its highest absolute value of $E_{hydrates}$ which was followed by Case II (THF) and Case IV (TBAB + DTAC), and Case I (no chemical additive). These results demonstrate that the presence of chemical additives can also reduce the energy consumption associated with CO_2 hydration.

The energy distribution in each case is displayed in Fig. 3. A significant reduction in all categories was well demonstrated in all cases where chemical additives were used. The presence of THF has resulted in the lowest total energy consumption among the four cases (Table 4). The significant impact of THF on the overall energy consumption profile is a result of both the drastic reduction in the hydrates formation pressure and the improved hydrates formation/dissociation kinetics. It is well known that the use of THF as a thermodynamic chemical additive encourages structure II hydrates to form, which allows CO_2 to occupy both small

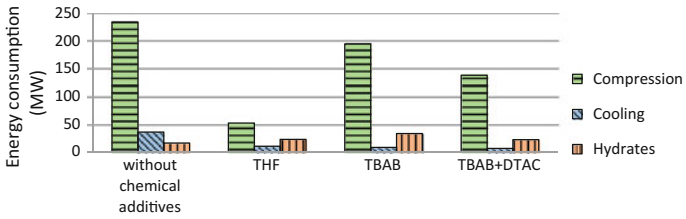

Fig. 3 The energy distribution (For better illustration, the absolute values of $E_{hydrates}$ are shown in this figure)

and large water cages at lower pressure [7, 39]. It is interesting to note that the total energy consumption in the presence of TBAB is not much lower than for Case I, although the lowest $E_{hydrates}$ is associated with the presence of TBAB. This is due to the fact that the changes in the hydrates-forming pressure and temperature are not sufficiently significant in Case III, therefore, the reduction in both compression and cooling is not apparent, although TBAB allows greater gas capacity and consequently higher conversion rates. On the other hand, using a mixture of TBAB and DTAC has produced a greater degree of energy reduction, since DTAC lowers the equilibrium pressure of CO_2 hydrates [22]. In general, energy consumption values in both the hydrate formation and dissociation stages are much lower than that during the cooling and compression processes.

When the total energy was converted into the energy demand per unit mass of captured CO_2, E_M, the results further confirmed that the addition of suitable chemicals can reduce the total energy associated with the HBCC processes. This, in turn, would lead to a reduction in the economic costs of HBCC. The economic impact of the chemical additives to the HBCC processes is currently under investigation.

Conclusions

In summary, a model has been developed to estimate the energy required at various stages during a hydrate-based CO_2 separation process. Application of the established energy analysis to the HBCC process in the presence of chemical additives has demonstrated that the chemical additives reduced the total energy consumed, through their impact on the pressures and temperatures at which CO_2 hydrates form and dissociate, and on the CO_2 hydration kinetics. Among the chemical additives investigated, THF has shown a significant reduction in the energy required in all stages, including the cooling, the compression, the formation and the dissociation of CO_2 hydrates. The quantitative analysis was proved to be effective in the comparison of the effectiveness of different chemical additives reported by various groups. The results also indicated that the chemical additives being able to reduce the operation pressure will bring more benefit to the ultimate application of the HBCC process.

Acknowledgment The authors wish to thank the Australia-China Natural Gas Technology Partnership Fund for financial assistance to this work.

References

1. Spencer DF (1999) Integration of an advanced CO_2 separation process with methods for disposing of CO_2 in oceans and terrestrial deep aquifers. In: Eliasson B, Riemer P, Wokaun A (eds) Greenhouse gas control technologies. Elsevier p. 89–94
2. Tam S et al (2001) A high pressure carbon dioxide separation process for IGCC plants. Paper presented at First National Conference on Carbon Sequestration, Washington DC, USA, 14–17 May 2001
3. Ho MT, Allinson GW, Wiley DE (2008) Reducing the cost of CO_2 capture from flue gases using pressure swing adsorption. Ind Eng Chem Res 47:4883–4890
4. Sloan ED, Koh CA (2008) Clathraye hydrates of natural gases. Taylor & Francis, New York
5. Herslund PJ, Daraboina N, Thomsen K, Abildskov J, Solms NV (2014) Measuring and modelling of the combined thermodynamic promoting effect of tetrahydrofuran and cyclopentane on carbon dioxide hydrates. Fluid Phase Equilib 381:20–27
6. Babu P, Linga P, Kumar R, Englezos P (2015) A review of the hydrate based gas separation (HBGS) process for carbon dioxide pre-combustion capture. Energy 85:261–279
7. Dashti H, Yew LZ, Lou X (2015) Recent advances in gas hydrate-based CO_2 capture. J Nat Gas Sci Eng 23:195–207
8. Xu CG, Li XS (2014) Research progress of hydrate-based CO_2 separation and capture from gas mixtures. RSC Adv 4:18301–18316
9. Herslund PJ, Thomsen K, Abildskov J, Solms NV (2013) Application of the cubic-plus-association (CPA) equation of state to model the fluid phase behaviour of binary mixtures of water and tetrahydrofuran. Fluid Phase Equilib 356:209–222
10. Herslund PJ, Thomsen K, Abildskov J, Solms NV (2014) Modelling of cyclopentane promoted gas hydrate systems for carbon dioxide capture processes. Fluid Phase Equilib 375:89–103
11. Verrett J, Renault-Crispo JS, Servio P (2015) Phase equilibria, solubility and modeling study of CO_2/CH_4 + tetra-n-butylammonium bromide aqueous semi-clathrate systems. Fluid Phase Equilib 388:160–168
12. Shi LL, Liang DQ (2015) Thermodynamic model of phase equilibria of tetrabutyl ammonium halide (fluoride, chloride, or bromide) plus methane or carbon dioxide semiclathrate hydrates. Fluid Phase Equilib 386:149–154
13. Englezos P, Kalogerakis N, Dholabhai PD, Bishnoi PR (1987) Kinetics of formation of methane and ethane gas hydrates. Chem Eng Sci 42:2647–2658
14. ZareNezhad B, Mottahedin M, Varaminian F (2015) A new approach for determination of single component gas hydrate formation kinetics in the absence or presence of kinetic promoters. Chem Eng Sci 137:447–457
15. Sun Q, Kang YT (2015) Experimental correlation for the formation rate of CO_2 hydrate with THF (tetrahydrofuran) for cooling application. Energy 91:712–719
16. Tajima H, Yamasaki A, Kiyono F (2004) Energy consumption estimation for greenhouse gas separation processes by clathrate hydrate formation. Energy 29:1713–1729
17. Duc NH, Chauvy F, Herri JM (2007) CO_2 capture by hydrate crystallization —A potential solution for gas emission of steelmaking industry. Energy Convers Manag 48:1313–1322
18. Kang SP, Lee H (2000) Recovery of CO_2 from flue gas using gas hydrate: thermodynamic verification through phase equilibrium measurements. Environ Sci Technol 34:4397–4400
19. Linga P, Adeyemo A, Englezos P (2008) Medium-pressure clathrate hydrate/membrane hybrid process for postcombustion capture of carbon dioxide. Environ Sci Technol 42:315–320

20. Belandria V, Mohammadi AH, Eslamimanesh A, Richon D, Sánchez-Mora MF, Galicia-Luna LA (2012) Phase equilibrium measurements for semi-clathrate hydrates of the (CO_2 + N_2 + tetra-n-butylammonium bromide) aqueous solution systems: Part 2. Fluid Phase Equilib 322–323:105–112
21. Fan S, Li S, Wang J, Lang X, Wang Y (2009) Efficient Capture of CO_2 from simulated flue gas by formation of TBAB or TBAF semiclathrate hydrates. Energy Fuels 23:4202–4208
22. Li XS, Xu CG, Chen ZY, Wu HJ (2010) Tetra-n-butyl ammonium bromide semi-clathrate hydrate process for post-combustion capture of carbon dioxide in the presence of dodecyl trimethyl ammonium chloride. Energy 35:3902–3908. http://www.sciencedirect.com/science/article/pii/S0360544210003233
23. Himmelblau DM, Riggs JB (2004) Basic principles and calculations in chemical engineering. Prentice-Hall International, N.J.
24. Ratcliffe CI, Ripmeester JA (1986) Proton and carbon-13 NMR studies on carbon dioxide hydrate. J Phys Chem 90:1259–1263
25. Kamath VA (1984) Study of heat transfer characteristics during dissociation of gas hydrates in porous media. PhD thesis, University of Pittsburgh
26. Gupta A, Lachance J, Sloan ED, Koh CA (2008) Measurements of methane hydrate heat of dissociation using high pressure differential scanning calorimetry. Chem Eng Sci 63:5848–5853
27. Handa YP (1986) Calorimetric determinations of the compositions, enthalpies of dissociation, and heat capacities in the range 85 to 270 K for clathrate hydrates of xenon and krypton. J Chem Thermodyn 18:891–902
28. Kang SP, Lee H, Ryu BJ (2001) Enthalpies of dissociation of clathrate hydrates of carbon dioxide, nitrogen, (carbon dioxide + nitrogen), and (carbon dioxide + nitrogen + tetrahydrofuran). J Chem Thermodyn 33:513–521
29. Delahaye A, Fournaison L, Marinhas S, Chatti I, Petitet JP, Dalmazzone D, Fürst W (2006) Effect of THF on equilibrium pressure and dissociation enthalpy of CO_2 hydrates applied to secondary refrigeration. Ind Eng Chem Res 45:391–397
30. Sabil KM, Witkamp GJ, Peters CJ (2010) Estimations of enthalpies of dissociation of simple and mixed carbon dioxide hydrates from phase equilibrium data. Fluid Phase Equilib 290:109–114
31. Peng DY, Robinson DB (1976) A new two-constant equation of state. Ind Eng Chem Fundam 15:59–64
32. Ribeiro CP, Lage PLC (2008) Modelling of hydrate formation kinetics: state-of-the-art and future directions. Chem Eng Sci 63:2007–2034
33. Shi BH, Fan SS, Lou X (2014) Application of the shrinking-core model to the kinetics of repeated formation of methane hydrates in a system of mixed dry-water and porous hydrogel particulates. Chem Eng Sci 109:315–325
34. Chen GJ, Guo TM (1996) Thermodynamic modeling of hydrate formation based on new concepts. Fluid Phase Equilib 122:43–65
35. Kim HC, Bishnoi PR, Heidemann RA, Rizvi SSH (1987) Kinetics of methane hydrate decomposition. Chem Eng Sci 42:1645–1653
36. Clarke MA, Bishnoi PR (2004) Determination of the intrinsic rate constant and activation energy of CO_2 gas hydrate decomposition using in-situ particle size analysis. Chem Eng Sci 59:2983–2993
37. Udachin KA, Ratcliffe CI, Ripmeester JA (2001) Structure, composition, and thermal expansion of CO_2 hydrate from single crystal X-ray diffraction measurements. J Phys Chem B 105:4200–4204
38. Yoon JH, Yamamoto Y, Komai T, Haneda H, Kawamura T (2003) Rigorous approach to the prediction of the heat of dissociation of gas hydrates. Ind Eng Chem Res 42:1111–1114
39. Park S, Lee S, Lee Y, Lee Y, Seo Y (2013) Hydrate-based pre-combustion capture of carbon dioxide in the presence of a thermodynamic promoter and porous silica gels. Int J Greenh Gas Control 14:193–199

Tar Removal from Hot Coke Oven Gas for H_2 Amplification with in Situ CO_2 Capture

Huaqing Xie, Qin Qin and Qingbo Yu

Abstract A novel sorption-enhanced steam reforming (SESR) process of hot coke oven gas (HCOG) was proposed for tar removal and H_2 amplification, and was studied with the comparison of conventional steam reforming (SCR) process. Both of the processes could remove tar effectively and improve the H_2 amount in the COG obviously. For CSR process, after the temperature and the S/HCOG ratio reached 700 °C and 2.4 respectively, the H_2 amplification factor kept 4.30 around, with its concentration less than 75%. However, for SESR process, the H_2 amount and concentration get improved further, with the optimal temperature moving toward low temperature. At 600 °C and the S/HCOG ratio of 2.4, the H_2 amplification factor and concentration could reach 4.91 and 97.55% respectively when the CaO/C ratio was 2.0. Under the respective optimal reforming conditions of the two processes, the energy consumption of the SESR process was lower than that of CSR process.

Keywords Hot coke oven gas · Hydrogen amplification · Tar removal
Steam reforming · Thermodynamic analysis · Adsorption-enhanced

Introduction

As the main co-product of coke-making process, the coke oven gas (COG) contains 48–55 mol% for H_2, and thus was as a high-quality fuel and chemical raw material [1]. For China as the largest COG producer in the world, over 200 billion Nm^3 per year COG was produced [2, 3]. COG emitted from the coking chamber, normally called hot COG (HCOG) with the temperature of 700–900 °C, is a complex mixture, containing tar components (such as benzene and naphthalene) aside from H_2, CH_4, CO, and CO_2. The tar components accounting for about 30% of the total

H. Xie (✉) · Q. Qin · Q. Yu
School of Metallurgy, Northeastern University, No. 11, Lane 3, WenHua Road, HePing District, Shenyang 110819, Liaoning, People's Republic of China
e-mail: huaqing_2008@163.com

Z. Sun et al. (eds.), *Energy Technology 2018*, The Minerals, Metals & Materials Series, https://doi.org/10.1007/978-3-319-72362-4_2

HCOG mass will become a kind of viscous liquid below about 500 °C, more likely causing equipment blockage [4]. At present, the main industrial method to remove tar from HCOG is ammonia solution spraying with high-efficient removal. However, the temperature of COG was cooled to less than 100 °C, causing huge amounts of high-quality sensible heat loss, and as a result of part of tar dissolved in water, substantial waste energy was lost, leading to serious secondary pollution [5]. Therefore, developing a new technology to convert COG into more energy-valued products or to recover COG more efficiently is urgent and significant for enhancing the energy efficiency of the coking enterprises and the steel enterprises [6].

Hydrogen, regarded as a promising energy carrier, is currently mainly produced from fossil fuels containing natural gas and coal via steam reforming, gasification, etc. However, as a result of the depletion of fossil fuel and the deterioration of the environment, finding a new approach for hydrogen production is attracting increasing attentions [7]. The industrial by-products may be potential alternatives for hydrogen production. Among them, COG is one of the most attractive sources and was considered as one of the raw materials to most likely realize large-scale economical hydrogen production in the short and medium term [8–10]. Currently, the main method for hydrogen production from COG is physical separation (such as pressure swing adsorption, PSA) of the cleaned COG (free-tar) [2]. But, this method just obtained the original H_2 in COG with other components (such as CO, CH_4, tar and other hydrocarbons) yet not rationally used (normally as fuel to be directly combusted) [11]. Besides, some chemical methods (such as steam reforming, partial oxidation, auto-thermal reforming, etc.) were put forward to reutilize CO, CH_4 and other hydrocarbons in the clean COG (free-tar) [1, 12–15]. Although up to 90% of these components could be converted, the H_2 concentration in the after-reacted COG was just about 70%, and their object mainly was COG after cleaning, causing the wastes of tar and high-temperature sensible heat of HCOG.

So, for H_2 amplification with utilizing the chemical energy of tar and the HCOG heat efficiently, the approaches via some chemical methods to deal with HCOG were reported. Among them, steam reforming was considered as a kind of feasible approaches for hydrogen production, since the more hydrogen can be produced not just from the COG, but also from the steam [16]. However, the relative reports on the steam reforming process of HCOG were rare. Although there is literature on the steam reforming reaction of tar compounds from HCOG, these heavy hydrocarbons were just converted to light fuel gases, such as CH_4, CO, H_2, with not reacting completely [17–19]. Commonly, just about 70 vol.% H_2 with over 20 vol.% CO_2 was in the produced gas via steam reforming, to limit the application of such a hydrogen-containing gas [20–22]. Thus, a novel sorption-enhanced steam reforming process of HCOG was put forward in this paper, through separating CO_2 from produced gas by the situ addition of CO_2 sorbent, not only improving the H_2 concentration, but also accelerating the steam reforming reactions so as to improve H_2 amount.

So, in this paper, the sorption-enhanced steam reforming (SESR) process of HCOG is investigated via thermodynamic analysis, with the comparison of the conventional steam reforming (CSR) process. The effects of temperature, S/HCOG

ratio (the ratio of the additional steam mole number and the total mole number of all the components of HCOG) and CaO/C ratio (the ratio of the additional CaO mole number and the total C mole number in HCOG) on the tar removal and H_2 amplification were discussed. And, the energy consumptions of the two processes were also analyzed comparatively.

Methodology

Feedstock

The components of HCOG are seen in the literature [11], with the tar simplified as 1-methylnaphthalene ($C_{11}H_{10}$), mainly because its reaction process under high temperature much approaches the conversion process of the real tar in HCOG. The key chemical reactions involved in the steam reforming process of HCOG were shown in Table 1.

Table 1 Key chemical reactions involved in the steam reforming process of HCOG

Reaction	Equation	$\Delta H^0_{800\ ^\circ C}$/kJmol^{-1}	No.
Thermal cracking	$nC_{11}H_{10} \rightarrow mC_xH_y + oH_2 + pCO + qCH_4 + rCO_2 + sC$	–	(1)
Hydrodealkylation	$C_{11}H_{10} + H_2 \rightarrow C_{10}H_8 + CH_4$	−53.89	(2)
Hydrocracking	$C_{11}H_{10} + 17H_2 \rightarrow 11CH_4$	−1075.82	(3)
	$C_{10}H_8 + 16H_2 \rightarrow 10CH_4$	−1021.93	(4)
	$C_6H_6 + 9H_2 \rightarrow 6CH_4$	−599.71	(5)
Steam reforming	$C_{11}H_{10} + 11H_2O \rightarrow 11CO + 16H_2$	1401.54	(6)
	$C_{11}H_{10} + 22H_2O \rightarrow 11CO_2 + 27H_2$	1026.27	(7)
	$C_{10}H_8 + 4H_2O \rightarrow C_6H_6 + 4CO + 5H_2$	478.64	(8)
	$C_6H_6 + 6H_2O \rightarrow 6CO + 9H_2$	751.58	(9)
	$C_xH_y + xH_2O \rightarrow xCO + (x + y/2)H_2$	–	(10)
	$CH_4 + H_2O \rightarrow CO + 3H_2$	225.22	(11)
Dry reforming	$C_{11}H_{10} + 11CO_2 \rightarrow 22CO + 5H_2$	1776.82	(12)
	$C_{10}H_8 + 4CO_2 \rightarrow C_6H_6 + 8CO + H_2$	615.10	(13)
	$C_6H_6 + 6CO_2 \rightarrow 12CO + 3H_2$	956.28	(14)
Carbon formation	$C_{11}H_{10} \rightarrow 11C + 5H_2$	−91.88	(15)
	$C_xH_y \rightarrow xC + y/2H_2$	–	(16)
Methanation	$CO + 3H_2 \leftrightarrow CH_4 + H_2O$	−225.22	(17)
	$C + 2H_2 \leftrightarrow CH_4$	−89.45	(18)
Water gas	$C + H_2O \leftrightarrow CO + H_2$	135.77	(19)
Water gas shift	$CO + H_2O \leftrightarrow H_2 + CO_2$	−34.12	(20)
Bell	$2CO \leftrightarrow C + CO_2$	−169.88	(21)

In the SESR presence, CaO was selected as CO_2 sorbent, due to the wide application of Ca-based sorbent in the sorption-enhanced steam reforming process [7, 20, 21]. CaO mainly occurred with the carbonation reaction (Eq. (24)) to adsorb CO_2:

$$CaO + CO_2 \leftrightarrow CaCO_3 \quad \Delta H^{\theta}_{800^{\circ}C} = -167.62\,kJ/mol \tag{22}$$

Process

For the novel SESR process and the CSR process of HCOG, the equilibrium of the involved chemical reactions was solved by minimization of the Gibbs free energy of the systems, using HSC chemistry software. Then, based on the equilibrium results, the energy consumption of the two processes can be investigated, with given mass-balances as the boundary conditions.

Figure 1a and b show the simplified flow diagram of CSR process and SESR of HCOG, respectively. For the CSR process, there is only one core unit, the reforming reactor, where the HCOG set at 800 °C and the 25 °C water are transported into and the reforming reactions occurred. Then, the reformed gas (H_2-rich gas and unreacted steam) from the reforming reactor was cooled to 25 °C. Because the reforming reactions of the main HCOG compositions are strongly endothermic reaction, extra heat has to be provided, to maintain the temperature of the reforming reactor. For the SESR process, there are two core units, the reforming reactor and the regenerator. Besides HCOG and water, 900 °C CaO from the regenerator is also transported into the reforming reactor. Due to the released heat from the CaO carbonation reaction, the extra heat added into the reforming reactor will be obviously reduced, compared to the CSR process. However, another extra heat is demanded to the regenerator, in which the endothermic decomposition reactions of calcium carbonate and calcium hydroxide transported from the reforming reactor occur. Note that the energy loss was ignored in the following calculation.

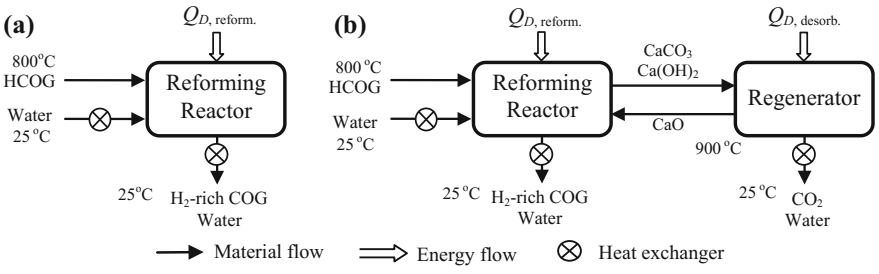

Fig. 1 Simplified flow diagram. **a** for CSR process and **b** for SESR process

Model Evaluation

In order to study and compare the two processes, the following indexes were chosen.

1. Tar removal rate, RE_{tar}, is defined as the ratio of the C mole number removal from the tar components and the C mole number of tar in the original HCOG.
2. H_2 yield, y_{H2}, was calculated as follows.

$$y_{H2} = \frac{H_2 \text{ amount in the reformed gas}}{\text{theoretical } H_2 \text{ amount after SR}} \times 100\% \tag{23}$$

where, the theoretical H_2 amount after SR was the amount when all the compositions of HCOG except the original (H_2 CO_2, N_2 and H_2O) reacted completely via steam reforming (SR) reactions (Eq. (6–11)) and water gas shift (WGS) reaction (Eq. (20)).

3. H_2 amplification factor, AF_{H2}, used to evaluate the amplification degree of H_2 after reforming, compared to the original H_2 in HCOG. And, it was defined as Eq. (24).

$$AF_{H2} = \frac{H_2 \text{ amount in the reformed gas}}{H_2 \text{ amount in the original HCOG}} \tag{24}$$

4. Composition concentration of the reformed gas, C_x, defined as

$$C_x = \frac{\text{moles of } x \text{ in the reformed gas}}{\text{total moles of the reformed gas}} \times 100\% \tag{25}$$

where, x represented H_2, CO, CH_4, CO_2 in the reformed gas, respectively.

5. C capture efficiency, $\eta_{C\text{-capture}}$, was applied to evaluate its adsorption performance and defined as

$$\eta_{C-capture} = \frac{\text{moles of } CaCO_3 \text{ after adsorption}}{\text{moles of C in original HCOG}} \times 100\% \tag{26}$$

6. $Q_{reform.}$, $Q_{desorb.}$, Q_{total} are defined as the energy consumed in the reforming reactor, the regenerator (for SESR process) and the whole process, kJ/mol_{HCOG}, respectively.

Results and Discussion

Steam Reforming in the Absence of CO_2 Sorbent

Figure 2 shows the effects of temperature and S/HCOG ratio on the CSR process. Through SR reactions, the tar and other hydrocarbons in the original HCOG were

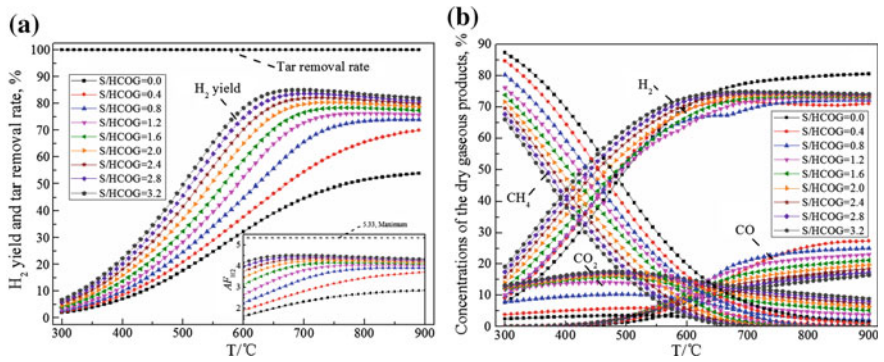

Fig. 2 Product distribution of the CSR process of HCOG

completely converted. The H_2 yield via the SR reaction was obviously higher than that via the own reaction, mainly attributed to Eqs. (6–11, 19, 20) accelerated by adding extra water. At lower temperatures, the H_2 yield was lower with higher CH_4 content, mainly because the hydrodealkylation reaction (Eq. (2)) and the hydrocracking reactions (Eqs. (3–5)) occurred. As the temperature rose, the endothermic reactions (Eqs. (6–14)) were accelerated, thus causing the decreases of CH_4 and the increases of H_2 and CO. But at higher temperatures, the amounts of H_2, CO, CO_2 flattened out, mainly because the WGS reaction was thermodynamically disfavoured at higher temperature. Noteworthy, due to no involvement of the reaction dynamics and the purpose of the Gibbs free energy minimization of the whole reaction system, the thermodynamic result to some extent was not very coherent with actual one.

As the S/HCOG ratio rose, the H_2 yield gradually increased, especially under high temperature zone, where yet the increase amplitude of H_2 yield was gradually decreased, with just a slight increase at the S/HCOG ratio above 2.4, indicating increasing blindly steam amount for hydrogen production is economically inadvisable. The temperature corresponding to the highest H_2 yield moved toward low temperature with the S/HCOG increase. When the S/HCOG ratio was above 2.4, the H_2 yield reached the maximum between 650 and 700 °C, yet just 80% around with the AF_{H2} lower than 4.5. Besides, the H_2 concentrations under such a temperature zone were concentrated around 70%.

Steam Reforming in the Presence of CO_2 Sorbent

Although the H_2 yield was obviously promoted via the CSR of HCOG, but the H_2 concentration in the gaseous products was undesired, just about 70%, to limit the application of such a hydrogen-containing gas. To improve the hydrogen content in

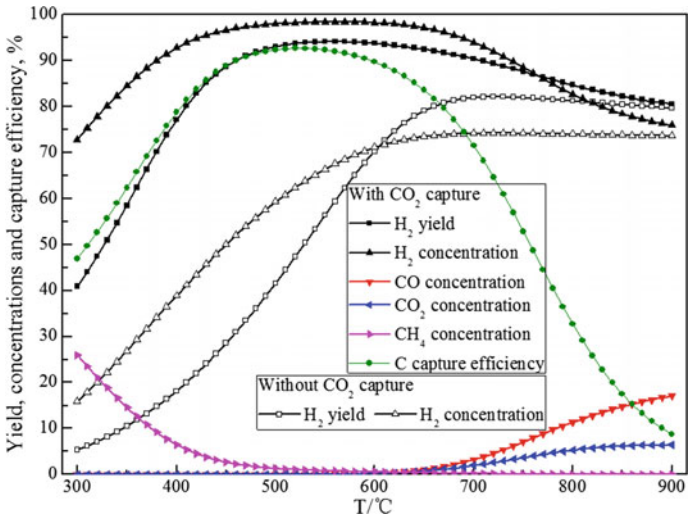

Fig. 3 Effect of temperature on the steam reforming process of HCOG in the presence of CO_2 sorbent

gaseous products, the steam reforming process of HCOG with suit in CO_2 adsorption will be discussed with thermodynamic analysis in the following.

Figure 3 shows the effect of temperature on HCOG steam reforming process in the presence of CO_2 sorbent, under the conditions: S/HCOG ratio of 2.4 and CaO/C ratio of 3.0. Compared with the case without CaO addition, the H_2 yield and concentration were improved obviously after the addition of CaO. Especially in the temperature range between 550 and 650 °C, they can improve to over 92% and over 97% both from 70%, respectively. This was attributed to the adsorption of CaO for CO_2. The above temperature range was beneficial to the carbonation reaction of CaO, so CO_2 from the SR reactions was capture and then the SR reactions in return were accelerated. From Fig. 3, the C capture efficiency was very high, 90% around, indicating that the majority C of HCOG was converted into CO_2 via SR reactions and then was captured by CaO. So, this also caused that the carbonaceous gases (CO, CO_2, CH_4) had just the concentrations close to zero in the reformed gas. It is worth to note that about 10% unreacted C in the HCOG was mainly converted into coke, attributed to the Bell reaction (Eq. (21)) accelerated due to the decrease of CO_2. So, the elimination of coke in the SESR process is an urgent problem to be solved before application, although it can obviously remove tar and improve H_2 amount.

Figure 4a and b show the effects of CaO/C ratio and S/HCOG ratio on the SESR process at 600 °C. From Fig. 4a, as the CaO/C ratio rose, the H_2 produced amount increase gradually, attributed to the SR equilibrium displaced to the direction of H_2 production, and after the CaO/C ratio reached 2.0, the amount flattened out. As the S/HCOG ratio rose, the H_2 amount also increased significantly, and then when the

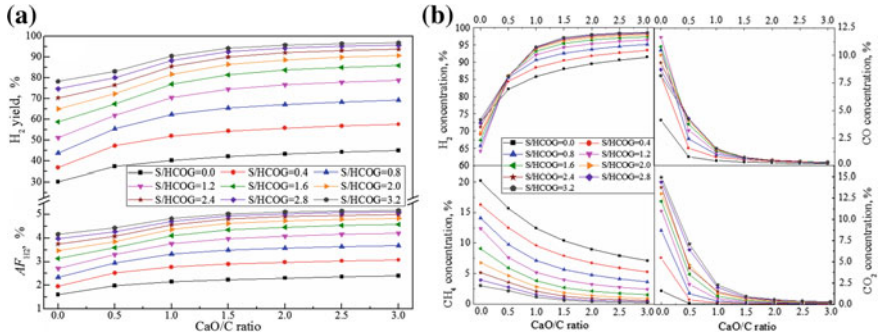

Fig. 4 Effects of CaO/C ratio and S/HCOG ratio on the steam reforming process of HCOG in the presence of CO_2 sorbent. **a** for the H_2 production, **b** for the concentrations of the reformed gas

S/HCOG ratio reached over 2.4, the change was not obvious any more, especially at the CaO/C ratio ≥ 2.0. Under such conditions, the H_2 yield and AF_{H2} can reach over 92% and 4.90, respectively. From Fig. 4b, as the CaO/C ratio and S/HCOG ratio rose, C_{H2} increase gradually on the whole, and then flattened out when the CaO/C ratio and S/HCOG ratio reached over 2.0 and 2.4, respectively, with the C_{H2} of over 97.5%. For other three main compositions (CO, CO_2, CH_4) of the reformed gas, they decreased with the increases of the CaO/C ratio and S/HCOG ratio, and they had just very trace amounts and no obvious change when the CaO/C ratio and S/HCOG ratio reached over 2.0 and 2.4, respectively.

Energy Consumption

From the above, for the CSR process the optimal SR conditions for H_2 production were the temperature of 700 °C and the S/HCOG ratio of 2.4. Under such conditions, although the tar components were removed from HCOG completely, the H_2 amplification factor was just 4.37 with the C_{H2} being just 74.17% (seen in Table 2). However, under the above same conditions with the CaO/C ratio of 2.0, the SESR process can obtain the AF_{H2} of 4.75 and the C_{H2} of 91.52%, and more importantly, the energy consumption of the novel process was lower than the conventional process. On the other hand, for SESR process the optimal SR conditions for H_2 production were the temperature of 600 °C, the S/HCOG ratio of 2.4 and CaO/C ratio of 2.0, where the H_2 amplification factor and the C_{H2} can reach 4.91 and 97.55%, respectively. At the same temperature and S/HCOG ratio, the CSR just had the AF_{H2} of 3.75 and the C_{H2} of 71.12%. Although SESR process had slightly higher energy consumption than the CSR process, the energy consumed for obtaining the same amount of H_2 was about 10% lower than the latter. Under the respective optimal reforming conditions of the two processes, the energy consumption of the SESR process was obviously lower than that of CSR process.

Table 2 Properties of both CSR and SESR processes of HCOG

Process	Reaction conditions				Evaluation indexes					
	Reforming reactor			Regenerator	Reforming indexes			Energy consumption, kJ/mol_{HCOG}		
	T, °C	S/HCOG	CaO/C	T, °C	RE_{tar}	AF_{H2}	C_{H2}	$Q_{reform.}$	$Q_{desorb.}$	Q_{total}
CSR	600	2.4		/	100%	3.75	71.12%	42.77	/	42.77
SESR			2.0	900		4.91	97.55%	−41.64	101.93	50.29
CSR	700	2.4		/	100%	4.37	74.17%	68.86	/	68.68
SESR			2.0	900		4.75	91.52%	−8.62	69.84	61.12

Conclusions

To realize the reutilization of the unused components (such as tar) in HCOG and the recovery of the waste heat of HCOG, a new hydrogen production technology from HCOG via SESR was put forward. The equilibrium compositions and energy consumption of the novel process were investigated, compared with CSR process. Although both of the processes can remove tar effectively, the CSR process just can obtain the AF_{H2} of 4.30 around and the C_{H2} of less than 75%. Compared the CSR process, the SESR process can improve the H_2 amount and concentration obviously, and the optimal temperature move toward low temperature. At 600 °C and the S/HCOG ratio of 2.4, the H_2 amplification factor and concentration could reach 4.91 and 97.55% respectively when the CaO/C ratio was 2.0. For energy consumption, although the energy consumed of SESR process has little difference with that of CSR process for disposing the same HCOG amount, the energy consumed of the former was lower than the latter for producing the same H_2 amount.

Acknowledgements This research was financially supported by the National Natural Science Foundation of China (51604077), the Fundamental Research Funds for the Central Universities (N150203006) and the Doctoral Scientific Research Foundation of Liaoning Province (201601004).

References

1. Koo KY, Lee JH, Jung UH, Kim SH, Yoon WL (2015) Combined H_2O and CO_2 reforming of coke oven gas over Ca-promoted Ni/$MgAl_2O_4$ catalyst for direct reduced iron production. Fuel 153:303–309
2. Cheng HW, Yao WL, Lu XG, Zhou ZF, Li CH, Liu JZ (2015) Structural stability and oxygen permeability of $BaCo_{0.7}Fe_{0.2}M_{0.1}O_{3-\delta}$ (M = Ta, Nb, Zr) ceramic membranes for producing hydrogen from coke oven gas. Fuel Process Technol 131:36–44
3. Qin ZF, Ren J, Miao MQ, Li Z, Lin JY, Xie KC (2015) The catalytic methanation of coke oven gas over Ni-Ce/Al_2O_3catalysts prepared by microwave heating: effect of amorphous NiO formation. Appl Catal B 164:18–30

4. Quitete CPB, Bittencourt RCP, Souza MMVM (2004) Steam reforming of tar using toluene as a model compound with nickel catalysts supported on hexaaluminates. Appl Catalysis A General 478:234–240
5. Xie HQ, Yu QB, Zhang JR, Liu JL, Zuo ZL, Qin Q (2017) Preparation and performance of Ni-based catalysts supported on $Ca_{12}Al_{14}O_{33}$ for steam reforming of tar in coke oven gas. Environ Progress Sustainable Energy 36(3):729–735
6. Xie HQ, Zhang JR, Yu QB, Zuo ZL, Liu JL, Qin Q (2016) Study on steam reforming of tar in hot coke oven gas for hydrogen production. Energy Fuels 30(3):2336–2344
7. Xie HQ, Yu QB, Zuo ZL, Wei MQ, Han ZC, Yao X, Qin Q (2016) Hydrogen production via sorption-enhanced catalytic steam reforming of bio-oil. Int J Hydrog Energy 41(4):2345–2353
8. Zhang YW, Li Q, Shen PJ, Liu Y, Yang ZB, Ding WZ, Lu XG (2008) Hydrogen amplification of coke oven gas by reforming of methane in a ceramic membrane reactor. Int J Hydrog Energy 33(13):3311–3319
9. Joseck F, Wang M, Wu Y (2008) Potential energy and greenhouse gas emission effects of hydrogen production from coke oven gas in US steel mills. Int J Hydrog Energy 33:1445–1454
10. Shen J, Wang ZZ, Yang HW, Yao RS (2007) A new technology for producing hydrogen and adjustable ratio syngas from coke oven gas. Energy Fuels 21(6):2592–3588
11. Xie HQ, Yu QB, Zuo ZL, Zhang JR, Han ZC, Qin Q (2016) Thermodynamic analysis of hydrogen production from raw coke oven gas via steam reforming. J Thermal Analy Calorim 126(3):1621–1631
12. Tao W, Cheng HW, Yao WL, Lu XG, Zhu QH, Li GS, Zhou ZF (2014) Syngas production by CO_2 reforming of coke oven gas over Ni/La_2O_3–ZrO_2 catalysts. Int J Hydrog Energy 39 (32):18650–18658
13. Cheng HW, Feng SH, Tao W, Lu XG, Yao WL, Li GS, Zhou ZF (2014) Effects of noble metal-doping on Ni/La_2O_3–ZrO_2 catalysts for dry reforming of coke oven gas. Int J Hydrog Energy 39(24):12604–12612
14. Shen SG, Chen PP, Li AQ, Qin HF, Li BB, Ren YP (2014) Effect of three processes on CO_2 and O_2 simultaneously reforming of coke oven gas to syngas. Chem Eng Process 75:75–80
15. Zhang JY, Zhang XH, Chen Z, Li L (2010) Thermodynamic and kinetic model of reforming coke-oven gas with steam. Energy 35(7):3103–3108
16. Chen WH, Lin MR, Yu AB, Dun SW, Leu TS (2012) Hydrogen production from steam reforming of coke oven gas and its utility for indirect reduction of iron oxides in blast furnace. Int J Hydrog Energy 37:11748–51178
17. Yue B, Wang X, Ai X, Yang J, Li L, Lu X et al (2010) Catalytic reforming of model tar compounds from hot coke oven gas with low steam/carbon ratio over Ni/MgO-Al_2O_3 catalysts. Fuel Process Technol 91(9):1098–1104
18. Yang J, Wang X, Li L, Shen K, Lu X, Ding W (2010) Catalytic conversion of tar from hot coke oven gas using 1-methylnaphthalene as a tar model compound. Appl Catalysis B Environ 96(1–2):232–237
19. Cheng HW, Lu XG, Hu DH, Ding WZ (2010) Catalytic reforming of model tar compounds from hot coke oven gas for light fuel gases production over bimetallic catalysts. Adv Mater Res 152–153:860–863
20. Xie HQ, Yu QB, Duan WJ, Yao X, Li XH, Qin Q (2015) Selection of CO_2 sorbent used in bio-oil steam reforming process for hydrogen production. Environ Prog Sustainable Energy 34(4):1208–1214
21. Xie HQ, Yu QB, Wang K, Shi XB, Li XH (2015) Thermodynamic analysis of hydrogen production from model compounds of bio-oil through steam reforming. Environ Prog Sustainable Energy 33(3):1008–1016
22. Authaynun S, Wiyaratn W, Assabumrungrat S, Amornchai A (2013) Theoretical analysis of a glycerol reforming and high-temperature PEMFC integrated system: hydrogen production and system efficiency. Fuel 105:345–352

An Evaluation Method for Material and Energy Conversion Effect with Steel Manufacturing Process Data

Shipeng Huang, Zhong Zheng, Xiaoqiang Gao, Shenglong Jiang and Zhaojun Xu

Abstract Steel enterprises in China are trending to improve material and energy conversion effect, because they are facing great challenges including energy saving and emission reduction, quality and efficiency improvement. According to the theory of metallurgical process engineering, with the process data in steel manufacturing, some novel indices are designed for quantifying the conversions in different metallurgical unit processes. By analyzing common technologic characteristics in different units, the main manufacturing units are divided into two categories: metallurgical reaction unit and other manufacturing unit. The novel concepts named as "material dissipation rate of unit process", "material accumulation rate of unit process", "enthalpy change of unit process" and "energy dissipation rate of unit process" are proposed for describing the effect and dynamic characteristics of the conversions in manufacturing units. Finally, material dissipation rate and energy dissipation rate in unit processes are calculated and analyzed respectively with the real-world process data from a steel plant in China.

Keywords Steel manufacturing · Manufacturing unit process · Material and energy conversion · Material dissipation rate · Energy dissipation rate

S. Huang · Z. Zheng (✉) · S. Jiang · Z. Xu
College of Materials Science and Engineering,
Chongqing University, Chongqing 400045, China
e-mail: zhengzh@cqu.edu.cn

S. Huang
e-mail: shipengh@cqu.edu.cn

X. Gao
College of Economics and Business Administration, Chongqing University,
Chongqing 400045, China

Z. Sun et al. (eds.), *Energy Technology 2018*, The Minerals, Metals & Materials Series, https://doi.org/10.1007/978-3-319-72362-4_3

Introduction

As one of the most important basic pillar industries of the national economy, iron and steel industry has made great contributions to the rapid economic development in China [1]. China's steel production has been the largest quantity in the world for more than 20 years. Moreover, China's crude steel production in 2016 has reached 808 million tons, accounting for 49.64% of global crude steel production [2]. However, steel industry is a resource and energy intensive process manufacturing industry, facing with serious problems such as overcapacity, high production costs, large resource and energy consumption, serious pollution and lack of competitiveness. Therefore, research on material and energy conversion in the steel manufacturing process has attracted more and more attentions of researchers.

At present, the research on energy and material conversion in steel manufacturing process is mainly based on the thermodynamic analysis method, such as thermal equilibrium analysis method, exergy equilibrium analysis method, energy level analysis method and thermal economic analysis method. Thermal equilibrium analysis method [3, 4], which calculating thermal equilibrium for the system (or equipment) and setting the thermal efficiency as an index, can analyze the conversion, transmission, use and loss of energy from the perspective of energy "quantity", but don't consider the decline of the energy "quality" resulting from various irreversible factors inside the energy system. Exergy equilibrium analysis method [5, 6], which setting the exergy efficiency of system (or equipment) as an index, can analyze the conversion, transmission, use and loss of energy from the perspective of energy "quality" so as to reveal the loss of system energy more efficiently, but don't analyze whether the supply of energy match the demand of user from the perspective of energy "quality". Energy level analysis method [7, 8], mainly applies "energy level difference" to analyze, evaluate, plan, and control the system, which makes the energy-using process rationalized, can match different energy levels between the supply and use of energy, but ignores the changes of energy "quantity". Thermal economic analysis method [9, 10], which takes thermodynamic analysis and economic factors into account uniformly, considers the problem of energy "quantity" and "quality" together, can track energy production process and cost formation process to get the solution of product cost. Besides, industrial metabolism [11] is also a quantitative method to research metabolic rule of material and energy in industrial system, describing a series of interrelated changes in the conversion from material and energy to final products and wastes. Based on the method, Brunner and Rechberger [12] put forward a new method of material flow analysis, which established the material total analysis model and the material use intensity model to analyze the input and output of materials. Then, Milford et al. [13] analyzed and predicted the development trend of material and energy consumption and carbon emission in steel manufacturing, by material flow analysis method based on process emission intensity.

For the problem to evaluate the effect of material and energy conversions in steel manufacturing process, according to conditions and industry characteristics in

China, different energy consumptions are converted into standard coal, so that process energy consumption, comprehensive energy consumption of per ton steel and comparable energy consumption of per ton steel can be used to evaluate the effect [14]. For example, Cai [15] analyzed the energy consumption status of iron and steel industry in China with the indices of comprehensive energy consumption of per ton steel and comparable energy consumption of per ton steel, and compared them between China and the advanced steel producing countries. Furthermore, Cai [15] proposed the potential direction of energy saving in the future for China's steel enterprises. Wang et al. [16] analyzed energy consumption in steel enterprises with comprehensive energy consumption of per ton steel and process energy consumption, then established a diagnosis model of energy consumption bottleneck and applied to develop energy saving programs. In addition, there were some other evaluation indices defined by the researchers. For example, Li et al. [17] proposed a new energy efficiency assessment system of steel enterprises on the basis of the existing indices such as comprehensive energy consumption, product energy consumption, crude steel energy consumption, sector energy consumption, process energy consumption, yield factors, production structure factors and energy intensity factors. From the differences of process flows and product structure, Zhang [18] proposed a new energy consumption index system of steel enterprises and changes of energy standard coal coefficient, which including 3 sub-indices (comprehensive energy consumption index, process section energy consumption index, terminal product energy consumption index) and 21 secondary-indices. Xu et al. [19] put forward a hierarchical energy consumption index system, according to the requirement of energy management, which focus on comprehensive energy consumption of per ton steel, modified process energy consumption, energy consumption of key energy consuming unit and key impact factors of energy consumption. Besides, Zhang et al. [20] proposed a methodology for the energy efficiency benchmarking of steel industry among different countries, taking into account the key factors, such as boundary definitions, energy efficiency index, energy conversion coefficient, electric furnace share, etc., to compare the energy efficiencies of steel industry in China with those in the United States.

The above works were on the basis of statistical calculation of the material and energy conversion or utilization of the whole manufacturing system or unit. Essentially, the methodologies were of static equilibrium. As a consequence, it is difficult to accurately express the dynamic characteristics of the real metallurgical process and to be used to guide the precise regulation of production process.

In this paper, by analyzing and classifying the characteristics of steel manufacturing unit process, the comprehensive quantitative indices of the interval products such as per ton iron, steel or rolled steel, in different unit process will be introduced with the production operational data. Then the material and energy conversion effect of each unit process will be quantitatively described. It is helpful for steel enterprises to analyze the difference of conversion effect among unit processes, get insight on the conversions or consumptions in each unit process, and search new methods for the precise regulation of manufacturing process.

Analysis and Description of Conversion Characteristics of Materials and Energy in Steel Manufacturing Process

The theory of metallurgical process engineering [21, 22] reveals the physical nature, structure and functional characteristics of the steel manufacturing process. From the theory, steel manufacturing process is regarded as a complex multidimensional logistics system in which material state transition, material property control and logistics control optimization are carried out [23]. It is composed of material flow (iron element flow), energy flow (carbon element flow) and a variety of key elements, with characteristics mixing discrete and continuous manufacturing process, as shown in Fig. 1. Material flow is mainly based on iron-based materials, and energy flow is mainly based on a variety of energy medium. The entire manufacturing process system consists of unit processes as subsystem with different physical or chemical changes, such as heating, melting, refining, solidification, phase change and plastic deformation. Each unit process can be abstracted into manufacturing unit nodes along the process path of iron element material flow and manufacturing process network which constituted by the unit nodes. So the material and energy conversion or use in manufacturing unit processes can be sufficient from process requirements and production planning.

Material and energy conversions occur in the metallurgical manufacturing unit process. Although different manufacturing units have different metallurgical function and manufacturing function, and there are differences of the characteristics in the process of the material flow conversion and the energy flow utilization, there are still some common characteristics. So, the manufacturing units can be divided into two main categories: the first category is metallurgical reaction unit, such as BF, BOF, LF/RH, etc., in which chemical reactions occur mainly. The second one is other manufacturing unit, such as CC, RHF, RM, etc., where physical changes occur mainly. Both of the two categories of manufacturing units constitute a

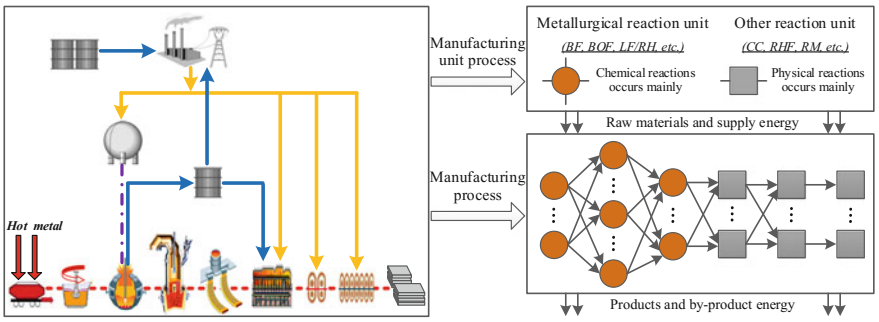

Fig. 1 The schematic diagram of unit processes and the whole process in real-world steel manufacturing (BF: blast furnace; BOF: basic oxygen furnaces; LF: ladle furnaces; RH: Ruhrstahl–Hausen vacuum refining furnace; CC: continuous caster; RHF: reheating furnace; RM: rolling mill.)

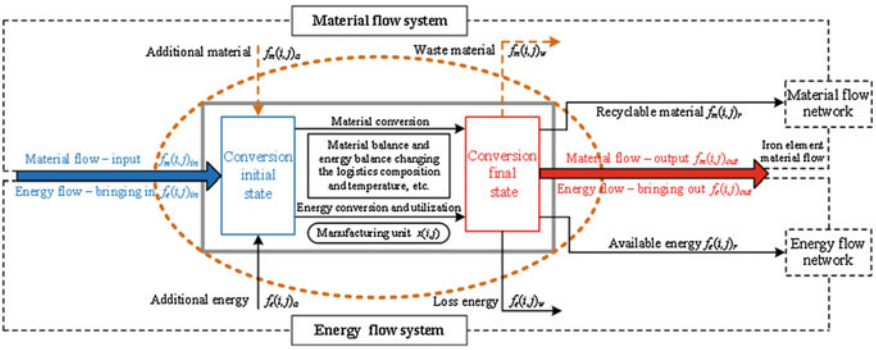

Fig. 2 The schematic diagram of material and energy conversion relationship in a manufacturing unit

complex manufacturing process system together, which achieve the goal of product production, material and energy conversion.

The material and energy conversion relationship of a manufacturing unit can be described in Fig. 2. The brown dashed ellipse represents a metallurgical reaction unit, i.e., a BOF. The brown dashed arrow represents the input (additional material) and the output (waste material) only load in metallurgical reaction units. The grey solid rectangle represents other manufacturing units such as a CC, where physical changes occur mainly, it barely involves chemical reaction, so the quantity of additional material and wastes are both supposed as zero. For a manufacturing unit process, the iron element material flow inputs in the initial state and outputs in the final state. In addition, material and energy conversions are finished in the manufacturing unit process. So, there are material and energy balance relationship in a certain manufacturing unit process $x(i,j)$ within a certain time range, which can be described as follows [24].

Material balance relationship,

$$f_m(i,j)_{in} + f_m(i,j)_a = f_m(i,j)_w + f_m(i,j)_r + f_m(i,j)_{out}, \tag{1}$$

Energy balance relationship,

$$f_e(i,j)_{in} + f_e(i,j)_a = f_e(i,j)_w + f_e(i,j)_r + f_e(i,j)_{out}, \tag{2}$$

For an other manufacturing unit,

$$f_m(i,j)_a = 0, f_m(i,j)_w = 0. \tag{3}$$

Quantitative Evaluation Method for Materials and Energy Conversion in Steel Manufacturing Process

According to above analysis of the basic characteristics of material and energy conversion in steel manufacturing unit process, with the real-world production operational data, several novel indices can be introduced to quantitatively evaluate the characteristics and effects of conversions by referring to the classical theory of thermodynamics and kinetic.

In this paper, *material dissipation rate of unit process* (α_{ij}) is defined to describe material consumption in manufacturing unit processes. It is the ratio of difference between the total input material quantity, which includes input iron element material quantity and additional material quantity, and the total output available material quantity, which includes output material quantity and recyclable material quantity, to the former in a manufacturing unit $x(i,j)$ within a certain time range. In other words, it is the ratio of material consumption in unit process, which can be formulated as follows,

$$\alpha_{ij} = \frac{[f_m(i,j)_{in} + f_m(i,j)_a] - [f_m(i,j)_{out} + f_m(i,j)_r]}{f_m(i,j)_{in} + f_m(i,j)_a}. \tag{4}$$

For the unit process mainly with chemical changes, the concept is *material dissipation rate* (*MDR*) in chemical reaction process based on per interval products. While, for the process mainly with physical changes, the concept is *material loss rate* in physical transformation process based on per interval products. In addition, there are *output product rate* (*OPR*) and *recyclable material rate* (*RMR*) in the processes. So, the material balance relationship between input and output in unit process is as follow,

$$(OPR + RMR) + MDR = 1. \tag{5}$$

In which, both of *output product rate* and *recyclable material rate* constitute the *effectively-utilized material rate* (*EUMR*) in unit process. They can be formulated as follows,

$$EUMR = OPR + RMR, \tag{6}$$

$$OPR = \frac{f_m(i,j)_{out}}{f_m(i,j)_{in} + f_m(i,j)_a}, \tag{7}$$

$$RMR = \frac{f_m(i,j)_r}{f_m(i,j)_{in} + f_m(i,j)_a}. \tag{8}$$

If there is an imbalance in the dynamic production process, that is to say, there is an input and output imbalance of iron element material flow in a manufacturing unit process, so the *EUMR* plus *MDR* in unit process not equal to 1. It will lead to *material accumulation* appear, for example, the liquid steel remaining in a BOF

after steel tapping, for which the concept named *material accumulation rate of unit process* (γ_{ij}) is introduced to describe the accumulation. Namely, it is defined as the ratio of the accumulated material quantity to the total input material quantity in unit process, can describe not only dynamic accumulated material quantity of iron element material flow but also flexible characteristics in unit process. Moreover, if it is 0, it means the unit process has no flexibility.

The *enthalpy change of unit process* (ΔH_{ij}^{p}) is defined to describe the total energy quantity without being effectively utilized at the final state after the material transformations of per material quantity in unit process within the certain time period. And *energy dissipation rate of unit process* (φ_{ij}) is defined as the ratio of the *enthalpy change of unit process* to the total input available energy quantity of per material quantity in unit process according to the time period. They can be formulated as follows,

$$\Delta H_{ij}^{p} = \frac{\left[f_e(i,j)_{in} + f_e(i,j)_a\right] - \left[f_e(i,j)_{out} + f_e(i,j)_r\right]}{f_m(i,j)_{in} + f_m(i,j)_a}, \tag{9}$$

$$\varphi_{ij} = \frac{\left[f_e(i,j)_{in} + f_e(i,j)_a\right] - \left[f_e(i,j)_{out} + f_e(i,j)_r\right]}{f_e(i,j)_{in} + f_e(i,j)_a}. \tag{10}$$

In the above formulas, the relevant data can be obtained from the real-world steel manufacturing process database.

For the process before steelmaking, the benchmark is set as per ton pig iron products; for the process of steelmaking-continuous casting, the benchmark is per ton steel products; for the process after continuous casting, the benchmark is per ton rolled steel products. Therefore, *material dissipation rate of unit process* can be, respectively, associated with the commonly used indices of iron ratio coefficient, steel ratio coefficient and material ratio coefficient. The indices of *enthalpy change of unit process* and *energy dissipation rate of unit process* are also similar, which can describe the energy dissipation and utilization in different processes. Besides, according to the multi-level and multi-scale characteristics of steel manufacturing process, the indices from unit processes can expand to describe conversions in the whole manufacturing process.

Researching and quantitatively describing of material and energy conversion of unit processes, is helpful for steel enterprises to get insight on the dynamical material and energy conversion or consumption in each unit process at all the time, which provide targeted measures to make decision for energy-saving and consumption-reducing.

Experiment and Discussion

The above indices can be used to describe an object steel production organization: heats in multi-processing processes. With the indices, it will be clear whether there are differences of material and energy conversion in the metallurgical process types of different steel grades.

Table 1 The production information of seven steel grades in production plan the day

Serial number	Steel grade	Processing route	Heats amount	Serial number	Steel grade	Processing route	Heats amount
1	DC01	LD-RH-CC	2	5	SPHC	LD-LF-CC	4
2	M4R30	LD-LF-CC	10			LD-RH-CC	6
3	Q235B	LD-LF-CC	9	6	St12	LD-LF-RH-CC	9
4	Q345B	LD-LF-CC	12	7	Stb34	LD-LF-CC	10

A few index cases for different steel products from a steel plant in China are shown in Table 1, which contains 62 heats of 7 steel grades in one day.

With the production data collected from the plant, the *material dissipation rate* and *energy dissipation rate* in the process of steelmaking-refining can be computed as an example. In the case, there are 2 BOFs at steelmaking phase, 2 LFs and 1 RH at refining phase. The material information including iron element material flow, additional material and other auxiliary material quantity and the energy information including temperature, power consumption and energy medium consumption in different stage can get from the real-world production process data. Consequently, *material dissipation rate of unit process* and *energy dissipation rate of unit process* in all BOFs and refining furnaces (LFs/RH) of all steel grades can be calculated. The statistical range (μ-2σ, μ+2σ) of the dissipation rate of materials and energy are, respectively, shown in Figs. 3, 4, 5, 6, 7, 8, calculated with all unit process of different steel grades. In which, μ is the mean value of the calculated dissipation rate, while σ is standard deviation of the calculated dissipation rate. As shown in Figs. 3, 4, 5, 6, 7, 8, the midpoint represents the value of μ, the top and bottom line represent the value of $\mu + 2\sigma$ and $\mu - 2\sigma$, which express the material or energy dissipation rate of all steel grades in all kinds of unit.

The above results show that the indices of *material dissipation rate of unit process* and *energy dissipation rate of unit process* are changed with steel grade,

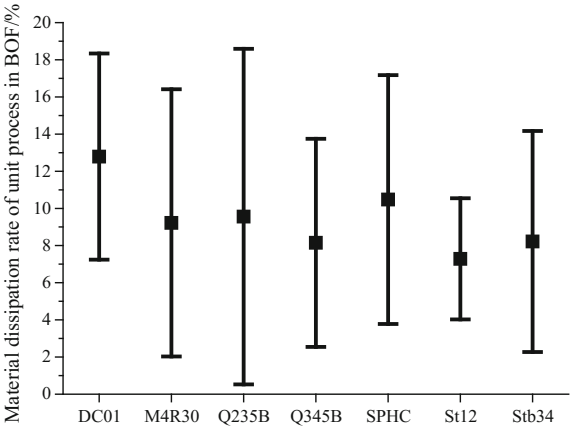

Fig. 3 The statistical range ($\mu - 2\sigma$, $\mu + 2\sigma$) of material dissipation rate with different grades (in BOFs)

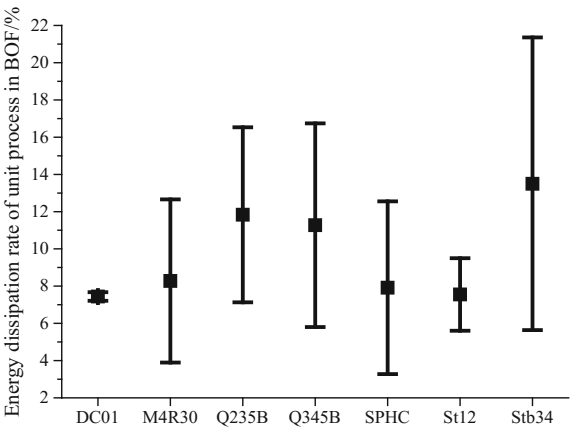

Fig. 4 The statistical range ($\mu - 2\sigma$, $\mu + 2\sigma$) of energy dissipation rate with different grades (in BOFs)

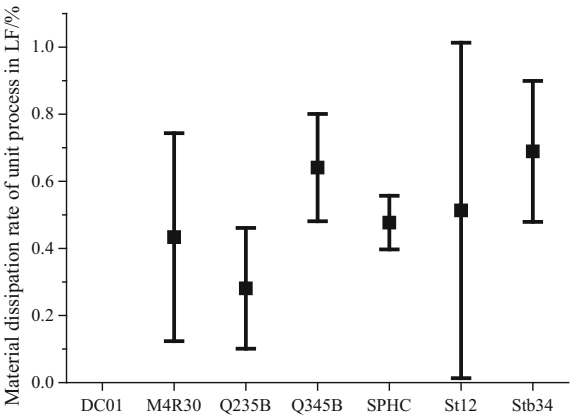

Fig. 5 The statistical range ($\mu - 2\sigma$, $\mu + 2\sigma$) of material dissipation rate with different grades (in LFs)

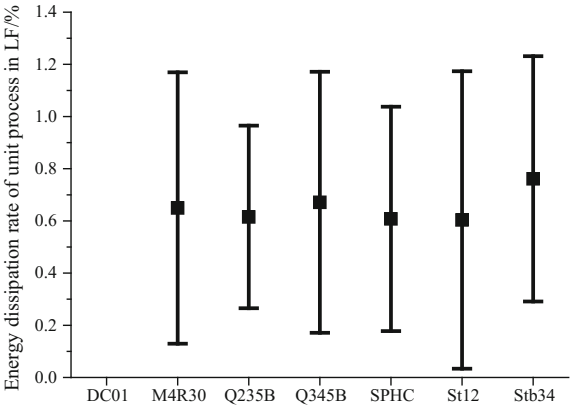

Fig. 6 The statistical range ($\mu - 2\sigma$, $\mu + 2\sigma$) of energy dissipation rate with different grades (in LFs)

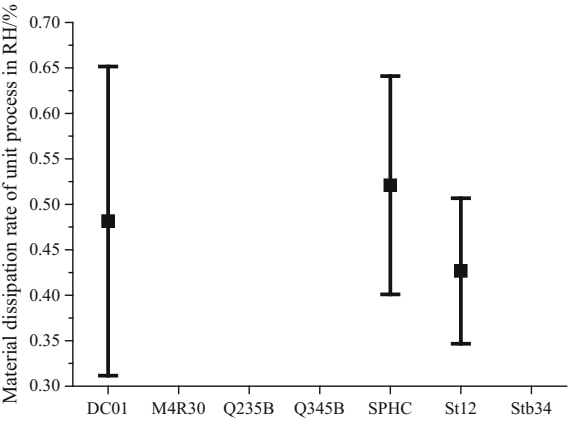

Fig. 7 The statistical range ($\mu - 2\sigma$, $\mu + 2\sigma$) of material dissipation rate with different grades (in RH)

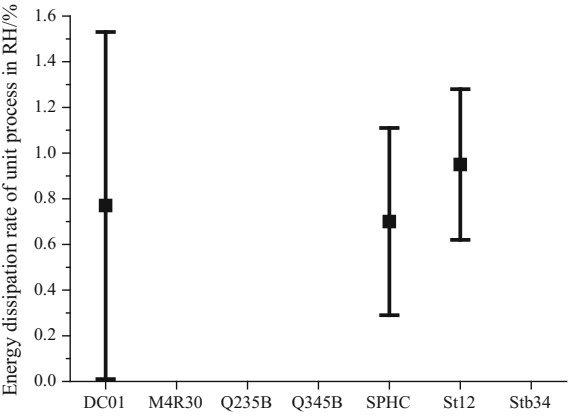

Fig. 8 The statistical range ($\mu - 2\sigma$, $\mu + 2\sigma$) of energy dissipation rate with different grades (in RH)

which means novel indices may expand the traditional evaluation indices, focusing on quantitatively evaluating the material or energy consumption of different steel grades and unit. However, convincing effect of the indices have to require more real-world production data, which certainly would be the future works.

Summary

In this paper, a few indices such as *material dissipation rate of unit process*, *material accumulation rate of unit process*, *enthalpy change of unit process* and *energy dissipation rate of unit process*, have been introduced to quantitatively evaluate material and energy conversion effect in steel metallurgical process. With the real-world production operational data, a few cases of *material dissipation rate*

and *energy dissipation rate* in unit processes have been calculated. There are differences of the indices among different steel grades or processes. It means that the novel indices could be indices for quantitatively describing materials and energy conversation in steel manufacturing unit processes. Nevertheless, more calculations and evaluations with real-world production data are needed, as they will be helpful for steel enterprises to achieve the production goals of *energy-saving and emission-reducing, cost-reducing and efficiency-increasing*.

Acknowledgements The authors gratefully acknowledge the financial support of the Key Program of the National Natural Science Foundation of China (No. 51734004), the National Key Research and Development Program of China (2017YFB0304005), the General Program of National Natural Science Foundation of China (No. 51474044).

Reference

1. Yin RY (2008) Development of steelmaking and continuous casting technology and prospect of this technology in 2010 in China. Steelmaking 06:1–12 (in Chinese)
2. World Steel Association (2016) World crude steel output increases by 0.8% in 2016 (https://www.worldsteel.org/media-centre/press-releases/2017/world-crude-steel-output-increases-by-0.8–in-2016.html, 2017-01-25/2017-08-10)
3. Fu QS (2005) Thermodynamic analysis method of energy system Xi'an Jiaotong University Press, Xi'an, 2005 (in Chinese)
4. Larsson M, Dahl J (2003) Reduction of the specific energy use in an integrated steel plant-the effect of an optimization model. ISIJ Int 10:1664–1673
5. Bisio G (1993) Exergy method for efficient energy resource use in the steel industry. Energy 09:971–985
6. Costa MM, Schaeffer R, Worrell E (2001) Exergy accounting of energy and materials flows in steel production systems. Energy 04:363–384
7. Cai JJ (2009) Research on energy flow and its network problems in iron and steel manufacturing process. In: Proceedings of the 7th China iron & Steel annual meeting. Beijing, China, 11–13 Nov 2009, pp. 189–195 (in Chinese)
8. Zhou JC, Zhang CX, Li XP et al (2013) Reasonable recycling methods of waste heat at steel plants based on energy level analysis. Iron Steel 02:80–85 (in Chinese)
9. Saidur R, Ahamed JU, Masjuki HH (2010) Energy, exergy and economic analysis of industrial boilers. Energy Policy 05:2188–2197
10. Lang DY (2011) Exergy analysis and thermoeconomic analysis of energy-saving technology in iron and steel enterprises. Northeastern University (in Chinese)
11. Ayres RU, Simonis UK (1994) Industrial metabolism: restructuring for sustainable development. United Nations University Press, Tokyo
12. Brunner PH, Rechberger H (2003) Practical handbook of material flow analysis. CRC Press, Florida
13. Milford RL, Pauliuk S, Allwood JM et al (2013) The roles of energy and material efficiency in meeting steel industry CO2 targets. Environ Sci Technol 07:3455–3462
14. Lu ZW, Cai JJ (2010) The foundation of systems energy conservation. Northeastern University Press, Shenyang (in Chinese)
15. Cai JJ (2009) Energy consumption analysis and energy-saving counter measure research for integrated steelworks. Angang Technol 02:1–6 (in Chinese)

16. Wang G, Bai H, Cang DQ et al (2009) Mathematical model for diagnosis of energy consumption bottlenecks in steel plants and its application. J Univ Sci Technol 09:1195–1199 (in Chinese)
17. Li Y, Zhao XY, Zhang Q (2015) Establishment and application of energy efficiency evaluation system for iron and steel enterprises. In: Proceedings of the 8th national conference on energy and thermal engineering. Dalian, Liaoning, China, 26–28 Aug 2015, pp. 720–727
18. Zhang GG (2013) Research and application of index system for evaluating energy consumption in iron and steel enterprises. Northeastern University (in Chinese)
19. Xu HL, Pan GY, Shao YJ et al (2017) Analysis of energy consumption evaluation indicator for iron and steel production. Energy Metall Ind 02:3–7 (in Chinese)
20. Zhang CX, Shangguan FQ, Li XP et al (2013) Study on energy efficiency benchmarking of the steel industry between China and the U.S. Iron and Steel 01, 87–92 (in Chinese)
21. Yin RY (2011) Metallurgical process engineering, 2nd edn. Metallurgical Industry Press, Beijing
22. Yin RY (2016) Theory and methods of metallurgical process integration. Metallurgical Industry Press, Beijing
23. Yin RY (1997) The multi-dimensional mass-flow control system of steel plant process. Acta Metall Sin 01:29–38 (in Chinese)
24. Zheng Z, Huang SP, Long JY et al (2017) Synergetic method between materials flow and energy flow in iron and steel intelligent manufacturing. Chin J Eng 01:115–124 (in Chinese)

Preparation and Characterization of Activated Carbon from Waste Ion-Exchange Resin for CO_2 Adsorption

Mengqi Wei, Qingbo Yu, Qiang Guo, Zongliang Zuo and Qin Qin

Abstract Activated carbons, derived from waste ion-exchange resin by CO_2 physical activation, were applied to separate CO_2 from flue gas against global warming. The BET specific surface areas of activated carbons at different activation temperatures and times were investigated. The CO_2 adsorption capacity was tested under non-isothermal and isothermal conditions. The experimental results show that when keeping the activation temperature constant, the specific surface area increases firstly and then decreases with increasing activation time. For the given activation time, the specific surface area rises firstly and then declines with increasing activation temperature. The adsorption capacity decreases with increasing temperature. The maximum adsorption capacity is 51.46 mg/g under the condition of 298 K and pure CO_2. Fractional order kinetic model is the best one to describe the kinetics of CO_2 adsorption. The activated carbons show the potential to be an effective adsorbent for the removal of CO_2 from flue gas.

Keywords Waste ion-exchange resin · Activated carbon · Carbon dioxide Adsorption · Kinetics

M. Wei · Q. Yu (✉) · Z. Zuo · Q. Qin
School of Metallurgy, Northeastern University, No 11, Lane 3, Wenhua Road, Heping District, Shenyang 110819, Liaoning, The People's Republic of China
e-mail: yuqb@smm.neu.edu.cn

Q. Guo
Hebei Construction & Investment New Energy Co. Ltd, Shijiazhuang 050051, Hebei, The People's Republic of China

Q. Yu
Northeastern University, No 11, Lane 3, Wenhua Road, Heping District, P.O, Box345, Shenyang, Liaoning, The People's Republic of China

Z. Sun et al. (eds.), *Energy Technology 2018*, The Minerals, Metals & Materials Series, https://doi.org/10.1007/978-3-319-72362-4_4

Introduction

Severe global climate change has been one of the most challenges with the sustainable development of human beings. Global warming leading by artificial greenhouse gas emissions has become an issue of major international concerns. Carbon dioxide (CO_2) whose amount is the largest among greenhouse gases is emitted into the surroundings from various sources, such as power plant, cement industry, iron and steel industry, ammonia industry, refinery and so on [1]. Carbon capture and storage (CCS) has been thought to be a promising technology to reduce the CO_2 emissions against global warming.

Adsorption is considered as one of the most promising CCS technologies for CO_2 capture from flue gases. Adsorption process, as a mature technology, is widely used in separation industry based on the high performance of the adsorbent materials. Activated carbon (AC) is a common adsorbent used in gas separation and depuration [2, 3], sewage treatment [4, 5], desulfurization and denitrification [6, 7] etc., whereby it provides a large range of pore structures and surface chemistry properties [8]. Generally, AC is relatively cheap, stable in acidic or basic solutions and has much more sources of raw materials. Besides, it is also insensitive to moisture and cost effective as it can be regenerated after being used [8, 9]. These above-mentioned features make it the candidate adsorbent materials for post-combustion capture [10–13].

Ion-exchange resins are mainly used for demineralization of boiler water, metal separation from aqueous solutions, health and medicine, and the metallurgical industry among others. Generally, they are wasted after being used for 3–5 years and do not readily degrade in the natural environment [14]. Waste ion-exchange resins have been found to be a suitable precursor to produce AC due to high carbon yield and low ash content [15, 16]. From the present papers, waste ion-exchange resins using for producing AC may be a very potential economic and ecological advantage. Bratek et al. [15] have produced AC with waste ion-exchange resin to clean the toluene-contaminated water efficiently. Gun'ko and his co-workers [16] have prepared to manufacture a series of ACs by stream activation with different waste commercial ion-exchange resins. Zhang [17] produced AC by cation exchange resin via KOH activation for high-performance super-capacitor.

However, few people apply the waste ion-exchange resin-based activated carbons (WIRACs) to CO_2 capture against global warming. Therefore, in this paper, WIRACs were produced by different activation conditions and the different pore structures and surface chemistry properties were compared. Then the CO_2 adsorption capacities of different WIRACs were measured. Different adsorption kinetic models were selected to describe the kinetics of CO_2 adsorption.

Experimental

Materials

The waste ion-exchange resins after being treated with demineralization of water were soaked in the absolute ethyl alcohol overnight to wipe off the organic impurity adsorbed on the surface of them. Then they were impregnated with 5% hydrochloric acid (HCl) for 24 h, washed with distilled water until the pH approached to 7. Then the resins were dried in the drying oven for 24 h.

Preparation of WIRACs

The treated resins were heated from room temperature to 1073 K in a corundum boat at the rate of 1.5 K/min and kept 60 min for carbonization under N_2 atmosphere in a horizontal cylindrical furnace. After carbonization, the char was activated at a designated temperature for a certain time with CO_2 in a vertical cylindrical furnace.

Characterization of WIRACs

The pore structure of WIRACs was examined using an automatic micromeritics NOVA 1200e volumetric adsorption analyzer by nitrogen adsorption-desorption isotherm at 77 K. The specific surface area (S_{BET}) was calculated by the BET equation; the total pore volume (V_t) was evaluated by converting the adsorption volume of nitrogen at relative pressure of about 0.985 to equivalent liquid volume of the adsorbate. The mesopore volume (V_{mes}) and the pore size distributions were determined by the BJH model.

WIRACs were ground and mixed with KBr at a mass ratio of 1:100 and then were ground into powders together. The 151.5 mg mixed powders were pressed into a slice and then subjected to Fourier Transform Infrared spectroscopy (FTIR) scan. 32 scans were taken at a wave number range of 400-4000 cm^{-1} with a resolution of 4 cm^{-1}.

Carbon Dioxide Adsorption Capacity

The CO_2 adsorption capacity of the WIRACs at atmospheric pressure was assessed with a thermogravimetric analyser (TGA). The WIRACs were loaded in a corundum crucible into the TGA and heated to 393 K in the atmosphere of N_2 to remove

CO_2 and H_2O on the surface of WIRACs before adsorption experiment. After the temperature decreased to the designated temperature, N_2 was changed to CO_2 until the weigh remained unchanged. Before adsorption experiment, the base line was done in the same condition.

Results and Discussion

Textural Characterization and Chemical Characteristics of WIRACs

Figures 1 and 2 illustrate the BET specific surface area of WIRACs. From Fig. 1, at the same activation temperature, the BET specific surface area of WIRACs increases to the maximum and then decreases with increasing activation time. When the activation reaction occurs, activation reagent molecules enter into the interior of char through the macropores on the surface of char and react with tar and amorphous carbon formed at the carbonization process. Due to the burning-off of the blocking pore, the BET specific surface area increases. The BET specific surface area is much bigger owing to the opening of blocking pore among the crystallites in succession. With activation time increasing, the micropores formed previously begin to be destroyed, and some of the micropores become mesopores. However, when the activation time is much longer, activation reaction is excessive. The formed mesopores become macropores, carbon matrix collapses, and the pore structure blocks, which lead to the reduction of the BET specific surface area.

The activation reaction of char with CO_2 is endothermic. At the low activation temperature, the reaction is controlled by the reaction rate. With the increase of activation temperature, the reaction rate of char with activation reagent becomes faster. Low temperature is disadvantageous to the activation reaction. With the

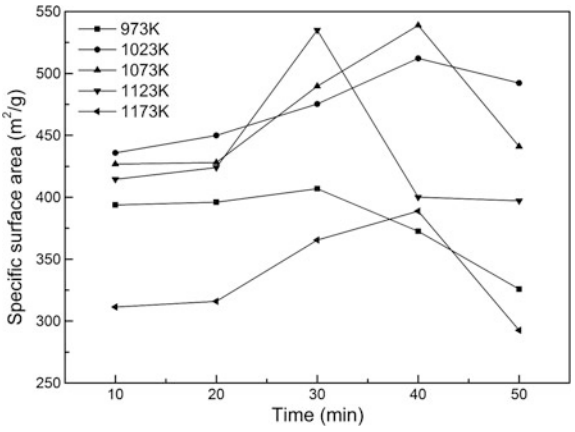

Fig. 1 The specific surface areas of the different activation times

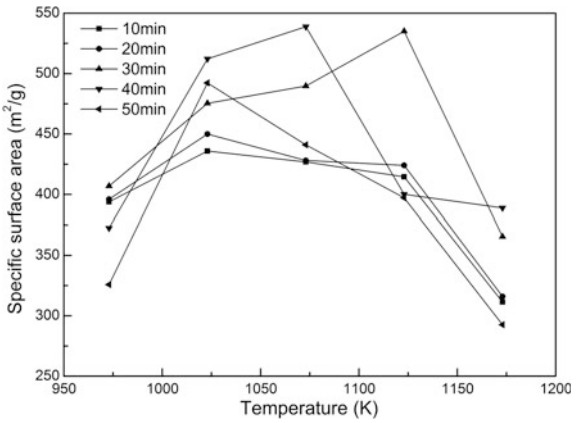

Fig. 2 The specific surface areas of the different activation temperatures

temperature increasing, the specific surface area of WIRACs increases before the optimum temperature, while starts to decrease on further increase of the temperature, as seen in Fig. 2. When temperature is higher than the optimum one, the specific surface area starts to reduce significantly due to the collapsing and vanishing of the micropores.

Among these WIRACs, five kinds of WIRACs were chosen according to their BET specific surface areas. The pore structure of the WIRACs was tested. The results and the pore size distributions can be seen in Table 1 and Fig. 3, respectively.

As revealed in Fig. 3, most pores of WIRACs are distributed in the pore size ranging from 1.4 nm to 3.8 nm, and the latter is much bigger than the former, especially sample C and D, which leads to the highest value of pore volumes of sample C and D among these samples. It is beneficial to adsorb small molecule substances for the micropores and mesopores with less than 3.8 nm diameter. From Table 1, with the increase of BET specific surface area, the pore volume presents a non-rule status. So the pore volume is not directly related to the BET specific surface area. The percentage of mesopores of the produced WIRACs is the largest, especially about 3.8 nm which can be seen in Fig. 3. The average pore diameters are from 3.821 nm to 3.854 nm. The WIRACs are mesoporous carbons, and the percentage of mesopores is from 88.57% to 97.34%.

Table 1 Pore structure parameters of WIRACs

Sample	S_{BET} (m^2/g)	V_t (cm^3/g)	V_{mic}/V_t (%)	V_{meso}/V_t (%)	D_{avg} (nm)	m (mg/g)
A	393.8	0.133	3.48	96.52	3.848	45.26
B	414.6	0.072	2.66	97.34	3.821	43.85
C	475.4	0.236	5.28	94.72	3.854	48.32
D	505.1	0.238	11.43	88.57	3.847	51.46
E	538.9	0.029	2.73	97.27	3.840	35.23

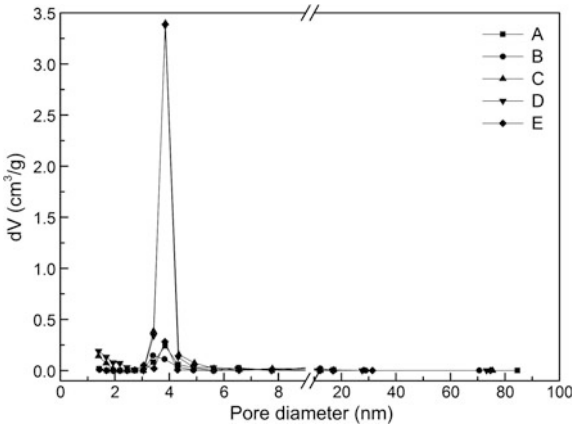

Fig. 3 The pore size distributions of the WIRACs

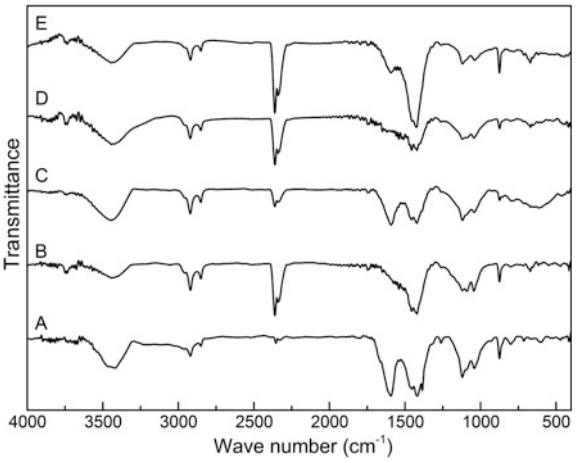

Fig. 4 FTIR of different WIRACs

To research the nature of the functional groups presenting on the surface of the WIRACs, FTIR analysis was tested. Figure 4 shows the results of FTIR measurement for WIRACs. The bands at 3402 cm^{-1} can be assigned to the -NH_2-. The peaks at 2917 and 2834 cm^{-1} are attributed to C-H stretching vibration of -CH_2-NH-CH_2-. The bands at 2350 cm^{-1} are related to C = C. The peaks at 1570, 1422, 1248 and 856 cm^{-1} can be due to C = O stretching vibration of ketones, aromatic ring, C-O stretching vibration and presence of C-H groups (located at the edges of aromatic ring).

Assessment of CO_2 Adsorption Capacity

The CO_2 adsorption capacity of WIRACs was tested by TGA. Firstly, non-isothermal adsorption was tested and the temperature was from 298 K to

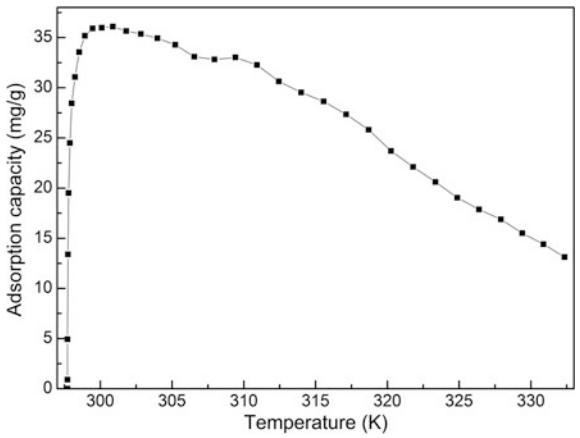

Fig. 5 Non-isothermal adsorption curve

333 K. As shown in Fig. 5, at the beginning, the adsorption capacity increases instantaneous to the highest. However, with the temperature increasing, adsorption capacity begins to reduce and desorption phenomenon occurs to some extent. With the temperature increasing, the adsorption capacity reduces obviously, indicating that CO_2 adsorption of WIRACs is a typical physical adsorption. As a rule of thumb for physical adsorption, it is an exothermal reaction. When the adsorption occurs, the molecules adsorbed on the surface of porous material can receive adsorption energy. If the energy is big enough, the molecules adsorbed will get away from the surface. The higher adsorption temperature is, the easier it is for molecules to escape from the surface. It is disadvantageous to CO_2 adsorption at high temperature due to the exothermic reaction of CO_2 adsorption by WIRACs. Even if the reaction rate becomes faster at higher temperature, less CO_2 is adsorbed onto the active sites due to the faster CO_2 desorption.

Figure 6 shows CO_2 isothermal adsorption curves at 298 K. As revealed in Fig. 6, the equilibrium times of WIRACs are similar, about 7 min. E is the first and C is the last. From A to E, the adsorption capacities are 45.26 mg/g, 43.85 mg/g, 48.32 mg/g, 51.46 mg/g and 35.23 mg/g, respectively. At the beginning, the adsorption capacity increases slowly, indicating hysteresis existing in the adsorption process. The hysteresis phenomenon is caused by CO_2 molecules diffusing from gaseous phase to pores.

Adsorption Kinetic Models

CO_2 adsorption kinetics of WIRACs is desirable to evaluate the performance of adsorbents and to understand the overall mass transfer in the CO_2 adsorption process. It is very important to design the adsorption process and determine the adsorption equipment. So it is necessary to study the adsorption kinetics. To

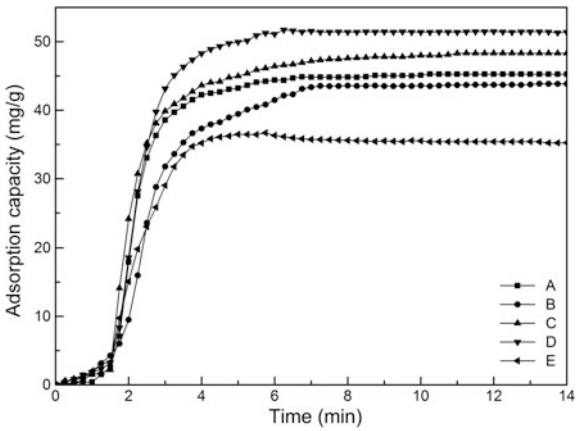

Fig. 6 Isothermal adsorption curves at 298 K

Table 2 Adsorption kinetic models

Kinetic model	Differential form	Equation
Pseudo-first order [18, 19]	$\frac{dq_t}{dt} = k_1(q_e - q_t)$	$q_t = q_e\left(1 - e^{-k_1 t}\right)$
Pseudo-second order [19, 20]	$\frac{dq_t}{dt} = k_2(q_e - q_t)^2$	$q_t = \frac{k_2 q_e^2 t}{1 + k_2 q_e t}$
Avrami's fractional-order [20, 21]	$\frac{dq_t}{dt} = k_A^{n_A} t^{n_A - 1}(q_e - q_t)$	$q_t = q_e\left(1 - e^{-(k_A t)^{n_A}}\right)$
Fractional order [19, 20]	$\frac{dq_t}{dt} = k_n t^{m-1}(q_e - q_t)^n$	$q_t = q_e - \frac{1}{\left[((n-1)k_n/m)t^m + \left(1/q_e^{n-1}\right)\right]^{1/(n-1)}}$

investigate the kinetics of CO_2 adsorption of WIRACs, the following four models were considered in Table 2.

The adsorption of different WIRACs was tested in the same condition. So the adsorption kinetics was studied by one kind of WIRACs. Figure 7 indicates the different kinetic models of CO_2 adsorption. Table 3 shows the parameters of different kinetic models.

The squared regression coefficients (R^2) related to the four kinetic models are all higher than 0.83, indicating that the fitted curves are well. So the four kinetic models all can describe the CO_2 adsorption process. The fractional order kinetic model is the best one, closely followed by Avrami's fractional-order kinetic model, pseudo-first order kinetic model and pseudo-second order kinetic model. According to the kinetic models fitted curves of Fig. 7, at the beginning stage of adsorption, adsorption capacity is overrated by pseudo-first order kinetic model and pseudo-second order kinetic model; and at the middle stage, adsorption capacity is underrated; at the end stage, adsorption capacity is overrated again. The final equilibrium adsorption capacity of the two models is higher than the real. The fitted result of Avrami's fractional-order kinetic model is well, except at the middle stage. The adsorption capacity is a little overrated. Compared with pseudo-first order kinetic model and pseudo-second order kinetic model, the overrated value is a little,

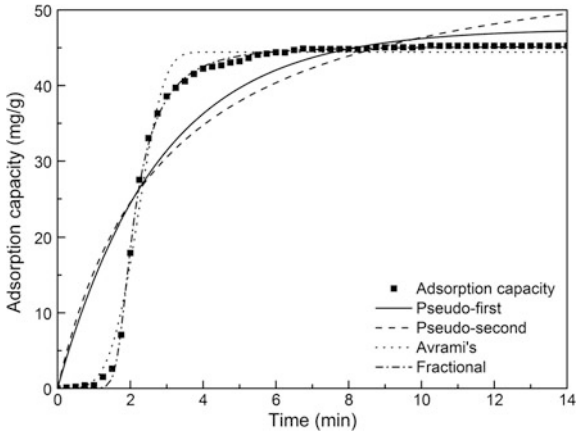

Fig. 7 Different kinetic models of CO_2 adsorption by WIRACs

Table 3 Different kinetic models parameters

	Pseudo-first order	Pseudo-second order	Avrami's fractional-order	Fractional order
q_e (mg/g)	47.51	59.64	44.42	45.14
k	0.36015	5.85×10^{-3}	0.41855	4.78×10^{-10}
m	–	–	–	13.58374
n	–	–	4.28647	4.99895
R^2	0.8711	0.8313	0.9910	0.9993

which can be ignored to a certain degree because R^2 of the kinetic model is 0.9910. Fractional order kinetic model is the best one, whose R^2 is 0.9993. The adsorption capacity is neither overrated nor underrated, and the overall process of adsorption can be described well. The final equilibrium adsorption capacity of Avrami's fractional-order and Fractional order kinetic models is very consistent with the real adsorption capacity.

Conclusions

Waste ion-exchange resin belongs to solid hazardous waste, and how to dispose it is a problem bothering people. And now waste ion-exchange resin is found to be a kind of suitable precursor to produce AC via CO_2 physical activation in this study. When keeping the activation temperature constant, the BET surface area rises and then decreases as activation time increases. For a given activation time, the BET surface area rises and then reduces with increase of activation temperature. The CO_2 adsorption capacity of WIRACs decreases with the increase of temperature. CO_2 adsorption by WIRACs with porosity is physical adsorption, and a higher

temperature is disadvantageous to CO_2 adsorption. So in practical application, the temperature of flue gas should be low. The maximum adsorption capacity is 51.46 mg/g under the condition of 298 K with pure CO_2. Fractional order kinetic model, whose R^2 is 0.9993, is the best kinetic model to describe the adsorption process. WIRACs used for CO_2 adsorption not only turns waste into wealth and solves the problem of waste resins difficult terminal dispose, but also reduces the cost of AC, indirectly reducing the cost of emissions reduction. The WIRAC is a promising porous adsorbent to CO_2 adsorption because of its good adsorption property and low cost.

Acknowledgements This research was supported by The Major State Research Development Program of China (2017YFB0603603), The National Natural Science Foundation of China (51576035, 51604077, 51604078), The Fundamental Research Funds for the Central Universities (N162504012).

References

1. Li L, Zhao N, Wei W, Sun Y (2013) A review of research progress on CO_2 capture, storage, and utilization in Chinese academy of sciences. Fuel 108:112–130
2. Arami-Niya A, Daud WMAW, Mjalli FS (2011) Comparative study of the textural characteristics of oil palm shell activated carbon produced by chemical and physical activation for methane adsorption. Chem Eng Res Des 89:657–664
3. Awadallah-F A, Al-Muhtaseb S (2013) Carbon dioxide sequestration and methane removal from exhaust gases using resorcinol–formaldehyde activated carbon xerogel. Adsorption 19:967–977
4. Awwad NS, Gad HMH, Ahmad MI, Aly HF (2010) Sorption of lanthanum and erbium from aqueous solution by activated carbon prepared from rice husk. Colloid Surf B 81:593–599
5. Zabihi M, Asl AH, Ahmadpour A (2010) Studies on adsorption of mercury from aqueous solution on activated carbons prepared from walnut shell. J Hazard Mater 174:251–256
6. Gao XA, Liu SJ, Zhang Y, Luo ZY, Cen KF (2011) Physicochemical properties of metal-doped activated carbons and relationship with their performance in the removal of SO_2 and NO. J Hazard Mater 188:58–66
7. Gaur V, Asthana R, Verma N (2006) Removal of SO_2 by activated carbon fibers in the presence of O_2 and H_2O. Carbon 44:46–60
8. Lee CS, Ong YL, Aroua MK, Daud WMAW (2013) Impregnation of palm shell-based activated carbon with sterically hindered amines for CO_2 adsorption. Chem Eng J 219:558–564
9. Mahurin SM, Górka J, Nelson KM, Mayes RT, Dai S (2014) Enhanced CO_2/N_2 selectivity in amidoxime-modified porous carbon. Carbon 67:457–464
10. Balsamo M, Budinova T, Erto A, Lancia A, Petrova B, Petrov N, Tsyntsarski B (2013) CO_2 adsorption onto synthetic activated carbon- Kinetic, thermodynamic and regeneration studies. Sep Purif Technol 116:214–221
11. Ello AS, de Souza LKC, Trokourey A, Jaroniec M (2013) Coconut shell-based microporous carbons for CO_2 capture. Micopor Mesopor Mat 180:280–283
12. Ello AS, de Souza LKC, Trokourey A, Jaroniec M (2013) Development of microporous carbons for CO2 capture by KOH activation of African palm shells. J CO_2 Util 2: 35–38
13. Samanta A, Zhao A, Shimizu GKH, Sarkar P, Gupta R (2012) Post-combustion CO_2 capture using solid sorbents a review. Ind Eng Chem Res 51:1438–1463

14. Long C, Lu JD, Li A, Hu D, Liu F, Zhang Q (2008) Adsorption of naphthalene onto the carbon adsorbent from waste ion exchange resin: equilibrium and kinetic characteristics. J Hazard Mater 150:656–661
15. Bratek K, Bratek W, Kulazynski M (2002) Carbon adsorbents from waste ion-exchange resin. Carbon 40:2213–2220
16. Gun'ko VM, Leboda R, Skubiszewska-Zie¸ba J, Charmas B, Oleszczuk P (2005) Carbon adsorbents from waste ion-exchange resins. Carbon 43: 1143–1150
17. Zhang ZJ, Cui P, Chen XY, Liu JW (2013) The production of activated carbon from cation exchange resin for high-performance supercapacitor. J Solid State Electr 17:1749–1758
18. Andreoli E, Cullum L, Barron AR (2015) Carbon dioxide absorption by polyethylenimine-functionalized nanocarbons: a kinetic study. Ind Eng Chem Res 54:878–889
19. Heydari-Gorji A, Sayari A (2011) CO_2 capture on polyethylenimine-impregnated hydrophobic mesoporous silica: experimental and kinetic modeling. Chem Eng J 173: 72–79
20. Liu Q, Shi JJ, Zheng SD, Tao MN, He Y, Shi Y (2014) Kinetics studies of CO_2 adsorption-desorption on amine-functionalized multiwalled carbon nanotubes. Ind Eng Chem Res 53:11677–11683
21. Serna-Guerrero R, Sayari A (2010) Modeling adsorption of CO_2 on amine-functionalized mesoporous silica. 2: Kinetics and breakthrough curves. Chem Eng J 161:182–190

Evaluation of Variation in the Life Cycle Based Environmental Impacts for Copper Concentrate Production

Will Sikora, Trevor Saldanha and Nawshad Haque

Abstract This study reported life cycle assessment (LCA) of six copper mines in Australia, Papua New Guinea and Portugal. Inventory data was sourced from published papers, sustainability reports by mining companies, independent technical reports and previous CSIRO studies. SimaPro software and various databases were used to evaluate life cycle based environmental impacts. The impact indicators were: global warming potential (GWP), acidification potential, water footprint, ecotoxicity potential, ozone depletion potential and human toxicity potential (carcinogenic and non-carcinogenic), abiotic resource depletion potential (minerals and fossil fuels), particulate matter and ionizing radiation. Generally, open pit mines were found to have a GWP of approximately 1.0 t CO2-eq/t Cu concentrate while underground mines had approximately 1.3 to 1.8 t CO2-eq/t Cu concentrate. Environmental impacts varied between mines considerably due to several factors, most notably: ore grade, mining method, flowsheets and ore mineralogy. Energy consumption and sources were significant contributors to most impact categories.

Keywords LCA · Copper · GHG · Sustainability · Concentrate

Introduction

Copper metal is an extremely important commodity in society being used in a wide range of applications such as electronics, electrical wiring and energy transfer technologies. With these applications expected to be remain in strong demand, copper production should continue to increase into the future. There is a need to understand the environmental impacts associated with products since an increase in general awareness and demand from the consumer. A focus on the environmental performance of products also drives an increased efficiency upstream processes such as raw material extraction and metal processing. Life cycle assessment (LCA),

W. Sikora · T. Saldanha · N. Haque (✉)
CSIRO Mineral Resources, Private Bag 10, Clayton South, VIC 3168, Australia
e-mail: Nawshad.Haque@csiro.au

Z. Sun et al. (eds.), *Energy Technology 2018*, The Minerals, Metals & Materials Series, https://doi.org/10.1007/978-3-319-72362-4_5

in particular, is an established tool for assessing environmental impacts, including in the mining and metals industry [1]. Environmental impacts of multiple products have been assessed using LCA methodologies and generated Environmental Product Declarations (EPDs) [2]. Product assessments of cars [3], tractors [4], beverage cans [5], wind turbines [6], and copper products such as tubes, sheets and wires [7] showed a significant impact from raw materials, particularly metals. For this reason, the understanding of the impact of copper mining and processing is inevitable. A study [8] showed 93% of Americans displayed a conscious willingness to incorporate sustainability into their lifestyle. Other studies [9] showed similar results that found 84% of surveyed consumers take varying actions to seek sustainable products when they shop. This consumer interest is one of the key drivers for sustainability. Without correct representation of the environmental impact of products, it is more difficult for consumers to actively participate in sustainability. Therefore, having more informative and consistently structured (i.e. based on international standards) environmental performance indicators using methodologies such as LCA and indicators in EPD can help society to make informed decisions to benefit the global environment.

Previous LCAs on metal production have focussed on representative data for production of various metals, lumping mining and mineral processing into one stage [10], which helped to provide a complete life cycle inventory. However, metal production LCAs have yet to compare the environmental performance of various mines to ascertain the variation of performance between sites, and thus to assess the sensitivity of the results.

This study conducted LCAs of copper concentrate (Cu con) production for six mines located in Australia, PNG and Portugal. Mining and mineral processing, in general, consume significant amounts of energy and have a large environmental impact associated with them [11]. Furthermore, the production of copper concentrate uses more energy than the refining stage of copper metal production [10]. This is different to the steel and aluminium industries which use more energy in the refining stage [10]. In addition, the contribution of the mining and mineral processing stages will significantly increase as ore grades continue to decrease over time due to a larger amount of material being processed [12]. This shows the importance of understanding the processing stage of copper production to evaluate environmental impacts.

Many LCAs [10, 13–15] analyse the global warming potential (GWP) of mines but ignore other major impact categories due to the lower certainty associated with their characterisation. This study recognises that there are limitations with these impact categories but utilises their usefulness in providing a basis for a more in depth comparison. Haque & Norgate [15] indicate the importance of evaluating other impacts that significantly influence public perception of environmental performance. Santero & Hendry [1] also recommends the assessment of five categories (including GWP) when performing LCAs of the metals industry and suggests inclusion of more impact categories as data becomes more refined. Beyond these categories, Heijungs et al [16] indicates the importance of considering dedicated models for human and ecosystem toxicity of metals. Inclusion of multiple impact

categories is important in copper processing in particular due to the number of influencing factors that lead to significant variation in performance between sites. This study looks in particular to explore these differences as understanding this variation helps to know where and how significant improvements can be made in environmental performance. Furthermore, through comparisons of mines limitations in LCA methodology can be highlighted and improved. There is also an opportunity to focus on and refine areas of mining and mineral processing that are key contributors to environmental impacts of metal production.

Though social relations and environmental regulations are key drivers for environmental performance reporting, there appears to be a lack of reporting when considering the extent of the environmental footprint of copper mining. Considering that there are significant savings that can be made in energy use and hence environmental damages, in depth reporting may benefit business too. This could allow peer to peer comparisons and allow for future opportunities to be seized. Green Research [17] conducted a study sponsored by PE-International that lists several benefits to businesses conducting LCAs including market access, increased revenue and brand enhancement. For these reasons this study further aims to highlight the importance of providing detailed information by showing how environmental performance can be better represented with the use of this information in combination with LCA.

Methodology

LCA evaluates the total environmental burdens and benefits over the entire life cycle for a product from 'cradle' to 'grave' including: material and energy used during extraction and processing of raw materials, manufacturing, transportation, use, recycling and end-of-life fate. International Standards (ISO 14046: 2006) provides guidelines on undertaking an LCA with recommended four stages: goal and scope definition, inventory analysis, impact assessment and interpretation.

The goal of this study was to determine the carbon emissions and other environmental impacts of several copper mines producing copper concentrate. Six copper mines, from Australia, Papua New Guinea and Portugal were selected to perform LCA.

The study adopts a cradle to gate approach (as shown in Fig. 1) which encompasses the entire operation from ore extraction to concentrate production. As only copper concentrate production was included in this study, sites with pyrometallurgical copper processing were considered. Hydrometallurgical copper processing sites do not produce copper concentrate. All energy, reagents and materials consumed within the system boundary were assessed, using a functional unit of 'one tonne of copper concentrate' as a basis for comparison.

The study considered the following impact categories:

- Global warming potential (GWP)
- Abiotic depletion potential (for mineral and fossil fuels) (ADP)

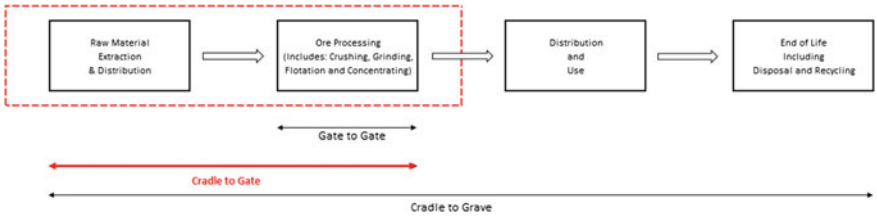

Fig. 1 Datasets included in gate to gate, cradle to gate and cradle to grave. 'Cradle to gate' approach was used in this study and is highlighted accordingly

- Ozone depletion potential (ODP)
- Photochemical oxidation creation potential (POCP)
- Acidification potential (AP)
- Eutrophication potential (EP)
- Particulate matter
- Human toxicity potential (HTP) (carcinogenic and non- carcinogenic)
- Ionizing radiation

Life cycle inventory data was collected from a number of publicly available sources. This included peer reviewed papers, sustainability reports from mining companies and independent technical reports. Inventory data from previous CSIRO studies [18] were also incorporated. Data included key mine information (e.g. tonnage, ore grade), electricity, flotation reagents and material consumption that also included explosives, grinding media, lime and flocculants.

The impact is calculated by multiplying each component within the inventory data by a relevant impact factor from the method in SimaPro (Version 8.4.1.0) LCA software environment and then summing the results. For example, electricity consumption was multiplied by its emission factor to calculate GWP for electricity use. These GWP contributions for all individual input items were then added up to obtain the total GWP for the particular mine. SimaPro was used to calculate the midpoint impact. SimaPro uses the Australian Life Cycle Inventory database as well as other international databases.

Results and Discussion

Mine Flowsheets and Overview

A significant difference was found in the flowsheets of separate mine sites. However, each mine contained the generic processes outlined in Fig. 2. The detailed individual process units differ in number, size, type and in configuration.

Relevant mine information including annual milled tonnage, ore grade, concentrate grade, predominant ore type and mine type are provided in Table 1 for the six mines analysed.

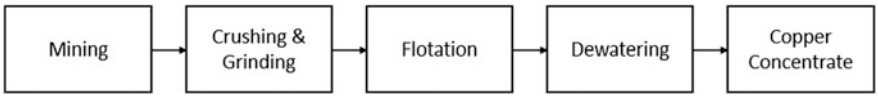

Fig. 2 General flow sheet for copper concentrate production process

Table 1 Overview data for selected concentrate producing mines

Mine	1	2	3	4	5	6
Annual Tonnage (Mt/annum)	9.54	5.25	9.84	2.00	22.19	2.69
Ore Grade (%)	1.32	0.82	0.69	1.23	0.84	2.72
Concentrate Grade (%)	50.85	33.60	28.56	26.50	25.76	24.30
Predominant Ore Type[a]	CC, B	B	M, CP	CP, P	CP	CP
Mine Type	OP	UG[b]	OP	UG	OP	UG

Notes [a]Ore types are: B—Bornite, CC—Chalcocite, CP—Chalcopyrite, M—Magnetite and P—Pyrite. Mine types are: OP—Open Pit, UG—Underground. [b]Mine 2 has both underground and open pit mines but sources most of its process ore from the underground mine and so has been assessed as an underground mine

Impact Results

GWP for each mine sites are shown in Fig. 3 as found and also with the assumption that all mines are using electricity from same source having same emission factors. This assists with the comparison and also to identify what other important possible variables are that can affect GWP. Table 2 shows other impact indicators.

Global warming potential is the most widely used impact category in LCA. A large effort has been allocated globally to this impact category by organisations such as the IPCC. The largest contributors to GWP were electricity and diesel consumption. Both are fossil fuels sources (with the exception of energy produced from renewable sources). The materials with the next biggest GWP contributions were explosives and grinding media consumption.

Figures 4, 5, 6, 7 provided a ranking (highest to lowest GWP) and indicated the relative annual tonnage (out of the six mines assessed). The GWP for 'base case' results (Fig. 4) showed a large variance between each mine. The problem with analysing this data is that the variance between sites depends on a number of factors (electricity fuel source, ore grade, ore mineralogy etc.). These factors each contribute differently to GWP and are not always a linear scaling of results. For this reason, the exact results give inadequate information on what exactly caused the variance between sites.

Figures 4, 5, 6 have been constructed for a number of scenarios that correspond to the variables considered to have a major influence on mine performance:

- Base Case Results: all results unaltered (Fig. 4)
- Common Fuel Type: electricity generation assumed to be from a common source (natural gas) (Fig. 5)

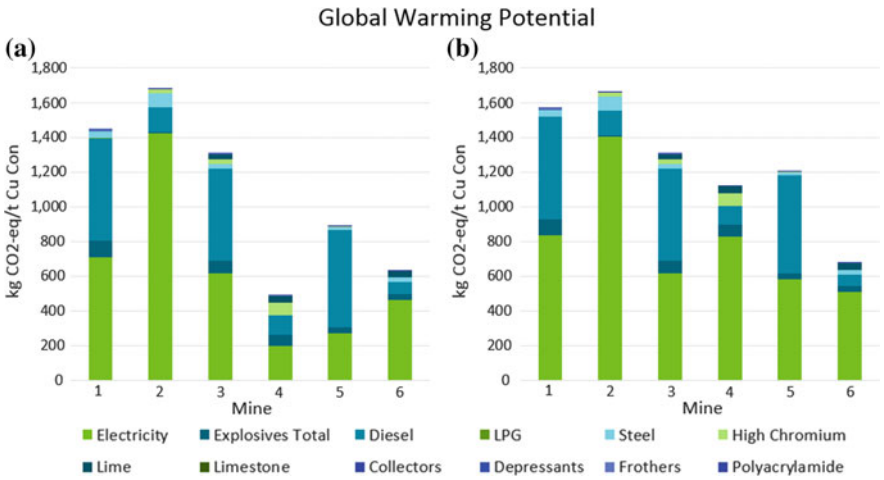

Fig. 3 Global Warming Potential breakdown for each mine for: **a** base case - no adjustments, **b** common fuel type adjusted

Table 2 Other impacts for each mine per tonne of concentrate produced

Mine	1	2	3	4	5	6
GWP ($kgCO_2$-e/t Cu Con)	1,450	1,680	1,310	488	890	633
AP (kg SO_2-e/t Cu Con)	9.67	4.26	9.74	3.02	4.45	7.20
EP ($kgPO_4$-e/t Cu Con)	1.04	0.379	0.963	0.408	0.966	0.343
HTP cancer (10^7 CTUh/t Cu Con)	6.27	24.3	29.0	66.1	14.6	6.71
HTP non-cancer (10^5 CTUh/t Cu Con)	7.16	3.11	7.47	3.46	7.55	1.80
ODP ($10^{6\ kg}$ CFC-11-e/t Cu Con)	44.5	25.2	48.4	18.3	1.48	41.4
POCP (kg C_2H_4-e/t Cu Con)	0.390	0.198	0.400	0.133	0.291	0.302
AETP (10^{-6} CTUe/t Cu Con)	3.03	3.61	2.76	1.08	1.71	1.68
ADP element (10^3 kg Sb-e/t Cu Con)	3.43	50.9	59.9	153	12.7	1.60
ADP fossil fuels (10^{-3} MJNCV/t Cu Con)	15.8	26.9	13.8	4.89	4.34	7.52
Particulate matter (kg PM2.3/t Cu Con)	0.452	0.272	0.453	0.232	0.172	0.675
Ionizing radiation (kg Bq U235-e/t Cu Con)	0.844	3.70	3.92	10.1	0.844	3.74

- Common Fuel Type and Ore Grade: common fuel type condition with a linear adjustment of GWP to a common ore grade of 1% (Fig. 6)
- Common Fuel Type, Ore Grade and Concentrate Grade: common fuel type and ore grade condition with a linear adjustment of GWP to a common concentrate grade of 30% (Fig. 7)

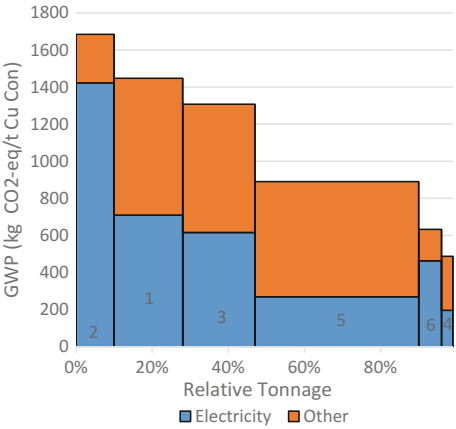

Fig. 4 Global Warming Potential ranked analysis for six mines assessed. 'Other' includes all inputs other than electricity

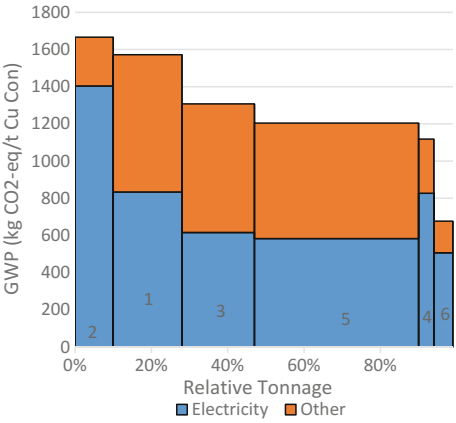

Fig. 5 Common fuel type (Natural Gas) adjusted Global Warming Potential ranked analysis for six mines assessed. 'Other' includes all inputs other than electricity

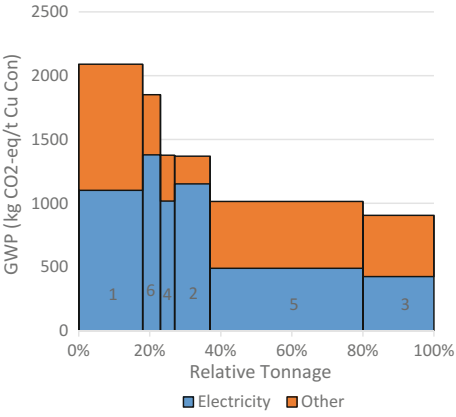

Fig. 6 Common fuel type (Natural Gas) and ore grade adjusted Global Warming Potential ranked analysis for six mines assessed. 'Other' includes all inputs other than electricity

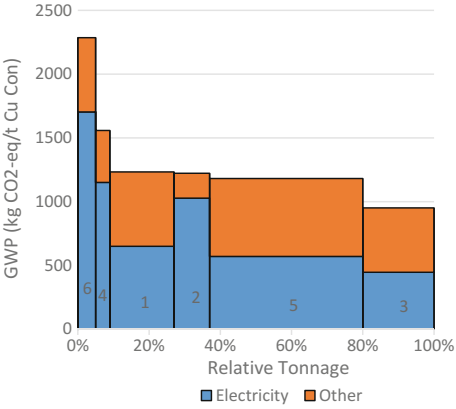

Fig. 7 Common fuel type (Natural Gas), ore grade and concentrate grade adjusted Global Warming Potential ranked analysis for six mines assessed. 'Other' includes all inputs other than electricity

Effect of Variables on GWP

Figures 4, 5, 6, 7 refer to a number of adjustments for GWP calculation that allowed comparisons between mines. Each mine is compared for each scenario by ranking mines by GWP (highest to lowest GWP from left to right). The relative tonnage is also displayed indicating a percentage milled for a particular mine out of the total milled tonnage (for all six mines assessed).

Common Fuel Type

The first notable contribution to variance in GWP can be seen from the variance in GWP factors for each fuel type used to generate electricity. Impact factors depend on the source of electricity, and range from 0.00076 for hyrdro to 1.13 kg CO_2-eq/kWh for coal. This difference in emission factors for fuel source is not particularly useful when comparing mine sites as electricity is often sourced from the grid and thus depends largely on location. This means some mines can run as a less efficient site and still contribute less towards global warming. Since electricity has such a large impact on environmental performance, it is assumed that all mines are using natural gas for electricity generation as a common basis. This allows mines to be compared in a more representative way of their actual energy consumption rather than a comparison of location/electricity grids.

Comparison of Figs. 4 and 5 show a significant change in electricity impacts. Whilst ranking did not change, the GWP for each mine (with the exception of Mine 6) became much more comparable ranging from approximately 1,100–1,600 kg CO_2-eq/t Cu con compared to the previous range of 500–1,600 kg CO_2-eq/t Cu con (Mine 6 excluded). Mine 6 changed by small amount due to the impact factor for the Portuguese electricity grid being similar to natural gas. Mine 6 also uses the

least amount of electricity for their copper plant (i.e. after proportionate mass based allocation for their other product (e.g. zinc)).

The largest changes from Figs. 4 and 5 are from Mine 5 and Mine 4. These mines both source electricity from predominantly hydroelectricity. This is expected as the GWP factor for hydroelectricity is approximately 30 times smaller than that of natural gas.

Common Fuel Type and Ore Grade

Since ore grade is known to influence energy consumption [19], the common fuel data was then scaled linearly to a common ore grade of 1%. Linear scaling was used since ore grades for the mines evaluated ranged from 0.69% to 2.72% over which the relationship between energy consumption and ore grade is approximately linear (see Fig. 8) [19]. This scaling resulted in mines originally with ore grades larger than 1% having a larger impact and mines originally with ore grades smaller than 1% having a reduced impact. The result of these three mines with a GWP over 1,000 kg CO_2-eq/t Cu con and three mines below. Two of the three mines below 1,000 kg CO_2-eq/t Cu con GWP had GWPs between 400 and 500 kg CO_2-eq/t Cu con.

There is still large variance between mines in terms of total GWP, namely Mine 1, which is more than one third larger than other mines evaluated. This suggests there are still more factors contributing individual mines energy and material consumption and the resulting impacts.

Common Fuel Type, Ore Grade and Concentrate Grade

The next variable that noticeably differed between sites was concentrate grade. A similar linear scaling to ore grade was used. This is justified by being similar to converting tonne of copper concentrate to tonne of contained copper.

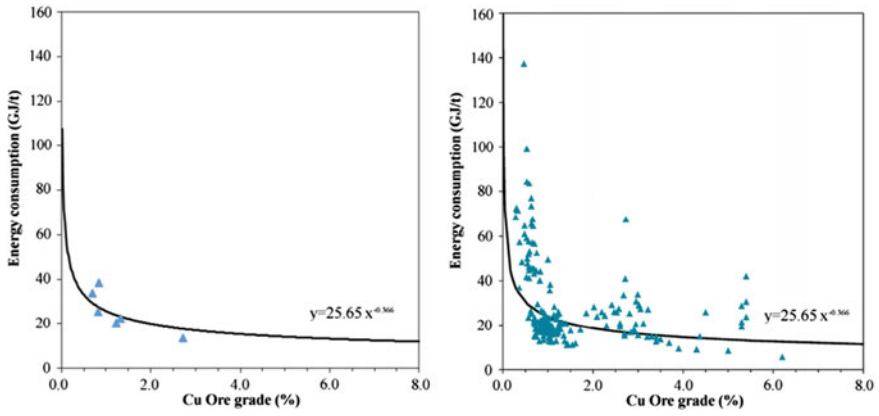

Fig. 8 Energy requirements (in GJ/t) for copper production as a function of the ore grade. (Left)-Results from this study, (Right)-Calvo et al [19]

The most notable change in the impact curve (Fig. 7) is an approximate halving of Mine 1's GWP and an approximate one third increase of Mine 6's GWP. These changes in ranking lead to two mines (Mine 6 and Mine 4) having GWP's larger than 1,500 kg CO_2-eq/t Cu con, three mines (Mine 5, Mine 1 and Mine 2) with GWP's of approximately 1,200 kg CO_2-eq/t Cu con and only one mine (Mine 3) having a GWP less than 1,000 kg CO_2-eq/t Cu con.

When scaled for common concentrate grade (i.e. approximately per tonne of copper metal) comparisons between mines show no clear relationship between energy and reagent consumption like ore grade does (see Fig. 8). This is expected since variance in ore mineralogy largely influences the concentrate grade (and extractable metal) [20]. Therefore only mines with similar ore mineralogy should be compared for this adjustment. However, information on orebodies was not always publicly available, with only dominant ore types being shown. Since orebodies can vary vastly (as discussed below in Ore Mineralogy section) and there are other factors publicly known such as mine type that influence this performance.

Open Pit Versus Underground

Comparing the GWPs of mines Mine 4, Mine 2 and Mine 6 with Mine 3 and Mine 5 in Fig. 6 suggests that the mine type influences performance. Mine 4, Mine 2 and Mine 6 are all underground mines and have significantly larger GWP from electricity consumption than diesel consumption. The open pit mines (Mine 5, Mine 3 and Mine 1), however, have a larger GWP associated with diesel consumption than electricity consumption. This difference in impact is attributable to the actual consumptions of each mine as open pit mines often use more diesel and less electricity than underground mines [18, 19].

Ore Mineralogy

Concentrate grade is affected by treatment processes and ore type [20]. For example chalcocite and bornite ores often result in concentrate grades of over 50% [20] similar to the 50% copper concentrate produced at Mine 1 while chalcopyrite ores produce concentrates of around 25% copper [20]. This further suggests that while some energy consumption depends on concentrate grade produced (due to treatment processes influencing the copper concentrate grade), the final concentrate grade is highly dependent on the ore type and thus the GWP cannot be linearly scaled for mines with different ore mineralogy.

Considering Table 1 it can be seen that there are two mines whose main copper bearing ores are bornite (one of which also has a large amount of chalcocite) both of which have the highest concentrate grades. This further supports the relationship between ore mineralogy and concentrate grade. This also suggests GWP differences depends more on the individual processes used at plants than the concentrate

grades. For example, the requirement at Mine 1 to have a regrind size of < 20 μm to remove fluorine bearing minerals increases the required comminution energy.

The gold only zone in Mine 1's orebody impacts comminution due to low grindability and high abrasivity [21]. This supports the theory that differences in ore mineralogy and hence orebody can influence GWP significantly. This is especially the case where the ore and its associated surrounding rock types are more difficult to mine and haul (increased fuel consumption) or more difficult to crush and grind (increased electricity consumption). Furthermore, Dance [22] stated that coarser or finer mill feed size can result in a ± 15% swing in tonnage for a similar hardness material. Ore hardness (bond work index) can also impact mill throughput [22] which in turn can increase the specific energy consumption of the mill. This suggests ore mineralogy can significantly affect an individual mines' environmental impact by influencing mill performance.

Mine 6 has a much larger adjusted electricity consumption than other underground mines when fuel type and ore grade are accounted for (see Fig. 6). This may be explained by the orebody containing higher levels of zinc ore (sphalerite) (for example in the massive copper-zinc ore) than other mines assessed. Sphalerite at Mine 6 can contain high levels of mercury [23]. The presence of sphalerite high in mercury can affect flotation (requiring finer grinding and extensive depression) [23]. Mine 6 also contains a cassiterite mineralisation, with an ore has a hardness up to 7 Mohs. Ore hardness is a major determinant in electricity use for grinding. The inclusion of the harder ore in the Mine 6 orebody, therefore, could explain the larger energy consumption. These factors all suggest Mine 6 should use more energy and hence have a larger GWP than mines without these ore types.

Finally, the gold only zone at Mine 1 and the range of non-copper ores contained in the Mine 6 orebody demonstrate the importance of ore body characteristics on performance. Figure 6 supports this by showing that mine sites with significant amounts of other ore/rock types in their orebody (Mine 1 and Mine 6) have a larger energy consumption compared to mines of the same type (open pit/underground).

Effect of Ore Grade on Primary Energy Consumption

Figure 8 shows a comparison of the results from this study with the results reported by Calvo et al [19]. The comparison shows a similar trends for energy consumption over a range of ore grades. This suggests that a significant variance in energy consumption is attributable to differences in ore grade.

Conclusions

Many LCA studies reported only a few impact categories largely due to the lack of certainty in impact factors. However, there is a significant wealth of knowledge available by including all available impact categories when assessing and comparing environmental impacts of mines. Inclusion of more LCA impact categories provides, at least, an indication of areas of improvement in both LCA data and mine site reporting. The lack of publicly available data reduces the ability to fully assess and progress environmental performance of individual mine sites and leads to a poor representation of the impact caused by the industry.

Key findings from this study included:

- Electricity, diesel, HiCr and steel grinding media, lime and explosives consumption consistently contributed significantly to each impact category.
- Energy consumption (diesel and electricity), in particular, largely dominated the environmental impact with a >50% contribution for most categories.
- Underground mines used more electricity than diesel compared to open pit mines and showed significant environmental savings can be made from energy efficiency and switching to renewable energy sources.
- When GWP was normalised for fuel type, the range of values reduced from 484–1,685 kg CO_2-eq/t Cu con to 677–1,666 kg CO_2-eq/t Cu con. This showed electricity grid mix was a large contributor to variance in environmental performance.
- Ore mineralogy appeared to influence energy consumption (and hence environmental impact) significantly through influencing comminution. This seemed to cause outlying values in GWP with values more than 500 kg CO_2-eq/t Cu con larger than other mines for Mine 1 and Mine 6 when data was normalised by fuel type and ore grade.
- Ignoring the outlying value of Mine 1, open pit mines were found to have a GWP of approximately 1,000 kg CO_2-eq/t Cu Con while underground mines had values between approximately 1,300–1,800 kg CO_2-eq/t Cu con. This further signifies the importance electricity grid mixes that can have on a mine's environmental performance.
- Flow sheeting and differences in mining and processing methods was shown to influence some categories. For example, Mine 2's block caving method and Mine 4's use of significant amounts of HiCr grinding media.
- There appears to compatibility issues when using impact factors for separate electricity sources. This limits the ability to compare environmental impacts of sites in locations with differing electricity grid mixes.

These results suggest that there is a potential for optimisation of environmental performance when all impact categories are taken into account. The large contribution of diesel consumption in open pit mines (approximately six times the use in underground mines) also indicates an area of improvement especially as ore grades continue to decrease and haulage energy costs increase as a result.

In general, environmental impacts varied between mines considerably due to several factors most notably: ore grade, mine type, flowsheets and ore mineralogy. This was mostly due to energy consumption being a significant contributor to most impact categories. Exploring each of these variables meant that most of the variance in environmental performance (in particular GWP) between sites could be attributed to four variables with further differences being explained by limitations in LCA and LCI data. This highlights the significance to the LCA community and mining industry of using comparative LCAs and how they can address issues associated with energy savings and correct environmental impact assessment.

Acknowledgements The authors acknowledge the financial support of CSIRO Mineral Resources through the Environmental LCA project. Input from A Roine (Technology Director, Modelling and Simulation, Outotec) is also greatly appreciated.

References

1. Santero N, Hendry J (2016) Harmonization of LCA methodologies for the metal and mining industry. Int J Life Cycle Assess 21(11):1543–1553
2. Del Borghi A (2013) LCA and communication: environmental product declaration. Int J Life Cycle Assess 18(2):293–295
3. Ford C (2015) Our value chain and its impacts-Sustainability Report 2014/15-Ford Motor Company. https://corporate.ford.com/microsites/sustainability-report-2014–15/strategy-value.html. Accessed 20 Feb 2017
4. Lee J, Cho H-j, Choi B, Sung J, Lee S, Shin M (2000) Life cycle assessment of tractors. Int J Life Cycle Assess 5(4):205–208
5. PE Americas (2010) Life cycle impact assessment of aluminium beverage cans. http://www.container-recycling.org/assets/pdfs/aluminum/LCA-2010-AluminumAssoc.pdf
6. Haapala K, Prempreeda P (2014) Comparative life cycle assessment of 2.0 MW wind turbines
7. European Copper Institute (2012) The environmental profile of copper products: a 'cradle-to-gate' life cycle assessment for copper tube, sheet and wire produced in Europe. http://copperalliance.eu/docs/default-source/resources/the-env-profile-of-copper-products_lifecycle.pdf
8. Hartmann Group (2007) The hartmann report on sustainability: understanding the consumer perspective. Bellevue, WA
9. Cone Communications/Ebiquity Global (2015) Cone Communications/Ebiquity Global CSR Study. http://www.conecomm.com/research-blog/2015-cone-communications-ebiquity-global-csr-study
10. Norgate T, Haque N (2010) Energy and greenhouse gas impacts of mining and mineral processing operations. J Clean Prod 18(3):266–274
11. Rankin J (2012) Energy use in metal production. Paper presented at high temperature processing symposium
12. Norgate T, Haque N (2013) The greenhouse gas impact of IPCC and ore-sorting technologies. Miner Eng 42:13–21
13. Suppen N, Carranza M, Huerta M, Hernández MA (2006) Environmental management and life cycle approaches in the Mexican mining industry. J Clean Prod 14(12):1101–1115
14. Mangena SJ, Brent AC (2006) Application of a Life Cycle Impact Assessment framework to evaluate and compare environmental performances with economic values of supplied coal products. J Clean Prod 14(12):1071–1084

15. Haque N, Norgate T (2014) The greenhouse gas footprint of in-situ leaching of uranium, gold and copper in Australia. J Clean Prod 84:382–390
16. Heijungs R, Ligthart T, De Koning A, Korenromp R (2004) Improvement of LCA Characterization Factors and LCA Practice for Metals. Apeldoorn, The Netherlands
17. Green Research (2011) Life Cycle Assessment: An Executive Overview of Applications, Market Drivers and Business Benefits
18. Northey S, Haque N, Cooksey M (2014) Variability in mine-site copper and gold LCI data: Reagent, fuel and electricity requirements. CSIRO, Australia
19. Calvo G, Mudd G, Valero A, Valero A (2016) Decreasing ore grades in global metallic mining: a theoretical issue or a global reality? Resources 5(4):36
20. McKay A, Miezitis Y, Porritt K, Britt A, Champion D, Cadman S, Towner R, Summerfield D, Whitaker A, Huston D, Jaireth S, Sexton M, Schofield A, Hoatson D, Senior A, Carson L (2014) Australia's identified mineral resources 2013. Commonwealth of Australia (Geoscience Australia)
21. Barns K, Colbert P, Munro P (2009) Designing the optimal flotation circuit-the prominent hill case. Paper presented at Tenth Mill Operators' Conference, Adelaide, SA
22. Dance A (2017) Grinding circuit design principles
23. Wardell Armstrong International Limited (2013) Technical Report for the Neves-Corvo Mine and Semblana Deposit, Portugal

Direct Reduction of Copper Slag Composite Pellets Within Lignite Using Biomass as Binder

Zongliang Zuo, Qingbo Yu, Huaqing Xie, Qin Qin and Mengqi Wei

Abstract The resource utilization of copper slag is an attractive option of iron resource. Thermal energy recovery and direct reduction (TER-DR) system was proposed in this study. By theoretical analysis, the exergy efficiency of this system can reach to 57.3%. To investigate the feasibility of TER-DR system, copper slag composite pellets within lignite were prepared. As a new binder, pine sawdust was added into the pellets. The diameter of pellets was 20 mm in experiments and the compressive strength of them was up to 831 N when the addition ratio of biomass was 29%. The results showed that the overall iron recovery reached to 90% and the separated iron concentrate was up to 93.5% when the temperature is at 1423 K for 90 min with CaO addition ratio of 0.3. The process reduces the secondary environmental pollution of copper slag and will be applied well in the future.

Keywords Copper slag · Waste heat recovery · Direct reduction
Biomass

Introduction

Copper smelting making process from blowing, refine and electrolysis is an essential copper production route. The production of copper has reached 16 million tons in recent years, and about 80% of it is produced by the smelting making process. As a kind of by-product of this method, for every ton of copper, about 2.2–3 tons of copper slag is produced [1]. Copper slag mainly combines of iron oxide with SiO_2 and forms to fayalite phase ($2FeO \cdot SiO_2$) and magnetite phase (Fe_3O_4). The temperature of molten copper slag is above 1573 K and the contents of iron in copper slag are 30–45%, which contains high recovery of thermal energy and its grade is much higher than that in some industrial iron ore [2, 3]. However, the thermal energy and valuable metals of copper slag can't be recovered efficiently by traditional quenching method.

Z. Zuo (✉) · Q. Yu · H. Xie · Q. Qin · M. Wei
School of Metallurgy, Northeastern University, Shenyang 110819, Liaoning, China
e-mail: zuozongliangneu@163.com

Z. Sun et al. (eds.), *Energy Technology 2018*, The Minerals, Metals & Materials Series, https://doi.org/10.1007/978-3-319-72362-4_6

Many practices have proved several methods that can be used to recover iron form copper slag. These methods include reduction method [4, 5], oxidation method [6, 7], grinding flotation method [8] and magnetic separation method [9]. Among these methods, reduction could obtain higher Fe recovery ratio and have obtained more attention. Direct reduction method is one of reduction method, and it has been applied well in the reduction of valuable metal containing wastes due to its feasibility to recovery iron [10]. Thus, it has been developed significantly in recent years, and it is an effective technology to dispose complex minerals or secondary resources containing ferrous. Followed by magnetic separation, melting separation or acid leaching separation, iron ore direct reduction process was studied [11].

Besides, thermal energy recovery of pyrometallurgy slags is a worldwide problem that is widely concerned for decades. Dry granulation presents an opportunity to produce slag particles, and the thermal energy from high-temperature slag particles is recovered by physical or chemical methods. At present, rotary cup atomizer (RCA) method, spinning disk method, rotating drum method, solid slag impingement method and air blasts method were put forward [12]. Due to the better productivity and controlled slag particle diameter afforded, RCA method has been extensively studied. Granulation characteristics of copper slag were studied by Liu [13]. There was just a small change in mean diameter of solid particles with an increase in rotating speed for copper slag with low viscosity and surface tension. This means that RCA method can be applied in waste heat recovery of copper slag.

Based on RCA method and direct reduction technology, a new thermal energy recovery and direct reduction system (TER-DR) for copper slag is put forward in this article. Enthalpy-exergy diagram was originally proposed as thermodynamic compass by Ishida [14]. Enthalpy-exergy diagram was employed for the comparison of heat recovery systems [15, 16]. This method is simple but very powerful for system design. The in-flow and out-flow enthalpy and exergy of system was calculated by this method [17]. In this study, the system was analyzed by thermodynamic compass method.

Based on the precedent experiment study, we found that biomass has wonderful adhesive property. The function of adhesion and capillary force is much higher than other reducer by cold pressed method. Thus, using biomass as binder, direct reduction characteristics and mechanism of copper slag composite pellets within lignite was studied.

System Description

Technology Process Introduction

TER-DR system is put forward in this article. Figure 1 shows a schematic of TER-DR system. TER-DR system mainly includes granulation and waste heat recovery process and direct reduction and waste heat recovery process. Granulation

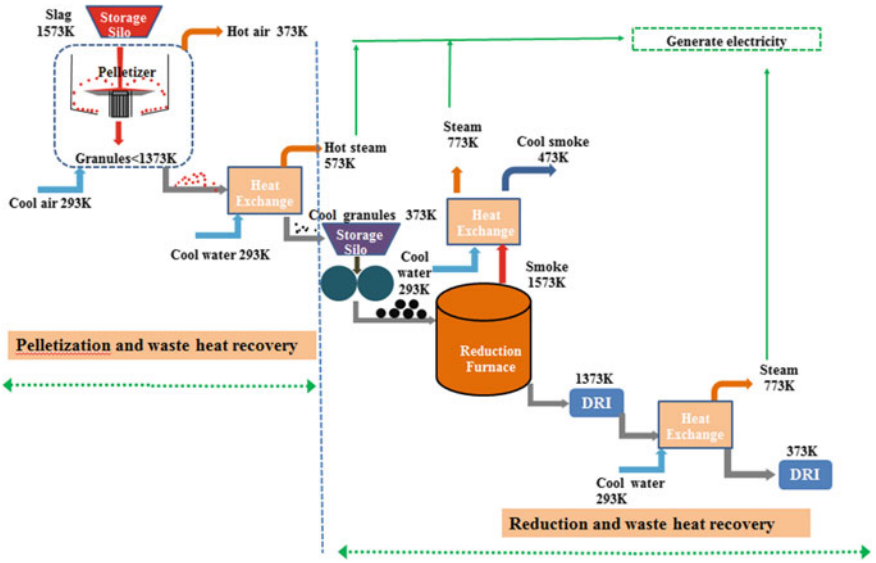

Fig. 1 Schematic of TER-DR system

and waste heat recovery process includes granulation, slag particles collection and waste heat recovery. For recovering thermal energy from high-temperature molten copper slag, molten copper slag is granulated in a rotary cup. The flying copper slag liquid drop is cooled rapidly by cold air from the bottom of particle collector. And then the copper slag particles fall into the gravity bed waste heat boiler [18]. In heat exchanger, the thermal energy of copper slag is recovered by water. After mixing with carbon contained reductants, binder and slag former, carbon-based pellets are prepared by pelletizer. After dried in drying oven, carbon-based pellets fall into reduction furnace and reduction reactions between copper slag and reductants take place. By separation of slag and iron matte, direct reduction iron (DRI) is obtained. The type of waste heat boiler is the same as above and is a gravity bed waste heat boiler. The thermal energy of high temperature flue gas is recovered by waste heat boiler.

Figure 2 shows the process schematic of TER-DR system. Unit 1–Unit5 stand for the process of Pelletizer, Waste Heat Boiler, Ball Press Machine, Rotary Hearth Furnace and Waste Heat Boiler.

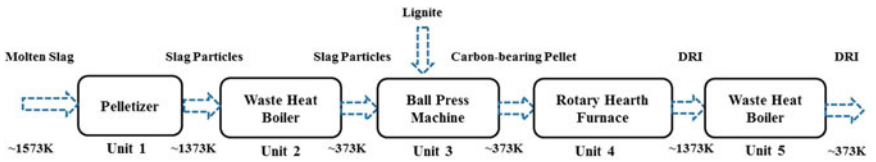

Fig. 2 The process schematic of TER-DR system

Thermodynamic Analysis

Thermodynamic analysis of designed system is a traditional method based on the first law and second law of thermodynamic. The quality of energy was in decreasing. The conversion principle could be expressed by Eqs. (1) and (2).

$$\sum_j \Delta \mathrm{H}_j = 0 \tag{1}$$

$$\sum_j \Delta \varepsilon_j \leq 0 \tag{2}$$

Where j is 1, 2, 3, 4…; $\Delta \mathrm{H}_j$ is the enthalpy change of in-flow and out-flow, MJ; $\Delta \varepsilon_j$ is the exergy change of in-flow and out-flow, MJ. We can plot any kinds of process as a vector of (ΔH, $\Delta \varepsilon$) in the enthalpy-exergy diagram. Thus, a process is expressed by a synthesis of energy process vectors. In-flow energy vector is put in the third quadrant and out-flow energy vector is put in the first quadrant. Based on the two vector lines, a parallelogram can be obtained and the diagonal coincided exactly with y axis is the exergy loss (EXL).

The calculate method of exergy change is defined as Eq. (3). If the waste heat recovery is by physical method without chemical reaction, Gibbs free energy change (ΔG) is zero. Exergy efficiency (EE) is the ratio of output exergy and input exergy.

$$\Delta \varepsilon = \Delta \mathrm{H} \cdot (T - \mathrm{T}_0)/T + \Delta \mathrm{G} \cdot \mathrm{T}_0/T \tag{3}$$

Based on different waste heat recovery methods, the energy utilization degree is determined on the follow conditions:

(1) 1 t copper slag is used in the system and the composition of copper slag is shown in Table 1.
(2) The temperature of molten copper slag put into the system is 1573 K. The solid product of the system is DRI and the production of DRI is 0.489 t. Average specific heat of the copper slag is 1100 $\mathrm{JK^{-1}kg^{-1}}$ and average specific heat of the DRI is 0.46 $\mathrm{JK^{-1}g^{-1}}$. The input enthalpy of system is 1320 MJ and the output exergy of system is 1070 MJ. The input enthalpy and exergy of pellet before reduction are 483 MJ and 770 MJ respectively.
(3) There is no thermal energy recovery in Pelletizer (Unit 1) and Ball Press Machine (Unit 3). Slag particles are heated in reduction furnace and the temperature of slag particles increases. This process isn't analyzed in this paper.

Table 1 The compositions of copper slag (wt%)

FeO	Fe_3O_4	CaO	Al_2O_3	MFe	SiO_2	Cu	MgO	S	Zn	Others
37.50	18.90	0.23	0.98	1.24	31.99	0.74	0.42	0.39	2.78	4.87

Thermodynamic Calculation Results

The assumed conditions are as follow. As shown in Fig. 2, the input temperature of copper slag in Unit 1, Unit 2 and Unit 3 are 1573 K, 1373 K and 373 K respectively. Carbon bearing pellet is heat at 1373 K in Unit 4 and DRI is cooled from 1373 K to 373 K. Hot steam is produced in Unit 2 and Unit 5 with temperature of 673 K. Besides, the thermal energy of smoke from Unit 4 is recovered. The temperature of smoke is cooled from 1573 K to 473 K and steam is produced with temperature of 773 K.

DRI is the products of direct reduction furnace and the mass of DRI is 0.489 t. The system does not deal with secondary dross from reduction furnace. Enthalpy-exergy diagram for the traditional water quenching method is shown in Fig. 3. The input exergy and enthalpy of system is 1088 MJ and 1342 MJ respectively and the output exergy of water quenching is 228 MJ. EXL of water quenching is 860 MJ. EE is 21.0%. Enthalpy-exergy diagram for the proposed system, 'Granulation and waste heat recovery process' and Unit 5 are shown in Figs. 4, 5 and 6 respectively. The EXL of 'Granulation and waste heat recovery

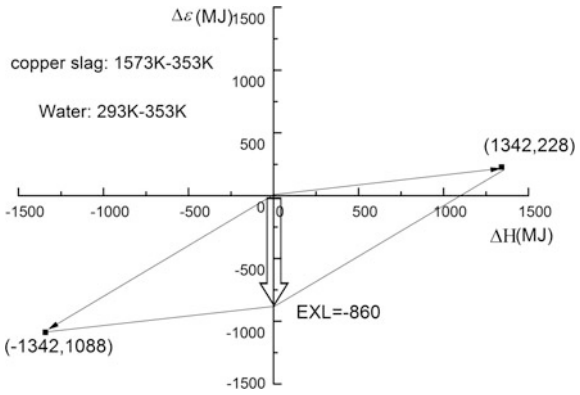

Fig. 3 Enthalpy-exergy diagram for traditional water quenching method

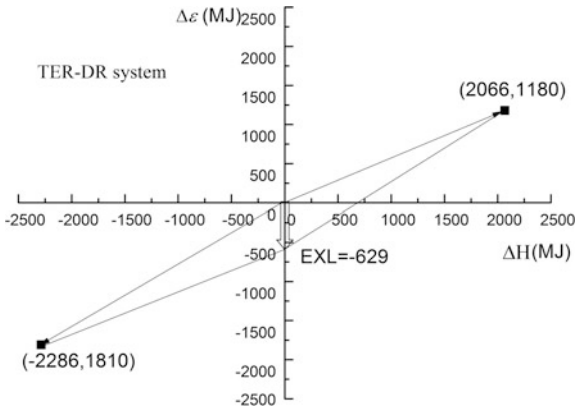

Fig. 4 Enthalpy-exergy diagram for TER-DR system

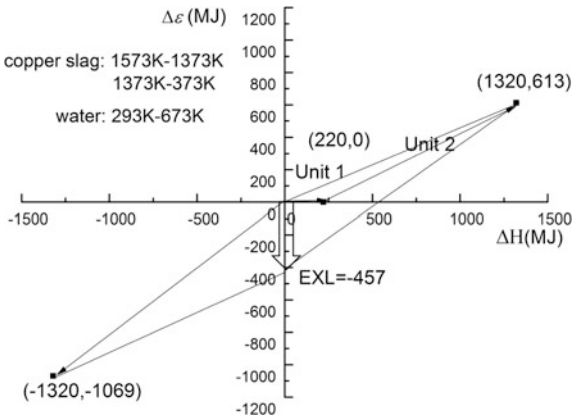

Fig. 5 Enthalpy-exergy diagram for 'Granulation and waste heat recovery process' in TER-DR system

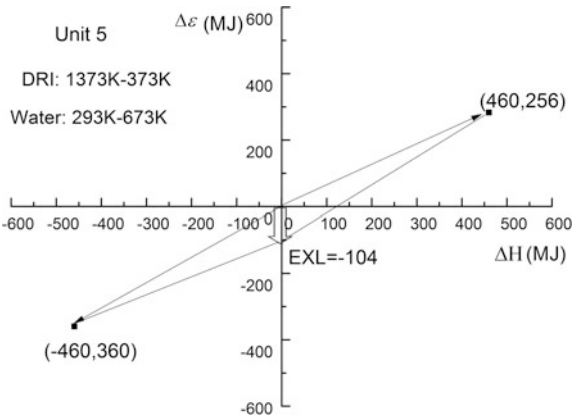

Fig. 6 Enthalpy-exergy diagram for Unit 5

process' and Unit 5 are 457 MJ and 104 MJ respectively. The EE of 'Granulation and waste heat recovery process' and Unit 5 are 57.3 and 71.1%. By TER-DR system, for every ton of copper slag, 993.7 kg steam (673 K) is acquired. Compared with conventional method, TER-DR system acquired higher quality thermal energy recovery from copper slag and the valuable metals in it are obtained. EXL of it is lower than conventional method.

Direct Reduction Feasibility Experiments

Copper slag composite pellets were prepared and the direct reduction characteristics were studied. Reducer in the experiments was lignite due to low-cost property. The proximate analysis of biomass and lignite were shown in Table 2. Copper slag, biomass, CaO and lignite were dried in vacuum drying oven at 393 K for 12 h and

Table 2 Properties of biomass and lignite

Analytical item	Biomass	Lignite
Proximate analysis (wt%)		
Moisture	5.68	3.13
Volatiles matter	85.14	32.78
Ash	1.77	29.30
Fixed carbon	7.41	34.79

then ground by crusher. The obtained copper slag, biomass and lignite samples were crushed to the size smaller than 150 μm. The experiments procedures could be described as follows: (1) Pellets preparation. The samples were mixed sufficiently. 8 g sample was put in a pellets mold. The diameter of pellets was 20 mm and then it was prepared by a ball press machine. The prepare pressure for carbon based pellets was 30–55 MPa. (2) Compressive strength test. (3) Weight. (4) Reduction. The pellets were filled into a crucible reduction reactor. The temperature was programmed and heat preservation for the reduction of copper slag. The temperature of reactor was measured. When the time was achieved, the pellets were cooled in liquid N_2. (5) Weight and analysis. After crushing and separating, DRI from reduced copper slag was analyzed by XRD and SEM-EDS.

Results and Discussion

Reduction Reactions of Copper Slag

The main iron oxides in copper slag are $2FeO \cdot SiO_2$ and Fe_3O_4.Thus, the reduction reactions of copper slag are the reduction of iron oxide with C (direct reduction) and CO (indirect reduction) as shown in Eqs. (4)–(8). Besides, gasification reaction Eq. (9) takes place at high temperature and promotes the indirect reduction of copper slag. The addition of CaO can promote the separation of Fe and Si in $2FeO \cdot SiO_2$, which is in favor of the reduction of copper slag.

$$Fe_3O_4 + C = 3FeO + CO(g) \tag{4}$$

$$FeO + C = Fe + CO(g) \tag{5}$$

$$2FeO \cdot SiO_2 + 2C = 2Fe + 2CO(g) + SiO_2 \tag{6}$$

$$Fe_3O_4 + CO(g) = 3FeO + CO_2(g) \tag{7}$$

$$FeO + CO(g) = Fe + CO_2(g) \tag{8}$$

$$2FeO \cdot SiO_2 + 2CO(g) = 2Fe + 2CO_2(g) + SiO_2 \quad (9)$$

$$C + CO_2(g) = 2CO(g) \quad (10)$$

$$2FeO \cdot SiO_2 + 2C + CaO = 2Fe + 2CO(g) + CaO \cdot SiO_2 \quad (11)$$

$$2FeO \cdot SiO_2 + 2CO(g) + CaO = 2Fe + 2CO_2(g) + CaO \cdot SiO_2 \quad (12)$$

Effects of Biomass and CaO Addition Ratio on Comprehensive Strength

The effects of pellets biomass addition and CaO addition ratio were shown in Figs. 7 and 8. With the addition of biomass, the comprehensive strength of composite pellets increased rapidly. It was as up to 831 N when the addition ratio of biomass was 29%. And when the composite pellet was mixed by biomass and copper slag exactly, the comprehensive strength was up to 2800 N. The figure illustrated that CaO can change the structure of pellets. And CaO in pellets can react with bound water of raw materials, which led to the volume expansion of pellets. The increase of volume produced small gap in pellets and decreased the compressive strength consequently.

Reduction of Copper Slag by Lignite

As shown in Fig. 9, the reduction ratios of pellets by lignite were analyzed from 1173 to 1473 K. With the increase of temperature, the reduction ratio of pellet increased gradually. And the reduction ratio of pellet with biomass as binder was

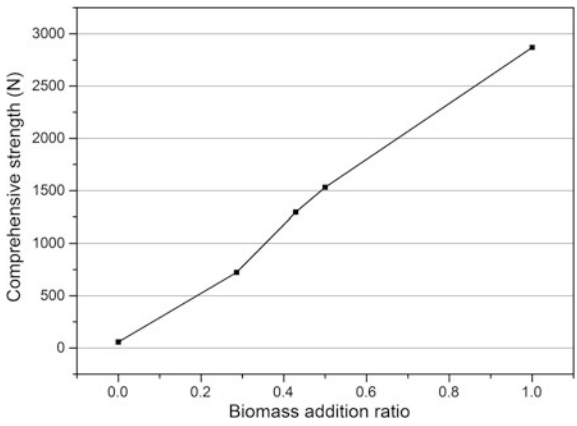

Fig. 7 Effects of biomass addition ratio on compressive strength of biomass composite pellets (50 MPa, 8 g, CaO addition = 0.3)

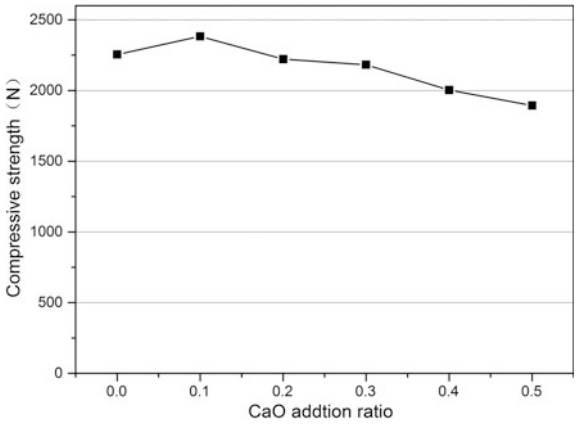

Fig. 8 Effects of CaO addition ratio on compressive strength of biomass composite pellets (50 MPa, 8 g, C/O = 1.0)

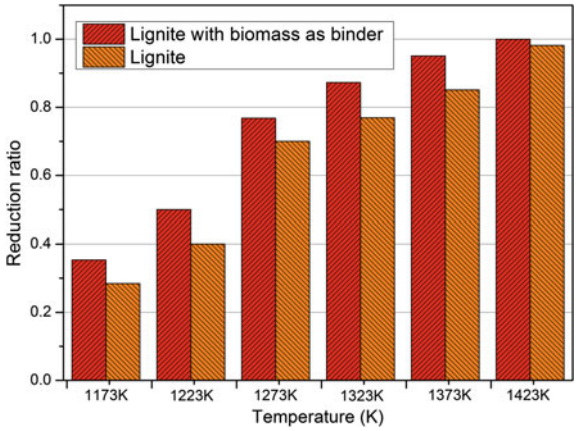

Fig. 9 Copper slag reduction ratio with the change of temperature (biomass addition 0.29, reduction time 90 min)

higher than lignite. And when the temperature was above 1423 K, reduction ratio of copper slag was higher than 0.95. The structure of biomass was porous and it increased the surface contact area of copper slag particles and biomass particles, which provided better direct reduction conditions.

Figure 10 is the SEM images of reduced composite pellets. The white spherical material was metallic iron. Human's sweating process was exactly familiar with the formation of metallic iron. The 'sweating metallic iron' reduced by lignite. Analysis by SEM images, metallic iron outflowed from cracks in pellet and it was in the formation of sphere under the effect of surface tension. With the extension of time, sphere metallic iron drops grew up. Adjacent sphere metallic iron drops would form into bulk. Therefore, massive metallic iron was formed by this method. The reduced iron was separated from pellets and the content of reduced iron and copper from copper slag are 93.5% and 2.07% respectively. It means that this method can be used to produce weathering resistant steel from copper slag.

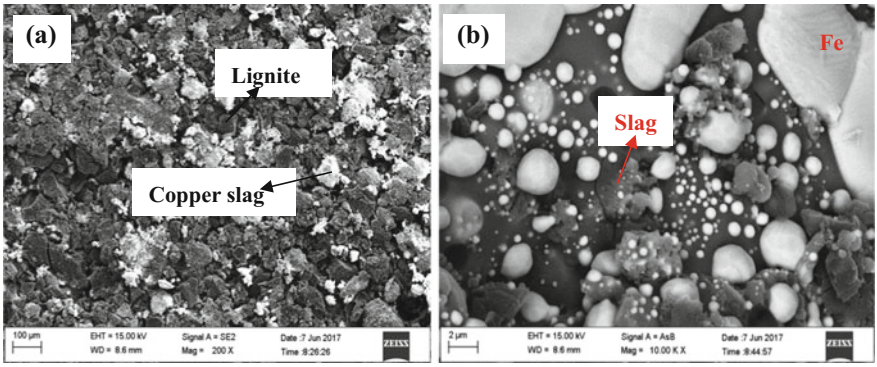

Fig. 10 SEM images of reduced composite pellets: **a** 200 X; **b** 10000 X

Conclusions

By TER-DR system based on thermodynamic compass method, for every ton of copper slag, 993.7 kg steam (673 K) is acquired. TER-DR system acquired higher quality thermal energy recovery from copper slag and the valuable metals in it are obtained. EXL of it is lower than conventional method.

To verify the feasibility of this system, direct reduction characteristics were studied. Copper slag-lignite composite pellet was prepared using biomass as binder. The compressive strength of composite pellets was improved with the addition of biomass. Human's sweating process was exactly familiar with the formation of metallic iron. The 'sweating metallic iron' was reduced by lignite. The process reduces the secondary environmental pollution of copper slag and will be applied well in the future.

References

1. Fan Y, Shibata E, Iizuka A, Nakamura T (2014) Crystallization behaviors of copper smelter studied using Time-Temperature-Transformation Diagram. Mater Trans 55(6):958–963
2. Gorai B, Jana RK, Premchand (2003) Characteristics and utilisation of copper slag—a review. Resour Conserv Recycl 39(4):299–313
3. Palacios J, Sánchez M (2011) Wastes as resources: update on recovery of valuable metals from copper slags. Miner Process Extr Metall 120(4):218–223
4. Heo JH, Kim BS, Park JH (2013) Effect of CaO addition on iron recovery from copper smelting slags by solid carbon. Metall Mater Trans B 44(6):1352–1363
5. Zhang H, Shi X, Zhang B, Hong X (2013) Reduction of molten copper slags with mixed CO-CH_4-Ar gas. Metall Mater Trans B 45(2):582–589
6. Zhang LZ, Zhang L, Wang MY (2005) Oxidization mechanism in CaO-FeOx–SiO_2 slag with high iron content. Trans Nonferr Met Soc China 15(4):938–943
7. Gyurov S, Rabadjieva D, Kovacheva D, Kostova Y (2014) Kinetics of copper slag oxidation under nonisothermal conditions. J Therm Anal Calorim 116(2):945–953

8. Bruckard WJ, Somerville M, Hao F (2004) The recovery of copper, by flotation, from calcium-ferrite-based slags made in continuous pilot plant smelting trials. Miner Eng 17 (4):495–504
9. Warczok A, Riveros G (2007) Slag cleaning in crossed electric and magnetic fields. Miner Eng 20(1):34–43
10. Wang CL, Yang HF, Jiang BP, Zhang JL, Lu LF, Tang QY (2014) Recovery of iron from lead slag with coal-based direct reduction followed by magnetic separation. Adv Mater Res 878:254–263
11. Yang HF, Dang CG, Xu W (2011) Preparation of geopolymer using the slag from direct reduction-magnetic separation of refractory iron ore (SDRMS). Adv Mater Res 383–390:911–915
12. Barati M, Esfahani S, Utigard TA (2011) Energy recovery from high temperature slags. Energy 36(9):5440–5449
13. Liu J, Yu Q, Zuo Z, Duan W, Han Z, Qin Q, Yang F (2016) Experimental investigation on molten slag granulation for waste heat recovery from various metallurgical slags. Appl Therm Eng 103:1112–1118
14. Ishida M (1995) Thermodynamics-its perfect comprehension and applications-(in Japanese). Baifukan (93)
15. Akiyama T, Oikawa K, Shimada T, Kasai E, Yagi J (2000) Thermodynamic analysis of thermochemical recovery of high temperature wastes. ISIJ Int 40(3):286–291
16. Duan W, Yu Q, Qin Q, Hou L (2014) Thermodynamic analysis of bf slag waste heat recovery system using enthalpy-exergy diagram. J Northeast Univ (Nat Sci) 35(11):1566–1570
17. Akiyama T, Yag J (1998) Methodology to evaluate reduction limit of carbon dioxide emission and minimum exergy consumption for ironmaking. ISIJ Int 38(8):896–903
18. Liu J, Yu Q, Peng J, Hu X, Duan W (2015) Thermal energy recovery from high-temperature blast furnace slag particles. Int Commun Heat Mass Transfer 69:23–28

Thermodynamic Analysis of Incineration Treatment of Waste Disposable Syringes in an EAF Steelmaking Process

Maryam Ghodrat and Bijan Samali

Abstract Disposal of waste syringes in a safe and eco-friendly way has been an issue of considerable scale for decades. The generated amount of waste syringes has escalated with the rapid growth in population and wide acceptance towards single-use medical devices. Some hospitals have their own on-site incinerators, but recent tightening of air quality regulations and landfill levies led to the closure of many on-site incinerators. The solution to this problem implicates the development of an environmentally-sound method that would employ these waste materials. This work investigates a thermodynamic modelling approach for incineration treatment of waste plastic syringes in Electric Arc Furnace (EAF) steelmaking. Mass balance was obtained from HSC Chemistry thermochemical package. The results indicate that the rate of iron oxide reduction in the slag is higher when coke is partially replaced by waste plastic syringes. Furthermore, the amount of dust and stack gas emission was reduced by around 0.4% and 1.25% respectively by replacing 20%-weight of pure coke with waste plastic syringes. The study demonstrates part of the coke can be successfully replaced by waste plastic syringes in electric arc furnace to provide additional energy from combustion without affecting the main process

Keywords Thermodynamic analysis · Waste plastic syringes · Incineration Electric arc furnace · Coke

M. Ghodrat (✉) · B. Samali
School of Computing, Engineering and Mathematics,
Centre for Infrastructure Engineering, Western Sydney University, Sydney, NSW, Australia
e-mail: M.ghodrat@westernsydney.edu.au

B. Samali
e-mail: B.Samali@westernsydney.edu.au

Z. Sun et al. (eds.), *Energy Technology 2018*, The Minerals, Metals & Materials Series, https://doi.org/10.1007/978-3-319-72362-4_7

Introduction

Medical waste, including waste syringes has raised serious concerns because of the possible inappropriate treatment and final disposal practices afforded to them. Inappropriate treatment can result in negative impacts to public health and to the environment. In recent years, Australia has experienced rapid population growth and seen the introduction of new legislation and agreements by the government to generate national waste management policies. Australia's reporting to the Basel Convention reveals that 59,000 tonnes per annum of medical waste is generated from medical facilities and pharmaceutical production waste. This accounts for 8.14% of the total waste generated in Australia [1]. Medical wastes historically have been disposed of in landfills or treated in incinerators located in the health care facilities or off-site [2]. Incineration has been the most widely used treatment technology for the disposal of medical waste especially waste syringes and has the potential to continue to be an important waste disposal option. The main reason is incineration sterilizes and detoxifies the wastes through combustion process and destroys pathogens and reduces the volume of waste [3]. Heat can also be recovered from the waste incineration process [4]. In the case of waste plastic syringes with a high calorific value of about 47 MJ/kg [5], the process of thermal disposal is an attractive option from the energy recovery point of view. Many researchers investigated the possibility of the heat recovery out of medical waste incineration. Kenyon described heat recovery from hospital systems of medical waste incineration [6]. He discussed the possibility of producing steam using waste heat from the incineration of medical waste. Bujak reported experimental studies of useful energy flux and the thermal efficiency coefficient of the system of thermal conversion of waste, including heat recovery [7]. On the other hand using waste plastic syringes in electric arc furnace (EAF) steelmaking has numerous benefits both economically and environmentally [8]. Waste plastic can partially replace coke as a carbon source with substantial savings in electricity and carbon usage [9]. Since carbon and hydrogen are the main components of waste plastics, they have the potential to be utilised as a substitute for coke in EAF [10]. Asanuma [11] studied the use of waste plastics in a commercial blast furnace and the raceway hot model at NKK Corporation and found the combustion performance is higher when plastics are involved. Kim et al., [12] measured the combustibility of polyethylene by changing experimental variables in a modelled blast furnace and found the energy efficiency escalated with increasing blast furnace temperatures, the amount of oxygen injected into the furnace and by using smaller particle size. Gupta [13] investigated the simultaneous combustion of polyethylene with coal and found no adverse effects on the combustion efficiency. The use of waste tyre as a partial fuel substitute for coke in EAF was also studied experimentally by [14, 15]. Using thermodynamic analysis to trace and explore industrial and environmental problems is well established [16]. Development of Gibbs energy models and computer codes for the calculation of complex equilibria have led the researchers to rely on the theoretical studies to explain the behaviour of a great number of chemical reactions under different

conditions [17]. In this study, a detailed thermodynamic analysis of incineration treatment of waste plastic syringes in EAF steelmaking has been carried out. The mass balance flowsheet of the process has been developed and compared with the conventional pyrometallurgical process in EAF with pure coke. Thermodynamic based modelling of waste plastic treatment by incineration can provide insights on the fundamental limit of the slag and off gas composition as well as the purity of the iron and how the waste behaves at the high temperature during the process. The results can then be used as a basis for the development of a complete flowsheet to evaluate the mass and energy balance, the techno-economic e.g. [8] and the life cycle analysis of the process e.g. [18, 19]. The present paper highlights the benefits brought by the usage of recycled materials in EAF to enhance its sustainability.

Process Overview

The primary raw material used in the EAF steelmaking process is ferrous scrap, which is melted using electric energy. Power is supplied to the furnace through the electrodes. After formation of electrical arc, the temperature is raised to 1600 ^{o}C. Additional inputs include fluxes and other alloying materials such as coke, waste plastic syringes, de-oxidation materials, etc. along with oxygen and natural gas also added to the molten scrap and mixed to remove some small amounts of impurities [20]. After that, the molten steel is tapped into the secondary refining furnace (special furnace such as ladle furnace (LF)) where the strong heat fluxes can be supplied to obtain the desired chemical composition of the steel. The whole system of EAF production processes of this study is shown schematically in Fig. 1.

Materials and Operating Condition

Electric Arc Furnace (EAF) uses different carbon based materials as foaming agents. In this study, the possibility of replacing coke with waste plastic syringes has been investigated. Waste plastic syringes were mixed in the proportion of 20:80

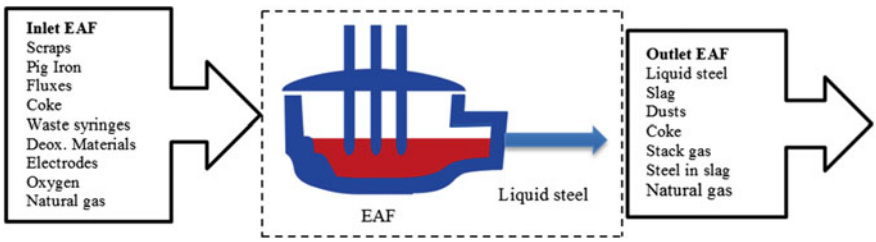

Fig. 1 Schematic for inlet and outlet materials in EAF

Table 1 Selected composition of scrap, pig iron and de-oxidation materials used in the feed of EAF (wt%)

wt%	Fe	C	Si	Mn	P	S	Cr	Ni	Mo	Cu	Al	Zn
Scrap	97.31	0.55	0.35	0.5	0.025	0.035	0.9	0.1	0.03	0.2	–	–
Pig Iron	94.27	3.5	–	1	0.15	1	–	–	–	–	–	–
De-oxidation materials	9	1.48	16	62	0.1	0.22	–	–	–	–	11	0.2

Table 2 Selected composition of flux used in the feed of EAF (wt%)

wt%	CaO	MgO	Al	CaCO3	SiO2	Ni	Zn	Ca	Al2O3	Fe2O3
Flux	50	40.03	1.72	6	1	0.1	1	0.15	–	–

Table 3 Selected composition of coke and waste plastic syringes used in the feed of EAF (wt%)

wt%	C	SiO2	Al2O3	Fe2O3	CaO	SiO2	H	N2	Cl	O2
Coke	88.5	4	5	1	1	0.5	–	–	–	–
Waste plastic syringes	78.38	–	–	–	–	–	11.62	0.25	1.16	15.453

with coke for combustion at the temperature range of 1100–1600 °C and oxygen partial pressure $pO10^{-1}$–$pO10^{-4}$. A total input rate of 65,430 kg/h of feed materials, composed of approximately 93 wt% ferrous scrap/metal oxides, and 7 wt% reductant (coke was chosen as reductant) was fed into the reduction furnace. 20% of the coke was replaced by the waste plastic syringes for the purpose of the modelling. This composition represents an amount of 180 kg/h (in weight) of waste plastic syringes input into the furnace. The compositions of the main feed utilised in this study are taken from [21] and presented in Tables 1, 2 and 3. The basic chemical reactions taking place in the electric arc furnace (EAF) are given in Table 4 and can also be found in Refs [22, 23].

Thermodynamic Modelling

In this study, combined chemical thermodynamic and process flowsheet modelling were conducted to assess and describe the material and energy flow during processing of ferrous scrap, reductant, metal oxide and waste plastic syringes in an EAF smelting route. It is assumed that 20% of the coke in the feed materials had been replaced by the waste plastic syringes. For simplicity, the considered scenario named (20% WS) throughout the paper. Thermochemical packages of FactSage 7.0 and HSC Chemistry Sim 8.0 were used for the modelling. The elements listed in

Table 4 Standard chemical reactions occurring in EAF

Reactions	
$2[Fe] + 3[O] \rightarrow [Fe_2O_3]$	$2[Cr] + 3[O] \rightarrow [Cr_2O_3]$
$[Fe] + [O] \rightarrow [FeO]$	$(CaO) + [S] \rightarrow (CaS) + [O]$
$[C] + [O] \rightarrow CO_{(g)}$	$(CaCO_3) \rightarrow (CaO) + CO_{2(g)}$
$[Si] + 2[O] \rightarrow [SiO_2]$	$2[Al] + 3[O] \rightarrow [Al_2O_3]$
$[Mn] + [O] \rightarrow [MnO]$	$[Ca] + [O] \rightarrow (CaO)$
$2[P] + 5[O] \rightarrow [P_2O_5]$	$[Zn] + [O] \rightarrow [ZnO]$

[]:Solid; ():liquid; (g):gas

Tables 1, 2 and 3 were included in the modelling. The HSC Chemistry Sim 8.0 was used to develop an Ellingham diagram to predict the stability of selected metal oxides (Fe_2O_3, MgO, CaO, SiO_2, Al_2O_3); as well as to develop the process flow sheet of EAF along with the mass balance. The HSC Chemistry 8.0 uses thermodynamics data from Barin and JANAF databases [24]. The FactSage 7.0 uses "Equilib" module to predict phase equilibria and to finalise the detailed elements and phases distribution in EAF as shown in Figs. 2 and 3. The "Equilib" module includes the Gibbs free energy minimization system to estimate the equilibrium of multicomponent systems at various processing states. Optimised databases for multicomponent systems and their related slags were used for this study; that include FactPS (for pure substances), FToxide (for oxides and slag), and FTmisc-FeLQ (for liquid iron) [25]. The multicomponent systems composed of FeO, Fe2O3, SiO2, CaO, and Al_2O_3 had been optimised for the whole range of compositions and valid for calculation between 1000 and 1600 °C. The liquid oxides (slags) were modelled using a modified quasichemical model which explains the short-range ordering of components [8]. It should be noted that FeO also considered as an integral component of slag in this study and assumed to follow ideal solution using rough interaction parameters. The equilibrium calculations

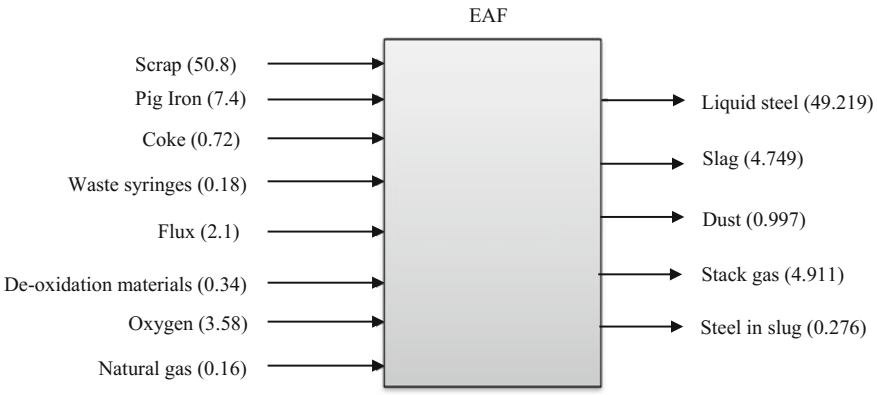

Fig. 2 Mass balance for incineration treatment of waste plastic syringes in an EAF (20%WS)-unit in tonne

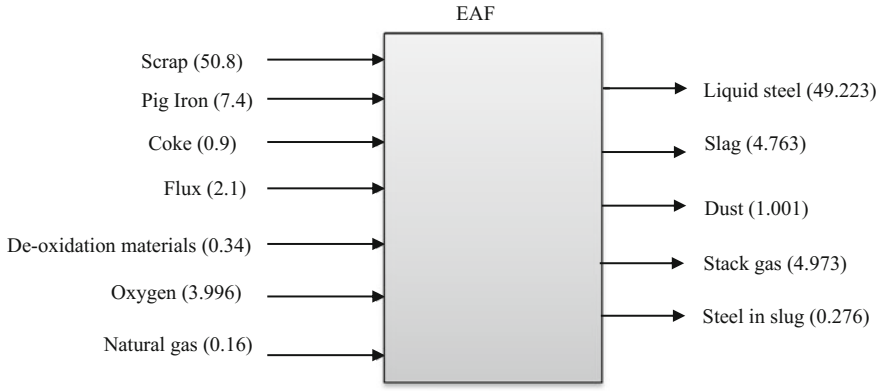

Fig. 3 Mass balance for conventional incineration process in EAF with pure coke (CI)-unit in tonne

were conducted at temperatures ranging from 1000 to 1600 °C with oxygen partial pressures (pO_2) varying from 10^{-1} to 10^{-4} atm (which shows different reducing conditions).

Results and Discussion

The result of the mass balance for incineration treatment of waste plastic syringes in an EAF process (20%WS) is shown in Fig. 2. The mass balance for conventional incineration process in EAF with pure coke (CI) is presented in Fig. 3. The values shown in the input and output streams of Figs. 2 and 3 indicate the amount of the materials flow in tonne. A comparison between the input and output values in Figs. 2 and 3 shows that the amount of dusts and stack gas emission was reduced up to around 0.4% and 3.1% respectively by replacing 20%-weight of pure coke with waste plastic syringes.

The EAF operation started with the charging of the furnace with the input materials. Refining operations in the electric arc furnace involved the removal of phosphorus, sulfur, aluminum, silicon, manganese and carbon from the steel. Oxygen was injected at the end of meltdown to reduce the carbon content to the desired level. Most of the compounds which are to be removed during refining have a higher affinity for oxygen than the carbon. Thus the oxygen will preferentially react with these elements to form oxides which float out of the steel as stack gas and into the slag. To understand the general stability of selected oxides present in the feed materials, an Ellingham diagram was developed, as shown in Fig. 4. The predicted order of stability at 1500 °C is from $Al_2O_3 > SiO_2 > CaO > MgO > FeO$. Therefore, in a suitable reducing condition, it could be expected that FeO reduced first before MgO, CaO, SiO_2, and Al_2O_3. During the reduction process in (20% WS) in EAF, most of the

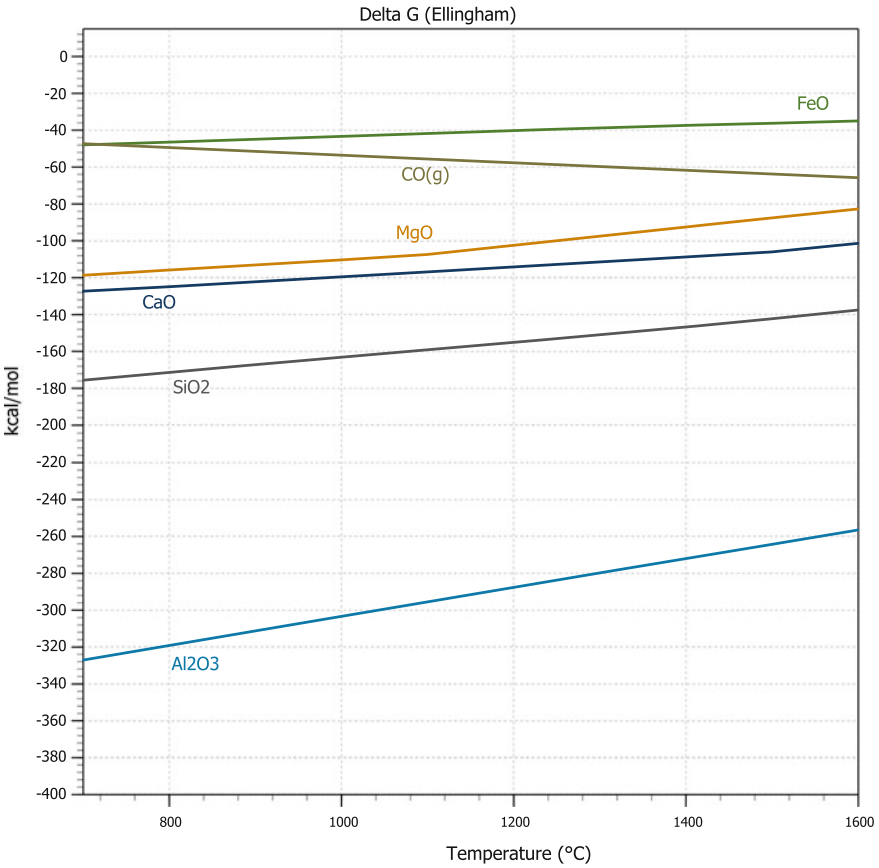

Fig. 4 Gibbs free energy formation of various oxides and CO (g)

impurities, such as Mg, Si, Ca, Al, Ni, and Zn, were predicted to segregate in the liquid steel, although some of them were also distributed to the slag and vapour phases. The simplified reactions for the major elements can be seen in the followings equations:

$$\mathrm{C} + 1/2\,\mathrm{O}_{2(\mathrm{g})} = \mathrm{Co}_{(\mathrm{g})} + \mathrm{heat} \tag{1}$$

$$(\mathrm{FeO}) + \mathrm{CO}_{(\mathrm{g})} = \underline{\mathrm{Fe}} + \mathrm{CO}_{2(\mathrm{g})} \tag{2}$$

$$(\mathrm{MgO}) + \mathrm{CO}_{(\mathrm{g})} = \underline{\mathrm{Mg}} + \mathrm{CO}_{2(\mathrm{g})} \tag{3}$$

$$(\mathrm{CaO}) + \mathrm{CO}_{(\mathrm{g})} = \underline{\mathrm{Ca}} + \mathrm{CO}_{2(\mathrm{g})} \tag{4}$$

$$(Al_2O_3) + 3CO_{(g)} = 2\underline{Al} + 3CO_{2(g)} \quad (5)$$

The bracket "()" indicates that the compound is in solution in liquid slag, and under bar "_" means that the metal is in solution in liquid iron. During the reduction process in EAF, the heat and the reducing condition were supplied by the combustion of excess coke plus waste plastic syringes by the oxygen supplied in the feed materials, which given in Eq. 1. The carbon monoxide which produced from Eq. 1 reduced some of the metal oxides into metals that are segregated in the liquid metal phase (liquid steel), as described in Eqs. 3–5. Fluxes were added to react with the unreduced oxides such as SiO2 from liquid slag.

Reduction of iron oxide by hydrogen, carbon and carbon monoxide are given in Eqs. 6–8 [9].

$$\underline{FeO} + H_{2(g)} = Fe_{(l)} + H_2O_{(g)} \quad (6)$$

$$\underline{FeO} + C_{(s)} = Fe_{(l)} + CO_{(g)} \quad (7)$$

$$\underline{FeO} + CO_{(g)} = Fe_{(l)} + CO_{2(g)} \quad (8)$$

The equilibrium concentration of Fe in the liquid steel (which also represents the iron purity) at various oxygen partial pressures (pO2) and temperatures was predicted for the incineration treatment of waste plastic syringes in EAF (20%WS) and shown in Fig. 5. It can be seen from Fig. 5 that at oxygen partial pressure (pO_2) of 10^{-4}, the purity of iron was predicted to increase from 69.2 to 99.2 wt% with increasing temperature from 1100 to 1600 °C. Similar trends were predicted with increasing temperatures at pO2 of 10^{-3}, 10^{-2}, and 10^{-1} atm. Overall, the purity of iron was predicted to increase with increasing temperature at the considered oxygen partial pressures. The changes in the impurities' concentrations (Cu, Ni, Mo and S) in the liquid phase with pO2 at 1500 °C for 20%WS was predicted and shown in Fig. 6. It was predicted that, at 1500 °C, pO2 has little effect (less than 1.2 wt%) on the equilibrium concentration of S in the liquid iron. However, the dissolution of Ni and Mo to the liquid iron was predicted to slightly increase when the pO2 is decreased to 10^{-4} atm. As it can be seen from Fig. 6, the dissolution of copper to the liquid phase marginally decreased with decreasing oxygen partial pressure.

The change in the slag composition during reduction with temperature for the 20%WS scenario is shown in Fig. 7. The liquid slag was predicted to mainly compose of Al_2O_3, SiO_2, CaO, MgO and FeO. At 1100 °C, the predicted percentage of FeO and CaO in slag is higher than 30 wt%, and Al_2O_3 is close to 10 wt%, as given in Fig. 7. At temperatures > 1500 °C, CaO, MgO and Al2O3 content in the slag decreased and predicted to become unstable and decompose and join to the off gases. SiO2 was predicted to increase with increasing of temperature up to 1500 °C and then decease with further rise in the temperature. The predicted amount of FeO in the slag is 35 wt% at 1500 °C and pO2 = 1.01 atm that represents the loss of iron in slag during the reduction process. The overall trend in

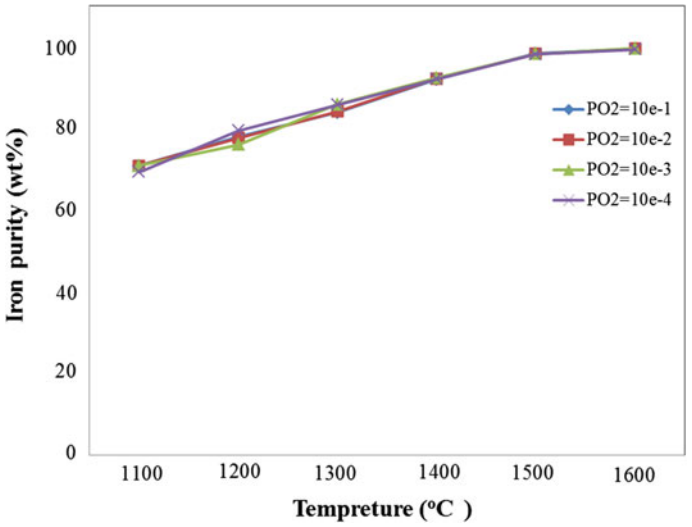

Fig. 5 Change in the iron purity as a function of temperature and oxygen partial pressure (pO_2)–20%WS

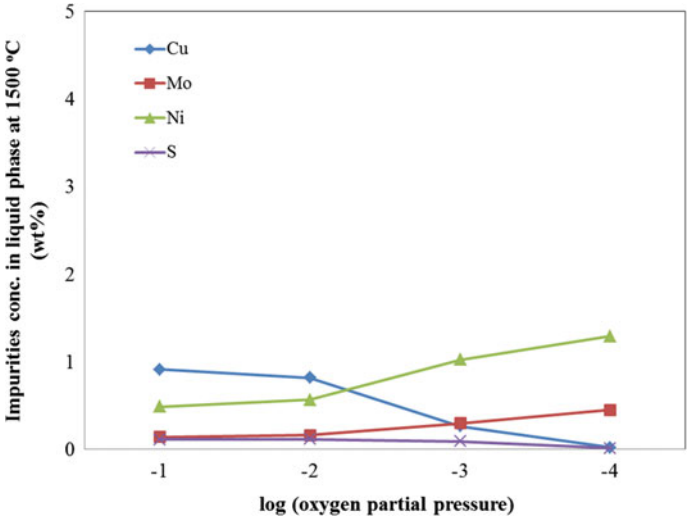

Fig. 6 Change in the concentrations of impurities in the liquid iron at 1400 °C at pO2 from 10^{-1} to 10^{-4} atm for 20%WS

Fig. 7 showed that temperatures above 1500 °C are required to avoid the formation of solid phases during reduction process in 20% WS scenario.

From the comparison of both scenarios, it could be suggested that, thermodynamically, the processing of waste plastic syringes through EAF steelmaking is

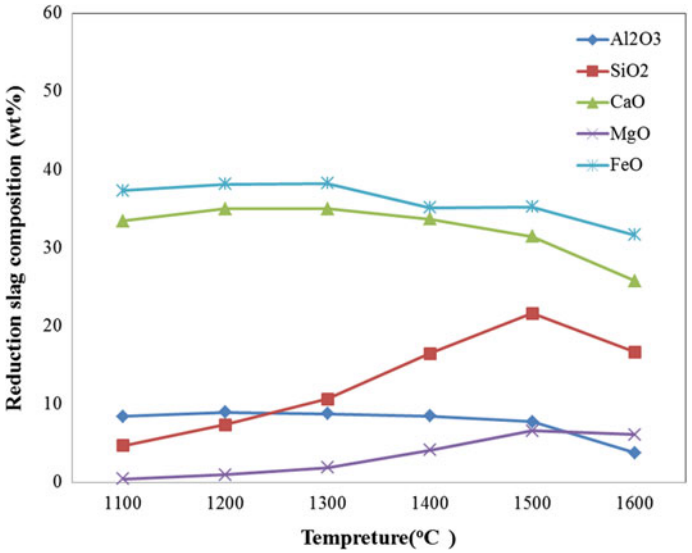

Fig. 7 Change in the slag composition in the reduction stage of the 20%WS with temperature at pO2 = 1.01 atm

feasible from two main points of view: first to provide additional energy from combustion and second to find a potential alternative for treating plastic medical waste and avoid sending them to the landfill. In the 20%WS scenario, the final recovery of steel was predicted to be slightly lower than CI. In contrast, the dust and stack gas emitted from 20%WS scenario is lower than CI scenario which led to better environmental impact for the proposed recycling route. One of the benefits of waste plastic syringes recycling is the utilisation of carbon as fuel and reductant in the EAF smelting process. In CI scenario, carbon (in the form of coke) supplied in the feed material which generates heat and acts as reducing agent (CO). On average, waste plastic syringes composed of 78–80% carbon. Replacing part of coke with this waste hence may result in better economic revenue for the process and reduce environmental burden associated with coke making.

Conclusion

In this study, the mass balance for two defined scenarios, 20%WS (incineration treatment of waste plastic syringes in an EAF process-20% of coke replaced by waste plastic syringes) and CI (conventional incineration in EAF with pure coke), supported by thermodynamic modelling have been developed using HSC Chemistry 8.0 and FactSage 7.0 thermodynamic packages. The results of the study indicated that the final recovery of steel in 20%WS scenario is slightly lower than

CI scenario. However the dusts and stack gas emitted from 20%WS scenario is marginally lower compared to that of CI scenario. This caused a lower environmental impact for the proposed recycling route of plastic medical waste (e.g. waste syringes). It was also predicted that temperatures above 1500 °C are required to avoid the formation of solid phases during reduction process in 20%WS scenario. Solid phases, such as CaS(s), SiS2(s), Al2S3(s) were predicted to form that remain stable below 1500 °C and, therefore, can adversely obstruct the plastic waste recycling process. The results also predicted that at 1500 °C, oxygen partial pressure (PO2) has insignificant effect on the concentration of impurities in the liquid iron. Based on the trial calculation of different waste plastic proportion in the coke it has also been concluded that a higher addition of waste plastic increases the slag generation, and therefore, the temperature of the liquid slag is shifted to higher temperature that requires the close monitoring of slag composition (e.g. addition of the appropriate amount of fluxes). It is also worthwhile to consider that the analysis presented in this study was based on thermodynamic online modelling aspect and did include the kinetic factors. Realistically, kinetic limitations can play an important role to the processing of waste through EAF smelting route.

References

1. Randell P, Pickin J, Grant B (2014) Environ Prot Agency Victoria. Publ Blue Environment Pty Ltd, Canberra
2. Hutchens SL, Strutz L (1998) Proceedings of a waste managematnt association annual meeting and exhibition, p 8
3. Lee B-K, Ellenbecker MJ, Moure-Ersaso R (2004) Waste Manag 24:143
4. Bujak JW (2015) Energy 90:1721
5. Sahajwalla V, Zaharia M, Kongkarat S, Khanna R, Rahman M, Saha-Chaudhury N, O'Kane P, Dicker J, Skidmore C, Knights D (2011) Energy Fuels 26:58
6. Kenyon D (1996) ASHRAE J 38
7. Bujak J (2009) Appl Energy 86:2386
8. Ghodrat M, Rhamdhani MA, Brooks G, Masood S, Corder G (2016) J Clean Prod
9. Dankwah JR, Koshy P, Saha-Chaudhury NM, O'Kane P, Skidmore C, Knights D, Sahajwalla V (2011) ISIJ Int 51:498
10. Sahajwalla V, Zaharia M, Kongkarat S, Khanna R, Saha-Chaudhury N, O'Kane P (2009) Energy Fuels 24:379
11. Asanuma M, Ariyama T, Sato M, Murai R, Nonaka T, Okochi I, Tsukiji H, Nemoto K (2000) ISIJ Int 40:244
12. Kim D, Shin S, Sohn S, Choi J, Ban B (2002) J Hazard Mater 94:213
13. Gupta S, Sahajwalla V, Wood J (2006) Energy Fuels 20:2557
14. Sahajwalla V, Zaharia M, Kongkarat S, Khanna R, Rahman M, Saha-Chaudhury N, O'Kane P, Dicker J, Skidmore C, Knights D (2012) Energy Fuels 26:58
15. Zaharia M, Yunos NF, Sahajwalla V (2012) Mater Struct Adv Innov 21
16. Hack K (2011) Pure Appl Chem 83:1031
17. Ghodrat M, Rhamdhani MA, Khaliq A, Brooks G, Samali B (2017) J Mater Cycles Waste Manag 1
18. Ghodrat M, Rhamdhani MA, Brooks G, Rashidi M, Samali B (n.d.) Environ Dev
19. Ghodrat M, Rhamdhani MA, Sharafi P, Samali B (2017) Metall Mater Trans E

20. Ekmekçi Ī, Yetisken Y, Çamdali Ü (2007) J Iron Steel Res Int 14:1
21. Çamdali Ü, Tunç M, Karakaş A (2003) Energy Convers Manag 44:961
22. Schroeder DL (1990) 48th electrical furnace configuration proceedings, pp 417–428
23. Lankford WT (1985) The making, shaping, and treating of steel (Association of iron and steel engineers)
24. Bale CW, Chartrand P, Degterov SA, Eriksson G, Hack K, Ben Mahfoud R, Melançon J, Pelton AD, Petersen S (2002) Calphad 26:189
25. Bale CW, Bélisle E, Chartrand P, Decterov SA, Eriksson G, Hack K, Jung I-H, Kang Y-B, Melançon J, Pelton AD, Robelin C, Petersen S (2009) Calphad 33:295

The Reduction Kinetic of the Combined Cu-Based Oxygen Carrier Used for Chemical Looping Gasification Technology

Kun Wang, Weipeng Luan, Qingbo Yu and Qin Qin

Abstract The oxygen uncoupling property of the oxygen carrier is essential for the chemical looping gasification process. In this paper, the combined Cu-based oxygen carrier were prepared by mechanical mixing method. XRD and SEM were used to characterize the oxygen carrier prepared. TG experiments were performed in a thermal analyzer to investigate the oxygen uncoupling property. The XRD pattern of the fresh oxygen carriers showed that the phases of the oxygen carriers were stable. The active phase of oxygen carrier was $Cu_xMn_{3-x}O_4$. With the increasing of heating rate, the starting and ending temperatures of the reduction reaction increased. However, the reaction time decreased and the reduction rate increased. With the increasing of oxygen concentration, the starting temperatures of the reduction reaction shifted to high level. Temperature had great effect on the reduction rate and the reduction rate increased with increasing of the reduction temperatures.

Keywords Chemical looping gasification · Biomass
Combined Cu-based oxygen carrier · Reduction · Property

Introduction

Biomass gasification is a process which converts biomass to gas fuel through thermal-chemical reaction. The main products of gasification are H_2, CH_4, CO, CO_2 and other hydrocarbons. At present, the gasification agents of biomass are mainly air, O_2, H_2O, CO_2 and H_2O/O_2, H_2O/air [1, 2]. Compared to other types of gasification agents, oxygen has advantages of high gasification efficiency, high carbonization rate, and high concentration of combustible gas in syngas [3]. However, the high energy consumption and high oxygen production cost of the present

K. Wang · W. Luan · Q. Yu (✉) · Q. Qin
School of Metallurgy, Northeastern University, No. 11, Lane 3, WenHua Road, HePing District, Shenyang 110819, Liaoning, People's Republic of China
e-mail: yuqb@smm.neu.edu.cn

Z. Sun et al. (eds.), *Energy Technology 2018*, The Minerals, Metals & Materials Series, https://doi.org/10.1007/978-3-319-72362-4_8

oxygen production technologies greatly increase the cost of pure oxygen gasification [4, 5].

Chemical looping gasification (CLG) is a novel gasification technique [6]. The principle of CLG is as follows: the lattice oxygen in the oxygen carrier reacts with fuel in the gasification reactor and then the reduced oxygen carrier absorbs the oxygen in the air reactor to regenerate. Compared to the traditional pure oxygen gasification, the CLG has the following advantages: The oxygen carrier provides lattice oxygen for the biomass gasification and the cost is low; the oxidation of the reduced oxygen carrier in the air reactor is exothermic and the heat released can be carried by the oxygen carrier from the air reactor to the gasification reactor; The metal oxygen carrier is catalytic on the tar cracking, which can reduce the tar content [7–9].

At present, Fe-based oxygen carrier was mostly used in CLG. Huang et al. investigated the CLG property of natural hematite as oxygen carrier in fluidized bed reactor. Results showed that the carbon conversion ratio and syngas production yields increased by 7.47 and 11.02% compared to traditional steam gasification [10, 11].

In this study, the combined oxygen carriers were prepared and used in the CLG technology. Compared to Fe-based oxygen carrier, these oxygen carriers have the capability of releasing oxygen, which can increase the gasification rate and reduce the reaction temperature. Meanwhile, the new combined oxygen carriers have high melting points, which can improve the anti-sintering property [12, 13]. This study was focused on the oxygen uncoupling property. The kinetics experiments were carried out to investigate the oxygen uncoupling properties of the combined oxygen carriers prepared.

Experimental

Materials

The combined oxygen carriers were prepared by mechanical mixing. CuO and Mn_2O_3 were selected as active phases and ZrO_2 was selected as binder. The mole mass ratios of CuO, Mn_2O_3 and ZrO_2 in the mixtures were 0.5:1:1, 1:1:1, 1.5:1:1 and 2:1:1. Graphite (10 wt%), a pore-forming additive, which can create a suitable macro-porosity to enhance the carrier reactivity after sintering, was added during the mixing process. Distilled water was added to the mixed powders until the mixtures were formed, and then the mixtures were dried at 80 °C for 12 h in a dryer and calcined at 950 °C for 6 h in a muffle furnace. Then the oxygen carriers were ground and sieved to obtain the desired particle size of 150–180 μm [14].

The characteristics of the oxygen carrier prepared were characterized by XRD and SEM. Figure 1 shows the phase analysis of Cu/Mn/Zr composite oxygen carriers. The phases of Cu/Mn/Zr composite oxygen carriers with different ratios were ZrO_2 and $Cu_xMn_{3-x}O_4$ (including $CuMn_2O_4$, $Cu_{1.4}Mn_{1.6}O_4$ and

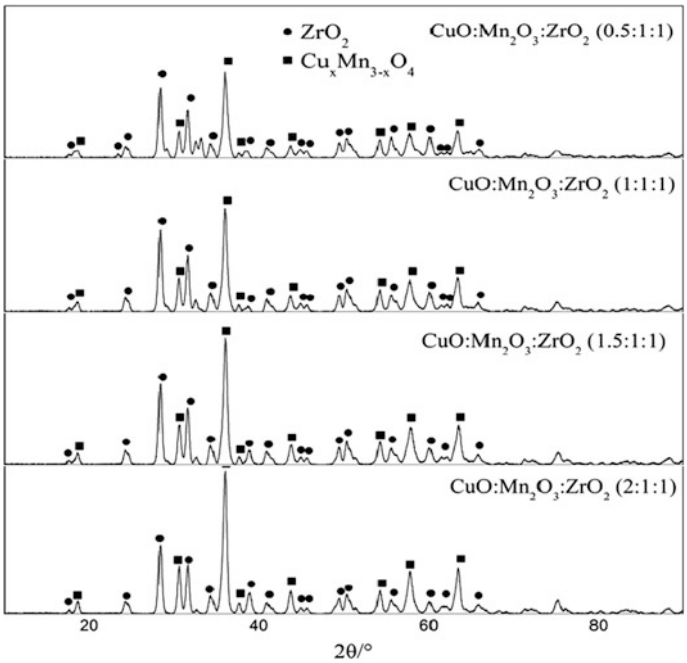

Fig. 1 The phase composition of Cu/Mn/Zr composite oxygen carriers

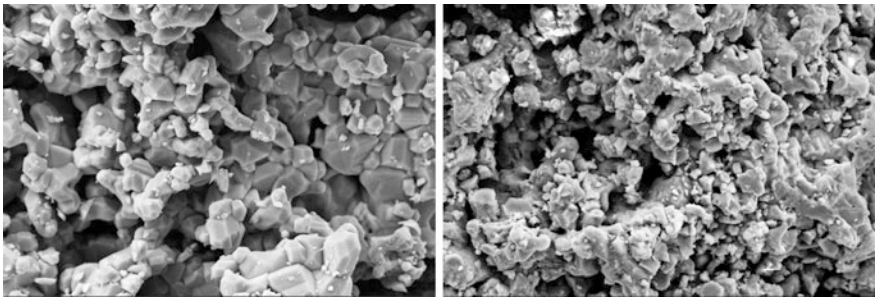

Fig. 2 SEM images of the Cu/Mn/Zr composite oxygen carriers (left-Cu/Mn/Zr = 1.5:1:1; right-Cu/Mn/Zr = 2:1:1)

$Cu_{1.5}Mn_{1.5}O_4$). The binder of ZrO_2 kept stable. However, CuO reacted with Mn_2O_3 and a new type of combined oxygen carrier was constructed by the composite method. The new phase replaced CuO or Mn_2O_3 as the active ingredient in the oxygen carrier, which could improve the oxygen uncoupling properties of CuO or Mn_2O_3 greatly.

Figure 2 shows the surface morphology of the combined oxygen carriers. The oxygen carriers prepared were porous. The different phases were staggered and the ZrO_2 binder could effectively prevent the agglomeration of the combined oxygen carriers.

Experimental Set-up

Experiments were performed in a thermal analyzer (Netzsch, Model STA409PC). N_2 or N_2/O_2 mixed gas with a flow rate of 30 ml/min was used as carrier gas during the reduction reaction. Sample was loaded in a crucible with a mass of about 10 mg. The sample was heated to 1000 °C at heating rates of 10, 15, 20 and 25 °C/min to investigate the effect of heating rate. Isothermal thermogravimetric experiments were performed to investigate the effect of reduction temperature. During the heating process in the reduction, air with a flow rate of 30 ml/min was used to avoid the oxygen releasing. N_2 was introduced when the reduction reaction temperatures of 800, 825, 850 and 875 °C were reached.

Data Processing

The weight variations were automatically recoded by the TGA, the reduction conversion ratio can be calculated according to following equation.

$$\alpha_{red} = \frac{m_{oxi} - m}{m_{oxi} - m_{red}} \tag{1}$$

Where m mass of the sample during the reduction and oxidation reaction, m_{oxi} mass of the fully oxidized sample, m_{red} mass of the fully reduced sample.

Results and Discussions

Effects of Mole Ratio

Figure 3 shows the mass changes of the Cu/Mn oxygen carriers under different mole ratios. The heating rate was 15 °C/min. With the increasing content of CuO, the mass changes of Cu/Mn oxygen carriers increased firstly and then decreased. The mass changes of Cu/Mn oxygen carrier with mole ratio of 1.5:1:1 was biggest, followed by mole ratio of 2:1:1. In order to heighten the gasification efficiency, the oxygen transport capacity should be high. Base on this, the optimal mole ratios of Cu/Mn/Zr were determined as 1.5:1:1 and 2:1:1.

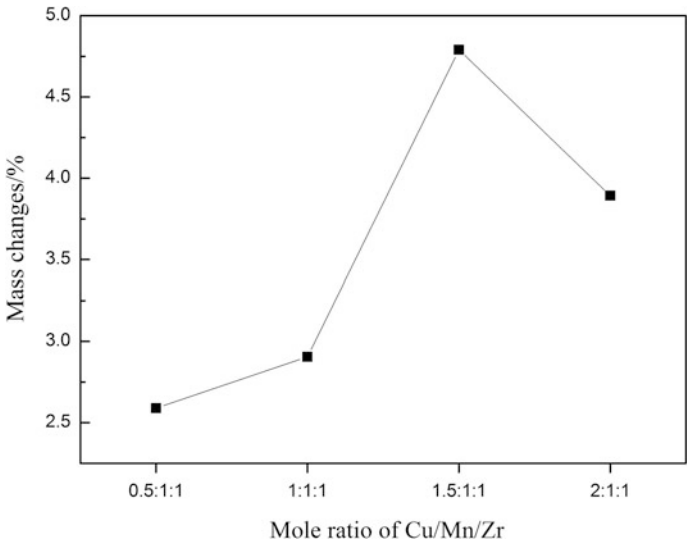

Fig. 3 The mass changes of the Cu/Mn oxygen carriers under different mole ratios

Effects of Heating Rate

Figure 4 shows the changes of reduction conversion with time under different heating rates. With the increase of heating rate, the reaction times shortened and the reaction rates increased. The reason was that the reaction temperatures regions increased with the increasing of heating rate, the reactivity of the oxygen carrier enhanced. The reaction temperatures under different heating rates of Cu/Mn oxygen carrier were listed in Table 1. With the increase of heating rate, the starting and ending temperatures of reduction reaction moved forward. The reason was that the internal and external temperature of the particle could not balance in time with an increasing of heating rate. The temperature differences between the internal and surface, the surface and the crucible lead to the thermal hysteresis of the system.

Effect of Oxygen Concentration

Figure 5 shows the changes of reduction conversion with temperature under different oxygen concentrations. In the beginning, the reaction rate was low. The reason was that the oxygen equilibrium partial pressures of the reduction reaction were small and the driving forces of the reduction reaction were consequently low, leading to slow reduction reaction rate. With the increase of reduction temperatures, the oxygen equilibrium partial pressures of the reduction reaction increased greatly and the reactivity of oxygen carrier increased greatly [15]. With the increase of

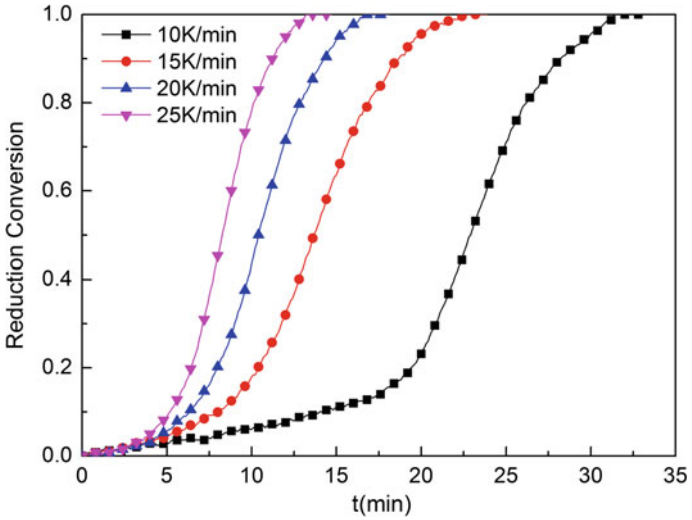

Fig. 4 The conversion ratio of oxygen carrier versus time under different heating rates

Table 1 The starting and ending temperatures of oxygen carrier under different heating rates

Oxygen carrier	10 °C/min	15 °C/min	20 °C/min	25 °C/min
Starting temperature/°C	606	625.5	632	642.5
Ending temperature/°C	920	963	966	972.5

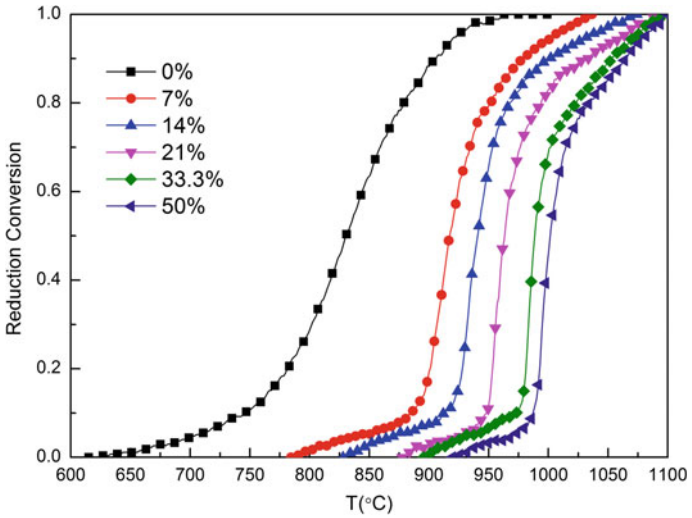

Fig. 5 The reduction conversion with temperature under different oxygen concentrations

oxygen concentration, the starting and ending reduction temperatures moved forward. However, the reaction time shortened and the reactivity of the oxygen carrier enhanced. On the one hand, high oxygen concentration could restrain the reduction of oxygen carrier and the reduction temperature should be heightened in high oxygen concentration. On the other hand, the oxygen carrier could release oxygen in high oxygen concentration, which can broaden the using range of Cu/Mn oxygen carriers.

Effect of Temperature

Figure 6 shows the reduction conversion with time under different temperatures. The reduction time shortened and the reaction rate increased greatly with the increase of the reaction temperatures. The reason was that the increase of temperature leaded to high energy in the reduction system. The collision among molecules was severe and the chemical chain was easy to generate and break. Moreover, with the increase of reduction temperatures, the oxygen equilibrium partial pressures of the reduction reaction increased. The driving forces of the reaction reactions increased. Thus, the reduction reactivity of Cu/Mn oxygen carrier was heightened with the increase of reaction temperatures [16].

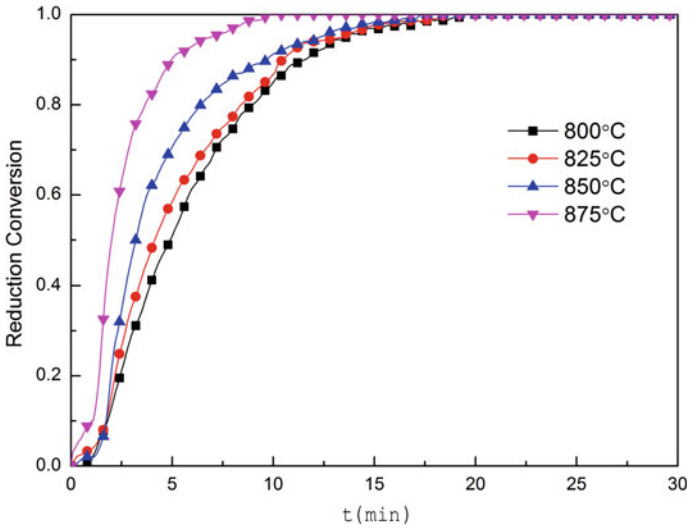

Fig. 6 The reduction conversion with time under different temperatures

Conclusions

In this study, the combined Cu/Mn oxygen carriers were prepared and the characterization and reactivity of oxygen carriers prepared were investigated. The following conclusions were drawn from the current study.

The XRD of oxygen carriers shows that the binder ZrO_2 does not react with metal oxides and two active oxides react to the new phase of $Cu_xMn_{3-x}O_4$, which has the property of releasing oxygen. The optimal mole ratios of Cu/Mn/Zr were determined as 1.5:1:1 and 2:1:1 according to the mass changes during the reduction process.

With the increase of heating rate, the starting and ending reduction temperatures increase. However, the reduction times shorten and the reaction rates increase. With the increase of oxygen concentration, the starting and ending temperatures of reduction reaction increase. High oxygen concentration is harmful for the reduction of Cu/Mn oxygen carrier. With the increase of reduction temperature, the reactivity of oxygen carrier increases greatly. High reaction temperature is beneficial to the reduction of Cu/Mn oxygen carrier.

Acknowledgements This research was financially supported by National Natural Science Fund of China (51604078, 51576035); Fundamental Research Funds for the Central Universities (N162504012); Post-Doctoral Science Foundation (2017M610185, 20170101).

References

1. Nhuchhen DR (2016) Prediction of carbon, hydrogen, and oxygen compositions of raw and torrefied biomass using proximate analysis. Fuel 180:348–356
2. Ding L et al (2015) Interaction and its induced inhibiting or synergistic effects during co-gasification of coal char and biomass char. BioResour Technol 173:11–20
3. Wang ZQ et al (2015) Gasification of biomass with oxygen-enriched air in a pilot scale two-stage gasifier. Fuel 150:386–393
4. Wang K et al (2016) Redox performance of Cu-based oxygen carrier used in chemical looping air separation combined oxy-fuel combustion technology. Appl Therm Eng 98:440–448
5. Wang K et al (2016) Evaluation of Cu-based oxygen carrier for chemical looping air separation in a fixed-bed reactor. Chem Eng J 287:292–301
6. Rydén M, Lyngfelt A, Mattisson T (2008) Chemical-looping combustion and chemical-looping reforming in a circulating fluidized-bed reactor using Ni-based oxygen carriers. Energy Fuels 22:2585–2597
7. Adanez J et al (2012) Progress in chemical-looping combustion and reforming technologies. Prog Energy Combust 38:215–282
8. Wang K et al (2016) Thermodynamic analysis of syngas generation from biomass using chemical looping gasification method. Int J Hydrog Energy 41:10346–10253
9. Liu Y et al (2012) Reaction mechanism of coal chemical looping process for syngas production with $CaSO_4$ oxygen carrier in the CO_2 atmosphere. Ind Eng Chem Res 51:10364–10373
10. Huang Z et al (2013) Synthesis gas production through biomass direct chemical looping conversion with natural hematite as an oxygen carrier. BioResour Technol 140:138–145

11. Huang Z et al (2014) Biomass char direct chemical looping gasification using NiO-modified iron ore as an oxygen carrier. Energy Fuels 28:183–191
12. Shulmana A et al (2011) Chemical-looping with oxygen uncoupling using Mn/Mg-based oxygen carriers-oxygen release and reactivity with methane. Fuel 90:941–950
13. Shulman A et al (2009) Manganese/iron, manganese/nickel, and manganese/silicon oxides used in Chemical-Looping With Oxygen Uncoupling (CLOU) for combustion of methane. Energy Fuels 23:5269–5275
14. Wang K, Yu QB, Qin Q (2013) Reduction kinetics of Cu-based oxygen carriers for chemical looping air separation. Energy Fuels 27:5466–5474
15. Wang K, Yu QB, Qin Q (2013) The thermodynamic method for selecting oxygen carriers used for chemical looping air separation. J Therm Anal Calorim 112(2):747–753
16. Xu L et al (2013) Experimental study of cement-supported CuO oxygen carriers in chemical looping with oxygen uncoupling (CLOU). Energy Fuels 27:1522–1530

Synergistic Effect Between Fat Coal and Poplar During Co-Pyrolysis with Thermal Behavior and ATR-FTIR Analysis

Qingyun Zhang, Shengfu Zhang, Rongjin Zhu, Shuxing Qiu and Yue Wu

Abstract Co-pyrolysis of biomass and coal was investigated as an effective way to reduce the greenhouse gas emission. The effects of poplar on the thermal behavior of fat coal were studied using thermogravimetric analyzer. The blended samples heated to characteristic temperature were subjected to attenuated total reflection Fourier transform infrared spectroscopy (ATR-FTIR) to characterize the macromolecular structure. The results indicated that the synergistic effects existed in co-pyrolysis process of blends since lower char yield than calculated values, and the synergistic effects presented positive and negative trend with the increase of temperature, respectively. The carbonyl/carboxyl C=O stretching vibration functional groups and aliphatic side chain from individual fuels were decomposed in advance during co-pyrolysis. Furthermore, the hydrocarbon-generating potential (A-factor) and thermal maturity(C-factor) of the mixtures showed nonadditivity performance.

Keywords Fat coal · Poplar · Co-pyrolysis · ATR-FTIR · Synergistic effects

Introduction

Fossil fuels are still the main energy of human survival and development, its massive consumption has caused global problems such as environmental pollution, ecological destruction and global warming. Biomass has been recognized worldwide as a promising renewable and carbon neutral energy source, which provides about 14% of the world's energy supply [1, 2]. The development and utilization of biomass can not only reduce the greenhouse effect and promote the benign circulation of ecology, but also is one of the important ways to solve the energy crisis and environmental problems by partly replacing fossil fuels such as petroleum and coal. Biomass is the most commonly used fuels in co-processing application with

Q. Zhang · S. Zhang (✉) · R. Zhu · S. Qiu · Y. Wu
College of Materials Science and Engineering, Chongqing University, Chongqing 400044, China
e-mail: zhangsf@cqu.edu.cn

Z. Sun et al. (eds.), *Energy Technology 2018*, The Minerals, Metals & Materials Series, https://doi.org/10.1007/978-3-319-72362-4_9

coal. Co-pyrolysis of blended biomass and coal for bio-coke can overcome the limited energy supplying of biomass, exert the advantages of biomass with large reserves, low sulphur and nitrogen content, and reduce the amount of coking coal consumption and economic cost. It is generally considered that biomass is easier to pyrolysis than that of coal because of its lower bond energy and simpler composition [3]. Whether the synergistic effect exists in the co-pyrolysis process of biomass and coal has been a focus of controversy in study. Synergistic effects exist in some researches. Benzene substitutes can be produced by the combination of H radicals and methoxyphenol respectively decomposed from aliphatic compounds and lignin in biomass, when pyrolysis temperature is larger than 400 °C [4–6]. Krerkkaiwant et al. [7] found that the phenols and oxygenated compounds in co-pyrolysis tar partially disappeared, while the aromatic compounds such as naphthalene, anthracene and pyrene increased. Biomass can provide hydrogen carriers for coal in the co-pyrolysis process, these carriers combine with the nitrogen and sulphur element into NH_3, H_2S and COS and then removed, which improves the denitrification and desulfurization rate [8]. However, some other works reported a lack of significant synergistic effects between biomass and coal. The devolatilization of biomass and coal may occur independently due to the different pyrolysis temperature interval, hydrogen-rich volatiles from biomass can't be effectively utilized by coal pyrolysis and thereby without significant interactions [9, 10]. Collot et al. [11] simulated co-pyrolysis of close contact and complete separation of biomass and coal particles, and found that the derivation of calculated and experimental values were less than 5%.

This work attempts to investigate the synergistic effects during the co-pyrolysis of biomass-coal blends with TGA and ATR-FTIR analysis. Poplar (P) was selected as biomass sample and then blended with a fat coal (FC). The co-pyrolysis characteristics of mixtures were studied, including co-pyrolysis rate, characteristic temperature and derivation of calculated and experimental values of TG curves. The ATR-FTIR spectra of chars were also investigated, especially the changes of functional groups. The structural parameters were deduced from ATR-FTIR spectra.

Experimental

Fat coal (FC) supplied from Anshan Iron and Steel Group Co., Ltd in northeast China and poplar (P) taken from Ganshu Province, located in northwest China were used in this study. Proximate and ultimate analysis of the fat coal and poplar are shown in Table 1. The fat coal and poplar were ground and collected the particle size of 0.150-0.212 mm for experiments. Fuel samples were dried at 110 °C for two hours to possibly reduce the effect of moisture content. The experiments carried out with manual blends of fat coal and poplar in different ratios, the addition ratios of poplar were 0%, 4%, 16%, 32%, and 100%, with names of FC, FCP4, FCP16, FCP32, and P, respectively.

Table 1 Proximate and ultimate analysis of samples

Sample	Proximate analysis (wt%)				Ultimate analysis (wt%)					
	M_{ad}	A_d	V_d	FC_d	C_d	H_d	O_d	N_d	S_d	Other
Fat coal	1.74	9.61	28.67	61.72	77.27	4.61	5.68	1.36	1.47	9.61
Poplar	4.18	5.52	76.56	14.74	45.95	6.30	41.92	0.18	0.13	4.52

Pyrolysis characteristics of fat coal, poplar and their blends were determined in a STA 449C TGA made by NETZSCH Instrument Manufacturing Co., Ltd. About 10 mg of the sample was weighted to mitigate the effect of heat and mass transfer limitations. The experiments carried out from room temperature to 1000 °C at the heating rate of 10 °C/min under high purity nitrogen with the flow of 50 ml/min. Pyrolysis characteristic parameters including T_{in}, T_i, R_i were defined by thermogravimetric (TG) and derivative thermogravimetric (DTG) and showed in Fig. 1. Where T_{in} is the initial decomposition temperature, T_i and R_i are the temperature and decomposition rate of DTG peaks, respectively. It is worth noting that all the parameters above obtained when the temperature is more than 150 °C.

To study the synergistic effect of co-pyrolysis of FC and P blend, the measured values of char yield were compared with calculated ones from individual fuels. The calculated values were obtained by additive model which assumed that there are no interactions between two samples during co-pyrolysis. So, the calculated values are the sum of values of individual samples with relevant to their blending weight ratio.

$$M_{cal} = aM_{FC} + bM_P \tag{1}$$

$$\Delta M = M_{cal} - M_{\exp} \tag{2}$$

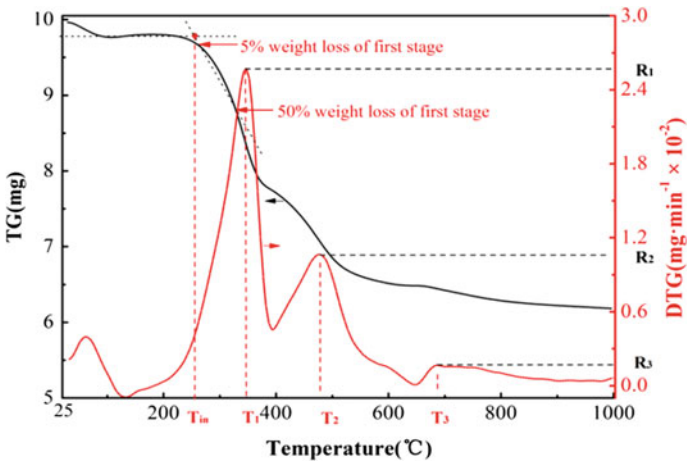

Fig. 1 Co-pyrolysis characteristics of FCP32 in TGA

Where M_{cal} is the calculated values from the additive model, a and b are the mass fraction of fat coal and poplar in the blends, M_{FC} and M_P are the measured experimental value from TG curves of fat coal and poplar separately. The ΔM was defined to further investigate the degree of the synergistic effects, and M_{exp} is the experimental value from TG curves of the blends.

Samples were heated to characteristic temperature at a heating rate of 10 °C/min. The residue chars collected from the pyrolysis were ground to under 0.074 mm and then subjected to ATR-FTIR. The ATR-FTIR spectra of the samples were obtained by a FTIR (model Nicolet iS5, made by Thermo Fisher in America) in the absorbance mode, equipping with the attenuated total reflection (ATR) diamond coupling. The samples were detected at room temperature, from a collection of 32 scans per spectrum measured at a resolution of 4 cm^{-1} in the frequency range of 4000–400 cm^{-1}.

To analyze the synergistic effect of blended fat coal and poplar during co-pyrolysis, the macromolecular structures of chars were analyzed through the spectrogram, including main functional groups and structural parameters. CH_2/CH_3, A-factor, C-factor were calculated by the peak area according to Suryeddu et al. [12], Xin et al. [13], and Wu et al. [14].

$$CH_2/CH_3 = (A2920cm^{-1})/(A2950cm^{-1}) \tag{3}$$

$$A - factor = (A3000 - 2800cm^{-1})/(A3000 - 2800cm^{-1} + A1650 - 1520cm^{-1}) \tag{4}$$

$$C - factor = (A1800 - 1650cm^{-1})/(A1800 - 1650cm^{-1} + A1650 - 1520cm^{-1}) \tag{5}$$

Results and Discussion

Pyrolysis Characteristics in TGA

Pyrolytic behavior of individual components and mixtures are shown in Fig. 2. Pyrolysis characteristic parameters of individual and mixed samples are listed in Table 2. The TG and DTG curves present different pyrolysis trends with the poplar increased. Thermal decomposition of FC appears to start at around 321 °C, and it continued over the whole temperature range at a relatively low and constant rate. The maximum weight loss rate is found to be 0.016 mg min^{-1} at 475 °C. On the other hand, thermal composition of P starts at around 240 °C and the maximum weight loss rate is 0.082 mg min^{-1} at 345 °C. The weight of residual char at 1000 °C decreases gradually as the mass ratio of P increase. The FCP mixture DTG curves exhibit two main peaks. The first peak intensity increases from 0.0049 to 0.026 mg min^{-1}. However, the second peak presents opposite trend which decreases

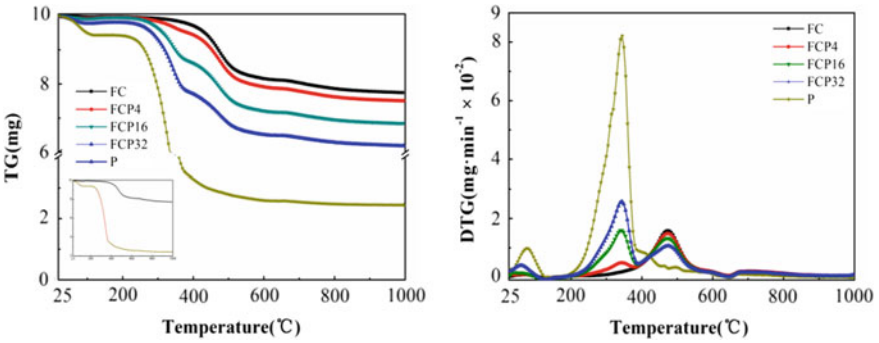

Fig. 2 TG and DTG curves for FC, P and their blends under various mass ratios

Table 2 Pyrolysis parameters of FC, P, and their blends

Sample	T_{in}/°C	T_1/°C	T_2/°C	T_3/°C	R_1/mg min^{-1}	R_2/mg min^{-1}	R_3/mg min^{-1}
FC	321	–	473	686	–	0.016	0.20
FCP4	297	346	474	686	0.0049	0.015	0.19
FCP16	245	345	473	684	0.016	0.013	0.18
FCP32	243	345	475	685	0.026	0.011	0.17
P	240	345	–	–	0.082	–	–

from 0.015 to 0.011 mg min^{-1}. The maximum weight loss rate mainly change from the second peak to the first one with the increase of the P mass ratio in the mixture. It also can be seen from Table 2 that T_1 and T_2 have little change, indicating the addition of P doesn't affect the peak temperature under same hating rate. It is worth noting that T_{in} decreases with the increase amount of P, and the more the amount of addition, the less the T_{in} decrease.

The different devolatilization rate between biomass (P) and coal (FC) is mainly caused by their structural properties. Biomass is mainly made up of hemicellulose, cellulose and lignin [15]. The macromolecular structure of those components are mainly joined by weak ether bonds (R-O-R) with bond energy of 380–420 kJ/mol and that will easy broken at lower temperature. On the contrary, the macromolecular structure of coal is mainly composed of polycyclic aromatic hydrocarbons and linked by alternate single and double bonds and is more resistant to thermal decomposition with high bond energy of 1000 kJ/mol [9]. The hemicellulose is the easiest pyrolysis among biomass components, and pyrolysis gas of hemicellulose could partly absorb on the surface of coal particles. Thus, the weight doesn't change significantly when the addition amount of biomass is little, which cause higher T_{in} compare with larger addition.

Synergistic Effects Between FC and P by TGA

The comparison of experimental and calculated values of the FCP blends TG curves are illustrated in Fig. 3. There are not consistent trends for the $M_{\text{experimental}}$ and $M_{\text{calculated}}$. The experimental values are similar to that of calculated under 200 °C due to the influence of unstable moisture content. For another, the values of calculated are higher than that of the experimental at the temperature range of over 200 °C. The more deviation with the greater addition amount of P, indicating that the synergistic effects exist between FC and P during co-pyrolysis, and this effect promotes the pyrolysis of FC for higher volatiles. According to the proximate analysis, Hydrogen-containing free-radicals are generated by depolymerization and dehydration during pyrolytic reaction of P. Those radicals inhibit the formation of aromatic rings and prevent recombination and cross-linking reactions of other free-radicals that increase char formation [16]. Alkali metals and alkaline earth metal contained in P ash can transfer the charge on the carbon skeleton of the char surface, which change the electron cloud distribution of the carbon atom and improve the surface activity [17, 18]. Consequently, more volatiles are produced during pyrolysis of the blend than that from individual pyrolysis of FC and P.

From Fig. 3, the values of ΔM in zone 2, 4, and 6 have no change remarkably with the temperature rising, while zone 1, 3, 5 are the opposite, especially zone 3 and 5 which. By contrast, the zone 3 shows promotion effect while zone 5 shows inhibition, indicating that interactions happen between FC and P. The hydrogen-rich pyrolysis gases and the heat released by pyrolysis of P make some of the aliphatic side chain of coal decomposed in advance, which accelerate the weight loss of mixture at the temperature range of 220–380 °C. The early decomposition of the FC's aliphatic side chain also allows for more energy to decompose in zone 5. Although the catalysis of inorganic of P present in zone 5, it does not play a leading role. Thus, compared with raw coal, the weight loss slows down. When the temperature is over 550 °C, the main pyrolysis of FC is nearing the end and it starts to form semi-coke, only a little of catalysis from P ash. That's why the deviation of

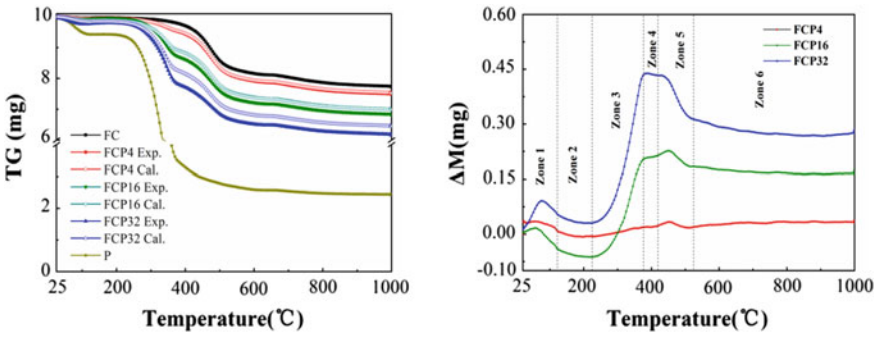

Fig. 3 Comparison of experimental and calculated values from FCP blends TG curves

each mixture is almost unchanged after 550 °C. From the whole process of pyrolysis, the addition of P has a positive and inhibitory effect on the FC pyrolysis process, while the former is more dominant than the latter and finally shows synergy.

ATR-FTIR Spectra of Char Obtained at Characteristic Temperature

To determine differences between the mixture and the individual fuels during pyrolysis process, the ATR-FTIR spectra of FC, P and FCP16 at different temperatures were obtained and presented in Fig. 4. Ten regions about band assignment from the ATR-FTIR spectra in this work are given in Table 3. All the samples under heating feature a similar distribution of functional groups. From Fig. 4a, the ATR-FTIR spectra of FC are characterized by stronger aromatic C-H stretching at 3100–3000 cm^{-1}, higher intensity aromatic C=C stretching vibrations at 1650–1520 cm^{-1} and C-H aromatic out-of-plane deformation at 950–750 cm^{-1} than that of P. On the contrary, the P is characterized by more aliphatic-related functional groups such as aliphatic ether C-O-C and alcohol C-O stretching at 1350–1150 cm^{-1}. What's more, more easily decomposed bonds such as ether bonds, ester bonds, C-O bonds and C=O bonds exist in the molecular structure of P. Those

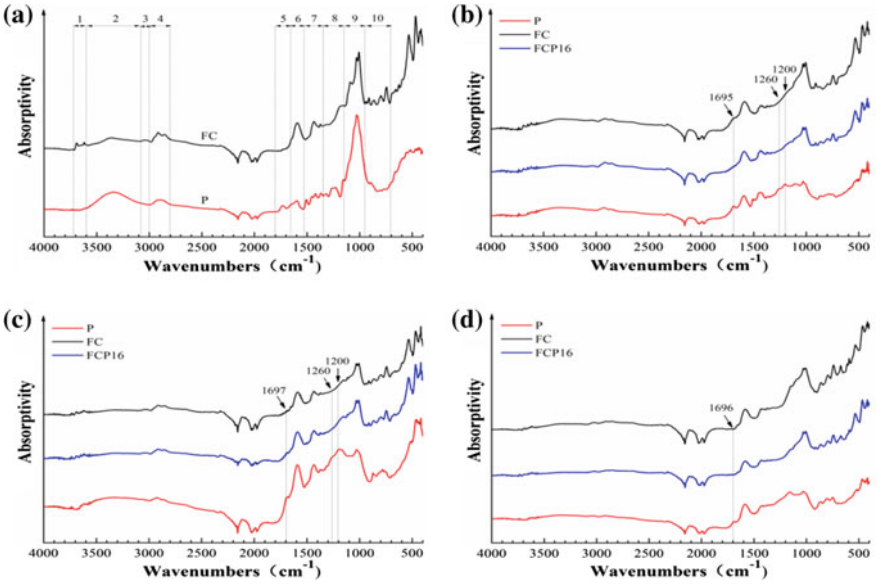

Fig. 4 ATR-FTIR spectra of FC, P and their blends at different temperature: **a** room temperature, **b** 345 °C, **c** 390 °C, **d** 450 °C

Table 3 Band assignments for ATR-FTIR spectra of samples

	Band (cm^{-1})	Assignments
1	3700–3600	Free −OH
2	3500–3300	−OH stretching
3	3100–3000	Aromatic C−H stretching
4	3000–2800	Aliphatic C−H stretching
5	1800–1650	Carbonyl/carboxyl C=O stretching
6	1650–1520	Aromatic C=C ring stretching
7	1520–1350	Aliphatic $-CH_2$ and $-CH_3$ deformation
8	1350–1150	Aromatic ether C–O–C, phenolic C–O, and ester C–O–O–C stretching
9	1150–950	Aliphatic ether C−O−C and alcohol C−O stretching
10	950–750	C−H aromatic out-of-plane deformation
	750–720	Polymethylenic chains ($n \geq 4$) rocking

above structure characteristics are consistent with the proximate analysis that P has more volatiles than FC. A broad region of 3500–3300 cm^{-1} is observed and related to –OH stretching vibrations. The P shows a stronger infra-red absorbance in this region than FC. This observation compared well with the moisture contents of the samples determined from proximate analysis in Table 1.

The intensity shows decrease trend in region 2 which can be attributed to moisture evaporation. The functional groups with lower bond energy can be decomposed generally into small molecule groups, some are released in the form of gas, and the other part is used to form macromolecular structure by addition reaction. The stretching intensity of the aromatic C=C ring is high at all temperatures due to the higher bond energy. It is worth noting that the intensity of aromatic C=C ring of P has an obvious increase under experimental temperature but not in the FC. A large number of volatiles of P were decomposed in the pyrolysis process. In addition, the aromatic C=C ring is the most stable in functional groups of P and does not decompose under 475 °C.

The obvious synergistic effects can be observed by comparing with the ATR-FTIR spectra of chars obtained from FC, P and FCP16 at the same temperature. Take Fig. 4b for example, the peak at 1695 cm^{-1} which is assigned to the aliphatic C=O and –COOH stretching vibrations was detected in the ATR-FTIR spectra of FC char and P char but not in FCP16 char. The peak at 1260 and 1200 cm^{-1} which were attribute to aromatic ether C-O-C and ester C-O-O-C stretching vibrations were observed in the ATR-FTIR spectra of P char but not in FCP16 char. These above phenomena indicate that interactions occurred between FC and P during co-pyrolysis process. The pyrolysis of P promoted the pyrolysis of FC in advance, which is consistent with the analysis of TGA. Meanwhile, the free radicals produced by FC pyrolysis also accelerated the decomposition of functional groups of P. The same situation present in Fig. 4c, d, and the interaction presents a downward trend due to a large number of P pyrolysis as the temperature increases.

Table 4 Structure parameters deduced from ATR-FTIR spectra of chars

Samples	A-factor	C-factor	CH_2/CH_3
FC 345	0.23	0.10	4.17
P 345	0.29	0.16	7.29
FCP16 345	0.37	0.03	3.87
FC 390	0.33	0.04	6.04
P 390	0.17	0.12	2.57
FCP16 390	0.31	0.03	5.33
FC 475	0.17	0.02	4.87
P 475	0.10	0.07	2.42
FCP16 475	0.17	0.03	2.35

Structural parameter of ratio CH_2/CH_3 can be used to evaluate the degree of branching and chain length of the aliphatic side functional groups within sample macromolecular structure [13]. A-factor represents changes in the relative intensities of the aliphatic groups, which reflects the hydrocarbon-generating potential of sample. C-factor represents the changes of C=O groups to aromatic C=C stretching groups, which reflects the thermal maturity of sample [19]. The calculation of CH_2/CH_3, A-factor and C-factor are based on Eqs. (3)–(5). The values of these structural parameters are listed in Table 4.

It can be seen that P char has higher values of A-factor and CH_2/CH_3 than that of FC at lower temperature (i.e. 350 °C). This is ascribed to hydrogen-rich characteristics of P. However, values of A-factor and CH_2/CH_3 of P char are lower than that of FC when temperature rises above 390 °C. A large number of volatiles of P has been decomposed at 390 °C, the residue is mostly charcoal powder with very little of hydrogen-containing branched chains. An interesting phenomenon was observed that the values of C-factor for P char are higher than FC char at any temperature. This situation compared well with the ATR-FTIR spectra in Fig. 4. P char contains more carbonyl/carboxyl C=O stretching than FC char and is still not fully decomposed at 475 °C, whereas the corresponding spectral bands of ketone functional groups show a very weak intensity. Besides, the stretching intensity of the aromatic C=C ring in FC char is higher than that of P char.

By the above analysis, it's not difficult to find that the structural parameters of FCP16 char are not related to that of FC char and P char, showing nonadditivity performance. The calculated values of structural parameters from FC char and P char are higher than that of FCP16 char for A-factor, while the opposite situation for C-factor and CH_2/CH_3. It turned out that the addition of P is beneficial to increasing the hydrogen-generating potential of FC and decreasing the thermal maturity and chain length of the aliphatic, which accordant with the analysis of ATR-FTIR spectra in Fig. 4.

Conclusions

This study investigates the thermal behavior and char structure during co-pyrolysis of blended fat coal (FC) and poplar (P). From TGA analysis, the influence of P on the pyrolysis of coal was not the pyrolysis temperature but the weight loss rate. A positive deviation existed between calculated values and experimental values of TG curves and showed larger with the addition of P. Interactions occurred between FC and P and showed both of promotion and inhibition trend with the increase of temperature. More volatiles were produced from co-pyrolysis due to the dominance of promotion effect. From ATR-FTIR spectra analysis, functional group peaks of carbonyl/carboxyl C=O, ether C-O-C and ester C-O-O-C stretching vibration in mixture char showed very weak intensity and even disappeared comparing with individual fuels at same temperature. The structural parameters of A-factor, C-factor and CH_2/CH_3 showed a nonadditivity performance. Synergistic effects exhibited during co-pyrolysis of FC and P mixtures, which caused higher hydrogen-generating potential, lower thermal maturity and chain length of the aliphatic.

Acknowledgements This work was supported by the Natural Science Foundation of China (Project No. 51474042 and 51774061) and the Fundamental Research Funds for the Central Universities (Project No. 106112017CDJQJ138801).

References

1. López-González D, Fernandez-Lopez M, Valverde JL et al (2013) Thermogravimetric-mass spectrometric analysis on combustion of lignocellulosic biomass. Bioresour Technol 143 (6):562–574
2. Zhang X, Yang W, Blasiak W (2011) Modeling study of woody biomass: interactions of cellulose, hemicellulose, and lignin. Energy Fuels 25(10):4786–4795
3. Chao CY, Kwong PC, Wang JH et al (2008) Co-firing coal with rice husk and bamboo and the impact on particulate matters and associated polycyclic aromatic hydrocarbon emissions. Bioresour Technol 99(1):83–93
4. Ulloa CA, Gordon AL, García XA (2009) Thermogravimetric study of interactions in the pyrolysis of blends of coal with radiata pine sawdust. Fuel Process Technol 90(4):583–590
5. Sharma RK, Wooten JB, Baliga VL et al (2004) Characterization of chars from pyrolysis of lignin. Fuel 83(11):1469–1482
6. Jones JM, Kubacki M, Kubica K et al (2005) Devolatilisation characteristics of coal and biomass blends. J Anal Appl Pyrolysis 74(1–2):502–511
7. Krerkkaiwan S, Fushimi C, Tsutsumi A et al (2013) Synergistic effect during co-pyrolysis/gasification of biomass and sub-bituminous coal. Fuel Process Technol 115(11):11–18
8. Cordero T, RodríGuez-Mirasol J, Pastrana J et al (2004) Improved solid fuels from co-pyrolysis of a high-sulphur content coal and different lignocellulosic wastes. Fuel 83(11–12):1585–1590
9. Sadhukhan AK, Gupta P, Goyal T et al (2008) Modelling of pyrolysis of coal-biomass blends using thermogravimetric analysis. Bioresour Technol 99(17):8022–8026
10. Masnadi MS, Habibi R, Kopyscinski J et al (2014) Fuel characterization and co-pyrolysis kinetics of biomass and fossil fuels. Fuel 117(8):1204–1214

11. Collot AG, Zhuo Y, Dugwell DR et al (1999) Co-pyrolysis and co-gasification of coal and biomass in bench-scale fixed-bed and fluidised bed reactors. Fuel 78(6):667–679
12. Shuaidan L, Xueli C, Li W et al (2013) Co-pyrolysis behaviors of saw dust and Shenfu coal in drop tube furnace and fixed bed reactor. Bioresour Technol 148(11):24–29
13. Dutta S, Hartkopf-Fröder C, Witte K et al (2013) Molecular characterization of fossil palynomorphs by transmission micro-FTIR spectroscopy: Implications for hydrocarbon source evaluation. Int J Coal Geol 115(4):13–23
14. Xin HH, Wang DM, Qi XY et al (2014) Structural characteristics of coal functional groups using quantum chemistry for quantification of infrared spectra. Fuel Process Technol 118 (2):287–295
15. Aicher T (2013) The effect of the biomass components lignin, cellulose and hemicellulose on TGA and fixed bed pyrolysis. In: Mitochondria and their role in cardiovascular disease, pp 371–383
16. HaykiRiAcma H, Yaman S (2010) Interaction between biomass and different rank coals during co-pyrolysis. Renew Energy 35(1):288–292
17. Keown DM, Hayashi JI, Li CZ (2008) Effects of volatile–char interactions on the volatilisation of alkali and alkaline earth metallic species during the pyrolysis of biomass. Fuel 87(7):1187–1194
18. Wu ZQ, Wang SZ, Zhao J et al (2014) Synergistic effect on thermal behavior during co-pyrolysis of lignocellulosic biomass model components blend with bituminous coal. Bioresour Technol 169(5):220
19. Guo Y, Bustin RM (1998) Micro-FTIR spectroscopy of liptinite macerals in coal. Int J Coal Geol 36(3):259–275

Flow Characteristic of Two-Phase Bubble Reactor for Slag Waste Heat Recovery

Wenjun Duan, Qingbo Yu, Zhimei Wang and Tianwei Wu

Abstract In order to recover the waste heat of molten blast furnace slag, a reactor with top-submerged lance was established. The numerical simulation and experiment study of the flow characteristic in the reactor were conducted. The mathematical model of reactor was established and the Euler-Euler model was employed to simulate the gas-liquid flow in molten slag bath. Meanwhile, the experiment results were obtained and compared with the simulation to testify the accuracy of the established model. According to the bubble behavior in bath, there were four stages: initial expansion stage, bubble detachment stage, freedom lift up stage and bubble broken stage. When the flow field in bath fully developed, the gas fraction decreased with the increasing of bath depth. During injection process, the area near the nozzle and lower the bath would first generate two symmetric heliciform flow regime, and then the flow regime in whole bath would become irregular because of bubble lifting up and rupturing. The gas fraction in bath, the average velocity and turbulence energy of slag would decrease before it increased to maximum and then it would keep fluctuate in a range.

Keywords Molten blast furnace slag · Waste heat recovery
Numerical simulation · Flow characteristic · Bubble behavior

W. Duan (✉) · Q. Yu · T. Wu
Northeastern University, No. 11, Lane 3, Wen Hua Road, He Ping District, Shenyang 110819, Liaoning, People's Republic of China
e-mail: duanwenjn@163.com

Z. Wang
Shenyang Metrology Testing Institution, No. 43, Shi Ji Road, Hun Nan District, Shenyang 110179, Liaoning, People's Republic of China

Z. Sun et al. (eds.), *Energy Technology 2018*, The Minerals, Metals & Materials Series, https://doi.org/10.1007/978-3-319-72362-4_10

Introduction

Iron and steel industry was among the main energy-intensive manufacturing systems worldwide: according to the International Energy Agency, the iron and steel sector was the second largest industrial user of energy [1]. However, huge energy consumption brought serious environmental pollution and the saving technologies of it were still below what would be possible [2]. Therefore, it was necessary to develop the energy saving technologies to improve the current situation.

Blast furnace slag (BFS) was one of the main by-products of iron and steel industry, which was discharged at about 1773 K, and the energy carried was about 1700 $MJ\cdot(t_{slag})^{-1}$. Approximately 0.3 tons of slag was produced for each ton of steel manufactured. In 2015, about 235 million tons of BFS were produced in China. The total energy carried by BFS amounted to 14 million tons standard coal [3, 4]. Therefore, developing an effective method to recover and utilize the waste heat of BFS was necessary.

Some dry waste heat recovery methods were developed, including mechanical crushing method, air blast method and centrifugal granulated method [5]. Although physical methods were gradually reaching commercial testing and acceptance, they had obvious disadvantages. With the development of the study, some researchers proposed chemical methods to recover the waste heat. Kasai et al. [6] proposed the method of methane reforming reaction to recover slag waste heat into chemical energy. Purwanto [7] indicated that the slag acted as not only heat carrier but also a good catalyst. MSW gasification using BFS heat was performed at atmospheric pressure in a fixed bed reactor at 873 $\sim$ 1173 K by Zhao [8]. The waste heat of BFS could provide the energy required in combustible gas production from MSW gasification. Luo [9] using slag heat to generate hydrogen-rich gas in a continuous moving-bed biomass gasification reactor. The maximum gas yield and H_2 content achieved $1.28Nm^3\cdot kg^{-1}$ and 46.56%, respectively. Sun [10] established a two-stage sludge gasification using the thermal heat in hot slags. The results indicated that an Avrami-Erofeev model could best describe the stage of char gasification and the potential CO yield achieved was estimated to be $1.92 \times 10^9 m^3$. A series of thermodynamic analysis and kinetic experiment studies on molten BFS waste heat recovery were conducted by Li [11, 12] and Duan [13, 14]. The theory optimal operation conditions were obtained by these methods. However, as authors' knowledge, the study of flow characteristic in the equipment of waste heat recovery was not still carried out. It was beneficial and necessary to obtain the flow characteristic of the molten slag to enhance the waste heat recovery efficiency and gasification reaction.

In this paper, the Euler-Euler model was used to simulate the gas-liquid flow in molten slag bath. Meanwhile, the cold model experiment was conducted to testify the accuracy of simulation model. The bubble behavior and gas fraction in the molten slag were simulated. In the injection process, the average velocity and turbulence energy of molten slag were also studied.

Mathematical Model

Model Description

The general layout of the waste heat recovery system was illustrated in Fig. 1. The pulverized coal and syngas were transported into the molten slag by top-submerged lance. The following assumptions were employed to simplify the analysis:

(1) Ignore the gasification reaction.
(2) The gas-liquid two-phase flows in the reactor were incompressible.
(3) The furnace wall was simplified as adiabatic and zero-thickness wall.
(4) The top-submerged lance was rigid structure.

Governing Equation

Based on assumptions that gas phase and liquid phase were regarded as continuous phases, an Euler-Euler model for simulating gas-liquid flow was established by combining Geo-Reconstruct method to track the gas-liquid interface.

(1) Continuity equation

$$\frac{\partial \rho}{\partial t} + \frac{\partial(\rho u)}{\partial x} + \frac{\partial(\rho v)}{\partial y} + \frac{\partial(\rho w)}{\partial z} = 0 \tag{1}$$

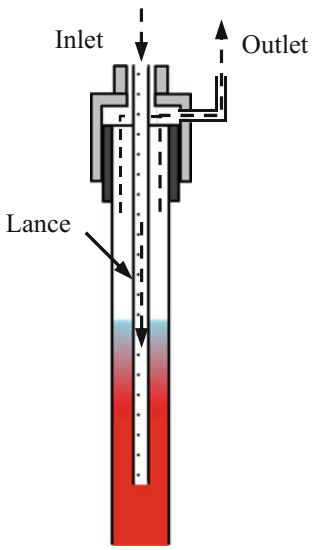

Fig. 1 The schematic diagram of reactor for to-submerged lance molten slag gasifier

where, ρ was the fluid density, kg·m^3; t was the time.

(2) Volume fraction equation

$$\frac{1}{\rho_q}\left[\frac{\partial(\alpha_q\rho_q)}{\partial t}+\nabla\cdot(\alpha_q\rho_q\vec{v_q})\right]=s_{\alpha q}+\sum_{p=1}^{n}(m_{pq}-m_{qp}) \tag{2}$$

where, α_q was the volume fraction of the q; ρ_q was the density of the q; $S_{\alpha q}$ was the quality source term of the q; m_{pq} was the mass transport from p to q; m_{qp} was the mass transport from q to p.

(3) Momentum equation

$$\frac{\partial\left(\rho\vec{v}\right)}{\partial t}+\nabla\cdot(\rho\vec{v}\vec{v})=-\nabla p+\nabla\cdot\left[\mu(\nabla\vec{v}+\nabla\vec{v^T})\right]+\rho\vec{g}+\vec{F} \tag{3}$$

where, p was the pressure; μ was the viscosity.

(4) Energy equation

$$\frac{\partial}{\partial t}(\rho E)+\nabla\cdot(\vec{v}(\rho E+p))=\nabla\cdot\left(k_{eff}\nabla T\right)+S_h \tag{4}$$

where, S_h was the source item; k_{eff} was the effective thermal conductivity; E was the energy.

The RNG k-ε model was selected to simulate the turbulent process in the waste heat recovery system. The equations were showed as followed:

$$\frac{\partial(\rho k)}{\partial t}+\frac{\partial(\rho k u_i)}{\partial x_i}=\frac{\partial}{\partial x_j}(\alpha_k\mu_{eff}\frac{\partial k}{\partial x_j})+G_k+G_b-\rho\varepsilon-Y_M-S_k \tag{5}$$

$$\frac{\partial(\rho\varepsilon)}{\partial t}+\frac{\partial(\rho\varepsilon u_i)}{\partial x_i}=\frac{\partial}{\partial x_j}(\alpha_\varepsilon\mu_{eff}\frac{\partial\varepsilon}{\partial x_j})+C_{1\varepsilon}\frac{\varepsilon}{k}(G_k+C_{3\varepsilon}G_b)-C_{2\varepsilon}\rho\frac{\varepsilon^2}{k}-R_\varepsilon-S_\varepsilon \tag{6}$$

Results and Discussion

Model Validation

In order to confirm the validity of the simulation model, the cold model experimental platform was established and high-speed camera was utilized to capture bubble behavior. Seen from Fig. 2, the bubble behavior of the numerical simulation result was developed to align with experiment result. Therefore, the established

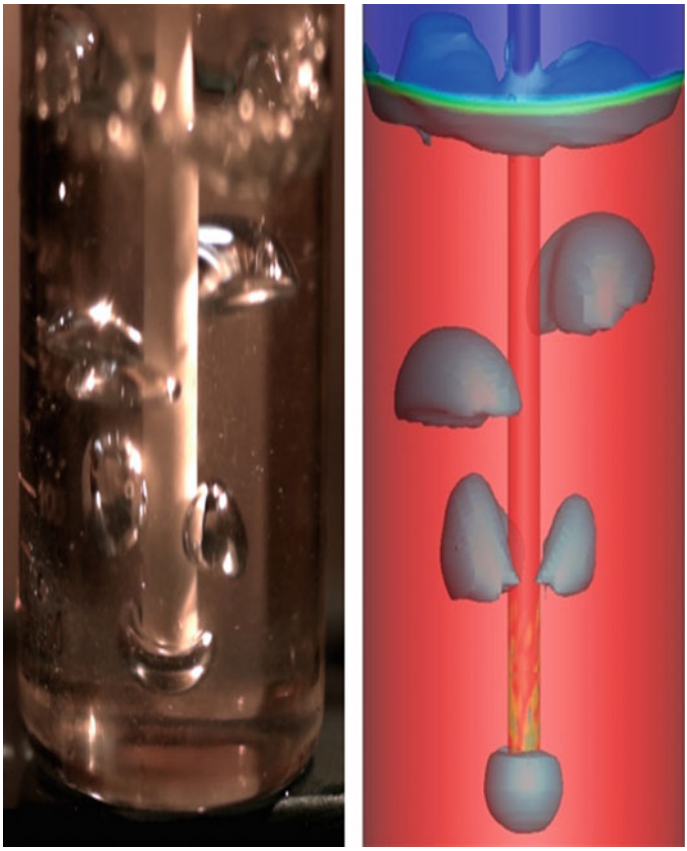

Fig. 2 The comparison between top-submerged lance cold model experiments results and the numerical simulation results

simulation model was completely right to describe the bubble behavior in the molten slag.

Bubble Behavior in the Bath

In the molten bath, the gas spurted from the lance at a certain rate and gradually formed bubble when the expansion velocity (μ) was higher than movement velocity (v). The jet impinging depth in the bath reached maximum when μ equaled to v. The bubbles would experience the detachment stage and freedom lift up stage when it separate from the lance. The bubble quickly reached to interface and became broken Fig. 3.

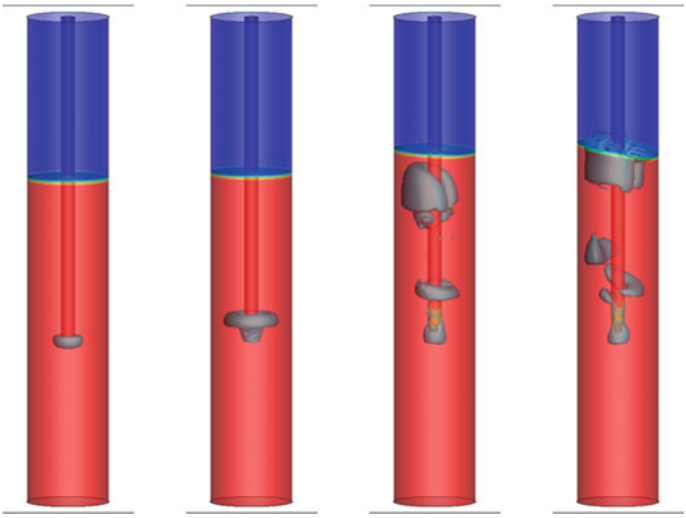

Fig. 3 The gas-liquid phase diagram in the bath for initial expansion stage, bubble detachment stage, freedom lift up stage and bubble broken stage

Distribution of Gas Phase in the Bath

The gas fraction at different time in the molten bath was shown in Fig. 4. With the injection of the gas, the gas fraction in the bath increased with the time increasing. The gas fraction reached maximum at 0.75 s, and then decreased sharply to a certain value with a certain range of fluctuation. It was because that the bubble completely submerged into the molten slag before 0.75 s, and the gas fraction began to decrease with the bubble broking.

Flow Field in the Bath

The distribution of path line in the molten bath for bubble behavior was shown in Fig. 5. The two symmetric heliciform flow regime was generated in the area near the nozzle and lower the molten bath when the bubble separated from the lance. However, this state was destroyed when the bubble reached to the gas-liquid interface. The broken of the bubble caused a sharp fluctuation at the gas-liquid interface and the distribution of trace in the molten bath became more irregular.

The average velocity and turbulence kinetic energy of the liquid were shown in Figs. 6 and 7, respectively. Seen from figures, these changes were consistent with the changing of the gas phase distribution. The more gas phase existed in the molten bath, the larger average velocity and turbulence kinetic energy.

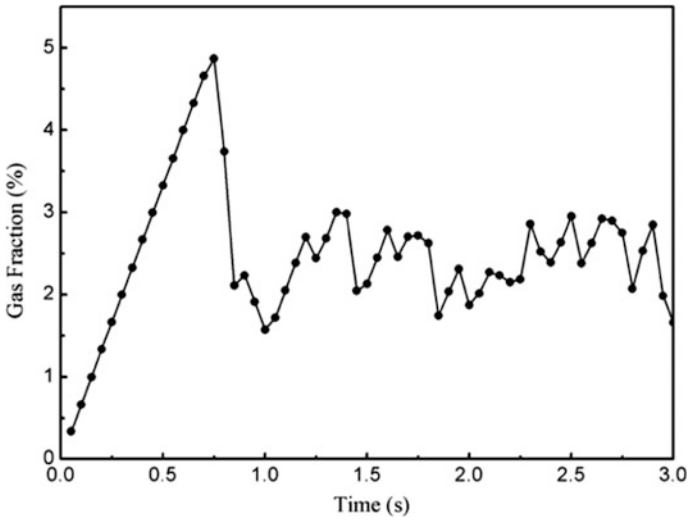

Fig. 4 The gas fraction at different time in the molten bath

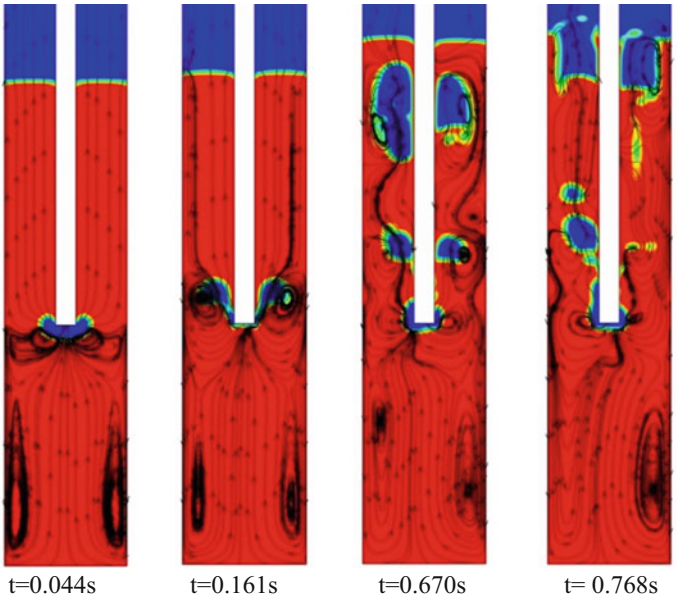

Fig. 5 The distribution of path line in the molten bath for initial expansion stage, bubble detachment stage, freedom lift up stage and bubble broken stage

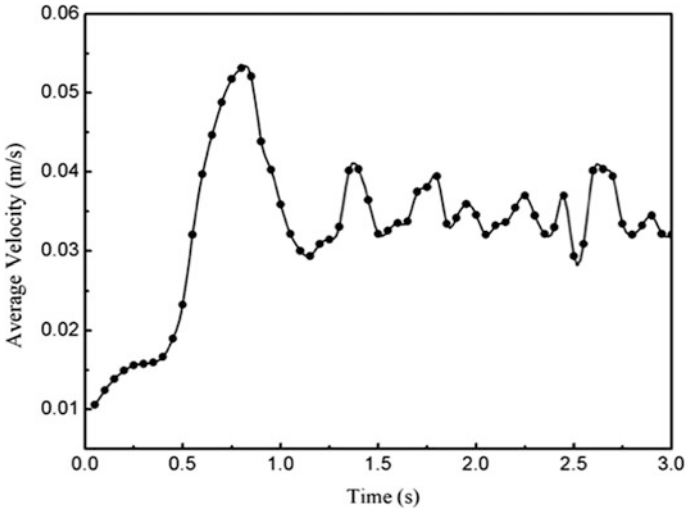

Fig. 6 The average velocity of liquid at different time in the molten bath

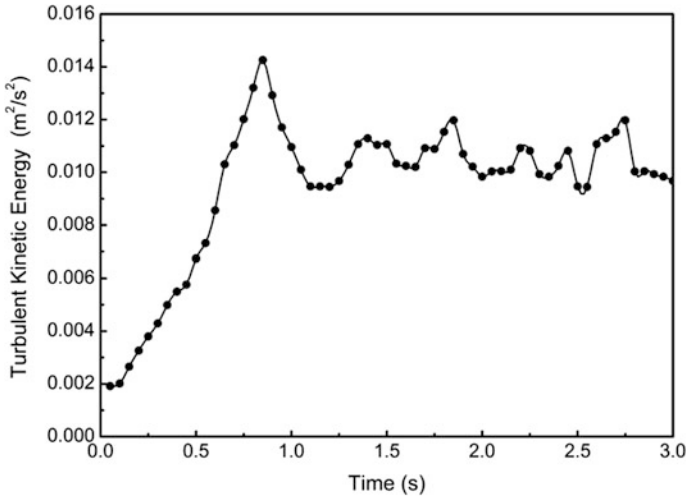

Fig. 7 The average turbulence kinetic energy at different time in the molten bath

Conclusions

In this paper, a numerical simulation model using VOF model and RNG k-ε model was established to study the flow characteristic of the two-phase bubble reactor for blast furnace slag waste heat recovery. The cold model experimental platform was established and high-speed camera was utilized to capture bubble behavior. The

established simulation model could describe the flow characteristic and the bubble behavior, gas phase distribution and flow field in the bath were investigated sufficiently.

Acknowledgements This research was supposed by National Natural Science Foundation of China (51704071); The National Postdoctoral Program for Innovative Talents (BX201600028).

References

1. Porzio GF, Fornai B, Amato A, Matarese N, Vannucci M, Chiappelli L, Colla V (2013) Reducing the energy consumption and CO_2 emissions of energy intensive industries through decision support systems-an example of application to the steel industry. Appl Energy 112:818–833
2. Li Y, Zhu L (2014) Cost of energy saving and CO_2 emissions reduction in China's iron and steel sector. Appl Energy 130:603–616
3. Liu JX, Yu QB, Peng JY, Hu XZ, Duan WJ (2015) Thermal energy recovery from high-temperature blast furnace slag particles. Int Commun Heat Mass Transf 69:23–28
4. Duan WJ, Yu QB, Wang K, Qin Q, Li LM, Yao X, Wu TW (2015) ASPEN Plus simulation of coal integrated gasification combined blast furnace slag waste heat recovery system. Energy Convers Manag 100:30–36
5. Wang H, Wang H, Zhu X, Qiu YJ, Li K, Chen R, Liao Q (2013) A waste heat recovery technologies towards molten slag in steel industry. Appl Energy 112:956–966
6. Kasai E, Kitajima T, Akiyama T, Yagi J, Satio F (1997) Rate of methane-steam reforming molten BF slag for waste heat recovery from molten slag by using a chemical reaction. ISIJ Int 37:1301–1306
7. Purwanto H, Akiyama T (2006) Hydrogen production from biogas using hot slag. Int J Hydrog Energy 31:491–495
8. Zhao LM, Wang H, Qing S, Liu HL (2010) Characteristics of gaseous product from municipal solid waste gasification with hot blast furnace slag. J Nat Gas Chem 19:403–408
9. Luo SY, Zhou YM, Yi CJ (2012) Hydrogen-rich gas production from biomass catalytic gasification using hot blast furnace slag as heat carrier and catalyst in moving-bed reactor. Int J Hydrog Energy 37:15081–15085
10. Sun YQ, Zhang ZT, Liu LL, Wang XD (2015) Two-stage high temperature sludge gasification using the waste heat from hot blast furnace slags. Bioresour Technol 198:364–371
11. Li P, Yu QB, Qin Q, Lei W (2012) Kinetics of CO_2/coal gasification in molten blast furnace slag. Ind Eng Chem Res 51:15872–15883
12. Li P, Lei W, Wu B, Yu QB (2015) CO_2 gasification rate analysis of coal in molten blast furnace slag-For heat recovery from molten slag by using a chemical reaction. Int J Hydrog Energy 40:1607–1615
13. Duan WJ, Yu QB, Liu JX, Wu TW, Yang F, Qin Q (2016) Experimental and kinetic study of steam gasification of low-rank coal in molten blast furnace slag. Energy 111:859–868
14. Duan WJ, Yu QB, Wu TW, Yang F, Qin Q (2016) Experimental study on steam gasification of coal using molten blast furnace slag as heat carrier for producing hydrogen-enriched syngas. Energy Convers Manag 117:513–519

Improving Energy Efficiency in Direct Method for Continuous Casting of Lead Sheets

Arun Prabhakar, Joanna Mielnicka, Mark Jolly and Konstantinos Salonitis

Abstract Lead sheets are widely used for roofing applications, radiation protection and sound proofing. Most of the sheets are either produced by rolling cast slabs of lead sheets or via the direct method (DM) of casting of the sheet continuously. The DM method comprises of a rotating water-cooled drum that is partly immersed in a bath of molten lead and sheets are cast out continuously. The direct method of casting lead is more energy efficient compared to the rolling process which requires a casting process before rolling to achieve the required thickness. This work investigates the energy consumption in different stages of the DM process and suggests pointers for improvement. An energy audit of the process is conducted and the consumption is analysed at different stages and compared with rolled lead.

Keywords Energy efficiency · Lead · Casting · Direct method

Introduction

Sustainability aspects in material processing industries are widely discussed these days. Metal processing is highly energy consuming and contributes significantly to carbon dioxide emissions. This sector is being examined these days as emission reduction is a key driver for finding more energy efficient solutions. Foundries are one of the most energy intensive industries. The average energy burden for the foundry sector in UK is 55 GJ/tonne which is more than double the target burden of 25.7 GJ/tonne as per the climate change agreement published by the

A. Prabhakar (✉) · J. Mielnicka · M. Jolly · K. Salonitis
Manufacturing Department, School of Aerospace Transport and Manufacturing, Cranfield University, Cranfield, UK
e-mail: a.prabhakar@cranfield.ac.uk

M. Jolly
e-mail: m.r.jolly@cranfield.ac.uk

K. Salonitis
e-mail: k.salonitis@cranfield.ac.uk

Z. Sun et al. (eds.), *Energy Technology 2018*, The Minerals, Metals & Materials Series, https://doi.org/10.1007/978-3-319-72362-4_11

UK government [1]. Metallurgical processes like melting, refining and casting have a crucial impact on environment and as a result assessing and controlling the emissions and energy consumptions are of supreme interest for continuous improvement initiatives.

Lead sheets are widely used for radiation protection and in the construction industry for roofing and flashing applications. Around 85% of the demand for lead sheets is for these kind of applications [2]. The high ductility, malleability and resistance to atmospheric oxidation make lead an ideal material for roofing applications. Lead is also a very dense metal and possesses a high attenuation coefficient especially for high energy X-rays which makes it an ideal material for radiation protection [3]. Moreover lead sheets are fully recyclable, durable, long lasting, needs low maintenance and has a low environmental impact [4]. Lead sheets used for construction purposes are mostly produced from recycled lead by two techniques. Majority of the sheets are produced by rolling, which involves casting lead slabs and then rolling them in a mill until the desired code/thickness is obtained. The other technique is a direct method in which sheet of a particular thickness is continuously cast. In this method, a water-cooled drum is immersed in a bath of molten lead and sheets are continuously cast upon rotation of the drum. There is a third method of manufacture of lead sheets by the traditional sand casting method [5]. The main markets for these sheets are in the heritage industry and they are used generally for renovation of old churches, cathedrals and castles.

More than 100,000 tonnes of lead sheet is used every year worldwide with a high demand from countries like Belgium, France, Spain, Germany, UK, Ireland and Netherlands [6]. Lead based products are easy to identify and economical to collect and recycle mainly due to its physical-chemical properties and product design. Lead is recycled more than any other metal and has one of the highest end-of-life recycling rates amongst commonly used metals [2]. The type of lead production has changed through the years. Previously lead was mainly obtained though primary lead production. Primary lead is mainly obtained from its ore galena by a roasting process [7]. However, by 2011 the secondary sources accounted for more than 77% of lead production in Europe. Scrap from lead roofing, flashings and lead-acid batteries are the main sources of raw materials for secondary lead manufacturing [8]. These days almost 50% of the lead that is produced worldwide is from secondary lead with high rates of production in Europe and America and high primary rate of production in China. Scrap lead from building and construction industries is often clean and is re-melted without smelting, however refining may be required [9].

Energy

The foundry industry is one of the most energy consuming sectors. The type of material is also a crucial factor that influences the amount of energy used. Secondary lead production requires much less energy than primary lead production

with the former taking up 5–10 GJ per tonne of lead, and the latter 7–20 GJ per tonne [9].

A modern casting process consists of different stages like melting, refining, moulding, pouring, etc. The cost of a process increases with increase in energy intensiveness [10]. In most foundries, melting, holding and refining consume majority of energy (around 70%). Melting and holding incurs a lot of energy loss which depends on a number of factors like, type and design of the furnace, insulation, frequency of metal charging, etc. [10]. Most furnaces are not very efficient, in fact there are very few furnaces with efficiencies more than 50% [11].

There are several factors that affect energy consumption. The current study compares energy consumption of the DM process with that of the rolling process. The energy data for the DM has been sourced from a foundry based in the UK. However, the values for rolling process have been theoretically calculated. It is assumed that the melting and refining values are the same for both process, since these activities stay unchanged irrespective of the process. The same rule accounts for cutting and transporting the spools, hence this data is omitted.

Direct Method

The Direct Method of casting of lead sheet was initially invented in 1956 for the production of lead sheets potentially based on a process invented by Sir Henry Bessemer for the production of sheets of iron based on the principle of molten metal solidifying over a cooling rotating drum [12]. In this process, a rotating drum which is water cooled, internally, dips into a pool of molten lead, picking the liquid metal and solidifies it into a sheet with the thickness depending on the depth of dip and speed of rotation as shown in the schematic diagram below.

The process starts with scrap lead which consists mostly of old roofing sheets and pipes, separated into two batches based on the bismuth content. It is then loaded into the melting furnace with appropriate proportions of the two batches as melting just the scrap with high bismuth content would result in large emissions from the furnace. The furnace is heated to 440 °C using a natural gas burner. Impurities and dross that arise during the melting process are collected using a mechanical skimmer. The dross collected is stored in metal barrels which are sent for further recovery.

The molten lead is transferred to a refining kettle where it is churned with an oxidising agent such as sodium nitrate for several hours (Harris Process). The scrap lead mostly consists of Antimony, Arsenic and tin as impurities. These elements are more reactive than lead and as a result can be chemically removed by preferential oxidation [13]. The impurities are separated from the lead and get suspended in the flux as sodium arsenate, antimonate and stannate (tin); any zinc is removed as zinc oxide. The flux and lead are separated and impurities may be extracted from the flux. The major product, sodium antimonate, is refined [9].

Table 1 Properties of lead

Property	Value
Heat of melting (H_m)	22.4 kJ/kg
Specific heat of solid lead(C_{ps})	0.126 kJ/kg/ °C
Melting point (T_m)	327.5 °C
Specific heat of liquid lead(C_{pl})	0.14 kJ/kg/ °C
Thermal conductivity	35 W/(m. K)

The refining process results in 99.99% pure lead which is then transferred to a large casting tank. This is the stage where casting of the sheet by DM begins. The casting tank consists of heating elements that keeps the melt at 400 °C. The depth of immersion of the drum in the lead bath is a major factor that controls the thickness of the sheet cast. To stabilise the level of molten lead and to eliminate the need to adjust the roll to a changing level, two tanks are provided adjacent to one another but at different heights/levels. A small pump is used to pump molten metal from the casting tank to the tray which is at a higher level. The tray is constructed in such a way that one of its edges is set lower than the other so that the excess melt can overflow through this edge and flow back into the lower tank. With this arrangement of pump and tanks, regardless of the quantity of lead withdrawn as sheet, the level of lead remains a constant in the casting tray [12]. The cast sheets are wound on a spool which is subsequently unrolled and cut into desired dimensions.

Data analysis and theoretical calculations are made based on thermodynamic properties of lead as well as from literature. The theoretical quantity of energy required to rise 1 tonne of pure lead from room temperature (22 °C) to its melting point, melt it and raise to the temperature of 440 °C can be calculated as 0.077 GJ as per the equation below (Table 1).

$$E = H_m + \left[(T_m - T_a) * C_{ps} \right] + \left[\left(T_p - T_m \right) * C_{pl} \right]$$

Figure below presents utilization of the machines in the direct machine casting process as per data received from a foundry in the UK. The refiner and scrapper are the most energy consuming segments of the process.

The main parts of the DM process are the scrapper, refiner, casting tank and casting tray (Figs. 1 and 2). Figure 3 shows the consumption at each stage of the process sourced from a foundry based in the UK in a calendar month. The company produced 316 spools of cast lead weighing 2010 tonnes.

Rolling Process

Metal sheet rolling was invented in 1500 s. However, it was only recognized as an alternative technique to traditional sand casting in the early 20th century. Rolled lead

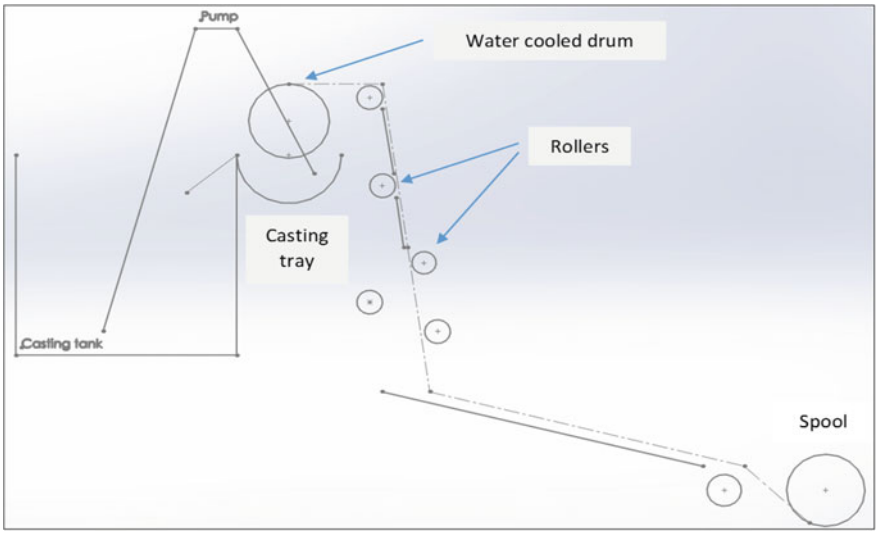

Fig. 1 Schematic diagram of the DM machine

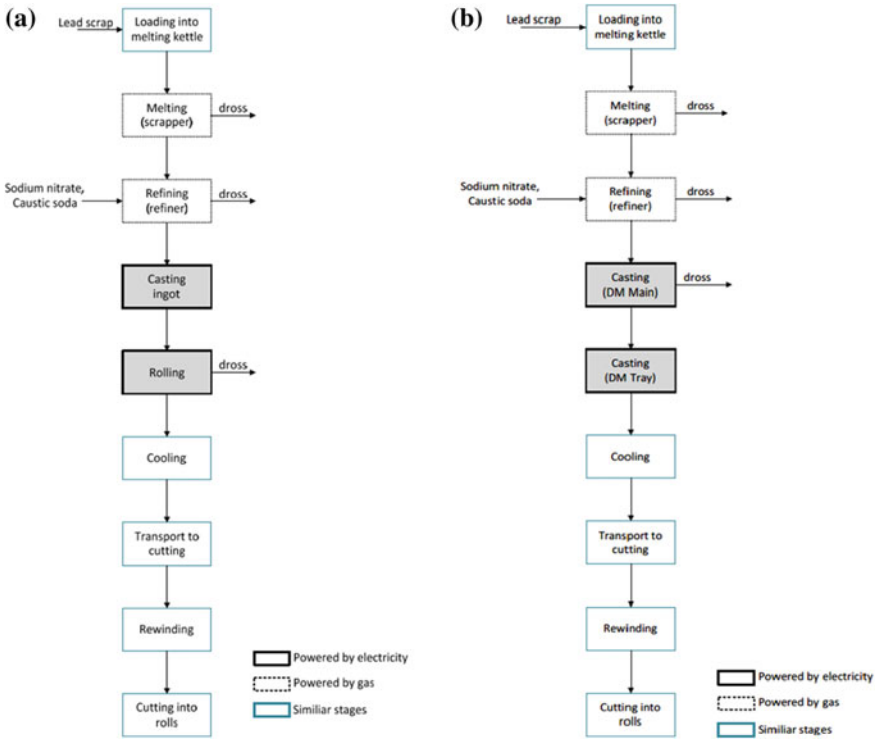

Fig. 2 **a**: Rolling; **b**: Direct Method

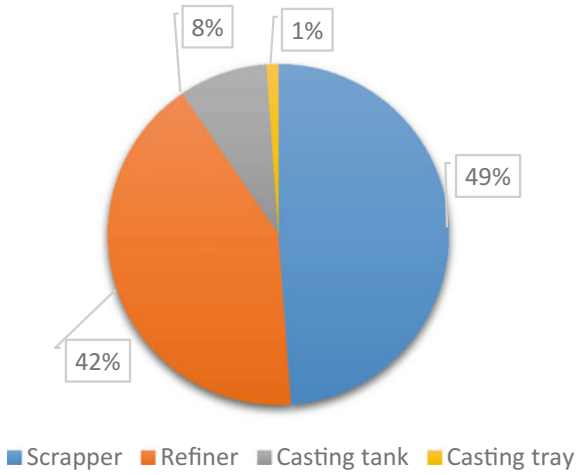

Fig. 3 Energy usage by different entities in DM

sheets have a shiny appearance compared to DM sheets which have a matte finish. However, DM sheets possess good creep resistance which increases with increasing copper content compared to rolled sheets with similar copper contents [14].

The process starts with melting lead scrap and then refining it. The refined lead is cast in moulds usually made of cast iron. These slabs are then passed through multiple rollers until the desired thickness is achieved [4]. The sheets are cut to the desired dimensions and packed for distribution as per the process flow diagram in Fig. 2. The usual thickness of production is 0.45 mm (code 1)—3.55 mm (code 8)—thicker rolled lead sheets up to 9.00 mm are also produced.

Metal in rolling process elongates with the rolling direction, speeding up. This means that the material moves faster on the exit side then on the entry [15]. The rolling calculations have been conducted based on equations for roll force and torque in flat-rolling [16]. The needed data are initial thickness of the billet (h_o), desired thickness (h_f), width of the material (w), number of revolutions per second of the rolls (N) and roll radius (R). At first roll-billet contact is given by the formula:

$$L = \sqrt{R(ho - \mathrm{hf})}$$

The roll force is calculated by the formula:

$$F = LwYavg$$

Where Y_{avg} is the average true stress. The total power is estimated by the equation:

$$P = \frac{2\pi FLN}{1000} * 10^6 \mathrm{kW}$$

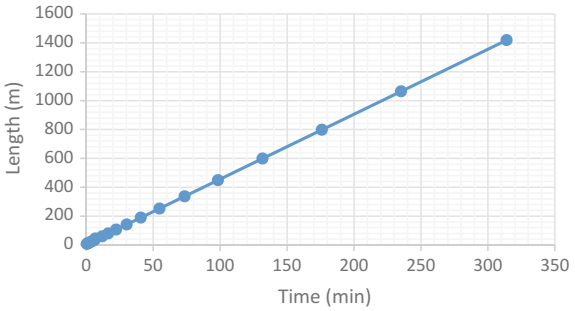

Fig. 4 Length of rolled sheet (l) versus total time taken (T)

Where N is the number of rotations per second. Since billets are not milled to the required thickness in one pass, multiple rolling approach has been applied. It assumes that with each pass the billet reduces its thickness by a percentage of its original thickness. The sheets are assumed to be constrained from the sides which means there is no change in the width of the sheets. The only parameters that change during the rolling process are length and thickness. This method produces multiple energy values which sum up to total energy of the process. The following assumptions are made to theoretically calculate the energy consumed.

Changing the length can be captured by comparison to the volume of the material, which stays the same though the whole process. Information regarding the velocity of the rolls enables calculating the time needed to roll given length. Next, multiplying the power by time gives the energy value presented in kJ. Density and volume provide the information about the mass of the material and the energy per tonne can be determined.

The graph shows the total time taken to attain a thickness starting from 5 mm thickness based on the assumed data. The graph is linear and the slope of the graph depends on the rate of reduction in thickness of the slab.

The maximum reduction in thickness (d) that can be attained is related to the coefficient of friction (μ) and radius of the roll (R) as per the following equation:

$$d = \mu^2 \mathrm{R}$$

Higher the value of μ, higher the reduction in thickness that can be attained. However, a higher coefficient of friction would result in higher consumption of energy (Fig. 4).

Cost Analysis of DM

As per Table 2, the overall energy consumed in the DM process is 539836 kJ/t. The energy consumed by the DM machine consisting of the main tank and the tray is 51412 kJ/t. The total energy consumed in reducing thickness from 5 mm to

Table 2 Energy data for DM process collected from a foundry based in UK for a calendar month

Element	Stage	Energy usage (GJ)	Energy usage per tonne (GJ/t)
Scrapper	Melting	529.57	0.263508
Refiner	Refining	452	0224915
Casting tank	Holding	91.19	0.045375
Casting tray	Casting	12.13	0.006037
Total		1084.91	0.539836

Table 3 Assumed data for theoretically calculating the energy consumed in rolling process

Data	Value
Initial thickness	50 mm
Pass reduction level	25%
Length	6 m
Width	1.4 m
Roll velocity	0.3 m/s
Roll radius	0.519 m
Average true stress (Y_{avg})	16 MPa

0.000376 is theoretically calculated to be 239142.4 kJ. The energy required per tonne for the rolling process can be calculated as 50210.46 kJ/t. This value is almost similar to the actual consumption of the DM process as per the energy audit from the foundry. The actual energy consumed in the rolling process would be much higher than the theoretically calculated values due to wastage through friction and loss of energy. Hence the Direct Method of casting is more energy efficient than rolling process (Tables 2, 3, 4 and 5).

There is a large difference between theoretical and actual energy consumption values in case of the DM. Though the theoretical value can never be achieved, this difference can be considered an opportunity for improvement. Tables 5 and 6 show a cost analysis of the DM. The scrapper and refiner are gas kettles and consume energy with the cost rate of £0.017202 per kWh. Direct casting machine is powered by electricity. The electricity rate is variable throughout the day but for simplicity the average cost has been taken.

Based on the actual cost data for the process, calculations can be made for the theoretical value of energy needed to melt and produce the same amount of lead that was manufactured via DM in a calendar month and this is calculated to be 155.23 GJ

This enables approximating energy values for each of the machines and possible cost. Mentioned calculations are shown in Table 6.

The huge difference between actual cost of energy of the DM and the cost estimated according to theoretical energy consumption shows that there is a potential for large amount of savings. Though reducing the energy consumption to attain the theoretical value of 0.077 GJ is impossible, there is plenty of room for improvement.

Table 4 Calculation of energy consumed in rolling process

Pass	Initial thickness h_o (m)	Final thickness h_f (m)	Change in thickness	Contact length L (m)	Force (MN)	Power (W)	Length of sheet (m)	Time (s)	Energy (kJ)
							6	20	
1	0.05	0.0375	0.0125	0.08054	1.804208	527.52	8	26.6666	14067.2
2	0.0375	0.028125	0.009375	0.06975	1.56249	395.64	10.66667	35.5555	14067.2
3	0.028125	0.021094	0.007031	0.06040	1.353156	296.73	14.22222	47.4074	14067.2
4	0.021094	0.01582	0.005273	0.05231	1.171868	222.547	18.96296	63.2098	14067.2
5	0.01582	0.011865	0.003955	0.04530	1.014867	166.910	25.28395	84.2798	14067.2
6	0.011865	0.008899	0.002966	0.03923	0.878901	125.183	33.71193	112.373	14067.2
7	0.008899	0.006674	0.002225	0.03398	0.76115	93.8872	44.94925	149.830	14067.2
8	0.006674	0.005006	0.001669	0.02942	0.659176	70.4154	59.93233	199.774	14067.2
9	0.005006	0.003754	0.001251	0.02548	0.570863	52.8115	79.90977	266.365	14067.2
10	0.003754	0.002816	0.000939	0.02207	0.494382	39.6086	106.5464	355.154	14067.2
11	0.002816	0.002112	0.000704	0.01911	0.428147	29.7065	142.0618	473.539	14067.2
12	0.002112	0.001584	0.000528	0.01655	0.370786	22.2798	189.4158	631.385	14067.2
13	0.001584	0.001188	0.000396	0.01433	0.32111	16.7099	252.5543	841.847	14067.2
14	0.001188	0.000891	0.000297	0.01241	0.27809	12.5324	336.7391	1122.46	14067.2
15	0.000891	0.000668	0.000223	0.01075	0.240833	9.39932	448.9855	1496.61	14067.2
16	0.000668	0.000501	0.000167	0.00931	0.208567	7.04949	598.6473	1995.49	14067.2
17	0.000501	0.000376	0.000125	0.00806	0.180625	5.28712	798.1964	2660.65	14067.2

Table 5 Actual cost analysis of DM

	Gas used (kWh)	Gas rate (£)	Electricity (kWh)	Electricity rate (£)	Total cost (£)
Scrapper	147103.16	0.017202	–	–	2530.47
Refiner	125558.96	0.017202	–	–	2159.87
DM tank	–	–	25330.86	0.075811265	1920.37
DM Tray	–	–	3370.20	0.075811265	255.50
					6866.20

Table 6 Theoretical cost analysis of DM

	% energy used	Energy consumed (GJ)	Energy in kWh	Type	Gas rate (£)	Average electricity rate (£)	Total cost (£)
Scrapper	48.81	75.7743427	21512.40	Gas	0.017202	–	370.0563
Refiner	41.66	64.6767050	18361.77	Gas	0.017202	–	315.8592
DM tank	8.41	13.0481862	3704.39	Electricity	–	0.075811265	280.8345
DM tray	1.12	1.736023107	492.86	Electricity	–	0.075811265	37.3642
							1004.114

Table 7 Analysis of lumps on a batch of 6 spools

Mass of spool (kg)	Mass of lump (kg)	Energy required to recast (GJ)
6136	1603	3.312434
6302	1144	3.402046
6098	1421	3.29192
6072	2091	3.277884
6152	1271	3.321071
6225	1551	3.360479

Energy Improvement Techniques for DM

There are several techniques for saving energy in foundries. Techniques like insulating furnaces, preheating scrap, reducing losses through convection, etc. are widely used. The following are two important areas of improvement in the DM method of lead casting:

Waste Reduction

Operational material efficiency (OME) is the ratio between the good casting shipped to customer and the total metal melted [17]. Improving the true yield is possibly the simplest way in which foundries can save energy, as this method focuses on increasing good casting production and reducing the total metal melted [18].

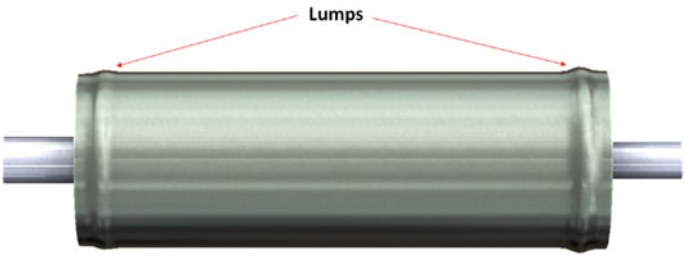

Fig. 5 Accumulation of edge deformation resulting in formation of lumps on DM spools

Casting in general results in formation of waste which are removed by machining. In many casting systems, wastage can be over 50% which are machined [18]. The DM process on the other hand is a distinct casting process in which the metal solidifies over the rotating drum layer by layer and wastage is substantially less compared to other casting processes. However, at times deformations can occur at the edges of the spool as shown in Fig. 5. This accumulation results in formation of a bulge or lump which is machined off and is re-melted, refined and recast to utilise materials resourcefully. However, this results in increased energy costs, labour and emissions. A reduction in the amount of material that needs to be machined can be considered as an opportunity to improve OME thereby making the process more energy efficient.

An analysis of the amount of wastage per spool in a day is shown in the table 7. Therefore, if the true yield of the casting can be improved, less metal will be required to produce the casting and the energy consumption for recasting could be reduced. Techniques to reduce these defects to the minimum would result in large energy savings and a higher OME can be attained.

Heat Recovery and Preheating of Scrap

Pre-heating of scrap can be very effective. It is very advantageous as it could remove any moisture and organic materials in the scrap, thereby preventing explosions in the furnace and reduce energy required for melting. Techniques like using flue gases from the melting furnace are being used by foundries these days [17]. In the DM process, the dross formed during melting is filled in metal barrels and is sent to a rotating recovery furnace. The metal barrels are loaded into the furnace which is heated to a temperature of over 420 °C and rotated. Recovery rates up to 65% are obtained. The barrels are taken out and then allowed to cool. Selvaraj et al. conducted studies on an innovative approach to preheat the scrap by using heat released by castings when they cool. The study reported 2.83% energy savings using this approach in which heat from the cast metals is recovered during cooling and used to preheat scrap [18]. A similar approach can be applied to use the heat from the recovery furnace and can be used to preheat scrap lead.

References

1. Department of Energy & Climate Change (2011)
2. Davidson AJ, Binks SP, Gediga J (2016) Lead industry life cycle studies: environmental impact and life cycle assessment of lead battery and architectural sheet production. Int J Life Cycle Assess 21(11):1624–1636
3. Haynes W (2015) CRC handbook of chemistry and physics. CRC Press, Boca Raton, FL
4. Construction| European Lead Sheet Industry Association (2017). http://elsia.org.uk/uses-benefits/construction/. Accessed 03 Aug 2017
5. Rocca E, Mirambet F, Steinmetz J (2004) Study of ancient lead materials: A gallo-roman sarcophagus—contribution of the electrolytic treatment to its restoration. J Mater Sci 3 (4):2767–2774
6. International Lead Zinc Study Group (2008) Principal uses of lead and zinc. http://www.ilzsg.org/static/home.aspx
7. Hofmann W (1970) Lead and Lead Alloys. In: Lead and lead alloys. Springer, Berlin Heidelberg, pp 25–320
8. Best Available Techniques (BAT) reference document for the non-ferrous metals industries (2014)
9. Thornton I, Rautiu R, Brush S (2001) Lead the facts. London
10. Salonitis K, Jolly MR, Zeng B, Mehrabi H (2016) Improvements in energy consumption and environmental impact by novel single shot melting process for casting. J Clean Prod 137:1532–1542
11. Jolly MR, Salonitis K (2017) Primary manufacturing, engine production and on-the-road CO 2: how can the automotive industry best contribute to environmental sustainability? In: 38th International Vienna Symposium, pp 379–398
12. European Lead Development Committee. and Lead Development Association (1967) Lead 65 edited proceedings. Pergamon Press
13. Randich E, Duerfeldt W, Mclendon W, Tobin W (2002) A metallurgical review of the interpretation of bullet lead compositional analysis. Forensic Sci Int 127(3):174–191
14. Whillock S, Charles JA, Smith GC (1989) Microstructures and mechanical properties of milled and continuously cast lead sheet Part 1 microstructures. Mater Sci Technol 5 (11):1074–1083
15. Kalpakjian S, Schmid SR, Sekar KSV (2013) Manufacturing Engineering and Technology, 7th edn
16. Zeng B, Jolly M, Salonitis K (2014) Manufacturing cost modeling of castings produced with CRIMSON process. In: Shape casting: 5th international symposium. Springer International Publishing, Cham, pp 201–208
17. Selvaraj J, Vignesh VS, Vishwam V (2014) Waste heat recovery from metal casting and scrap preheating using recovered heat. Procedia Eng 97:267–276
18. Salonitis K, Zeng B, Mehrabi HA, Jolly M (2016) The challenges for energy efficient casting processes. Procedia CIRP 40:24–29

Research on High Efficiency Energy Conversion Technology for Modern Hot Blast Stove

Fuming Zhang, Xin Li and Zurui Hu

Abstract High blast temperature is one of the important technical characteristics of modern blast furnace (BF), which is also an important technical approach for the green development of ironmaking. Increase blast temperature can improve and promote the BF operation smooth and stable, reduce coke rate, fuel consumption and CO_2 emission. Top combustion hot blast stove technology has been applied in Shougang Jingtang's 5500 m^3 BF for 8 years. Under the condition of burning single BF gas, high efficiency energy conversion and over 1250 °C high blast temperature have achieved. The combustion and heat transformation process were researched by numerical simulation technology to optimize the structure design. The high efficiency annular ceramic burner and checker brick were developed and applied, the flue gas waste heat was recovered and reused to preheat the combustion air and gas. Prominent achievement of high blast temperature under the condition single BF gas burning has been realized.

Keywords Blast furnace · Hot blast temperature · Top combustion hot blast stove Waste heat recovery · Combustion · Energy transformation

F. Zhang (✉)
General Engineer Office of Shougang Group Co Ltd, Beijing, China
e-mail: zhangfuming@bsiet.com

X. Li
Technology and Quality Department of Beijing, Shougang International Engineering Technology Co., Ltd, Beijing, China
e-mail: lx091516@163.com

Z. Hu
Ironmaking Department of Beijing, Shougang International Engineering Technology Co., Ltd, Beijing, China
e-mail: 246mp5@163.com

Z. Sun et al. (eds.), *Energy Technology 2018*, The Minerals, Metals & Materials Series, https://doi.org/10.1007/978-3-319-72362-4_12

Introduction

Reducing energy consumption and cost of ironmaking process are very important to improve the market competitiveness of iron and steel industry, [1] because energy consumption of ironmaking process accounts for about 70% of the total energy consumption of iron and steel manufacturing, and cost of pig iron accounts for about 50% the total cost of iron and steel manufacturing. High temperature blast provides about 20% of the heat in BF smelting, and high blast temperature is an important technical characteristic of modern BF ironmaking, which is also an important way to realize high efficiency energy conversion. High blast temperature has the following important meaning: [2]

- Reducing fuel consumption, saving coke, reducing the production cost.
- Increasing the temperature of tuyere raceway, increasing quantity of pulverized coal injection, further reducing coke rate.
- Increasing the hearth heat, which is helpful for the BF operational performance.
- Improving production efficiency, reducing CO_2 emissions.

Chinese steel workers have studied the key technologies of hot blast stove from their respective needs. The research they have made are as follow: The research for the reason caused the piping broken and optimizing design [3], Study on standards of refractory used for hot blast pipes between blast furnace and hot blast stove [4], The optimization of hot blast stove quantity and operation [5], The optimization of hot blast stove control system [6], High radiative coating used in checker bricks [7].

Acquisition, transmission and utilization of high blast temperature is a systematic project, which is composed of a series of key technologies, including low heat-value gas utilization technology, high efficient and clean combustion technology, high efficient heat transfer technology in regenerator, low stress piping system, etc. This paper focused on joint research which combined numerical simulation and experimental research, and also focused on analyzing and verifying the influence of checker brick on heat transfer process. The purpose of the research is to increase the energy conversion efficiency of hot blast stove.

Promote Blast Temperature by Low Heat Value BF Gas

Technological Philosophy

Shougang Jingtang steel plant is an annual production capacity of approximate 10 million tons of large iron and steel union enterprises, product positioning for high grade plate and strip, cold rolled products ratio is 54.6%, the steel products processing facilities complete, so the high calorific value of coke oven gas, converter gas to supply in steelmaking, rolling process, hot blast stove only the low calorific value of BF gas as fuel. With the progress of BF operational technology, the

utilization rate of gas is continuously increasing, and the calorific value of BF gas is decreasing gradually, which is about 3000–3200 kJ/m^3. The top combustion hot blast stove can only reach 1200–1300 °C, with the single BF gas, and so it is difficult to reach the high blast temperature above 1250 °C [8].

Shougang Jingtang's 5500 m^3 BF in the design process, in order to realize the high blast temperature reaches 1250–1300 °C [9], which fuel of hot blast stove only the BF gas, a large amount of research, comprehensive analysis and demonstration of various technical measures of high temperature at home and abroad have been applied, the design and development of BF gas and combustion air, preheating process with innovation [10, 11].

Theoretical Combustion Temperature and Dome Temperature

During the hot blast stove burning, the main source of heat is the chemical heat of the gas, and the preheated temperature of the combustion air and gas is fixed. When all the heat is used to heat the combustion products, no other heat losses, the temperature which can reach called the theoretical combustion temperature of hot blast stove.

During the operation of the hot blast stove, actually the dome temperature of hot blast stove is lower than the theoretical combustion temperature 30–50 °C because of heat dissipation of stove wall and incomplete combustion. Practice has proved that the theoretical combustion temperature is the main contradiction to limit the increase of blast temperature in hot blast stove, and the formula is shown in Eq. 1.

$$t_T = \frac{Q_A + Q_G + Q_{DW}}{C_P V_P} \tag{1}$$

In formula: t_T-theoretical combustion temperature, °C; Q_A-combustion air sensible heat, kJ/m^3; Q_G-Gas sensible heat, kJ/m^3; Q_{DW}-low calorific value of gas, kJ/m^3; C_P-heat capacity of combustion product at t_T, kJ/(m^3·°C); V_P-volume of combustion product, m^3.

It can be seen from formula 1, that the theoretical combustion temperature of the hot blast stove can be improved by increasing the physical heat (sensible heat) of the combustion air and gas. Increase the preheat temperature of combustion air and gas can improve their physical heat effectively. Figure 1 shows the theoretical combustion temperature under the condition of preheating combustion air and gas.

During the blasting period, the cold blast absorb heat from checker brick, then flow into the hot blast pipeline and blast into the BF through the tuyere. The hot blast temperature which is received by the BF is called the blast temperature. During the whole blasting period, the hot blast temperature at the hot blast outlet is gradually decreased with the increase of the heat exchange between the cold blast and the checker brick. BF operation requires constant blast temperature, so we

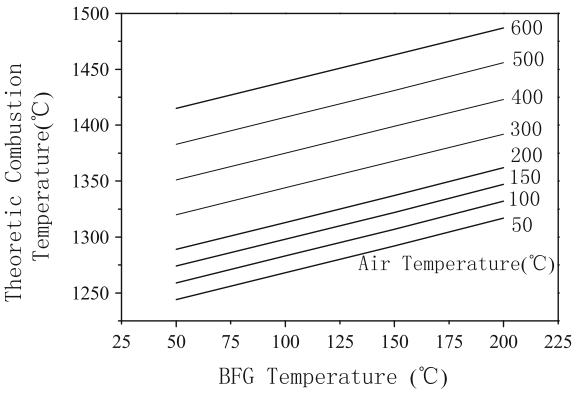

Fig. 1 The theoretical combustion temperature of hot blast stove under the condition of combustion air and gas preheating

usually mix cold blast into the hot blast pipeline system, and maintain the constant blast temperature by adjusting the mix cold flow at different stages of blasting.

High Efficiency Preheating Technology

It is a worldwide problem to realize high temperature only by burning BF gas. The blast temperature of Japan, Europe and other advanced BFs have reached 1250 °C, were blended with some high calorific value gas (such as natural gas, coke oven gas, converter gas and so on). Research shows that, the dome temperature of hot blast stove is depending on the theoretical combustion temperature, according to theoretical combustion temperature calculation formula can be found that improve the physical heat of gas and air are the effective technical measures to improve the flame temperature at the same gas calorific value. According to the combustion calculation, the BF gas should be preheated to 200 °C and the combustion air should be preheated to over 500 °C to achieve high blast temperature at 1300 °C [12].

At the beginning of 21st Century, the combustion air preheating technology was adopted to increase dome temperature and achieve industrial application success in Shougang. The existing 4 seats of Shougang's type top combustion hot stove which belong to Shougang's No. 2 BF were put into production in 1979 No. 2 BF rebuilt in 2002, focusing on the innovative design of high temperature combustion air preheating process, mainly in the following aspects:

- Remove two old top burning hot stoves, Nos. 1 and 2, which have been running for more than 23 years. Nos. 3 and 4 top combustion hot blast stoves were used as preheating furnace for high temperature preheated combustion air.
- The three high temperature internal combustion hot stoves introduced from Corus were applied, which combustion air was preheated to 600 °C by the original Shougang's top combustion stove. The blast temperature reaches 1250 °C only by burning BF gas. Figure 2 is a photo of Shougang's No. 2 BF after renovation.

Preheating Process Integration

The comprehensive advantages and disadvantages of various preheating process, and combined with a large number of engineering practice in the field of accumulation, in the design of hot blast stove preheating system of 5500 m^3 BF of Shougang Jingtang steel plant, the longevity of independent intellectual property rights of the two stage double preheating system. The technology is developed and designed successfully on the basis of high temperature preheating technology of combustion air in shougang. The main technical principle is: the separated type heat pipe heat exchanger, using hot BF flue gas waste heat preheating gas and combustion air is preheated gas and combustion air temperature can reach 200 °C, this process is called a double preheating. Two sets of regenerative combustion air temperature preheating stove used to preheat the combustion air, the temperature is raised to 550 °C. The combustion air preheating furnace gas and combustion air through the heat pipe heat exchanger preheating, by burning through a preheated BF gas to preheat furnace after heating, the dome temperature can reach 1300 °C, and then used for combustion air heating hot blast stove use, after combustion air temperature after heating temperature can reach 1200 °C for export and then, after a mixed combustion air preheating, the combustion air to control the temperature of 550 ~ 600 °C, this process is called two preheating. This is a process of self-circulating preheating process, significantly improve the physical heat of air and gas, the dome temperature of hot blast stove also improved, which can effectively improve the air temperature, hot blast stove system overall efficiency is significantly improved. Figure 3 shows the two stage dual preheating system with high blast temperature in the hot blast stove system.

With the development of plate heat exchanger, it has shown many advantages, such as longer service life, less fouling, and gradually began to replace the traditional tubular heat exchanger.

Fig. 2 Photo of Shougang's No. 2 BF hot blast stove

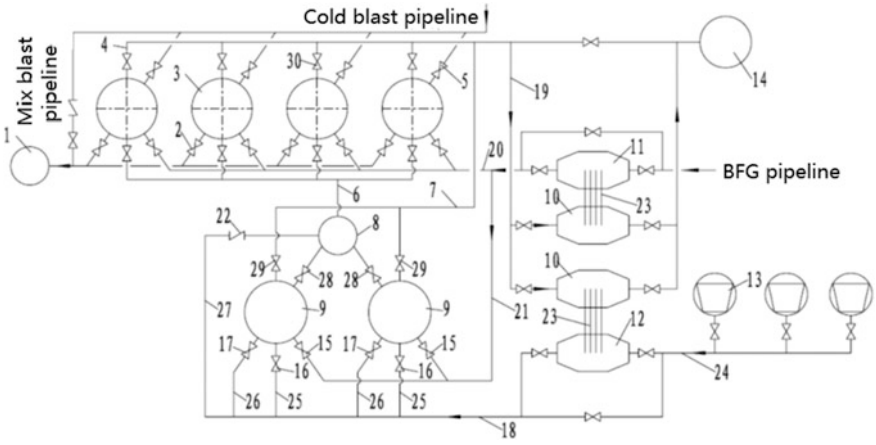

Fig. 3 Process flow chart of two stage double preheating system for hot blast stove

The system has been put into operation in May 2009, and the practice has proved that the system can satisfy the thermal air temperature of 1250 ~ 1300 °C under the condition of using a single BF gas [13].

Comparison of Efficiency of Hot Blast Stove

The two processes of two stage double preheating and only heat exchanger preheating are calculated and compared:

(1) The thermal efficiency of the main body of the hot blast stove
The two process gas temperature is basically the same, the two stage double preheating process of blast temperature is 1300 °C higher than the low temperature preheating 1200 °C, so the body slightly high thermal efficiency of hot blast stove. The thermal efficiency of the two stage double preheating process was calculated to be 77.01%, and the thermal efficiency of the hot blast stove was 74.84% at the low temperature preheating process, and the former was 2.17% higher than that of the latter [14].
(2) The cooling, heat dissipation of the shell, pipe and valve of the hot blast stove system
Table 1 shows the comparison of the heat dissipation of two kinds of preheating process.
(3) Comparison of thermal efficiency of hot blast stove system

Table 1 Heat dissipation of different preheating process

Process	Shell (kJ/Nm^3 blast)	Pipe (kJ/Nm^3 blast)	Valve cooling (kJ/Nm^3 blast)
Two stage high temperature preheating	52.58	71.23	17.71
Low temperature preheating	44.42	57.12	8.51
Different (%)	15.5	26.2	51.9

Table 2 Comparison of different preheating process

Process	Blast temperature (°C)	BF gas flow (Nm^3/h)	Air flow (Nm^3/h)	Coke rate (kg/tHM)	Thermal efficiency of hot stove (%)	Thermal efficiency of the hot blast stove system (%)
Two stage high temperature preheating	1300	338089	218406	290	77.01	83.76
Low temperature preheating	1200	303776	196240	305	74.84	84.05
Different (%)	100	34313	22166	−15	2.17	−0.29

Overall, the two stage high temperature double preheating process has improved 100 °C blast temperature, reducing coke rate 15 kg/tHM, but low temperature preheating process to consume 34313 Nm^3/h gas, the thermal efficiency of the hot blast stove system is reduced by 0.29%, but for the entire system of BF, the energy consumption is reduced (Table 2).

Numerical Simulation and Experimental Study

Burner is very important as the core equipment of hot blast stove. During the research and design of huge high temperature top combustion hot blast stove, hot blast stove accurate design system have been established, which is based on the theoretical research, experimental investigation, industrial trial, 3-D precision design. The system integrated application of a variety of advanced research methods, and developed several calculation programs independent. Research group not only analyzed and calculated the hot blast stove theoretically, but also did the cold/hot test and industrial test to verify the calculation results. The 3-D design method also was used to enhance design efficiency and precision, and to optimize design scheme.

Numerical Simulation of Top Combustion Hot Blast Stove

The combustion type in the dome combustion hot blast stove is turbulent non-premixed combustion, which is simulated by the mixed fraction *k*- ε- *g* model. The control equations include:

Continuity equation:

$$\frac{\partial \rho}{\partial t} + \nabla \cdot (\rho U) = 0 \tag{2}$$

Momentum Equation:

$$\frac{\partial \rho U}{\partial t} + \nabla \cdot (\rho U \times U) - \nabla \cdot (\mu_{eff} \nabla U) = -p^{'} + \nabla \cdot (\mu_{eff} (\nabla U)^{T}) + B \tag{3}$$

In the equation, ρ is density of main stream, U is average velocity of main stream; μ_{eff} is effective viscosity, which is defined as: $\mu_{\text{eff}} = \mu + \mu T$, μT is eddy viscosity, B is body force.

k-ε Equation:

$$\frac{\partial \rho k}{\partial t} + \nabla \cdot (\rho U k) - \nabla \cdot \left(\left(\mu + \frac{\mu_T}{\sigma_k} \right) \nabla k \right) = P + G - \rho \varepsilon \tag{4}$$

In the equation, k is the turbulent kinetic energy, ε is the turbulent dissipation rate, P is shear generated, G is volume generated, σ_k and σε respectively represent Prandtl number of k and ε. In the calculation, $\sigma_k = 1.0$, $\sigma_\varepsilon = 1.3$. C_1, C_2 and C_3 are empirical constant, $C_1 = 1.44$, $C_2 = 1.92$, $C_3 = 0.09$.

Considering that combustion in hot blast stove is diffusion combustion, a non-premixed PDF model is used. The main fuel of hot blast stove is BF gas, which produce CO_2, H_2O and N_2 after combustion. CO_2 and H_2O belongs to polar molecules gas, within a certain wavelength radiation and energy absorption. In common engineering combustion equipment, radiation heat transfer is the main method to transfer heat, up to 90%. So radiation model must be used when we simulate the combustion in hot blast stove. For radiation heat flux q_r:

$$-\nabla q_r = aG - 4a\sigma T^4 \tag{5}$$

The expression of $-\nabla q_r$ can be directly introduced to the energy equation, thereby obtaining the heat source caused by the radiation. The absorption coefficient and scattering coefficient of a given mixture are required for the use of this radiation model. Because the mixture contains CO_2 and H_2O, the absorption coefficient is calculated by using the gray gas weighted average model (WSGGM). Boundary conditions: set flow, temperature and composition of air and gas inlet, resistance coefficient of checker brick.

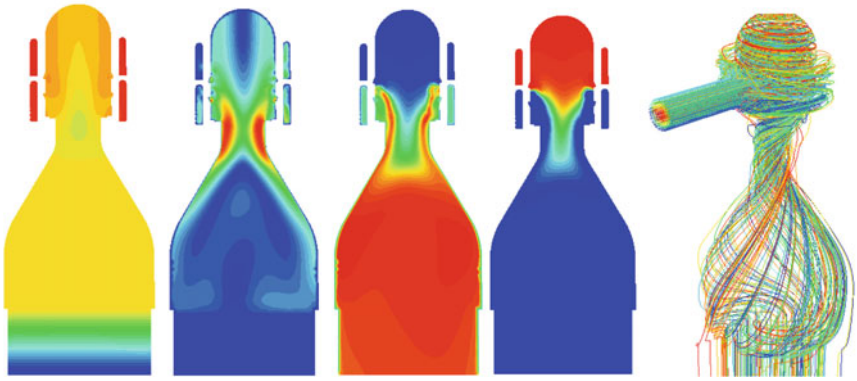

(1)-Pressure distribution, (2)-Velocity distribution, (3)-Temperature distribution, (4)-CO concentration distribution, (5)-Flow field distribution

Fig. 4 Results of CFD simulation for top combustion hot blast stove

Through iterative calculation, pressure distribution, velocity distribution, temperature distribution, CO concentration distribution and flow field distribution of the dome combustion hot blast stove are obtained, as shown in Fig. 4.

It is found by calculation that, after flowing into the premix chamber, velocity of air and gas increase quickly when they down through the throat because of flowing area decreases which is caused by shrinkage throat. A mixture of air and gas here is greatly enhanced, and nonuniformity caused by upper stream is also effectively reduced. Through the strengthening mixture of the throat, velocity distribution, temperature distribution and concentration field distribution in the combustion chamber are axisymmetric. CO is fully burned in the combustion chamber before flowing into the checker brick, avoid the occurrence of secondary combustion within the checker brick and to extend the service life of checker brick. The uniform swirling flow field in dome combustion hot blast stove avoids the production of local high-temperature zone, which can produce a large number of NO_x.

Cold Blast Distribution Uniformity of Top Combustion Hot Blast Stove

During blasting period, the cold blast flow into the bottom of the stove through the branch pipe, and then flow into the regenerator chamber. After exchanging heat in regenerator chamber, the cold blast become hot blast, and leave the hot blast stove from hot blast outlet. In order to improve the efficiency of the use of regenerator chamber, and make the heat in regenerator chamber to be taken away evenly and

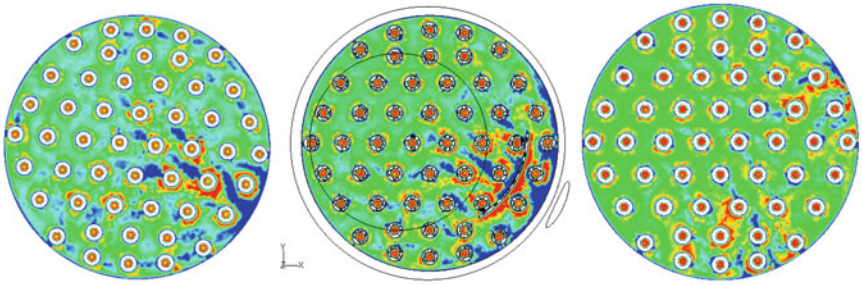

(1) Single cold blast inlet pipe; (2) Single cold blast inlet pipe with guide plate;
(3) Using the two waste gas branch pipes as cold blast inlet pipes

Fig. 5 Velocity distribution of cold blast in the blasting chamber

fully as much as possible, cold blast should be distributed evenly into the chamber, avoid nonuniformity.

Three schemes are designed: (1) Single cold blast inlet pipe; (2) Single cold blast inlet pipe with guide plate; (3) Using the two waste gas branch pipes as cold blast inlet pipes. After analyzing simulation results of three schemes, it is found that if used single cold blast inlet, whether guide plate used or not, there are wide range of high speed area and low speed area near the inlet. If two waste gas branch pipes are used as cold blast inlets, it could decrease the high speed area and low speed area obviously. The distribution of cold blast is more uniform, which is beneficial to improve the heat exchanging efficiency of the regenerator chamber. Figure 5 shows the velocity distribution of cold blast in the blasting chamber.

Industrial Cold Test of Top Combustion Hot Blast Stove

The cold industrial test for hot blast stove of Shougang Jingtang's 5500 m^3 huge BF was carried out to verify the numerical simulation. The testing content included air jet velocity, gas jet velocity (medium was air), velocity in throat, regenerator chamber upper velocity distribution, regenerator chamber lower velocity distribution, flow field inside the stove, etc.

Test results show that the distribution of air and gas among nozzles are not uniform. The speed of nozzles which are near the branch pipe is higher than others. The gas jet velocity is more uniform than air's. The test results are consistent with the numerical simulation, so we believe that the simulation is reliable. Because air and gas swirl down through the throat, and flow near the wall, the velocity near the wall is higher, and velocity in center of the combustion chamber is lower, which covers an area of about 10% of the regenerator chamber upper area.

Hot Condition Simulating Trial

For further study of transfer theory of combustion, gas flow and heat transfer process of dome combustion type hot blast stove, 2 hot blast stoves for hot condition trial based on prototypical of dome combustion hot blast stove of Jingtang's 5500 m^3 BF are established. The "one stove burning and one stove blasting" working mode is applied to simulate real working process of the hot blast stove.

The 2 hot blast stoves for hot condition trial are provided with 289 temperature meters and corresponding gas flow meters for many times of hot condition test of hot blast stove. On-line detection is used to test temperature variety of checker brick in the regenerator chamber at combustion and blasting statuses of hot blast stove, and with combination of pressure detection and fume composition detection to analyse temperature field distribution status and combustion status in the experimental hot blast stoves. The results of hot condition test of hot blast stove prove that, the results of the flow field numerical simulation of combustion chamber and the numerical simulation of regenerator chamber are correct. The simulation and the test provide theoretic and experimental basis for optimal design of the hot blast stove and configure checker brick reasonably.

Research on Regenerator Chamber

Regenerator chamber has the characteristics of periodic heat absorption and exothermic, and is another key part of hot blast stove. The design of checker brick and channel regenerator chamber, and selection of refractory material are emphasized during the design of hot blast stove.

Optimization of Checker Brick

The checker brick should meets the following conditions:

- Having large heating surface, can satisfy the requirements of the heat transfer rate;
- Having enough filling rate, can satisfy the heat storage capacity;
- Having enough compressive strength, can support regenerator chamber;
- Checker bricks in high temperature zone have excellent creep resistance;
- Easy to be manufactured, low cost, quality is stable.

Figure 6 shows the three kinds of checker bricks currently are used in a wide range. Table 3 shows the specification comparison of these three checker bricks.

Compare with checker brick A, checker brick C has smaller hole and living area. Under the same simulation condition, the pressure loss will increase with smaller

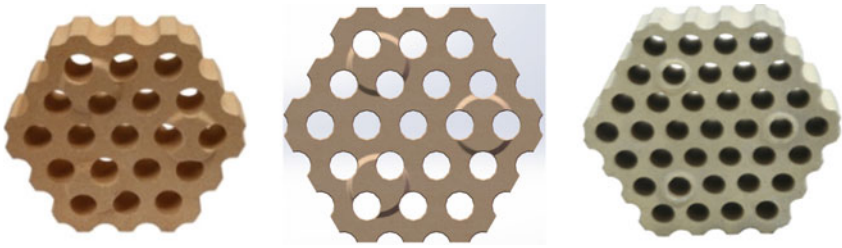

(A) 19 holes- ϕ30mm (B) 19 holes- ϕ25mm (C) 37 holes- ϕ20mm

Fig. 6 Three types checker brick

Table 3 Specification comparison of three checker bricks

Items	A	B	C
Diameter of hole (mm)	30	25	20
Numbers of hole	19	19	37
Filling rate (-)	0.612	0.627	0.655
Active area (-)	0.388	0.373	0.345
Thickness of brick (mm)	120	120	120
Heating area per volume (m^2/m^3)	48.6	56.1	64.7
Equivalent depth (mm)	25.2	22.4	20.2
Thickness between holes (mm)	17.3	15.2	13.5

hole. If we use checker brick A (ϕ30 mm) as the benchmark, when the hole of checker brick decrease to 25 mm, the pressure loss will increase 50%, and when the hole of checker brick decrease to 20 mm, the pressure loss will increase 150%, as shown in the Fig. 7.

In order to reduce pressure loss, a series of method should be used after using small hole checker brick, like increasing the diameter of regenerator chamber and flow area, and lowering gas velocity. The convective heat transfer coefficient of the

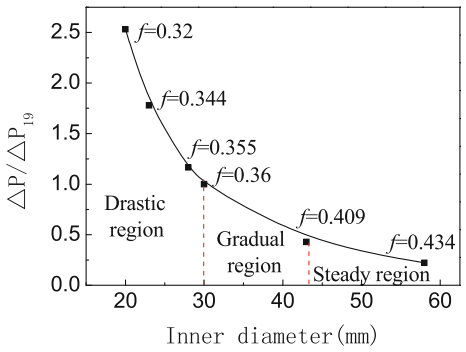

Fig. 7 Relationship between checker brick hole and pressure loss

Table 4 Specification comparison with 3 different checker bricks

Items	Option A	Option B	Option C
Effective volume of BF (m^3)	5500	5500	5500
Blast volume (Nm^3/min)	9300	9300	9300
Blast temperature (°C)	1300	1300	1300
Diameter of regenerator chamber (m)	10.89	10.0	10.89
Height of regenerator chamber (m)	17.48	22.5	21.48
Ratio of height to diameter	1.61	2.25	1.97
Diameter of checker brick hole (mm)	20	25	30
Average Reynolds number	1504	2036	1980
Pressure loss of regenerator chamber (Pa)	616	783	446
Heating area of hot blast stove (m^2/HBS)	104452	96524	95885
Weight of checker bricks per hot blast stove (t/HBS)	2164	2175	2435
Heating area of checker brick per volume of blast ($m^2 \cdot m^{-3} \cdot min^{-1}$)	47.48	41.52	41.24
Height of hot blast stove (m)	46.2	50	50.2

fluid has a great relationship with the flow condition, which is showed by the Reynolds number. The calculation formula of the Reynolds number is:

$$Re = \rho v d / \mu \tag{7}$$

In formula 7, ρ is density of the fluid, v is velocity, d is diameter of checker brick hole, μ is dynamic viscosity. Table 4 shows regenerator chamber specification comparison with 3 different checker bricks.

Option A uses checker brick with diameter 20 mm hole. In this situation, the height of regenerator chamber should be less than 18 m, in order to control the pressure loss, and avoid blocking the hole. So the diameter of the regenerator chamber should be increased to get enough checker brick weight for storing heat. Average Reynolds number of option A is just 1504, which is less than option B, when they have the same pressure loss. This is not good for heat convection.

If the checker brick diameter 20 mm like option C is adopted, and keep the heating area as same as option A and B, the weight of regenerator chamber will increase about 12%. The Reynolds number is same as option B. So we can get balance easily between heating area and weight, and we also can get higher using efficiency of regenerator chamber when we use diameter 30 mm checker brick like option B.

During the hot blast stove repair, it was founded that on the upper surface of the wall and inner surface of upper silicon checker brick there was a thick and loosened layer of residue which was formed by reaction of silicon bricks and dust under high temperature condition. Colors of the residue were earth yellow and dark gray, and the original color of silicon brick was pale yellow. After cooling to room temperature, the residue began to crack and peel from the checker brick. It was clean on

Fig. 8 Erosion of upper silicon checker brick in hot blast stove

the top surface of regenerator chamber and no residue, because the gas velocity here was too high to keep dust staying. But silicon checker brick was eroded because of being long-term exposed under high temperature and gas condition. The relatively weak part of the silica brick was eroded seriously, and surface of the weak part became honeycomb. The damaged checker brick details were shown in Fig. 8.

The internal erosion of hot blast stove is mainly determined by the chemical composition of BF gas and the surface temperature of refractory lining. After testing of BF gas gravity dust, it is found that the main composition of BF gas dust were MgO, CaO, Fe_2O_3, K_2O, Na_2O and ZnO, which is related to the reaction taking place inside the BF. There will be some small particles that have not been removed as the gas flows into the hot blast stove. When the BF gas react in hot blast stove, the products of combustion will adhere to the surface of the refractory lining under high temperature condition. This will cause damage to the silica and aluminium siliceous refractory which always happen in BF.

Hot blast stove always works under the condition of high temperature and high pressure. For long-term used hot blast stove which is designed to use for 25 $\sim$ 30 years, it has big risk to use smaller hole (like diameter 20 mm) checker brick.

Considering the above factors, it is advisable to use diameter 25 mm checker brick which has large heating area, a moderate amount of pressure loss and unblocked characteristic, to achieve high efficiency, long service life and low cost.

Numerical Simulation and Optimization of Regenerator Chamber

The hot blast stove is a typical heat exchanger, which is made of a large number of checker bricks. Due to the periodic characteristics of the hot blast stove, the heat storage and heat release of the hot blast stove have the characteristic of hysteresis

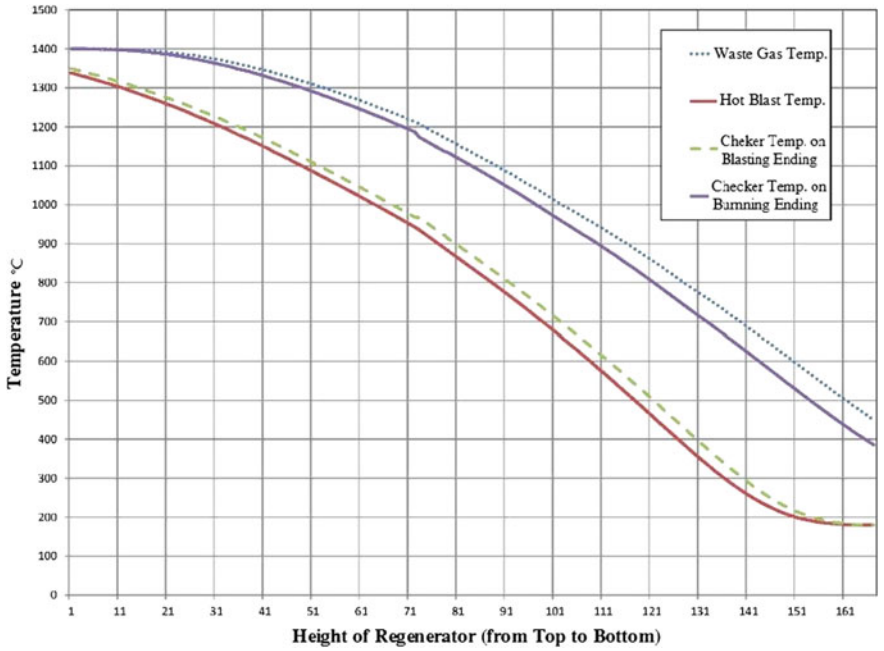

Fig. 9 Temperature distribution curve in regenerator chamber

and nonlinearity. The calculation of hot blast stove regenerator chamber has been based on several empirical formulas for a long time [15].

The hot blast stove regenerator chamber calculation program developed by BSIET, is based on the German H. Hausen theory to calculate the vertical temperature field of regenerator chamber. After practical use and continuous optimization and improvement of the program for several years, it can accurately calculate the temperature distribution in regenerator chamber, and provide effective guidance for hot blast stove precise design. Figure 9 shows the temperature distribution curve of regenerator chamber of hot blast stove of Tonggang's new No. 2 BF. It was calculated by the program. With the guidance of the calculation result, we could choose different refractory material for different part of the regenerator chamber. For example, the height of the silicic checker brick eventually identified as 70 × 120 mm = 8400 mm high, which was considered with both the calculation result and the requirement of the temperature range 1200 ∼ 950 °C. With the understanding of the temperature change along the height of the regenerator chamber in different time, we could reasonably choose the refractory materials of different parts to ensure the long-term stable operation of the hot blast stove.

Design of Low Stress and no Overheat System for Hot Blast Pipeline

Static Force Analysis of Pipeline

The hot blast pipe, main pipe and ring pipe in hot blast stove system are high temperature and high pressure pipes, and they are the most complicated piping design of hot blast stove. Hot blast pipeline is an important link to achieve high hot blast temperature, and is the guarantee of stable transportation of high temperature hot blast.

In the design through the flexible structure with rigid structure should be designed with a combination of low power pipeline, pipe system using professional analysis software design and calculation of pipeline (Fig. 10), reasonable design of pipe, corrugated expander, pipe rack, pipe rod, so that the hot blast pipeline into a low stress system. Effectively guarantee the normal service life of the pipe system. The hot blast duct and three fork pipe fixing bracket, a fixed bracket on both sides of duct axial compensator for thermal displacement, absorption duct, is arranged between the fixed bracket and compound compensator is used to heat the hot blast stove, hot blast stove and the hot blast rising displacement absorption branch. The hot blast duct with rigid rod body, overcome the expansion force, the whole pipeline system of thermal pressure force, the end of the hot blast duct is used to absorb the hot blast duct compensator, and the elongation of the rod thermal expansion displacement, to overcome the blind plate force hot blast duct, hot blast duct of the low stress drop. Through the optimization design of refractory in the pipeline, a no overheating system of hot blast pipe was established.

Design Optimization of Hot Blast Branch Pipe

The hot blast duct and three fork branch intersection is the position of stress concentration. Through the pull beam structure is arranged in a hot blast pipe on the triangle layout, the characteristics of triangle stability, improve the stability of steel

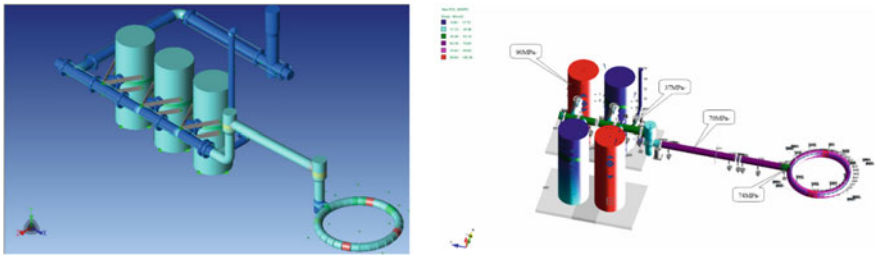

Fig. 10 Force analysis of hot blast pipe system

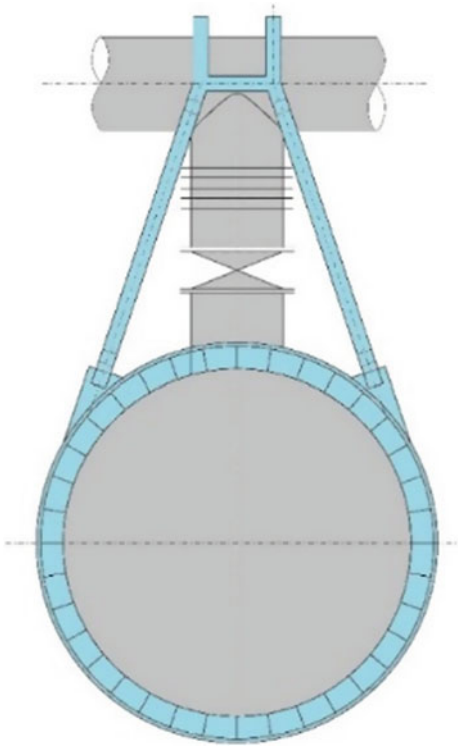

Fig. 11 Triangular tension beam structure

pipe/hot blast duct three forks (Fig. 11). Special method should be used because the hot blast outlet exists larger vertical displacement after heating up the hot blast stove. A vertical displacement between hot blast main pipe and hot blast outlet should be kept when hot blast outlet is installed (Fig. 12). The hot blast outlet will rise up with the heating of hot blast stove. When elevation of hot blast outlet and hot blast valve is same, the hot blast valve should be installed. This method could decrease stress of hot blast outlet.

Design Optimization of Corrugated Compensator

Hot blast pipe compensator stiffness is relatively small, high temperature and high pressure and harsh working conditions, refractory heavy load makes the compensator has become a weak link in hot blast pipe system. The load of the compensator is improved by adding the structure of the ripple compensator. The expansion joint of traditional double axial compensator has wide width and is prone to overheat and even wind. By optimizing the form of compensator structure and adopting the

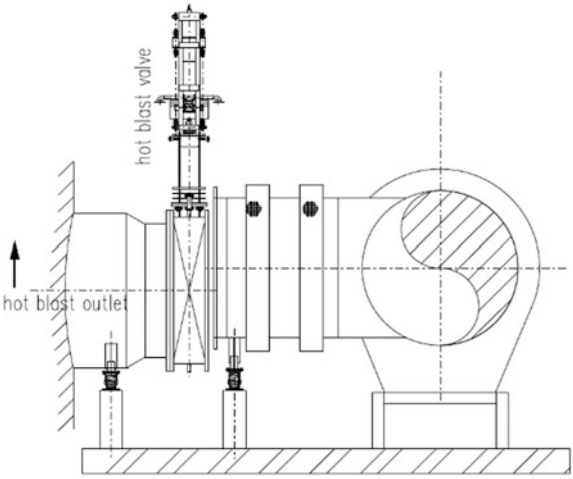

Fig. 12 Staggered installation of hot blast valve

Fig. 13 Optimization of hot blast pipe system compensator

compound form of hinge and axial, the width of expansion joint of compensator is reduced, and the tightness of refractory material is improved (Fig. 13).

Optimization of Refractory Structure Design

The hot blast pipeline adopts a heavy brick, three layer of heat insulation brick, spraying a layer of unshaped refractory. The upper part of the pipeline Section 120

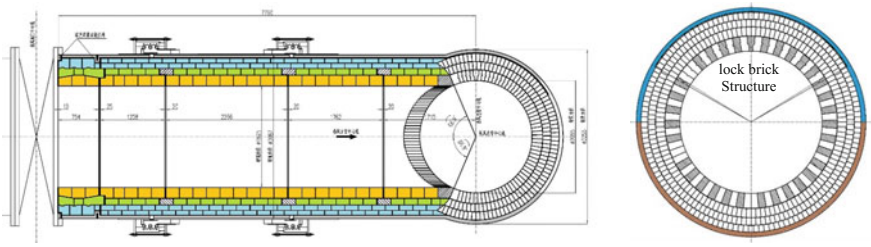

Fig. 14 Optimization of refractory structure for hot blast pipe

degree heavy brick with locking structure, improve the structural stability of lift. The expansion joint is designed reasonably in the axial direction of the pipe, and the expansion joint is protected by heavy bricks. Hot blast valve located near the expansion joints, convenient maintenance for the valve, avoid change valve, damage the overall stability of the pipeline refractories (Fig. 14).

Application

Top combustion hot blast stove and efficient energy conversion technology has applied to the Shougang Jingtang's 5500 m^3 huge BF, Qiangang's No. 1 BF (2650 m^3), the new No. 2 BF (2650 m^3) of TISCO, No. 8 BF (3052 m^3) of Liangang, No. 2 BF (1950 m^3), the new No. 3 BF (1800 m^3) of Xiangtan Iron & Steel Co. Which is the first BF of Shougang Jingtang's 5500 m^3 the application of the technology huge BF, after the commissioning of monthly average hot blast temperature reached 1300°C, the combustion condition of single BF gas, BF hot blast temperature stable design index reached 1300 °C, has created considerable economic benefits and good social benefits for the user.

The new technology in Qiangang's No. 2 BF (2650 m^3) application, the production index steadily, gas preheating temperature 180 ~ 200 °C, combustion hot blast preheating temperature 350 ~ 400 °C, hot blast stove burning BF gas, can provide 1250 °C hot blast temperature to improve the stability of BF.

Conclusions

With the using of two stage double preheating process, hot blast stove of Shougang Jingtang 5500 m^3 hot blast furnace could get hot blast as high as 1300 °C with fully using of blast furnace gas.

With the using of joint research combined with numerical simulation, cold condition test and hot condition experiment, the flow field in combustion chamber and cold blast distribution in blasting chamber are optimized.

It is advisable to apply diameter 25 mm checker brick which has large heating area, a moderate amount of pressure loss and unblocked characteristic, to achieve high efficiency, long service life and low cost.

Pay attention to design optimization of hot blast pipeline, no overheat and low stress hot blast pipeline system is applied with structure optimization, refractory optimization and using of advanced design system.

Top combustion hot blast stove and high efficient energy conversion technology has been applied to several hot blast furnaces, which scale from 1800 to 5500 m^3. The practical application prove that the technology can increase the blast temperature efficiently, economically and steadily.

References

1. Shourong Z (2012) Development and problems of ironmaking industry after entering the 21st century in China. Ironmaking 31(1):1–6
2. Fuming Z (2012) Cognition of some technical issues on contemporary blast furnace ironmaking. Ironmaking 31(5):1–6
3. Yao T, Ruihai Z, Zhihong L (2016) The study of design concept of hot blast piping of high temperature hot blast stove. Ironmaking 35(4):30–33
4. Guotao X, Wuguo X, Xibo W (2017) Study on standards of refractory used for hot blast pipes between blast furnace and hot blast stove. Res Iron Steel 45(1):58–62
5. Wenquan T, Cuiping W (2015) The comparation and optimization of quantity of hot blast stove. Metall Econ Manag:37–39
6. Lihong Z, Han H, Jie W (2016) Intelligent optimal control method study of burning process for hot blast stove. Comput Meas Control 24(5):74–77
7. Fengjun T, Chuansheng S, Changfu L (2017) The applied research and progress of high radiative coating technology. Energy Metall Ind 36(Supplement):20–22
8. Fuming Z (2012) Technical features of super large sized blast furnace in earlier 21st century. Ironmaking 31(2):1–8
9. Fuming Z (2013) Developing prospects on high temperature and low fuel ratio technologies for blast furnace ironmaking. China Metall 23(2):1–7
10. Fuming Z, Shichong Q, Ruiyu Y (2012) Blast furnace enlargement and optimization of manufacture process structure of steel plant. Iron Steel 47(7):1–9
11. Fuming Z, Shichong Q, Jian Z (2011) New technologies of 5500 m^3 blast furnace at shougang jingtang. Iron Steel 46(2):12–17
12. Hongqi W (2010) Application and practices of 1300 °C air temperature in Shougang Jingtang united iron and steel Co., Ltd. Ironmaking 29(4):7–10
13. Zhang Fuming H, Zurui CS (2012) Combustion technology of BSK dome combustion hot blast stove at Shougang Jingtang. Iron Steel 47(5):75–81
14. Qingwu M, Fuming Z, Jianliang Z et al (2010) Design and research of new type high temperature top combustion hot stove for super large sized blast furnace. Ironmaking 29(4):1–6
15. Fuming Z, Conghua M, Guangyu Y (2012) Design study on BSK dome combustion hot blast stove of Shougang Jingtang 5500 m^3 blast furnace. China Metall 22(3):27–32

An Exergy Study of Cowper Stove Operations with an Iron Blast Furnace

Patrick E. Krane and Matthew John M. Krane

Abstract This study examines the operations of the Cowper stoves attached to an iron blast furnace from a Second Law perspective. The exergetic efficiency of a 3-stove system operating at cyclic steady state is determined using a model accounting for the thermal, mechanical, and chemical flow exergies of the top gas and blast air, as well as the thermal exergy stored and released in the stoves. The analysis covers the heating and mixing of blast gas in one on-blast stove, and the combustion of top gas and its use to heat two on-gas stoves. The effect of different cycle times, and blast furnace operating conditions on the exergetic efficiency of the cycle is examined, and the optimal cycle time for different blast temperatures found. In addition, a study of the combustion parameters quantifies the advantages of using enriched oxygen in the combustors.

Keywords Cowper stove · Blast furnace · Exergy

Introduction

Energy is a large part of the cost of blast furnace ironmaking and one effort to save on that cost is the use of Cowper stoves [1]. These devices are regenerative heat exchangers, burning furnace waste gases and storing the heat to later preheat the blast gas.

One metric for the analyzing and improving the performance of such an energy intensive system is the use of exergy analysis. Exergy is the part of an energy stream that produces useful work and so it is therefore the part of that stream with economic value; it can be stored in thermal, mechanical, and/or chemical form.

P. E. Krane (✉)
School of Mechanical Engineering, Purdue University, West Lafayette, IN 47907, USA
e-mail: pkrane@purdue.edu

M. J. M. Krane
Purdue Center for Metal Casting Research, School of Materials Engineering, Purdue University, West Lafayette, IN 47907, USA

Z. Sun et al. (eds.), *Energy Technology 2018*, The Minerals, Metals & Materials Series, https://doi.org/10.1007/978-3-319-72362-4_13

While *energy* is conserved when transferred or used in any way, it is degraded in usefulness and so *exergy* is destroyed during real processes. Exergy destruction minimization has been used successfully in the energy systems community for the purpose of optimizing design parameters in a variety of energy-intensive systems [2–6]. This capture of waste gases and heat minimizes exergy losses from steel production and increases the overall efficiency of the mill [1].

Some previous studies have applied exergy analyses to blast furnaces. Bisio [7] studied the interactions of the blast furnace, Cowper stoves, and a gas turbine system. They noticed that the use of more blast furnace gas in the turbine and less natural gas lessened exergetic losses. Ziebik and Stanek [8] showed an exergy analysis of a blast furnace and stoves from which approximately half of the exergy left in the pig iron, a quarter was destroyed internally, and the rest was lost in other effluents. A more detailed analysis of only the blast furnace using the Rist model [9] was done by Rasul et al. [10], who found improvements with changes in composition of the solid charge and higher blast temperatures. These studies are all based on steady state models, but exergy analyses of simple thermal systems has shown the optimization of cyclic, transient processes is different from steady state/steady flow systems [4, 6]. The current study examines the operations of a Cowper stove system, which is inherently a transient process, using exergy analysis to understand where in the system exergy is destroyed or lost and how that might be mitigated.

Model Description

A diagram of the three Cowper stove system studied in this model can be seen in Fig. 1. These three stoves run in a cycle with two stoves "on-gas" and one "on-blast" at any given time, and thus each stove spends twice as much time on-gas as on-blast. Figure 2 shows the behavior of the stove temperatures changing through an entire cycle.

The model performs exergy calculations during one-third of a full cycle at cyclic steady state, where one stove is on-blast, one on-gas (low temperature), and the third on-gas (high temperature). Because each stove has identical losses and destructions as the other stoves during each complete cycle, the system behavior and efficiency for one-third of the cycle is the same as for the full cycle. The inputs to this system are the top gas of the blast furnace (including CO), methane, and air for the combustors (3,13), and air for the blast (6). The product of the system is the blast for the furnace at the specified temperature (10), and the on-gas stoves exhaust of hot combustion products to the environment (5).

To begin the model, the following assumptions are made:

(a) all gas flows in the cycle are steady except through the mixer and on-blast stove;
(b) the combustion of carbon monoxide from the top gas and methane in the combustion gas in the combustor is complete;

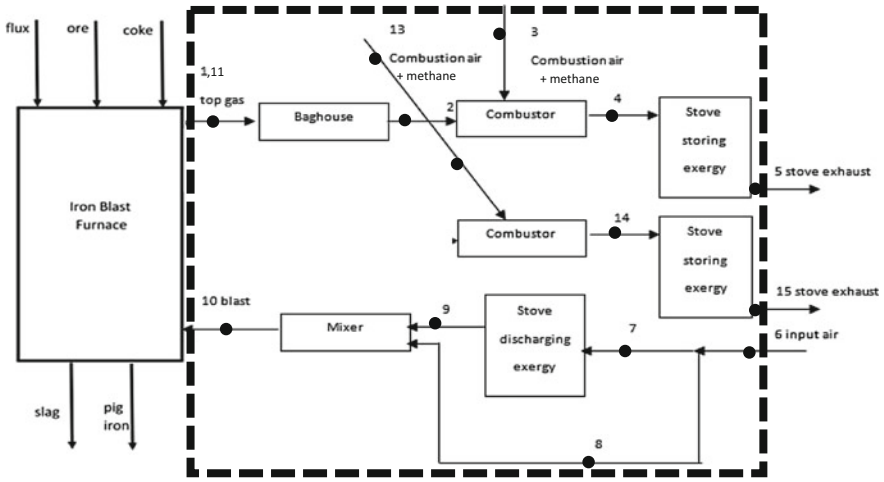

Fig. 1 Diagram of model three-stove system

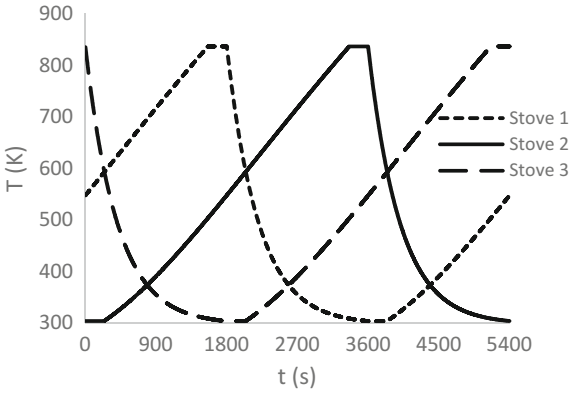

Fig. 2 Temperatures at the bottom of the 3 stoves over the course of a complete cycle (τ = 5400 s)

(c) all devices in the system are adiabatic;
(d) the only significant pressure losses are due to friction in the stoves, and an equivalent loss in the mixer;
(e) gas exits the on-gas stove at atmospheric pressure, and enters the blast furnace at $3*p_{atm}$ and T_{blast};
(f) air flow through the stove flues is turbulent and fully-developed;
(g) axial conduction in the stoves is negligible;
(h) the lateral temperature distribution in the ceramic of each stove is uniform at any height;
(i) gas flow through the stoves is evenly distributed over stove area, and so all the evenly-spaced, circular flues have the same mass flow rate.

Heat Transfer, Flow, and Combustor Models

Each device in the system is modelled to determine the temperature, pressure, and composition changes within it. The iron blast furnace is a source of exergy (mostly chemical) and the load on the stove system (requiring blast gas at T_{blast}). The Rist model, as described in [9], is used to approximate steady furnace behavior, in particular, to predict the top gas flow rate, composition, and temperature for a given T_{blast} and blast rate. It is assumed, based on practice, that 60% of the top gas is diverted for alternate methods of waste exergy recovery and 20% is used in each on-gas stove.

As the top gas enters the stove system (node 1), it is saturated with water vapor in the baghouse and cooled to $T_2 = T_o$, completely destroying all thermal exergy in the gas. The gas exits the baghouse and enters two combustors, in which CO from the blast furnace and added CH_4 are burnt; the overall reaction is:

$$\begin{aligned} &n_2^{CO}CO + n_2^{CO_2}CO_2 + n_2^{H_2O}H_2O + \left(n_2^{N_2} + n_3^{N_2}\right)N_2 + n_3^{O_2}O_2 \\ &\quad + n_3^{CH_4}CH_4 \overset{\text{yields}}{\longrightarrow} n_4^{CO_2}CO_2 + n_4^{N_2}N_2 + n_4^{H_2O}H_2O \end{aligned} \tag{1}$$

The temperature of the gas leaving the combustor is found from the enthalpy balance for the combustor:

$$\begin{aligned} &n_2^{CO}(h_{2,CO} + \Delta H_{f,CO}) + n_2^{CO_2}h_{2,CO_2} + n_2^{N_2}h_{2,N_2} + n_2^{H_2O}h_{2,H_2O} + n_3^{CH_4}(h_{3,CH_4} + \Delta H_{f,CH_4}) \\ &\quad + n_3^{N_2}h_{3,N_2} + n_3^{O_2}h_{3,O_2} = n_4^{CO_2}h_{4,CO_2} + n_4^{N_2}h_{4,N_2} + n_4^{H_2O}h_{4,H_2O} + \left(n_4^{CO_2} - n_2^{CO_2}\right)\Delta H_{f,CO_2} \\ &\quad + \left(n_4^{H_2O} - n_2^{H_2O}\right)\Delta H_{f,H_2O} \end{aligned} \tag{2}$$

For modelling the heat transfer within stoves, they are divided into a set of circular control volumes of equal radius and height and centered around a representative flue through which gas flows. Because all flues have identical geometries and mass flow rates, the temperature profiles around each flue is identical.

The convection heat transfer coefficient for the gas flow in the flues is found from the correlation [11]:

$$Nu = \frac{hd_{flue}}{k_{air}} = 0.023Re^{0.8}Pr^{0.33} \tag{3}$$

The effectiveness of one axial section of the stove is

$$\varepsilon = 1 - e^{-\frac{hA_s}{\dot{m}_{flue}c_{p,air}}} \tag{4}$$

and the heat flow rate from the gas to the stove is

$$q = \varepsilon \dot{m}_{flue} c_{p,air} \left(T_{gas,i} - T_{stove,i,old} \right) \tag{5}$$

The gas and stove temperatures used to find the heat transfer (q) change during the cycle. At each time step (Δt) in the cycle, Eq. 5 is solved using the temperature of the gas entering the (i)th section of the flue ($T_{gas,i}$) and the local stove temperature from the previous time step ($T_{stove,i,old}$).

The new temperature in each stove section and the gas exiting that section can be found from:

$$T_{stove,i} = T_{stove,i,old} + \frac{q\Delta t}{\rho_{cer} c_{cer} V_{section}} \tag{6}$$

and

$$T_{gas,i+1} = T_{gas,i} - \frac{q\Delta t}{\dot{m}_{flue} c_{p,air}}. \tag{7}$$

The axial distribution of stove and gas temperatures are found by marching Eqs. (5)–(7) from where the gas enters the flue, with the last gas temperature being the output stove temperature. To reflect actual stove operation, the direction of the flow is reversed depending on whether the stove is on-gas (flowing from top) or on-blast (flowing from bottom).

The mixer after the on-blast stove bleeds in air at ambient temperature in order to bring the temperature entering the furnace down to T_{blast}. The mass and energy balance give the output mass flow and temperature:

$$\dot{m}_{10} = \dot{m}_8 + \dot{m}_9 \tag{8}$$

$$T_{10} = \frac{\dot{m}_8 T_8 + \dot{m}_9 T_9}{\dot{m}_{10}}. \tag{9}$$

At each time step, as the temperature of the gas exiting the stove decreases, the on-blast section calculations were iterated to find the values of $\dot{m}_8$ and $\dot{m}_9$ that result in the required blast temperature, $T_{10} = T_{blast}$, and flow rate, $\dot{m}_{10}$.

Exergy Analysis

The flow exergy at each node, j, is the sum of thermal (th), mechanical (m), and chemical (ch) exergy:

$$\dot{E}_j = \dot{E}_{j,th} + \dot{E}_{j,m} + \dot{E}_{j,ch} \tag{10}$$

$$\dot{E}_{j,th} = \dot{m}_j c_{p,air} (T_{node} - T_0) - T_0 \ln\left(\frac{T_j}{T_0}\right) \tag{11}$$

$$\dot{E}_{j,m} = \dot{m}_j T_0 R_{gas} \ln\left(\frac{P_j}{P_0}\right) \tag{12}$$

Chemical exergy is calculated as the sum of the chemical exergies of each compound in the gas, where the chemical exergy of a compound (X) found in air at dead state at fraction $y_{x,0}$ is calculated as follows:

$$\dot{E}_{ch,X} = \dot{m}_{X,j} T_0 R_X y_{X,j} \ln\left(\frac{y_{X,j}}{y_{X,0}}\right) \tag{13}$$

For a compound not found at dead state, the chemical exergy is

$$\dot{E}_{ch,X} = \dot{m}_{X,j} T_0 R_X y_{X,j} \left(\frac{E_{ch,std}}{T_0 R_{gas}} + ln\left(y_{X,node}\right)\right) \tag{14}$$

For all exergy calculation, dead state was T_0 = 298 K, $P_0 = 1.01 \times 10^5$ Pa, and composition being air at 50% humidity calculated based on data in [12].

In addition to these terms, the tare exergy (the exergy stored in the charging stoves during one-third of a cycle at cyclic steady state [6]) was calculated as follows, with the stove temperatures being the temperatures at the end of one-third of a cycle:

$$E_{tare} = \sum_{j=1}^{n} T_o \rho_{cer} c_{cer} V_{section} \ln\left(\frac{T_{j,stove3}}{T_{j,stove2}}\right) \tag{15}$$

At cyclic steady state, an equal quantity of exergy is lost in the discharging stove, so the tare exergy is treated as both an input and an output in the equation for system efficiency:

$$\eta = \frac{\dot{E}_{10} + \dot{E}_{tare}}{\dot{E}_1 + \dot{E}_3 + \dot{E}_6 + \dot{E}_{11} + \dot{E}_{13} + \dot{E}_{tare}} \tag{16}$$

The exergy destruction in the baghouse, combustor, and mixer were calculated using the equation:

$$\dot{E}_{dest} = \sum \dot{E}_{in} - \sum \dot{E}_{out} \tag{17}$$

In the stoves, the exergy destruction is calculated using the following equation:

$$\dot{E}_{dest} = \sum \dot{E}_{in} - \sum \dot{E}_{out} - \dot{E}_{stove} \tag{18}$$

In this equation, the change in stove exergy over one-third the cycle time (τ) is found as follows:

$$\Delta E_{stove} = \rho_{cer} c_{cer} V_{section} \left(\int_0^{\tau} \sum_{j=1}^{n} T_j - T_{j,old} - T_0 \ln\left(\frac{T_j}{T_{j,old}}\right) dt \right) \tag{19}$$

For each subsystem (j), the entropy generation number is calculated as follows:

$$N_{S,j} = \frac{\dot{E}_{d,j} + \dot{E}_{L,j}}{\dot{E}_1 + \dot{E}_3 + \dot{E}_6 + \dot{E}_{11} + \dot{E}_{13} + \dot{E}_{tare}}, \tag{20}$$

where every subsystem destroys exergy $\left(\dot{E}_{d,j}\right)$ and only the on-gas stoves have exergy losses to the environment $(\dot{E}_{L,j})$.

The sum of all entropy generation numbers is related to overall system efficiency:

$$\eta = 1 - \sum_j N_{S,j} \tag{21}$$

A study comparing different cycle times at different blast temperatures and one examining the effect of different air compositions added to the top gas in the combustor, were conducted using this model and the values for stove geometry found in Table 1. Thermodynamic property values were taken from [9].

Results and Discussion

Two parametric studies were performed using this model. Both studies used the blast furnace Rist model [9] to generate different top gas states and flow rates of top gas and blast for different blast temperatures.

Effects of Blast Temperature

For the first study, conditions were evaluated at three values of T_{blast}. At each blast temperature, the Rist model data (Table 2) were used as inputs into the Cowper stove model operating over a range of cycle periods (τ).

Table 1 Cowper stove geometry used for all cases in this study. Volume ratio is ratio of ceramic volume/flue volume in stove

Number of flues	21000
Flue length (m)	36.2
Flue diameter (m)	0.025
Volume ratio	1.5
Number of axial flue sections	100
Blast Furnace Wind Rate (Nm^3/hr)	1.6×10^5
ceramic density (ρ, kg/m^3)	1500
ceramic specific heat (c, J/kgK)	1000

Table 2 Outputs of the rist blast furnace model different T_{blast}

T_{blast} (K)	1200	1350	1500
$\dot{m}_{top\ gas}$ (tonne/stove/hr)	132	135	138
$T_{top\ gas}$ (°C)	340	304	269
%mass $CO_{top\ gas}$	19.1	19.1	19.1
%mass CO_2, $_{top\ gas}$	35.3	36.4	37.5
%mass N_2, $_{top\ gas}$	45.6	44.5	43.4
$\dot{m}_{blast\ gas}$ (tonne/hr)	393	392	391

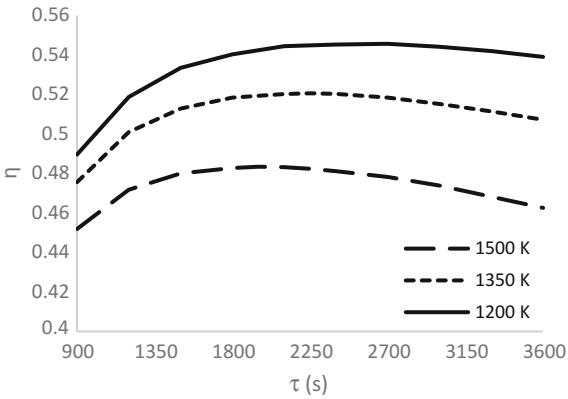

Fig. 3 Efficiency of the Cowper stove system at different cycle times and blast temperatures

Figure 3 shows the exergetic efficiency of the stove system over the range of τ. This efficiency decreases with higher blast temperatures, primarily because at lower blast temperatures, the combustor does not destroy as much exergy heating gas to as high a temperature. However, a higher blast temperature does improve the exergetic performance of the blast furnace itself [10], so an analysis of the entire stove-furnace system is needed to understand the details of these tradeoffs. It should be noted that the slope of the η-τ curve near the optimal cycle time is shallow, especially for low T_{blast}, so gains from altering the cycle time near the optimum point are small.

By plotting $N_S(\tau)$, Fig. 4 shows in which devices exergy destructions and losses occur when operating at T_{blast} = 1500 K. The exergy destructions in the baghouse and mixer are so small that they are not included on this graph. As can be seen, the dominant sources of exergetic inefficiency are the exergy destruction in the combustor, and the exergy destructions and losses in the on-gas stove.

While the destruction in the combustor changes very little with cycle time, the exergy destroyed in the on-gas stove increases as cycle time decreases, while the exergy lost from the on-gas stove increases with cycle time. This exchange of a destruction for a loss in the on-gas stoves is because, when cycle time increases, the gas spends more time moving through a stove that has already been heated by the earlier gas. The consequent lower temperature difference between stove and gas results in less exergy destruction, but less heat is removed from the gas, resulting in

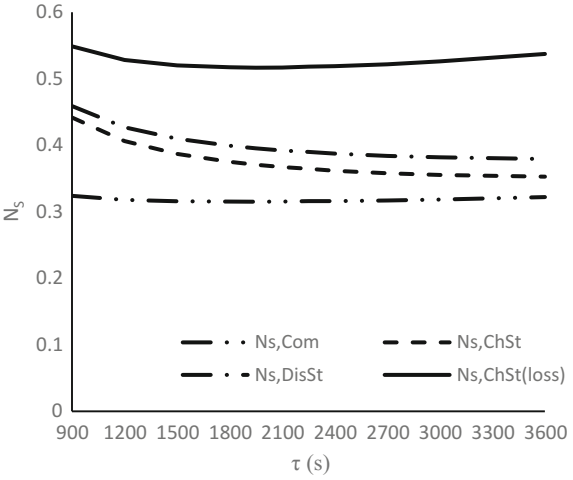

Fig. 4 Exergy destructions and losses at T_{blast} = 1500 K, by subsystem. For each subsystem, N_S is the difference between the curve and the one below. For components in the on-gas subsystem, the values from each of the two stoves are combined

a greater exergy loss at the stove exit. One practical implication of this tradeoff is that running the stove at cycle times greater than optimum would make economic sense if some way of re-capturing the exergy lost in the stove exhaust is found.

Effects of combustor air composition

The cycle time study was run assuming that the air in the combustor was a standard composition of oxygen and nitrogen (21% O_2, 79% N_2), and that exactly the oxygen required for complete combustion is used. However, in a real stove, to ensure complete combustion, the air would be in excess of that required for combustion, and could be enriched with oxygen to increase efficiency. To see the effects of combustor air composition, a study was run at a cycle time of 30 min and a blast temperature of 1500 K, looking at combustor air flows between 100 and 150%, at 10% intervals, of the requirements for complete combustion, at compositions of 21, 25, and 30% oxygen. Figure 5 shows the resulting efficiencies of the system under these conditions, as a function of the mole fraction of the air reacted (the fraction of the air that is oxygen used in the reaction, as compared to unused oxygen or nitrogen).

One thing that can be seen in this plot is that the effect of the composition of the unreacted gas (whether it is oxygen or nitrogen) is negligible. The decreased efficiency from adding excess air (for complete combustion) will be made up by the increased proportion of oxygen in the air, resulting in the same molar flow rate of air going into the combustor. It can also be seen that there are large efficiency gains for increasing the mole fraction reacted by lower values, but as the mole fraction increases past around 0.22, there are diminishing returns in efficiency. This decreasing slope suggests that when running with excess air in the combustor, oxygen enrichment to a composition of 30% would bring substantial benefits, but at some point beyond that, it would no longer be worthwhile.

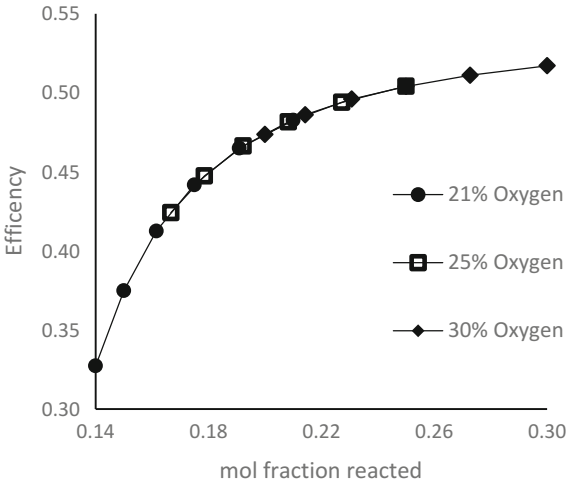

Fig. 5 Efficiency of the system compared to the mole fraction of air in the combustor reacted. Mole fraction reacted is increased by oxygen enrichment, and decreased by excess air

The exergy destructions and losses in the different devices as a function of air composition are seen in Fig. 6. This plot shows that the increase in efficiency with increased mole fraction reacted is due mainly to decreased exergy destruction in the combustors and decreased losses from the on-gas stoves. One reason for the increased destruction in the combustor for lower reacted mole fractions is that the combustor must heat up a larger amount of air for it to still heat the stove to the same temperature, and so needs to burn more natural gas to do so. Exergy losses also increase for lower mole fractions reacted because there is a greater mass flow of gas exiting the stove. This trend suggests that the more excess air used in the

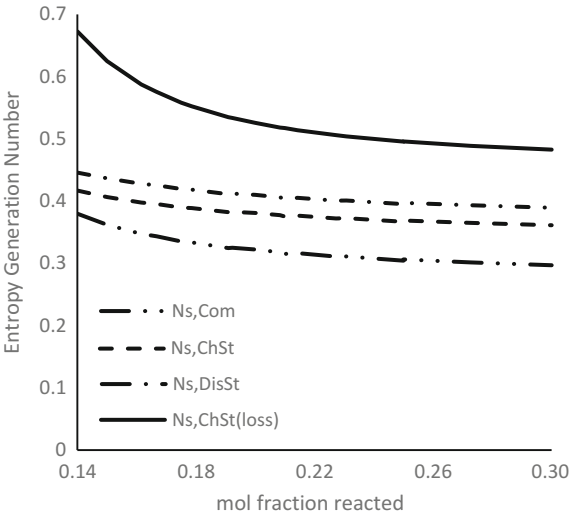

Fig. 6 Exergy destructions and losses as functions of mole fraction of air reacted in the combustor

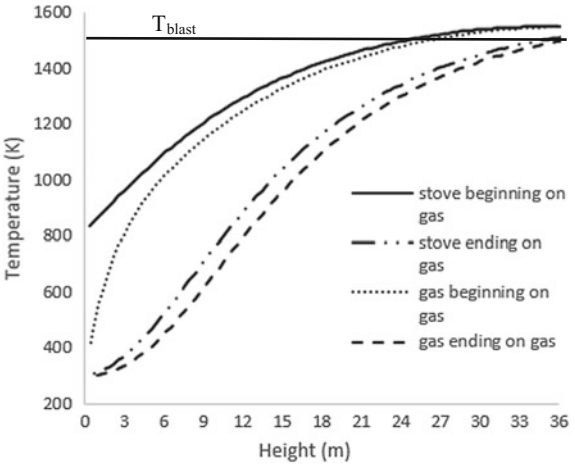

Fig. 7 Axial temperature profiles of the ceramic in the stove and the blast air flowing through it, from bottom to top, at the beginning and end of the on-blast cycle

combustor, or the less oxygen-enriched it is, the more potential for improvement there is in recapturing some of the exergy in the air leaving the stoves.

Cyclic thermal response of a stove

To better see how the stove changes over the course of a cycle, Fig. 7 shows the axial temperature profile of the stove and the gas flowing through it at the beginning and end of the on-blast state when operating at 40% excess air, 25% oxygen. Because the system is operating at cyclic steady state, the temperature distribution at the start of the on-blast state is that at the end of the on-gas state, and vice versa.

It can be seen from Fig. 7 that the stove is not fully heated in the on-gas state, except at the top. There is very little change in temperature over time because the top of the stove must be above 1500 K during all the on-blast condition to keep the blast gas above T_{blast}. As the cycle goes on, the axial variation in temperature along the stove increases, while the differences between the stove and gas temperatures decrease.

Finally, it should be noted that, in all cases, the changes in thermal and chemical exergy account for effectively all the exergy destruction, while the destruction of mechanical exergy is negligible, only equaling 0.06% of the total exergy input for the case. Any significant exergy improvements should focus on the economical prevention of destruction and loss of thermal and chemical exergy, not mechanical.

Conclusions

A model was developed to study the exergy destructions and losses in the Cowper stove system attached to an iron blast furnace. The first part of this work used this model to find an optimal cycle time for each blast temperature. It would be economical for the stoves to run at a cycle time longer than the optimum if there is a

way to use the exergy lost in the stove exhaust. The second part of the study revealed that oxygen enrichment in the combustor up to 30% would produce significant gains in exergetic efficiency, but that the benefits from further enrichment would be smaller. Finally, an examination of the types of losses that occur in the system shows that efforts to improve efficiency should focus on the destruction of thermal and chemical exergy, and not mechanical. It should be noted that these values depend on the geometry and operating conditions of a specific stove system and blast furnace, and are not general results. However, the conclusions about the general trends in behavior would still apply to other similar systems.

Acknowledgements The authors thank Mr. Robert Steiger of Paul Wurth, Inc., for helpful discussions concerning practical aspects of Cowper stove operations.

References

1. Ghosh A, Chatterjee A (2010) Ironmaking and steelmaking: theory and practice. PHI
2. Kotas TJ (1985) The exergy method of thermal plant analysis. Butterworths
3. Szargut J, Morris DR, Steward FR (1988) Exergy analysis of thermal, chemical, and metallurgical processes. Hemisphere
4. Bejan A (2006) Advanced engineering thermodynamics. Wiley, New York
5. Proceedings of the 27th international conference on efficiency, cost, optimization, simulation and environmental impact of energy systems, ECOS 2014, 15–19 June 2014
6. Krane RJ (1987) A second law analysis of the optimum design and operation of thermal energy storage systems. Int J Heat Mass Transf 30:43–57
7. Bisio G (1998) A second-law analysis of the 'hot blast stove/gas turbine' combination by applying the parameter 'usable exergy'. Energy Convers Mgmt 39:217–227
8. Ziebik A, Stanek W (2006) Influence of blast-furnace process thermal parameters on energy and exergy characteristics and exergy losses. Int J Energy Res 30:203–219
9. Peacey JG, Davenport WG (1979) The iron blast furnace: theory and practice. Pergamon Press
10. Rasul MG, Tanty BS, Mohanty B (2007) Modelling and analysis of blast furnace performance for efficient utilization of energy. Appl Therm Eng 27:78–88
11. Incropera F, DeWitt D, Bergman T, Lavine A (2011) Fundamentals of heat and mass transfer, 7th edn. Wiley, New York
12. Moran MJ, Shapiro HN (2004) Fundamentals of engineering thermodynamics, 4th edn. Wiley, New York

Waste Heat Recovery from Aluminum Production

Miao Yu, Maria S. Gudjonsdottir, Pall Valdimarsson and Gudrun Saevarsdottir

Abstract Around half of the energy consumed in aluminum production is lost as waste heat. Approximately 30–45% of the total waste heat is carried away by the exhaust gas from the smelter and is the most easily accessible waste heat stream. Alcoa Fjarðaál in east Iceland produces 350 000 tons annually, emitting the 110 °C exhaust gas with 88.1 MW of heat, which contains 13.39 MW exergy. In this study, three scenarios, including organic Rankine cycle (ORC) system, heat supply system and combined heat and power (CHP) system, were proposed to recover waste heat from the exhaust gas. The electric power generation potential is estimated by ORC models. The maximum power output was found to be 2.57 MW for an evaporation temperature of 61.22 °C and R-123 as working fluid. 42.34 MW can be produced by the heat supply system with the same temperature drop of the exhaust gas in the ORC system. The heat requirement for local district heating can be fulfilled by the heat supply system, and there is a potential opportunity for agriculture, snow melting and other industrial applications. The CHP system is more comprehensive. 1.156 MW power and 23.55 MW heating capacity can be produced by CHP system. The highest energy efficiency is achieved by the heat supply system and the maximum power output can be obtained with the ORC system. The efficiency of energy utilization in aluminum production can be effectively improved by waste heat recovery as studied in this paper.

Keywords Aluminum production · Waste heat recovery · ORC
District heating · Combined heat and power

M. Yu (✉)
Key Laboratory of Efficient Utilization of Low and Medium Grade Energy, MOE, School of Mechanical Engineering, Tianjin University, No.135 Yaguan Road, Haihe Education Park, Tianjin 300350, China
e-mail: miao16@ru.is

M. Yu · M. S. Gudjonsdottir · P. Valdimarsson · G. Saevarsdottir
School of Science and Engineering, Reykjavik University, Menntavegi 1, Reykjavik 101, Iceland

Z. Sun et al. (eds.), *Energy Technology 2018*, The Minerals, Metals & Materials Series, https://doi.org/10.1007/978-3-319-72362-4_14

Introduction

Aluminum production is a power-intensive industry. Around 72.3% of produced electricity in Iceland was consumed by aluminum production in 2016 [1]. Approximately half of the energy consumed in aluminum production is lost as waste heat and the 30–45% of total waste heat is carried away by the exhaust gas from the aluminum smelter as seen in Fig. 1. Alcoa Fjarðaál is an aluminum plant, producing 350 000 tons aluminum per year, in east Iceland close to the town of Reyðarfjörður. The space heating demand of Reyðarfjörður is estimated at approximately 4.05 MW_{th}.

Power generation and direct heat utilization are two approaches to utilize the low-temperature energy. The conventional Rankine cycle is widely used in power generation from high-temperature heat sources. The ORC system is considered as a low-temperature heat recovery technology for power generation, using an organic substance with a low boiling point as the working fluid. A temperature-entropy diagram of the ORC system is shown in Fig. 2 The Kalina Cycle is a power generation cycle which converts low-temperature thermal energy to mechanical power, using a mixture of ammonia and water as the working fluid [2]. Thermoelectric generator (TEG) can convert thermal energy from a temperature gradient into electric energy by Seebeck effect. Comparing the three methods for power generation, the technology of ORC is considered to be the most feasible one.

As a consequence of the second law of thermodynamics, the conversion of low-temperature heat to electricity has low efficiency. From the view of the first law of thermodynamics, higher energy efficiency can be obtained by direct heat utilization. Various approaches are possible to utilize thermal energy directly, such as space heating, snow melting, swimming pools, agriculture applications and industrial use [3]. Power generation by the Rankine cycle and Brayton cycle to

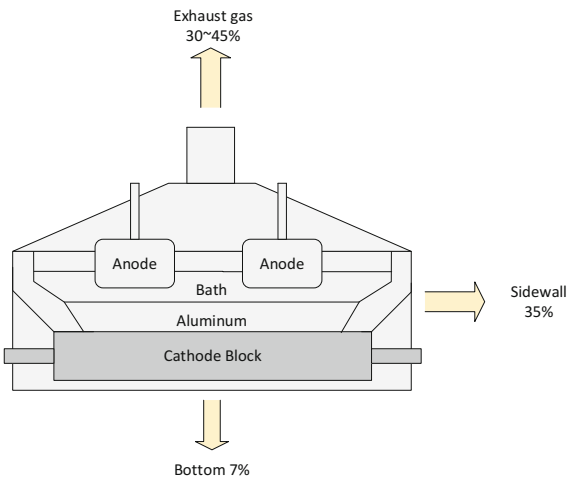

Fig. 1 Heat loss distribution in aluminum smelter [6]

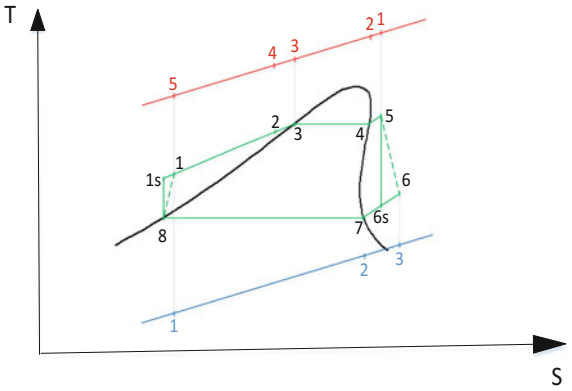

Fig. 2 Temperature-entropy diagram of an ORC system

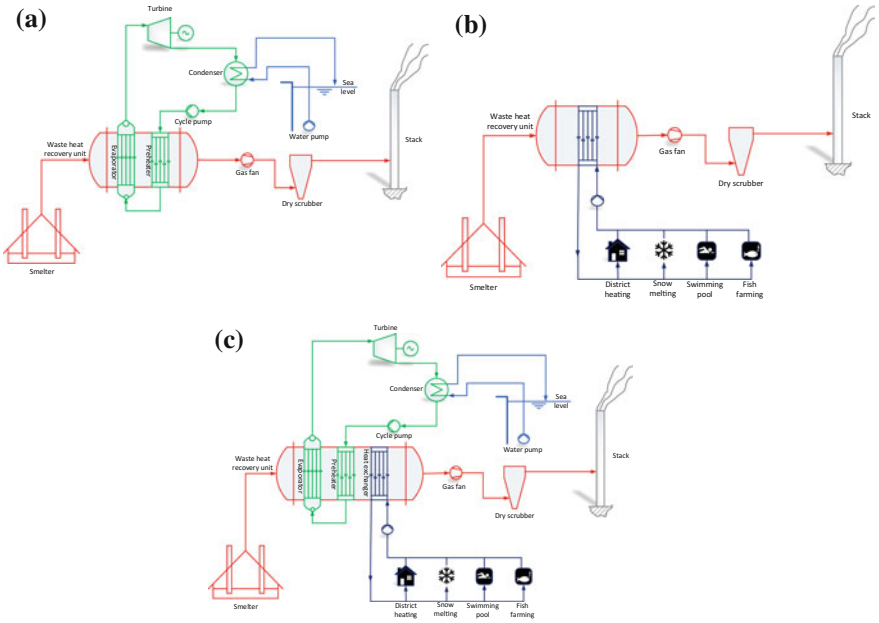

Fig. 3 Sketch of **a** ORC system. **b** Direct heating system. **c** CHP system

recover the waste heat from aluminum smelter exhaust gas was studied by Ladam et al. [4]. An ORC system was designed by Ke (2009) to recover the heat from aluminum production [5]. Most research focuses on electricity generation from the waste heat in aluminum production, but ignore the heating potential and the combination of electricity generation and heat utilization.

Nomenclature			
Ex	exergy (kW)	cond	condenser
h	specific enthalpy (kJ/kg)	eva	evaporator
m	mass flow rate (kg/s)	fan	fan
P	pressure (bar)	hex	heat exchanger
Q	heat transfer rate (kW)	gas	state of gas
S	entropy (kJ/kg K)	gen	generator
T	temperature (°C)	gral	general
U	heat transfer coefficient (kW/m^{2}K)	mid	middle
v	specific volume (m^3/kg)	net	net amount
w	Power (kW)	pin	pinch point
η	efficiency	pre	preheater
		sup	superheater
Subscripts		sys	system
amb	ambient	turb	turbine
cw	cooling water	wf	working fluid

In this study, three scenario studies were carried out, concentrating on both electricity generation and heat utilization. A proper multiple-objective target function was proposed for the power generation scenario and CHP scenario. The optimal parameters for each scenario were found by optimization.

System Description

The three scenarios are composed of four modules, which are the heat source module, the power module, the cooling module and the heating module (Table 1). The heat source module is the same module in all scenarios. The cooling module serves the power module as the cold sink. An interface for the heating system can be provided by the heating module.

Table 1 System module component

	Heat source module	Power module	Cooling module	Heating module
Power generation system (Fig. 3a)	✓	✓	✓	✓
Heat supply system (Fig. 3b)	✓			✓
CHP system (Fig. 3c)	✓	✓	✓	✓

Model

To simplify the model, the assumptions are made:

- The system and heat source is at a steady state. The temperature of the exhaust gas is 110 °C and the volumetric flow rate is 910 m^3/s.
- The heat sink of the cycle is the sea water, which is close to the aluminum smelter. The temperature is assumed at 6 °C, the mean temperature of the local sea surface [7].
- 2 °C of superheat and 2 °C of subcooling are assumed at the outlet and inlet of the evaporator.
- On the working fluid side, the pressure drops and heat losses to the environment in the evaporator, condenser, turbine, and pump are neglected.
- The thermal resistance of conduction in heat exchanger pipes/walls is neglected.
- The pressure drop in the heat source module after waste heat recovery unit is considered constant.

The T-s diagram of ORC system is shown in Fig. 2. The thermal energy content of the exhaust gas can be calculated by

$$\dot{Q}_{gas} = C_{p,gas}\rho_{gas}\dot{V}_{gas}\left(T_{gas,1} - \bar{T}_{amb}\right) \tag{3.1}$$

The $C_{p,gas}$ is the heat capacity of the gas. The ρ_{gas} is the density of the gas. The heat transfer through preheater can be given as following equations.

$$\dot{Q}_{pre} = \dot{m}_{wf}\left(h_{wf,2} - h_{wf,1}\right) \tag{3.2}$$

$$\dot{Q}_{pre} = \dot{m}_{gas}c_{p,gas}\left(T_{gas,4} - T_{gas,5}\right) \tag{3.3}$$

Heat exchanger area can be calculated by

$$area = \frac{\dot{Q}}{U\Delta T_m} \tag{3.4}$$

The logarithmic mean temperature difference can be calculated by

$$\Delta T_m = \frac{\Delta T_{\max} - \Delta T_{\min}}{\ln \frac{\Delta T_{\max}}{\Delta T_{\min}}} \tag{3.5}$$

In general, the overall heat transfer coefficient can be calculated by

$$\frac{1}{U} = \frac{1}{U_{inside}} + \frac{\delta}{\lambda} + \frac{1}{U_{outside}} \tag{3.6}$$

The heat resistance of conduction, $\frac{\delta}{\lambda}$, is ignored, then

$$\frac{1}{U} = \frac{1}{U_{inside}} + \frac{1}{U_{outside}} \tag{3.7}$$

The minimum temperature difference between the hot and cold stream in the heat transfer unit is referred to as the pinch point temperature difference (PPTD). The pinch position in a heat exchanger emerges at the place where the heat transfer is the most constrained [8]. Therefore, the PPTD is the critical parameter in an evaporator and condenser. The heat transfer area and cycle performance are influenced by PPTD. The PPTD in evaporator is

$$\Delta T_{pin,eva} = T_{gas,3} - T_{wf,3} \tag{3.8}$$

The heat transfer in the evaporator can be given by following equations.

$$\dot{Q}_{eva} = \dot{m}_{wf}\left(h_{wf,5} - h_{wf,2}\right) \tag{3.9}$$

$$\dot{Q}_{eva} = \dot{m}_{gas} c_{p,gas}\left(T_{gas,1} - T_{gas,4}\right) \tag{3.10}$$

Where the $\dot{Q}_{rhs}$ refer to the heat transfer in the evaporator excluding the preheat section.

The power of turbine is given as

$$\dot{W}_{turb} = \dot{m}_{wf}\left(h_{wf,5} - h_{wf,6}\right) \tag{3.11}$$

The efficiency of turbine is

$$\eta_{turb} = \frac{h_{wf,5} - h_{wf,6}}{h_{wf,5} - h_{wf,6s}} \tag{3.12}$$

The generator power output is given as

$$\dot{W}_{gen} = \eta_{gen}\dot{W}_{turb} \tag{3.13}$$

The heat transfer in condenser can be given as following equations.

$$\dot{Q}_{cond} = \dot{m}_{wf}\left(h_{wf,6} - h_{wf,8}\right) \tag{3.14}$$

$$\dot{Q}_{cond} = \dot{m}_{cw} c_{p,cw}\left(T_{cw,3} - T_{cw,1}\right) \tag{3.15}$$

Where $\dot{Q}_{cond,con}$ is the heat transfer rate in the condensation section in condenser.

The power of working fluid pump is calculated as

$$\dot{W}_{wf,pump} = \dot{m}_{wf}\Delta h_{wf,pump} \tag{3.16}$$

$$\eta_{pump} = \frac{h_{wf,1s} - h_{wf,8}}{h_{wf,1} - h_{wf,8}} \tag{3.17}$$

The power of cooling seawater pump can be calculated by

$$\dot{W}_{cw,pump} = \frac{\dot{m}_{cw}(\rho_{cw} g\Delta h + \Delta p)}{\rho_{cw}\eta} \tag{3.18}$$

The power of gas fan can be calculated by

$$\dot{W}_{gas,fan} = \frac{\dot{v}_{gas}\left(p_{gas,1} - p_{gas,5}\right)}{\eta_{gas,fan}} \tag{3.19}$$

The volume flow was changed by the temperature drop of the exhaust gas. The power consumption of original fan module reduces with the less volume flow after cooling, which originally exists in the gas treatment center (GTC). The flow rate of the exhaust gas at the outlet of waste heat recovery unit can be calculated by the following equation:

$$\dot{V}_{gas,out} = \dot{V}_{gas,in}\frac{T_{gas,out}}{T_{gas,in}}\frac{P_{gas,in}}{P_{gas,out}} \tag{3.20}$$

The original fan power is saved by the volume flow rate descending:

$$\dot{W}_{fan,save} = \frac{\dot{V}_{gas,in}\Delta P_{gas}}{\eta_{fan,ori}} - \frac{\dot{V}_{gas,out}\Delta P_{gas}}{\eta_{fan,ori}} \tag{3.21}$$

The net power output is considered as

$$\dot{W}_{net} = \dot{W}_{gen} - \dot{W}_{gas,fan} - \dot{W}_{cw,pump} - \dot{W}_{wf,pump} \tag{3.22}$$

The saving power of the gas fan module is considered as a part of power output by the ORC system. Therefore, the *general net power output* can be defined as

$$\dot{W}_{net,gral} = \dot{W}_{gen} - \dot{W}_{gas,fan} - \dot{W}_{cw,pump} - \dot{W}_{wf,pump} + \dot{W}_{fan,save} \tag{3.23}$$

The general thermal efficiency of the system is

$$\eta_{sys,thermal} = \frac{\dot{W}_{net,gral}}{\dot{Q}_{gas}} \tag{3.24}$$

The enthalpy exergy of gas can be calculated by

$$\dot{E}_{x,gas} = \dot{m}_{gas}\left(c_p(T - T_0) + RgT_0 ln\frac{p}{p_0} - c_p T_0 ln\frac{T}{T_0}\right) \tag{3.25}$$

The general exergy efficiency of system

$$\eta_{sys,exergy} = \frac{\dot{W}_{net,gral}}{\dot{E}_{x,gas}} \tag{3.26}$$

For the heat supply system, the heat transfer in the waste heat recovery unit is considered as

$$\dot{Q}_{heat} = \dot{m}_{gas} c_{p,gas}\left(T_{gas,5} - T_{gas,out}\right) \tag{3.27}$$

$$\dot{Q}_{heat} = \dot{m}_{water} c_{p,water}\left(T_{water,in} - T_{water,out}\right) \tag{3.28}$$

The power input for the heat supply system is

$$\dot{W}_{input} = \dot{W}_{fan,save} - \dot{W}_{gas,fun} - \dot{W}_{water,pump} \tag{3.29}$$

The thermal efficiency of heat supply system is

$$\eta_{heat} = \frac{\dot{Q}_{heat}}{\dot{Q}_{gas}} \tag{3.30}$$

Optimization

Objective Function

A multi-objective function, which combines various single objective functions, can make the optimization comprehensive. The scalarization method is an efficient approach to obtain the multi-objective function from multiple individual objective functions [9]. For the power generation system, the objective function and direction are shown below:

$$max : \dot{W}_{net} \tag{4.1}$$

$$max : \eta_{sys,exergy} \tag{4.2}$$

$$min : Area \tag{4.3}$$

Three objective functions are integrated into two functions and keep the same direction. These two objective functions can be combined into $F(x)$ with the weighting factors φ, ψ.

$$max : f_1 = \frac{\dot{W}_{net}}{Area} \tag{4.4}$$

$$max : f_2 = \eta_{sys,exergy} \tag{4.5}$$

$$max : F(x) = \varphi F_1(x) + \psi F_2(x) \tag{4.6}$$

Therefore, the objective function is proposed as

$$max : F(x) = \varphi \frac{\dot{W}_{net,gral}}{Area} + \psi\left(100 \cdot \eta_{sys,exergy}\right) \tag{4.7}$$

By the similar principle, the objective function of optimization for CHP system is

$$F(x) = \varphi \frac{\dot{W}_{net,gral}}{A_{ORC}} + \psi \frac{\dot{Q}_{heat}}{A_{hex}} \tag{4.8}$$

In the condition, the dimension and magnitude of two terms are same. The weighting factor can be decided by following equations [10].

$$\varphi = \frac{F_2^1 - F_2^2}{\left(F_1^2 - F_1^1\right) + \left(F_2^1 - F_2^2\right)} \tag{4.9}$$

$$\psi = \frac{F_1^2 - F_1^1}{\left(F_1^2 - F_1^1\right) + \left(F_2^1 - F_2^2\right)} \tag{4.10}$$

Where F_1^1 is the maximum value of $F_1(x)$; F_2^2 is the maximum value of $F_2(x)$; F_1^2 is the value of $F_1(x)$ when $F_2(x)$ reaches the maximum; F_2^1 is the value of $F_2(x)$ when $F_1(x)$ reaches the maximum.

Iteration Procedure

The design variables for power generation system are $T_{wf,eva}$, $T_{wf,cond}$, $\Delta T_{pin,eva}$ and $\Delta T_{pin,cond}$. When the differences between the input and results of design variables are less than 0.05%, convergence condition is met and then output the result. Otherwise, the next iteration will be conducted, shown in Fig. 4. For CHP system, the design variables are $T_{gas,mid}$, $T_{wf,eva}$, $T_{wf,cond}$ and $\Delta T_{pin,cond}$, shown in Table 4. A critical parameter, the gas temperature at the outlet of evaporator, is defined as the *middle temperature* $T_{gas,mid}$.

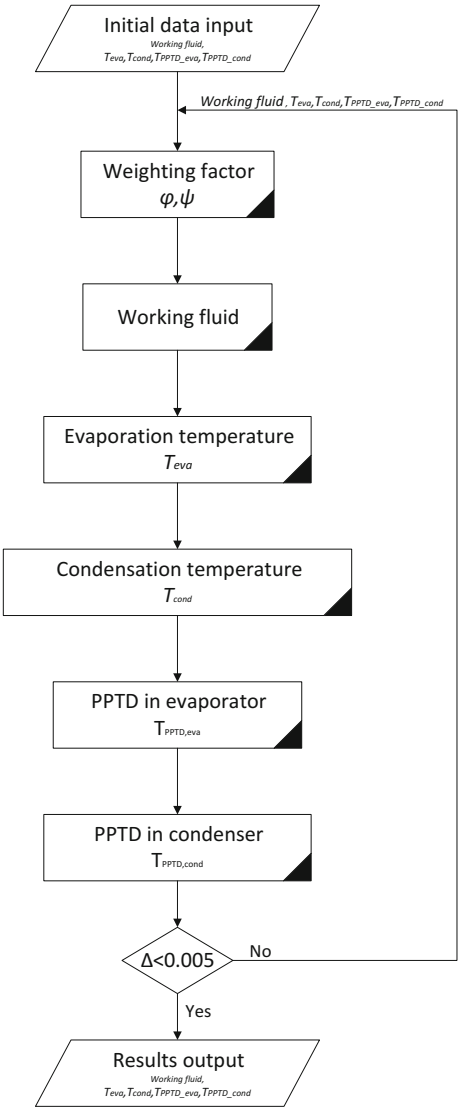

Fig. 4 Iteration procedure of optimization

Result and Discussion

Figure 5 shows the variation of the objective function with the various evaporation temperature for 14 different working fluids. Five working fluids, R-236fa, R-245fa, R-236ea, R-123 and R-600a, have good thermodynamic performance. The environmental issue and safety of the working fluid are considered as well. R-123 has good environmental friendly property, comparing with R-236fa, R-245fa, and R-236ea, shown in Table 2. The high flammability makes R-600a a low safety.

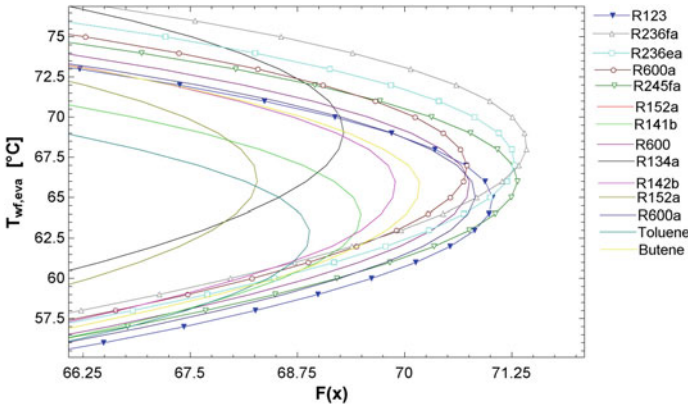

Fig. 5 Working fluid selection for ORC system

Therefore, R-123 is selected as working fluid in the iteration. The optimal parameters of the power generation system and CHP system are shown in Table 3.

In the condition of the same temperature drop for the exhaust gas, the optimal performance of each system is shown in Table 4. A considerable difference of the evaporation temperature between the power generation system and CHP system is owing to the different heat source conditions for the two systems.

The highest exergy efficiency of 19.22% is obtained and 2.573 MW electricity is produced by the power generation system. The thermal efficiency of 48.1% and heating capacity of 42.34 MW are obtained by the heat supply system. The power output and heating capacity of CHP system are 1.156 and 23.55 MW separately. The gas fan power consumption in the three systems are considerable. More heat exchanger area is required by CHP system than heat supply system.

From the thermodynamic view, the low emission temperature of the gas is the more thermal energy is recovered by the waste heat recovery unit. However, the temperature is also limited by the acid dew point temperature in the exhaust gas and cannot reach too low. The dew point temperature is influenced by the partial pressure of the acid in the exhaust gas. The absolute pressure of exhaust gas is as low as 0.96 bar. Therefore, a *low acid dew point temperature* is possible, which will pose an effective lower temperature limit on exhaust gas temperature The further quantitative analysis should be taken in the future.

Table 2 Properties of working fluids [11]

	R-236fa	R-245fa	R-236ea	R-123	R-600a
Molecular formula	$CF_3CH_2CF_3$	$CF_3CH_2CHF_2$	$CF_3CHFCHF_2$	$CHCl_2CF_3$	$CH(CH_3)_3$
ODP	0	0	0	0.02	0
GWP(100 years)	9810	1030	1370	77	3

Table 3 Iteration results of optimal parameters

System	Working fluid	Evaporation temperature (°C)	Condensation temperature (°C)	PPTD in evaporator (°C)	PPTD in condenser (°C)
Power generation system	R-123	61.22	16.33	9.469	3.501
CHP system	R-123	76.02	17.10	Middle temperature	3.857
				86.43	

Table 4 System performance of three scenarios

Parameters	ORC	Heat supply	CHP
$\dot{W}_{gral}$	2.573 MW	−0.104 MW	1.156 MW
$\dot{Q}_{heat}$	0	42.34 MW	23.550 MW
η_{exergy}	19.220%	0	8.63%
$\eta_{thermal}$	2.921%	48.1%	28.05%
$Area$	21115 m^2	14412 m^2	25509 m^2
$\dot{W}_{net}$	1.248 MW	0	−0.195 MW
$\dot{W}_{gen}$	4.17 MW	0	2.344 MW
$\dot{W}_{gas,fan}$	−2.417 MW	−1.39 MW	−2.295 MW
$\dot{W}_{fan,save}$	1.325 MW	1.324 MW	1.351 MW
$\dot{W}_{cw,pump}$	−0.465 MW	0	−0.194 MW
$\dot{W}_{wf,pump}$	−0.0403 MW	−0.03792 MW	−0.0291 MW
$T_{gas,outlet}$	58.84°C	58.89°C	58°C
$\dot{m}_{wf}$	207.4 Kg/s	0	91.97 Kg/s
$\dot{m}_{cw}$	1278 Kg/s	0	533.1 Kg/s
$\dot{m}_{heat}$	0	252.81 Kg/s	140.61 Kg/s

Conclusion

In this study, the low-temperature waste heat of exhaust gas from the aluminum smelter is recovered the three different scenarios. The ORC technology is used in the power generation system and CHP system. A multiple-objective function and a

new optimization method were proposed for the optimization of the ORC system. Four design variables were selected by the optimization iteration procedures. From the result, the main conclusion can be summarized as follows:

1. At the optimal condition, 2.573 MW_e electricity can be produced by the power generation system. For CHP system, 1.156 MW_e power and 23.55 MW_{th} heating capacity can be produced. 42.34 MW_{th} heating capacity can be produced by heat supply system. The considerable potential of waste heat recovery from aluminum production was established.
2. The performance of ORC is significantly influenced by selection of working fluid and design parameters.
3. Comparing various scenarios, the highest exergy efficiency, 19.22%, can be obtained by power generation system and the highest energy efficiency of 48.1% can be obtained by the heat supply system. The efficiency of organic Rankine cycle is limited by the low temperature of the exhaust gas. A high energy efficiency can be obtained by heat direct utilization.
4. The system selection should be integrated with the local demand. For the town of Reyðarfjörður in east Iceland, the basic space heating load can be amply met by the heat supply scenario or CHP scenario. More direct thermal utilizations can be developed with this considerable heat potential, such as snowing melting, greenhouse, desalinization, drying industry and other industrial applications.

Acknowledgements Gratefully acknowledge Alcoa Foundation for the financial support of this work. The authors also wish to acknowledge Jón Steinar Garðarsson Mýrdal at Austurbrú, Hilmir Ásbjörnsson, Unnur Thorleifsdottir at Alcoa Fjarðaál and Þorsteinn Sigurjónsson at Fjarðabyggð Municipal Utility for their assistance.

References

1. Orkustofnun (2017) OS-2017-T016-01: development of electricity consumption in Iceland. http://os.is/gogn/Talnaefni/OS-2017-T016-01.pdf. Accessed 30 Aug 2017
2. Zhang X, He M, Zhang Y (2012) A review of research on the Kalina cycle. Renew Sustain Energy Rev 16(7):5309–5318
3. Popovski K, Andritsos N, Fytikas M, Sanner B, Sanner S, Valdimarsson P (2010) Geothermal energy. Skopje
4. Ladam Y, Solheim A, Segatz M, Lorentsen OA (2011) Heat recovery from aluminum reduction cells. Light Met 2011:393–398
5. Ke W (2009) Research on waste heat power generation of aluminum reduction cells flue based on ORC. MSc thesis, Central South University, Changsha
6. Fleer M, Lorentsen OA, Harvey W, Palsson H, Saevarsdottir G (2010) Heat recovery from the exhaust gas of aluminum reduction cells. Minerals, Metals Materials Society/AIME (420 Commonwealth Dr., P. O. Box 430 Warrendale PA 15086 USA [np] 14–18 Feb)
7. Sea surface temperature 1998 + (1 Month MWOI). NASA. https://neo.sci.gsfc.nasa.gov/servlet/RenderData?si=1710746&cs=gs&format=SS.CSV&width=250&height=125. Accessed 4 Sep 2017

8. Dimian AC, Bildea CS, Kiss AA (2014) Integrated design and simulation of chemical processes, vol. 13. Elsevier
9. Caramia M, Dell'Olmo P (2008) Multi-objective management in freight logistics: increasing capacity, service level and safety with optimization algorithms. Springer
10. WU SY YITT, XIAO L (2014) Parametric optimization and performance analysis of subcritical organic Rankine cycle based on multi-objective function. CIESC J 65(10):4078–4085
11. Daniel JS, Velders GJM, Douglass AR, Forster PMD, Hauglustaine DA, Isaksen ISA, Kuijpers LJ, McCulloch A, Wallington TJ (2006) Halocarbon scenarios, ozone depletion potentials, and global warming potentials. Scientific assessment of ozone depletion, pp 8–1

Leaching and Carbonation of Electric Arc Furnace (EAF) Slag Under a Microwave Field for Mineral Carbonation

Zhibo Tong, Guojun Ma, Xiang Zhang, Junjie Liu and Langsha Shao

Abstract The aqueous mineral carbonation process that leaching alkaline earth metals from industrial residues by ammonium salt and carbonation thereafter is one of the potential technologies for CO_2 sequestration. In this paper, the effect of particle size of waste slag on the leaching rate of metals under a microwave field and effect of microwave irradiation on the carbonation process were investigated. It was found that the initial leaching ratio of Ca decline seriously with the particle size of EAF slag increasing, and the Ca leaching ratio is relatively low during 120 min leaching. The lower leaching ratio of Ca with large particle size is due to the existence of a silica product layer produced on the surface of calcium silicates. Moreover, due to the microwave irradiation, the leaching ratio of calcium and the crystallization rate of calcium carbonate increase, though the particle size and distribution range of calcium carbonate reduce.

Keywords Leaching · Mineral carbonation · Kinetics · EAF slag Carbonation

Introduction

Carbon capture, utilization and storage (CCUS) has been considered as one of the effective solutions to regulate anthropogenic CO_2 emissions in which mineral carbonation, as one of the major proposed options for CO_2 sequestration, occurs spontaneously in nature and involves the reaction between atmospheric CO_2 and alkaline earth metals contained silicate minerals, with the formation of chemically

Z. Tong · G. Ma (✉) · X. Zhang · J. Liu · L. Shao
The State Key Laboratory of Refractories and Metallurgy,
Wuhan University of Science and Technology, Wuhan, China
e-mail: gma@wust.edu.cn

Z. Tong
The Key Laboratory of Extroadinary Bond Engineering and Advanced Materials Technology,
Yangtze Normal University, Fuling, Chongqing 408100, China

Z. Sun et al. (eds.), *Energy Technology 2018*, The Minerals, Metals & Materials Series, https://doi.org/10.1007/978-3-319-72362-4_15

stable carbonate forms [1, 2]. Natural minerals has been tested as alkaline feedstock for mineral carbonation from the very beginning, particularly including forsterite, serpentine and wollastonite [3–6]. As the research moves along, it is noticed that industrial residues show more reactive properties than natural ores, moreover, the site where produce industrial waste is often close to the source of CO_2 emissions, which is in favour of saving the transportation cost [7–9]. Typically, these industrial wastes are basic, such as steelmaking slag, fly ashes from combustion processes [10, 11], cement kiln dust [12], cement waste [13], and mining residue [14].

Kakizawa et al. puts forward that the lower acidity and recyclable ammonium salt, such as ammonium chloride can be used as extracting agent [5]. The main reacption equations are shown as the following:

$$2CaO \cdot SiO_2(s) + 4\,NH_4Cl(aq) \rightarrow 2CaCl_2(aq) + 2H_2O + SiO_2(s) \downarrow + 4\,NH_3(aq) \quad (1)$$

$$4\,NH_3(aq) + 2CO_2(aq) + 2CaCl_2(aq) + 4H_2O(l) \rightarrow 2CaCO_3(s) \downarrow + 4\,NH_4Cl(aq) \quad (2)$$

Only calcium ions can be extracted at the pH range of 8.0–10.5 in the leaching system, and precipitate calcium carbonate as the by-product is of high purity. In addition, the extraction agent can be recycled to effectively reduce the process cost, nevertheless, the leaching rate of ammonium chloride as extraction medium is relatively lower than that with strong acid.

In order to improve the reaction rate at leaching experiments, numerous researchers succeeded in promoting the extraction reaction by various methods, such as physically activated [6], heat activated [15], ultrasonic [16] and microwave [17]. Microwave irradiation helps the leaching of alkaline earth metal form slag on account of its thermal effect and non-thermal effect [17], and our previous study indicated that the calcium leaching ratio from EAF steelmaking slag at the constant temperature under microwave field increases about 10% than that under the water bath [18]. However, the calcium leaching mechanism from EAF steelmaking slag by ammonium salt and effects of microwave on the precipitation of calcium carbonate are still not clear. In this study, the effect of particle size of waste slag on the leaching rate of metals under a microwave field and effect of microwave irradiation on the carbonation process were investigated.

Experimental Procedure

The EAF steelmaking slag was collected from a local steelmaking plant in northern China. The as-received slag had undergone magnetic separation to obtain the metallic iron content and contains mainly 39 wt% CaO, 28 wt% Fe_2O_3, 12 wt% SiO_2, 8 wt% MgO and 4 wt% Al_2O_3. The slag samples were dried in an oven at 110 °C for 24 h to remove residual moisture, and then comminuted in a vibratory

disk mill to achieve a fine particle size. The fine milled samples were then sieved into 4 size fractions, i.e., 54–74, 74–97, 97–150 and 150–340 μm. The sieved EAF steelmaking slag portion were stored separately in the drying apparatus for further use. The calcium contents of the four size fractions are 37.84 wt%, 38.11 wt%, 38.51 wt%, 39.6 wt% for the portions of 54–74, 74–97, 97–150 and 150–340 μm, respectively.

Calcium leaching experiments from EAF slag by ammonium chloride under microwave filed were carried out in a microwave chemical reactor (Model: MCR-3) which can provide a stable temperature with variable microwave power output. It operated with a continuous microwave at 2.45 GHz and equipped a continuous monitoring of the measured temperature with a trifluoroethylene thermocouple. The leaching system was stirred by a magnetically stirrer. The leaching experiments in a microwave field, were carried out in a 500 ml flat bottom narrow neck flask, which reactor was positioned in the middle of the microwave chemical reactor and equipped with condenser system to minimize the evaporation losses of leaching system.

The typical leaching experiment were conducted as follows: the 500 ml glass reactor filled with 340 ml of 2 mol/l ammonium chloride solution was firstly heated to the desired leaching temperature. Then, 17 g EAF steelmaking slag with certain particle size was added into the leaching solution, agitation of the solution was maintained at three-quarters of the maximum agitation speed, and small portion of samples were drawn at designed time schedule of 2, 5, 10, 20, 30, 60, 90, 120 min and whereafter filtered. Calcium ion contents in the filtrates were titrated with EDTA. The leached residues were triply washed by Reverse Osmosis water (RO) and dried for scanning electron microscopy (SEM) (Nova 400 Nano SEM, FEI, Hillsboro, OR, USA) -energy dispersive spectrometer (EDS) (INCAIE 350 PentaFET X-3 EDS, Oxford, UK) analysis. The as-received EAF slag sample were also analyzed with SEM-EDS.

The carbonation experiments were conducted either in a microwave field (microwave chemical reactor MCR-3) or with conventional precipitation method. In the microwave assisting carbonation process, the synthetic solution (2.4 mol/l NH_4Cl-0.8 mol/l $CaCl_2$-1.6 mol/l $NH_3{\cdot}H_2O$, 400 ml) was placed in a microwave reactor, then the high purity carbon dioxide gas was bubbled and the time was started. After the sampling time was reached, 2 ml of the reaction slurry was transferred to the filter by a syringe and the concentration of calcium ions in filtrate was measured. Moreover, the filtered residue was triply washed with distilled water and rinsed to a 50 ml beaker with ethanol, then diluted with 20–30 ml of ethanol. Finally, the beaker containing calcium carbonate and ethanol was placed in a water bath with ultrasound processing for 10 min, a drop of the slurry was removed on the silicon plate with a capillary and sprayed with gold for SEM analysis. The particle size distribution of the remaining residue-alcohol emulsion was immediately measured with laser particle analyzer (Malvern Mastersizer 2000). In the conventional carbonation experiment under a water bath, the synthetic solution was heated to the experimental temperature for half an hour. The rest of the steps were the same as that in the carbonation experiment under a microwave field.

Results and Discussion

Calcium Leaching Process from Different Size Particles of EAF Steelmaking Slag with Ammonium Chloride

The effects of particle size on the calcium leaching rate from EAF slag by ammonium chloride were studied at 60 °C under microwave filed, as the higher temperature is conducive to calcium leaching while resulting in dissolved ammonia leakage from leaching solution. Four size fractions were chosen to verify the effect of particle size on the leaching rate (Fig. 1). It can be seen from Fig. 1 that the initial calcium leaching ratio decline seriously with the increase of particle size of EAF slag, and the leaching ratio is relatively lower during 120 min though it is improved and tend to balance as leaching time goes on. This is due to the smaller specific surface area, leaded by the larger EAF particle size, the smaller contact area of the leaching solution and particles, which reducing the calcium leaching rate under the same leaching condition.

Microstructure Analysis of the as-Received EAFSlag and Leached Residues

SEM Analysis of the as-Received EAF Slag

As calcium silicate, calcium ferroalumnates and RO phase are the main phases in EAF slag [19], the SEM analysis will be focused on these three phases. It is shown in Fig. 2 that the particle surface of calcium silicate phase is smooth and dense, and the calcium content of which is much higher than iron and silicon. Figure 3 is the SEM image of typical three-phase symbiosis containing calcium silicate, calcium

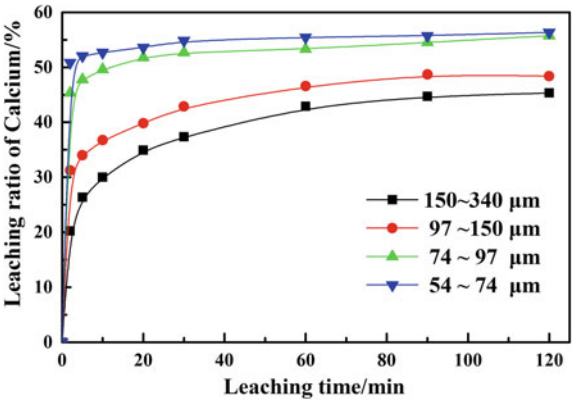

Fig. 1 The effect of particle size on the leaching rate of calcium

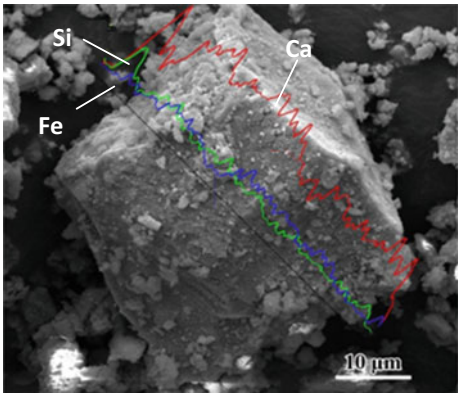

Fig. 2 SEM image of calcium silicate in EAF slag

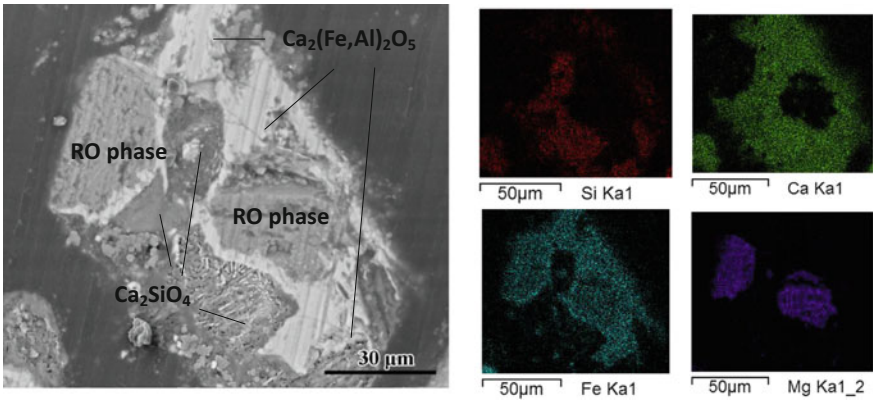

Fig. 3 SEM image of typical three-phase symbiosis

ferroalumnates and RO phase, from which it can be found that the slag particle mainly contains iron, as well as large amounts of magnesium and calcium. Moreover, iron and silicon usually exist with calcium and does not coexist.

Calcium silicate, with good hydration activity, is the mainly phase in EAF slag, and it usually coexist with low hydration activity phases such as calcium ferroalumnates and RO phase. As aluminum element often dissolves into calcium ferrite and the average ratio of $CaO/(Fe_2O_3 + Al_2O_3)$ is close to 2, the Al-bearing phase was usually expressed as $Ca_2(Al, Fe)_2O_5$ [19, 20].

RO phase is a solid solution, which mainly contains iron, magnesium and small amount of manganese. During the steelmaking process, CaO as a free state usually leads to the crystallization precipitation of MgO, FeO and MnO from steelmaking slag when the content of CaO increasing. Moreover, it is helpful to form a limited solid solution for the ion radius difference among magnesium, iron and manganese

less than 15% [19, 20]. In this study, RO phase is wustite and difficult to react with other phases due to its small value of KM according to the KM properties of RO phase (KM = w(MgO)/w(FeO + MnO) < 1).

SEM Analysis of the Leached EAF Slag Residues

Figure 4 shows the typical microstructure of the leached EAF slag residues at certain leaching time. Figures 4a, b are SEM images of 54–74 μm leached residues at leaching time of 2 min and 120 min respectively. It can be seen from Fig. 4a that calcium is completely extracted from calcium silicate while it is difficult to extract from the phase riching in iron and aluminum. As the leaching time was prolonged (Fig. 4b), it still can't be extracted from calcium ferroalumnates. However, the micro-crack generated among different phases of particles under microwave field (the dashed area Fig. 4b), which is leaded by the thermal stress due to different capacity of absorbing microwave for different phases, expands the exposed surface area, and this is beneficial to the calcium leaching. Furthermore, the RO phase contains less calcium and do not react with ammonium chloride. Therefore, it explains the leaching curve of 54–74 μm EAF slag in Fig. 1 that the calcium

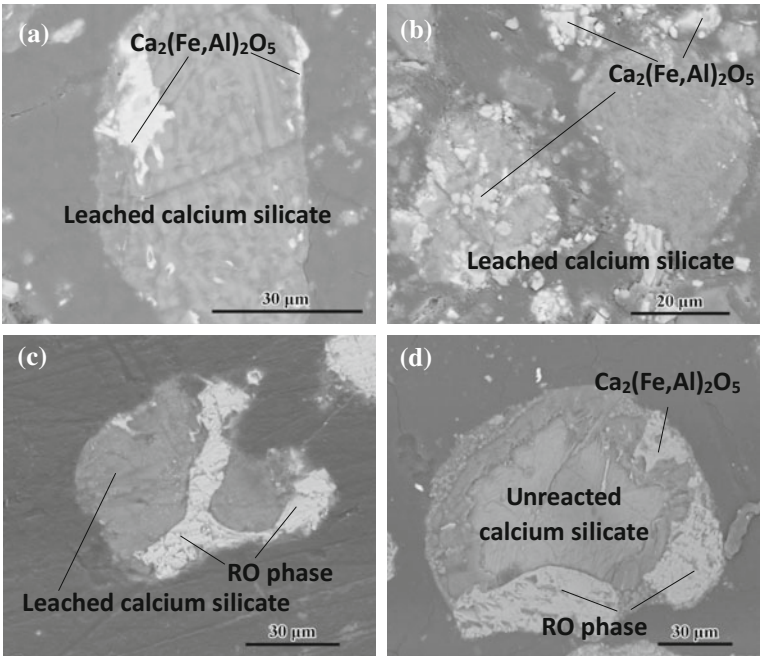

Fig. 4 SEM image of leached residues **a** 54–74 μm, 2 min; **b** 54–74 μm, 120 min; **c** 97–150 μm, 2 min; **d** 97–150 μm, 120 min

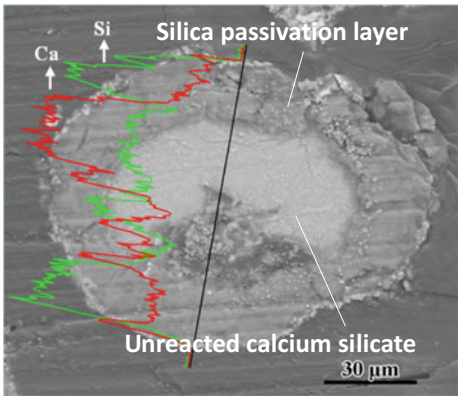

Fig. 5 SEM image of separate calcium silicate phase (97–150 μm, 2 min)

leaching rate rise obviously within 2 min due to the leaching reaction of the calcium silicate, while it tends to balance in subsequently leaching time.

As the SEM image of larger leached residues (such as 97–150 μm) at leaching time of 2 min shows in Fig. 4c, the calcium silicate phase which is associated with RO phase and calcium ferroalumnate has not been fully leached. However, calcium continues to be leached with the increase of leaching time and the calcium silicate phase which is associated with RO phase and calcium ferroalumnates has also been leached partly. The reaction is hindered by silica (leached calcium silicate), on the particle surface (Fig. 4d).

Figure 5 is the SEM image of separate calcium silicate phase (97–150 μm and 2 min). It can be seen that there is a silica passivation layer coming from the calcium silicate phase on the particle surface after leaching, of which is loose and with a certainty thickness. It indicates that when the loose silica passivation layer has a certainty thickness for larger size, the leaching reaction of the separate calcium silicate phase will be prevented as the leaching time goes on, and the center of particles will be difficult to react. It is in keeping with the leaching curve of larger size particle that calcium leaching rate is relatively slower at the start of experiment and become more slower as the core of particles will be difficult to react due to the silica passivation layer.

The Leaching Mechanisms of Different Phase in EAF Slag

As RO phase, one of the main three phases in the EAF slag, contains a small amount of calcium, the main calcium sources leached from EAF slag are calcium silicate and calcium ferroaluminate at the leaching process. According to the Gibbs free energy thermodynamic theory, calcium ferroaluminate can react with ammonium chloride [17]. However, experiments in this study verify that calcium ferroaluminate almost does not participate in the leaching reaction. This is probably

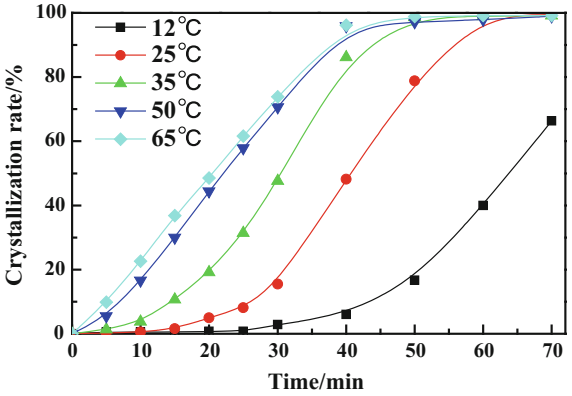

Fig. 6 The effect of water-bath temperature on the crystallization rate of calcium carbonate (2.4 NH_4Cl-0.8 $CaCl_2$-1.6 $NH_3 \cdot H_2O$, 160 mL/min, 350 rpm, water-bath)

due to that the dissolved Al(III) and Fe(III) at the leaching reaction completely hydrolysis into passivation layer on the particle surface, and hampering diffusion of ammonium chloride and further calcium leaching considering the fact that Al(III) and Fe(III) will complete hydrolysis in the system of NH_3-NH_4Cl-H_2O [21]. Therefore, the main involved calcium-bearing phase in EAF slag reacting with ammonium chloride is calcium silicate.

Based on the calcium leaching curve and SEM analysis of different granularity of EAF slag, it is shown that a silica product layer will be produced in the dissolving process of calcium silicate, and the silicate solid product layer under microwave field has permeability. When the particle size is small (54–74 μm), calcium silicate phase participates in leaching reaction completely. However, when the particle size is large (97–150 μm), calcium is difficult to be extracted from calcium ferroaluminate and calcium silicate. The final calcium leaching ratio is lower than that of small size particle due to a silica product layer produced on the surface of calcium silicate.

Effects of Microwave on the Carbonation Process

In the conventional carbonation process, the crystallization rate of calcium carbonate at different water bath temperatures was shown in Fig. 6. It is shown that the reaction rate is low, and the crystallization rate is only 66% at 70 min with the crystalline temperature of 12 °C. With the increase of the crystalline temperature, the crystallization rate of calcium carbonate is accelerated. When the temperature increases up to 50 °C, the carbonation reaction stops in 50 min. While keep in heating to higher temperature, the crystallization rate does not increases significantly. This could be due to the rate of diffusion and reaction accelerated with the crystallization temperature [22], while when the temperature reaches a certain

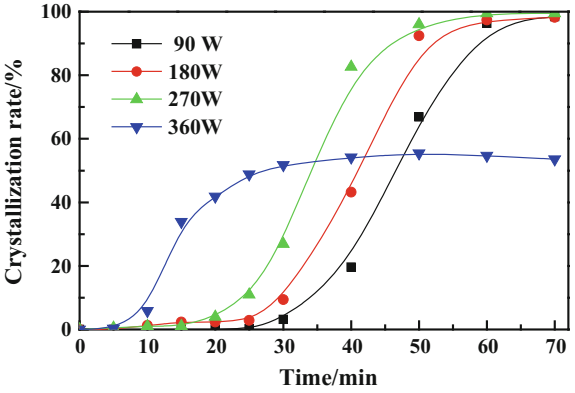

Fig. 7 The effect of microwave power on the crystallization rate of calcium carbonate (2.4 NH_4Cl-0.8 $CaCl_2$-1.6 $NH_3{\cdot}H_2O$, 160 mL/min, 350 rpm, microwave)

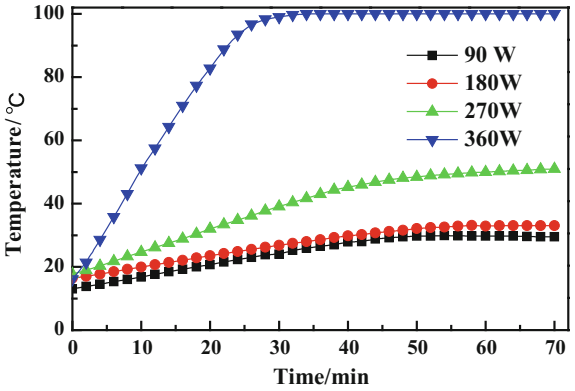

Fig. 8 The heating curve of the solution under different microwave power (2.4 NH_4Cl-0.8 $CaCl_2$-1.6 $NH_3{\cdot}H_2O$, 160 mL/min, 350 rpm, microwave)

degree, ammonia will evaporate and thus affects the dissolution of carbon dioxide, and the crystallization rate of calcium carbonate does not increase significantly.

Figures 7 and 8 show the crystallization rate of calcium carbonate and the heating curve of the solution under different microwave powers, respectively. The results show that the crystallization rate increases with an increase of microwave power. When the microwave power increases to 360 W, the solution will boil in 30 min leading to the difficulty of dissolving carbon dioxide into the solution and thus the crystallization reaction of calcium carbonate is unable to continue. Comparing to Fig. 6, it can be seen that the crystallization rate is very low at the initial stage in the microwave irradiation environment. However, with the increase of reaction time, the crystallization rate increased rapidly until the end of the carbonation reaction. From the crystallization curve, it can be deduced that the formation of nuclei is delayed under the action of microwave. As the carbonation reaction time increased, the crystallization rate increases rapidly until the reaction ends, and this explosive homogeneous nucleation is favorable for the refinement of the crystal and concentration of the particle size distribution.

Figure 9 shows the effect of different water bath temperatures on the particle size of calcium carbonate. It can be seen that with the temperature increases, the particle size of calcium carbonate increases and the distribution range becomes larger. That is due to the fact that increasing the crystallization temperature promotes crystallization reaction rapidly, thus increasing the supersaturation of the calcium carbonate in the reaction system and promoting nucleation of calcium carbonate. At the same time, the higher temperature can improve the crystal surface activity and growth rate, resulting in the increase of the grain size [23].

It can be seen from Fig. 10 that the grain size of calcium carbonate is changed insignificantly under microwave irradiation with different microwave power of 90, 180 and 270 W. but it is obviously smaller and more concentrated than that in water bath (except water bath at 12 °C), which agrees with the crystallization rate of calcium carbonate under different microwave power. As the microwave irradiation can affect the internal energy of the solution, and water and other polar molecules will vibrate and activate after microwave absorption which result in the decreased of surface tension and viscosity coefficient of the solution, thus increasing the

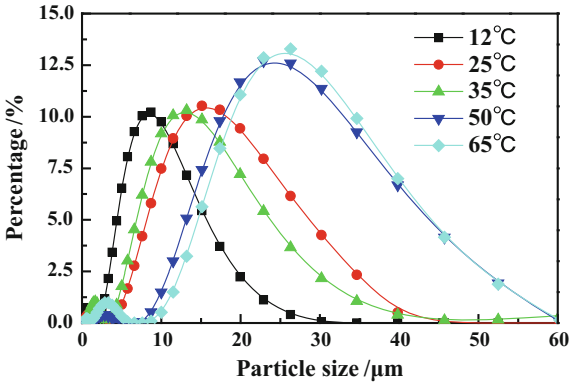

Fig. 9 The effect of temperature on particle size of calcium carbonate (70 min)

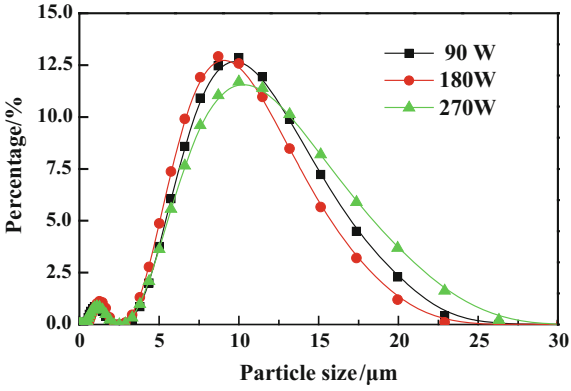

Fig. 10 The effect of microwave power on particle size of calcium carbonate (70 min)

nucleation rate and reducing the critical nucleation radius. In addition, the microwave irradiation can heat the solution evenly which provides the power for homogeneous nucleation [24].

It can be seen from Figs. 9 and 10 that there are two peaks on the particle size distribution curve. The peak of small particle size is between 0.4 and 2.5 μm which corresponds to the initial crystalline particle size, comparing the effects of different time under microwave irradiation on the particle size distribution of calcium carbonate. And peak of larger particle size may be due to the large agglomeration of many particles, which is the same as that reported in the literature [25].

Conclusions

(1) The initial leaching ratio decline seriously with the particle size of EAF slag increasing, and the leaching ratio is relatively lower during 120 min though it is improved and tends to balance as time goes on.
(2) When the particle size is small (54–74 μm), calcium silicate phase participate in leaching reaction completely, however, when the particle size is large (97–150 μm), calcium is difficult to be extracted from calcium ferroaluminate and calcium silicate.
(3) The final leaching ratio is lower than that of small size particle due to a silica product layer produced on the surface of calcium silicate.
(4) Due to the microwave irradiation, the leaching ratio of calcium and the crystallization rate of calcium carbonate increase, though the particle size and distribution range of calcium carbonate reduce.

Acknowledgements The authors gratefully acknowledge the Natural Science Research Foundation of China (51374161) for financial support.

References

1. Polettini A, Pomi R, Stramazzo A (2016) Carbon sequestration through accelerated carbonation of BOF slag: influence of particle size characteristics. Chem Eng J 298:26–35
2. Li Y, Ma X, Wang W, Chi C, Shi J, Duan L (2017) Enhanced CO_2 capture capacity of limestone by discontinuous addition of hydrogen chloride in carbonation at calcium looping conditions. Chem Eng J 316:438–448
3. Lackner KS, Wendt CH, Butt DP, Jr ELJ, Sharp DH (1995) Carbon dioxide disposal in carbonate minerals. Energy 20(11):1153–1170
4. Kojima T, Nagamine A, Ueno N, Uemiya S (1997) Absorption and fixation of carbon dioxide by rock weathering. Energ Convers Manage 38(36):237–242
5. Kakizawa M, Yamasaki A, Yanagisawa Y (2001) A new CO_2 disposal process via artificial weathering of calcium silicate accelerated by acetic acid. Energy 26(4):341–354

6. Park AHA, Fan LS (2004) CO_2 mathcontainer loading mathjax mineral sequestration: physically activated dissolution of serpentine and pH swing process. Chem Eng Sci 59(22–23):5241–5247
7. Huijgen WJ, Witkamp GJ, Comans RN (2005) Mineral CO_2 sequestration by steel slag carbonation. Environ Sci Tech 39(24):9676
8. Lekakh SN, Rawlins CH, Robertson DGC, Richards VL, Peaslee KD (2008) Kinetics of aqueous leaching and carbonization of steelmaking slag. Metall Mater Trans B 39(1):125–134
9. Tong Z, Ma G, Zhang X (2017) Microwave activation of electric arc furnace (EAF) slag for strengthening calcium extraction with ammonium chloride solution. J Solid Waste Technol Manag 43(2):137–144
10. Li X, Bertos MF, Hills CD, Carey PJ, Simon S (2007) Accelerated carbonation of municipal solid waste incineration fly ashes. Waste Manage 27(9):1200–1206
11. Nyambura MG, Mugera GW, Felicia PL, Gathura NP (2011) Carbonation of brine impacted fractionated coal fly ash: implications for CO_2 sequestration. J Environ Manage 92(3):655–664
12. Huntzinger DN, Gierke JS, Sutter LL, Kawatra SK, Eisele TC (2009) Mineral carbonation for carbon sequestration in cement kiln dust from waste piles. J Hazard Mater 168(1):31
13. Jo H, Park SH, Jang YN, Chae SC, Lee PK, Jo HY (2014) Metal extraction and indirect mineral carbonation of waste cement material using ammonium salt solutions. Chem Eng J 254:313–323
14. Assima GP, Larachi F, Molson J, Beaudoin G (2014) Impact of temperature and oxygen availability on the dynamics of ambient CO_2 mineral sequestration by nickel mining residues. Chem Eng J 240:394–403
15. Pasquier LC, Mercier G, Blais JF, Cecchi E, Kentish S (2014) Parameters optimization for direct flue gas CO_2 capture and sequestration by aqueous mineral carbonation using activated serpentinite based mining residue. Appl Geochem 50:66–73
16. Huajuan DI, Yang L, Pan D (2012) Enhancement of carbon dioxide sequestration with calcium-based residues by ultrasonics. Ciesc J 63(8):2557–2565
17. Zhang X, Ma G, Tong Z, Xue Z (2017) Microwave-assisted selective leaching behavior of calcium from basic oxygen furnace (BOF) slag with ammonium chloride solution. J Min Metall 53(2):139–146
18. Tong Z, Ma G, Zhang X, Cai Y (2017) Microwave-supported leaching of electric arc furnace (EAF) slag by ammonium salts. Minerals 7(7):119
19. Dong O, Xie Y (1991) Composition, mineral morphology and cementitious properties of converter slag. J Chin Ceramic Soc, Beijing
20. Hou G, Li W, Guo W, Chen J, Luo J, Wang J (2008) Microstructure and mineral phase of converter slag. J Chin Ceramic Soc 36(4):436–443
21. Ju S (2006) Study on hydrometallurgical thermodynamics of metal (Cu, Ni, Au) in the system of Me-NH_4Cl-NH_3-H_2O and heap leaching process of their low-grade ores. Ph.D. thesis, Central South University
22. Yan X, Wang P, Su J (2007) Key technologies on nano calcium carbonate. Chemical Industry Press, Beijing
23. Lin R (1997) Study on the crystalline kinetics and reaction parameters of precipitate calcium carbonate. Master thesis, Guangxi University
24. Rodriguez-clemente R, Gomez-morales J (1996) Microwave precipitation of $CaCO_3$ from homogeneous solutions. J Cryst Growth 169(2):339–346
25. Xiang L, Wen Y, Wang Q, Jin Y (2006) Formation and characterization of dispersive Mg substituted $CaCO_3$. Mater Lett 60(13–14):1719–1723

A Novel Preparation of Bi_2O_3 and Their Potent Photocatalytic Activity Under Visible-Light Irradiation

C. Jun, Z. Jing, L. Qihou, Z. Yumeng and L. Hui

Abstract Three phases of Bi_2O_3 were first synthesized by extraction-stripping-precipitation and post decomposition from $BiCl_3$ leaching solution. The as-prepared Bi_2O_3 were characterized by X-ray powder diffraction (XRD), Fourier transform infrared spectra (FT-IR), scanning and transmission electron microscopy (SEM, TEM), UV-vis diffuse reflectance spectroscopy (UV-vis DRS), Brunauer-Emmett-Teller (BET) and X-ray photoelectron spectroscopy (XPS). The photocatalytic performances of the oxides were investigated by decomposing rhodamine B (RB) under visible irradiation. It shows that the Bi_2O_3 with different crystal structures and morphology were obtained under different decomposition temperature. The band gaps of as-prepared samples were 2.36, 2.41, and 2.78 eV for β-Bi_2O_3, α-Bi_2O_3, and δ-Bi_2O_3, respectively, and the photocatalytic activities followed the order: β-Bi_2O_3 > α-Bi_2O_3 > δ-Bi_2O_3, which was in good accordance with the photoluminescence spectra measurement results. The β-Bi_2O_3 exhibited the best photocatalytic performance which can effectively degrade 99.23% RB within 240 min.

Keywords B-Bi_2O_3 · A-Bi_2O_3 · Δ-Bi_2O_3 · Photocatalysts · Degradation

C. Jun · Z. Jing (✉) · L. Qihou · L. Hui
School of Metallurgy and Environment, Central South University, Changsha 410083, People's Republic of China
e-mail: zhanjing2001@hotmail.com

C. Jun
e-mail: Cj_csu@163.com

L. Qihou
e-mail: liqihou@csu.edu.cn

L. Hui
e-mail: leolau@csu.edu.cn

Z. Yumeng
College of Environmental and Resources, Xiangtan University, Xiangtan 411104, People's Republic of China
e-mail: 462312402@qq.com

Z. Sun et al. (eds.), *Energy Technology 2018*, The Minerals, Metals & Materials Series, https://doi.org/10.1007/978-3-319-72362-4_16

Introduction

The depletion of the fossil energy and the pollution of the environment are two severe global problems. That is why the photocatalytic oxidation technology, which utilizes renewable clean solar energy to curb environmental pollution, is a very promising technology, by which the organic pollutions are oxidized and degraded to even carbon dioxide and water under light, especially sunlight, irradiation at ambient temperature in the presence of photocatalysts [1–3]. Nowadays, many semiconductor materials including TiO_2 [1, 4, 5], ZnO [6, 7] and $SrTiO_3$ [4, 8] have been investigated as photocatalysts in degradation of organic pollutants for water treatment. However, these photocatalysts have a rapid recombination rate of photo-generated electronehole pairs, a low efficiency for utilizing solar light, and a high band gap energy, which significantly restrict its practical applications. Bi_2O_3, a p-type semiconductor, has been proven to be one of interesting photocatalyst due to its significant energy band gap, fresh-construction, and well-dispersed valence bands by the hybridization of Bi 6 s and O 2p orbits [9–12].

Bi_2O_3 exhibits four main polymorphs that are consisted of α-, β-, γ-, and δ-Bi_2O_3. The α-Bi_2O_3 phase and δ-Bi_2O_3 phase are stable at room and high temperature, respectively, while others are all metastable phases [13]. It is commonly considered that the phase structure of crystals plays a crucial parameter in the determination of their properties. Moreover, the photocatalytic activity of Bi_2O_3 strongly depends on its crystalline structure [14]. Though, many researches on α-Bi_2O_3 [15–17] have been reported, there were only a few on β-Bi_2O_3 and δ-Bi_2O_3 [18–21]. What's more, Bi_2O_3 was prepared usually using analytical grade bismuth material or high-purity bismuth as raw materials, there was no reported on prepared three polymorphs of Bi_2O_3 from $BiCl_3$ leaching solution. In this paper, synthesis of three polymorphs Bi_2O_3 using $BiCl_3$ leaching solution as raw materials was first investigated. The photocatalytic activity and the effects of crystal type on it were also investigated, taking the degradation of RB under visible light.

Experimental Details

Materials

Tributyl phosphate (TBP), hydrochloric acid, oxalic acid, ammonium hydroxide, sulfonated kerosene (0.8 g/mL) and ethanol were provided by Xilong Chemical Co. Ltd., China. All the chemicals used in this study were of analytical grade without further purification. The $BiCl_3$ leaching solution was obtained according to previous report use low grade bismuthinite and pyrolusite ores [22], and followed by purified, the contents of $BiCl_3$ leaching solution showed in Table 1.

Table 1 Contents of $BiCl_3$ solution

Elements	Bi	Fe	Cu	Mn	Pb
Concentration (g/L)	19.0566	4.3939	0.0896	0.9009	0.6114

Synthesis of Bi_2O_3

The Bi_2O_3 was synthesized by extraction-stripping-precipitation and post decomposition. The typical synthesis procedure was as follows. 100 mL of $BiCl_3$ (19.0566 g/L) leaching solution was extracted with 100 mL of 60% v/v TBP-sulfonated kerosene use separatory funnel and then the organic-aqueous phases were separated by separatory funnel. An equal volume of the stripping phase (15 g/L oxalic acid) was used to strip and precipitate Bi from organic phase at a temperature of 25 °C. After phase separation, the white precipitate was separated and washed with ethanol for several times successively, and then was dried at 80 °C for 12 h. The white precipitate was known as precursor, usually. Finally, as-prepared precursor was calcined in a tube furnace with temperature increased at a rate of 5 °C/min to a certain temperature (300, 500, 730 °C) and then held there for 2 h.

Characterization

X-ray diffraction (XRD-6000, Shimadzu Inc., Japan) pattern of the samples were obtained for phase identification. The morphologies were examined by scanning electron microscopy (SEM, Quanta 200 F, Japan) and transmission electron microscopy (TEM, JEOL, JEM-2100, Japan). The banding energy of the elements was investigated by X-ray photoelectron spectra spectrometer (XPS, VG Multilab 2000, USA). The specific surface area of product was determined according to the Brunauer-Emmett-Teller (BET, ASAP2020 M, Mike instruments inc., USA) method in the relative pressure range (P/P_0) of 0.01–0.3. Equilibration interval was controlled at 10 s. Photoluminescence spectra were taken using Horbia Fluorolog@3 spectrophotometer. Ultraviolet-visible diffuse reflectance spectra were recorded on a JASCO V-550 UV-Vis spectrophotometer. Fourier Transform Infrared (FT-IR) spectra for the photocatalysts were monitored using Agilent, Cary 660, USA.

Photocatalytic Experiments

The photocatalytic activity for the photocatalysts were evaluated for the degradation of aqueous RB under visible light illumination. A 300 W Xenon lamp was used as a

light source ($\lambda > 400$ nm). 25 mL RB aqueous solution (10^{-5} M) and 0.025 g (1 g/L) Bi_2O_3 sample were put into a glass reactor, the temperature of which was kept at 25 °C in a following water bath. Before light illumination, RB with catalyst was stirred under dark condition to attain adsorption-desorption equilibrium. At a given time interval, supernatant was collected, centrifuged and transferred to 3 mL of quartz cuvette for measuring the UV-vis absorbance value.

Results and Discussion

Preparation of Bi_2O_3 Photocatalysts

TBP was used as the extracting agent. The $BiCl_3 \cdot xTBP$(x = 2 or 3) complexes was obtained from $BiCl_3$ leaching solution and TBP in the extraction process and the precipitation stripping reaction between the $BiCl_3 \cdot xTBP$ complexes and oxalic acid may be written as the following Eq. (1) [23]: The $Bi_2(C_2O_4)_3 \cdot 7H_2O$ can be further decomposed to prepare the Bi_2O_3 photocatalysts.

$$2\overline{BiCl_3 \cdot xTBP} + 3H_2C_2O_4 + 7H_2O = Bi_2(C_2O_4)_3 \cdot 7H_2O_{(s)} + 2x\overline{TBP} + 6HCl \quad (1)$$

Figure 1 was the XRD patterns of the prepared precursor and it can be indexed as a triclinic lattice of $Bi_2(C_2O_4)_3 \cdot 7H_2O$ with crystal cell constants $a \neq b \neq c$, and a = 9.43Å, b = 9.18Å, c = 11.17Å, $\alpha = 78.3°$, $\beta = 101.0°$, $\gamma = 73.7°$, which are close to the JCPDS file data (PDF no. 38–0548). The sharpness of the peaks suggested that the obtained precursor was well crystallized. The Fig. 2 showed that the precursor was hierarchical flower-like. Thus, the main contents of as-prepared Bi_2O_3 was listed in Table 2. It obviously showed that the main impurity was iron.

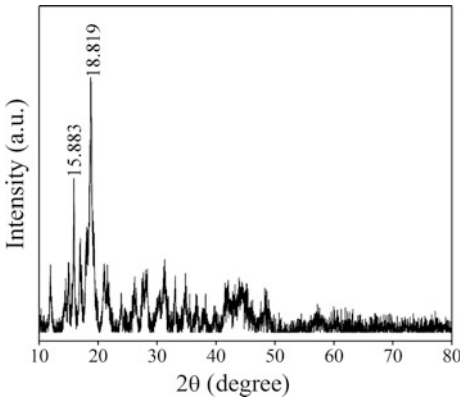

Fig. 1 XRD patterns of precursor

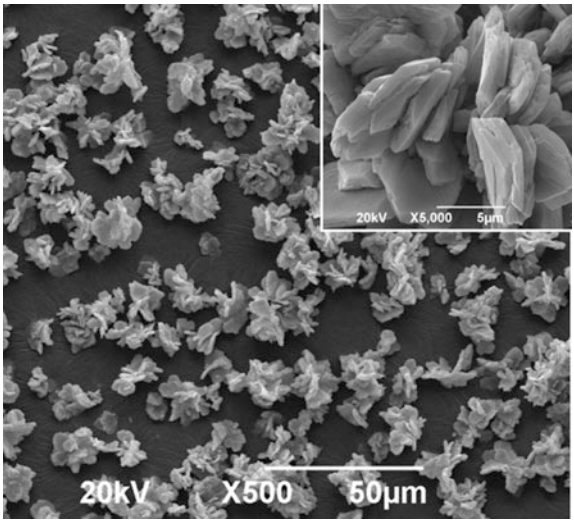

Fig. 2 SEM images of precursor

Table 2 Contents of Bi_2O_3

Element	Al	K	Fe	Cu	Mo	W	Bi_2O_3
Unit (wt%)	13.6×10^{-6}	19×10^{-6}	99×10^{-6}	12.8×10^{-6}	11.7×10^{-6}	28.1×10^{-6}	99.929

The XRD patterns of the as-prepared Bi_2O_3 was depicted in Fig. 3. The product calcined at 300 °C can be indexed to well crystallized β-Bi_2O_3 (PDF no. 78–1793). As the decomposition temperature increased to 500 °C, metastable β-Bi_2O_3 changed into α-Bi_2O_3 (PDF no. 41–1499). When the decomposition temperature increased to 730 °C, the α-Bi_2O_3 changed into δ-Bi_2O_3 (PDF no. 65–2366). Meanwhile, the results revealed that the samples have strong and sharp diffraction peaks, which revealed a high degree of crystallization. The apparent diffraction peaks of the three curves show that the all as-prepared Bi_2O_3 samples can be

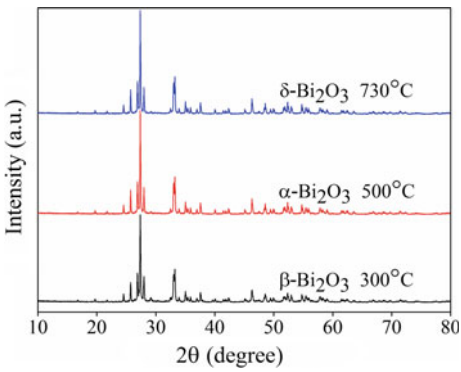

Fig. 3 XRD patterns of the Bi_2O_3 calcined at different temperature

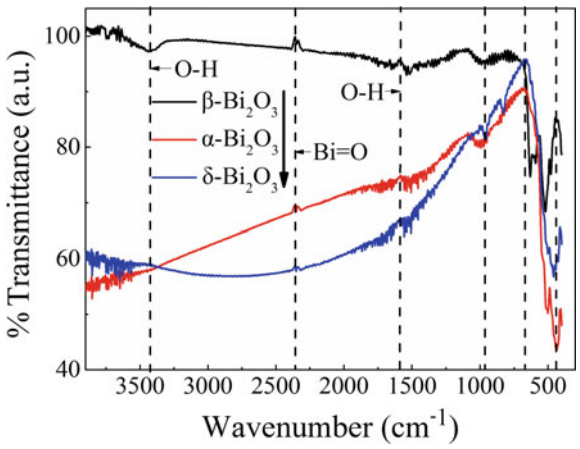

Fig. 4 FT-IR spectra of Bi_2O_3

indexed closely to the single phases of Bi_2O_3 semiconductor; β-, α-, and δ-Bi_2O_3 phase.

The FT-IR spectra of the as-prepared Bi_2O_3 photocatalyst was depicted in Fig. 4. The bands observed near 3423 and 1637 cm^{-1} correspond to the O-H stretching and banding vibration of residual H_2O molecules absorbed from the environment [24, 25]. The bonds appearing in the wavenumber rang of 400–1000 cm^{-1} were assigned to the Bi-O-Bi and the Bi-O [23, 26, 27]. Additionally, the bands located at 2400 cm^{-1} were assigned to the Bi = O group vibrations in Bi_2O_3.

SEM and TEM analysis was carried out to identify the effect of crystal type on morphology of Bi_2O_3 photocatalyst. Figure 5a–c shows SEM images of different crystal type Bi_2O_3. It can be seen that the morphology was transformed from aggregated microplates into micromesh under the different decomposition temperature. As displayed in Fig. 5d–f, the integer appearance of the microplates remained. Combined with high magnification TEM (Fig. 5f), the lattice fringes of 0.3190 nm was measured, corresponding to (201) plane of β-Bi_2O_3. In the Fig. 5d and f, the dark portion may resulted by the smooth surface.

To investigate BET and porous nature of the product further, the N_2 adsorption-desorption isotherm of the β-Bi_2O_3 sample measured at 77.5 K was displayed in Fig. 6. Meanwhile, the BET of prepared Bi_2O_3 was listed in Table 3. The smaller specific surface area may be due to the higher decomposition temperature that makes part of the sample sintered. The specific surface area can provide more reaction adsorption-desorption sites for photocatalytic reaction. The photocatalytic performance of the sample can benefit from the specific surface area of photocatalyst, which provides a large number of adsorption sites [28].

In order to study the chemical state of the surface elements, XPS analysis of Bi_2O_3 was carried out. Figure 7a showed the survey XPS spectra of Bi_2O_3, in which only the element Bi and O were observed, except for inevitable carbon contamination. Figure 7b showed the high-solution spectra of Bi in the Bi_2O_3. The characteristic Bi peaks at 158.77 and 164.08 eV show a high degree of symmetry.

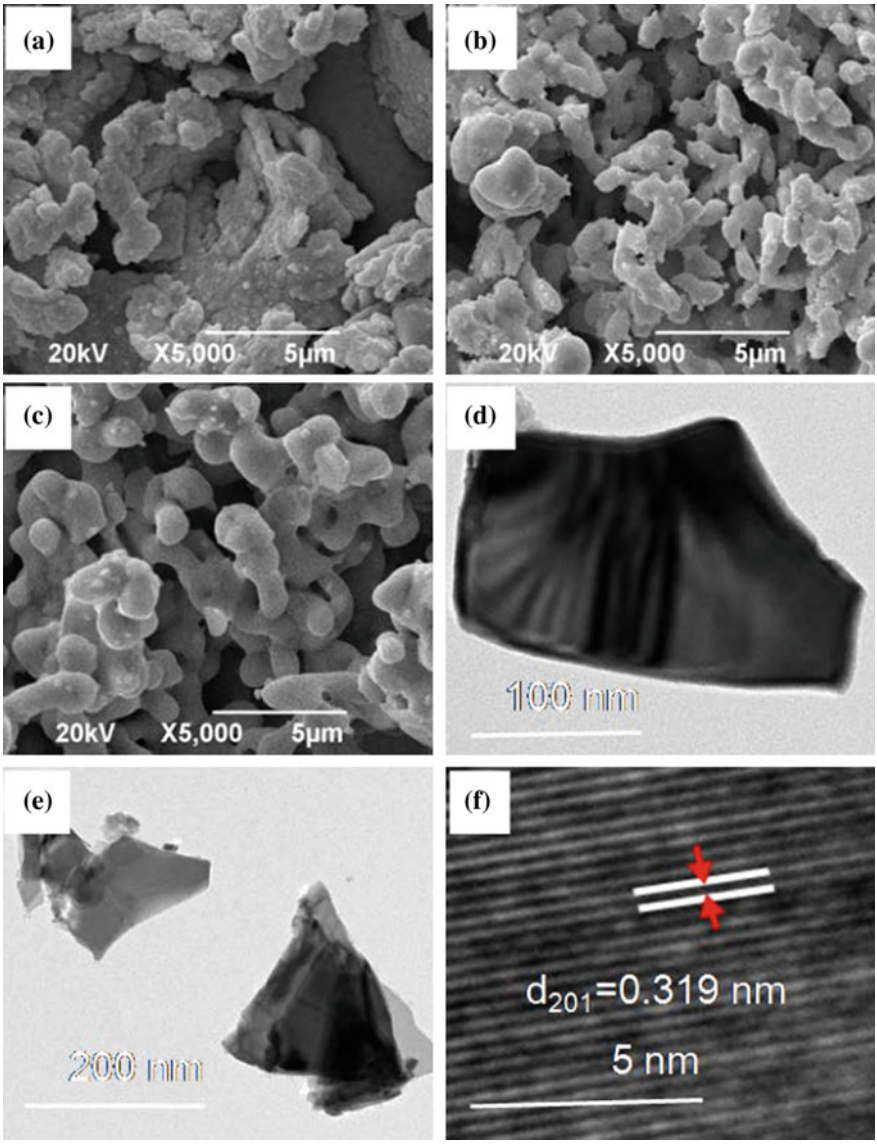

Fig. 5 SEM images of β-Bi_2O_3 (**a**), α- Bi_2O_3 (**b**) and δ-Bi_2O_3 (**c**) and the TEM images of β-Bi_2O_3 (**d–f**)

They belong to $Bi4f_{7/2}$ and $Bi4f_{5/2}$. Along with the sharp features of the Bi4f XPS spectra, those values indicate that the Bi was Bi^{3+} state. The high-resolution XPS spectra of O can be resolved into two peaks by deconvolution (Fig. 7c). The binding energy at 529.5 and 531.1 eV were assigned to the lattice oxygen (O_L), and the O^{2-} ion located in an imperfect lattice with oxygen deficiencies (O_M),

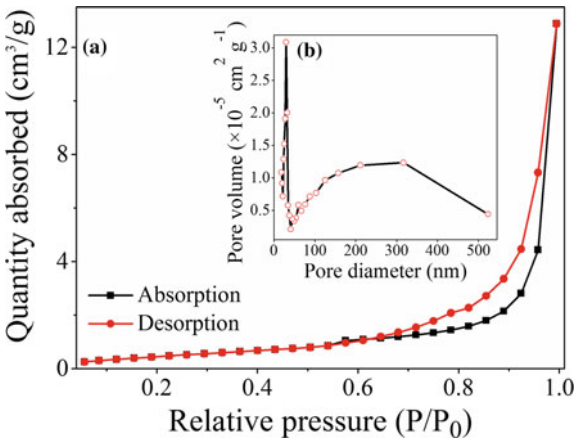

Fig. 6 N_2 adsorption-desorption isotherms (**a**) and BJH pore size distribution polts of β-Bi_2O_3 (**b**)

Table 3 Specific surface area of photocatalysts

Photocatalysts	β-Bi_2O_3	α-Bi_2O_3	δ-Bi_2O_3
S_{BET} (m^2/g)	2.3496	1.4783	0.5181

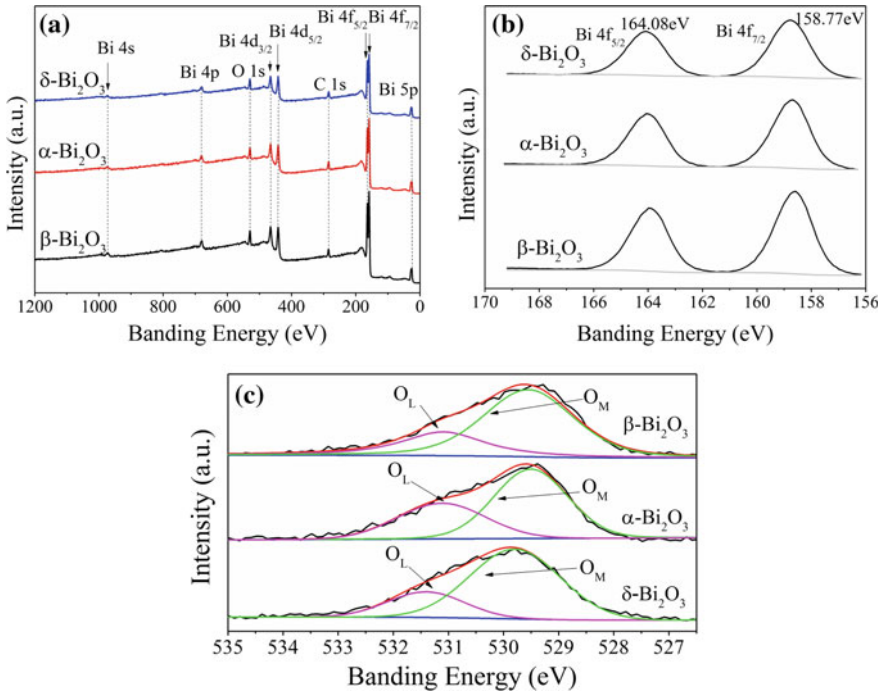

Fig. 7 **a** wide XPS survey of Bi_2O_3. **b** O1 s XPS spectra of Bi_2O_3. **c** Bi4f XPS spectra of Bi_2O_3

respectively [29]. The area ration of O_M to O_L provides a semiquantitative method to determine the concentration of oxygen vacancy. The calculated values of O_M/O_L were 0.79, 0.59, and 0.31 for the β, α, and δ-Bi_2O_3, respectively. This strongly suggests the presence of a significant amount of oxygen deficiencies in the Bi_2O_3, this is consistent with the photocatalytic activities of Bi_2O_3.

Photocatalytic Properties

The absorption performance and the band gaps of the prepared Bi_2O_3 were shown in Fig. 8. The absorption edges of the products calcined at 300, 500 and 730 °C, which have been evidenced by XRD to be β-Bi_2O_3, α-Bi_2O_3 and δ-Bi_2O_3 were located at 465 nm, 545 nm and 552 nm, respectively, showing high absorption till visible light region. As crystalline semiconductors of direct transition, their optical near the bang edge follows the formula $(\alpha h\nu)^2 = A(h\nu E_g)$, where α, h, ν, A, and E_g were the absorption coefficient, Plank constant, light frequency, a constant and band gap energy, respectively. The band gap energies of β-Bi_2O_3, α-Bi_2O_3 and δ-Bi_2O_3 were estimated to be 2.36 eV, 2.41 eV and 2.78 eV, respectively, below to those were reported [17, 19], indicating the high absorption of Bi_2O_3 in wide visible light region and implying the higher photocatalytic activity under visible light irradiation.

Photoluminescence (PL) emission spectra can be obtained to study the separation of photogenerated electrons and holes in the semiconductor photocatalysts. Figure 9 shows the room temperature PL spectra of the Bi_2O_3 polymorphs with the excitation wavelength at 300 nm. We can observed that both α-Bi_2O_3 and δ-Bi_2O_3 show a strong broad emission peak around 460 nm [30], implying the high recombination rates of the photoinduced carries. However, β-Bi_2O_3 shows a rather

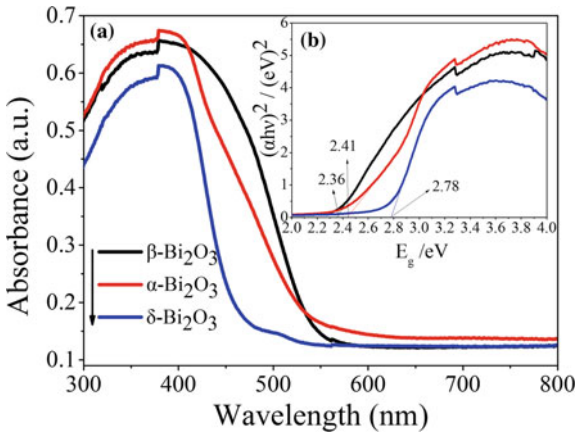

Fig. 8 **a** UV-vis absorption spectra of Bi_2O_3 photocatalysts recorded in diffuse reflectance spectra (DRS) and **b** Tauc plot of Bi_2O_3 photocatalysts

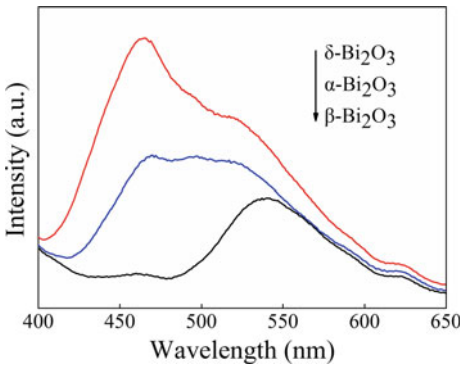

Fig. 9 PL spectra of the different Bi_2O_3 polymorphs (λ_{exc} = 300 nm)

Table 4 Decolorization rate of contrast experiments

Contrast experiment	Blank	Adsorption/desorption		
		β-Bi_2O_3	α-Bi_2O_3	δ-Bi_2O_3
Decolorization rate (%)	0.387	26.11	14.62	12.27

lower intensity, which means the high efficient separation rate of the carriers in β-Bi_2O_3 structure.

The decolorization rate of blank and adsorption-desorption to RB was listed in Table 4. The results demonstrated that the RB has a high stability under visible light, the photocatalysts have a certain absorption effect on the RB and the absorbility of the photocatalyts followed the order: β-Bi_2O_3 > δ-Bi_2O_3 > α-Bi_2O_3.

The removal of RB with Bi_2O_3 as photocatalyst irradiated by Xenop lamp were shown in Fig. 10a and c. It shows that after 240 min of irradiation, 95.4%, 97% and 99.23% of RB was photocatalytically degrade by the δ-Bi_2O_3, α-Bi_2O_3, and β-Bi_2O_3, respectively. Therefore, it's clear that the photocatalytic activities of β-Bi_2O_3 are higher than other phases, which was in consistent with what has been reported [16]. To further compare the catalytic activity of the α-Bi_2O_3, β-Bi_2O_3 and δ-Bi_2O_3, the pseudo-first order model was used to fit the experimentally obtained data. Since the initial concentration was low, the photocatalytic degradation of organic pollutants in water follows the pseudo-first order model given by Eq. (2) [31]:

$$\ln(C_0/C) = K_{app}t \tag{2}$$

where C_0 and C are the concentrations of RB in an aqueous solution at time 0 and t, respectively, and K_{app} was the pseudo-first order rate constant. The relation between $\ln(C_0/C)$ and irradiation time was plotted in Fig. 10b. The excellent fitness indicates that the photoreaction follows the way of first-order reaction kinetics. The K_{app} of the β-Bi_2O_3, α-Bi_2O_3 and δ-Bi_2O_3 were 0.02022 min^{-1}, 0.01614 min^{-1} and 0.01263 min^{-1}, respectively. A photocatalyst that can function for a long time would lead to significant reduction of cost. For this reason, the Bi_2O_3 were tested in

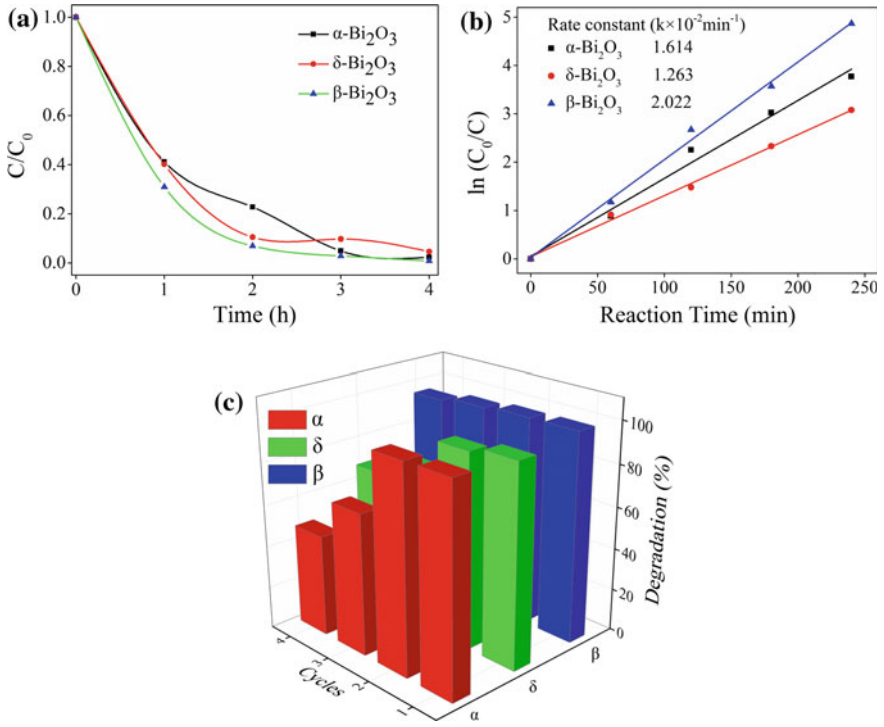

Fig. 10 **a** and **c** Removal of RB under visible light irradiation with Bi_2O_3. **b** Kinetic linear simulation curve of RB photocatalytic degradation by Bi_2O_3. **c** Cycling runs in the photocatalytic degradation of RB by Bi_2O_3

four runs for the degradation of RB under visible light irradiation. As shown in Fig. 10c, the photocatalytic activity of β-Bi_2O_3 did not obviously decrease after four successive cycles of degradation tests, indicating that the β-Bi_2O_3 was fairly stable under the studied conditions. On the basis of the results, the main reason may be discussed to explain the high photocatalytic activity of Bi_2O_3. The high photocativity of Bi_2O_3 can be ascribed to the Fe ions introduced between the conduction and valence band of Bi_2O_3, from which the electrons can be promoted to the conduction band [32, 33]. Fe doping increases the trapping sites while enhancing effective trapping sites for charge carriers [32–35].

Conclusions

Three different phases of Bi_2O_3 were synthesized via extraction-stripping-precipitation and post decomposition method. The microplates of β-Bi_2O_3 was obtained at a temperature of 300 °C of decomposition in the air. Decomposition at 500 and 730 °C were

obtained for the micaomesh of α-and δ-Bi_2O_3 in the air, respectively. The BET of β-, α-, and δ- Bi_2O_3 were 2.3496, 1.4783 and 0.5187 m^2/g, respectively. The band gaps of as-prepared samples were 2.36, 2.41, and 2.78 eV for β-Bi_2O_3, α-Bi_2O_3, and δ-Bi_2O_3, respectively. The photocatalytic experiments indicated that β-Bi_2O_3 displayed much higher photocatalytic performance and high stability than other phases and the photocatalytic activities of Bi_2O_3 polymorphs followed the order: β-Bi_2O_3 > α-Bi_2O_3 > δ-Bi_2O_3. After 240 min of irradiation, 95.4%, 97% and 99.23% of RB was photocatalytically degraded by the δ-Bi_2O_3, α-Bi_2O_3, and β-Bi_2O_3, respectively. These results indicated that the synthesized β-Bi_2O_3 photocatalyst was a potential candidate for environmental remediation processes.

Acknowledgements The authors would like to express sincere thanks to Department of Science and Technology of Hunan Province (2010SK2010) and the Nonferrous Foundation of the Hunan Province, China in supporting this research project (2010SK2010).

References

1. Kazuya N, Tsuyoshi O, Taketoshi M, Akira F (2012) Photoenergy conversion with TiO_2 photocatalysis: new materials and recent applications. Electrochim Acta 84(12):103–111
2. Akpan UG, Hameed BH (2009) Parameters affecting the photocatalytic degradation of dyes using TiO_2-based photocatalysts: a review. J Hazard Mater 170(2–3), 520–529
3. Adrián AV, Mehrdad K, Madjid M (2011) Composite template-free TiO_2 photocatalyst: synthesis, characteristics and photocatalytic activity. Appl Catal B Environ 104(1–2):127–135
4. Olim R, Mirabbos H, Claudia F, Ralf R (2017) Fabrication of lanthanum and nitrogen-co-doped $SrTiO_3$-TiO_2 heterostructured macroporous monolithic materials for photocatalytic degradation of organic dyes under visible light. J Alloy Compd 699:144–150
5. Seabra MP, Pires RR, Labrincha JA (2011) Ceramic tiles for photodegradation of orange II solutions. Chem Eng J 171(2), 692–702
6. Xiaobo Z, Shuai S, Guangli W, Caizhu L, Zhe Q, Xiangdong L, Jianguo Z (2017) Facile synthesis of the flower-like ternary heterostructure of Ag/ZnO encapsulating carbon spheres with enhanced photocatalytic performance. Appl Surf Sci 406:44–150
7. Qingzhi L, Xiaolian Y, Xiaoxiao Z, Desong W, Rong Y, Xueyan L, Jing A (2017) Facile preparation of well-dispersed ZnO/cyclized polyacrylonitrile nanocomposites with highly enhanced visible-light photocatalytic activity. Appl Catal B Environ 204:304–315
8. Wei Z, Nianqi L, Hongxing W, Lihao M (2017) Sacrificial template synthesis of core-shell $SrTiO_3$/TiO_2 heterostructured microspheres photocatalyst. Ceram Int 43(6):4807–4813
9. Ruiping H, Xin X, Shunheng T, Xiaoxi Z, Junmin N (2015) Synthesis of flower-like heterostructured β-Bi_2O_3/$Bi_2O_2CO_3$microspheres using $Bi_2O_2CO_3$ self-sacrifice precursor and its visible-light-induced photocatalytic degradation of o-phenylphenol. Appl Catal B Environ 163(vember), 510–519
10. Lisha Z, Wenzhong W, Jiong Y, Zhigang C, Wenqing Z, Lin Z, Shengwei L (2006) Sonochemical synthesis of nanocrystallite Bi_2O_3 as a visible-light-driven photocatalyst. Appl Catal A Gen 308(7):105–110
11. Yongfu Q, Minlin Y, Hongbo F, Yuanzhi Z, Youyuan S, Yongjun X, Xiaoxi Y, Shihe Y (2011) Nanowires of α-and β-Bi_2O_3: phase-selective synthesis and application in photocatalysis. Cryst Eng Comm 13(6):1843–1850

12. Ming-Sheng G, Wei-De Z (2012) A facile preparation strategy for hollow-structured Bi_2O_3/Bi_2WO_6 heterojunction with high visible light photocatalytic activity. J Phys Chem Solids 73 (11):1342–1349
13. Gujar TP, Shinde VR, Lokhande CD, Mane RS, Han SH (2005) Bismuth oxide thin films prepared by chemical bath deposition (CBD) method: annealing effect. Appl Surf Sci 250(1), 161–167
14. Yunhai Y, Zhaoxian Z, Xiaohua Z, Jianguo Z (2014) A controlled anion exchange strategy to synthesize core-shell β-bismuth oxidebismuth sulfide hollow heterostructures with enhanced visible-light photocatalytic activity. J Colloid Interf Sci 435(435C):91–98
15. Ya-Jing H, Yue-Qing Z, Hong-Lin Z, Jin-Jian W (2016) Hydrothermal synthesis of Bismuth (III) coordination polymer and its transformation to nano α -Bi_2O_3 for photocatalytic degradation. J Solid State Chem 239:274–281
16. Hicham O, Souad R, Fahd T, Al W, Khalaf JA, Ahmed O, Mouslim M, Mostafa A (2015) Synthesis, characterization and photocatalytic activity of α-Bi_2O_3nanoparticles. J Taibah Univ Sci 9(4):508–512
17. Yunhui Y, Zhaoxian Z, Yun C, Lili Q, Cuiping G, Jianguo Z (2014) Template-free fabrication of α-and β-Bi_2O_3 hollow spheres and their visible light photocatalytic activity for water purification. J Alloy Compd 605:102–108
18. Suiqi H, Jia L, Kailun Y, Jun L (2015) Fabrication of a β-Bi_2O_3/BiOI heterojunction and its efficient photocatalysis for organic dye removal. Chin J Catal 36(12):2119–2126
19. Deyi L, Yonggang Z, Yalei Z, Xuefei Z, Sujin G (2013) Fabrication of bidirectionally doped β-Bi_2O_3/TiO_2-NTs with enhanced photocatalysis under visible light irradiation. J Hazard Mater 258–259(258–259C), 42–49
20. Guo L, Shuai L, Yuanyuan L, Jing Z, Zhaochi F, Can L (2016) Controllable synthesis of α-Bi_2O_3 and γ-Bi_2O_3 with high photocatalytic activity by α-Bi_2O_3 → γ-Bi_2O_3 → α-Bi_2O_3 transformation in a facile precipitation method. J Alloy Compd 689:787–799
21. Zuoshan W, Shala B, Yingpeng W, Pengjie H, Min Z (2017) Optical properties of a new $Bi_{38}Mo_7O_{78}$ semiconductor with fluorite-type α-Bi_2O_3 structure. Appl Surf Sci 399(31):506–514
22. Fenghua D, Jing Z, Zhijian W, Liyuan C, Chuanfu Z (2016) Simultaneous leaching of low grade bismuthinite and pyrolusite ores in hydrochloric acid medium. Hydrometallurgy 166:279–284
23. Zhi-jian W, Feng-hua D, Jing Z, Chuan-fu Z (2016) Solvent extraction mechanism and precipitation stripping of bismuth (III) in hydrochloric acid medium by tributyl phosphate. J Cent South Univ 23(12):3085–3091
24. Hezam A, Namratha K, Drmosh QA, Yamani ZH, Byrappa K (2017) Synthesis of heterostructured Bi_2O_3-CeO_2-ZnO photocatalyst with enhanced sunlight photocatalytic activity. Ceram Int 43(6), 5292–5301
25. Faisal M, Khan SB, Rahman MM, Jamal A, Akhtar K, Abdullah MM (2011) Role of ZnO-CeO_2 nanostructures as a photo-catalyst and chemi-sensor. J Mater Sci Technol 27(7), 594–600
26. Aslam M, Soomro MT, Ismail IM, Qari HA, Gondal MA, Hameed A (2015) The facile synthesis, characterization and evaluation of photocatalytic activity of bimetallic $FeBiO_3$ in natural sunlight exposure. RSC Adv 5(124), 102663–102673
27. I. A, Simona C, Dorina R, (2008) EPR and FT-IR spectroscopic studies of Bi_2O_3-B_2O_3-CuO glasses. Phys. B 19–20(403), 3682–3685
28. Jianzhang L, Junbo Z, Xiyang H, Shengtian H, Jun Z, Jinjin H, Wangling S (2013) Enhanced photocatalytic activity of Fe_2O_3 decorated Bi_2O_3. Appl Surf Sci 284(11):527–532
29. Zhou S, Xuelin D, Nan W, Linhua Z, Zhihong L, Jindong F, Caihua X (2017) Efficient photocatalytic defluorination of perfluorooctanoic acid over BiOCl nanosheets via a hole direct oxidation mechanism. Chem Eng J 317(1):925–934
30. Hefeng C, Baibiao H, Jibao L, Zeyan W, Binxin X, Xiaoyan Q, Xiaoyang Z, Ying D (2010) Synergistic effect of crystal and electronic structures on the visible-light-driven photocatalytic performances of Bi_2O_3 polymorphs. Phys Chem Chem Phys 12(47):15468–15475

31. Xiaogang G, Xueming L, Wulin L, Daixiong Z, Zhongshu X (2015) Cathodic electrophoretic deposition of bismuth oxide (Bi_2O_3) coatings and their photocatalytic activities. Appl Surf Sci 331:455–462
32. Tina H, Majid M (2014) Fe^{3+}:Ag/TiO_2 nanocomposite: synthesis, characterization and photocatalytic activity under UV and visible light irradiation. Appl Catal A Gen 473(5):104–115
33. Lu L, Huiyao W, Wenbin J, Ahmed R M, Pei X (2017) Comparison study on photocatalytic oxidation of pharmaceuticals by TiO_2-Fe and TiO_2-reduced graphene oxide nanocomposites immobilized on optical fibers. J Hazard Mater 333, 162–168
34. Yong G, Meng H, Baoxia M (2014) Membrane surface modification with TiO_2-graphene oxide for enhanced photocatalytic performance. J Membr Sci 455(4):349–356
35. Wang XH, Li JG, Kamiyama H, Moriyoshi Y, Ishigaki T (2006) Wavelength-sensitive photocatalytic degradation of methyl orange in aqueous suspension over Iron(III)-doped TiO_2 nanopowders under UV and visible light irradiation. J Phys Chem B 110(13), 6804–6809

Energy Conservation in Sintering Ignition Process Based on Comprehensive Ignition Intensity

Wen Pan, Xia Zhao, Si-bin Zhang, Jun-hua Zhao, Huai-ying Ma and Zhi-xing Zhao

Abstract Ignition is the start point of the sintering circuit, which plays an important role during the whole sintering process. The gas consumption accounts for 80% energy cost in the sintering ignition process. Therefore, gas flow reduction is of great significance to energy conservation in the sintering ignition process. In current study, the concept of comprehensive ignition intensity (CII) was introduced to determine the ignition effect. The experimental results indicate that the value of CII increases with higher air-fuel ratio at gas flow of 550 and 600 Nm^3/h. From another point of view, given constant CII value, lower gas flow can be achieved with higher air-fuel ratio. Based on the comprehensive ignition intensity, the ignition parameters were optimized and the gas flow was subsequently reduced. By increasing the air-fuel from 5.5 to 6.6, the gas flow is reduced from 450 Nm^3/h (8.1 GJ/h) to around 350 Nm^3/h (6.3 GJ/h).

Keywords Ignition parameters · Air-fuel ratio · Gas flow
Comprehensive ignition intensity

Introduction

Ignition process is a connecting link between the preceding and the following processes of the iron ore agglomeration circuit, which has great influence on the quality of iron ore sinter, the permeability of sinter layer, the return fine ratio, etc. [1].

W. Pan (✉) · H. Ma · Z. Zhao
Research Institute of Technology Shougang Group Co., LTD, Beijing 100043, China
e-mail: panwen@shougang.com.cn

X. Zhao
Shougang Institute of Technology, Beijing 100041, China

S. Zhang
Chief Engineer Office Shougang Group Co., LTD, Beijing 100043, China

J. Zhao
Beijing Shougang Co., LTD, Qian'an 064400, China

Z. Sun et al. (eds.), *Energy Technology 2018*, The Minerals, Metals & Materials Series, https://doi.org/10.1007/978-3-319-72362-4_17

The fuel consumption is affected by the ignition process as well. For the past few years, a large amount of research work has been conducted on the sintering ignition process [2]. Structural design of the ignition furnace [3–5], ignition fuel selection [6, 7], and the ignition parameters optimization [8, 9], etc. are included in the above research. The ignition parameters involve fuel flow, air flow, air-fuel ration and so on. Currently, the ignition parameters are adjusted or optimized based on the temperature within the ignition furnace which measured by several thermocouples installed in the ignition furnace. In current study, the concept of comprehensive ignition intensity (CII) was introduced based on the heat perception of the sintering layer. The comprehensive ignition intensity can be used to determine the ignition effect. Along with the research result on the combustion characteristic of the solid fuel in sinter mixture, the ignition parameters were optimized and the gas flow was subsequently reduced.

Experimental Procedure

The temperature of burden surface in the sintering ignition furnace was recorded continuously as shown in Fig. 1. Based on the temperature curve, the absolute ignition intensity of high temperature, the absolute ignition intensity of medium temperature, the comprehensive ignition intensity of high temperature and the comprehensive ignition intensity of medium temperature are defined in Eqs. (1)–(4), respectively. Where, AII_1 is the absolute ignition intensity of high temperature (°C.Sec), AII_2 is the absolute ignition intensity of medium temperature (°C.Sec), CII_1 is the comprehensive ignition intensity of high temperature (°C.m), CII_2 is the comprehensive ignition intensity of medium temperature (°C.m), T is the temperature of burden surface (°C), t is the amount of time the burden spends in the ignition furnace (sec), t1 is the intersection point between the high temperature base line and the upward section of the temperature curve (sec), t2 is the intersection point between the high temperature base line and the downward section of the temperature curve (sec), t3 is the intersection point between the medium temperature base line and the upward section of the temperature curve (sec), t4 is the intersection point between the medium temperature base line and the downward section of the temperature curve (sec), V is the speed of sinter machine (m/sec).The complete combustion temperature of the solid fuel in sinter mixture is defined as the high temperature base line. The temperature at which the solid fuel begins to decompose is defined as the medium temperature base line.

$$AII_1 = \int_{t1}^{t2} T(t) \times dt \tag{1}$$

$$AII_2 = \int_{t3}^{t4} T(t) \times dt - \int_{t1}^{t2} T(t) \times dt \tag{2}$$

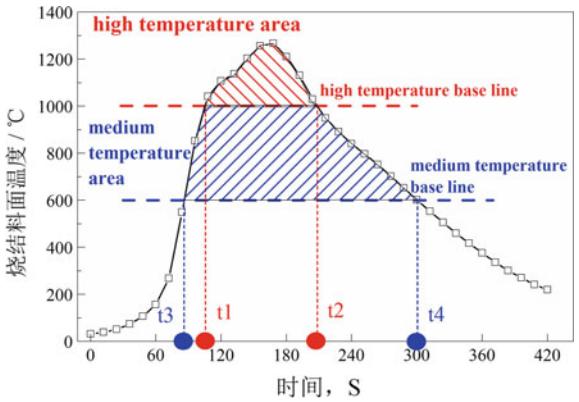

Fig. 1 Temperature curve of burden surface in the sintering ignition furnace

$$CII_1 = \frac{V \times \int_{t1}^{t2} T(t) \times dt}{60} \tag{3}$$

$$CII_2 = \frac{V \times \left(\int_{t3}^{t4} T(t) \times dt - \int_{t1}^{t2} T(t) \times dt \right)}{60} \tag{4}$$

To investigate the optimal ignition parameters, a series of experiments were conducted in the ignition furnace of Shougang, as shown in Table 1.

Table 1 Experimental conditions of current study

No.	Gas flow/(Nm^3/h)	Air flow/(Nm^3/h)	Air-fuel ratio/-
0	600	3300	5.5
1	600	3600	6.0
2	600	3900	6.5
3	600	4200	7.0
4	600	4500	7.5
5	550	3025	5.5
6	550	3300	6.0
7	550	3575	6.5
8	550	3850	7.0
9	550	4125	7.5
10	520	3900	7.5

Combustion Characteristics of the Solid Fuel in Sinter Mixture

The combustion characteristics were analyzed by using thermogravimetric analysis under oxygen partial pressure of 16.5% and 21% respectively, as shown in Figs. 2 and 3. The solid fuel begins to decompose at temperature around 620 °C. At 720 °C, the weight loss rate reaches its peak. The combustion of solid fuel completes at around 920 °C . Based on this, the high temperature and medium temperature base line in Fig. 1 are 920 °C and 620 °C respectively.

By comparison, the initial temperature of combustion decreases from 625 to 601 °C with higher oxygen partial pressure. Meanwhile, higher oxygen partial pressure may lead to better burning effect of the solid fuel. The total mass loss after combustion increases from 73.71 to 82.44% with higher oxygen partial pressure. So, it can be inferred that the combustion process of the solid fuel in the ignition furnace can be improved by increasing the air-fuel ratio to get higher oxygen partial pressure within the ignition furnace.

Experimental Results

The ignition and sintering parameters are listed in Table 2, in which mean temperature is the average temperature measured by the thermocouples within the ignition furnace. Figure 4 shows the maximum temperature of the burden surface under the ignition furnace at air-fuel ratio of 5.5–7.5 and gas flow of 550 Nm^3/h and 600 Nm^3/h, respectively. It can be seen that, at the same air-fuel ratio, the maximum temperature of burden surface increases by around 60 °C with higher gas flow. While at the same gas flow, there appears to be a slight decline with the maximum temperature of burden surface at higher air-fuel ratio. Figures 5 and 6 show the time duration at high and medium temperature at air-fuel ratio of 5.5–7.5 and gas flow of

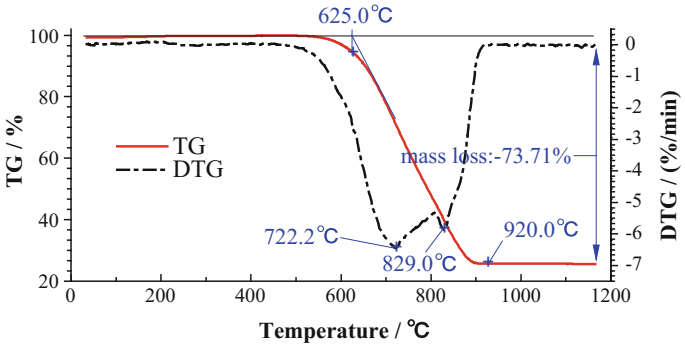

Fig. 2 TG and DTG curves of the solid fuel under oxygen partial pressure of 16.5%

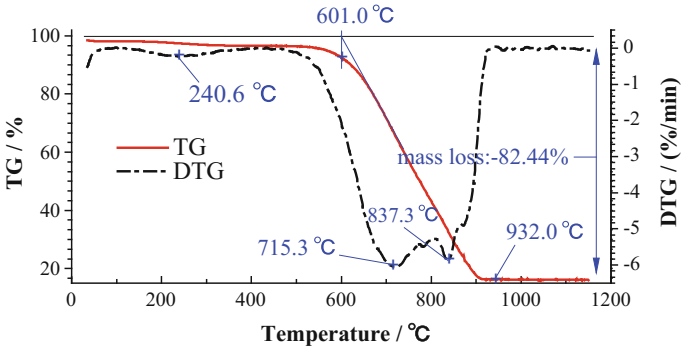

Fig. 3 TG and DTG curves of the solid fuel under oxygen partial pressure of 21%

550 Nm^3/h and 600Nm^3/h, respectively. At the same air-fuel ratio, the time duration at high temperature and medium temperature both increase with higher gas flow. With the gas flow being kept constant, the time duration at high temperature and medium temperature increase with high air-fuel ratio as well.

According to Eqs. (3) and (4), the comprehensive ignition intensity of high temperature (CII_1) and medium temperature (CII_2) are calculated, as shown in Figs. 7 and 8, respectively. Similar to maximum temperature and time duration of high, medium temperature, the comprehensive ignition intensity of high temperature and medium temperature increase with higher gas flow at the same air-fuel ratio. With constant gas flow, CII_1 and CII_2 increase linearly with higher air-fuel ratio.

Table 2 Ignition and sintering parameters

No.	Mean temperature/ °C	Pressure within ignition furnace/Pa	Air flow/ (m^3/h)	Gas flow/ (m3/h)	Velocity of sinter machine/(m/min)	Actual air-fuel ratio/-
0	1062.43	−8.83	3400.00	610.20	0.80	5.60
1	1067.59	−8.42	3607.15	606.05	0.80	6.00
2	1118.27	−8.21	3938.05	604.85	0.80	6.50
3	1084.39	−8.70	4348.95	608.00	0.78	7.15
4	1119.99	−7.88	4542.80	607.35	0.82	7.45
5	981.38	−9.40	2984.05	559.65	0.78	5.35
6	1024.36	−8.66	3319.40	556.80	0.67	6.00
7	995.25	−8.66	3624.25	558.55	0.71	6.45
8	1048.84	−8.30	3937.80	557.25	0.80	7.05
9	1067.51	−8.44	4210.10	554.80	0.78	7.60
10	1020.57	−8.30	3894.20	516.10	0.75	7.55

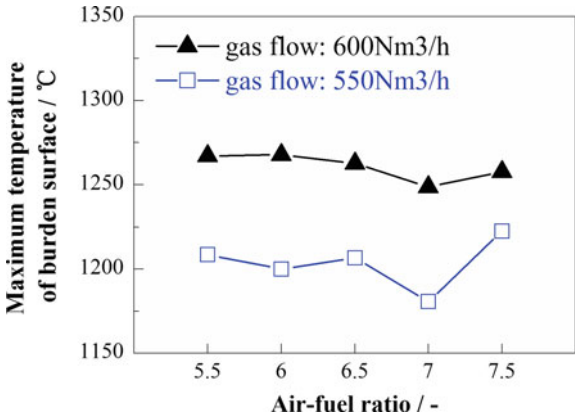

Fig. 4 Maximum temperature of burden surface at various air-fuel ratio and gas flow

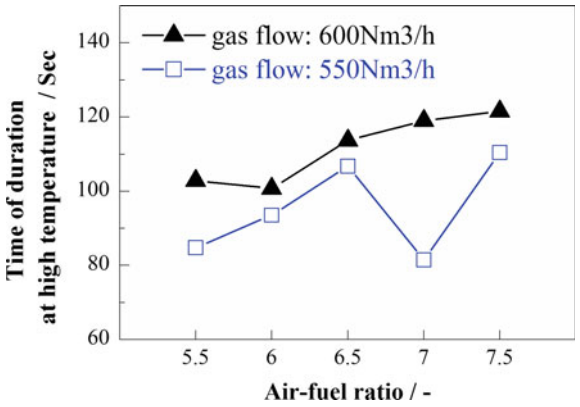

Fig. 5 Time of duration at high temperature

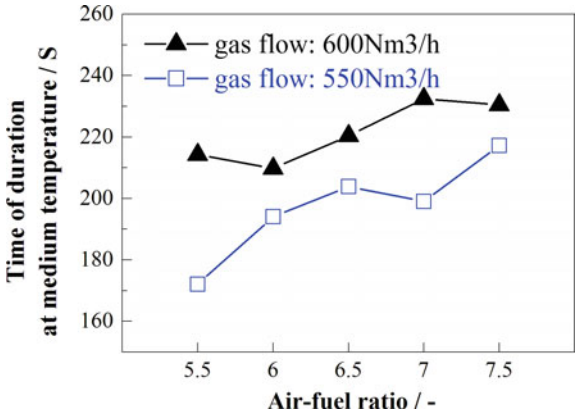

Fig. 6 Time of duration at medium temperature

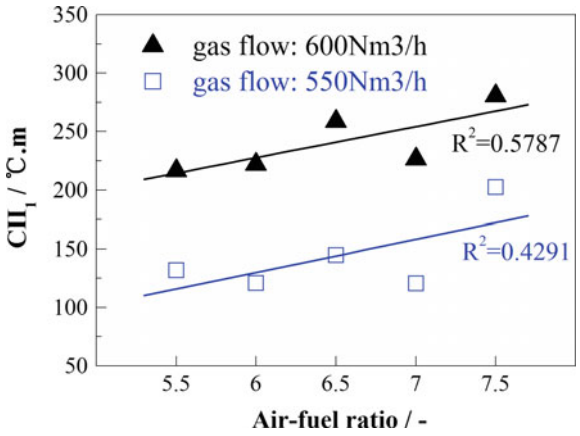

Fig. 7 Comprehensive ignition intensity of high temperature (CII_1) at various air-fuel ratio and gas flow

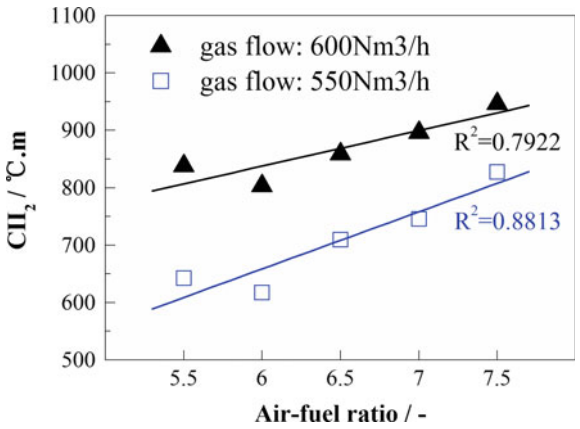

Fig. 8 Comprehensive ignition intensity of medium temperature (CII_2) at various air-fuel ratio and gas flow

From another point of view, better combustion effect and lower gas consumption may both be achieved by increasing the air-fuel ratio to some extent. But the gas consumption cannot decrease unlimitedly even at high air-fuel ration, as shown in Figs. 9 and 10. When the air-fuel ratio increases from 5.5 to 7.5, gas flow decreases from 600 to 550 Nm^3/h, similar comprehensive ignition intensity of high temperature and medium temperature can be achieved with air-fuel ratio at 5.5 and gas flow at 600 Nm^3/h. With the gas flow further decreasing to 520 Nm^3/h, the combustion effect deteriorates dramatically even at air-fuel ratio of 7.5. The comprehensive ignition intensity of high temperature drops to only a quarter of the value at air-fuel of 5.5, gas flow of 600 Nm^3/h.

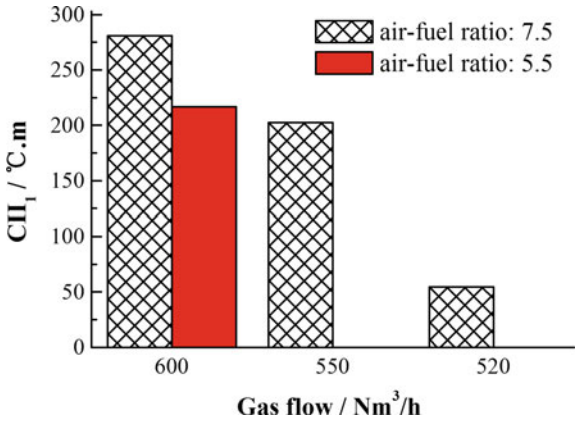

Fig. 9 Comprehensive ignition intensity of high temperature (CII_1) at air-fuel ratio of 5.5 and 7.5

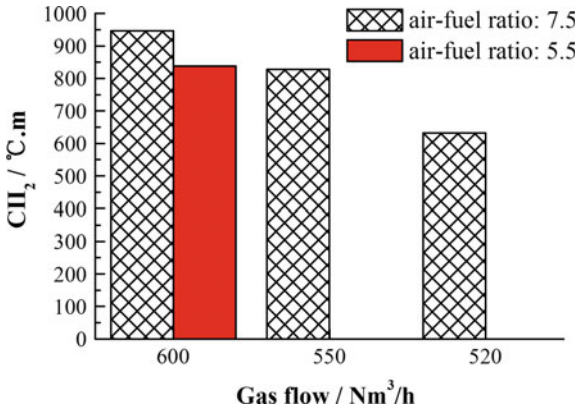

Fig. 10 Comprehensive ignition intensity of medium temperature (CII_2) at air-fuel ratio of 5.5 and 7.5

Industrial Test

Based on the above experimental research results, industrial test on adjusting ignition parameters was conducted. Figure 11 shows the gas flow at air-fuel ratio of 5.5 and 6.6 in the sintering ignition furnace of Shougang. By increasing the air-fuel from 5.5 to 6.6, the gas flow is reduced from 450 Nm^3/h (8.1 GJ/h) to around 350 Nm^3/h (6.3 GJ/h).

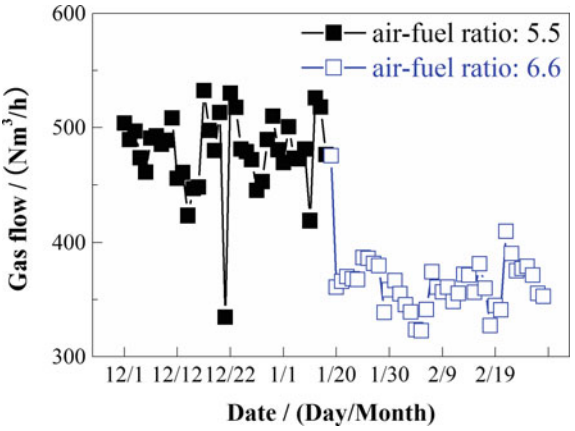

Fig. 11 Industrial test result

Conclusions

(1) Based on the combustion characteristics analysis results of the solid fuel in the sinter mixture, the combustion process of the solid fuel can be improved by increasing the air-fuel ratio to some extent to increase the oxygen partial pressure in the ignition furnace.
(2) The temperature curve of the burden surface within the ignition furnace was recorded continuously. Derived from the above temperature curve, the concept of comprehensive ignition intensity was introduced in current study, with which the combustion effect could be quantificationally measured.
(3) The comprehensive ignition intensity of high temperature and medium temperature at various air-fuel ratio and gas flow have been tested. The results showed that the comprehensive ignition intensity of high temperature and medium temperature were positively correlated with air-fuel ratio in the range of 5.5 to 7.5. In other words, the gas consumption can be reduced by increasing the air-fuel ratio to some extent.
(4) According to the above fundamental research results, industrial test was conducted in the ignition furnace of Shougang. By increasing the air-fuel from 5.5 to 6.6, the gas flow is reduced from 450 Nm^3/h (8.1 GJ/h) to around 350 Nm^3/h (6.3 GJ/h).

References

1. Haoyu Z, Zhiqing D, Fei Z (2011) Measures for improving side ignition quality and their effect. Sinter Pellet 36(5):19–33
2. Dajun J, Muguang H (2014) Technology advancement and practices on save ignition energy consumption of ore sintering. Energy Metall Ind 33(1):10–13

3. Senqi H, Wang Y, Zhu F, Ning D (2014) Technology advancement and practices on save ignition energy consumption of ore sintering. Energy Metall Ind 33(1):10–13
4. Xia Dehong W, Jie GY, Bencang T (2014) Development and application of focusing and radiating sinter igniter. Energy Metall Ind 21(2):11–13
5. Yujie C (2003) Design and application of ignition in sintering machine. Ind Furn 25(1):38–40
6. Wenhui L, Wenbo Z (2015) Application technology discussion of BFG ignition furnace. Ind Furn 37(1):36–38
7. Xia Dehong W, Jie ZY (2002) The application of coal-water slurry in the igniter of sintering machine. Energy Metall Ind 21(3):40–43
8. Guanhua Q, Jing S, Dechun Y (2013) Control of sinter ignition and its application. Ind Control Appl 32(10):8–10
9. Xiaohong Y, Guoxin Z, Chunna Z (2012) Optimal control algorithm of burn through point temperature and ignition intensity for sintering system. Sinter Pellet 37(5):12–15

Part II
Deriving Value from Challenging Waste Streams: Recycling and Sustainability Joint Session

Behavior of Co, Ni and Precious Metals in Copper Converting Process: Experimental Study

Keiran Holland, Dmitry Sukhomlinov, Ville Naakka, Ari Jokilaakso and Pekka Taskinen

Abstract This study is focused on distribution of Co, Ni, Ag, Au, and Pd between molten copper and molten copper sulfide ('white metal') phases in copper converting conditions. The behavior of the elements selected was studied experimentally at 1300 °C and at various sulfur dioxide partial pressures (0.01, 0.05, 0.1, 0.5, and 1 atm). The experimental technique employed involves a high temperature equilibration followed by rapid quenching in ice water, with subsequent quantitative elemental analysis of the equilibrium phases with an electron micro probe analyzer. The distribution coefficients $L_{Me}^{Cu/wm}$ determined in this work can be arranged in the following sequence: Co < Ag < Ni < (Au, Pd).

Keywords Distribution · Trace elements · White metal · Matte

Introduction

Conventional copper converting process is conducted in Peirce-Smith converters, where crude 'blister' copper is produced from copper-iron-sulfur melt ('matte'). In this batch process, iron is oxidized by oxygen-enriched air blowing and reacts with silica flux forming slag phase. Slag is skimmed when remaining iron concentration in matte has been reduced to less than one weight percent. The molten phase produced is mainly comprised of copper and sulfur ('white metal') and it is further processed by blowing oxygen-enriched air to oxidize the remaining sulfur and to make blister copper [1].

K. Holland · D. Sukhomlinov (✉) · A. Jokilaakso · P. Taskinen
Department of Chemical and Metallurgical Engineering, Aalto University, Espoo, Finland
e-mail: dmitry.sukhomlinov@aalto.fi

V. Naakka
Boliden Harjavalta Oy, Harjavalta, Finland

Z. Sun et al. (eds.), *Energy Technology 2018*, The Minerals, Metals & Materials Series, https://doi.org/10.1007/978-3-319-72362-4_18

Copper concentrates as well as secondary copper bearing scraps contain a wide range of impurities. These impurities dissolve and distribute between immiscible liquids formed in the processing. Behavior of cobalt, nickel and precious metals in the copper converting conditions has been investigated in several previous fundamental studies and their distribution coefficients between molten copper and white metal phases have been measured at various temperatures and gas atmospheres. However, data are in some degree inconsistent and scarce for some elements.

Distribution coefficient of nickel ($L_{Ni}^{Cu/wm}$) was measured by Asano at 1200 °C by equilibrating the sample in an evacuated fused silica ampoule to be 3.059 [2]. Another study suggests a temperature correlation with $L_{Ni}^{Cu/wm}$ derived from experimental data, $L_{Ni}^{Cu/wm} = 7.296 - 0.0035T/^{\circ}C$ (1150 to 1250 °C) [3]. In addition, the effect of sulfur dioxide partial pressure on $L_{Ni}^{Cu/wm}$ was investigated by Kashima et al. [4] and Yazawa [5] and it was found to be insignificant. Cobalt distributes rather evenly between copper and white metal phases. The distribution coefficient ($L_{Co}^{Cu/wm}$) was reported to be nearly independent of sulfur dioxide partial pressure [4, 5]. Its value was reported to be 1.124 [2] at 1200 °C, and between 1.03 [4]–1.14 [5] at 1300 °C.

Among the precious metals selected, distribution of silver is the most studied one, while data concerning gold and palladium are rather scarce. The distribution coefficient of silver between copper and white metal ($L_{Ag}^{Cu/wm}$) was measured in previous studies [6–9] from 1127 to 1250 °C to be in the range from 2.17 to 2.93. In addition, $L_{Ag}^{Cu/wm}$ was investigated at 1200 °C as a function of sulfur dioxide partial pressure and a gradual rise from 2.8 to 3.6 was reported in the range of 0.7–20 kPa by Kashima et al. [4]. Schlitt and Richards reported $L_{Au}^{Cu/wm}$ determined at 1200 °C in a protective atmosphere of N_2 to be 125 [7], while Asano measured a higher value 171.5 at the same temperature [9]. Sinha et al. measured distribution coefficient of gold at 1127 and 1227 °C to be 102 and 127, respectively [8]. Data concerning palladium distribution are particularly scarce. $L_{Pd}^{Cu/wm}$ was reported to be 166.67 at 1200 °C [7], measured in a protective atmosphere of N_2. Burylev et al. experimentally measured $L_{Pd}^{Cu/wm}$ at 1150 and 1300 °C to be 94 and 62, respectively [10].

Consequently, the aim of this study was to determine the distribution coefficients of Co, Ni, Ag, Au, and Pd between molten copper and white metal phases at 1300 °C as a function of sulfur dioxide partial pressure, applying a reliable and well-established experimental technique [11–13]. Such fundamental data show a potential to improve recovery of the metals selected as by-products in the copper converting process.

Experimental

Distribution of the selected trace elements between molten copper and molten copper sulfide ('white metal') phases was studied experimentally by applying equilibration and quenching technique, followed by electron probe micro analyzer (EPMA) employed for elemental analysis of the equilibrium phases.

A master alloy comprised of 1 wt% of Co, Ni, Ag, Au, Pd, 0.25 wt% Fe (to mimic real converting process) and 94.75 wt% Cu was synthesized from pure metals (Table 1). The weighed amounts of the metals were sealed in a fused silica ampoule flushed with Ar gas (99.999 vol.%, AGA, Finland) and evacuated to $3 \cdot 10^{-5}$ atm. The ampoule was heat-treated for 120 h at 1200 °C and quenched in ice water. The sample produced was analyzed with a LEO 1450 (Carl Zeiss Microscopy GmbH, Jena, Germany) scanning electron microscope (SEM) coupled to an Oxford Instruments X-Max 50 mm^2 energy dispersive spectrometer (EDS) (Abingdon, Oxfordshire, UK) and its homogeneous composition was confirmed.

The synthesized master alloy and pure copper sulfide (Cu_2S) were utilized as starting materials mixed in the equal mass fractions and pressed into a pellet. The mass of the pellet was about 0.2 g. Flat-bottomed calcia-stabilized zirconia (CSZ) crucibles (10–12 mm in diameter) were cut along the axis and produced halves were utilized as an inert container for equilibration of the pellets. Such a shape of the container improves exposure of the sample to the gas phase during the equilibration. The CSZ crucible with the sample inside (Fig. 1a) was put into a basket made of a platinum wire (0.5 mm diameter, Johnson Matthey, UK). The basket was introduced into the alumina working tube of the furnace from below with a platinum suspension wire.

A Lenton vertical resistance furnace (PTF 15/–/450) with a gas-impermeable alumina work tube (38/45/1100 mm, Friatec) was employed for the equilibration experiments (Fig. 1b). Eurotherm PID controllers 3216 were employed for temperature control. The experimental temperature was measured with a calibrated S-type Pt/Pt-10%Rh thermocouple (Johnson Matthey, UK) right next to the sample during the entire equilibration (accuracy of ±2 °C). The thermocouple was connected to a multimeter (Keithley 2010 DMM, USA). A Pt100 resistance

Table 1 Chemicals utilized in the study, their purity and suppliers

Chemical	Purity, wt%	Supplier
Co	99.99	Koch-Light Laboratories (UK)
Ni	99.996	Alfa Aesar (Germany)
Ag	99.99	Alfa Aesar (Germany)
Au	99.95	Alfa Aesar (Germany)
Pd	99.9	Alfa Aesar (Germany)
Fe	99.99	Alfa Aesar (Germany)
Cu	99.999	Alfa Aesar (Germany)

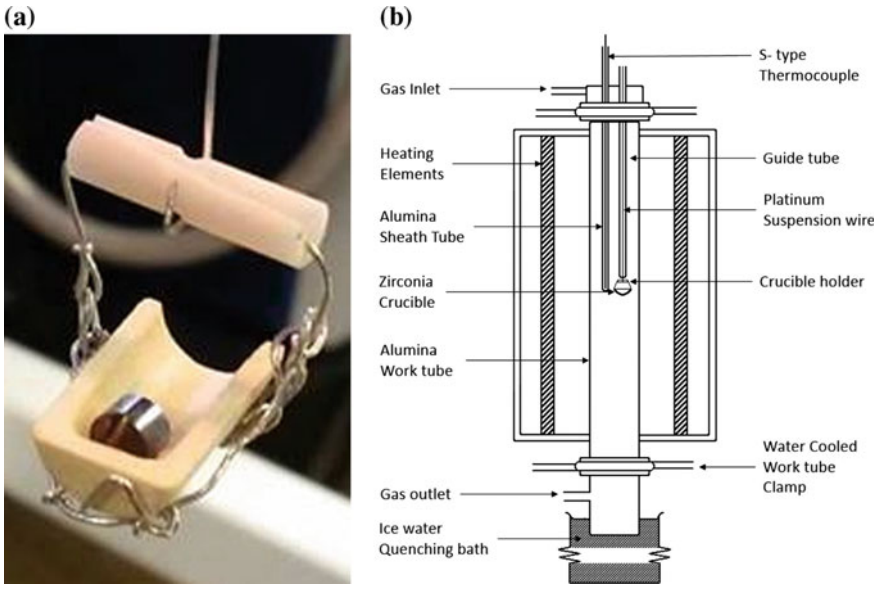

Fig. 1 **a** The CSZ crucible with the sample inside and **b** the schematics of the experimental setup

thermometer (SKS-Group, Finland) connected to a multimeter (Keithley 2000 DMM, USA) performed the cold junction compensation.

The sulfur dioxide partial pressure was fixed by mixtures of SO_2 (99.98 vol.%) and Ar (99.999 vol.%) both supplied by AGA (Finland). The gas flowrates were controlled with Alborg DFC26 mass-flow controllers (USA). The total flow rate was 300 ml/min.

The experiments were conducted at 1300 °C and sulfur dioxide partial pressures were controlled to 0.01, 0.05, 0.1, 0.5, and 1 atm. The necessary and sufficient equilibration time was found in a series of preliminary experiments to be 16 h. After equilibration, the samples were rapidly quenched in ice water. The small sample size facilitated a rapid quenching rate. The quenched samples were dried at room temperature and mounted in EpoFix epoxy resin (Struers, Denmark). Metallographic methods of wet grinding and polishing were applied to prepare cross-sections. After carbon coating, the polished sections were examined with Cameca SX100 microprobe (Cameca SAS, France) EPMA equipped with five wavelength dispersive spectrometers (WDS). The number of identical measurements per phase was eight. The PAP matrix correction procedure [14] was applied for the raw data. The beam diameter employed was varying from 20 to 100 µm. The accelerating voltage employed was 20 kV and beam current was 60 nA. Table 2 shows EMPA detection limits for every element analyzed.

Table 2 EPMA detection limits

Phase	Detection limit, ppm								
	Cu	S	O	Fe	Co	Ni	Pd	Ag	Au
Copper metal	347	147	1061	176	178	260	171	355	553
White metal	335	147	1248	182	187	257	171	347	534

Results and Discussion

A micrograph presented in Fig. 2 shows a typical microstructure of the quenched samples. It was comprised of CSZ crucible with multiple cracks occurring in quenching due to the thermal shock, copper metal and white metal phases.

The distribution of a solute element Me between molten copper and white metal phases can be described by the following equilibrium reaction [4]:

$$\mathrm{Me} + [\mathrm{Cu_2S}] = \mathrm{MeS} + (2\mathrm{Cu}), \tag{1}$$

where () and [] refer to the copper metal and white metal phases, respectively.

The distribution coefficient of the solute elements between copper metal and white metal phases was defined with Eq. (2):

$$\mathrm{L}_{\mathrm{Me}}^{\mathrm{Cu/wm}} = \frac{(\mathrm{wt\%Me})}{[\mathrm{wt\%Me}]}. \tag{2}$$

The uncertainty of the distribution coefficients measured in the study was calculated as:

$$\frac{\mathrm{L_{Me}}}{\mathrm{L_{Me}}} = \left(\frac{\Delta \mathrm{wt\%Me}}{\mathrm{wt\%Me}}\right) + \left[\frac{\Delta \mathrm{wt\%Me}}{\mathrm{wt\%Me}}\right], \tag{3}$$

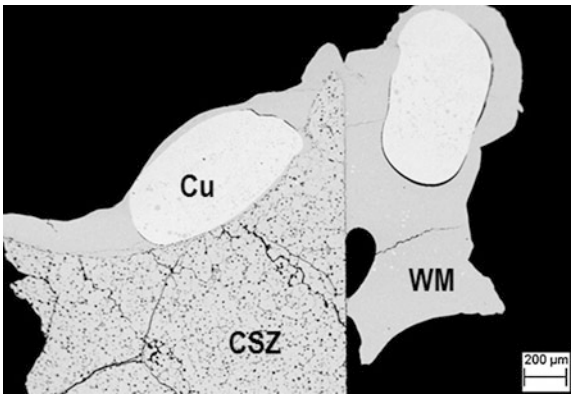

Fig. 2 A typical microstructure of the quenched samples: CSZ is the crucible, Cu is the copper alloy phase, and WM is the white metal phase

where wt%Me and Δwt%Me stand for the average concentration of Me in the phase and the standard deviation, respectively.

The distribution coefficients of Ni, Co and Ag determined at 1300 °C as a function of sulfur dioxide partial pressure (P_{SO2}) in the present work are depicted in Fig. 3. An explicit dependence between $L_{Co}^{Cu/wm}$ and P_{SO2} can be seen. $L_{Co}^{Cu/wm}$ decreases from 0.87 to 0.22 with increasing P_{SO2}, within the range studied. These findings contradict to the previous reports [4, 5], which claimed that $L_{Co}^{Cu/wm}$ is nearly independent of P_{SO2}, probably due to lower accuracy of the analytical measurements in the previous studies. However, $L_{Co}^{Cu/wm}$ values measured at the lower SO_2 partial pressures are close to those reported previously [2, 4, 5]. The similar trend of $L_{Ni}^{Cu/wm}$ can be noticed. Its value decreases from 2.64 to 1.57 within the P_{SO2} range studied, but in the previous reports [4, 5] it was stated that $L_{Ni}^{Cu/wm}$ dependence of P_{SO2} is negligible, as in the case of Co. Nevertheless, the values reported previously [2–5] are in a good agreement with those measured in the present work at the lower P_{SO2} side.

The distribution coefficient of silver ($L_{Ag}^{Cu/wm}$) seems to be practically independent of P_{SO2} and its value is about 1.35 at 1300 °C throughout the P_{SO2} range studied (Fig. 3). In the previous studies $L_{Ag}^{Cu/wm}$ was measured at lower temperatures, from 1127 to 1250 °C and higher values were reported [6–9], what is reasonable. However, a gradual rise of $L_{Ag}^{Cu/wm}$ at 1200 °C was reported in the P_{SO2} range of 0.7–20 kPa [4], which was not observed at 1300 °C in the present work.

The detection limits of EPMA were insufficient to analyze the equilibrium concentrations of Au and Pd dissolved in the white metal phase reliably. These precious metals mostly distribute into the copper alloy phase. Therefore, their distribution coefficients between copper and white metal phases were roughly estimated based on their equilibrium concentrations in the metal phase and the respective detection limits of EPMA for the white metal phase. The distribution coefficient of palladium is higher than 50, while the distribution coefficient of gold

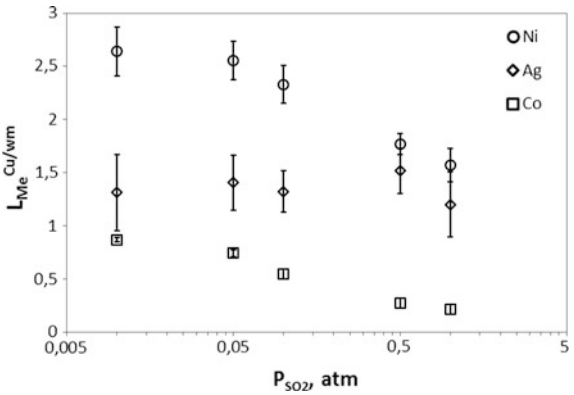

Fig. 3 The distribution coefficients of Ni, Co and Ag between copper and white metal phases at 1300 °C as a function of partial pressure of SO_2

is higher than 15. Probably, these values are highly underestimated, but an analytical technique that is more sensitive than EPMA is essential for the accurate evaluation.

Conclusions

High temperature equilibration followed by rapid quenching in ice water with subsequent quantitative elemental analysis of the equilibrium phases was employed to determine the distribution coefficients between the copper metal and white metal phases of the solute metals of interest. The equilibration experiments were conducted at 1300 °C within the P_{SO2} range from 0.01 to 1 atm. The distribution coefficients of the solute metals between copper and white metal $L_{Me}^{Cu/wm}$ measured in the present work can be arranged in the following sequence: Co < Ag < Ni < (Au, Pd). However, the distribution of Au and Pd was only roughly estimated, due to difficulties in the analytical technique applied to detect the low concentrations in the white metal phase.

The correlations between $L_{Me}^{Cu/wm}$ and P_{SO2} were determined. Ni and Co distribute more to the copper metal phase at lower partial pressures of sulfur dioxide, while the behavior of Ag at 1300 °C seems to be essentially independent of P_{SO2}.

Acknowledgements The present research work was conducted as a part of an EIT-Raw Materials upscaling project. Geological Survey of Finland (GTK) and particularly Mr. Lassi Pakkanen are acknowledged for conducting the EPMA analysis.

References

1. Schlesinger ME, King MJ, Sole KC, Davenport WGI (2011) Extractive metallurgy of copper, 5th edn. Elsevier, Oxford
2. Asano N. (1965) Showa 40 years mining relations association joint autumn meeting (Kyoto) subcommittee materials document. Jpn Min Assoc Nat Coal Min Eng Assoc H1(5):32–37
3. Asano N, Ichio T (1962) Distribution of nickel and lead between copper and cuprous sulfide. Trans Min Metall Kyoto (Suiyokaishi, Japan) 14(9):467–470
4. Kashima M, Eguchi M, Yazawa A (1978) Distribution of impurities between crude copper, white metal and silica saturated slag. Trans JIM 19(3):152–158
5. Yazawa A (1980) Distribution of various elements between copper, matte and slag. Erzmetall 33(7–8):377–382
6. Taylor JR (1983) A thermodynamic study of the distribution of metals between copper matte and bullion. In: Sohn HY, George DB, Zunkel AD (eds) Proceedings of the 1983 international sulfide smelting symposium on advances in sulfide smelting, San Francisco, California, USA, November 6–9, 1983. The Metallurgical Society of AIME, Warrendale, Pennsylvania, USA, pp 217–229. ISBN: 0-89520-463-0
7. Schlitt WJ, Richards KJ (1975) The distribution of silver, gold, platinum and palladium in metal-matte systems. Met Trans B 6(2):237–243

8. Sinha SN, Sohn HY, Nagamori M (1985) Distribution of gold and silver between copper and matte. Met Trans B 16(1):53–59
9. Asano N, Wase K, Kobayashi M (1971) Distribution of gold, silver, and selenium between liquid copper and cuprous sulfide. Nippon Kogyo Kaishi 87(998):347–352
10. Burylev BP, Mechev VV, Tsemekhman LSh, Romanov VD, Vaisburd SE (1974) Distribution of Pd and Pt between metal and sulfide melts Cu-S and Cu-Ni-S. Metals 2:82–86
11. Avarmaa K, Johto H, Taskinen P (2016) Distribution of precious metals (Ag, Au, Pd, Pt, and Rh) between copper matte and iron silicate slag. Met Trans B 47(1):244–255
12. Strengell D, Avarmaa K, Johto H, Taskinen P (2016) Distribution equilibria and slag chemistry of DON smelting. Can Met Quart 55(2):234–242
13. Tirronen T, Sukhomlinov D, O'Brien H, Taskinen P, Lundström M (2017) Distributions of lithium-ion and nickel-metal hydride battery elements in copper converting. J Clean Prod 168:399–409
14. Pouchou JL, Pichoir F (1987) Basic expression of "PAP" computation for quantitative EPMA. Proc ICXOM 11:249–253

Recycling of EAF Dust Through Source Separation

Naiyang Ma

Abstract Along with fast growth of EAF steelmaking, better ways of treating EAF dust have been continuously pursued for better environmental protection and better economic benefits. In this contribution, various ways of collecting EAF dust in EAF off-gas cleaning systems are reviewed, and generation of dust and concentration of zinc in the dust from various collecting devices are examined. Accordingly, recycling of EAF dust through source separation is discussed.

Keywords EAF steelmaking · EAF dust · Recycling · Source separation
Zinc

Introduction

EAF steelmaking generates EAF dust, and the EAF dust is a listed hazardous solid waste [1]. There are only three ways to treat the EAF dust allowed by environmental protection authorities: disposal of the dust at landfills for permanent storage, recycling of the dust at zinc recycling facilities for zinc recovery and selling the dust to exempt markets [2–5].

Selling EAF dust to exempt markets has not been well developed, and hence this treatment method of the EAF dust plays an insignificant role in solving issues of the EAF dust.

In treating EAF dust by landfilling, the dust is first chemically stabilized and then shipped to well-lined landfills and stored. [2–4] Disposal of the EAF dust at landfills may jeopardize EAF dust producers with potential environmental liabilities. It is increasingly difficult to obtain new permits for landfilling the EAF dust due to increasing public resistance. In addition, environmental regulations are

N. Ma (✉)
ArcelorMittal Global R&D—East Chicago Laboratories, 3001 E Columbus Dr, East Chicago IN 46312, USA
e-mail: Naiyang.Ma@arcelormittal.com

Z. Sun et al. (eds.), *Energy Technology 2018*, The Minerals, Metals & Materials Series, https://doi.org/10.1007/978-3-319-72362-4_19

increasingly becoming tougher. Consequently, landfilling of the EAF dust is increasingly becoming unpopular and has been dramatically decreased [5].

When recycling EAF dust at zinc recycling facilities, there is a fundamental limitation to EAF dust producers. The EAF dust must contain at least 15% zinc, to be economically treatable [1]. The minimum zinc content is generally associated with recycling fees charged by zinc recyclers. If zinc concentration in the EAF dust becomes higher, zinc recyclers will offer credits to EAF dust producers to subsidize part of the recycling fees.

Clearly, concentration of zinc in EAF dust is a crucial parameter affecting recyclability of the EAF dust, recycling cost paid by EAF dust producers and profitability of EAF dust recyclers. High concentration of zinc in the EAF dust will secure recyclability of the dust and will help maintain strong financial stability for both EAF dust producers and recyclers. As a result, how to increase concentration of zinc in the shipped EAF dust in economic ways becomes a critical step for EAF dust producers to keep recyclability of the EAF dust and to lower their financial burden in recycling of the EAF dust. In the same time, high concentration of zinc in EAF dust is also beneficial to EAF dust recyclers.

Recycling of EAF dust back into EAF furnaces has been regarded as an important step to increase concentration of zinc in the shipped EAF dust and has been widely tested in many EAF steelmaking plants. [2–4, 6–11] Iron, lime and carbon are beneficial components for EAF steelmaking, but zinc is not needed by the EAF steelmaking process. As a matter of fact, since reduction and vaporization of zinc in EAF bath are associated with huge energy consumption, it is often questionable whether recycling of all the EAF dust back into the EAF for zinc enrichment makes any economic senses. In addition, it is also often a concern that too much zinc in the EAF furnaces may interfere with EAF operation and harm steel quality [12].

Therefore, when recycling the EAF dust back into the EAF furnaces, it is beneficial to minimize zinc looping in the EAF steelmaking process. As such, in this contribution, various ways of collecting EAF dust in EAF off-gas cleaning systems are reviewed, generation of dust and concentration of zinc in the dust from different collecting devices are examined, and source separation of the various EAF dusts based on concentration of zinc and source recycling of the lesser-zinc EAF dusts are discussed for increment of concentration of zinc in the shipped EAF dust.

Overview of Various Collecting Devices in EAF off-gas Cleaning Systems

A modern EAF steelmaking shop generally has two off-gas cleaning systems. One is the primary off-gas cleaning system which captures gas and dust emissions directly extracted through the fourth hole of the furnace during melting and refining. The other is the secondary off-gas cleaning system which collects dust and fumes

from the furnace through canopy suction when the furnace is open for charging and tapping, and captures fugitive dust inside the EAF shop from the roof.

The primary off-gas cleaning system consists of at least a combustion chamber and primary baghouses. For some EAF shops, there might exist one or more cooling dropout boxes and reaction chambers between the combustion chamber and the primary baghouses for cooling the off-gas and for removing contaminants [7, 13–16].

The combustion chamber, the dropout box(es) and the reaction chambers may also act as dust collectors besides their primary functions for burning combustibles in EAF off-gas, for cooling the off-gas and for removal of contaminants from the off-gas.

The secondary off-gas cleaning system may also receive off-gas and dust from ladle metallurgy furnace (LMF) shops and other dust sources [13]. In some EAF shops, the secondary off-gas cleaning systems may have their own fans and baghouses. In other EAF shops, the secondary off-gas cleaning systems may share fans and baghouses with the primary off-gas cleaning systems [13, 16]. The secondary off-gas might mix with the primary off-gas partially or in full to cool the primary off-gas.

Some electric arc furnaces might be equipped with scrap preheating facilities. [17–19] The scrap being preheated in the scrap preheaters can capture dust from the primary EAF off-gas while the hot and dirty off-gas is passing through the scrap.

As a summary, EAF shops might have the following devices that can capture EAF off-gas dust: scrap preheaters, combustion chambers, cooling dropout boxes, reaction chambers, primary baghouses and secondary baghouses.

Generation of EAF Dust by Various Devices in EAF off-gas Cleaning Systems

As discussed in last section, EAF dust can be captured not only by primary baghouses, but also by many other devices in the off-gas cleaning systems, including scrap preheaters, combustion chambers, cooling dropout boxes, reaction chambers and secondary baghouses.

Generation of EAF dust by these various devices depends on many factors, and may vary greatly. It is estimated that generation rate of primary EAF dust ranges from 7.5 to 20 kg per tonne of liquid steel, and the generation rate of secondary EAF dust varies from 0.5 to 3.5 kg per tonne of liquid steel [20]. As a result, ratio of the secondary EAF dust to the total EAF dust could change from about 6% to around 15%. Estimated by another source, the secondary EAF dust is about one tenth of the primary EAF dust [4]. The ratio could be higher if the secondary off-gas cleaning systems also capture fumes from LMF shops and other dust sources.

For EAF shops equipped with scrap preheating facilities, considerable amounts of EAF dust in off-gas can be filtered out. It is estimated that up to 20–30% of total EAF dust could be caught by scrap in scrap preheaters [17, 21].

Combustion chambers are also very important in collecting large EAF dust particles. Based on experience of some ArcelorMittal EAF steelmaking plants, the combustion chambers could collect about 10% of the total EAF off-gas dust.

A cooling dropout box might not capture significant amount of EAF dust, perhaps about 1% of the total EAF dust according to experience of some ArcelorMittal EAF steelmaking plants.

Activated carbon is often used in reaction chambers for removal of contaminants in EAF off-gas. Depending on whether the reaction chambers use fixed activated carbon beds or injected activated carbon, the reaction chambers may or may not capture EAF dust. For the reaction chambers with activated carbon beds, considerable amounts of EAF dust particles can be absorbed in the beds.

In summary, scrap preheaters can capture up to 20–30% of the total EAF dust, generation of the secondary EAF dust is up to 15% of the total EAF dust, combustion chambers can collect about 10% of the total EAF dust, cooling dropout boxes may catch about 1% of the total EAF dust, reaction chambers of activated carbon may or may not capture EAF off-gas dust, and primary baghouses collect most of the EAF off-gas dust.

Concentration of Zinc in EAF Dust Collected by Various Devices in EAF off-gas Cleaning Systems

Two ArcelorMittal EAF steelmaking plants, denoted by A and B, are used as examples in the following discussion. A plant primary off-gas cleaning system consists of a combustion chamber and baghouses. Its secondary off-gas cleaning system shares fans and baghouses with the primary off-gas cleaning systems. Dusts generated by the combustion chamber and the baghouses were sampled and analyzed for zinc. The results are shown in Fig. 1.

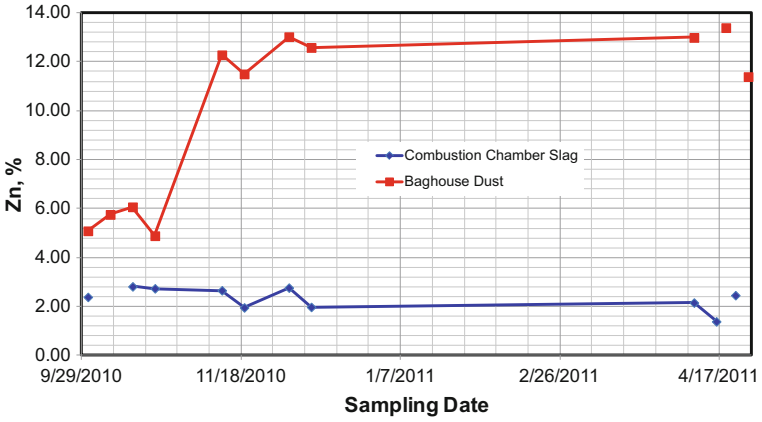

Fig. 1 Variation of concentration of zinc in EAF offgas dusts of ArcelorMittal A EAF Steelmaking Plant

Table 1 Generation of dust and concentration of zinc in the dust from various collecting devices at ArcelorMittal B EAF steelmaking plant

Device	Combustion chamber	Dropout box	All baghouses combined	Secondary baghouses
Percentage out of total dust, %	10	1	89	10
Zn, %	4	6.407	19.405	1

From Fig. 1, one can see that the combustion chamber dust contained significantly less zinc than the baghouse dust, and the concentration of zinc in the combustion chamber dust did not fluctuate very much as the baghouse dust did over the sampling period. The combustion chamber dust was treated as EAF slag, and the baghouse dust was chemically stabilized and landfilled.

ArcelorMittal B EAF steelmaking plant primary off-gas cleaning system collects dust via direct evacuation through the fourth hole and indirect evacuation through the canopy hood. The primary off-gas cleaning system has a combustion chamber, a cooling dropout box and baghouses. Its secondary off-gas cleaning system receives dust from the EAF shop and the LMF shop, and has a dedicated fan and dedicated baghouses. The combustion chamber dust is treated as EAF slag, and the dropout box dust and the baghouse dust are sent to the zinc recycler. The dropout box dust and the baghouse dust are separately sent to the zinc recycler, but the primary baghouse dust and the secondary baghouse dust are combined.

The generation of dust and concentration of zinc in the dust from various collecting devices of the B EAF steelmaking plant are presented in Table 1. Based on the data in Table 1, concentration of zinc in the primary baghouse dust can be calculated out and is 21.735%. Clearly, EAF offgas dusts collected by other devices contain significantly less zinc than the primary baghouse dust and cannot be economically recycled in zinc recycling facilities.

Source Separation and Source Recycling of EAF Dust Based upon Concentration of Zinc in the Dust

From the data presented in previous sections, EAF off-gas dusts collected in other devices in EAF off-gas cleaning systems contain much less zinc than primary EAF baghouse dust. Therefore, only primary EAF baghouse dust should be shipped out to zinc recyclers while other EAF off-gas dusts could be recycled back to the source—EAF furnaces for zinc enrichment and for recovery of valuable components in the EAF dust.

In the two ArcelorMittal EAF steelmaking plants, combustion chamber dust was treated as EAF slag, iron in the dust was recovered by magnetic separation, and residual slag was sold to construction industry. The combustion chamber dust could also be directly recycled back into the EAF furnaces for zinc enrichment and

utilization of iron, lime and carbon in the dust. Separation of the combustion chamber dust from primary baghouse dust can be readily facilitated. It is possible to significantly increase the ratio of the combustion chamber dust to the total EAF off-gas dust for recovering more iron in the combustion chamber dust and for significantly raising zinc levels in the primary baghouse dust by adopting in-process separation strategy [22, 23].

Since the secondary EAF off-gas dust contains very small amount of zinc, it should not be mingled with the primary EAF baghouse dust if it is separately collected. For ArcelorMittal B EAF steelmaking plant, separation of the secondary EAF off-gas dust from the primary EAF baghouse dust can increase zinc content of the shipped EAF dust from 19.405 to 21.735%. The secondary EAF off-gas dust can be recycled back to the EAF furnace for reuse of iron, lime and carbon in the dust.

Zinc content in the cooling dropout box dust is far below the minimum zinc requirement. Therefore, it is not worth to ship the dust to the zinc recycler.

For EAF shops with scrap preheaters, the retained dust in the scrap will go back to the EAF furnaces by nature with the preheated scrap. This dust presumably contains high iron and lime and little zinc. Enhancing the filtration capability of the scrap preheater could be a very effective method to increase zinc content in the shipped EAF baghouse dust and to reduce quantity of the total shipped EAF baghouse dust.

Conclusions

Beside primary EAF baghouses, EAF steelmaking off-gas cleaning systems are composed of various other collecting devices like scrap preheaters, combustion chambers, cooling dropout boxes, reaction chambers and secondary baghouses, which also collect EAF off-gas dusts. The EAF off-gas dusts collected by these different devices are quite different and should be classified for adopting different treatment methods. In general, other EAF off-gas dusts contain much less zinc than the primary EAF baghouse dust. As a result, only the primary EAF baghouse dust should be shipped out for zinc recycling, and other EAF off-gas dusts could be recycled back to EAF furnaces for zinc enrichment and for utilization of iron, lime and carbon in the dusts. Concentration of zinc in the shipped EAF dust can be significantly increased simply by source separation and source recycling of the EAF dusts collected by other devices rather than the primary EAF baghouses. Further greater increment of concentration of zinc in the shipped EAF dust can be facilitated by adopting in-process separation strategy.

References

1. US EPA (1991) Land disposal restrictions for electric arc furnace dust (k061). https://www.epa.gov/sites/production/files/2016-03/documents/fr95.pdf. Accessed Aug 20 2017
2. International Iron and Steel Institute (1994) The management of steel plant ferruginous by-products. Committee on Environmental Affairs and Committee on Technology, Brussels
3. American Iron and Steel Institute (2010) Steel technology roadmap—iron unit recycling. US DOE web. https://energy.gov/sites/prod/files/2013/11/f4/roadmap_chap3.pdf. Accessed Aug 2017
4. Remus R, Aguado Monsonet MA, Roudier S, Sancho LD (2013) Best available techniques (BAT) reference document for iron and steel production. Publications office of the European Union, Luxembourg. http://eippcb.jrc.ec.europa.eu/reference/BREF/IS_Adopted_03_2012.pdf. Accessed Aug 2017
5. Liebman M (2000) The current status of electric arc furnace dust recycling in North America. In Stewart D, Stephens R, Daley JC (eds) Recycling of metals and engineered materials IV, (Warrendale, PA: The Minerals, Metals and Materials Society of AIME, 2000), pp 237–250
6. Sasamoto H, Fujisawa A (1997) Behavior of zinc on dust recycling in EAF. In Paper presented at the 55th electric furnace conference, Chicago, Illinois, USA, November 9–12, 1997), pp 123–125
7. Jensen J, Wolf K (1997) Reduction of EAF dust emissions by injecting it into the furnace. MPT-Metallurgical Plant Technol Int, 3, 58–62
8. Lopez F, Lopez-Delgado A (2007) Enhancement of electric arc furnace dust by recycling to electric arc furnace. J Environ Eng 128:1169–1174
9. Krishnan ER, Kemner WF (1986) Recycling of dust from electric arc furnaces–an experimental evaluation. In Paper presented at the 44th electric arc furnace conference, Warrendale, PA, USA, December 9–12, 1986, pp 355–365
10. Evans LG, Hogan JC (1986) Recycling of EAF dust by direct injection. In Paper presented at the 44th electric arc furnace conference, Dallas, TX, USA, December 10–12, 1986, pp 367–372
11. Tsubone A et al (2012) Development of EAF dust injection technology in Aichi Steel. In AISTech 2012 Proceedings, pp 163–172
12. Pruszko R et al (2003) An assessment of energy, waste, and productivity improvements for North Star Steel Iowa. US DOE project report, sub-contract No. 4000013389, April 2003
13. Smith M (2008) Consideration of staff recommendation regarding financing projects using baghouse technology. CPCFA staff summary, July 2008. http://www.treasurer.ca.gov/cpcfa/meeting/staff/2008/20080723/4a.pdf. Accessed Aug 20 2017
14. Kashiwaya Y et al (2004) Thermodynamic analysis on the dust generaion from EAF for the recycling of dust. ISIJ Int, 44(10), 1774–1779
15. Lehner J et al (2004) Low-cost solutions for the removal of dioxin from EAF offgas, La Metallurgia Italiana, 4, 67–70
16. Nakayama M, Kubo H (2001) Progress of emission control system in electric arc furnace melt-shops. NKK Technical Review, pp 16–23
17. EPRI report (2000) Electric arc furnace scrap preheating. Tech Commentary, http://infohouse.p2ric.org/ref/10/09048.pdf. Accessed Aug 20 2017
18. EPA report (2012) Available and emerging technologies for reducing greenhouse gas emissions from the iron and steel industry. http://www.epa.gov/nsr/ghgdocs/refineries.pdf. Accessed Aug 20 2017
19. Nakano H, Uchida S Arita K (1999) New scrap preheating system for electric arc furnace (UL-BA), Nippon Steel Technical Report No, 79, 68–74
20. Ontario ministry of the environment technology status report: electric arc furnace fume systems and control technologies (1997). https://ia600304.us.archive.org/5/items/technologystudye00ontauoft/technologystudye00ontauoft.pdf. Accessed Aug 20 2017

21. Fanutti G, Pozzi M (2004) Environmental control and the CONSTEEL process. Millennium Steel, pp 106–110
22. Ma N-Y (2011) On in-process separation of zinc from EAF dust, TMS. Collected Proc EPD Congress 2011:947–952
23. Bronson TM, Ma N-Y, Zhu LZ et al (2017) Oxidation and condensation of zinc fume in steelmaking off-gas systems. Mater Metallurgical Trans B 48:908–921

A Sustainable Methodology for Recycling Electric Arc Furnace Dust

Joseph Hamuyuni, Petteri Halli, Fiseha Tesfaye, Maria Leikola and Mari Lundström

Abstract In a race to save the planet of its rapidly depleting natural resources, the use of Secondary Raw Materials (SRMs) as replacements in several processes is currently intensively pursued. In fact, this is currently one of the European Union (EU)'s mandates. Valorization of SRMs is consistent with circular economy, where resource efficiency is maximized for the benefit of both businesses and the environment. In line with this mandate, this paper focuses on investigating process phenomena related to hydrometallurgical recycling of Electric Arc Furnace (EAF) dust. In the experimental study, selective dissolution of zinc and other metals is investigated to acquire a recyclable leach residue. Based on the experimental and theoretical investigations, zinc could be extracted from the EAF dust and a recyclable leach residue produced, having chemical composition suitable as a feed material into electric arc furnace.

Keywords SRMs · Recycling · EAF dust · DSC-TGA curves
Alkaline roasting

Introduction

Recovery of valuable metals and energy from secondary raw materials (SRMs) has a two-fold effect on natural resources. Firstly, using SRMs lessens the pressure on the earth's fast depleting raw materials, thereby ensuring extended supply of metals and other products for a foreseeable future. Secondly, since SRMs emanate from waste streams, recovering resources from them ensures a cleaner environment [1].

J. Hamuyuni (✉) · P. Halli · M. Leikola · M. Lundström
Department of Chemical and Metallurgical Engineering (CMET),
School of Chemical Engineering, Aalto University, 16200, 00076 Aalto, Finland
e-mail: joseph.hamuyuni@aalto.fi

F. Tesfaye
Laboratory of Inorganic Chemistry, Johan Gadolin Process Chemistry Centre, Åbo Akademi University, Piispankatu 8, 20500 Turku, Finland

Z. Sun et al. (eds.), *Energy Technology 2018*, The Minerals, Metals & Materials Series, https://doi.org/10.1007/978-3-319-72362-4_20

Using SRMs also keeps metals in circulation, a process often referred to as a circular economy. This is why for example, the European Union (EU), has outlined a detailed plan through the European Commission (EC) [2] on how to move towards a more circular economy.

Electric Arc Furnace (EAF) dust, is a potential SRM. Currently, up to 20 kg of EAF dust is generated per tonne of steel [3]. This is an enormous amount of material considering the total amount of steel produced by this method [4]. Presently, EAF dust is classified a toxic waste and cannot end up in landfills or be recycled through the conventional methods [5, 6]. This is because of the presence of Pb, Cr and Zn among other metals. Hexavalent chromium (Cr^{6+}) [7, 8] and lead (Pb) [2, 9] are carcinogenic while zinc renders direct EAF dust recycling process impracticable: high zinc content in recycled scrap would react and cause damage to the refractory of the electric furnace [3]. It would also choke the gas uptake, which may lead to the entire process shut down.

Several studies have been conducted to offer a solution to use EAF dust as a SRM. However, these studies are dominated by direct inorganic acid leaching using acids such as sulphuric, nitric and hydrochloric acids [10–14]. The problems and limitations related to inorganic acids, such as poor selectivity, low zinc recovery and problematic leach residues are discussed in a recent study of Halli et al. [1]. In a quest to overcome these limitations, a method that is both selective and generates a recyclable iron rich residue is investigated in the current study.

Experimental Section

Materials and Method

The composition of the five metals of interest in the EAF dust raw material employed in the study, were Zn (33.16%), Fe (17.89%), Mn (2.52%), Pb (1.64%), and Cr (0.23%). Additionally, the EAF steel dust also contained oxides of alkalis (Na, K, Mg, and Ca), silica, and carbon. Silica and alkalis are useful as slag formers in the EAF feed material and carbon will be easily removed through decarburization during the high temperature process. Therefore, the leaching behaviour of these elements is not critical to the quality of the leach residue to be recycled back to the EAF process. In the first part of the project, 16 leaching media were utilized for mapping experiments and they are detailed in Halli et al. [1].

EAF steel dust was homogenized at Geological Survey of Finland laboratory, before experiments. Roasting was performed at 450 °C in a Scandia oven, (Type K4/PDI 40). A 1000 mL lab scale reactor and a LAUDA Aqualine AL 25 water bath were employed for leaching experiments. The bath was used to maintain the leaching temperature. During leaching, constant stirring speed of 500 RPM using a four blade lab agitator stirrer was maintained. A digital Glass Body pH Electrode HI 11310 (Hanna Instruments) and an In Lab Ag/AgCl 3 M KCl (Mettler Toledo)

were employed for pH and Redox potential measurement, respectively. After the leaching experiments, dried residues were analyzed using XRD (X-Ray Diffraction), X'Pert PRO Powder, NL (with Rietveld method, PANalytical HighScore Plus software version 4.0) [15, 16]. The leach solutions were analyzed using AAS for extractions of Zn, Fe, Mn, and Pb. Cr was analyzed by ICP-OES due to its high vaporization temperature.

Roasting was done at an EAF dust/NaOH ratio of 1.94, NaOH being $\leq 99.5\%$ assay (VWR Chemicals Belgium). During leaching experiments, sampling was done at various intervals (5, 15, 30, 60, 120 min) to map the progress of dissolution of metals. Solid/liquid ratio for all leaching experiments was kept at 100 g/L under oxygen purging. The yield of each element was determined by dividing the analyzed metal concentration with the metal concentration obtained after total leaching of equal amount of solids into an equal volume of 100% aqua regia.

Thermal Analysis

Thermal analyses of the EAF-dust mixed with NaOH were conducted by using a TA Instruments SDT Q600 simultaneous TG/DTA. The calorimeter was calibrated with the melting temperatures of high purity zinc, aluminium, and gold. The average measurement accuracies of temperatures were determined to be ± 2 °C.

Two calorimetric measurements were performed for the sample under the same experimental conditions. In all runs, mass change and heat flow during linear heating were measured simultaneously. The runs were performed under a protective 99.999% pure N_2 atmosphere. In both runs the furnace was heated up to 450 °C and then maintained isothermally for 1 h. The heating rate was 5 °C/min, and the flow rate of gas was 100 ml/min. Al_2O_3 crucibles were used as sample holders and references during all runs.

Results and Discussion

The study was conducted in two phases. The first part where 16 leaching media were used serves as a mapping phase while the second part using citric acid as the only leaching medium is an optimization phase. Key observations from the mapping phase are documented in Halli et al. [1]. From this study, it was concluded that citric acid was the optimal leaching medium to be employed in the optimization phase. Table 1 shows performance of investigated organic acids in the absence of pretreatment of EAF dust.

From Table 1 it can be seen that citric acid resulted in the highest Zn extractions and more selectivity for Fe among all investigated organic acids. Furthermore, the

Table 1 The performance of organic acids as leaching media for EAF dust. The extraction results are ranked with highest Zn extraction to solution (>75% or >50%) and with the lowest Fe extraction (<5% or <20%). Pb removal is considered advantageous in terms of preventing accumulation

Leaching media	Zn >75%	Zn >50%	Zn >10%	Zn <1%	Fe <1%	Fe <5%	Fe <20%	Fe >80%	Pb %
H_2CO_2 (Formic acid), 0.27 M			X				X		49
H_2CO_2 (Formic acid), 2.7 M				X		X			0.6
$C_6H_8O_7$ (Citric acid), 0.09 M			X				X		0.3
$C_6H_8O_7$ (Citric acid), 0.94 M	X						X		49
$C_2H_2O_4$ (Oxalic acid), 0.16 M				X	X				18
$C_2H_2O_4$ (Oxalic acid), 1.6 M				X				X	22
$C_2H_4O_2$ (Acetic acid), 1.75 M		X				X			60
$C_2H_4O_2$ (Acetic acid), 17.5 M			X				X		35

Pb dissolution was considered an added advantage. Therefore, citric acid was selected as preferred candidate for further experimentation.

Citric Acid Leaching

The influence of time, concentration, temperature, and pH on metals extraction in the citric acid solution, were predicted using MODDE Version 8.0. Table 2 shows the impact of each parameter on the metal (Fe, Zn, Mg, Cr, Pb) leaching behaviour, scale 1–3 describing the importance of the parameter.

From Table 2, it can be deduced that within the investigated parameter ranges, concentration, followed by temperature had greatest (positive) influence on the yields of all the five metals. Moreover, whilst the concentration coefficient had a positive influence, temperature displayed a negative effect on the yields of all metals. This is assumed to be due to degradation of the citric acid with increasing temperature

Table 2 Scaled and centred coefficients for iron, zinc, manganese, chromium, and lead metals yields. The numbers in brackets () represents the magnitude of the influence of each parameter on the yield of a particular metal. The parameters t, c, and T are time, concentration and temperature, respectively

Parameter and scale	Fe	Zn	Mg	Cr	Pb
t (0–120 min)	↑ **(1)**	↑ **(1)**	↑ **(1)**	**Invalid**	**Invalid**
C(0.05–0.8 M)	↑ **(3)**	↑ **(3)**	↑ **(3)**	↑ **(3)**	↑ **(3)**
T (25–50 °C)	↓ **(2)**	↓ **(2.5)**	↓ **(2)**	↓ **(2)**	↓ **(1.5)**
pH (1–8)	↓ **(2.5)**	↓ **(2)**	↓ **(2.5)**	↓ **(2)**	↓ **(2.5)**

MODDE is an experimental design and statistical analytical tool

Roasting—Leaching

In the study, it was observed further that the highest zinc extraction achievable by direct organic acid leaching was only 78%, which is well below the target of 90%. Therefore, the mineralogy of the sample was studied in more detail. It was observed that zinc was present not only as zinc oxide and minor zinc sulphide, but also partially as zinc ferrite ($ZnFe_2O_4$). Zinc ferrite is known to be more refractory and thus insoluble in citric acid in the investigated environment, resulting zinc extraction below 80%. Figure 1 shows the main phase composition of EAF dust (XRD).

In order to transform the zinc ferrite into a more leachable form, a roasting step was introduced. Roasting of EAF dust and specifically zinc ferrite in the presence of NaOH supports the formation of sodium zincate and sodium ferrate, following Eq. (1):

$$ZnFe_2O_4(s) + 4NaOH(s) = Na_2ZnO_2(s) + 2NaFeO_2(s) + 2H_2O\uparrow \quad (1)$$

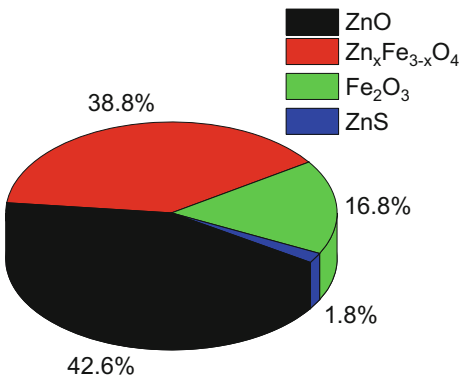

Fig. 1 A chart showing composition of EAF dust by phases present in large fractions. Beside zinc oxide, a significant amount of zinc exist in the ferrite phase

The DSC-TGA curves in Fig. 2 illustrate the decomposition and formation of compounds during the roasting phase of the experiments. As can be observed from the figure, there are mass losses below 200 °C which are due to evaporation of water. This phenomenon is common for the Zn-based and NaOH containing phases. There is one small peak before isothermal temperature has been reached (onset: 267 °C and Peak: 280 °C). This is due to chemical reaction during the formation of the Na_2ZnO_2. From this study, it may be deduced that decomposition of zinc ferrite and formation of the two compounds Na_2ZnO_2(s) and $2NaFeO_2$ occurs at temperatures lower than 300 °C. Such a low temperature would require less energy for the roasting of EAF dust, a feature that makes the method more lucrative.

After adopting the pre-treatment step of alkaline roasting at T = 450 °C (established from literature to be high enough), the citric acid leaching was conducted for the roasted EAF dust. Figure 3 shows the extraction of Fe, Zn and Pb into the citric acid solution for this pre-treated dust material. Zinc present in the roasted EAF dust was shown to be easily soluble and reached high extraction after only 5 min. This suggests that zinc ferrite was transformed into sodium zincate during the roasting process and furthermore, that zincate was easily soluble into citric acid. At the same time, iron extraction into the solution was low (<10%) due to leaching pH > 3, keeping iron in a solid form [17]. Thus, pH monitoring and control can support the selective leaching process of EAF dust.

Figure 3 illustrates the effect of alkaline roasting on selective dissolution of zinc, iron, and lead. Leaching with citric acid was shown to improve both zinc extraction and selectivity between zinc and iron. It can be observed that zinc extraction reached 100% while iron extraction remained below 10%, a feature supporting the recyclability of EAF dust back into the steel process. Additionally, lead extraction was over 80%.

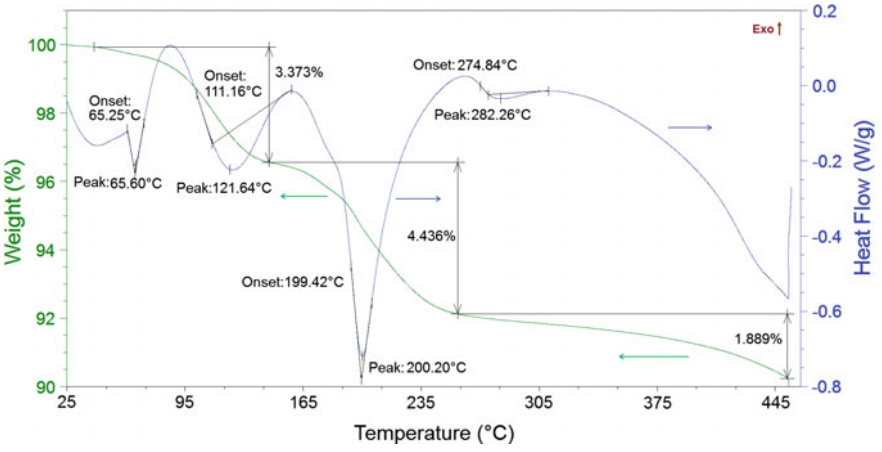

Fig. 2 DSC-TGA curves for the sample composed of EAF-dust mixed with NaOH heated up to 450 °C and kept isothermal for 1 h

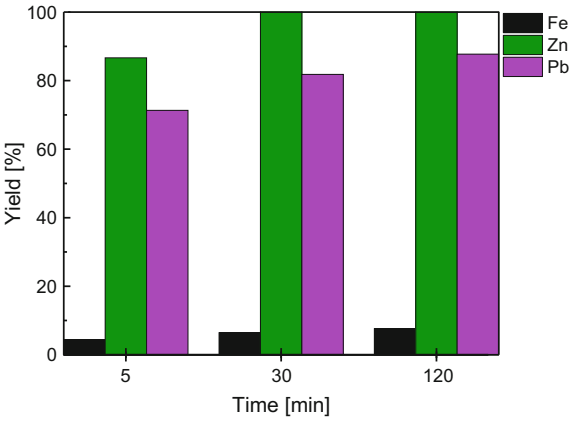

Fig. 3 The yields of Fe, Zn, and Pb after NaOH roasting. Leaching was performed at 40 °C in 0.8 M citric acid concentration

Conclusions

The current study was aimed at observing the phenomena related to EAF dust recycling, producing an iron rich solid with low Zn and Pb, suitable as a secondary feed material to the EAF. The organic acids were discussed as potential lixiviants for Zn leaching. Both citric acid (0.94 M) and acetic acid (1.75 M) could result in high Zn extraction (>75% and >50%, respectively) into the solution whereas acetic acid dissolved initially lower iron (<5%) compared to citric acid (<20%). As a result, the factors affecting EAF dust leaching in citric acid media were investigated. The main parameters affecting metal extraction (Fe, Zn, Mg, Cr, and Pb) were citric acid concentration (increased all metals extraction) and temperature (decreased all metal extraction). The latter was suggested being due to decomposition of the organic acid. It was observed further that the highest zinc extraction achievable by direct citric acid leaching was only 78% due to Zn being partially present as zinc ferrites. This was addressed by applying an alkaline roasting pretreatment prior to citric acid leaching of the EAF dust, increasing the Zn extraction up to 100%.

Acknowledgements This work has been financed by the Association of Finnish Steel and Metal Producers (*METSEK project*) and supported by "*RawMatTERS Finland Infrastructure*" (RAMI) by Academy of Finland and *CMEco*-project (Finnish Funding Agency for Innovation, 7405/31/2016). Some part of the work has been also done as part of the activities of the Johan Gadolin Process Chemistry Centre at Åbo Akademi University under the project "Thermodynamic investigation of complex inorganic material systems for improved renewable energy and metals production processes", which is also financed by the Academy of Finland. The provider of the raw material, Ovako Imatra Oy, is also greatly acknowledged by the authors.

References

1. Halli P, Hamuyuni J, Revitzer H, Lundström M (2017) Selection of leaching media for metal dissolution from electric arc furnace dust. J Clean Prod 164:265–276
2. European Commission DG ENV.E3 (2002) Heavy metals in waste, final report, project ENV. E3/ETU/2000/0058.COWI A/S, Denmark
3. Dutra AJB, Paiva PRP, Tavares LM (2006) Alkaline leaching of zinc from electric arc furnace steel dust. Miner Eng 19(5):478–485
4. Holappa LEK (2017) Energy efficiency and sustainability in steel production. In: Applications of process engineering principles in materials processing, energy and environmental technologies. Springer International Publishing, pp 401–410
5. Pelino M, Karamanov A, Pisciella P, Crisucci S, Zonetti D (2002) Vitrification of electric arc furnace dusts. Waste Manag 22(8):945–949
6. Council EU (2003) Council Decision 2003/33/EC of 19 December 2002 establishing criteria and procedures for the acceptance of waste at landfills persuant to Article 16 of and Annex II to Directive 1999/31/EC. Off J Eur Communities 16(2003):L11
7. Petrilli FL, De Flora S (1977) Toxicity and mutagenicity of hexavalent chromium on Salmonella typhimurium. Appl Environ Microbiol 33(4):805–809
8. Vutukuru SS (2005) Acute effects of hexavalent chromium on survival, oxygen consumption, hematological parameters and some biochemical profiles of the Indian major carp, Labeo rohita. Int J Environ Res Public Health 2(3):456–462
9. Needleman H (2004) Lead poisoning. Annu Rev Med 55:209–222
10. Montenegro V, Agatzini-Leonardou S, Oustadakis P, Tsakiridis P (2016) Hydrometallurgical treatment of EAF dust by direct sulphuric acid leaching at atmospheric pressure. Waste Biomass Valoriz 7(6):1531–1548
11. Montenegro V, Oustadakis P, Tsakiridis PE, Agatzini-Leonardou S (2013) Hydrometallurgical treatment of steelmaking electric arc furnace dusts (EAFD). Metall Mater Trans B 44(5):1058–1069
12. Cruells M, Roca A, Núnẽz C (1992) Electric arc furnace flue dusts: characterization and leaching with sulphuric acid. Hydrometallurgy 31(3):213–231
13. Caravaca C, Cobo A, Alguacil FJ (1994) Considerations about the recycling of EAF flue dusts as source for the recovery of valuable metals by hydrometallurgical processes. Resour Conserv Recycl 10(1–2):35–41
14. Langová Š, Leško J, Matýsek D (2009) Selective leaching of zinc from zinc ferrite with hydrochloric acid. Hydrometallurgy, 95(3): 179–182
15. Izumi F, Young RA (1993) The Rietveld method. In: Young RA (ed) International union of crystallography, p 13
16. Bish DL, Howard SA (1988) Quantitative phase analysis using the Rietveld method. J Appl Crystallogr 21(2):86–91
17. Pourbaix M (1974) Atlas of electrochemical equilibria in aqueous solutions

Thermal Separation and Leaching of Valuable Elements from Waste-Derived Ashes

Daniel Lindberg, Emil Vainio and Patrik Yrjas

Abstract Recovery of trace elements from different industrial waste streams is important in realizing the goals of the circular economy. Ash streams from waste combustion can contain high levels of both toxic and valuable trace elements. These elements can be separated during the combustion process based on volatilization and condensation, as well as being separated in post-combustion processes, through thermal or leaching treatment. In this study, an overview is given of the thermal methods for recovery of valuable elements from ash fractions derived from waste incineration. In addition, a case study is presented of the behaviour of ash-forming elements in combustion of MSW and demolition wood, with special focus on the elements Co, Cu, and Sb. In conclusion, it is shown that thermodynamic modeling of high temperature processes can be a useful tool to predict ash behavior both during combustion and in the post combustion treatment of the ash.

Keywords Ash treatment · Thermodynamic modeling · Waste incineration
Thermal processing

Introduction

Different types of ash fractions and various types of APC (air pollution control) residues are formed in thermal conversion of waste-derived fuels. The solid residues from WtE (Waste-to-Energy) plants may contain harmful components, such as toxic metal compounds and organic micropollutants, which may lead to problems in the utilization or safe disposal of the material. Various treatment methods and processes can be used to reduce the leachability of harmful residue constituents, destroy toxic organic compounds (organic micropollutants), reduce residue volume, and produce material suitable for utilization.

D. Lindberg (✉) · E. Vainio · P. Yrjas
Johan Gadolin Process Chemistry Centre, Åbo Akademi University,
Piispankatu 8, 20500 Åbo/Turku, Finland
e-mail: daniel.lindberg@abo.fi

Z. Sun et al. (eds.), *Energy Technology 2018*, The Minerals, Metals & Materials Series, https://doi.org/10.1007/978-3-319-72362-4_21

Van der Sloot et al. [1], Sabbas et al. [2], Quina et al. [3], Whiticar and Ralph [4], and Zacco et al. [5] have recently reviewed different approaches in the management of the ash and solid APC residues from waste combustion. The two main approaches are safe disposal and recycling or reuse of the ash. In order to safely dispose of or reuse/recycle the ash, separate treatment processes are often required.

The main treatment methods for ash and APC residues can be divided into three groups: (1) separation process (physical or chemical); (2) stabilization and solidification; (3) thermal treatment. Table 1 gives an overview of the principles and methods for treatment of MSW (municipal solid waste) ash, based on the reviews of the International Ash Working Group [6], van der Sloot et al. [1], Sabbas et al. [2], and Whiticar and Ralph [4].

Lindberg et al. [7] recently reviewed different thermal treatment methods of MSW ash residues. The main categories for thermal treatment are vitrification, fusion/melting, and sintering. The thermal methods are mainly differentiated based on the characteristics of the process product, rather than the process itself. In vitrification, a glassy phase is produced, whereas in fusion processes, a crystalline or heterogeneous product is formed by melting the ash or residue. In sintering, the residues are heated to achieve a reconfiguration of solid materials.

Table 1 Overview of principles and methods of treatment of ash residues from WtE plants [1, 2, 4, 6]

Treatment principle	Processes/Methods and unit operations
Chemical and physical separation	Washing
	Chemical precipitation
	Crystallization/evaporation
	Ion exchange
	Density and particle size based separation
	Distillation
	Electrolysis
	Electrokinetic separation
	Magnetic separation
	Eddy-current separation
	Chemical extraction/mobilization
	Adsorption
Stabilization and/or solidification	Solidification/stabilization with hydraulic binders and pore-filling additives
	Chemical stabilisation
	Ageing/weathering
Thermal treatment	Sintering
	Vitrification
	Melting
	Vaporization/condensation

In addition, thermal separation processes may also be combined with the above-mentioned processes to vaporize harmful trace elements from the bulk material. Thermal treatment processes are among the best methods to destroy harmful organic compounds, such as dioxins and furans, present in the solid residues.

Most of the thermal methods are processes that are separate from the thermal conversion of the fuel. One exception is the gasification-melting process or the direct melting process [8–10]. MSW is gasified in a fluidized bed reactor and the syngas is used as the heat source for the ash melting. The gasification-melting process may lead to better separation of different elements compared to traditional MSW incineration, with elements distributed between a silicate slag, the fly ash in the process and a metallic phase [10]. Pb, Zn, and Cl tend to form fly ash, whereas Fe and Cu form a metallic phase. Other common ash-forming elements are distributed in both fly ash and the silicate slag.

Another in situ process for elemental separation into different fractions is the use of hot cyclones in the combustion unit. During combustion or gasification, heavy metals such as Cd and Pb volatilize. The volatilized metals condense when the gas is cooled and will be found in the fly ash or filter ash. The use of a hot cyclone prior to the heat exchanger could make it possible to separate the heavy metals from the fly ash. In a hot cyclone separation concept, the fly ash is collected in a hot cyclone, where volatilized heavy metals continue with the flue gas stream and is collected as filter ash. In an ideal case, the cyclone ash is heavy-metal free, and can be used directly as a product, while the filter ash is highly enriched in heavy metals and may be more easily handled due to lower volumes of hazardous ash.

Ljung and Nordin [11] studied the fate of different elements during combustion of a fast-growing energy tree (Salix spp.) and hot cyclone separation in theory using chemical equilibrium model calculations. Calculation results indicated that hot cyclone separation might be possible for Cd, Pb and Cu due to their relatively low volatilization temperatures. According to the calculations Ni, Zn and V would be difficult to separate with the hot cyclone due to their high volatilization temperatures. The calculations were in good agreement with results from previous field studies.

Obernberger and Biedermann [12] compared a combustion plant (Lofer) and a plant with integrated fractionated heavy metal separation (Straβwalchen). The temperature in the combustion zones was varied to check the influence on the heavy metal concentrations. A high-temperature cyclone was placed behind the furnace in Straβwalchen. The temperature in the cyclone varied between 950 and 1050 °C. The Cd concentrations in the bottom ashes were about 20 times lower in the new plant compared to the old. Cd levels in combustion zone fly ash and fly ash from the high-temperature cyclone were also lower for the new plant. Cd concentrations in hot-precipitated fly ash showed clear temperature dependence. The Cd concentrations decreased with increasing temperature of ash precipitation. Zn concentrations in the bottom ash were 5 times lower in the ash from the new plant compared to the old. Zn concentration in the combustion zone fly ash were lower than in hot-precipitated fly ashes produced in the old plant but considerably higher in the

fly ash precipitated in the high-temperature cyclone. Zn showed no temperature dependence in the investigated range in either plant. The amounts of fly ashes produced were lower in the new plant and the amount of condensation sludge higher. Coarse fly ash particles could be separated from in the combustion zone at high temperatures with a hot cyclone catching the large scale particles between the furnace and the boiler of the plant. The temperature in the hot cyclone has to be above 900 °C to be efficient for heavy metal fractionation.

According to calculations Cd, Pb and Cu could be removed by hot cyclone separation from the fly ash [11]. Due to higher volatilization temperatures Ni and Zn would be difficult to separate from the fly ash. According to Obernberger et al. [12, 13] the cyclone temperature has to be over 900 °C for efficient separation.

Objective and Approach

The objective of the study is to investigate the ash chemistry in combustion of waste-derived fuels (SRF) with emphasis on the separation of ash-forming elements in different ash streams during the thermal conversion of the fuel. The main division between different ash element streams is between elements that stay in a condensed form during the main conversion process and elements that form volatile species at temperatures prevailing at the conversion temperatures and air/fuel ratios. Predictions of this separation is done by using thermodynamic modeling based on Gibbs Energy Minimization. Thermodynamic modeling predicts the amount and composition of stable phases and components at chemical equilibrium at a specified temperature, total pressure and overall elemental composition. The approach does not require any prior knowledge of specific chemical reactions or initial speciation of elements. In the general approach, chemical kinetics cannot be considered. However, Kangas et al. [14, 15] have utilized a so-called constrained Gibbs Free Energy Method, where kinetic limitations can be considered for certain reactions. This is however not included in the present study.

Thermodynamic Equilibrium Calculations

Thermodynamic equilibrium calculations were made to predict the speciation of the ash-forming elements as a function of temperature for both oxidizing and reducing conditions. The advanced thermodynamic modeling was performed using the software package Factsage, version 6.4 [16]. A tailor-made thermodynamic database was used for the calculations. The data for the gas phase and the stoichiometric solid phases of the elements C−H−O−N−S−Cl–Na−K−Zn−Pb–Ca−Mg–Fe−Al–Si−P−Ti−Co−Cr−Cu−Mn−Sb−Sn were taken from the FACT Pure substance database in the Factsage software. It was assumed that N_2 was the only stable nitrogen compound as the formation of NO_x compounds in biomass combustion is

strongly dependent on kinetics and N-speciation in the fuel. A multicomponent molten salt phase including $NaCl-KCl-Na_2SO_4-K_2SO_4-Na_2CO_3-K_2CO_3$ was also included together with corresponding solid solutions [17]. A molten silicate/slag phase is available in the thermodynamic databases in Factsage but was excluded due to calculational limitations. All condensed silicate phases are therefore considered as stoichiometric phases in the current calculations.

The main fuel studied in the present report is SRF (solid recovered fuel). SRF is mainly the non-recoverable paper, plastics and textiles fractions from MSW that has been shredded and dehydrated for incineration. The chemical composition of the fuel is given in Table 2. It was based on the chemical composition of a SRF fuel that has been burned in an BFB (Bubbling Fluidized Bed) plant in Anjalankoski, Finland operated by Stora Enso.

Table 2 Fuel composition of SRF used as input for the calculations

Ultimate analysis (dry solids)	C	*wt% (d.s.)*	51.0
	H	*wt% (d.s.)*	6.5
	S	*wt% (d.s.)*	0.2
	O	*wt% (d.s.)*	37.4
	N	*wt% (d.s.)*	0.7
	Cl	*wt% (d.s.)*	0.258
	F	*wt% (d.s.)*	0.003
	Br	*wt% (d.s.)*	0.001
Element concentrations in the dry substance	Al	*g/kg*	3.324
	Si	*g/kg*	8.936
	Ti	*g/kg*	1.067
	Na	*g/kg*	1.772
	Mg	*g/kg*	1.421
	K	*g/kg*	1.612
	Ca	*g/kg*	17.884
	Fe	*g/kg*	1.596
	P	*g/kg*	0.559
Heavy metals concentrations in the dry substance	Sb	*mg/kg*	3.58
	As	*mg/kg*	0.73
	Cd	*mg/kg*	0.24
	Cr	*mg/kg*	50.16
	Co	*mg/kg*	0.44
	Cu	*mg/kg*	24.44
	Pb	*mg/kg*	42.63
	Mn	*mg/kg*	378.38
	Ni	*mg/kg*	9.91
	Sn	*mg/kg*	15.91
	V	*mg/kg*	3.30
	Zn	*mg/kg*	159.44

The fuel compositions taken from Table 2 were used as input for the calculations. The calculations were made as a function of temperature and air-to-fuel ratio (λ). The air-to-fuel ratio was varied between 0.4 and 1.2 with steps of 0.01 and the temperature was varied between 400 and 1300 °C with steps of 10 °C. Additional calculations with either double amounts of Cl and S or completely Cl- and S-free fuels have been calculated, but the detailed results are not shown here.

Results

The predicted main ash phases and the minor gas components of ash forming elements (>1 ppm) are shown in in Fig. 1 as a function of temperature for reducing and oxidizing conditions (λ = 0.7 and λ = 1.2). Ca–Al—and Ca–Mg-silicates dominate the condensed phases, whereas HCl, KCl, and SO_2 (oxidizing conditions) or H_2S (reducing conditions) are the main alkali, sulfur or chlorine species.

The elements Co, Cu, and Sb are of special interest in the present study for assessing the viability to recycle these elements from the ash [18–20]. It was concluded that these elements often occur in the waste ashes at levels higher

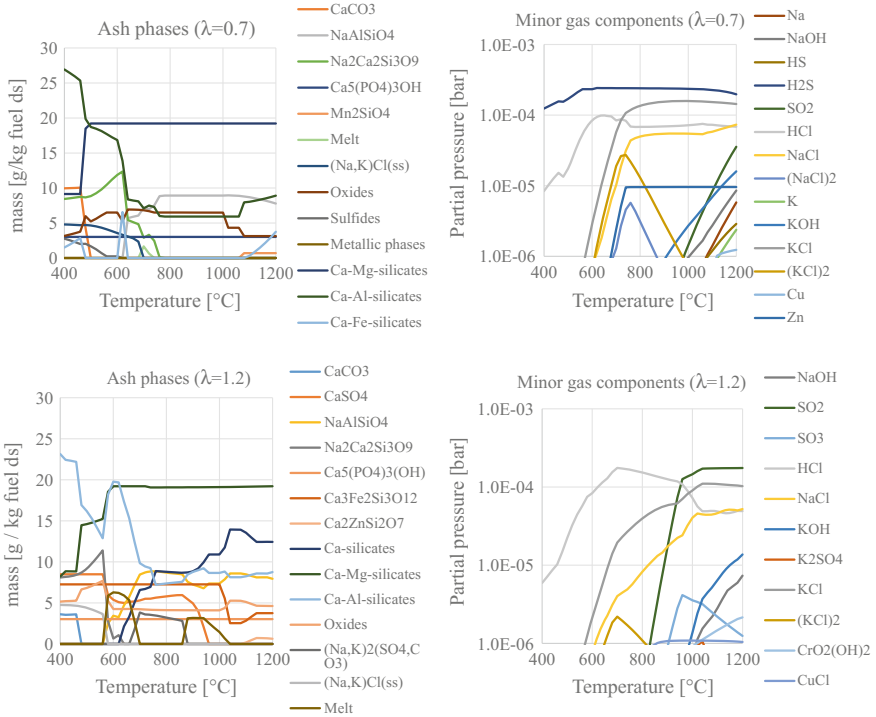

Fig. 1 Predicted condensed phases (left), and minor (right) gas components as a function of temperature for SRF conversion at λ = 0.7 (top) and λ = 1.2 (bottom)

compared to other sources, and therefore may have a potential to be recovered from the ash. In the present study, where solid recovered fuel was studied, Cu has the highest concentration in the fuel and Co has the lowest. It is of interest to predict if these elements can be enriched in the flue gas so that they may be captured in filter ash instead of fly ash or bottom ash.

Cobalt is predicted to be present as Co(s, g), Co_9S_8(s), $CoCl_2$(g) at reducing conditions and Co_3O_4(s), $CoCr_2O_4$(s), $CoCl_2$(g) at oxidizing conditions. Copper is predicted to present as Cu (s,l,g), Cu_2S(s), Cu_5FeS_4(s), CuCl(g) at reducing conditions, and CuO(s), $CuFeO_2$(s), CuCl(g) at oxidizing conditons. Antimony is predicted to be present as SbO(g), and Sb_2S_3(g) at reducing conditions and SbO(g), and Sb_2O_5(s) at oxidizing conditons. At reducing conditions, no condensed antimony compounds were predicted to be stable at temperatures above 400 °C.

The fraction of volatile Co, Cu, and Sb as a function temperature and air-to-fuel ratio is shown in Fig. 2. In addition, the volatile fraction of the important ash-forming elements Pb, Zn, K, and Na, as well as Sn, are shown. It can be seen that Co is volatilized mainly at reducing conditions and at temperatures above 1100 °C. If the chlorine content in the fuel is doubled, the volatilization of cobalt becomes considerable at temperatures above 700 °C. Copper is volatilized at 600–700 °C at oxidizing conditions except if there is no Cl or S present, where temperatures above 1100 °C are needed for copper to volatilize. At reducing conditions, copper is volatilized at temperatures above 1000 °C. Antimony is predicted to be in a condensed phase only at temperatures below 500 °C and only at oxidizing conditions. Sn and Zn are mainly in the condensed phase at oxidizing conditions up to 1000 °C, whereas Pb is volatilized at oxidizing conditions even down to around 500 °C. K is the main volatilized alkali element, occurring as KCl(g), KOH(g) or KOH(g), and Na occurs as condensed $NaAlSiO_4$(s) up to high temperatures.

Enrichment of Co, Cu, Sb in gas phase

The enrichment of Co, Cu, and Sb in relation to the other ash-forming elements were calculated for the four different compositional input conditions. The enrichment was calculated as follows:

$$Enrichment\,factor\,of\,element\,in\,gas = \frac{m(i, gas)/m(total\,metals,\ gas)}{m(i, fuel)/m(total\,metals,\ fuel)}$$

In addition to the metals, phosphorus was also included, whereas the halogens and sulfur were excluded. The calculated enrichment factors for Co, Cu, and Sb are shown in Fig. 3 at air/fuel ratios of 0.7 and 1.2. An enrichment factor <1 means that the element is preferentially stable in the condensed phases, whereas values >1 means an enrichment in the gas phase. It can be seen that cobalt is depleted in the gas phase except for high temperatures at reducing conditions and at around 600 °C at oxidizing conditions. Copper becomes enriched in the gas phase above 900 °C at reducing conditions and above 600 °C at oxidizing conditions. Antimony is predicted to be strongly enriched in the gas phase, especially at lower temperatures. There is a thousandfold enrichment of Sb at both reducing and oxidizing conditions

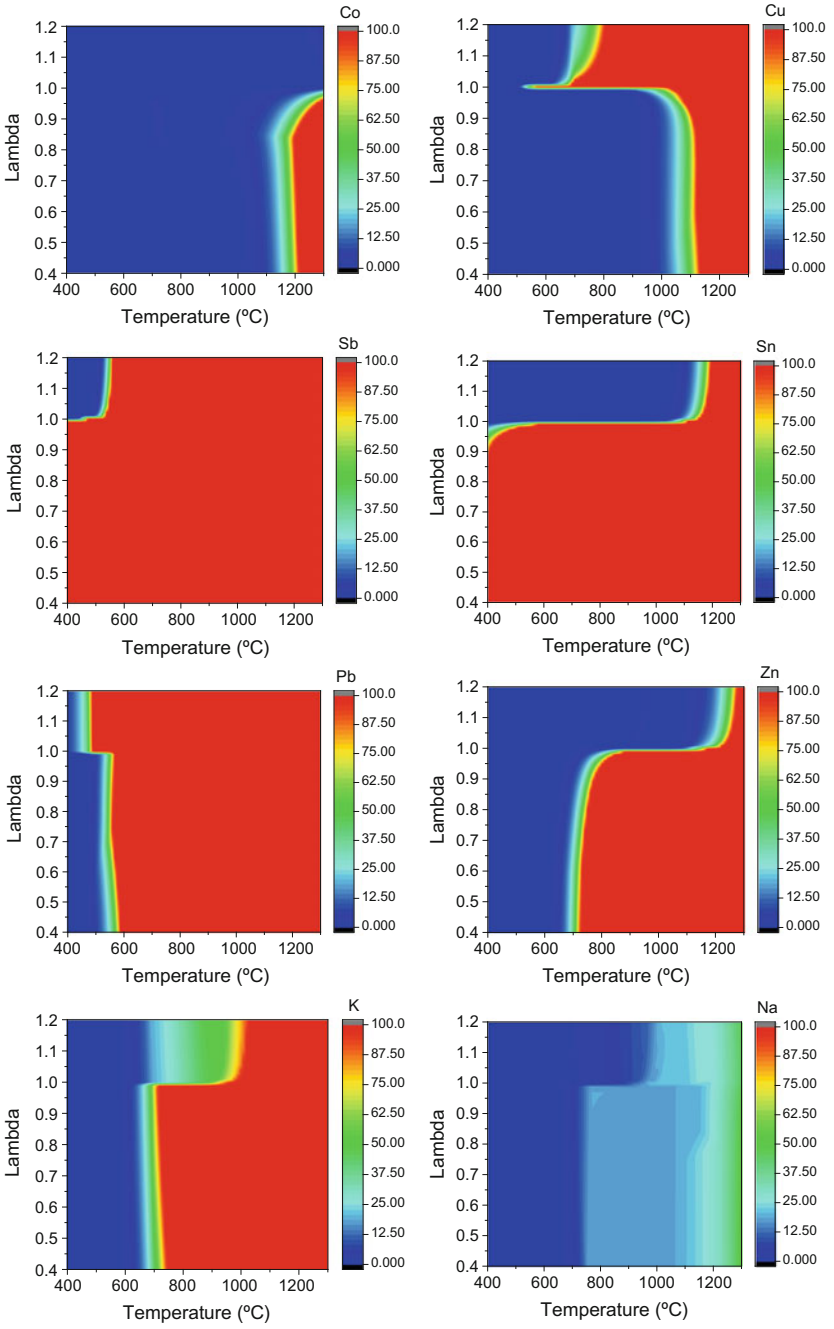

Fig. 2 Fraction of Co, Cu, Sb, Sn, Pb, Zn, K, and Na in the gas phase as a function of temperature and air-to-fuel ratio (lambda) for the normal case

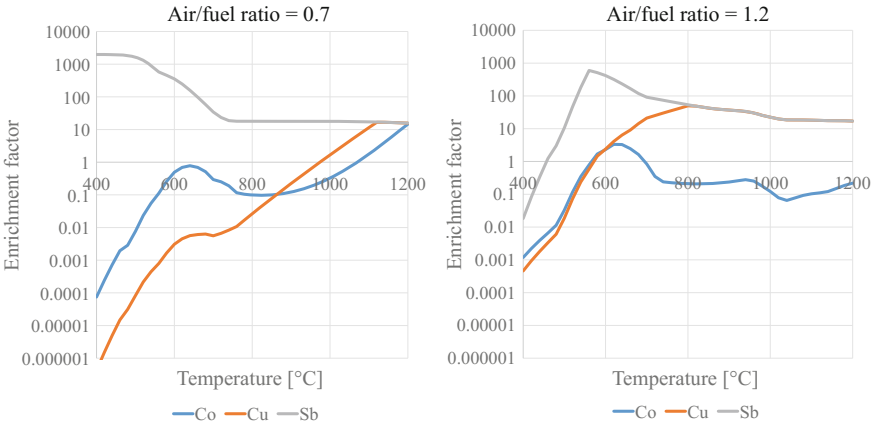

Fig. 3 Enrichment factors of Co, Cu, and Sb as a function of temperature for air/fuel ratios of 0.7 (left) and 1.2 (right) for the base case

below 600 °C. At higher temperatures, the level of volatilized ash-forming elements, such as K, Na, Pb, start to become significant.

Cobalt is mainly depleted from the gas phase and is therefore expected to be found in the bottom ash of different combustion units. The bottom ash fraction is typically considerably larger than fly ash or filter ash fractions, which makes it unlikely of finding high levels of cobalt in any ash fraction.

Copper enrichment in the gas phase is predicted to be the highest at oxidizing conditions at around 600–900 °C. Antimony is predicted to exist mainly for the studied conditions, with the exception of low temperatures at oxidizing conditions. The highest enrichment is predicted to be mainly at temperatures below 600 °C at reducing conditions.

Discussion and Conclusions

In a previous report [19], thermodynamic predictions of the speciation of Co, Cu, and Sb in MSW ash showed that the elements mainly occur as different oxides, such as Co_3O_4, CuO, Sb_2O_5. Experimentally determined speciation of Cu and Sb suggest similar results. Additional Cu compounds were also observed, such as $CuSO_4$ and $Cu_3(PO_4)_2$. Firing MSW fuels containing high concentrations of halogens may lead to formation of metal halides. We have performed leaching tests in a continuous flow reactor [18, 19, 21] and analyzed the metals that were leached from different waste-derived ashes online by inductively coupled plasma optical emission spectrometry (ICP-OES). It was shown that Co, Cu and Sb are not leached out from the ash in H_2O to any notable extent, except for Sb if the leaching is continuous for 24 h (about 40% for CFB boiler ash from waste wood). If the leaching agent is

changed from H_2O to 5% HNO_3 solution, total leaching of Co, Cu, and Sb will reach roughly 40–70% of the original content. If the initial H_2O leaching stage is longer (24 h), larger fractions of Co, Cu and Sb will dissolve compared to shorter H_2O leaching stages (30 min). It was shown that Co, Cu and Sb can be leached out from the ash in acids. However, more experiments are needed to optimize the leaching processes.

In the present study, the speciation and volatilization of Co, Cu, and Sb in thermal conversion of SRF at various temperatures and air/fuel ratios were studied using thermodynamic equilibrium modeling. The main goal was to determine if there are conditions in the combustion unit where it is possible to separate and enrich these elements in relation to the bulk ash composition. Based on the predicted results, cobalt occurs mainly in the condensed phases and is not feasible for enrichment in fly ash or filter ash. Copper is enriched in the gas phase at especially oxidizing conditions if chlorine levels in the fuel is high. Controlled conditions in relation to local temperature of the flue gas and air staging are possible methods to form fly ash or filter ash enriched in copper compounds. In general, concentration of copper is considerably higher than antimony and cobalt in waste-derived fuels. Antimony is predicted to be mainly in the flue gas except at oxidizing conditions below 600 °C, and it is therefore possible to enrich antimony in filter ash if a hot cyclone is utilized to separate condensed fly ash particles from the flue gas stream that contains the volatilized ash forming elements.

The effect of sulfur and chlorine on the ash chemistry was not very pronounced in the present study. Higher chlorine levels increased volatility of alkali species, Pb, Zn, and Co, but Cu and Sb were not affected to any large extent. Increase of sulfur levels had only minor effects. Complete removal of sulfur and chlorine decreased the volatility of Pb and the alkali metals at lower temperatures.

As a final example to study the possible overall chemistry of ash phases and flue gas in SRF combustion, a case where the condensed fly ash/bottom ash composition as well as the possible compounds condensating from the flue gas was calculated.

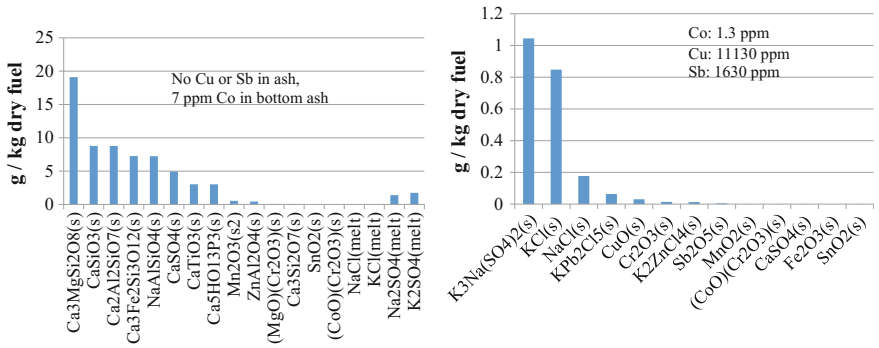

Fig. 4 Left graph shows the predicted stable condensed phases at air/fuel ratio = 1.2 and 900 °C; right graph shows predicted stable condensed phases that will form if the flue gas is cooled from 900 to 200 °C

The calculated condensed phases at 900 °C show that Cu and Sb are predicted to be in the gas phase, whereas the Co concentration in the condensed phases (bottom ash/condensed fly ash) is only 3 ppm. If the corresponding flue gas is cooled to around 200 °C or lower, the Co concentration in the condensate is only 1 ppm, but the Sb concentration is 1630 ppm and the Cu concentration is 11130 ppm (Fig. 4).

This suggests that Cu and Sb concentrations in filter ash condensates are considerably higher than the levels in the bulk fuel. However, uncertainties in the calculations stemming from missing or uncertain thermodynamic data, or applicability of the thermodynamic equilibrium assumption for the predictions, are issues that need to be studied, and the predicted results need to be verified with experimental data.

Acknowledgements The study was performed within the ARVI-Material Value Chains Research Program, coordinated by CLIC Innovation Oy and financed by Tekes – the Finnish Funding Agency for Innovation.

References

1. van der Sloot HA, Kosson DS, Hjelmar O (2001) Characteristics, treatment and utilization of residues from municipal waste incineration. Waste Manag 21:753–765
2. Sabbas T, Polettini A, Pomi R, Astrup T, Hjelmar O, Mostbauer P, Cappai G, Magel G, Salhofer S, Speiser C, Heuss-Assbichler S, Klein R, Lechner P (2003) Management of municipal solid waste incineration residues. Waste Manag 23:61–88
3. Quina MJ, Bordado JC, Quinta-Ferreira RM (2008) Treatment and use of air pollution control residues from MSW incineration: an overview. Waste Manag 28:2097–2121
4. Whiticar DM, Ralph J (2011) Waste to energy. A Technical Review of Municipal Solid Waste Thermal Treatment Practices—Final Report. Stantec Consulting Ltd, p 339. http://www.env.gov.bc.ca/epd/mun-waste/reports/pdf/BCMOE-WTE-Emissions-final.pdf
5. Zacco A, Borgese L, Gianoncelli A, Struis RPWJ, Depero LE, Bontempi E (2014) Review of fly ash inertisation treatments and recycling. Environ Chem Lett 12:153–175
6. C. IAWG (International Ash Working Group) AJ, Eighmy TT, Hartle´n O, Kosson D, Sawell SE, van der Sloot H, Vehlow J (1997) Municipal solid waste incinerator residues. studies in environmental science. Elsevier
7. Lindberg D, Molin C, Hupa M (2015) Thermal treatment of solid residues from WtE units: A review. Waste Manag 37:82–94
8. Tanigaki N, Manako K, Osada M (2012) Co-gasification of municipal solid waste and material recovery in a large-scale gasification and melting system. Waste Manag Oxford, U. K. 32:667–675
9. Jung CH, Matsuto T, Tanaka N (2005) Behavior of metals in ash melting and gasification-melting of municipal solid waste (MSW). Waste Manage Amsterdam Neth 25:301–310
10. Arena U, Di Gregorio F (2013) Element partitioning in combustion- and gasification-based waste-to-energy units. Waste Manage Oxford, U. K. 33:1142–1150
11. Ljung A, Nordin A (1997) Theoretical feasibility for ecological biomass ash recirculation: chemical equilibrium behavior of nutrient elements and heavy metals during combustion. Environ Sci Technol 31:2499–2503

12. Obernberger I, Biedermann F (1997) Fractionated Heavy metal separation in biomass combustion plants-possibilities, technological approach, experiences. In: The impact of mineral impurities in solid fuel combustion, Engineering Foundation, New York, United States, Kona, Hawaii, USA
13. Obernberger I, Biedermann F, Widmann W, Riedl R (1997) Concentrations of inorganic elements in biomass fuels and recovery in the different ash fractions. Biomass Bioenerg 12:211–224
14. Kangas P, Koukkari P, Lindberg D, Hupa M (2014) Modelling black liquor combustion with the constrained Gibbs energy method. J Sci Technol For Prod Process 3:6–15
15. Kangas P, Koukkari P, Brink A, Hupa M (2015) Feasibility of the constrained free energy method for modeling NO formation in combustion. Chem Eng Technol 38:1173–1182
16. Bale CW, Bélisle E, Chartrand P, Decterov SA, Eriksson G, Hack K, Jung I-H, Kang Y-B, Melançon J, Pelton AD, Robelin C, Petersen S (2009) FactSage thermochemical software and databases—recent developments. CALPHAD: Comput Coupling Phase Diagr Thermochem 33:295–311
17. Lindberg D, Backman R, Chartrand P (2007) Thermodynamic evaluation and optimization of the ($NaCl + Na_2SO_4 + Na_2CO_3 + KCl + K_2SO_4 + K_2CO_3$) system. J Chem Thermodyn 39:1001–1021
18. Vainio E, Lindberg D, Yrjas P (2015) Characterisation and on-line measurements of ashes—continuous leaching analysis of ashes. Arvi - material value chains, project report. https://portal.cleen.fi/_layouts/IWXmlPublications.aspx?Source=ARVI&FileId=265
19. Lindberg D, Vainio E, Yrjas P (2015) Critical review of thermodynamic data for heavy metals in aqueous solutions and thermodynamic calculations of solubility of heavy metal compounds in ash. Arvi—material value chains, project report. https://portal.cleen.fi/_layouts/IWXmlPublications.aspx?Source=ARVI&FileId=266
20. Laine-Ylijoki J, Bacher J, Tommi Kaartinen K, Korpijärvi M, Wahlström M, Castell-Rüdenhausen z (2015) Review on Elemental Recovery Potential of Ashes. Arvi—material value chains, project report. https://portal.cleen.fi/_layouts/IWXmlPublications.aspx?Source=ARVI&FileId=220
21. Vainio E, Hupa E, Eriksson J-E, Lindberg D, Yrjas P (2017) Continuous leaching analysis of ashes. Arvi—material value chains, project report. https://portal.cleen.fi/_layouts/IWXmlPublications.aspx?Source=ARVI&FileId=689

Different Methods for the Characterization of Ash Compositions in Co-Firing Boilers

J.-E. Eriksson, T. Khazraie and L. Hupa

Abstract With increased co-firing of coal and different biomasses in power plants, there is a growing need to study and characterize the produced, often heterogeneous ashes and to assess their utilization as secondary raw materials. In this work, we compare different methods for characterizing the ash compositions. These methods include scanning electron microscopy-energy dispersive X-ray analysis (SEM-EDS), X-ray fluorescence (XRF) and inductively coupled plasma emission spectroscopy (ICP-OES). The content of carbonaceous residues in the ashes was measured with CHNS analyzer. The methods and the pretreatment required for each of the analysis were studied in detail for three ashes: (1) coal, (2) peat and wood, (3) peat and wood residue with dolomite addition. The limitations of each method will be discussed. This work gives guidelines for selecting a rapid and reliable method for analyzing the suitability of the ash for a particular application.

Keywords Ash characterization · Biomass · SEM-EDS · XRF · ICP-OES

Introduction

In modern circular economy, industrial, agricultural and municipal waste and side streams are becoming increasingly important as secondary raw materials as such or as sources for separation and refining of metals and other valuable elements. Ashes belong to waste streams which are widely used as landfilling or as substitutes for minerals e.g. in ceramics and for Portland cement in concrete [1, 2]. Today, the utilization of ashes as added-value materials is intensively studied. In order to ensure safe reuse and recycling, various treatments are often needed to eliminate harmful residue constituents or toxic components from the ashes [1, 3]. To select a suitable ash treatment, the ashes must be analyzed and characterized by suitable

J.-E. Eriksson (✉) · T. Khazraie · L. Hupa
Johan Gadolin Process Chemistry Centre, Åbo Akademi University,
Piispankatu 8, 20500 Turku, Finland
e-mail: jan-erik-eriksson@abo.fi

Z. Sun et al. (eds.), *Energy Technology 2018*, The Minerals, Metals & Materials Series, https://doi.org/10.1007/978-3-319-72362-4_22

methods. The composition of ashes depends on the fuel composition, the site of the collection in the combustion device, and the combustion technique used.

The composition of the ash is usually classified according to the major elements present, or according to the mineral composition. Based on their concentrations, the elements in ashes are divided into three categories: major elements (>10,000 mg/kg), minor elements (1,000–10,000 mg/kg, and trace elements (<1000 mg/kg). Besides the inorganic elements and compounds, the ashes may contain organic micropollutants such as polycyclic hydrocarbons, chlorobenzenes, polychlorinated biphenyls, furans, etc. [3]. Apart from limiting the utilization of the ashes as secondary raw materials, the elements in the ashes may also create problems in furnace operation or lead to degradation of materials used in boilers [4]. The increasing utilization of biomass-based fuels, waste incineration and co-combustion of various solid fuels challenge the lifetime of the metals and refractories used in the boilers [4–6]. The challenges with safe reuse and circulation of the ashes and efficient boiler operation call for reliable methods to analyze the chemical composition of the ashes. Traditionally, the chemical composition of fuels is characterized according to standard methods to reveal the amount of moisture, mineral residues (ash), volatile matter and fixed carbon. These analyses are essential when studying the fate of the ash-forming elements during combustion and estimating their effect on the boiler operation. In contrast, for ash recycling purposes the elemental and mineralogical composition of the sample collected from a certain site is crucial.

The chemical composition of ashes can be measured by different techniques. Often, the oxide composition of ashes is characterized using one of the following methods: Scanning electron microscopy (SEM-EDS), X-ray fluorescence (XRF) or inductively coupled plasma emission spectrometer (ICP-MS) [7–9]. Recently, Romero et al. used all these methods for chemical analyses of ashes [10]. ICP-MS was employed to measure the total concentration of major to trace elements in ashes after digestion in aqua regia, while the major elements were characterized using XRF. They used SEM-EDS to study the morphology and composition of individual ash particles. Finally, the mineralogical composition of the ashes was studied using XRD, while different surface-functional groups were analyzed by FTIR [10]. However, the differences in the ash analyses obtained by these different methods have rarely been compared.

Though detailed analysis provides crucial information of the suitability of the ashes to various reuse purposes, a first reliable screening of the ash composition gives guidelines for the further steps needed to analyze and treat a particular ash for recycling as a secondary raw material. This work compares commonly used instrumental methods of ash elemental analysis. The ashes used as examples were fly ashes but the methods utilized are valid also for other inorganic waste streams.

Experimental

In this work, the chemical composition of fly ashes from full-scale boilers using three different types of solid fuels was characterized. (i) Ash A—coal ash from circulating fluidized bed boiler, (ii) Ash B—peat (60%) and wood (40%) ash from circulating fluidized bed boiler, and (iii) Ash C—peat (45%) and wood residue (55%) ash with a dolomite addition from bubbling fluidized bed boiler.

SEM-EDS

The elemental composition and morphology of the ash particles were studied using scanning electron microscope equipped with energy dispersive X-ray analysis (SEM-EDS, Leo 1530 Gemini, Thermo Scientific UltraDry SDD X-ray detector). To study the impact of sample preparation on the ash analysis results, two types of ash samples are prepared: First, the ash particles were directly fixed to the carbon tape on aluminum plates. Five samples of each ash were analyzed. Typical analysis area was $\sim$12 mm^2.

Second, the ashes were pressed into pills (diameter 10 mm, thickness 3–4 mm) to give a large homogeneous measurement area. The pills were prepared by placing 300–400 mg of each ash in a sample holder and then applying hydraulic pressure (220 bar, 30 s). Five pills of each ash were studied. The pills were first put into the SEM without any further preparation to determine if they could be analyzed without a conducting coating. However, due to the low conductivity, the samples had to be coated with a thin carbon layer to prevent charging effects. The coating was created with an "Emscope TB 500" carbon evaporator. In the SEM-EDS, the accelerating voltage was set at 15 kV and the area that was analyzed was $\sim$12 mm^2. In the analysis, carbon was excluded. To verify that the carbon amount was negligible, the total carbon content of the ashes was measured with CHNS elemental analyzer; FLASH 2000 organic elemental analyzer (Thermo Scientific, UK)

XRF

The elemental composition of the ashes was also analyzed using energy dispersive X-ray fluorescence analyzer (ED-XRF, PANanalytical Epsilon 3X) with Rh anode. For each sample, 8 g of ash and 2 g of wax (Licowax C micro powder PM) were weighed and mixed thoroughly, after which pellets with diameter 40 mm and thickness 5–8 mm were pressed under 20 tons. The spectrum of each pellet was analyzed for elements with 5 alternative settings for different elements from Na to Am using the Omnian software.

ICP-OES

The third analysis method was inductively coupled plasma optical emission spectroscopy (ICP-OES, Perkin Elmer Optima 5300 DV). When preparing the solution for the analysis, 0.1 g of dried ash was weighed in a polytetrafluoroethylene (PTFE) bomb after which 2 ml 65% HNO3 and 2 ml 85% H_3PO_4 and 2 ml 50% HBF_4 were added for total dissolution of the ash. The bomb was placed in a microwave sample preparation system (Perkin Elmer Multiwave 3000), ramped to 1400 W in 15 min, held for 20 min and then cooled for 20 min. After this pre-treatment, no solid residue was observed in the solution. The element concentrations were then analyzed with the ICP-OES using the Perkin Elmer multi-standard 25 for simultaneous analysis of all ash-forming elements at preferred wavelengths. For each ash, three samples were analyzed.

Finally, the element concentrations measured with the three methods were calculated into typical oxide composition of the ash. For each ash, the contribution of different carbon-containing (char, carbonate, etc.) species is not taken into account.

Results and Discussion

SEM-EDS

The SEM micrographs in Fig. 1 show the shape and size of the ash particles. Element mapping images of the ash particles in the ashes are given in Fig. 2. Ash A shows typical small (mainly Al, Si, O) and larger (Si, Ca, O) spherical particles of coal fly ash while the Ash B (peat and wood) has irregular particles of various shapes and size. Besides Si and Al, the particles also contain Fe, Ca and K. Ash C from the combustion of peat and wood with dolomite addition consists mainly of irregular rather large particles along with some spheres (Fig. 1).

According to the overall composition analysis of the ashes, the major elements include Al, Ca, Fe, K, Mg, Na, Si. Minor elements are Ba and Ti (see also Fig. 4). It should be pointed out that trace elements are difficult to detect with SEM-EDS. The detection limit is around 1000 ppm depending on the element. The variations in the element concentrations between the parallel samples were low as indicated by the standard deviations of each element analyzed and calculated to oxides (Fig. 4). Thus, although the thickness of the ash particle layer was small, the large surface area used in the EDX analysis gave a reasonable accuracy of the composition of a material consisting of particles of varying size and composition. It should be noted that the carbon tape used to fix the particles on the substrate was partly uncovered and therefore its contribution is seen in the overall analysis of the SEM powder spectra in Fig. 3.

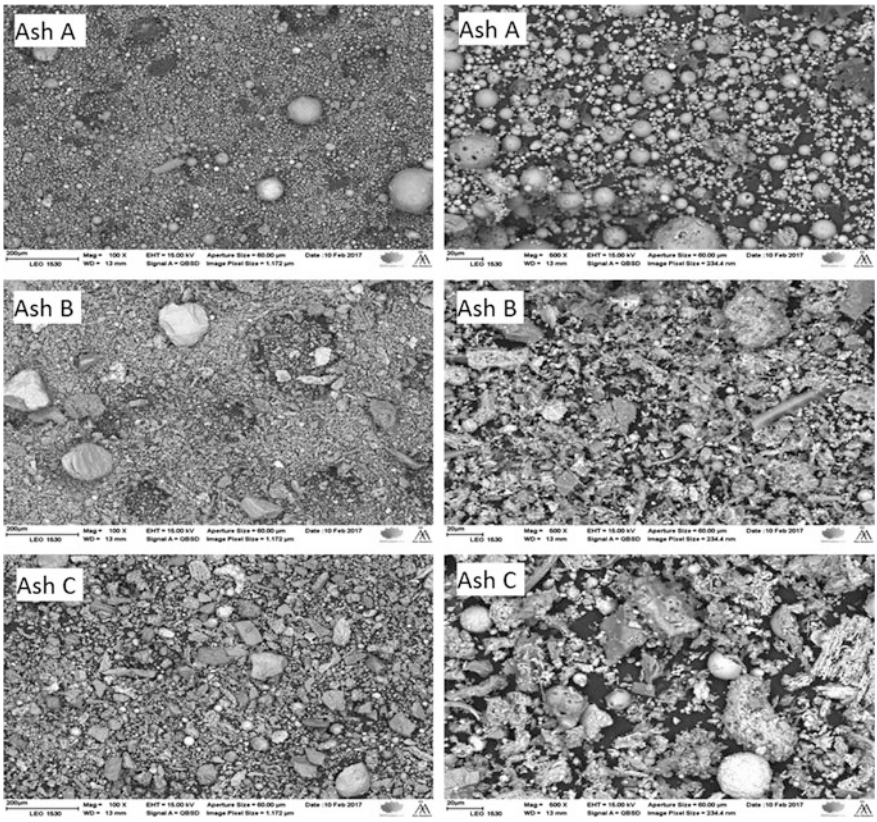

Fig. 1 SEM micrographs of ash A, B, and C

The analyzed elements of five pills and powders of each ash from SEM-EDX were converted to the relevant stable oxide compounds. Then the oxide contents were normalized to 100 by calculating the percentage of each. The normalized oxide composition is shown in Fig. 4. To be able to compare the results from different methods, all ash compositions were normalized. Thus, the impact of organic species could be neglected. In general, the variation of the oxide contents between the five parallel samples was minor, thus suggesting that the pills give a good basis for repeatable SEM analysis of heterogeneous ashes. Although the pills had to be coated with a thin carbon layer, the contribution of carbon is markedly smaller than with powders as shown by the EDX spectra for Ash B analyzed for powder and pills in Fig. 3. According to the CHNS analysis, the total carbon content of the ashes was below 1% Thus, neglecting its contribution to the total composition was justified. On the other hand, the relative carbon content as suggested by the SEM-EDS of the pills gives also appropriate concentrations of the

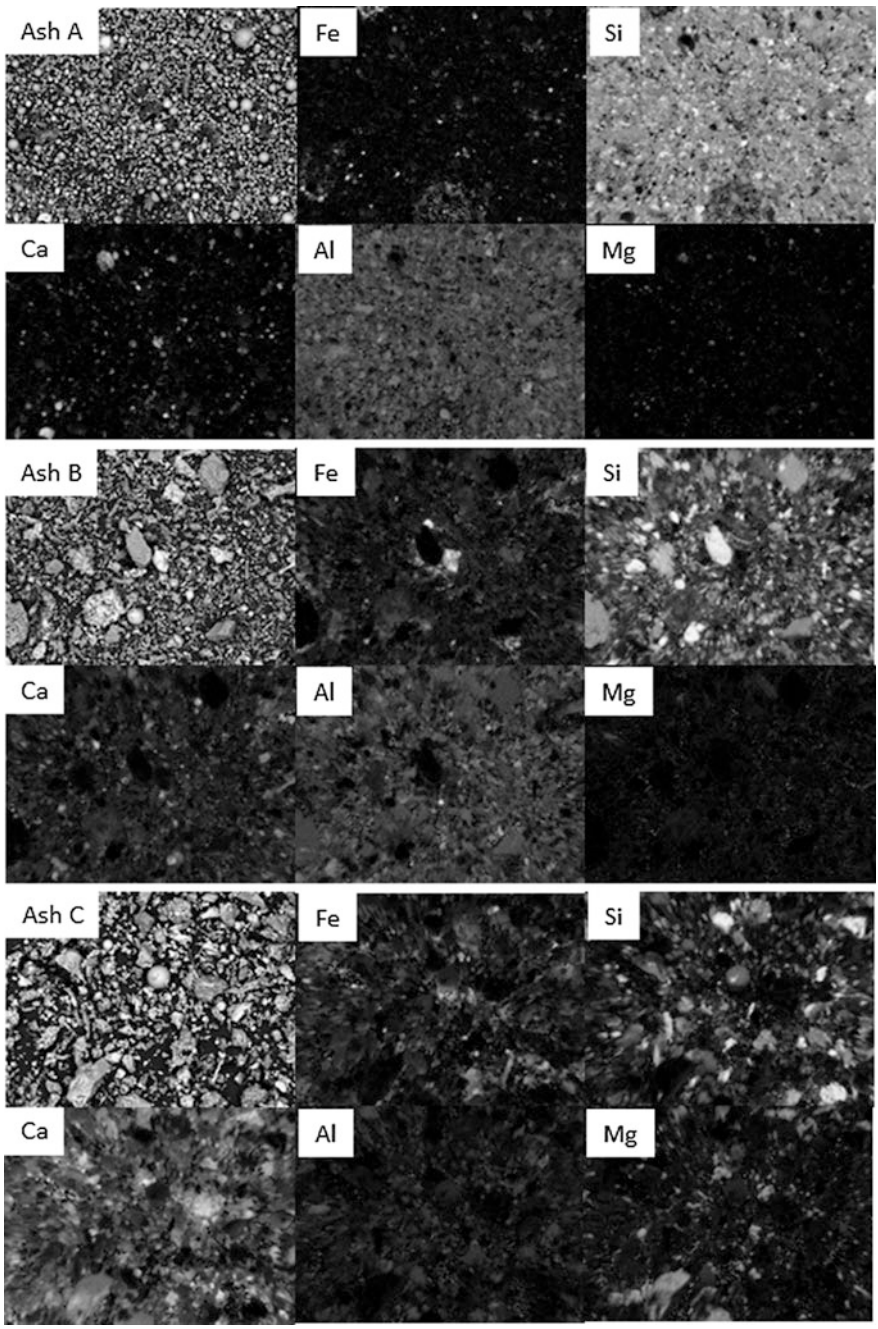

Fig. 2 SEM elemental mapping of the compositions of the particles in the ashes

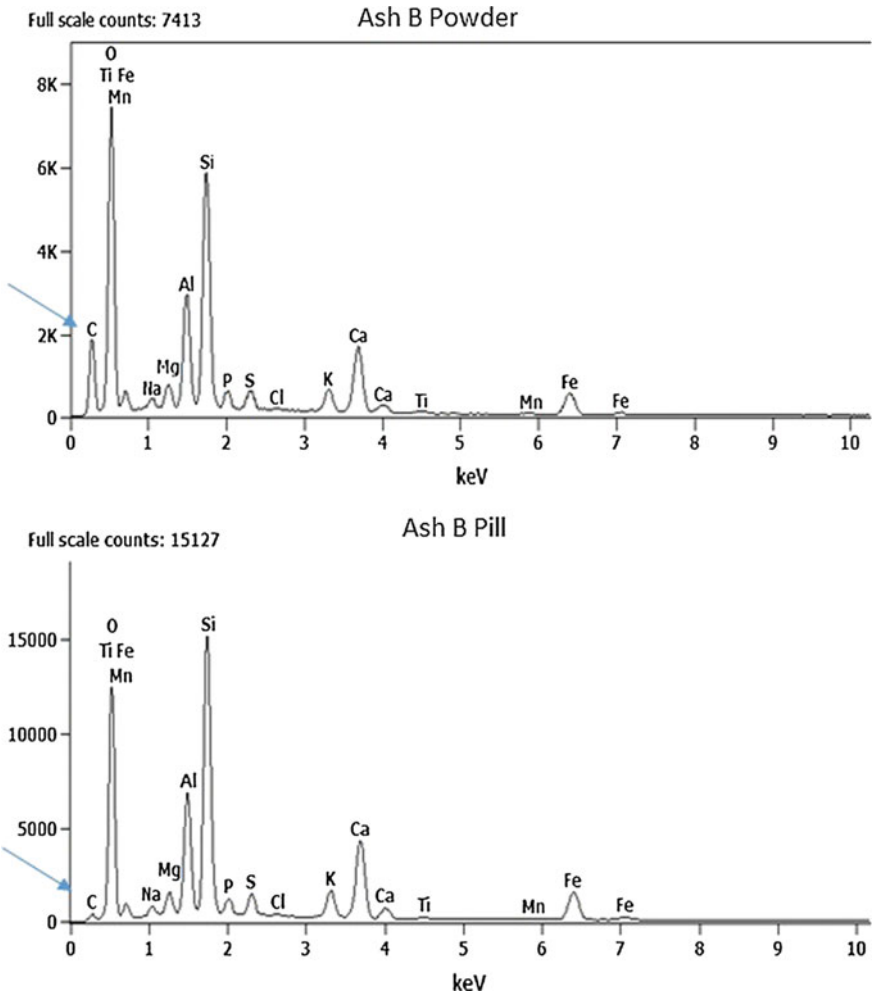

Fig. 3 EDX spectra (counts) of powder (above) and pills of Ash B (below) showing the relative carbon content in the samples. The carbon peak is indicated with an arrow

total carbon content in the sample. Accordingly, the contribution of the carbon coating to the total analysis is minor. When the carbon in the EDS results was neglected, no essential differences were seen between the powder or pill samples (Fig. 4). The minor differences seen for some oxides were assumed to depend on the share of the elements in the particles of various sizes in the sample surface. Larger hard particles may be partly embedded in the finer particles of another composition.

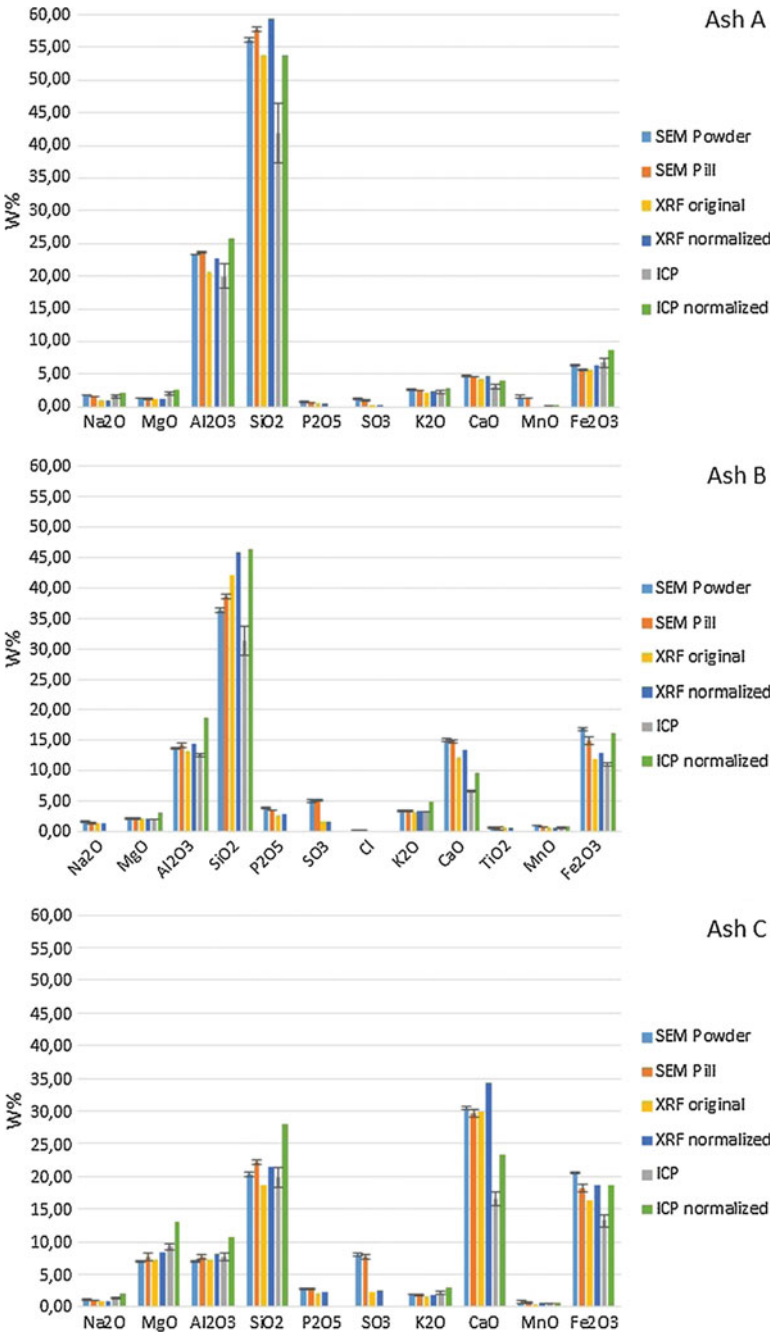

Fig. 4 The composition of the ashes (wt%) using different analysis methods

XRF

Figure 4 compares the oxide compositions calculated from the elemental compositions analyzed using different techniques: SEM of ash powder, SEM of ash pills, XRF of ashes and ICP-OES of dissolved ash solutions. XRF samples consisting of the ash and wax do not give any signal for carbon-containing species but gives concentrations of typical (harmful) trace elements present. The trace elements identified were V, Ni, Cu, Zn, Sn, Pb, Br. SEM-EDS was not able to detect any of the trace elements.

For comparison with the other methods, the concentration of the major and minor elements (excluding Ba) were normalized to 100% of oxides. The oxide composition of the ashes calculated for the measured and normalized values are given in Fig. 4. In general, slightly higher Si contents were measured with XRF than with SEM-EDS. The original values, however, can be used as an indication of the true content of each element, if present as an oxide, in the ash. However, any accurate analysis is possible only through identifying all the compounds present e.g. through appropriate standards for various compounds and/or X-ray diffractometry.

ICP-OES

The ash analysis with ICP-OES requires first a total dissolution of the ash into the highly acidic solution. Some of the elements such as S were likely to partly evaporate during the solution preparation. Moreover, the addition of H_3PO_4 in the solution prevents the P analysis. The concentrations of the other major and minor oxides as suggested by ICP-OES are given in Fig. 4. In the ICP-OES analysis, the trace elements present in the Multistandard 25 used could be identified. The trace elements recorded were V, Cr, Cu, Zn, Pb, As, most of which are the same as suggested by XRF. In this work, we did not use ICP-MS, which would enable a more accurate analysis of the trace elements. In general, comparing the ICP-OES data with the other methods gives very similar trends—given as the relative amounts of the oxides- but the absence of S and P affected the overall analysis. Taking this into account still, suggests that ICP-OES results differed from the composition suggested by SEM-EDS and XRF. Although the ashes appeared to dissolve completely into the acidic solution, incomplete dissolution of some minerals in the ash may affect the result.

Summary

A comparison of different methods for the analysis of the chemical composition of ashes suggests that each method has its own pros and cons.

- SEM-EDS is fairly easy to perform and, with pressed pills, also enables an estimation of the total carbon content. The presence of some trace elements can

be identified. SEM also enables the estimation of the morphology and particle size distribution of the sample.
- In contrast, XRF also enables the analysis of trace elements but fails to give elements lighter than Na. The sample preparation is more laborious than the sample preparation for SEM-EDS.
- ICP-OES requires total dissolution of the solid sample. This extra step may be cumbersome and time-consuming. If the elements to be analyzed are present in the sample in very different concentrations, the detection limits of certain elements may affect the results, especially when performing simultaneous analysis of all the elements. Thus, several dilutions are often needed for one and the same sample. However, when using ICP-OES, and especially ICP-MS, very low concentrations can be detected. This can be of importance for the analysis of harmful trace elements.

Conclusions

Different instrumental techniques were used to analyze the oxide composition of three ash samples. SEM-EDS was suitable as a rapid technique for analyzing the major and minor elements and also to give indications of some trace elements present in the samples. SEM-EDS is thus suitable for overall analyses. XRF successfully gave major, minor and trace elements in the ashes. This method is thus recommended when studying samples, which are likely to contain harmful trace elements. Finally, ICP-OES also enabled the analysis of major, minor and trace elements. However, the preparation of the sample for the analysis, total dissolution of the ash, may be difficult. Also, several dilutions are needed to give an accurate analysis of all the elements present. Thus, the method is laborious and requires, like the two other methods studied, skilled personnel.

Acknowledgements This work is part of the activities of the Johan Gadolin Process Chemistry Center at Åbo Akademi University. The support of Tekes INKA EAKR programme, the industrial partners Renotech Oy, Crisolteq Oy, Nanol Technologies Oy, VG-Shipping Oy, Ecomation Oy, Kierto Ympäristöpalvelut Oy, Mirka Oy is acknowledged. Linus Silvander, Jaana Paananen, and Tor Laurén are thanked for the SEM and XRF analyses.

References

1. Schabbach LM, Andreola F, Barbieri L, Lancellotti I, Karamanova E, Ranguelov B, Karamanov A (2012) Post-treated incinerator bottom ash as alternative raw material for ceramic manufacturing. J Eur Ceram Soc 32:2843–2852
2. Al Bakri MM, Mohammed H, Kamarudin H, Khairul Niza I, Zarina Y (2011) Review on fly ash-based geopolymer concrete without Portland cement. J Eng Technol Res 3(1):1–4

3. Lindberg D, Molin C, Hupa M (2015) Thermal treatment of solid residues from WtE units: A review. Waste Manag 37:85–94
4. Zevenhoven M, Yrjas P, Hupa M (2010) Ash-forming matter and ash-related problems. In: Lackner M, Winter F, Agarwal AK (eds) Handbook of Combustion, Solid Fuels, vol 4. WILEY-VCH Verlag GmbH & Co. KGaA, Weinheim, pp 495–531
5. Enestam S, Boman C, Niemi J, Boström D, Backman R, Mäkelä K, Hupa M (2011) Occurrence of zinc and lead in aerosols and deposits in the fluidized-bed combustion of recovered waste wood. Part 1: Samples from boilers. Energy Fuels 25(4):1396–1404
6. Li N, Vainio E, Hupa L, Hupa M, Coda-Zabetta E (in press) High-temperature corrosion of refractory materials in biomass and waste combustion—Method development and tests with alumina refractory exposed to a K2CO3-KCl mixture. Energy and Fuels
7. Garzon E, Morales L, Martinez-Blanes JM, Sanchex-Soto PJ (2017) Characterization of ashes from greenhouse crops plant biomass residues using X-ray fluorescence analysis and X-ray diffraction. X-ray Spectrometry 1–10
8. Vamvuka D, Kaniadakis G, Pentari D, Alevizos G, Papapolikarpou Z (2017) Comparison of ashes from fixed/fluidized bed combustion of swine sludge and olive by-products. Properties, environmental impact and potential uses. Renew Energy 112:74–83
9. Aboustaita M, Kim T, Ley MT, Davis JM (2016) Physical and chemical characteristics of fly ash using automated scanning electron microscopy. Constr Build Mater 106:1–10
10. Romero E, Quirantes M, Nogales R (2017) Characterization of biomass ashes produced at different temperatures from olive-oil-industry and greenhouse vegetable wastes. Fuel 208:1–9

Utilization CFA-Derived Tobermorite Fiber as Crystallization Revulsive in Autoclaved Concrete Block Production

Pengxu Cao, Jun Luo, Guanghui Li, Yijia Dong, Mingjun Rao and Zhiwei Peng

Abstract Coal fly ash (CFA), as a by-product generated from coal fired power stations, is widely used for autoclaved concrete block production. It has been found that the generation of tobermorite is great benefit to the block strength during autoclaving. In this study, the tobermorite fibers synthesized from CFA and lime via the hydrothermal process are used as the revulsive to promote the mechanic strength of the concrete blocks. The results show that tobermorite fibers with 0.01–0.5 μm in diameter and 1–3 μm in length are obtained at 200 °C for 0.2 h. As the addition of prepared tobermorite fibers increases from 0 wt% to 2.0 wt%, the compression strength of concrete block increases from 24.6 to 40.5 MPa, and the compression strength of aerated concrete block produced under the optimized conditions can reach above 7.5 MPa.

Keywords Coal fly ash · Tobermorite fiber · Autoclaved concrete block Mechanic strength

Introduction

About 1,000 million tons of CFA annually is produced around the world, and the utilization ratio keeps below 50% [1, 2]. This means large amount of CFA is obliged to be discharged into the environment, which brings about series of problems, such as decreasing the agriculture acreage, polluting the atmosphere and ground water, and so on. Owing to the high temperature combustion, CFA is characterized as fine particle size, high pozzolanic activity and rich in silicon- and aluminum-bearing constituents, making it a potential raw material for production of cement, concrete and construction materials [3–7].

P. Cao · J. Luo · G. Li (✉) · Y. Dong · M. Rao · Z. Peng
School of Minerals Processing and Bioengineering, Central South University, Changsha 410083, Hunan, China
e-mail: liguangh@csu.edu.cn

Z. Sun et al. (eds.), *Energy Technology 2018*, The Minerals, Metals & Materials Series, https://doi.org/10.1007/978-3-319-72362-4_23

Utilization of CFA as material for producing autoclaved concrete blocks is a mature technology [6, 7]. The compressive strength, volume-weight and thermal conductivity are considered as the most important indexes of the products, which are associated with tobermorite generation during autoclaving [6, 7]. As has been reported in the literature [8–12], tobermorite is a rare mineral but can be synthesized from various siliceous materials via the hydrothermal method. The synthesized tobermorite was certified to be efficient in the disposal of harmful emissions [8–10], and heat-insulating and fire-resistant materials made from it can meet the standards [11, 12].

To discharge the silicon-based lye obtained from the silicate minerals after alkali-leaching metallic resources, we have synthesized fibrous tobermorite via the hydrothermal method at 240 °C for 3 h with 100 g/L NaOH, Ca/Si 1.0, Ca/Al 5.0 and Ca/Cl 5.0 [13, 14]. Then synthesizing tobermorite fiber from CFA was certified to be feasible in our patent [15], and our recent development found that tobermorite fiber synthesized at the lower temperature for a shorter duration possesses good activity when used as the material for construction materials.

This study extends the knowledge of using the synthesized tobermorite fiber as the crystallization revulsive for producing high-mechanical-performance autoclaved concrete blocks. The specific focus was placed on the optimal revulsive dosage for the autoclaving process, and function mechanism of revulsive on mechanical strength of the autoclaved concrete blocks was illuminated.

Experimental

Materials

Raw materials used in this experiment including CFA, lime, Ordinary Portland Cement (OPC), phosphogypsum (PG) and powdery metallic aluminum, were all taken from Tongling, Anhui province of China. The sodium hydroxide was analytic reagent.

The main chemical compositions of CFA, lime, OPC and PG are listed in Table 1. The morphology of CFA particles, in Fig. 1, shows as solid spheres, hollow spheres and irregular granules. The phase compositions of CFA (in Fig. 2) include quartz (SiO_2), mullite ($3Al_2O_3{\cdot}2SiO_2$) and amorphous substance. The active CaO content in lime tested by hydrochloric titration is 71.94 wt%.

Table 1 Main chemical compositions of raw materials/wt%

Materials	SiO_2	Al_2O_3	CaO	Fe_2O_3	MgO	Na_2O	K_2O	P_2O_5	SO_3
CFA	57.44	34.15	1.62	3.39	0.64	0.24	0.79	0.11	–
Lime	9.60	2.64	83.30	0.64	2.40	–	0.33	0.02	–
OPC	22.87	6.19	63.99	2.31	2.11	–	0.82	0.07	–
PG	10.22	1.63	36.73	–	0.06	0.19	0.47	1.35	48.10

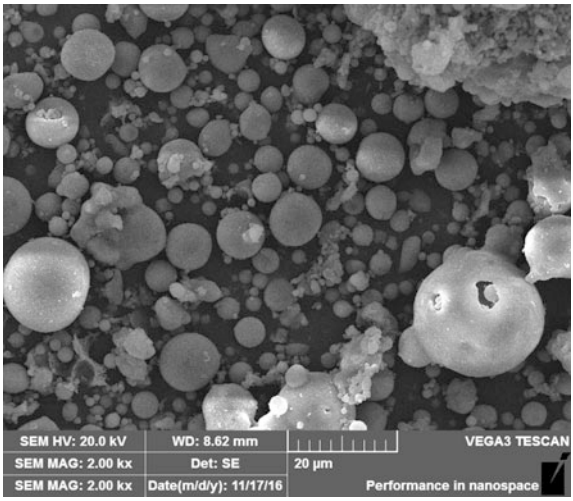

Fig. 1 SEM image of CFA

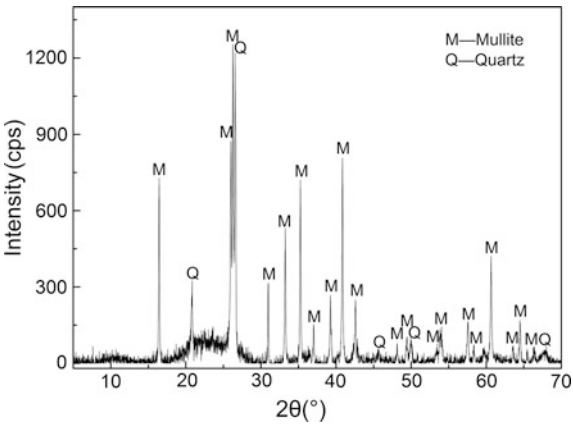

Fig. 2 XRD result of CFA

Methods

Hydrothermal Synthesis

The CFA and fresh slaked lime were mixed under the conditions of Ca/Si molar ratio of 1.0, liquid-solid ratio of 20 mL/g and in the presence of 20 g/L NaOH. Then the mixture was transformed into a 1 L electromagnetic-stirring autoclave and electrically heated with 200 rpm stir. The mixture was kept at 200 °C for 0.2 h, and then it was water-cooled to room temperature. The product was taken out, filtrated, washed with tap-water three times and utilized in the downstream autoclaving procedure.

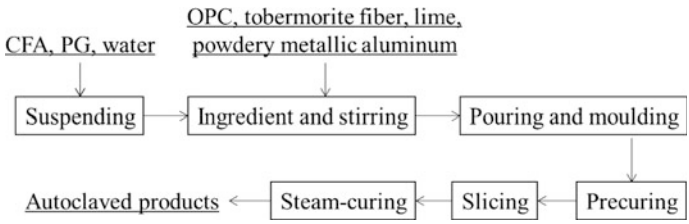

Fig. 3 The autoclaving procedure

Autoclaving Procedure

The autoclaving process was shown in Fig. 3. The suspension was mixed by ball-milling with 58 wt% CFA, 3 wt% PG and 39 wt% water, the fineness was controlled by the overflow of ball mill. The suspension was stirring all the time until it was pumped into the agitating vessel, then 8 wt% OPC, 0–2 wt% tobermorite fiber, 10 wt% lime and 0.085 wt% powdery metallic aluminum were successively added with violent agitation. Then the mixture was poured and moulded within 45 s and sent to be precured. After procuring for 60–90 min, the preformed bodies were sliced and sent to be autoclaved at 185 °C for 5 h. Finally, the autoclave was depressurized and cooled below 55 °C. The obtained autoclaved products were cut into cubes of 10 cm in size for mechanic strength tests.

Characterization

The chemical composition, phase and morphology of the samples were tested by X-ray fluorescence (XRF, Axios mAX, PANalytical, Netherlands), X-ray diffraction (XRD, D500, Siemens, Germany) and scanning electron microscope (SEM, JSM-6360LV, JEOL, Japan), respectively.

Results and Discussion

Characterization of Synthetics Obtained via Hydrothermal Process

It was shown in Fig. 4 that the main phases of the products synthesized from the CFA and lime mixture were tobermorite, portlandite ($Ca(OH)_2$), mullite and quartz. Due to the short treatment time, tobermorite was of poor crystallization in the (002) direction ($2\theta = 7.76°$). The mullite and quartz in CFA were not completely

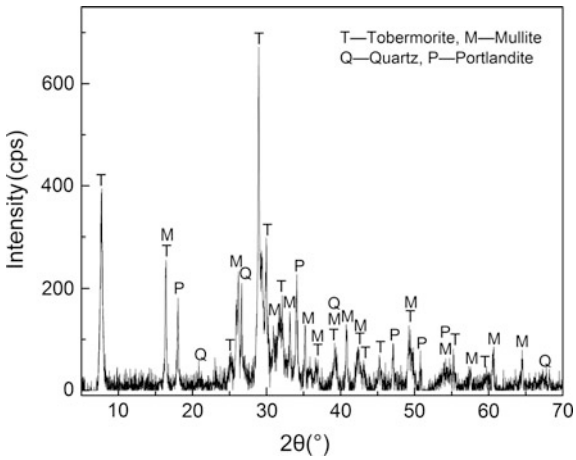

Fig. 4 XRD result of the synthetic

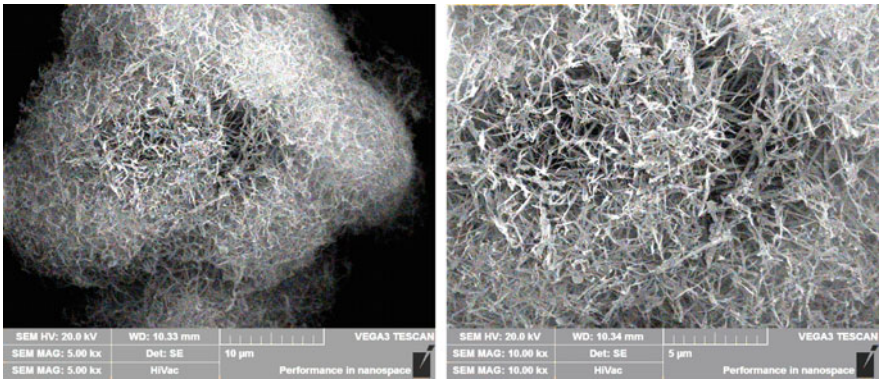

Fig. 5 SEM images of the synthetic

dissolved in the slurry and the redundant Ca^{2+} was transformed into potlandite ($Ca(OH)_2$). Morphology of the synthetics was shown in Fig. 5, tiny tobermorite fibers with 1–3 μm in length and 0.01–0.5 μm in diameter and assembled as spherical particles with 30–50 μm in diameter were obtained.

As the binder of autoclaved concrete blocks [7], the generation of tobermorite is advantageous to the mechanical performance of the products. The synthesized tobermorite fiber is of small crystal size that possesses large specific surface area, which is fittingly used as the crystallization revulsive in concrete block production via the autoclaving process.

Effect of Crystallization Revulsive on Autoclaved Concrete Blocks

Effect of Revulsive on Autoclaved Concrete Blocks

The effect of revulsive dosage on compressive strength and volume-weight of the autoclaved concrete blocks was shown in Fig. 6. The compressive strength of autoclaved concrete blocks was improving with the increasing revulsive dosage, and it was enhanced rapidly when the dosage was below 1.0 wt%, yet the enhancement was slowed down as the revulsive usage increased above 1.0 wt%. While the volume-weight of the products was continuously enhancing with the increasing revulsive dosage from 0 to 2.0 wt%. Therefore the suitable revulsive dosage is recommended as 1.0 wt%. Contrast with production without revulsive addition, the compressive strength of the products increased from 24.6 to 40.3 MPa when 1.0 wt% was added, the corresponding volume-weight increased from 1564 to 1650 kg/m^3, and the enhancement ratio increased 63.82% and 5.50%, respectively.

Effect of Revulsive on Autoclaved Aerated Concrete Blocks

As can be obtained from Fig. 6 that with addition of revulsive, the compressive strength of autoclaved concrete blocks was improving from 24.6 to 40.5 MPa as the revulsive dosage increased from 0 to 2.0 wt%. And similar improvement was observed from Fig. 7, the compressive strength of autoclaved aerated concrete

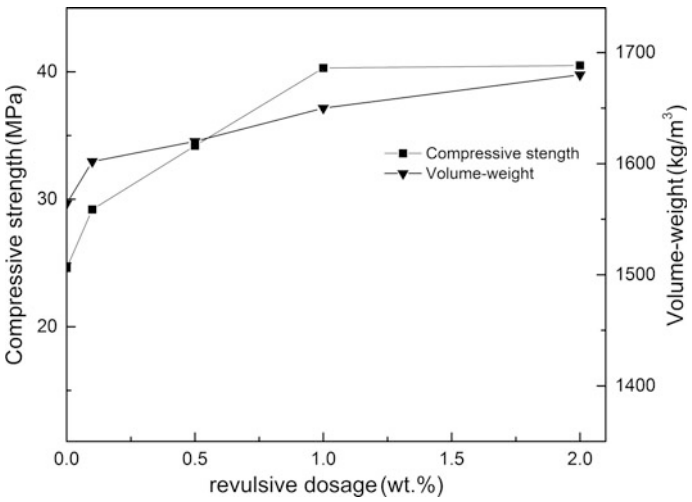

Fig. 6 Effect of revulsive dosage on autoclaved concrete blocks

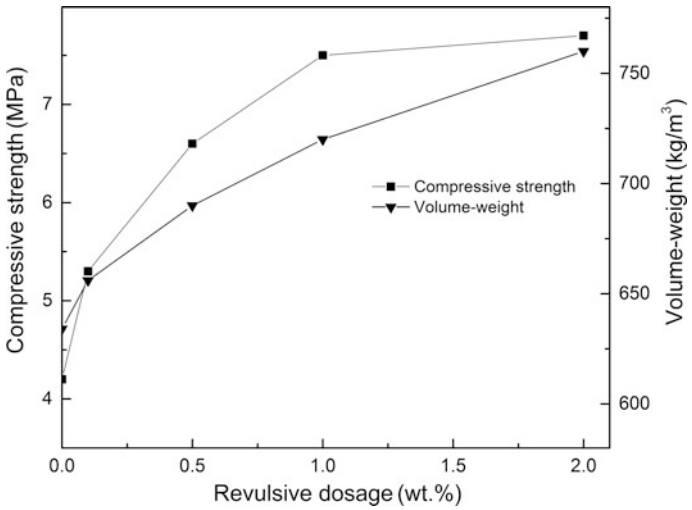

Fig. 7 Effect of revulsive dosage on autoclaved aerated concrete blocks

blocks was improved from 4.2 to 7.8 MPa with revulsive addition increasing from 0 to 2.0 wt%. The compressive strength increased obviously when the revulsive dosage was below 1.0 wt% and leveled off when the revulsive dosage increased above 1.0 wt%, while the volume-weight of autoclaved aerated concrete blocks was increasing with the increased revulsive dosage all the time. Therefore the optimal revulsive addition is recommended as 1.0 wt%, and the corresponding compressive strength of autoclaved aerated concrete blocks reaches 7.5 MPa with the volume-weight of 700–725 kg/m^3 under laboratory conditions, which meets A7.5 grade of the Chinese national standard.

Mechanism on Strength Improvement of Autoclaved Concrete Blocks

The phase composition and morphology of the autoclaved products with and without adding 1.0 wt% tobermorite fiber were shown in Figs. 8 and 9, respectively. The main phases of the product obtained without revulsive addition were quartz, mullite and katoite. When 1.0 wt% revulsive was added, tobermorite was generated and the katoite peaks were enhanced, and the quartz and mullite diffraction peaks were weakened simultaneously.

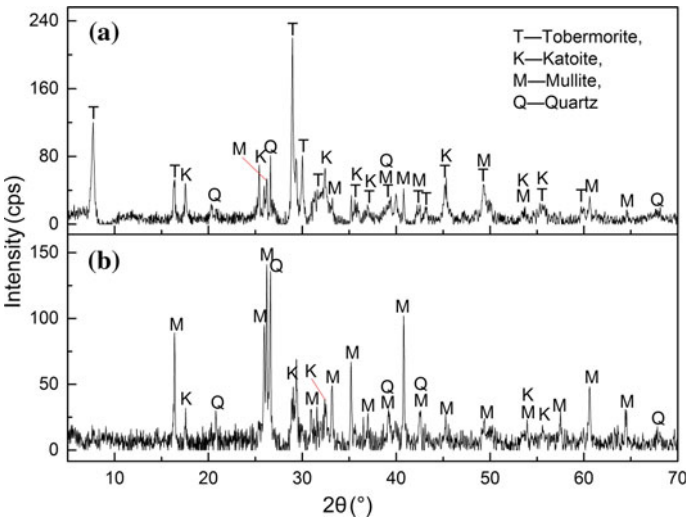

Fig. 8 Effect of revulsive utilization on phase species of the products **a**—none revulsive addition; **b**—1.0 wt% revulsive addition

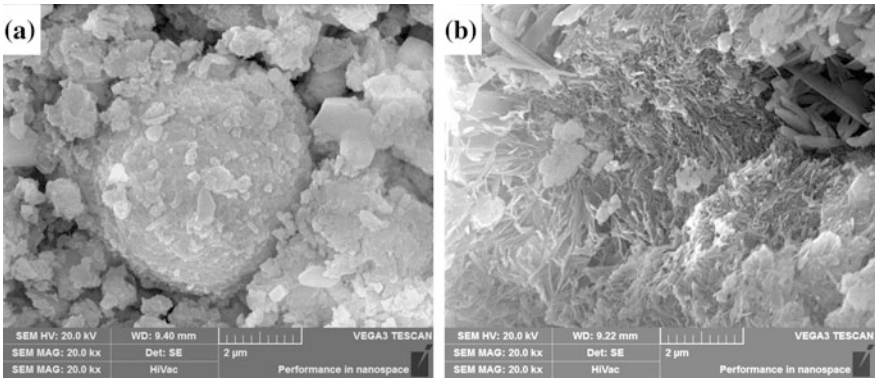

Fig. 9 Effect of revulsive utilization on microstructure of the products **a**—none revulsive addition; **b**—1.0 wt% revulsive addition

Morphology of the autoclaved products was unconnected tiny particles without revulsive addition, it was transformed into the interconnected fibers when 1.0 wt% revulsive was added. This is because the hydration of silicon-bearing components in CFA was accelerated and the generation of tobermorite fibers was promoted when crystallization revulsive was used, thus the compressive strength of the products was heightened.

Conclusions

This study was dedicated to use tobermorite fiber as crystallization revulsive to improve the mechanic strength of the autoclaved concrete blocks, and therefore promoting the comprehensive utilization of CFA in construction materials. The compressive strength of autoclaved concrete blocks and autoclaved aerated concrete blocks enhanced 63.82% and 85.71% when 1.0 wt% tobermorite fiber was added as the crystallization revulsive during the autoclaving process, and the volume-weight of the materials just increased 5.50% and 13.56%, respectively. The results showed that adding tobermorite fiber is beneficial to tobermorite generation during the autoclaving process. Additional work is underway to optimize the ratio of ingredients and enhance the mechanical performance of the blocks further.

Acknowledgements The authors wish to express their thanks to the National Natural Science Foundation of China (Nos. 51234008 and 51174230) for the financial support of this research. This work was also financially supported by Co-Innovation Center for Clean and Efficient Utilization of Strategic Metal Mineral Resources.

References

1. Blissett RS, Rowson NA (2012) A review of the multi-component utilization of coal fly ash. Fuel 97:1–23
2. BP Statistical Review of World Energy (2007). http://www.bp.com/content/dam/bp/en/corporate/pdf/energy-economics/statistical-review-2017/bp-statistical-review-of-world-energy-2017-full-report.pdf. Accessed June 2017
3. Bentz DP, Ferraris CF, Varga IDL, Peltz MA, Winpigler J (2010) Mixture proportioning options for improving high volume fly ash concretes. Int J Pavement Res Tech 3:234–240
4. Bentz DP, Hansen AS, Guynn JM (2011) Optimization of cement and fly ash particle sizes to produce sustainable concretes. Cem Concr Compos 33:824–831
5. Donatello S, Palomo A, Fernández-Jiménez A (2013) Durability of very high volume fly ash cement pastes and mortars in aggressive solutions. Cem Concr Compos 38:12–20
6. Naganathan S, Mohamed AYO, Mustapha KN (2015) Performance of bricks made using fly ash and bottom ash. Constr Build Mater 96:576–580
7. Çicek T, Çinçin Y (2015) Use of fly ash in production of light-weight building bricks. Constr Build Mater 94:521–527
8. Coleman NJ, Brassington DS, Raza A, Mendham AP (2006) Sorption of Co^{2+} and Sr^{2+} by waste-derived 11 Å tobermorite. Waste Manag 26:260–267
9. Reinik J, Heinmaa I, Kirso U, Kallaste T, Ritamäki J, Boström D, Pongrácz E, Huuhtanen M, Larsson W, Keiski R, Kordás K, Mikkola JP (2011) Alkaline modified oil shale fly ash: Optimal synthesis conditions and preliminary tests on CO_2 adsorption. J Hazard Mater 196:180–186
10. Tsutsumi T, Nishimoto S, Kameshima Y, Miyake M (2014) Hydrothermal preparation of tobermorite from blast furnace slag for Cs^{+} and Sr^{2+} sorption. J Hazard Mater 266:174–181
11. Ding J, Tang Z, Ma S, Wang Y, Zheng S, Zhang Y, Shen S, Xie Z (2016) A novel process for synthesis of tobermorite fiber from high-alumina fly ash. Cem Concr Compos 65:11–18
12. Chen M, Lu L, Wang S, Zhao P, Zhang S (2017) Investigation on the formation of tobermorite in calcium silicate board and its influence factors under autoclaved curing. Constr Build Mater 143:280–288

13. Li G, Zhang J, Luo J, Chen H, Zeng J, Jiang T (2012) Preparation of tobermorite whisker from sodium silicate solution. J Chin Ceram Soc 40:1721–1727 (In Chinese)
14. Luo J, Li G, Jiang T, Peng Z, Rao M, Zhang Y (2016) Conversion of coal gangue into alumina, tobermorite and TiO_2-rich material. J Cent South Univ 23:1883–1889
15. Li G, Jiang T, Peng Z et al (2016) A method of synthesizing tobermorite fibers using coal fly ash as raw material. Chinese patent: CN 105780121A, 20 Juy 2016 (in Chinese)

An Electrochemical Procedure for Copper Removal from Regenerated Pickling Solutions of Steel Plants

Esra Karakaya, Mustafa Serdal Aras, Metehan Erdoğan, Sedef Çift Karagül, Merve Kolay Ersoy and İshak Karakaya

Abstract Pickling is the treatment of metal surfaces by removing oxide layer, rust, scale, inorganic contaminants or other impurities from ferrous metals, copper or precious metals. A strong inorganic acid such as hydrochloric acid is used for plain carbon or low alloy steel pickling. When the concentration of copper in the pickling solution exceeds about 100 mg/L, reversion may take place and randomly plating of copper onto the steel strips which causes visual incompatibility occur. Furthermore, efficiency of pickling decreases with the increase of copper content. The reversion may be delayed to higher Cu concentrations by adding fresh acid to the line. Increased acid consumption only delays the time to discard the solution but increases the cost and hazardous nature effect on the environment. An experimental electrochemical procedure has been conducted to remove copper from pickling solution to reduce the concentration below 100 mg/L. Within this scope, effects of applied current density, copper concentration and electrolysis duration on copper

E. Karakaya (✉) · İ. Karakaya
Department of Metallurgical and Materials Engineering, Middle East Technical University, Üniversiteler Mahallesi, Dumlupınar Bulvarı no:1, 06800 Ankara, Çankaya, Turkey
e-mail: esra.karakaya@metu.edu.tr

İ. Karakaya
e-mail: kkaya@metu.edu.tr

E. Karakaya · M. S. Aras
MEGAP Co., ODTÜ Teknokent Gümüş Blok (a) no:15-a, 06800 Ankara, Çankaya, Turkey
e-mail: aras.mustafa.s@gmail.com

M. Erdoğan
Department of Metallurgical and Materials Engineering, Yıldırım Beyazıt University, Esenboğa Mah. Atatürk Cad, 06760 Ankara, Çubuk, Turkey
e-mail: metehanerdogan@ybu.edu.tr

S. Ç. Karagül · M. K. Ersoy
Borusan Technology Department and R & D Co., Büyükhanlı Plaza Defne Sok. no:3, 34758, İstanbul, Ataşehir, Turkey
e-mail: sckaragul@borusan.com

M. K. Ersoy
e-mail: mkersoy@borusan.com

Z. Sun et al. (eds.), *Energy Technology 2018*, The Minerals, Metals & Materials Series, https://doi.org/10.1007/978-3-319-72362-4_24

deposition were studied. Current density was determined as the most effective parameter to remove copper from the regenerated pickling solutions of steel plants.

Keywords Pickling solution · Copper · Electrochemical treatment
Environmental treatment · Current density

Introduction

Surface treatment of metals involves plating, galvanizing, anodizing, painting, heat treating, and many other operations. Degreasing, cleaning, pickling, and etching are processes used to prepare metal surfaces for subsequent surface treatment processes. Pickling is a chemically cleaning process employing strong inorganic acids [1], used to get rid of oxide layer, rust, scale, inorganic contaminants or other impurities coming from ferrous metals, copper or precious metals [2]. Very large amount of acid is spent during the pickling process. The spent pickling acid contains dissolved metals and metal salts. In order to purify the acid, regeneration process is carried out.

In the regeneration process, the spent acid is cleaned from its impurities except for copper ion. When this copper waste ion concentration exceeds the level of 100 mg/L, in hydrochloric acid used in this study at 60–80 °C, the copper starts to plate indiscriminately onto the steel. It was detected that the copper ion in the solution comes from the steel itself. During the production of steel, especially from scrap, little amount of copper is infused in the iron and this copper cannot make alloy with the iron so it remains free in the structure. Hence copper from the steel quickly dissolves in the acid, because it is highly soluble in hydrochloric acid, during the pickling process.

There are many mills that add new fresh acid to the line to delay the problem. But this action is not economical and cause environmental concerns. Removal of copper from pickling solution can be considered as an alternative to reduce acid consumption. Use of a consumable copper precipitant, ion exchange, electroplating or other relevant technology may be considered for this purpose.

Recently, there is a rising attention in the effective electrochemical methods for the removal of metal ions from waste solutions [3, 4]. Although it is possible to recover metal ions from dilute solutions by using ion exchange or other methods employing organics, the use of electrochemical process may be considered advantageous, because it doesn't need any other consecutive application [5, 6].

Electrochemical removal of copper from 30% HCl containing regenerated pickling solution at 60 °C was performed to reduce copper level below 100 mg/L. The recovery of valuable metallic copper product and possible extension of the life of pickling solution was aimed to answer economical and environmental concerns.

Experimental

Experimental tests were conducted in the laboratory. The electrochemical reactor used in this study was composed of a 300 ml Pyrex glass beaker, which was closed by a polypropylene cover at the top. A graphite anode and a copper cathode were installed into the reactor as electrodes. Anode was made of cylindrical graphite bar and cathode was made of copper foil of 0.5 mm thickness. Both anode and cathode had 5 cm^2 effective areas. The experiments were held at a constant temperature of 60 °C. A schematic drawing of the electrochemical test apparatus is shown in Fig. 1. Effects of current density, electrolysis duration and copper concentration on copper deposition were studied.

The electrochemical reactor was operated at a constant current mode. The applied current density values were changed from 0.005 to 0.02 A/cm^2. The values were chosen in this range in order to apply similar electrode potential values as realized from the linear sweep voltammetry measurements. The electrolysis experiments were done using Agilent B2901A power supply. Experiments were performed for 2–6 h durations. Liquid samples and deposited cathode samples were collected after each experiment to determine the mass of copper removed from the pickling solution.

The pickling solution that contained 85 mg/L copper was delivered by Borcelik Inc. As copper cementation was observed on the steels when the copper amount in the pickling solution was above 100 mg/L, the copper content of the stock solution was increased by dissolving appropriate amount of $CuCl_2$ powder. Therefore, experiments were performed in pickling solutions containing 85 to 154 mg/L copper. The extent of copper removal was determined by chemical analysis and by gravimetry. Chemical analyses were performed by Inductively Coupled Plasma—Mass Spectrometer (ICP-MS).

Three levels of parameters; applied current density, electrolysis duration and initial copper concentration were used in the full factor analysis using Minitab® Statistical Software [7] to determine experimental routes shown in Table 1.

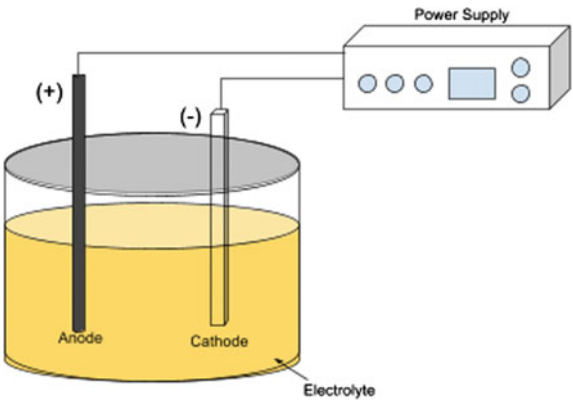

Fig. 1 The schematic drawing of experimental apparatus for The electrochemical tests

Table 1 Experimental routes determined by full factor analysis and averages of gravimetric and ICP-MS analysis results on the amount of Copper removal from 300 ml pickling solution

Run order	Copper concentration (mg/L)	current density (A/cm^2)	Duration (hour)	Average (g)
1	154	0.020	4	0.02010
2	85	0.010	6	0.00087
3	127	0.010	6	0.00586
4	85	0.020	2	0.00923
5	154	0.005	6	−0.01049
6	127	0.020	2	0.00045
7	127	0.010	4	0.01462
8	154	0.010	2	0.00114
9	85	0.010	4	−0.00434
10	85	0.005	4	0.00578
11	154	0.005	4	0.00282
12	154	0.005	2	0.00005
13	85	0.020	6	0.01551
14	85	0.010	2	−0.00402
15	127	0.005	6	0.00851
16	85	0.005	2	−0.00105
17	154	0.010	4	0.00673
18	127	0.010	2	0.00574
19	127	0.020	4	0.00609
20	127	0.005	2	0.00365
21	154	0.020	6	0.02567
22	154	0.020	2	0.00756
23	127	0.020	6	0.00468
24	85	0.005	6	0.00029
25	85	0.020	4	0.00192
26	154	0.010	6	0.01446
27	127	0.005	4	−0.00793

Results and Discussion

The gravimetric results were obtained from the difference between the weight of copper foil cathode before and after each experiment. In addition, the initial and final ICP-MS analysies of solutions were used to determine copper removal for all experiments. Effects of current density, copper concentration and electrolysis duration were evaluated.

Current density is the amount of electrical current passing through a unit area. The range of applied current density was from 0.005 to 0.02 A/cm^2 to make a detailed discussion. The initial copper concentrations of the pickling solution were 85–154 mg/L. The electrolysis duration of the experiments were 2–6 h.

The averages of gravimetric and ICP-MS analysis results on the amount of copper removal from 300 ml pickling solution are given in Table 1 for each experiment. The data were used to construct Fig. 2 to show main effects of current density, initial copper concentration and the duration of electrolysis on the amount of copper removal. The graphical representation was obtained by using Minitab® Statistical Software.

Minitab® is a statistical software that helps to analyze data. By using full factorial design, a chart and a run order were created for the experiments due to the variables that were given by the executer. After performing the experiments, the results were written to the chart and the graphs and performed statistical analyses were created by the software. With the help of this software, results for the test conditions can be predicted without performing any new experiments.

The main effects graphics were chosen to drive statistical conclusions on the effects of parameters on the small amount of copper collected from the solution. Each graph shown in Fig. 2 was constructed by Minitab® Statistical Software using the results of all 27 experiments given in Table 1. They were plotted against three different experimental parameters. Since three parameters had three levels, each point on these graphs was the average value of 9 experiments of that level of the parameter.

It can be seen from Fig. 2 that the copper removal was not possible when current density was 0.005 A/cm^2. Further increase in current density increased copper removal from the pickling solution. Furthermore, copper removal was increased with increase in electrolysis duration.

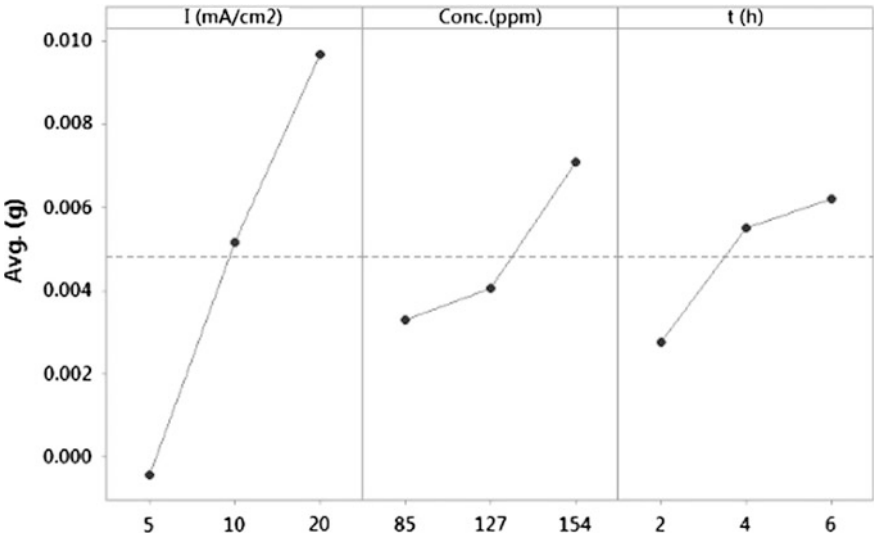

Fig. 2 The main effects of current density, initial Copper concentration and duration of electrolysis on the amount of Copper removal from 300 ml pickling solution

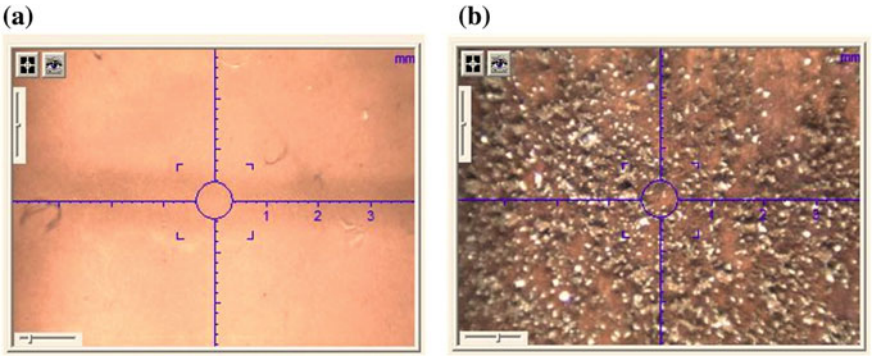

Fig. 3 XRF images of surface morphology of electrodeposited Copper foils at **a** 0.01 A/cm^2 current density for 2 h and **b** 0.02 A/cm^2 current density for 2 h

It was observed that the deposited copper layers were more compact for 0.01 A/cm^2 current density than 0.02 A/cm^2 and there were powdered electrodeposition at higher current density values. Figure 3a, b shows the XRF images of surface morphologies of electroplated copper foils from 154 mg/L copper containing regenerated pickling solutions at 0.01 and 0.02 A/cm^2 current densities respectively. The powdered accumulation was increased with increasing electrolysis duration. Figure 4a, b shows the effect of electrolysis duration at 0.02 A/cm^2 current density after 2 and 6 h of electrolysis. The deposited layer was found to contain 99.9% Cu together with 0.1% Fe as determined by Fischerscope X-Ray XDV-SDD 604-447, XRF.

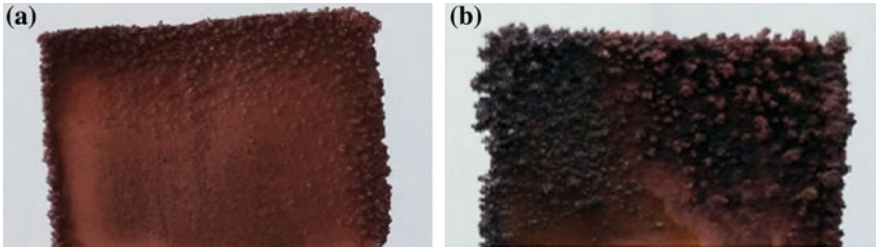

Fig. 4 Pictures of cathodes showing the effect of electrolysis duration at 0.02 A/cm^2 current density after **a** 2 h and **b** 6 h of electrolysis

Conclusion

Based on the laboratory studies the current density parameter was more influential on the copper removal from the regenerated pickling solutions of steel plants.

In order to have a sleekier morphological electrodeposition and not to loose the collected copper, less than 0.02 and more than 0.005 A/cm^2 current density is more feasible.

Longer electrolysis duration results in the more copper collection as expected.

Increase in initial copper concentration increases the amount of copper collection, but final concentration after copper removal increases with increased initial concentration as expected.

Copper removal from dilute pickling solution by electrolysis technique is a promising and environmentally friendly method for steel plants.

Acknowledgements Authors express their gratitude to Borusan Technology Department and R&D Co. for the economical support in the project.

References

1. Agrawal A, Kumari S, Sahu KK (2009) Iron and copper recovery/removal from industrial wastes. Metal Extraction and Forming Division, National Metallurgical Laboratory, India
2. Devi A, Singhal A, Gupta R (2013) A review on spent pickling liquor. Int J Environ Sci 4
3. Spitzer M, Bertazzoli R (2004) Selective electrochemical recovery of gold and silver from cyanide aqueous effluents using titanium and vitreous carbon cathodes. Hydrometallurgy 74(3–4):233–242
4. Kim EY, Kim MS, Lee JC, Jha MK, Yoo K, Jeong J (2008) Effect of cuprous ions on Cu leaching in the recycling of waste PCBs, using electro-generated chlorine in hydrochloric acid solution. Miner Eng 21(1):121–128
5. Kanzelmeyer TJ, Adams CD (1996) Removal of copper from a metal-complex dye by oxidative pretreatment and ion exchange. Water Environ Res 68(2):222–228
6. Fernando K, Tran T, Laing S, Kim MJ (2002) The use of ion exchange resins for the treatment of cyanidation tailings Part 1—Process development of selective base metal elution. Miner Eng 15(12):1163–1171
7. Minitab 17 Statistical Software (2017). [Computer software]. State College, PA: Minitab, Inc. www.minitab.com

Upgrading the Copper Value in a Waste Copper Smelter Dust with the Falcon Gravity Concentrator

D. O. Okanigbe, A. P. I. Popoola, A. A. Adeleke and O. M. Popoola

Abstract The physical, chemical, mineralogical and morphological characteristic of the waste copper smelter dust (CSD) from Palabora Copper (PTY), Limpopo, South Africa, has been reported in the open literature. The bulk of this material falls within the −53 μm particle size fraction with a copper weight percent of 18.02 as determined with the XRF. The high presence of reactive gangue minerals such as mullite (42.97 wt%) and quartz (11.45 wt%) necessitates that the waste CSD be first upgraded of its copper value in the falcon gravity concentrator before subsequent hydrometallurgical treatment. As an initial step, a sample preparation was carried out to make the sample amenable to both real density determination and copper upgrade experiment, thus resulting in 97% of the particles passing the 300 μm sieve aperture (d_{97} = 300). The laser particle size analyzer (LPSA) was used to analyze the d_{97} = 300 and the results showed a %change from 90.82% to 95.59%, with a real density of 2.830 for the waste CSD. The result of the copper upgrade showed that test 8 with treatment combination of 80 rpm and 4.5 l/min gave the highest % copper grade of 1.37 which is still less than the %grade of copper in the feed (1.49%). It thus lead to the recommendation that another type of centrifugal separator that will allow the introduction of the feed as slurry so that the pulp density

D. O. Okanigbe (✉) · A. P. I. Popoola
Department of Chemical Metallurgical and Materials Engineering,
Tshwane University of Technology (TUT), Pretoria 0183, South Africa
e-mail: okanigbedo@tut.ac.za

A. P. I. Popoola
e-mail: PopoolaAPI@tut.ac.za

A. A. Adeleke
Department of Materials Science and Engineering,
Obafemi Awolowo University, Ile-Ife 220002, Nigeria

O. M. Popoola
Centre for Energy and Electric Power (CEEP),
Tshwane University of Technology (TUT), Pretoria 0183, South Africa
e-mail: popoolao@tut.ac.za

Z. Sun et al. (eds.), *Energy Technology 2018*, The Minerals, Metals & Materials Series, https://doi.org/10.1007/978-3-319-72362-4_25

and feed rate can factored into the whole upgrade experiment, consequently reducing the significant amount of losses and the chances of an improved grade and recovery of copper from this waste CSD.

Keywords Fine gravity method · Waste copper smelter dust · Characterization EPS · Slurry · Mass balance

Introduction

The metallurgical industries produce huge quantities of different types of wastes such as the electric arc furnace (EAF) dust, basic oxygen furnace (BOF) sludge, jarosite residue and dust of secondary copper smelting [1, 4, 14].The loss of copper in form of waste copper smelter dust (CSD) during copper smelting is put at 5–10% [3]. On the basis of this value, no less than one million tons of these wastes have been produced in China per year [5], while at the Palabora copper (PTY), Limpopo, South Africa an annual average dust deposition at the smelter, vermiculite operation plant and Phalaborwa town, between 23rd of June 2009 to 23rd of June 2010 of 77,223.09 mg/m^2/annum of CSD was calculated [8]. At present, the disposal of metallurgical wastes such as waste CSD is becoming costly owing to increasingly stringent environmental regulations [6], because the physical and chemical nature of waste CSD (such as the content of heavy metals) causes it to be classified as hazardous waste [13]. In South Africa, the South African National Standard (SANS) annual target level of dust is 300 mg/m^2/day and the industrial action level of dust is reported to be 1200 mg/m^2/day [15].

In view of the above, there has been an increasing interest in developing processes for the recovery of metal value from this waste [11]. But existing process options for metal recovery are higher with respect to capital and operating costs than revenue from the recovered metal [16]. It becomes necessary to investigate a processing method by which contaminants could be separated from the metal value in the waste CSD, while maintaining an acceptable level of revenue metals in the resultant concentrate. In addition, it would be profitable if this could be done in an economic manner so as to justify the treatment of stockpiled dust [12]. Mineral processing techniques can be used to reduce/remove impurities in the waste CSD, prior to it being subjected to hydrometallurgical processing [2]. Since, it is expected to serve the purpose of upgrading its contained value metal(s), at the barest minimal slimes loss. Furthermore, as a requirement for effective separation is a marked difference in specific gravity between minerals contained in the waste CSD as reported in the open literature by [10], according to the authors a clear difference in Specific gravity (S.G.) exists between some of the minerals contained in the waste CSD; a good example is Tenorite (S.G. = 6.50) and Arsenolite or Gunningite (3.20 and 3.87 respectively); for which separation is possible as it satisfies the concentration criterion (CC), which is essential for effective separation; expressed mathematically as follows:

$$\frac{D_1 - D_3}{D_2 - D_3} > \pm 2.5 \quad (1)$$

Where D_1 is the specific gravity of the heavy mineral, D_2 is the specific gravity of the light mineral, and D_3 is the specific gravity of medium which is more often than not water [16]. But with the average size of this dust falling within the size range of 5–50 μm [3], [7], [9] and, [10] only the modern gravity techniques (Knelson and Falcon concentrators) have proven to be efficient for beneficiation of materials in this particle size range of up to 50 μm [16].

In the light of the above, this study is aimed at using the Falcon gravity concentrator (FGC) to upgrade the copper value in the −300 μm waste copper smelter dust (CSD) from Palabora Copper (PTY) Ltd (PC), Limpopo, South Africa prior to a hydrometallurgical treatment [17].

Material and Method

Ore Handling and Sampling

The copper smelter dust (CSD) used in this study was obtained from Palabora Copper (PTY) Ltd (PC), Limpopo, South Africa. The dust was collected over a 7-day period during the smelting operation from the electrostatic precipitator (EPS) attached to the reverberatory furnace. Exactly 120 kg of the waste CSD was received from the contact person at the mines, which was confirmed at the mineral processing and extractive metallurgy laboratory at the Tshwane University of Technology, Pretoria, South Africa. The as-received waste CSD sample was first re-weighed and subsequently homogenized by subjecting it to coning and quartering sample preparation method; after which, aliquot samples were derived from the homogenized CSD sample, using a riffle splitter, to be used for subsequent work in the course of this study.

From the aliquot samples produced, the 300 μm sieve was used to separate the waste CSD into two portions, the undersized and oversized particles. The oversize was subjected to grinding to further reduce the particles in order to eliminate the effect of porosity and particle size on the real density test and gravity separation experiment respectively. The ground oversized waste CSD was sieved with the 300 μm sieve again to produce undersized particles which were mixed with the previously produced undersize CSD, thus forming the −300 μm waste CSD (d_{97} = 300), used for this study. The laser diffraction particle size analyzer (LDPSA) was then used to ascertain the reduction/removal of particle size distribution on the sample preparation. The results can be seen in Table 3 and Fig. 1.

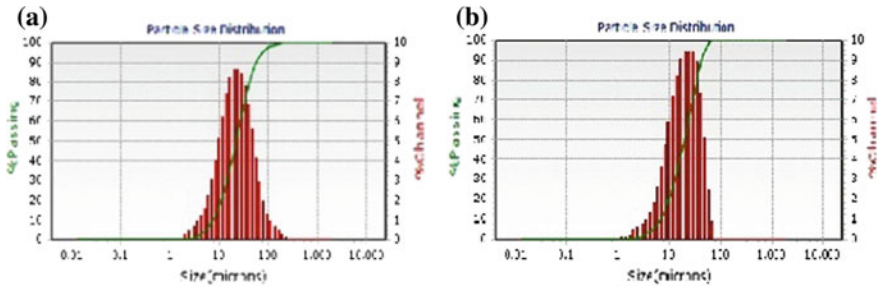

Fig. 1 Particle size distribution of **a** Homogenized waste CSD **b** milled Homogenized waste CSD

Moisture Content Determination

The moisture content of the sample was determined prior to subsequent study of the waste CSD. The determination of the surface moisture was done by placing 1 g of the waste CSD into three pre-weighed porcelain crucibles, which were (porcelain crucibles + CSD) reweighed and were subsequently placed in the open to be air dried for 48 h. At the end of this period the three sets of porcelain crucibles plus waste CSD were re-weighed and the mass recorded, the results can be seen in Table 4.

Density Determination

A number of pycnometers were tested simultaneously and one validation sample of silica material (SICER) was run in parallel with the real density measurements carried out and these results were added and compared with previous results in the proficiency file. The ambient temperature in the laboratory was recorded (24 °C).

The empty pycnometer was first cleaned dried at 110 °C and allowed to cool to within 5 °C of ambient. The number on the pycnometer and its stopper were recorded. The empty clean pycnometers with their individual stoppers in position were weighed to the nearest 0.0002 g(m_0). The −300 µm waste CSD (d_{97} = 300) was carefully added to the pycnometers until they were about one-third (1/3) full. The outer surfaces of the pycnometers were cleaned with a dry paper towel and afterwards weighed to the nearest 0.0002 g. The mass of the pycnometer with sample were subtracted from the respective mass of the empty pycnometer. The result thus represents the mass of the −300 µm waste CSD (d_{97} = 300) in the pycnometer (m_1).

De-aerated boiled water was added to the pycnometer containing the dry −300 µm waste CSD (d_{97} = 300) until the pycnometer was filled to two-third (2/3) its capacity. The pycnometers were then placed in a desiccator and exposed to a vacuum where the pressure was not greater than 25 mbar until no more air bubbles

were seen to rise. The pycnometers were then shaken to ensure complete wetting. The pycnometers were then removed from the desiccator and were filled almost completely with water. The contents of the pycnometers were allowed to settle until the liquid was only slightly cloudy. The glass stoppers were inserted and the water that overflowed was carefully wiped. The pycnometers were put in a thermostatically controlled bath and the temperature was raised to 5 °C above ambient temperature; while maintaining the temperature constant to within ±0.5 °C. A thermometer was placed in the bath and the temperature of the water was recorded. Care was taken to remove any overflows of water from the stopper as the temperature rises. At the point where no more water comes out from the capillary bore the pycnometer is believed to have attained the test temperature. This took an average of 20 min. The pycnometers were removed from the bath, wiped dry with care and weighed to the nearest 0.0002 g, this is mass m_2.

Empty and clean the pycnometers afterwards fill them almost completely with water. The glass stopper was carefully inserted, while eliminating overflows of water. The pycnometers were put in a thermostatically controlled bath which was raised to a temperature of 5 °C above ambient temperature. It was ensured that the temperature of the water was the same as recorded earlier. Whilst maintaining the temperature to within ±0.5 °C. The water that overflowed from the stopper as a result of rise in temperature was carefully removed. At the point where no more water comes out from the capillary bore, it is believed that the pycnometer has attained the test temperature. The pycnometer is eventually removed from the bath, wiped dry and weighed to the nearest 0.0002 g, this is mass m_3. The result of the real density is shown in Table 5.

Slurry Preparation

The slurry is a combination of water and waste CSD at a constant ratio. The determination of particle density for the waste CSD played a vital role in the preparation of the slurry for the Falcon gravity concentrator experiment. The Slurries were prepared using Eq. 1 below, to determine the volume of the pulp needed to make up 35% solids ratio for the gravity separation.

$$V_{pulp} = V_{solid} + V_{water} \tag{2}$$

Where:

V_{pulp} = Volume of pulp (l)
V_{solid} = Volume of waste CSD (l)
V_{water} = Volume of water (l)

The result of these calculations can be seen in Table 6.

Upgrading CSD via Fine Gravity Separation Method

The falcon gravity concentrator (FGC) with model number SB4-VFD was used for the copper upgrade experiment. A summary of parameters considered during the experiment are detailed in Table 1. Naturally, the more information that can be obtained the better. Unfortunately, obtaining more information often requires increased experimentation and the resources available may become a limiting factor. The shortage of any necessary resource, whether it be time, money or materials can greatly hinder the conduct of the experiment and even preclude obtaining the desired amount of information from the experimentation. Howbeit, in a full factorial experiment at least one trial is required for all possible combinations of factors and levels. This exhaustive approach makes it impossible for any interactions to be missed as all factor interactions are accounted for. Furthermore, when factors are taken at three levels instead of two, the scope of an experiment increases and as such becomes more informative; such that a study to examine if a change is linear or quadratic is possible when the factors are at three levels. Hence, a system of factorial effects for 3 k factorial designs based on orthogonal polynomials on equally spaced levels is known as the linear-quadratic system. Computer methods are used almost exclusively for the analysis of factorial and fractional designs. But, the Yates's algorithm can be modified for use in the 3 k factorial design. Hence, the design of experiment (DOE) was carried out using the 2 by 3 full factorial design methods, as shown in Table 2. The resulting concentrates and tailings from the experiment were dried in preparation for subsequent analyses; the results of these analyses can be seen in Tables 7 and 8 and in Figs. 2 and 3.

Table 1 Parameters considered at three levels

S/N	Parameters	Low (0)	Medium (1)	High (2)
1	Rotational bowl speed (rpm)	40	60	80
2	Fluidized water flow rate (l/min)	3.0	4.5	6.0

Table 2 DOE for PC's waste CSD copper upgradeusing the 3^2 full factorial design

Tests	RBS (G)	FWFR (l/min)	Treatment combination
1	0	0	00
2	0	1	01
3	0	2	02
4	1	0	10
5	1	1	11
6	1	2	12
7	2	0	20
8	2	1	21
9	2	2	22

Table 3 Result of LPSA for both as-received and milled as-received waste CSD

Category	Serial. No.	Particle size fraction	% passing
As-received waste CSD	A	−300 to 74 μm	9.18
	B	−63 μm to pan	90.82
300 μm to pan (d_{97} = 300) waste CSD	A	−300 to 74 μm	4.41
	B	−63 μm to pan	95.59

Table 4 Results of moisture content determination

Tests	W_1 (g)	CSD (g)	W_2(g)	W_3 test 1 (g)	W_3 test 2 (g)	W_3 test 3 (g)	Avg MC%
A	249.95	3.00	252.92	252.90	252.90	252.89	0.8
B	219.52	3.00	222.52	222.52	222.48	222.51	0.6
C	223.16	3.00	226.16	226.16	226.12	226.13	0.8
Mean MC%							0.73

Table 5 Results of real density calculation of the −300 μm waste CSD (d_{97} = 300) at CSIR

Sample	PYC NO. 1	PYC (g)	m_0 (g)	m_1(g)	BATH (°C)	m_2(g)	m_3 (g)	LD (g/cm^3)	RD (g/cm^3)
SICER	1	22.5127	29.5725	7.0598	27	52.7592	48.3496	0.9965	2.655
WCSD									
A_1	2	22.4596	27.8584	5.3988	27	52.9906	47.4825	0.9965	2.845
A_2	3	22.3683	29.8042	7.4359	27	52.4643	47.6626	0.9965	2.813
A_3	4	24.5317	31.7441	7.2124	27	53.9232	49.2481	0.9965	2.833
MEAN									2.830
SD									0.016

Key: PYC NO. = Pycnometer number; PYC (g) = mass of Pycnometer; m_0 =mass of Pycnometer and −300 μm waste CSD; m_1=mass of the −300 μm waste CSD; m_3 =mass of pycnometer filled with water and −300 μm waste CSD; LD = liquid density; RD = real density; SD = standard deviation; WCSD = homogenized copper smelter dust

Results and Discussion

Laser Particle Size Analyzer (LPSA)

The laser particle size analyzer (LPSA) was used to analyze the d_{97} = 300 and the results showed a % change from 90.82% to 95.59% (Table 3). A look at the distribution curve of the as-received waste CSD (Fig. 1a) presents an almost symmetric distribution with one half of the distribution almost mirroring the other half. But after grinding the waste CSD the distribution curve (Fig. 1b) became skewed to the left making the distribution asymmetric, giving a good illustration of

Table 6 Results of slurry calculations of the −300 μm waste CSD (d_{97} = 300)

S/N	Parameters	Values	Units
1	Volume of pulp	0.50	l
2	Density of solids	2,830	g/l
3	% water	85	%
4	% solids	15	%
5	Mass of pulp	553.7077	g
6	Mass of water	470.6515	g
7	Mass of solids	83.0562	g
8	Volume of water	0.4706	l
9	Volume of solid	0.0294	l
10	Density of water	1,000	g/l

Table 7 Mass of copper and iron in the as-received waste CSD and its concentrates

Chemical composition (wt %)	As	T1C1	T2C1	T3C1	T4C1	T5C1	T6C1	T7C1	T8C1	T9C1
CuO	14.60	14.83	14.47	14.68	14.68	14.79	14.80	14.68	14.94	14.85
Fe_2O_3	10.52	10.94	11.03	10.72	10.78	10.71	10.72	10.64	10.91	10.84

Key: T1C1 = Test 1 concentrate 1, T2C1 = Test 2 Concentrate 1, T3C1 = Test 3 Concentrate 1, T4C1 = Test 4 Concentrate 1, T5C1 = Test 5 Concentrate 1, T6C1 = Test 6 Concentrate 1, T1C7 = Test 7 Concentrate 1, T8C1 = Test 8 Concentrate 1, T9C1 = Test 9 concentrate 1

Table 8 %grade and %recovery of the copper and iron at optimum test conditions using the XRD (FGC)

Tests	%grade of Cu (1)	%grade of Fe (1)	%grade of Cu (2)	%grade of Fe (2)	%recovery of Cu (2)	%recovery of Fe (2)
8	1.49	2.10	1.37	4.89	??	77.80

Key: 1 = as-received; 2 = concentrate; Cu = Copper; Fe = Iron

the effect of the grinding during the sample preparation of the waste CSD for its appropriateness for the separation experiment.

Moisture Content (MC)

The percentage moisture content (%MC) of the −300 μm waste CSD (d_{97} = 300) were determined as % dry −300 μm waste CSD (d_{97} = 300) weight. The moisture of the sample as received was less than 1.0% (Table 4).

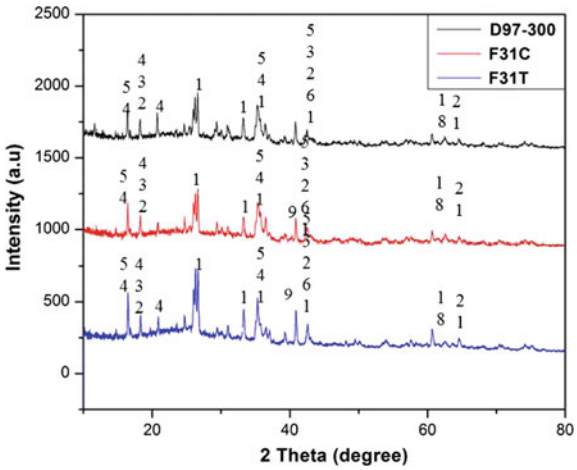

Fig. 2 X-ray diffractogram of waste CSD: ***As-received (D97-300)***: 1-Aluminum Silicon Oxide, 2-Silicon Oxide, 3-Copper Aluminum Sulphate, 4-Iron Oxide, 5-Copper Sulfate Hydroxide, 6-Copper Oxide, 7-Calcium Sulfate Hyroxide, 8-Titanium phosphate; ***Concentrate (F31C) and Tailing (F31T)***: 1,2,3,4,5,9-Copper Selenate Hydroxide

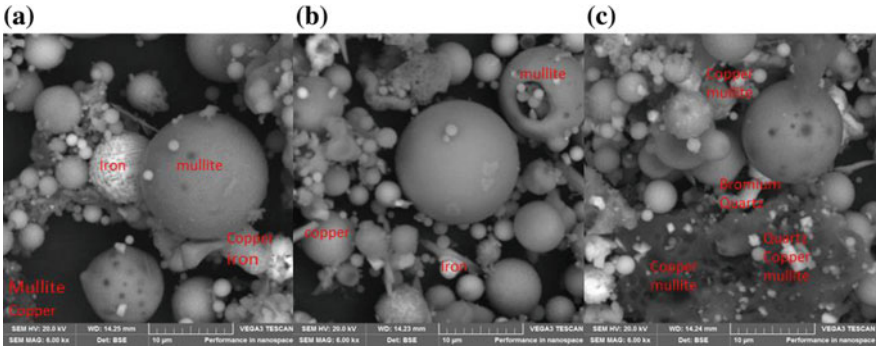

Fig. 3 Morphology and interaction between copper, iron, calcium, bromium, Aluminum and silicon in the as-received, concentrate and tailings produced at test 8

$$MC\% = \frac{W_2 - W_3}{W_3 - W_1} X100 \tag{3}$$

Where:

MC% = percentage moisture content
W_1 = weight of tin (g)
W_2 = weight of −300 μm waste CSD (d_{97} = 300) + tin + lid (g)
W_3 = weight of dried −300 μm waste CSD (d_{97} = 300) + tin + lid (g)

Density Determination

An initial density determination was carried out, but the set-up was not placed under vacuum, so that the result produced was not the real density but the apparent density. But when this test was done again with the set up placed under vacuum, the result gotten which is also shown in Table 5 (real density-2.830) is greater than that earlier obtained, (apparent density-2.691). The difference in results can be clearly attributed to the presence and absence of porosity; hence the later result can be conveniently referred to as the real density of the waste CSD.

Slurry Determination

The liquid to solid ratio can be seen in Table 6.

Gravity Separation Experiment

Weight Percent (Wt%) of Copper and Iron Before and After Upgrade

See Table 7.

Grade and Recovery of Copper and Iron Before and After Upgrade

The maximum iron recovery of 77.80% to the concentrate was discovered at test conditions of 80 rpm and 4.5 l/min fluidization rate with a copper grade of 1.37% less than the grade of copper in the feed (1.49%). This was further corroborated by the results obtained from the qualitative and quantitative mineralogical analyses using the EDS, SEM and XRD in Figs. 2, 3 and Table 9 respectively; from which it can be deduced that there was no significant separation of the heavy reactive gangue material: aluminum, silicon magnesium, calcium. But rather an increase in the grade of the hematite phase from 2.10% to 4.89%, which runs contrary to the aim of the study, which is to reduce the amount of Iron and other contaminants in the waste CSD (Table 8).

Table 9 EDS spot analysis of as-received, concentrate and tailings before and after upgrade experiment (test 8)

Waste CSD	Elements (wt%)						
	Cu	Fe	Al	Si	Ca	Ti	S
As	29.10	17.73	25.60	48.13	11.67	1.30	4.15
Concentrate	4.52	5.38	13.20	13.62	6.36	0.52	0.82
Tailing	3.04	5.52	10.72	21.62	1.56	0.78	3.86

Mineralogical Interaction Before and After Upgrade

Corroborating the results from the XRD analysis, the SEM images in Fig. 3 show amore copper minerals than iron in the concentrate than the as-received and tailings at test conditions of 80 rpm and 4.5 l/min; with the bulk of the particles been spherical an indication of the process that produced this waste CSD, as the molten metals solidified into spherical shaped after the parent ore was pretreated via roasting. Also Fig. 3b shows two generation of minerals a younger and older one. The older playing host to the most recent, pointing to two products of different condensation. Mineral logically, copper predominates in terms of amount, while mullite, quartz and gypsum are more pronounce in the as-received and tailings. Even though the separation of this unwanted materials.

Conclusions

The concentrates from the copper upgrade of the PC's waste CSD using the FGC with model number SB4-VFD, whilst varying parameters such as the rotational bowl Speed and the fluidization Water Flow rate; the effect of mineralogical phases, density and an almost constant particle size were also established. From which the following deductions were made:

- That based on the calculated CC from the specific gravity difference between the heavy minerals like tenorite, hematite, chalcopyrite, bornite (6.50, 5.30, and 5.30 respectively) and the host light minerals which are majorly quartz, mullite and gypsum (2.72, 3.16 and 2.4 respectively) separation was predicted.
- The maximum iron recovery of 77.80% to the concentrate was discovered at test conditions of 80 rpm and 4.5 l/min fluidization rate with a copper grade of 1.37% less than the grade of copper in the feed (1.49%).
- This was further corroborated by the results obtained from the qualitative and quantitative mineralogical analyses using the EDS, SEM and XRD, which indicated no significant separation of the heavy reactive gangue material: aluminum, silicon magnesium, calcium. But rather an increase in the grade of the hematite phase from 2.10% to 4.89%.

- So therefore, it will be said that the results were not in agreement with the hypothesis that states that the upgrade of the waste CSD will lead to the reduction/removal of reactive gangue minerals which should invariably affect the recovery of copper from this dust during the leaching process.
- This failure to achieve the set ojectives can be attributed to the type of Falcon gravity concentrator used; this equipment is designed to take the feed as solid instead of slurry, Thus resulting in significant amount of waste CSD been blown off in the process. Based on these limitations/challenges the feed rate and pulp density were factored into the upgrade study, which would have had significant impact on the outcome of this study.

Hence, it is recommended that another type of centrifugal separator be used, one that will allow the introduction of the material into the equipment as slurry, avoiding loss as a result of the rotating bowl and discharging water.

Acknowledgements The authors would wish to thank the Council for scientific and industrial research (CSIR), Pretoria, South Africa, for the financial support it gave in the course of this project, while also appreciating PC for providing the waste CSD used for this study. We also thank Tshwane University of Technology (TUT) and Vaal university of Technology (VUT) both in South Africa, for allowing the use of their facilities.

References

1. Dvorak P, Jandova J (2006) Zinc recovery from chloride-bearing galvanizing waste. Acta Metall Slovaca 12:90–94
2. Geldenhuis JMA (2002) Recovery of valuables from flue dust fines. Miner Eng 15(1):95–98
3. Ha TK, Kwon BH, Park KS, Mohapatra D (2015) Selective leaching and recovery of bismuth as Bi 2 O 3 from copper smelter converter dust. Sep Purif Technol 142:116–122
4. Ju SH, Zhang YF, Zhang Y, Xue PY, Wang YH (2011) Clean hydrometallurgical route to recover zinc, silver, lead, copper, cadmium and iron from hazardous jarosite residues
5. Li JS, Zhu JT, Yang HB, Yang SF (2011) Status on the treatment of EAF dust in China. Henan Metall 19:1–5
6. Montenegro V, Sano H, Fujisawa T (2008) Recirculation of Chilean copper smelting dust with high arsenic content to the smelting process. Mater Trans 49(9):2112–2118
7. Morales A, Cruells M, Roca A, Bergó R (2010) Treatment of copper flash smelter flue dusts for copper and zinc extraction and arsenic stabilization. Hydrometallurgy 105(1):148–154
8. Neveling U (2011) Palabora mining company annual report on ambient air quality monitoring
9. Okanigbe DO, Popoola API, Adeleke AA (2017) Characterization of copper smelter dust for copper recovery. Procedia Manufacturing 7:121–126
10. Okanigbe DO, Popoola API, Adeleke AA (2017) Hydrometallurgical processing of copper smelter dust for copper recovery as nano-particles: a review. In: Energy technology. Springer International Publishing, pp 205–226
11. Qiang L, Pinto IS, Youcai Z (2014) Sequential stepwise recovery of selected metals from flue dusts of secondary copper smelting. J Clean Prod 84:663–670
12. Raborar SC, Campos MB, Penaranda AH (1991) Philippine associated smelting and refining corporation. Process for removing impurities from flue dusts. US Patent 5,032,175

13. Regulation EC (1999) No 1907/2006 of the European Parliament and of the Council of 18 December 2006, concerning the Registration. Evaluation, Authorisation and Restriction of Chemicals (REACH), establishing a European Chemicals Agency, amending Directive, 45, pp 1–849
14. Reuter M, van Schaik A (2008) Thermodynamic metrics for measuring the "sustainability" of design for recycling. JOM 60(8):39–46
15. SANS (2005) South African National Standard: ambient air quality–limits for common pollutants
16. Wills BA, Napier-Munn T (2015) Wills' mineral processing technology: an introduction to the practical aspects of ore treatment and mineral recovery. Butterworth-Heinemann
17. Yin ZB, Caba E, Barron L, Belin D, Morris W, Vosika M, Bartlett R (1992) Copper extraction from smelter flue dust by lime-roast/ammoniacal heap leaching. Residues Effl Process Environ Consid pp 255–267

Towards Commercialization of Indium Recovery from Waste Liquid Crystal Display Screens

Thomas Boundy and Patrick Taylor

Abstract Indium recovery from liquid crystal display (LCD) waste has been the subject of over 50 peer reviewed publications over the last decade; however, the first commercial recycling facilities are just beginning to be built. The low value of indium in the LCD screen material has posed a major challenge to would-be recyclers. Uncommon material combinations and geometries have further challenged development. A review of published literature regarding extraction of indium from LCDs will be presented and themes of advantageous processes will be highlighted. Barriers to rapid expansion of any recycling technology in the form of manufacturing practices, environmental regulations, and geographic constraints will be discussed.

Keywords Indium · LCD · Recycling

Introduction

The cathode ray tube (CRT) displays are commonly recognized as an enormous burden on the recycling industry. The low value of the contained materials combined with the high costs of managing leaded glass waste for which there is no longer a market in CRT manufacture have required government intervention to keep recyclers operating and prevent abandonment or mismanagement of these materials. In a similar fashion, however, the technological replacement for the CRT, the liquid crystal display (LCD), poses challenges to recyclers. Like CRTs, safe dismantling of LCDs requires great attention. Unlike CRT glass in the U.S., LCD glass is not considered potentially hazardous and is not subject to the regulations for hazardous waste, whether or not it is recycled. Currently, LCD glass lacks end-use

T. Boundy (✉) · P. Taylor
Department of Metallurgical and Materials Engineering,
Colorado School of Mines, Kroll Institute for Extractive Metallurgy,
1500 Illinois St, Golden, CO, USA
e-mail: tiboundy@mines.edu

Z. Sun et al. (eds.), *Energy Technology 2018*, The Minerals, Metals & Materials Series, https://doi.org/10.1007/978-3-319-72362-4_26

markets that would support its recycling and is not recycled as a specific commodity in the U.S. Extraction of indium from LCD glass is currently not part of the process of recycling LCDs in the U.S.

While the human health and environmental concerns drive much interest in LCD recycling, interest in LCD recycling has been further stimulated by a desire for responsible indium supply chain management. Some of the unique properties of indium in transparent conductive oxides and light emitting diodes make it extremely valuable in clean energy photovoltaics and low energy lighting applications. Currently, the majority of indium consumption is used for manufacturing LCDs (the European Commission estimated 74% went towards flat panel displays as early as 2010 [1]). The approach to indium stewardship must begin, therefore, with the approach to waste LCD stewardship.

While environmental and resource stewardship considerations make used LCDs an important material to recycle, the labor-intensive processing and low material values make recycling difficult. Despite these difficulties, the first few processors worldwide have begun to recover indium from LCDs. This paper will review LCD construction and material values, dismantling approaches, indium recovery approaches, global policy and industrial environments with relevance to processing decisions, and the themes of processors currently recycling LCDs with a focus on indium recovery.

LCD Materials and Construction

Naturally, recycling practices for LCD-containing devices are dictated by the material composition and construction of such devices. Such devices have become ubiquitous in modern society in the form of mobile phones, computer monitors, and televisions. In each of these classes of devices, LCDs produce an image for a viewer by creating a uniform flux of white light across the display from which red, green, and blue light can be selectively filtered in small localized regions forming individual pixels. Therefore, a number of fundamental components enable operation: a white backlight, optical diffusers capable of presenting a uniform light flux to the screen, a grid of color filters, and a means of controlling the amount of light passed through each color filter.

The backlight of choice for LCD manufacturers prior to 2009 were mercury-containing cold cathode fluorescent lightbulbs (CCFLs). In about 2009, the shift towards light emitting diodes (LEDs) began, and by 2013 LEDs largely displaced CCFLs as backlights.

For both of these backlight options, various plastic diffuser and reflector sheets are used to present a uniform flux to the display for localized filtering.

The localized light filtering apparatus is characterized by a layered structure as shown in Fig. 1. Outer plastic layers are often composed of tri-acetyl cellulose and poly(vinyl alcohol) as light polarizers [3]. Alkali-free sheet glass composes the next outermost layer [4]. Organic color filter and electrode layers of which indium tin

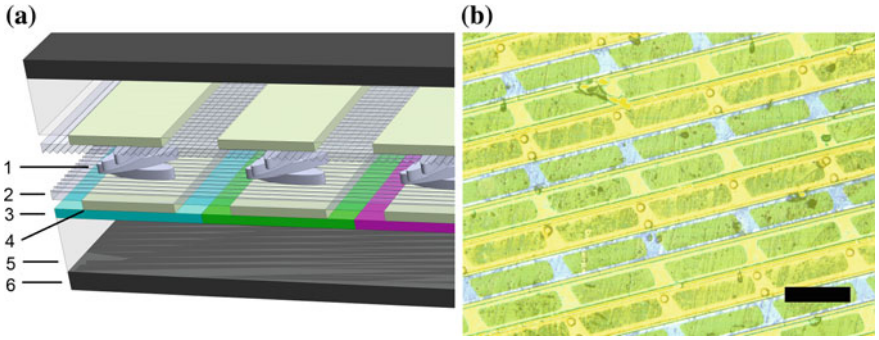

Fig. 1 **a** A simplified diagram of the structure of a typical LCD screen. 1 = liquid crystals, 2 = orientation layer, 3 = color filter, 4 = ITO layer, 5 = glass sheet, and 6 = polarizer. Not drawn to scale. **b** Micrograph of shredded LCD screen showing the individual pixels composed of three adjacent, independently controlled regions. Scale bar = 200 microns. Adapted from Boundy et al. [2]

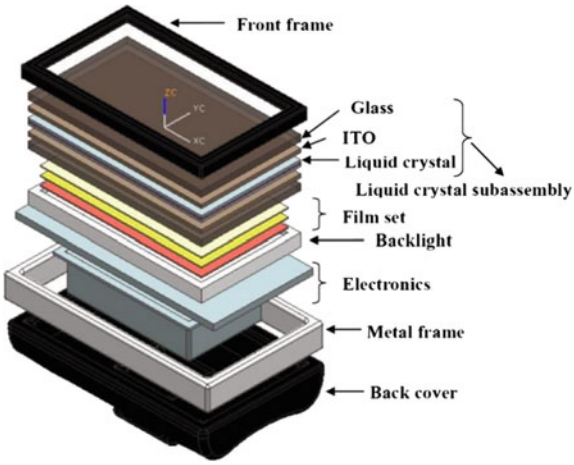

Fig. 2 An exploded view of a generalized LCD monitor adapted from Zhao et al. [6]

oxide (ITO) is the innermost coat the inner layer of the glass sheets [5]. Liquid crystal blends fill the gap between these glass plates. The liquid crystal blends themselves are used to control the light flux through each color filter by manipulating the voltage applied to the individual ITO domains. As such, a computer and attendant printed circuit boards (PCBs) must be electrically connected to the device.

A typical configuration for all of these components is shown in Fig. 2. Components are mated together through screws, plastic and metal clips, and adhesives.

Material Values

Salhofer et al. in collaboration with Saubermacher (a recycling company in Austria) performed a thorough characterization of LCD material composition and values based upon previously stockpiled LCDs in 2009 [7]. The material compositions and expected revenues generated from them are presented in Table 1.

Ryan et al. characterized average material fractions present in 17 large monitors (between 20 and 40 inch displays) [8]. These data are compared with those of Salhofer et al. [7] in Fig. 3.

Rotter et al. presented a review of indium content in the LCD screens of mobile phones and computer monitors and presented some of their own data as well [9]. The reviewed literature reported widely varying indium concentrations in LCD screens (58.5–1102 mg indium/kg screen). Rotter et al. report based on indium content determination in 23 computer monitors and 11 mobile phone displays contents of 175 ± 60 and 320 ± 160 mg/kg, respectively [9]. The reported standard deviations give an indication as to the widely variable manufacturing practices and indium content present in various displays. These data compare favorably with more recently published values of indium content in both computer monitors and mobile phones as reviewed by Boundy et al. [2]. Ueberschaar et al. have performed the most thorough characterization of indium content in LCD screens for various device types [10]. Their results are shown in Fig. 4.

Table 1 Material composition of LCDs and suggested associated values reported by Salhofer et al. [7]

Material	Composition monitors	Composition TV-sets	Revenues	Revenue monitors	Revenue TV-sets
	(kg/tonne)	(kg/tonne)	(euro/kg)	(euro/tonne)	(euro/tonne)
Ferrous metal	409	535	0.04	16	21
Aluminum	52	6	0.55	29	3
PCBs	81	61	2	163	122
Cables	11	9	0.7	8	7
Backlight	3	11	−0.7	−2	−8
LC display	81	77	−0.6	−49	−46
ABS	120	179	0.13	16	23
PC-ABS	43		0.13	6	
PMMA	124	17	0.15	19	2
PS	5	43	0.05	0	2
Other plastics	20	36	−0.16	−3	−6
FR plastics	50	26	−0.16	−8	−4
Total	1000	1000		194	117

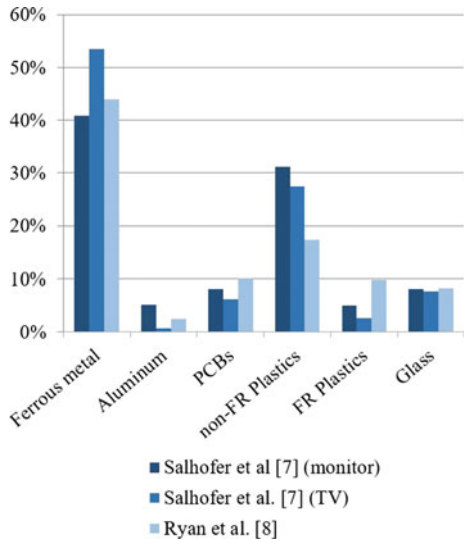

Fig. 3 A comparative bar graph for the selected material fractions found in LCDs by Salhofer et al. [7] and Ryan et al. [8]

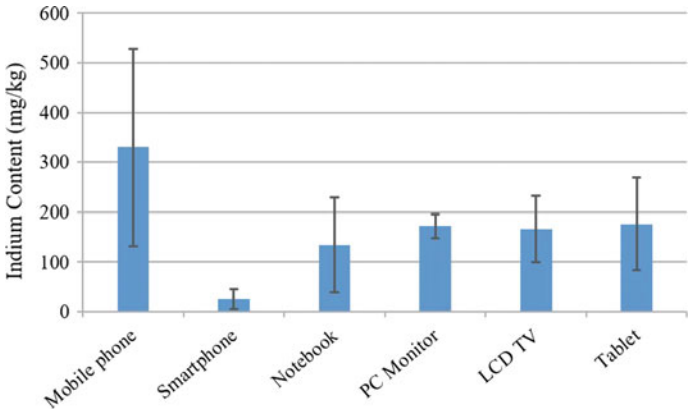

Fig. 4 Indium content determined by [10] in various types of LCD-containing devices with error bars representing standard deviations

As previously discussed, the indium content is often used to recommend LCD recycling from a criticality perspective. When approached from an economic perspective; however, the challenge emerges. Assuming 200 mg indium per kg of screen and the recent market price of $200/kg, the indium content in one tonne of waste screens is $40 or about $0.01 per 14-inch screen. Even during the indium price spike of 2014 when indium reached about $700/kg, the economics make processing decisions difficult.

LCD Disassembly

The major challenge with LCD disassembly is handling the mercury-containing CCFL backlight. Zhao et al. noted that recyclers are unable to shred these devices as a whole due to the emission of mercury into the atmosphere and products [6]. Because of this, the majority of recycled LCDs are manually dismantled. Ardente et al. thoroughly reviewed LCD dismantling practices and challenges and present some of their own findings as well. Disassembly times for LCD devices are commonly found to be in the range of five to 15 min with disassembly time increasing with screen size [11]. It has been noted that partial rather than complete disassembly is often employed. In the case of one Italian study, manual dismantling is utilized to remove CCFLs, LCD screen, PCBs, and PMMA sheets [11]. In these incomplete disassembly situations, the remainder of the attached materials are sent to shredding and subsequent particulate separations.

The relatively high labor costs and required dismantling times have driven some innovation in automated disassembly process capable of safety managing associated mercury risks; however, many features of the LCD-containing devices such as thin, heterogeneous materials and device variability make design of such automated processes difficult [12]. One commercial solution has been developed as an industrial shredding device capable of capturing mercury through gas and fines collection and sequestration. The other common approach to mercury management through automated processes has been mechanical cutting of the screen and recovery of the intact CCFLs. The remains of the device can then be safely submitted to a conventional electronics shredder. At the time of this writing, such automated LCD dismantling equipment is now being sold by a number of vendors across Europe.

As a greater fraction of LCD-containing devices with LED backlights reach end-of-life management operations, automated device characterization equipment will become increasingly economical to separate devices that require CCFL removal from those that do not.

Indium Recovery from Screens

In traditional extractive metallurgical processes, separations are designed to progressively increase the concentration of a value material while rejecting waste or gangue materials. These processes can be separated into physical/mechanical or chemical processes. Physical/mechanical processes tend to be relatively low-cost and non-polluting, with the exception of the carbon used to power them. Chemical processes, by contrast, are often more expensive, but enable concentration and often reduction of value materials to states that cannot be achieved by mechanical/physical means.

Chemical methods are more commonly employed in published investigations of indium recovery from LCD screens. These investigations have been reviewed in detail by Boundy et al. [2], Ueberschaar et al. [10], and Zhang et al. [13]. The results are as expected. Nitric acid, sulfuric acid, and hydrochloric acid are all effective, low-cost leachants, and leaching kinetics can be improved with increased temperature. These techniques, however, are found to be economically unfeasible for this low-grade indium feedstock in a commercial environment due to the relatively high losses due to low solution concentration and high costs of acids required to leach low-grade feedstocks. One metallurgical engineering approach to address the challenges of leaching low-grade ores is counter-current leaching. This technique enables greater solid to liquid ratios to be achieved in the leaching process than could be achieved if the leaching is confined to a single mixed slurry. A modified cross-current leach has been demonstrated for indium recovery from LCD screens by Rocchetti [14].

High-temperature pyrometallurgical processes have also been investigated taking advantage of the unique volatility of a number of indium species. He et al. have demonstrated recovery of indium through carbothermal reduction and vaporization of the In_2O species under vacuum [15]. Takahashi et al. reported using HCl to convert the In_2O_3 in ITO to $InCl_3$ and recoveries of greater than 80% at 400 °C [16]. The economics of these approaches have not been reported in any published research.

Investigations into mechanical/physical processes for indium beneficiation from LCD screens have been sparingly published. Without specifics, Rotter et al. suggested among many possible approaches that due to the surface confinement of indium on the LCD glass, an abrasive approach might be a viable method of producing an indium concentrate [9]. Dodbiba et al. demonstrated an electrical disintegration approach to increase the availability of indium to the leachant, but with no apparent subsequent separation [17]. Boundy et al. report an autogenous attrition scrubbing process in which inter-particle abrasive action causes the removal of the indium containing semi-conductor film as fine particulate which is separated from the coarse shredded glass by screening to produce an indium concentrate of approximately 2000 mg/kg [2]. In the same month Zhang et al. published a description of a mechanical stripping process whereby whole LCD screens, once separated from their respective devices, are opened to expose the indium and ground with a roller brush to remove the indium as fine particulate [18]. The produced fine particulate containing about 8% indium is contaminated with a large fraction (53%) of liquid crystals which must be vaporized under inert atmosphere in order to be separated from indium particulate enabling the indium to be further refined without harming downstream operations [18].

Geopolitical Processing Environments

Processing possibilities and decisions for waste LCDs are dictated by the geopolitical environments within which recyclers operate. Many variables including government policy, population density, recycling rates, labor costs, access to capital, proximity to purchasers of products, equipment availability, and technical understanding contribute to processing decisions by recyclers. Historically, LCD glass along with the roughly 200 mg/kg of indium have been landfilled or used as flux in lead or zinc smelters [18] which may recover indium from the off-gas. Primary indium circuits are estimated to recover only about 35% of indium in the feed material [19].

Europe

The European Union has passed the most aggressive measures with regard to waste electrical and electronic equipment (WEEE) with the most recent legislation (WEEE Directive 2012/19/EU) requiring recovery of mercury containing components such as backlighting bulbs and the screens of LCD units and that 70% of the material shall be prepared for re-use or recycling [20]. There exists some contention about the environmental risk associated with liquid crystals. MERCK, a major liquid crystal blend manufacturer, has published studies failing to demonstrate any ecotoxicity or human health risk associated with common liquid crystal blends [21]. It should be noted that these blends often contain halogenated organic compounds; therefore the same cannot be said of the combustion products [18]. Nonetheless, the EU has mandated that LCD screens themselves be collected and disposed of separately [22]. In addition to mandating segregation of certain hazardous materials and a weight fraction of the overall devices to be recycled, the EU has removed the burden of recycling costs from the consumer in an effort to improve WEEE collection. This legislation has led to relatively high recycling rates across Europe, which, when combined with a relatively large population density, gives recyclers access to relatively large economies of scale.

It is worth noting that the EU adopted some of the first WEEE recycling mandates, and with the recognition of the high costs of labor and manual disassembly, research and development into automated dismantling processes began early. These technologies were developed in light of EU mandate that LCD screens as well as backlights be collected separately. As recyclers with economies of scale grew and gained access to increasing capital, the developed automated dismantling technology began to be deployed across Europe. This produces conditions very favorable to one interested in recovering indium from these devices as large volumes are processed within a fairly limited geographical area and the screens are recovered in a fairly pure form without contamination of other plastics or low value materials that might otherwise be left in the waste fraction. While a government sponsored entity has begun operating a pilot plant, no commercial ventures recycling the LCD screens have begun.

United States

The United States have not passed meaningful federal legislation but have instead allowed individual states to legislate their own agendas. Notably, California has implemented extended producer responsibility legislation requiring manufacturers to contribute to the costs of recycling enabling consumers to drop off monitors at no cost. A fee ($10–25 per device) is associated with disposal of LCD TVs and monitors in all other states. Landfill bans on flat panel displays currently exist in 17 states [23]. It is common for many of the states with electronic waste legislation to require that recyclers be certified by either E-Stewards or R2. Therefore, processors are generally required to refurbish when possible, perform testing to assure quality of refurbished or re-used components, and recycle material values instead of landfill disposal or recovering energy value through incineration.

While the landfill bans and non-consumer paid recycling fees increase recycling rates for LCDs in the US, many obstacles to processing remain. One major barrier lies in the low population density of the US and much of its non-coastal area in particular. These low population densities lead to low throughput and revenue in processing facilities which makes capital investment and automation for these recyclers unreasonable. As the low value of LCD containing devices makes shipping these devices to larger urban centers for recycling uneconomical, the value of the screen by-product after local dismantling is even more prohibitive. Urban centers in the coastal areas have the population density to support larger plant revenues and capital investment; however, because the LCD screen is not classified as a hazardous material, after the CCFLs have been manually removed, the remaining monitor is often subjected to shredding. This leads to the accumulation of LCD screens either intact or as shredder residue mixed with other materials whose value did not justify separation from the waste stream. Dispersed in multiple forms and purity levels, the relatively small quantities of LCD screen scrap generated in the U.S. have also not found a commercial recycling route.

China

In 2011, China implemented a tax on electronics manufacturers to fund subsidies for disposal of WEEE (CLI.2.114171 Article 7). Recyclers must apply for the funds based on the volume of waste electronics processed [24]. While the funding mechanisms are not as mature as in the EU, China has much lower labor costs than the EU. Li et al. found that recycling of monitors (CRTs and LCDs together) in China, cost between $7.6 and $13.5 per unit with an average of 7% of the cost attributable to labor [24]. Zeng et al. recently reviewed the experience of China in

implementing environmental and waste management strategies with respect to WEEE and suggest that the government programs have increased the recycling rate as high as 35% in 2014 [25].

China also has a distinct technological and population density advantage over both the EU and the US. With the LCD manufacturing industry operating predominantly out of Asia, companies in and around China have been recycling LCD screens rejected by their manufacturing lines (reject rates in manufacturing lines can be as high as 5 to 15% [26]) for years [27]. It has been demonstrated that after subjection to color filter stripping solution the glass surface can be regenerated and coated once again with ITO without a significant decrease in performance [28]. If truly commercially achievable, regeneration of LCD glass at a value on the order of $\$1/ft^2$ has the potential revenue to justify these transistor stripping operations so long as an interested manufacturer can be found. Indium concentrates, too, have an easy processing route as China is the world's leading producer of indium, contributing 44% of the world's production in 2016 [29].

It is with this government commitment to recycling, high population density, technical capability, and local manufacturing industry that Ningda Noble Metal Co. Ltd. permitted the first large scale indium recovery facility from end-of-life LCD units in 2016 in Yangzhou, China. While the long-term success of this facility remains to be seen, it appears China has taken the first step towards stewardship of indium from end-of-life LCDs.

Conclusions

Investigations into policy and processing routes for recovery of rare and valuable materials have become common themes of research in recent years. If the recovery of indium from LCDs is of any use as a case study, however, a few additional themes emerge. Recycling involves the practice of converting a used or obsolete product or material into a useable material with value for another. Especially with materials which are difficult or costly to transport, processes will be most successful when preparing products that are appealing to manufacturers of reasonably close proximity. Additionally, especially within a world of increasingly complex proprietary technology and manufacturing methods, it is often the manufacturers or a product or at least those with intimate knowledge of manufacturing practices most equipped to recycle it.

Acknowledgements The authors would like to acknowledge Fangyu Liu for assistance translating Chinese publications and David Wagger for helpful insight into global regulatory environments for end of life materials.

This research is supported by the Critical Materials Institute, an Energy Innovation Hub funded by the U.S. Department of Energy, Office of Energy Efficiency and Renewable Energy, Advanced Manufacturing Office.

References

1. European Commision (2010) Annex V to the Report of the Ad-hoc Working Group on defining critical raw materials
2. Boundy T, Boyton M, Taylor P (2017) Attrition scrubbing for recovery of indium from waste liquid crystal display glass via selective comminution. J Clean Prod 154:436–444
3. J Ma, X Ye, Jin B (2011) Structure and application of polarizer film for thin-film-transistor liquid crystal displays
4. Ellison A, Cornejo IA (2010) Glass Substrates for Liquid Crystal Displays. Int J Appl Glas Sci 1(1):87–103
5. Kondo K, Kinugawa K, Konishi N, Kawakami H (1997) Wide-viewing-angle 13.3-in. XGA displays with in-plane switching mode of nematic LCs addressed by TFTs. J Soc Inf Disp 5 (1):37
6. Zhao F, Lagro A, Mendis G, Handwerker C (2014) Recycling of liquid crystal displays for maximum resource recovery. In: Proceedings of the ISSST, vol 2
7. Salhofer S, Spitzbart M, Maurer K (2011) Recycling of LCD screens in Europe—State of the art and challenges. pp 454–458
8. Ryan A, O 'donoghue L, Lewis H (2011) Characterising components of liquid crystal displays to facilitate disassembly. J Clean Prod 19:1066–1071
9. Rotter VS, Chancerel P, Ueberschaar M (2013) Recycling-oriented product characterization for electric and electronic equipment as a tool to enable recycling of critical metals in REWAS 2013. Springer International Publishing, Cham, pp 192–201
10. Ueberschaar M, Schlummer M, Jalalpoor D, Kaup N, Rotter V (2017) Potential and recycling strategies for LCD panels from WEEE. Recycling 2(1):7
11. Ardente F, Mathieux F, Recchioni M (2014) Recycling of electronic displays: analysis of pre-processing and potential ecodesign improvements. Resour Conserv Recycl 92:158–171
12. Elo K, Sundin E (2014) Automatic dismantling challenges in the structural design of LCD TVs. Procedia CIRP 15:251–256
13. Zhang K, Wu Y, Wang W, Li B, Zhang Y, Zuo T (2015) Recycling indium from waste LCDs: a review. Resour Conserv Recycl 104:276–290
14. Rocchetti L et al (2015) Cross-current leaching of indium from end-of-life LCD panels. Waste Manag 42:180–187
15. He Y, Ma E, Xu Z (2014) Recycling indium from waste liquid crystal display panel by vacuum carbon-reduction. J Hazard Mater 268:185–190
16. Takahashi K, Sasaki A, Dodbiba G, Sadaki J, Sato N, Fujita T (2009) Recovering indium from the liquid crystal display of discarded cellular phones by means of chloride-induced vaporization at relatively low temperature. Metall Mater Trans A 40(4):891–900
17. Dodbiba G, Nagai H, Wang LP, Okaya K, Fujita T (2012) Leaching of indium from obsolete liquid crystal displays: comparing grinding with electrical disintegration in context of LCA. Waste Manag 32(10):1937–1944
18. Zhang L, Wu B, Chen Y, Xu Z (2017) Treatment of liquid crystals and recycling indium for stripping product gained by mechanical stripping process from waste liquid crystal display panels. J Clean Prod 162:1472–1481
19. Werner TT, Mudd GM, Jowitt SM (2015) Indium: key issues in assessing mineral resources and long-term supply from recycling. Appl Earth Sci 124(4):213–226
20. Directive 2012/19/EU of the European Parliament and of the Council of 4 July 2012 on waste electrical and electronic equipment (WEEE) Text with EEA relevance. 2012
21. Simon-Hettich B et al (2001) Ecotoxicological properties of liquid-crystal compounds. J Soc Inf Disp 9(4):307
22. O'Donoghue L, Leen J, Ryan A, Ruiz J (2014) STRIVE 122—State-of-the-Art recycling technology for liquid crystal displays
23. Landfill Bans (2017) Electronics Recycling Coordination Clearinghouse

24. Li J, Dong Q, Liu L, Song Q (2016) Measuring treatment costs of typical waste electrical and electronic equipment: a pre-research for Chinese policy making. Waste Manag 57:36–45
25. Zeng X, Duan H, Wang F, Li J (2017) Examining environmental management of e-waste: China's experience and lessons. Renew Sustain Energy Rev 72:1076–1082
26. Longzhu L, Huidong T, Yonghong X, Yuanyuan S (2014) Research progress in resource-rization of waste liquid crystal display. China Resour Compr Util 32(6):23–26
27. Tsujiguchi M (2012) Indium recovery and recycling from an LCD panel. In: Design for innovative value towards a sustainable society, Springer Netherlands, Dordrecht, pp 743–746
28. Hong S-J, Kim M-S, Kim J-W, Shin M Characteristics of Indium-Tin-Oxide (ITO) glass re-used from old TFT-LCD panel
29. Tolcin A (2017) Mineral commodity summaries: indium. United States Geological Survey

Engineering, Scientific, and Policy Inputs for Developing a Levelized Cost of Energy Storage Model

Timothy W. Ellis, John A. Howes and Roger D. Feldman

Abstract Scope: The new generation of more powerful, energy-intensive devices for communications, industrial production, energy storage and other purposes is creating new challenges to guard against environmental harm and protect national security. Many devices are designed, used and disposed of in a linear, rather than circular manner. This causes scientific, legal and economic issues because the life-cycle costs of components are not adequately considered. Dealing with these issues in isolation from each other can lead to unintended consequences. New models to confront these issues are being defined. This paper suggests a fundamental tool for dealing with material science issues while taking into account the engineering, economic and policy perspectives. That tool is the development of a true, levelized cost of energy storage model with a wide spectrum of inputs for comprehensive analysis. This paper will discuss inputs and the process which can yield meaningful, useful comparisons among batteries and energy-intensive products.

Keywords Circular economy · Recycling · Batteries · Lithium
Life cycle · Levelized cost

T. W. Ellis (✉)
SAE Battery Recycling Committee; Advanced Lead-Acid Battery Consortium,
RSR Technologies, Inc, 4828 Calvert St, Dallas, TX 75247, USA
e-mail: tellis@rsrtechnologies.com

J. A. Howes
American Bar Association Energy Infrastructure, Siting, and Reliability Committee,
Redland Energy Group, 1875 Eye St., NW, Suite 500, Washington, DC 20006, USA
e-mail: Jahowes@redlandenergy.com

R. D. Feldman
American Bar Association Energy Infrastructure, Siting and Reliability Committee,
and of Counsel, Andrews Kurth, 1350 I Street, NW, Suite 1100, Washington, DC 20005,
USA
e-mail: RogerFeldman@andrewskurth.com

Z. Sun et al. (eds.), *Energy Technology 2018*, The Minerals, Metals & Materials
Series, https://doi.org/10.1007/978-3-319-72362-4_27

Introduction

Lithium-ion (Li-ion) batteries, introduced commercially in the latter part of the 20th century, have become commonplace in a variety of held-held electronic appliances because of the favorable energy density of the batteries compared to other commercially available rechargeable batteries. Within the past 20 years, Li-ion battery cells assembled in larger-format battery packs have been entering the market for use in hybrid and electric vehicles. They now are also being used increasingly for uninterruptible power supply and electric grid functions. However, risks associated with the safe operation and end-of-life management of Li-ion batteries have grown and are receiving considerable attention from government, insurance underwriters, consumer advocates and the environmental community [1].

The purpose of this paper is to view some of the major design, operational, safety and, especially, end-of-life recycling issues through scientific, economic and legal perspectives.

Scientific Perspective

Several characteristics about lithium-ion batteries contribute to the difficulty in recycling them. Among them:

- Lithium-ion batteries have been designed in a "linear" manner, meaning they have been designed without considering how battery materials can be recovered for reuse, remanufacturing or recycling.
- Lithium-ion batteries are part of a complex family of chemistries that utilize lithium and contain certain materials (copper, nickel, lead, fluoride compounds, etc.) that are potentially toxic. They also contain organic electrolytes that can cause fire hazards [2]. Care must be taken in the storage of these batteries to guard against leaching into landfills [3].
- Because of the complexity of designing lithium batteries from such a wide spectrum of materials, a recycling process used for one lithium battery design may not be as compatible with others.
- An infrastructure to collect from consumers the lithium batteries when they reach their end-of-life is in its early development stage.

These factors contribute to the low recycling rate of lithium-ion batteries, which is less than five per cent [4]. This suggests a gap exists between how lithium batteries presently are designed in a linear manner and how they might be designed in a "circular" manner. It is a gap that requires research into how battery materials can be recycled with the resulting materials becoming economically competitive with virgin materials. Addressing this gap is a priority in the automotive industry as hybrid and electric vehicles utilizing lithium-ion batteries enter the marketplace.

This stands in contrast to lead-acid batteries, which are recycled at a rate reaching 99%. Lead-acid batteries, which have been recycled for more than 100 years, are an example of how a product can be designed, manufactured, used and recycled in a "circular" manner. Materials in a lead-acid battery, lead, plastic, acid, are continually recovered and reprocessed for use in new batteries. Among the reasons for the high recycling rate of lead-acid batteries is that they are manufactured with fewer materials than lithium batteries and those materials have residual value when the battery no longer is used [5].

The U.S. Environmental Protection Agency (EPA) has in place strict guidelines for recycling lead-acid batteries that enable the recycling process to be classified under "universal waste" regulations. Lead-acid recycling plants must be fully enclosed to prevent the escape of lead micro particles. Smokestacks must be fitted with scrubbers. To check for possible escape of lead particles into the outside air, the plant perimeter must be surrounded with lead-monitoring devices.

Lead-acid battery recycling plants not only must comply with stringent waste processing standards, they must also be on guard for lithium batteries mixed into the waste stream of lead-acid batteries fed into secondary lead recycling smelters, either inadvertently or on purpose. This has resulted in several explosions as the lithium-ion batteries are crushed by the equipment used to crush lead-acid batteries. In addition, the absence of comparable waste processing standards for lithium batteries in the U.S. has, in effect, resulted in "pollution havens" being created. Not only have lithium-ion batteries been placed in the waste streams of U.S. recycling facilities, batteries also have been exported to recycling facilities in other countries that lack emission and safety standards comparable to those in the U.S [6].

Continued research is needed to address the challenges of bringing a closed loop design that is the hallmark of lead-acid batteries to products that use advanced chemistries like lithium. Among these challenges are the juxtaposition of various recycling processes with the variety of lithium battery designs. Will manufacturers have confidence in the quality of recycled materials compared to virgin materials? Can recycling be factored economically into the design of materials as well? Do such decisions depend only on price?

Economic Perspective

Consumer demand for high efficiency products has created increased use of materials, such as rare earths and specialty metals like lithium, that are not readily and economically recycled. After the consumer is finished with the batteries, the question of what to do with them is left to the consumer. In some instances, they can be sold at a cost lower than the original purchase price, placed in a container designated for shipment to a waste treatment facility or, in most cases, thrown into landfills or other waste streams.

Presently, the average cost of recycling lithium-ion batteries exceeds the cost of sending them to landfills. According to one study, the cost of collecting spent

lithium-ion batteries is approximately $1,120 per ton and the tipping fee paid to landfill operators for taking them is approximately $45 per ton [7]. The estimated cost of recycling lithium batteries is approximately 20–30% more than cost of transporting them to a landfill. It is conceivable that end-of-life processing costs could be in part recovered if recycled materials were of comparable quality and competitively priced with virgin materials used in lithium-ion batteries.

Not only is the cost of recycling lithium-ion batteries more expensive than simply discarding them into landfills or other waste streams, there is no nationwide legal requirement throughout the U.S. for lithium battery manufacturers to collect batteries at their end-of-life. Therefore, the expenses associated with managing these spent batteries are considered "externalities" or costs borne by society. With batteries becoming increasingly utilized in automotive and electric power applications, several economic studies [8] have undertaken levelized cost calculations to compare various battery chemistries on an equitable economic basis. However, in most comparisons, end-of-life costs are not included.

Since end-of-life costs are included in the retail price of all lead-acid batteries, such costs must be included in the assessment of batteries using lithium and other chemistries if a true equitable, levelized model is to be developed.

Internal costs are those upon which a business calculates the price of a product. The internal cost reflects variable costs such as materials and purchased items, direct labor and overhead. These internal costs also reflect fixed costs such as general administration, sales, research and development, depreciation and profits after taxes [9]. However, when costs such as product disposal, environmental degradation and toxic substance leaching are not included in the calculation of a product price, they become "external" costs that are borne by society. Such costs can be handled by the imposition of taxes to finance disposal or penalties assessed against polluters. Estimates for mandatory take-back costs can range as high as 40% of variable costs [10].

The chart below (Fig. 1) illustrates how the internal and external costs, plus associated profit, are embedded in the retail price of lead-acid batteries (average price $150/kWh). While the internal costs, plus associated profit, are embedded in the average retail price ($250/kWh) of lithium-ion batteries, they do not include end-of-life disposal costs which must be borne by society. These end-of-life costs for lithium-ion batteries are therefore "external" costs that must be borne by society.

To achieve sustainability on an ongoing basis, the way in which production and disposal cycles are integrated will come into focus more sharply as the market for lithium-ion batteries continues to grow and resulting solid waste disposal issues become more apparent. This will result in the need for a more circular approach that has been a hallmark of lead-acid batteries, one that will be needed for lithium-ion. This discussion also will be enhanced by technological developments in the recycling of lithium-ion batteries sponsored by government and industry.

Economies of scale for the recycling of lithium-ion batteries are as important as the recycling technology itself to justify sufficient investment in the technology. For

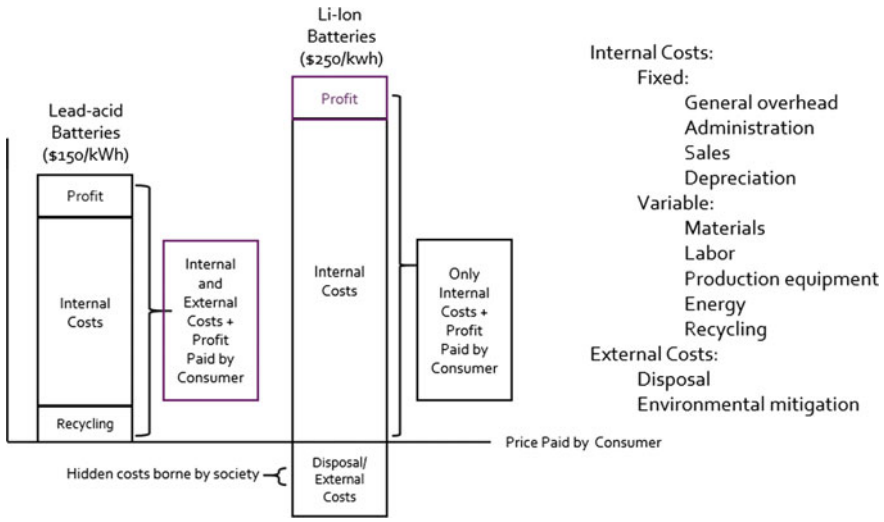

Fig. 1 Internal and external costs, plus associated profit, embedded in the retail price of lead-acid batteries (average 131 price $150/kWh)

smaller recycling facilities including typical electronic waste processors, it may be difficult to achieve economies of scale due to their limited resources and recycling capacity.

Legal Perspective

Bringing together scientific, economic and legal analysis can be useful in addressing the primary challenges of bringing lithium-ion batteries into a circular profile similar that that of lead-acid batteries. These challenges include the lack of design for recycling, inadequate collection infrastructure and insufficient incentives for consumers to place discarded batteries into recycling facilities rather than into landfills or other linear waste streams.

Various public policy proposals have been advanced in the lithium recycling discussion. The proposals range from an outright ban on the landfill disposal of batteries to integrating end-of-life protocols into the design and manufacture of lithium batteries.

Throughout Europe, many countries have enacted extended producer responsibility (EPR) laws requiring producers to take back rechargeable batteries, including lithium-ion, to manage them in an environmentally beneficial manner. In the U.S., such laws have not been legislated by the U.S. Congress. The Mercury-Containing and Rechargeable Battery Management Act of 1996 (Battery Act) requires that certain batteries (mercury-based, nickel-cadmium, and lead-acid) are considered hazardous waste and fall under the standards for universal waste management.

While the Battery Act mandates guidelines for disposal of hybrid, plug-in hybrid and electric vehicle batteries, the EPA universal waste rule does not consider lithium-ion batteries to be hazardous and, therefore, they are excluded. However, a regulatory system could be adapted to include lithium-ion batteries in anticipation of a high volume of these batteries that will be removed from hybrid and electric vehicles at their end-of-life [11]. In the meantime, only California, New York and Minnesota have enacted laws restricting the landfill disposal of lithium-ion, and other rechargeable batteries. (Lead-acid recycling laws are commonplace throughout the U.S.).

The question is what comprises a legal framework for the effective solution of practical problems affecting environmental concerns, energy infrastructure development, and the use of natural resources law that is consistent with how markets operate and equitable to all parties. There are three areas of law within which battery end-of-life are considered:

- Public law, which is created by governmental mandates and formal policy guidance.
- Private governance, which is established through sustainability metrics that companies develop and implement on their own, and structured market initiatives which private firms banding together have developed.
- Private law, which is an application by governments of law relating to things like supply chain relationships and project credit enhancement techniques.

The application of public law in the U.S. has been uneven in the treatment of lithium-ion batteries. Nevertheless, a type of private environmental governance through public-private partnerships has begun to emerge that is facilitating the creative adoption of commercial law related to sustainability through scientific and economic analysis [12].

This type of private governance can take into account the financeability of innovative technologies and facilitate the introduction of innovative technologies on a basis that is positive for the overall societal benefit. One public-private enterprise is the U.S. Center for Automotive Research (USCAR), a collaboration between the U.S. automakers (General Motors, Ford and Fiat Chrysler) and the U.S. Department of Energy (DOE). USCAR has initiated competitive awards to several firms undertaking lithium recycling research and development programs [13].

Another example is the creation of public-private programs in which money is provided by both government and the private sector to develop products where certain procurement standards are met and where revenue streams will support the public interest in assuring the sound financing of these new technologies using lithium-ion batteries and other products [14]. The manner in which procurement decisions are made is important to ensure that manufacturers produce batteries in accordance with industry standards and tests.

Financeability involves not just how much money is made, but how firm is the cash flow. Is the transaction one that bankers will find well organized? Are there assurances of performance? Is the sustainability of the performance long-lasting

enough that the process can be relied upon by the public? Another is by encouraging public and private models resourcing and supporting each other in the research and commercialization of resource efficient products.

Other policies have emerged in the context of private law that identify procedures to deal with the operational and end-of-life risks of lithium-ion batteries. These operational risks can be managed to consider the battery technology, electrical protection, fire detection systems, etc.

The insurance industry has undertaken such initiatives in policy underwriting [15]. Risks are being classified in the following manner:

- Chemical and mechanical risks result from a battery sustaining mechanical damage which causes internal shorting of the battery and can liberate corrosive and flammable electrolyte from the battery.
- Electrical risks include issues associated with current flow in the battery, such as short circuits, overcharging, rapid-discharge, battery cell shorting, etc.
- Operational risks include those that result from the loss of a critical battery function. Examples include loss of emergency systems, failure of high asset value systems and failure of equipment to shut down properly.

While most of these insurance underwriting procedures deal with the safe operation of lithium-ion batteries, the procedures can also extend to safe end-of-life battery treatment.

Levelized Cost of Storage Model

One way to assess the economic impact of public law, private governance and private law is the development of a levelized cost of storage model that will apply certain criteria (internal and external) costs on an equitable basis. These criteria include the costs of materials, production, energy/water consumption, emissions control, end-of-life management and commodity recovery (recycling). resolution.

Using a levelized cost methodology encourages the incorporation of "circular" considerations into the design of batteries (and by extension other products) so that manufactured goods ultimately will have a lower cost profile for the benefit not only of battery consumers, but society (and the environment) at large. The process of using a true levelized cost model that reflects all internal and external costs in a single formula promotes a net value gain in the batteries themselves and, by extension, the materials used in them.

An estimated baseline manufacturing cost of a typical lithium-ion battery unit in a plug-in hybrid electric vehicle has been developed by Argonne National Laboratory [16]. Variable costs (materials, purchased items, direct labor and variable overhead) account for approximately 72% of the total battery cost, while fixed costs (administration, research/development, depreciation and profit after taxes) account for the rest. This calculation, however, does not consider expenses

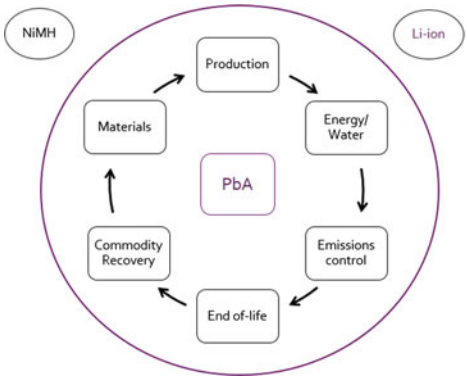

$$\text{LCOS} = \frac{\sum(Capital + O\&M + \text{Fuel} + \text{EOL})}{\sum MWh}$$

Where:

Capital	= Total capital expenditures in year
O&M	= Fixed operation and maintenance costs in year
Fuel	= Charging cost in year
EOL	= End-of-Life costs in year
MWh_t	= The amount of electricity discharged in MWh year measured for capacity factor

Fig. 2 The relationship of criteria for lead-acid (PbA), lithium-ion (Li-ion), and nickel metal hydride (NiMH) battery cost

associated with end-of-life battery management. An estimated cost for collecting and recycling spent lithium-ion batteries, from a separate analysis, has been estimated to be between 40–60% of variable costs [17]. Taking these data together, a 40% increase in variable costs would raise the total levelized cost of a typical 12-volt lithium-ion battery by approximately 28%. The cost of a 12-volt lithium-ion battery, about $250/kWh, would increase to approximately $320/kWh. It is important to note that this approximate increase in the total levelized-cost of a lithium-ion battery is entirely dependent upon (1) the material composition of the battery, (2) whether recycling has been incorporated into the battery design and (3) the degree to which materials emerging at the end of the recycling process would be of comparable quality to materials from virgin sources.

The relationship of these criteria for lead-acid (PbA), lithium-ion (Li-ion) and nickel metal hydride (NiMH) can be visualized (Fig. 2) in a circular diagram accompanying a simplified calculation formula that incorporates end-of-life management costs. In this instance, lead-acid (PbA) batteries can be considered within the circular paradigm by virtue of their 99% recycling rate, which is based on the quality of recycled materials being competitive (in both cost and quality) with virgin materials. In contrast, neither nickel metal hydride (NiMH) nor lithium-ion (Li-ion) can be considered to be within the circular diagram since nickel recovered from spent batteries is used primarily for steel plating and the recycling rate of lithium-ion batteries is only approximately five per cent.

$$\text{LCOS} = \frac{\sum(Capital + O\&M + \text{Fuel} + \text{EOL})}{\sum MWh}$$

Where:

Capital= Total capital expenditures in year
O and M= Fixed operation and maintenance costs in year
Fuel= Charging cost in year

EOL= End-of-Life costs in year
MWh_t= The amount of electricity discharged in MWh year measured for capacity factor

A preliminary cost estimated in a simplified formula such as the one above shows that more research is required. By providing an all-encompassing list of criteria for the circular management of all battery chemistries in a levelized economic modelling format, a clearer picture of battery costs on a truly comparative basis will emerge.

References

1. Marlair G (2012) Protection issues pertaining to large storage of new and used lithium-based batteries. INERIS. In: High challenge storage protection workshop, NFPA/FPRF, Paris
2. Kang DHP, Chen M et al (2013) Potential environmental and human health impacts of rechargeable lithium batteries in electronic waste. University of California, Irvine
3. Li L, Dunn J, Gaines L Recovery of metals from spent lithium-ion batteries with organic acids as leaching reagents and environmental assessment. J Power Sources, 233:180–189
4. Patel P (2017) How green is your electric vehicle, MRS Bull, Energy Quarterly
5. Gaines L (2014) The future of automotive lithium-ion battery recycling: charting a sustainable course, Sustain Mater Technol
6. Commission for Environmental Cooperation (2013) Hazardous trade?, An examination of US-generated spent lead-Acid battery exports and secondary lead recycling in Canada, Mexico, and the United States
7. Wang X, Gaustad G et al (2013) Economies of scale for future lithium-ion battery recycling infrastructure, Rochester Institute of Technology
8. Lazard, Levelized Cost of Storage Analysis, 2015
9. Nelson P et al (2009) Factors determining the manufacturing costs of lithium-ion batteries for PHEVs. In: Argonne national laboratory, EV24 International battery, hybrid and fuel cell electric vehicle symposium
10. Wang, op. cit
11. Richa K (2016) Sustainable management of lithium-ion batteries after use in electric vehicles, Rochester Institute of Technology
12. Feldman R (2017) Developing laws and deals to facilitate public-private circular economy loops, paper delivered at ISWA World Congress
13. Recommended practice for recycling of xEV electrochemical energy storage systems (2014) U.S. Center for Automotive Research
14. An example is the Electronic Product Environmental Assessment Tool, developed in a collaborative process between the U.S. Environmental Protection Agency and private sector entities. https://www.epa.gov/greenerproducts/electronic-product-environmental-assessment-tool-epeat
15. AIG (2013) Managing Lithium-Ion Battery Exposures, AIG Insight|COM-CG-07-0032
16. Nelson, op. cit
17. Wang, Gaustad, op. cit

Recovery of Gallium and Arsenic from Gallium Arsenide Semiconductor Scraps

Dachun Liu, Guozheng Zha, Liang Hu and Wenlong Jiang

Abstract In this paper, a novel technique for recovery of gallium and arsenic by thermal decomposition under vacuum is presented. The effects of distillation temperature on the volatilization behavior of each component were investigated. Theoretical calculations and experimental studies have shown that the method is feasible. The results show that under optimum conditions, highly pure Ga can be extracted with advantages over conventional techniques, including simple operation and environmental friendliness. For example, metallic gallium (purity > 99.99%) is obtained at 1273 K after 3 h under 3–8 Pa. Arsenic is obtained in the form of a elementary substance which could be preserved with relative ease.

Keywords GaAs · Vacuum thermal decomposition · Volatilization Recovery · Gallium

With the continuous consumption of gallium resources and the impact of energy shortage recovery from secondary resources containing gallium is particularly important. GaAs is the most important and most advanced semiconductor material. It is widely used in the field of light, electron and microelectronics and so on. In existing processes for GaAs production, the final yield is often less than 15%, and the remaining GaAs is discarded as debris [1]. GaAs waste has become an important raw material for the production of recycled gallium, in which the content of Ga is close to

D. Liu · G. Zha · L. Hu · W. Jiang (✉)
National Engineering Laboratory for Vacuum Metallurgy,
Kunming University of Science and Technology, Kunming 650093, China
e-mail: jiangwlkg@foxmail.com

G. Zha
The State Key Laboratory of Complex Non-Ferrous Metal Resources Clean Utilization,
Kunming University of Science and Technology, Kunming 650093,
People's Republic of China

D. Liu · G. Zha · L. Hu · W. Jiang
Key Laboratory of Vacuum Metallurgy for Nonferrous Metal of Yunnan Province,
Kunming University of Science and Technology, Kunming 650093, China

Z. Sun et al. (eds.), *Energy Technology 2018*, The Minerals, Metals & Materials Series, https://doi.org/10.1007/978-3-319-72362-4_28

50%. How to separate and recover gallium in a simple, low consumption and efficient way without pollution is of great significance for realizing the comprehensive utilization and sustainable development of the secondary resources.

For many years, researchers have worked on waste treatment and extraction of gallium. Hydrometallurgy and pyrometallurgy are the two main processes. Matsumura Tadanori et al. [2] dissolved waste material with nitric acid. The organic solvent such as Diisooctyl phosphate(P204)was extracted, and then the gallium was extracted by adjusting the pH of the solution obtained by the reverse extraction, finally the gallium can be obtained by electrolysis. Gallium nitrate was recovered from gallium arsenide waste by neutralization and precipitationin a plant in China [3]. Guo Xueyi et al. [4] in Central South University recover the gallium by nitric acid decomposition and sulfide precipitation, and obtained 99.99% purity gallium by electrolysis, the recovery rate of arsenic was 99%, and the loss of gallium slag was 0.3 to 1.5%. The hydrometallurgy process is basically by acid leaching and electrolysis. It has the disadvantages of long process, serious environmental pollution such as the generation of waste acid, waste alkali, waste gas (NO_2) and other pollutants. Another is pyrometallurgy. Mitsubishi Metal Corp [5] chloridize the waste containing gallium with chlorine, $AsCl_3$ and PCl_3 were separated by distillation, the resulting $GaCl_3$ was converted to a lower melting point $GaCl_2$, then the metal was reduced by metals such as Zn, and finally the residual impurities were removed by vacuum distillation. Masayoshi Inooka [6] reported that the waste containing gallium was mixed with oil to be calcined at 400 °C, turn oil into coke, and then mixed into a vacuum furnace to obtain molten metal gallium. It would produce a great deal of $AsCl_3$ in the process of pyrometallurgical chlorination, with considerable risks, and other methods [6, 7] also have disadvantage of long process.

Vacuum metallurgy [8–12] has been widely applied because of its low energy consumption, simplicity and environment-friendliness. In view of these, a vacuum thermal decomposition method was chosen to treat gallium arsenide waste. The influence of distillation temperature and distillation time on the separation efficiency of Ga and As was studied, under the condition of vacuum (3–8 Pa). The optimum technological conditions for vacuum pyrolysis of gallium arsenide wastes were investigated, which provided theoretical and technical basis for the comprehensive recovery of valuable metals such as Ga and As.

Theoretical Analysis of GaAs Vacuum Thermal Decomposition

Thermodynamic Analysis

GaAs is chemically stable and does not react chemically with oxygen or water vapor in air, nor does it react with with non-oxidizing acids, at room temperature. It does decompose at higher temperature. Equations (1)–(4) are the main reactions

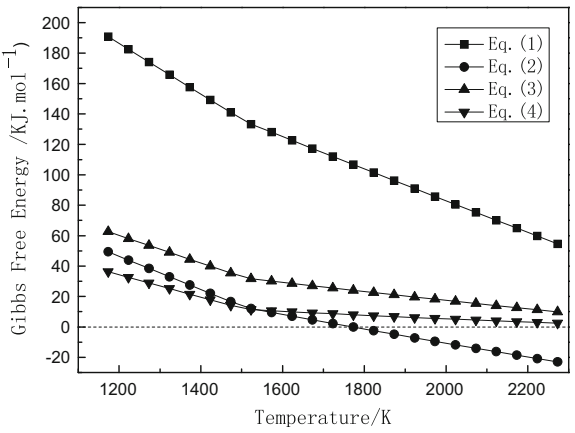

Fig. 1 Relationships between Gibbs free energy and temperature at a atm. pressure

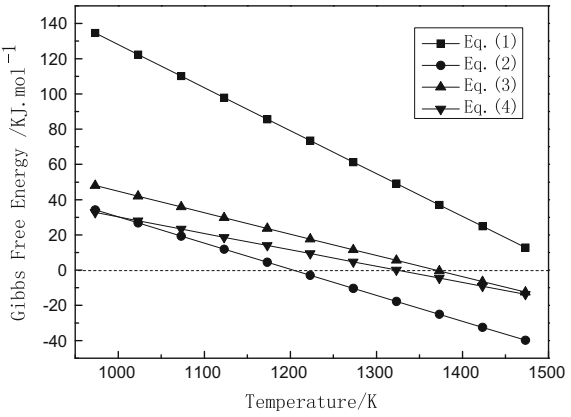

Fig. 2 Relationships between Gibbs free energy and temperature at 10 Pa

that may occur during its thermal decomposition. Taking into account that the vacuum thermal decomposition experiment is carried between 1 and 100 Pa, the relations between Gibbs free energy (ΔG_T) and temperature (T) are shown in Figs. 1 and 2.

$$\mathrm{GaAs} = \mathrm{Ga} + \mathrm{As(g)} \tag{1}$$

$$\mathrm{GaAs} = \mathrm{Ga} + 1/2\mathrm{As_2(g)} \tag{2}$$

$$\mathrm{GaAs} = \mathrm{Ga} + 1/3\mathrm{As_3(g)} \tag{3}$$

$$\mathrm{GaAs} = \mathrm{Ga} + 1/4\mathrm{As_4(g)} \tag{4}$$

Figure 1 shows that, at atmospheric pressure, the direct thermal decomposition temperature of GaAs is 1773 K, with formation of As2(g) following Eq. (2). If the system pressure is 10 Pa, as shown in Fig. 2, GaAs begins to react at 1204 K,

also with generation of As_2 gas. The equilibrium temperatures of Eq. (4) and Eq. (3) are 1326 and 1370 K, whereas the Gibbs free energy of Eq. (1) is still positive at 1500 K. Thus, working under vacuum allows a much lower temperature for the decomposition of GaAs, whose initial reaction temperature dropped from 1773 K to 1204 K.

Vapor Pressure Criterion for Metal Separation in Alloys

A metal has a fixed vapor pressure at a certain temperature. Whether a binary alloy can be separated by vacuum distillation depends on the difference in vapor pressure between components at a given temperature. The elements with high saturation vapor pressure are preferentially volatilized into the condenser, and another element is not volatilized at all and remains for separation purposes. The relationship [13] between vapor pressure and temperature of pure substances can be expressed as

$$\lg p = AT^{-1} + B \lg T + CT + D \tag{5}$$

Where A, B, C and D are the evaporation constants for each element, which can be obtained from the literature [14]. The relation between the saturated vapor pressure and the temperature of pure substances such as arsenic and gallium is obtained by substituting them (5). Drawing the results of the calculation into a lgp-T diagram, gives Fig. 3. P is vapor pressure, T is temperature.

It can be seen that at the same temperature, the saturated vapor pressure of As is much larger than Ga, and the difference between them is more than 10^6. Thus, we can control the temperature to make As preferentially evaporate over Ga, so that gallium and arsenic can be separated.

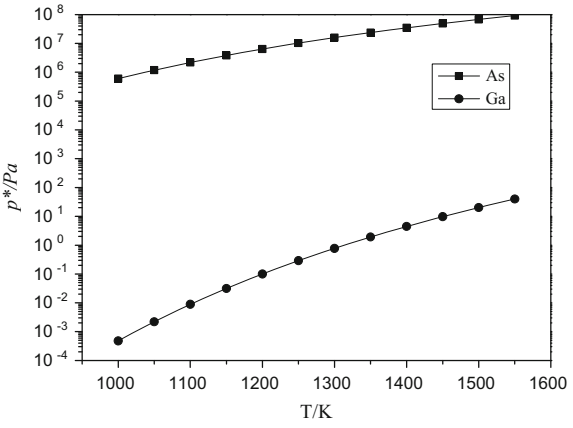

Fig. 3 lgp-T diagram of element As and Ga in pure state

Separation Factor β Criterion for Metal Separation in Alloys

Since the vapor pressure of the alloy composition is different from the vapor pressure of its pure material, each component evaporates in different degrees and has some component in the vapor, which affects the purity of the evaporated main metal. In order to further determine the possibility of separation of alloy components, the separation coefficient can be introduced,

$$\beta_A = \frac{\gamma_A}{\gamma_B} * \frac{P_A^\theta}{P_B^\theta} \tag{6}$$

Where γ is activity coefficient, P^θ is a saturated vapor pressure of pure component. When $\beta_A > 1$, the larger the separation coefficient is, the easier it is to separate. For binary alloy of A-B, the metal A with large saturated vapor pressure will be enriched in vapor phase and metal B with small saturated vapor pressure is enriched in liquid phase. When $\beta_A < 1$,in the same way, alloys can be separated,with A will be enriched in the liquid phase, while B will be enriched in the vapor phase. When $\beta_A = 1$, alloy components A and B are difficult to separate by vacuum distillation. Figure 4 shows the separation factor β of As and Ga at different temperatures. It can be seen that the separation coefficients of As and Ga are far greater than 1. Arsenic and gallium are more easily separated during vacuum distillation. Arsenic is volatilized into the vapor phase and gallium remains.

Phase Diagram Analysis

From the binary alloy phase diagram Ga-As [15], we can see that the 'Homogeneous melting point compound'is formed between Ga and As, and the intermolecular force is stronger. The solid GaAs below 1083.15 K is so stable that

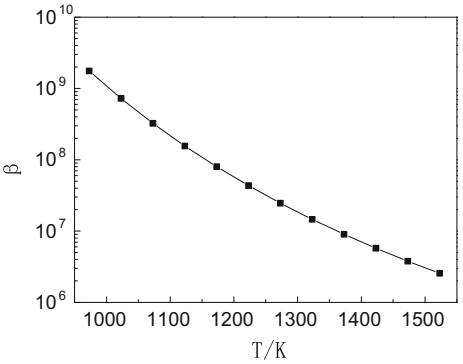

Fig. 4 Separation coefficients β of As and Ga

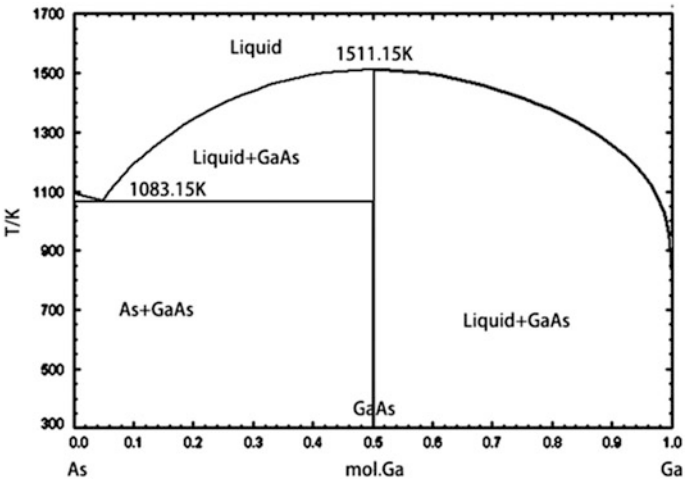

Fig. 5 Ga-As binary phase diagram

gallium and arsenic are not easily separated. Above 1083.15 K, it is possible to separate gallium from arsenic because of the formation of liquid phase (Fig. 5).

Figure 6 shows the relationship between the pressure and temperature of the Ga-As [16], It can be seen that more than 700 K, the saturated vapor pressure of As_2 was much higher than that of gallium, As_2 is more volatile and separates gallium and arsenic. Moreover, with the increase of partial pressure and temperature, the vapor phase changed from As_2 to mixture of As_2 and As_4. When the temperature above 1373 K, the content of gallium in vapor phase will be significantly increased, resulting in condensate containing gallium more, and affect the recovery of gallium.

Experiment

Experimental Materials and Equipment

The raw material used in the experiment is gallium arsenide waste material from a semiconductor plant in Japan, and the main phase is GaAs. The results of chemical analysis are shown in Table 1.

Experimental Process

The experimental setup is shown in Fig. 7. The operation process is as follows. The experimental material is placed in the crucible in the vacuum furnace. The furnace

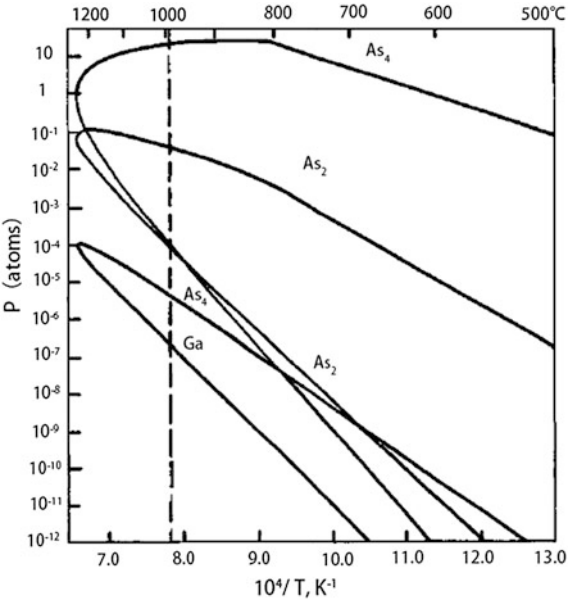

Fig. 6 Pressure-temperature equilibria for the Ga-As system

Table 1 Assay of semiconductor scraps

Component	Ga	As	Zn	Cu	Fe	Si	Others
wt%	48.20	49.82	1.0	0.3	0.03	0.1	0.55

is sealed, the cooling water and the vacuum pumps are turned on..When the limit vacuum (3 Pa) of vacuum furnace is reached, the experimental temperature is increased to 1073–1373 K at a rate of 8–12 K/min. After 1–3 h The vacuum and cooling are kept on until the temperature drops to room temperature. Finally, samples are taken for analysis.

Results and Discussion

Effect of Distillation Temperature on Residue Quality

Figure 8 shows the relationship between distillation temperature and mass of residue under different temperatures at the condition of 3–8 Pa and 2 h of distillation time. It can be seen that when the temperature was below 1123 K, the residue quantity was 100 g, i.e. no reaction occurred. The reaction started around 1173 K. As the temperature increased, the reaction was more intense and the mass decreased more rapidly. At 1273 K, 50.30 g residue was obtained, the surface of which was coated with a layer of slag, which indicated that the material was not fully reacted at

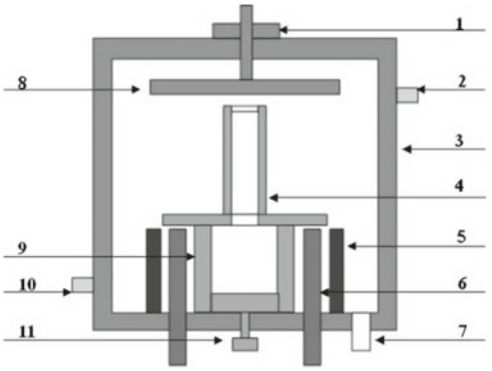

1-Adjustment knob; 2-Cooling water outlet; 3-Wate-cooled walls; 4-Graphite condensing system; 5-Thermal insulating layer; 6-Graphite heater; 7-Vacuum pump; 8-Steel condensing system; 9-Reaction crucible; 10-Cooling water inlet ; 11-Thermocouple

Fig. 7 Schematic diagram of vacuum furnace 1-Adjustment knob; 2-Cooling water outlet; 3-Wate-cooled walls; 4-Graphite condensing system; 5-Thermal insulating layer; 6-Graphite heater; 7-Vacuum pump; 8-Steel condensing system; 9-Reaction crucible; 10-Cooling water inlet; 11-Thermocouple

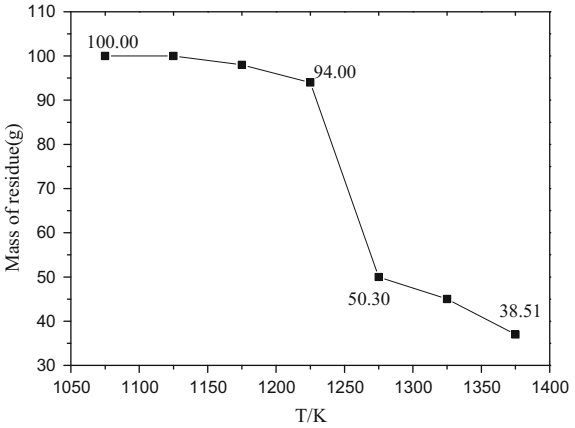

Fig. 8 Relationship between temperature and mass of residue

this time. When the temperature was 1373 K, the mass of residue was 38.51 g, much lower than its theoretical content of 48.20 g. The reaction temperature is so high, that the gallium volatilizes into the vapor, resulting in a greater loss of gallium.

Effects of Distillation Temperature on Gallium Volatilization

As arsenic has a low boiling point and is volatile, the arsenic produced by pyrolysis of gallium arsenide has substantially evaporated into the condensate at a lower

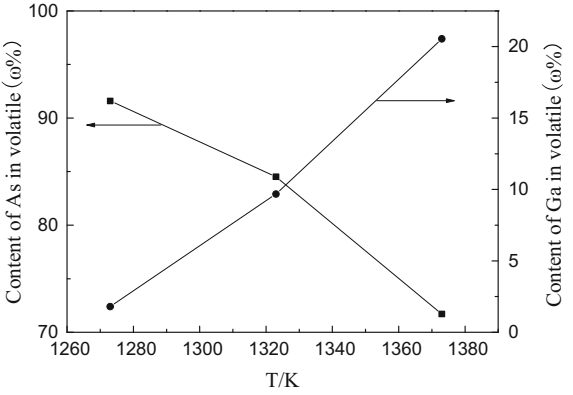

Fig. 9 Relationship between temperature and content of As and Ga in volatile

temperature. Figure 9 shows the relationship between the distillation temperature and arsenic content in the volatiles at the system pressure of 3–8 Pa and the distillation time of 2 h. The arsenic content in the volatiles decreases as the temperature increases, because the increase in temperature promotes the volatilization of Ga, and the higher the temperature, the higher the gallium content in the volatiles, which affects the recovery rate of gallium. When the temperature is 1373 K, the condensate contains gallium up to 20.54%, so to maximize the removal of arsenic and enrichment of gallium, the distillation temperature should be kept below 1373 K.

Effects of Distillation Temperature Time

In order to realize the maximum enrichment of Ga and As, the effect of distillation time on the components was investigated at the system pressure of 3–8 Pa, taking into account the influence of the distillation temperature discussed above. The results are shown in the Table 2.

It can be seen from the table, the condensate containing gallium at least when the distillation temperature is 1273 K, time 2 h, and the volatile content of gallium is 1.80% at this time, thus the amount of the upper layer of more weight 7.83 g, not fully react. Followed by 1273 K, 3 h, the volatiles in gallium containing 6.72%, upper slag mass is 5.23 g.

Then, we used the VG9000 Glow Discharge Mass Spectrometer from Thermo Elemental Company in UK to analyze the total element content of the residue gallium obtained at the distillation temperature of 1273 K and the constant temperature for 2 and 3 h. The samples were tested by liquid nitrogen cooling. The results are shown in Table 3.

As can be seen from Table 3 above, when the distillation temperature is 1273 K and the distillation temperature time is 3 h, the product gallium is obviously purer

Table 2 The experimental condition and products

NO.	Distillation temperature/°C	Distillation time/h	Mass of raw material/g	Residue		Volatiles		Upper slag
				Experimental value/g	Theoretical value/g	Ga/%	As/%	Mass/g
1	1050	1	100	47.22	48.20	8.90	90.98	5.51
2	1000	2		50.30		1.80	91.59	7.83
3	1050	2		45.22		9.68	84.52	2.88
4	1000	3		47.96		6.72	92.97	5.23

Table 3 Results of GDMS test of Ga

Element contents (ppm)	Na	Mg	Al	Si	Ca	Ti	V	Cr	Mn	Bi
Ga (1273 K,2 h)	10	<0.03	0.2	3.4	5	1.1	<0.009	<0.04	1.8	<0.07
Ga (1273 K,3 h)	0.07	<0.002	0.22	3.6	0.62	0.49	<0.3	0.03	0.8	<0.003
Element contents (ppm)	[a]Fe	Ni	Cu	Zn	Ge	In	Cd	Sn	Hg	Pb
Ga (1273 K,2 h)	58	<0.6	<0.1	<0.2	<0.3	<0.07	<0.7	<0.2	<0.5	<0.08
Ga (1273 K,3 h)	70	<0.007	<0.009	<0.02	<0.03	<0.003	<1	<0.01	<0.04	<0.006

Note: [a] possible interference

than that obtained at 1273 K and 2 h. The detection of iron is not reliable. The remaining impurities are lower than the quality of rough gallium standards [16]. Based on the above results, the optimum experimental conditions for the thermal decomposition of gallium arsenide waste are 1273 K for distillation temperature and 3 h for distillation time, and the content of gallium in the condensate is less. It can be seen that the experimental results are basically consistent with the previous theoretical analysis.

TG-DTG Analysis of Raw Materials

The thermal analysis of non-constant temperature TG-DTG from room temperature to 1323 K is carried out by German Chi-Chi STA449F3A-0046-M synchronous thermal analyzer, which can study the quality of gallium arsenide waste during heating with temperature changes. Thermogravimetry under vacuum and the protection of nitrogen at room temperature, sample is weighed and put into the balance on the instrument. Then continue to pass through the nitrogen for 10 min, turn off the intake valve, and start the vacuum pump.

When the instrument pressure is reduced to 10 kPa, which began to programmed temperature, heating rate is 10 K/min, the experimental results are shown in Fig. 10.

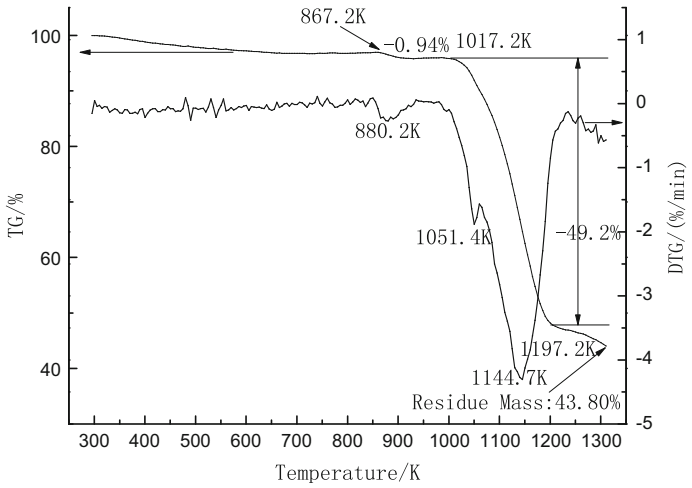

Fig. 10 The TG-DTG curves of GaAs scraps

As shown in Fig. 10, from 867.2 K to 968 K, there is a smaller reduction in weight (?), about 0.94%, mainly because of a small excess of arsenic in the waste material and near the boiling point of 887 K, endothermic sublimation. In the temperature range of 1017.2–1197.2 K, the TG curve is very steep and the weight loss is fast, which is 49.2%. During the period, a violent chemical reaction occurred and the gallium arsenide waste was decomposed to produce gallium and arsenic. The theoretical weight loss rate is 51.80%, which is close to the experimental value. The temperature from 1197.2 K has been increased to 1323 K, TG curve is relatively flat, weight loss rate becomes smaller, and the final residue of the amount of 43.80%, less than the theoretical residue of 48.20%, because some of the gallium heat and volatile at this time.

Conclusion

(1) For gallium arsenide waste, vacuum heat decomposition method can effectively recover the metal gallium, and the product obtained is higher than the quality requirement of crude gallium. Compared with the traditional process, this method has the advantages of simple process, no waste water, waste gas and other pollutants. Arsenic is recovered in the form of arsenic. It can not only reduce environmental pollution, but also change waste into treasure, avoid waste of resources, and meet the development needs of cleaner production in metallurgical industry.

(2) The distillation temperature and distillation time have great influence on the enrichment of gallium and arsenic. When the temperature is higher than

1373 K, the gallium is volatile and the content of gallium in the gas phase increases greatly, which affects the recovery of gallium. When at the condition of 3–8 Pa, 1273 K and constant time is 3 h, the quality of the residual gallium is better, the purity is greater than 99.99%, and the content of arsenic in the volatile matter is 87.97%, containing gallium 6.72%.

(3) Due to strong interaction between gallium and arsenic, which leads to the incomplete decomposition of raw materials, the condensate containing few gallium, thus affecting the recovery of gallium. For this problem, we can solve it by second distillation to the scum and condensate, or the improvement of existing methods and equipment.

References

1. Lee HS, Nam CW (1998) A study on the extraction of gallium from gallium arsenide scrap. Hydrometallurgy 49(1/2):125–133
2. Matsumura T, Fujimoto A et al (1986) Recovery of gallium from material containing intermetallic compound of gallium and arsenic. JP: 61215214A, 1986-09-25
3. Lingzhi Z, Gang C (2008) Extraction and metallurgy of rare metals. Metallurgical Industry Press, Beijing, pp 343–348
4. Guo X, Ping L, Kai H et al (2005) A methods for recovery of gallium and arsenic from gallium arsenide industrial waste . CN: 200510031531.8, 2005-11-09
5. Mitsubishi Metal Corp. Recovering of High-purity Gallium. JP: 0104434. 1989- 01
6. Inooka M, Yokohama (1989) Process for recovering metallic gallium from gallium compound-containing waste. JP: 4812167, 1989-03-14
7. Fang H (2010) Gallium and arsenic purification and recovery methods for waste gallium arsenide. CN: 101857918A, 2010-10-13
8. Dai YN, Yang B, Wen-Hui MA et al (2004) Advances in vacuum metallurgy of nonferrous metals. Vacuum
9. Yang B, Kong LX, Bao-Qiang XU et al (2015) Recycling of metals from waste Sn-based alloys by vacuum separation. Trans Nonferrous Met Soc China 25(4):1315–1324
10. Liu DC, Yang B, Dai YN et al (2004) Study on recovering Ga from GaAs scraps by vacuum metallurgy. Vacuum
11. Jiang WL, Deng Y, Yang B et al (2013) Application of vacuum distillation in refining crude indium. Rare Met 32(6):627–631
12. Zhan L, Xu Z (2008) Application of vacuum metallurgy to separate pure metal from mixed metallic particles of crushed waste printed circuit board scraps. Environ Sci Technol 42 (20):7676
13. Dai YN, Yang B (2004) Non-ferrous metal vacuum metallurgy, Metallurgical Industry Press, Beijing, pp 24–28
14. Dai YN (2009) Atlas of two element alloy phase. Beijing Metallurgical Industry Press, pp 80–83
15. Stringfellow Gerald B (1989) Organometallic vapor-phase epitaxy: theory and practice. Academic Press, London, pp 39–46
16. Liu DC, Yang B, Dai YN et al (2004) Study on GaAs gallium scrap recycling vacuum processing. Vacuum 41(3):18–20

Rapid Removal of Pb(II) from Acid Wastewater Using Vanadium Titanium-Bearing Magnetite Particles Coated by Humic Acid

Manman Lu, Yuanbo Zhang, Zijian Su, Bingbing Liu, Guanghui Li and Tao Jiang

Abstract Acid wastewater containing toxic metal ions has become increasingly important global environmental concern and lead (Pb) is one of the prime toxic heavy metal ions. Humic acid (HA), a kind of natural organic matter, has been proven to have a great adsorption capacity for metal cations (Pb^{2+}, Cu^{2+}, etc.). Our previous study has verified that HA has excellent adsorbing ability on vanadium titanium-bearing magnetite(VTM) particles. In this study, VTM-HA complex magnetic particles were prepared for removing Pb(II) from acid wastewater, which could be easily recycled by magnetic separation. The effects of pH value, ionic strength and VTM-HA concentration on the removal ratio of Pb(II) were determined by isothermal adsorption tests. The results indicated that Pb(II) adsorption was subject to pH and ionic strength. When initial Pb(II) concentration is 100 mg/L, the residual concentration and removal ratio of Pb(II) reach 0.17 mg/L and 99.83%, respectively, which are much lower than the discharge standard.

Keywords Acid wastewater · Removal of Pb(II) · Humic acid
V, Ti-bearing magnetite

Introduction

Water pollution due to the indiscriminate disposal of metal ions and organic contaminants has been a rising worldwide environmental concern. [1] Lead (Pb) has been considered as one of the most hazardous heavy metals. [2] Nowadays, adsorption has become one of the major methods for removing Pb(II) from wastewater owing to the high removal efficiency, environmentally friendly, excellent recyclability, etc. [3] Many researches indicate that preparing an efficient, green and easy-recycled absorbent is critical to all of the adsorption methods.

M. Lu · Y. Zhang (✉) · Z. Su · B. Liu · G. Li · T. Jiang
School of Mineral Processing and Bioengineering, Central South University, Changsha 410083, Hunan, China
e-mail: zybcsu@126.com

Z. Sun et al. (eds.), *Energy Technology 2018*, The Minerals, Metals & Materials Series, https://doi.org/10.1007/978-3-319-72362-4_29

Humic acid (HA) is a kind of natural organic matter extracted from lignite, weathered coal, soil, etc. [4] As reported, HA has great adsorption capacity with metal cations (Pb^{2+}, Cu^{2+}, etc.) due to the skeleton of alkyl and aromatic ring attached by the oxygen-containing groups (carboxyl, hydroxyl, etc.). [5] HA was ever used as natural adsorbents to remove heavy metal ions from wastewater [6]. However, high concentration of HA would increase the chemical oxygen demand (COD) of water and deteriorate the water quality [7]. Therefore, HA adsorbents must be combined with efficient carriers to prevent them from entering into the water.

Previous literatures demonstrated that iron oxides, especially Fe_3O_4, were good carriers for HA adsorbents [8–10]. The synthetic Fe_3O_4/HA complex sorbents are easily recycled due to the strong magnetism. Liu, et al. reported that the removal ratios of Cu(II), Cd(II), Hg(II) and Pb(II) by Fe_3O_4/HA complex were much higher than those by single Fe_3O_4 particles, especially at low pH value range. [11] Other studies showed that iron oxides could react with heavy metal ions so as to improve the adsorption effect. Jiang, et al. found the Fe(II) in magnetite can initiate the reduction of Cr(VI) to Cr(III). Then, Cr(III) can be complexed with the functional groups (hydroxyl, carboxyl, etc.) of HA. [12] Most of previous literatures indicated that synthetic iron oxide nanoparticles were used as the carriers for HA. However, there was almost no investigation that natural iron minerals (hematite, magnetite, etc.) particles were applied to be carriers for HA. In addition, the iron oxide nanoparticles are highly susceptible to air oxidation, easily aggregated in various water systems [13] and are expensive, which restricts the large-scale application in environment remediation.

Vanadium titanium-bearing magnetite (VTM) is a kind of natural iron minerals, the main components of which include magnetite, titanomagnetite, ilmenite, etc. [14] The previous researches conducted by the author's group reported that HA had special affinity to the VTM particles compared with other natural iron oxide minerals (magnetite, hematite, etc.). [15]

In this study, therefore, we put forward to use the VTM microparticles as magnetic carriers for HA adsorbents. Then, the VTM-HA magnetic complex was used to remove Pb(II) from acid wastewater. The effect of pH, ionic strength and VTM-HA concentration on removal of Pb(II) were determined.

Materials and Methods

Materials

The VTM samples from Sichuan province in China were firstly ground to a small particle size ($d_{0.5}$ = 2.94 μm, specific surface area = 9.23 m^2/g) for preparing the magnetic carriers for HA adsorbents. HA was extracted from the lignite samples taken from Shanxi province in China. [16] The properties of HA have been reported

in our previous publication [17]. All the reagents were purchased from Sinopharm Chemical Reagent Co., Ltd. (Shanghai, China). Ultrapure water (>18 mΩ) was used to prepare all of the solutions.

Adsorptive Experiments

The naked VTM particles were put into HA solution and stirred for 24 h to prepare the VTM-HA complexes particles. The adsorption experiments were carried out under isotherm conditions by using batch techniques. The Pb(II) solution prepared from $Pb(NO_3)_2$ (AR) was used in adsorptive experiments. 50 mL Pb(II) solution with different concentration was poured into an Erlenmeyer flask. Then the VTM-HA complexes were weighted and added into the Erlenmeyer flask, oscillating for 24 h at 298 K to achieve the adsorption equilibrium state. Next, the suspension was filtered using a 0.45 μm membrane filter. Pb(II) concentration of filtrate was analyzed by ICP-MS, which was identified as the equilibrium concentration of Pb(II). The amount of Pb(II) adsorbed by the VTM-HA complex under different experimental conditions was obtained from the following equation:

$$q_e = \frac{(C_o - C_e) \cdot V}{m} \tag{1}$$

Where q_e is the adsorbing amount of Pb(II) on VTM-HA, C_o and C_e are the initial and equilibrium concentrations of Pb(II) ($mg \cdot L^{-1}$), respectively; V is the volume of Pb(II) solution (L); m is the weight of VTM-HA adsorbent (g).

The effect of pH and ionic strength on removal of Pb(II) was measured using the same procedure mentioned above, the pH value was adjusted from 3 to 8 and the ionic strength was adjusted to 0.001, 0.01 and 0.1 M by adding a certain amount of $NaNO_3$ powders.

The isotherm adsorption experiments were conducted under 298, 308 and 318 K, respectively. Meanwhile, the initial concentration of Pb(II) varied from 5 to 150 mg/L and the pH value was fixed as 5. The suspension was filtered immediately when the adsorptive time reached at 30 s, 1 min, 2 min, 3 min, 5 min, 7 min, 10 min, 20 min, 30 min, 60 min, 120 min, respectively. The adsorption kinetics were measured by changing the adsorptive time.

Results and Discussions

Effect of PH on Adsorption of Pb(II)

The pH value of the solution plays an important role on the adsorption of Pb(II) on VTM-HA complexes. Figure 1 showed that the adsorption of Pb(II) on VTM-HA at

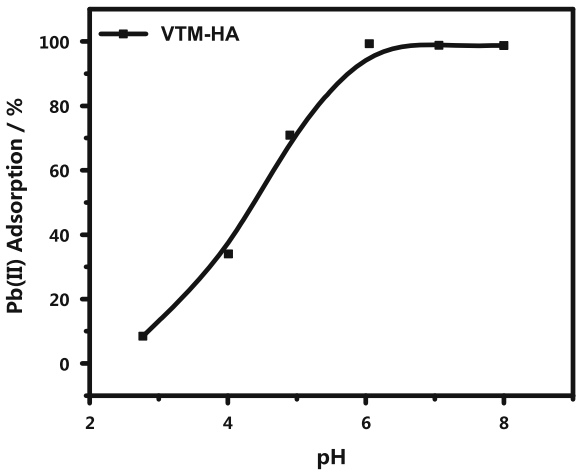

Fig. 1 The adsorption of Pb (II) on VTM-HA at various pH value *(Pb* $(II)_{initial}$ *= 10 mg/L, VTM-HA concentration (m/V) = 0.4 g/L, I = 0.01 M* $NaNO_3$*, T = 298 K)*

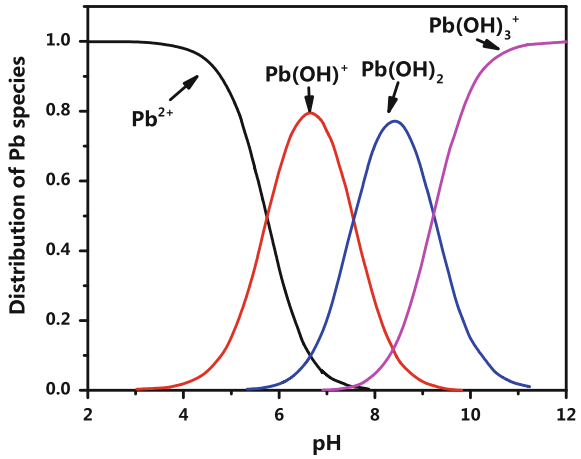

Fig. 2 The distribution of Pb species at different pH values

various pH value. The adsorption of Pb(II) increased quickly within the pH value range of 3 ~ 6, then maintained nearly constant within pH range of 6 ~ 8. It was known that lead species presented in the forms of Pb^{2+}, $Pb(OH)^+$, $Pb(OH)_2$ and $Pb(OH)_3^-$ at different pH values. Figure 2 is the present forms of lead at different pH values. When pH is less than 4, the dominant lead specie was Pb(II) and the removal of Pb(II) was mainly accomplished by adsorption reaction. At the low pH, the competition between H^+ and Pb(II) on the surface sites impeded the adsorption of Pb(II). On the other hand, the agglomeration degree of HA was extremely high at low pH, [5] therefore the adsorption sites for Pb(II) on the VTM-HA complex surface were reduced, decreasing the adsorbing efficiency of Pb(II). The main species of Pb at pH 5 ~ 8 were $Pb(OH)^+$ and $Pb(OH)_2$ and thus the adsorption of Pb was possibly accomplished by adsorption of $Pb(OH)^+$ and simultaneous

precipitation of $Pb(OH)_2$. With the increasing of pH value, the agglomeration degree of HA weakened. [5] These reasons facilitated the adsorption of Pb on the VTM-HA. From the results, it was verified that the suitable pH values for Pb(II) removal were 6–8.

Effect of Ionic Strength on Adsorption of Pb(II)

The ionic strength of solution was also a factor worthy of attention to Pb(II) adsorption. Figure 3 shows the adsorbing characteristics of Pb(II) at different ionic strength, and the electrolyte was sodium nitrate. As shown in Fig. 3, with increasing ionic strength, the adsorption of Pb(II) decreased slightly, indicating that higher ionic strength of solution was detrimental to Pb(II) adsorption. The main cause was likely that with the increase of ionic strength, the activity coefficient of Pb(II) was declined, impeding the diffusion of Pb(II) onto the surface of VTM-HA.

Effect of VTM-HA Concentration on Adsorption of Pb(II)

The emission monitoring of wastewater manifested that the Pb(II) concentration of wastewater was around 100 mg/L in general. Next, the effect of adsorbent dosage on Pb(II) adsorption was conducted under the condition of Pb(II) concentration of 100 mg/L. As shown in Fig. 4, the Pb(II) adsorption was promoted with the increasing of VTM-HA concentration. Under the optimum condition, the removal and residual amount of Pb(II) could achieve 99.83 wt% and 0.17 mg/L respectively, which is far below the emission standard (0.5 mg/L). The results showed

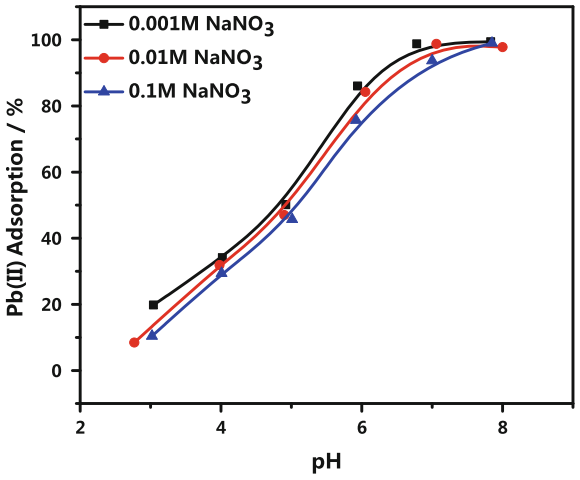

Fig. 3 The adsorption of Pb (II) on VTM-HA at various ionic strength *(Pb $(II)_{initial}$ = 10 mg/L, VTM-HA concentration (m/V) = 0.4 g/L, T = 298 K)*

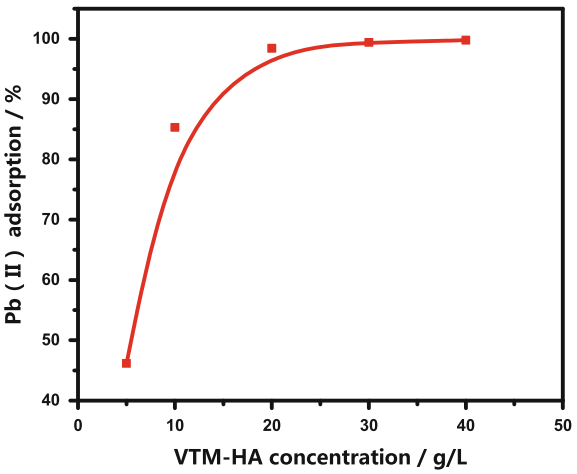

Fig. 4 The effect of VTM-HA concentration *(Pb $(II)_{initial}$ = 100 mg/L, pH = 5, T = 298 K)*

that higher VTM-HA concentration could provide more adsorbing site for Pb(II), thus the Pb(II) adsorption increased with the increasing of VTM-HA concentration.

Adsorption Kinetics

The Pb(II) adsorption kinetics was analyzed for investigating the adsorption process of Pb(II) onto VTM-HA. The adsorption of Pb(II) as a function of adsorption time was showed in Fig. 5, which were analyzed according to pseudo-second-order

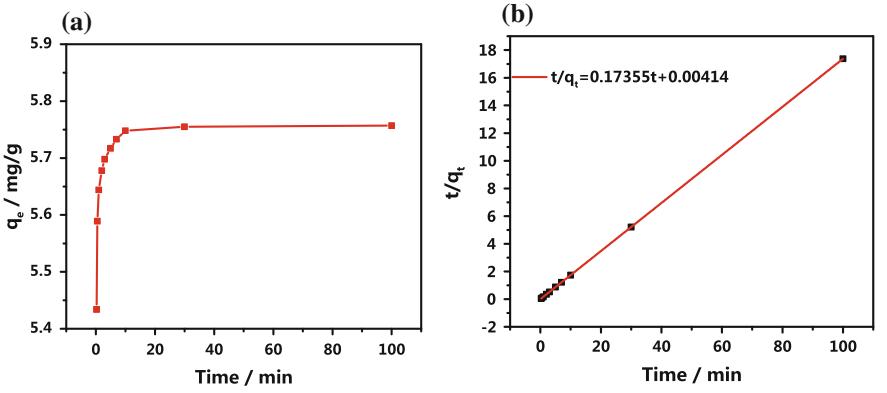

Fig. 5 Relationship between adsorption capacity of VTM-HA to Pb(II) and adsorbing time (**a**). The fitting curves of the pseudo-second-order model (**b**) *($Pb(II)_{initial}$ = 10 mg/L, VTM-HA concentration (m/V) = 0.4 g/L, I = 0.01 M NaNO3, pH = 5 and T = 298 K)*

kinetics model. [2] The linear form of the equation that represents this model is as follows:

$$\frac{t}{q_t} = \frac{1}{k_2 q_e{}^2} + \left(\frac{1}{q_e}\right) t \tag{2}$$

Where k_2 (g/ mg·min^{-1}) is the pseudo-second-order rate constant of adsorption, q_e and q_t (mg·g^{-1}) are the amounts of the Pb(II) adsorbed at equilibrium and at time t.

As shown in Fig. 5, the Pb(II) was adsorbed onto VTM-HA rapidly, and the adsorption equilibrium achieved at about 10 min. The result indicated that the VTM-HA adsorbent has a strong combination with Pb(II). The plot of t/q_t versus t yielded a well-fitted straight line with a good correlation coefficient (R^2 = 0.999), suggesting that the adsorption on the VTM-HA complex followed a pseudo-second-order kinetic model. It proved that the Pb(II) adsorption on VTM-HA belonged to chemisorption.

Adsorption Isotherms

The adsorption isotherms of Pb(II) onto VTM-HA at 298, 308 and 318 K were given in Fig. 6. As shown in Fig. 6, the adsorption capacity of VTM-HA to Pb(II) was the highest at 318 K, indicating that the higher temperature promoted the adsorption of Pb(II). The experimental data for Pb(II) adsorption onto VTM-HA were analyzed by Langmuir and Freundlich model. The form of the Langmuir isotherm can be represented by the following equation:

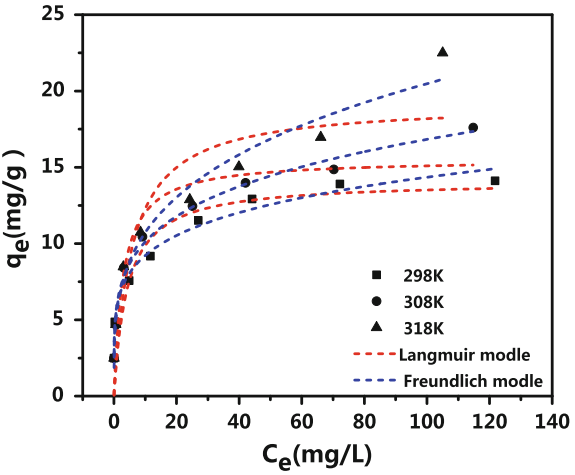

Fig. 6 Adsorption isotherms and the Langmuir, Freundlich models fitting for Pb(II) on VTM-HA at three different temperatures *($Pb(II)_{initial}$ = 5 −150 mg/L, I = 0.01 M $NaNO_3$, VTM-HA concentration (m/V0 = 2 g/L, pH = 5)*

Table 1 Parameters for Langmuir and Freundlich models of Pb(II) adsorption on VTM-HA

T (K)	Langmuir			Freundlich		
	q_{max} (mg/g)	b ($L \cdot mg^{-1}$)	R^2	k_F ($mg^{1-n} \cdot L^n \cdot g^{-1}$)	n	R^2
298	14.088	0.235	0.811	5.918	0.192	0.986
308	15.53	0.346	0.898	6.075	0.165	0.990
318	19.21	0.178	0.844	5.620	0.281	0.976

$$q_e = \frac{bq_{max}C_e}{1 + bC_e} \tag{3}$$

Where q_e (mg/L) is the amount of Pb(II) adsorbed per weight unit of solid after equilibrium, C_e ($mg \cdot L^{-1}$) is the equilibrium concentration of Pb(II) remained in solution, q_{max} ($mg \cdot L^{-1}$) is the amount of Pb(II) at complete monolayer coverage and b ($L \cdot mg^{-1}$) is a constant that relates to the heat of adsorption.

Another common adsorption isotherm model is Freundlich model which is usually used for several kinds of adsorption sites on the solid surface and represents properly the adsorption data at low and intermediate concentrations on heterogeneous surface. The model equation was shown below:

$$q_e = k_F C_e{}^n \tag{4}$$

Where q_e (mg/L) is the amount of Pb(II) adsorbed per weight unit of solid after equilibrium, k_F ($mg^{1-n} \cdot L^n \cdot g^{-1}$) represents the adsorption capacity when Pb(II) ion equilibrium concentration equals to 1, C_e ($mg \cdot L^{-1}$) is the equilibrium concentration of Pb(II) remained in solution and n represents the degree of dependence of adsorption at equilibrium concentration.

The adsorption of Pb(II) on VTM-HA were regressively fitted with Langmuir and Freundlich model, and the fitting curves were shown in Fig. 6. The related values fitted by these two model and the model parameters were listed in Table 1. The R^2 values posted in Table 1 illustrated that the Pb(II) adsorption isotherms were more subject to Freundlich model compared with Langmuir model. The result manifested that the Pb(II) adsorbing sites on the surface of VTM-HA were non-uniform and the Pb(II) ion was probably adsorbed on the VTM-HA in multilayer. Further investigation would be carried out on this phenomenon.

Conclusions

The study indicated that the VTM-HA complex adsorbent can effectively remove Pb(II) from the wastewater. From the results, it is concluded that the Pb(II) adsorption on VTM-HA is strongly dependent on pH value and ionic strength of the solution. The appropriate pH range for Pb(II) adsorption is at 6–8, and the low ionic

strength is favorable for the Pb(II) adsorption. Under the optimal conditions, the removal rate and residual amount of Pb(II) could achieve 99.83 wt% and 0.17 mg/L, respectively.

The adsorption isotherm of Pb(II) by VTM-HA complex is more consistent with Freundlich model, indicating that the Pb(II) was adsorbed onto the VTM-HA in multilayer. In addition, the adsorption of Pb(II) was positively related to the temperature. Further investigation will be carried out and reported in future.

Acknowledgements The authors would express their heartful thanks to Central South University Innovation Foundation for Postgraduate (2017zzts128).

References

1. Zhou G, Luo J, Liu C (2016) A highly efficient polyampholyte hydrogel sorbent based fixed-bed process for heavy metal removal in actual industrial effluent. Water Res 89(2):151–160
2. Huang G, Wang D, Ma S, Chen J, Jiang L, Wang P (2015) A new, low-cost adsorbent: Preparation, characterization, and adsorption behavior of Pb(II) and Cu(II). J Colloid Interface Sci 445(1):294–302
3. Fenglian F, Wang Q (2011) Removal of heavy metal ions from wastewaters: a review. J Environ Manag 92(3):407–418
4. Zhang Z, Liu J, Cai X, Jiang W, Luo W, Jiang G (2011) Sorption to dissolved humic acid and its impacts on the toxicity of imodazolium based ionic liquids. Environ Sci Technol 45 (4):1688–1694
5. Zhou Y, Zhang Y, Li G, Yudong W, Jiang T (2015) A further study on adsorption interaction of humic acid on natural magnetite, hematite and quartz in iron ore pelletizing process: Effect of the solution pH value. Powder Technol 271:155–166
6. Klučáková M, Pavlíková M (2017) Lignitic humic acid as environmentally-friendly adsorbent for heavy metals. J Chem 3:1–5
7. Lowe J, Hossain M (2008) Application of ultrafiltration membranes for removal of humic acid from drinking water. Desalination 218(1–3):343–354
8. Peng L, Qin P, Lei M, Zeng Q, Song H, Yang J (2012) Modifying Fe3O4 nanoparticles with humic acid for removal of Rhodamine B in water. J Hazard Mater 209–210(1):193–198
9. Niu H, Zhang D, Zhang S, Zhang X, Meng Z, Cai Y (2011) Humci acid coated Fe3O4 magnetite nanoparticles as highly efficient Fenton-like catalyst for complete mineralization of sulfathiazole. J Hazard Mater 190(1–3):559–565
10. Illés E, Tombácz E (2003) The role of variable surface charge and surface complexation in the adsorption of humic acid on magnetite. Colloid Surf Physicochem Eng Asp 230(1–3):99–109
11. Liu J, Zhao Z, Jiang G (2008) Coating Fe3O4 magnetic nanoparticles with humic acid for high efficient removal of heavy metals in water. Environ Sci Technol 42(18):6949–6954
12. Jiang W, Cai Q, Wei X, Yang M, Cai Y, Dionysiou DD, O'Shea KE (2014) Cr (VI) Adsorption and Reduction by Humic Acid Coated on Magnetite. Environ Sci Technol 48 (14):8078–8085
13. Yang S, Zong P, Ren X, Wang Q, Wang X (2012) Rapid and highly efficient preconcentration of Eu(III) by core-shell structured Fe3O4@Humic acid magnetic nanoparticles. Appl Mater Interfaces 4:6891–6900
14. Li W, Fu G-Q, Chu M-S, Zhu M-Y (2017) Oxidation induration process and kinetics of Hongge vanadium titanium-bearing magnetite pellets. Ironmak Steelmak 44(4):294–303

15. Zhang Y, Zhou Y, Jiang T, Han G, Li G, Bin X (2012) Applications of MHA binder in oxidized pellets preparation from vanadium, titanium-bearing magnetite concentrates. J Cent South Univ Sci Technol 43(7):2459–2465
16. Jiang T, Li G, Zhang Y, Yang Y, Huang Y, Guo Y, Fan X, Chen X, Qiu G (2009) An organic copolymer binder for iron ore pellets and its application method. China Patent No. 200910309383.X
17. Zhou Y, Zhang Y, Li P, Li G, Jiang T (2014) Comparative study on the adsorption interactions of humic acid onto natural magnetite, hematite and quartz: Effect of initial HA concentration. Powder Technol 251(1):1–8

Study of the Synthesis of $MgAl_2O_4$ Spinel Refractory from Waste Chromium Slag of a Chrome Plant in China

Jinxia Meng, Weiqing Chen, Jizeng Zhao and Li Liu

Abstract This paper discusses the utilization of chromium slag, which presently has no useful application in China, as a resource. The following research has been done in this paper: (1) After determining the composition and properties of chromium residue we decided to test the idea of using chromium slag as a component in synthetic $MgAl_2O_4$ spinel material. (2) Through experiments on sintering and electric melting of refractory materials we determined the best conditions for a practical process. (3) We compared the performance of the refractory material obtained with traditional spinel refractory materials and confirmed the excellent performance of our system. The results show the feasibility of preparing $MgAl_2O_4$ spinel material from chromium slag by electric melting.

Keywords Chromium slag · $MgAl_2O_4$ spinel · Refractory raw material Electric-melting method · Sintering method

Introduction

Magnesium aluminate ($MgAl_2O_4$) spinel is the only compound in the MgO-Al_2O_3 system. It possesses a high melting point (2135 °C) and is known for its high refractoriness, low thermal expansion, chemical stability, thermal shock resistance and corrosion resistance [1–5]. In recent years, the primary high aluminum ore resources are becoming increasingly scarce and the cost is increasing. Chromium slag is at the low-end of the market, not only the price is low, and the sales volume is not high, but there is the problem of toxicitye of the hexavalent chromium. Some ferroalloy enterprises began to consider using chromium slag to make a high-end

J. Meng (✉) · W. Chen
State Key Laboratory of Advanced Metallurgy,
University of Science and Technology Beijing, Beijing 100083, China
e-mail: ustbmjx@163.com

J. Zhao · L. Liu
Beijing Lier High-Temperature Materials Co. Ltd., Beijing 102200, China

Z. Sun et al. (eds.), *Energy Technology 2018*, The Minerals, Metals & Materials Series, https://doi.org/10.1007/978-3-319-72362-4_30

refractory material. The higher value would support the cost of the detoxification treatment. Therefore, we studied preparation of magnesium aluminate spinel refractory materials from chromium slag.

Materials and Methods

Material

Origin of Chromium Slag

Chromium slag is a waste residue produced in the smelting of chromium. The slag we tested came from a large ferroalloy plant in China. It is high in Al_2O_3. The composition, the physical and chemical properties of the slag are shown in Tables 1 and 2. As of November 2015, the this inventory of chromium slag in the plant was 42000t. Due to the continuous smelting of chromium metal, the plant's chromium slag inventory increases by 25000 to 35000t per year.

Process

The slag is produced by the thermite method,. The process uses elemental aluminum to react with chrome oxide to make chromium metal.

The equation for the chemical reaction is:

$$Al + Cr_2O_3 = Al_2O_3 + Cr. \quad (1)$$

The process involves intense reaction of aluminum powder and chromium oxide in the molten state, then rapid transition from alumina to corundum, and a small amount of unreacted Cr_2O_3 forms a solid solution with the reaction product Al_2O_3, namely the aluminum chromium slag, referred to as the chromium slag.

Process Design for Preparation of Refractory Raw Material from Chromium Slag

According to the research of the predecessors, generally two methods are used for the synthesis of $MgAl_2O_4$ spinel i.e. sintering and electric melting. Taking into

Table 1 Chemical composition of chromium slag studied in this paper (%)

Al_2O_3	Fe_2O_3	MgO	CaO	SiO_2	Na_2O	Cr_2O_3
72–82	0.2	0.5	1.4–2.4	0.3	1.5–2.0	13–18

Table 2 Physical characteristics of chromium slag

Bulk density, g/cm^3	Porosity, %	Water absorption, %	Mohs hardness	Refractoriness, °C	Load softening temperature of $T_{0.6}$, °C
3.68	5.24	1.48	9	$\geq$ 1950	$\geq$ 1750

account the characteristics of the raw material, we designed the experiments as follows: First, conduct the one-step process sintering experiments (that is, the typical synthesis methods of refractory materials), then the two-step sintering experiments, and finally the experiments where the raw materials are melted in an electric furnace.

Experimental Design of Sintering Method

The sintering process is a method of synthesizing $MgAl_2O_4$ spinel by calcination at high temperature. The calcination equipment used in China is mainly the rotary kiln. First, grind the material to a fine powder, then press it into pellets in the dry state, and calcine it finally into the rotary kiln. The process is shown schematically in Fig. 1a.

(1) Design of the one-step sintering experiments

The chemical indicators of main raw materials are shown in Table 3. Light burning magnesium and chromium slag using different ratios (see Table 4). The raw material is mixed, trapped, shaped, dried and sintered at first, and then sintered at

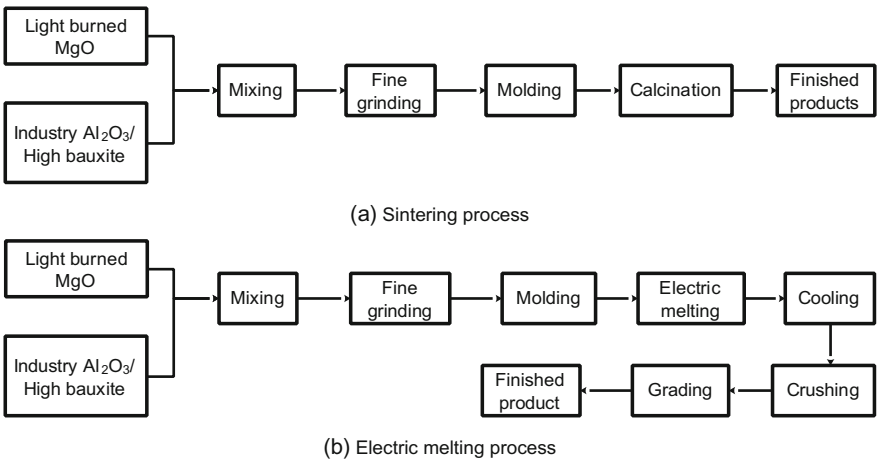

Fig. 1 Process routes of the synthesis of $MgAl_2O_4$ spinel. **a** Sintering process, **b** Electric melting process

Table 3 Chemical analysis of main raw materials for sintering experiment (%)

	Al_2O_3	Fe_2O_3	MgO	CaO	SiO_2	Na_2O	Cr_2O_3	Burning reduction	Total
Chromium slag	81.07	0.18	0.65	1.56	0.33	1.99	13.86	0.00	99.64
Light burned magnesium	0.01	0.43	95.41	1.19	0.78	/	/	1.93	99.76

Table 4 Tests on different ratios of chromium slag and light burned magnesium (%)

	Particle size/ mesh	A	B	C	D	E	F
Chromium slag	200	95.00	84.00	72.00	60.00	48.00	34.00
Light burned magnesium	200	5.00	16.00	28.00	40.00	52.00	66.00

1500, 1600, 1700, and 1750 °C, in average temperature for 3 h, finally examine the performance of the synthesis of refractory materials.

(2) Design of the two-step sintering experiments

First, the sample was calcined at 1350 °C for 3 h, then ground, put in molds, and finally sintered at different temperatures.

Design of Electric-Melting Experiments

First, a suitable block of material is melted into an arc furnace with a three-phase electrode, and then cooled into a solid MgAl2O4 spinel (see Fig. 1b). Due to the high temperature of the arc, the raw material is completely melted into liquid, so the MgAl2O4 spinel structure is expected to be more compact. Power consumption will be relatively high, however, and so will be the. In industry, electric-melting method is usually used in the production of high-purity MgAl2O4 spinel.

The ratio of MgO and the cooling rate of the melt have great influence on the crystallinity and density of the spinel, which are the main factors of this stage. We did tests at 3 different scales: (1) a semi-industrial, small-volume electric melting furnace, (2) a large-volume industrial electric melting furnace and (3) small laboratory electric melting equipment..

(1) Design of small-volume electric melting experiment

In a factory in Dengfeng City, we carried out a small-volume electric melting experiment to study the effect of different cooling methods on spinel density. Use the following three cooling methods: natural cooling, the cooling of circulating water and poured into the crucible quenched.

Table 5 Raw material composition of large -volume electric melting synthesize experiment (%)

Name	Al_2O_3	Fe_2O_3	MgO	CaO	SiO_2	Na_2O	Cr_2O_3	Burning reduction
Chromium slag	81.07	0.18	0.65	1.56	0.33	1.99	13.86	0.00
95 magnesia	1.05	0.78	95.50	1.40	1.18	/	/	0.05

(2) Design of large-volume electric melting experiment

The experiment was carried out in the shell furnace of Anshan City Lantian magnesia production co., LTD. Raw materials including chromium slag 70%, 95 magnesia 30%, and the chemical composition of the materials as shown in Table 5.

(3) Experimental design of laboratory test

In order to further the study of chromium residue synthetic spinel materials, we performed tests with different proportions of magnesia and chromium slag. The contents of MgO were: 5, 10, 15, 20, 25, 27 and 30%.

Design of Performance Test

The performance of materials is directly related to the life of refractory materials. The properties to be studied include: refractoriness, refractoriness under load, high temperature creep, high temperature stability, thermal shock resistance and slag resistance, etc. Because thermal shock and chemical erosion are the two main reasons for the damage of refractory materials, the thermal shock resistance and slag resistance of refractory materials are very important. We plan to compare the advantages and disadvantages of the $MgAl_2O_4$ spinel prepared by the best process and the traditional $MgAl_2O_4$ spinel, to judge whether the research purpose of this paper can be realized.

(1) Design of slag resistance test xxx

Slag resistance: it refers to the ability of the refractory material to resist the erosion and erosion of slag at high temperature. There are many methods for testing the slag resistance of refractories, it can be roughly divided into two categories: a class is static method, namely in the process inspection refractories is stationary, and another kind is the dynamic method, namely in the process inspection refractories is movement. Static method slag experiment includes crucible method, induction furnace method, dipping method and dropping slag method. The most common slag resistance test method in the laboratory is the crucible method.

Crucible experiment matrix was used traditional $MgAl_2O_4$ spinel powder and chromium slag synthetic $MgAl_2O_4$ spinel fine powder, aggregates were used brown corundum and white corundum, and samples were added to 4%wt Al_2O_3 powder and bonded by ρ-Al_2O_3. There are two kinds of slag used in slag resistance experiment, and the composition is in Table 6.

Table 6 Composition of the slag used in the slag resistance furnace experiments (%)

Ingredients	Al_2O_3	Fe_2O_3	MgO	CaO	SiO_2	MnO
Slag used for the first time	5.65	1.08	12.2	45.7	30.82	2.86
Sslag used for the second time	3.25	18.11	9.16	32.64	29.34	3.86

(2) Design of thermal shock resistance test

As the production of refractory lining materials and components used at high temperatures, in addition to withstand high temperature, but also to resist damage to its rapid change of temperature. The effect of temperature change on refractory material is called thermal shock. The ability of refractory material to resist the rapid change of temperature is the thermal shock resistance of refractory material, which is referred to as thermal stability. Thermal shock damage is one of the refractory two damaged reasons, and therefore, thermal shock resistance of refractory material is its important properties.

How accurate characterization and evaluation of thermal shock resistance of refractory material is an important but difficult problem. Although the predecessors have made a lot of work, but is not yet a good way to have a recognized. In the practical work of the most common method is to make the refractory samples through repeated heating–cooling cycle, with the damage degree of sample to evaluate the stand or fall of thermal shock resistance.

We design the thermal shock resistance of test sample size is 70 mm × 70 mm × 70 mm, 1100 °C by 0.5 h, circulating water cooling. The sample matrix was used traditional $MgAl_2O_4$ spinel powder and chromium slag synthetic $MgAl_2O_4$ spinel fine powder, aggregates were used brown corundum and white corundum, and samples were added to 4%wt Al_2O_3 powder and bonded by ρ-Al_2O_3. In the first thermal shock resistance experiment, the use of small-volume electric melting spinel, aggregate use of brown corundum; second thermal shock experiments in the use of large-volume electric melting spinel, aggregate use of white corundum.

Results and Discussion

Experimental Results and Discussion of Sintering Method

(1) Experimental results of the one-step process sintering: As the sintering temperature increases, the volume density of the sample increases gradually, but the bulk density of the sample is still not satisfactory even at 1750 °C. Here we only listed the data for 3 h at 1750 °C sintered samples (see Fig. 2). It can be seen that the results of one-step sintering method is not ideal, especially the bulk density is low, cannot meet the requirements of refractory raw materials.

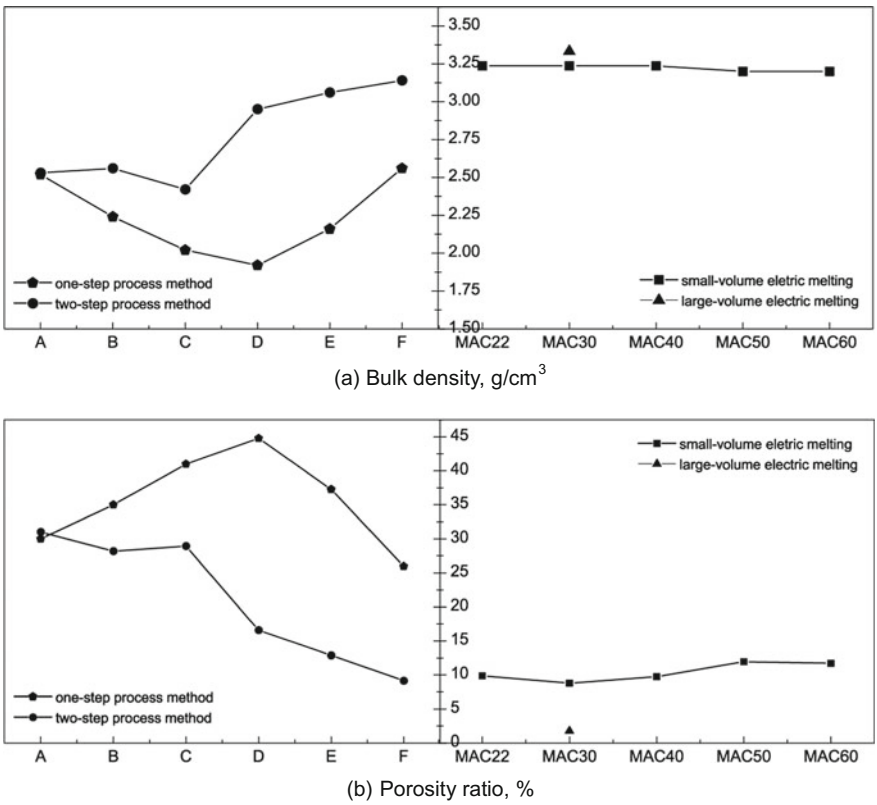

Fig. 2 Physical properties of samples synthesized by sintering method and electric melting method. **a** Bulk density, g/cm^3, **b** Porosity ratio, %

(2) Experimental results of the two-step process sintering: The relative data of sintered samples after heat insulation 3 h at 1750 °C is listed in Fig. 2. It can be seen that with the increase of the two sintering temperature, the volume density of the sample is getting higher and higher. Table 7 lists the results of chemical analysis of samples, it can be seen that the sample after high temperature sintering, Cr_2O_3 content increased significantly, which shows a large amount of metal chromium oxidation, but the Na_2O content has not changed. Comprehensive Fig. 2, Table 7, shows that the two-step process sintering method in the higher temperature, the heat preservation time is longer, the alkali metal is not effectively removed, and the physical properties of $MgAl_2O_4$ spinel material is not ideal.

Table 7 Chemical analysis results of the spinel synthesized by the two-sintering method (%)

Name	Chemical composition of samples after treatment at 1750 °C									
	Al_2O_3	Fe_2O_3	MgO	CaO	SiO_2	Na_2O	P_2O_5	Cr_2O_3	Burning reduction	Total
A	68.75	0.95	5.10	1.56	0.40	1.65	0.15	21.33	0.06	99.95
B	64.13	0.94	15.69	1.73	0.86	1.60	0.23	14.68	0.09	99.95
C	56.13	0.89	26.75	1.66	1.21	1.09	0.15	12.08	0.17	100.13
D	47.05	0.86	37.86	1.74	1.62	0.43	0.22	10.07	0.05	99.90
E	36.82	0.81	49.61	1.64	2.02	0.47	0.31	8.19	0.10	99.97
F	25.52	0.72	63.45	1.62	2.19	0.42	0.24	5.75	0.16	100.07

Experimental Results and Discussion of Electric-Melting Method

(1) Experimental results of small-volume electric melting experiment: The experimental results of small-volume electric melting are shown in Table 8. From the point of view of the experimental results, the furnace cooling should be adopted after the electric melting. With the furnace cooling of the sample is obviously a three-layer structure: lower density, the middle is a loose honeycomb structure, the upper part is a dense layer. Because of using graphite electrodes for heating, the sample will produce gas and cooling speed affects the gas discharge: too fast cooling, gas cannot be in the solidified samples timely discharge, resulting in the specimen structure is loose; with the furnace cooling can prolong the clotting time, the gas is expelled completely, more compact structure can be obtained.

Table 8 Small-Volume electric melting experiments of chromium slag under different conditions

Heat	Electro melting time/min	Cooling way	Discharged amount/kg	Electro fusion effect
1	11	Charcoal pan quench	20	Honeycomb, porosity and more large, crisp, not strength
2	24	Charcoal pan quench	20	Honeycomb, porosity and more large, crisp, not strength
3	14	Natural cooling	130	The bottom and top of the dense, high strength, hardness of the ceramic, central honeycomb
4	12	Circulating water cooling	25	Honeycomb, porosity and more large, crisp, not strength
5	18	Natural cooling	130	The bottom and top of the dense, high strength, hardness of the ceramic, central honeycomb, at the bottom of the dense material increase

Table 9 Related parameters of small- volume electric melting synthesize experiments

	MAC22	MAC30	MAC40	MAC50	MAC60
Light burning MgO powder/200 mesh	22%	30%	40%	50%	60%
Chromium slag/200 mesh	78%	70%	60%	50%	40%
Mixed material handling mode	Press the ball	Press the ball	Press the ball	Press the ball	Press the ball
Electro melting time/min	15	25	40	40	40
Cooling-down method	Furnace cooling	Furnace cooling	Furnace cooling	Furnace cooling	Furnace cooling

Table 10 Chemical compositions of different ratio samples after fusion

Name	Chemical composition, %							
	Al_2O_3	Fe_2O_3	MgO	CaO	SiO_2	Na_2O	Cr_2O_3	Total
MAC22	61.01	0.96	22.03	1.86	0.72	1.14	12.12	99.84
MAC30	53.42	0.70	33.43	1.47	0.74	0	9.99	99.75
MAC40	47.52	0.91	39.97	1.66	0.82	0	8.97	99.85
MAC50	38.11	0.70	52.14	1.31	0.60	0	7.06	99.92
MAC60	31.52	0.69	59.51	1.20	0.86	0	5.68	99.46

With the furnace cooling conditions, we investigate the different ratio of light burned magnesium and chromium residue synthetic fused material performance, test conditions and results as shown in Table 9. We can see that the fused material is still three layers: the upper and lower dense, central to the honeycomb. After testing, the composition and physical properties are shown in Table 10, and Fig. 2. These results are compared with the experimental results. It is showed that the performance of the fused materials is obviously better than that of the sintered materials, and the basic requirements of refractory raw materials are met after the melting of chromium slag. Low yield is the main problem of the small-volume electric melting.

(2) Experimental results of large-volume electric melting experiment

Large-volume electric melting experiment share 12 tons of raw materials, smelting process of 5 h, power consumption is 11720 KWH. Electric melting experiment the feeding and discharging data are shown in Table 11. Electric melting of spinel aggregate real as shown in Fig. 3, the chemical composition of the electric melting of spinel as shown in Table 12 below, which in Fig. 3 A, B two physical index as shown in Table 13.

Large-volume electric melting experiment of $MgAl_2O_4$ spinel micro structure as shown in Fig. 4 and figure in light gray is $MgAl_2O_4$ spinel, dark gray is periclase. In Fig. 4, the metal chromium is reduced and dispersed, and the structure is still uniform and dense under the electron microscope magnification 200 times.

Table 11 Feeding and discharging data of large-volume electric melting experiment (ton)

Charge		Discharge		
Chromium slag	95 magnesia	Finished products	Semi-finished products	Epidermis, lining
8.4	3.6	4.0	6.0	2.0

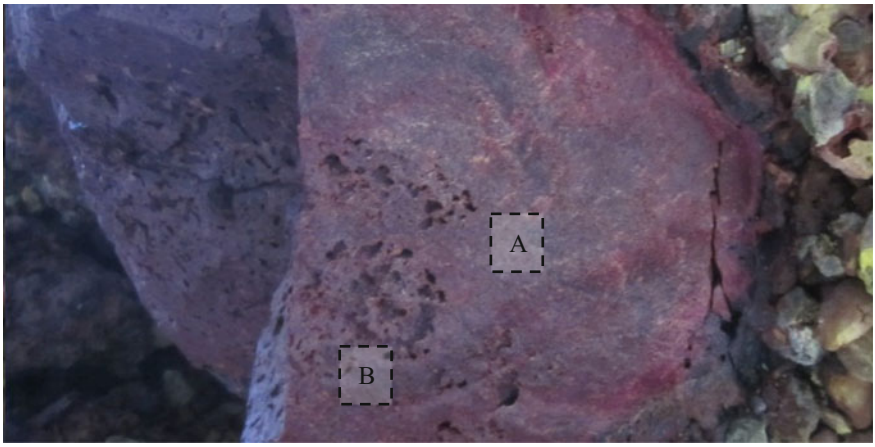

Fig. 3 SEM photos of electric-melting method sample

Table 12 Compositions of $MgAl_2O_4$ spinel prepared by electric melting experiment (%)

	Al_2O_3	Fe_2O_3	MgO	CaO	SiO_2	Na_2O	Cr_2O_3	Cr(VI)/ppm
$MgAl_2O_4$ spinel	55.35	0.11	32.91	1.47	0.92	0.69	7.86	87.4

Table 13 Physical indicators of $MgAl_2O_4$ spinel prepared by electric melting experiment

	Bulk density, g/cm^3	Porosity,%	Water absorption rate,%
$MgAl_2O_4$ spinel (A)[a]	3.47	1.67	0.51
$MgAl_2O_4$ spinel (B)[a]	3.43	4.74	1.40

[a]A, B refers to the location in Fig. 3

The results of comprehensive large quantities of electric melting experiments, we can see that: Large quantities of fused better performance than small quantities of fused refractory materials obtained, the yield is also higher. In the large-scale enterprises electric melting production, will further increase the rate of finished products of product performance, and greater efficiency.

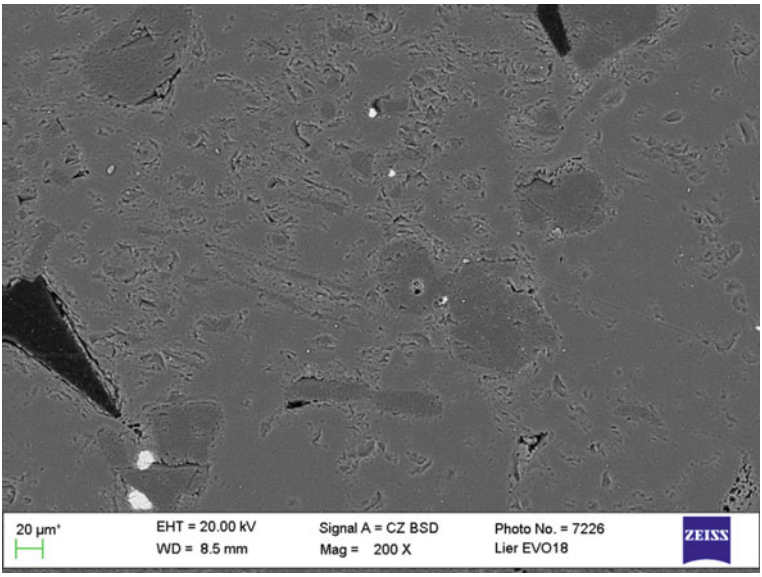

Fig. 4 Microstructure and morphology of electric-melting method sample under SEM

(3) The experimental results of fused $MgAl_2O_4$ spinel synthesized in the laboratory

The composition detection results after electro fusion are shown in Table 14, the typical spinel is shown in Fig. 5, and the XRD test is shown in Fig. 6. There are 8 XRD curves from the figure in order that raw slag, adding MgO powder were 5, 10, 15, 20, 25, 27 and 30% of the test results of synthetic spinel materials. By the detection results show that the original slag of high content of alkali metal and after fused synthesis, the alkali metals are effectively removing, and synthetic materials are primarily $MgAl_2O_4$ spinel. In short, through the process of chromium slag synthetic spinel, we get the expected material.

Table 14 Chemical analysis of chromium slag and $MgAl_2O_4$ spinel materials of different proportions of chemical analysis results (%)

Name	Al_2O_3	Fe_2O_3	MgO	CaO	SiO_2	Cr_2O_3	K_2O	Na_2O
Chromium slag	81.78	0.08	0.44	2.35	0.10	13.34	–	1.83
A	85.22	0.028	5.56	3.89	0.67	2.50	0.01	1.85
B	81.16	0.015	11.17	2.11	0.76	3.30	–	1.24
C	77.51	0.015	13.39	4.79	0.38	2.68	–	1.05
D	74.85	0.019	19.21	4.79	0.39	0.50	–	0.05
E	68.87	0.014	25.96	3.18	0.32	1.35	–	0.04
F	68.46	0.014	27.70	2.37	0.29	0.73	–	–
G	63.65	0.019	30.98	4.39	0.43	0.28	–	–

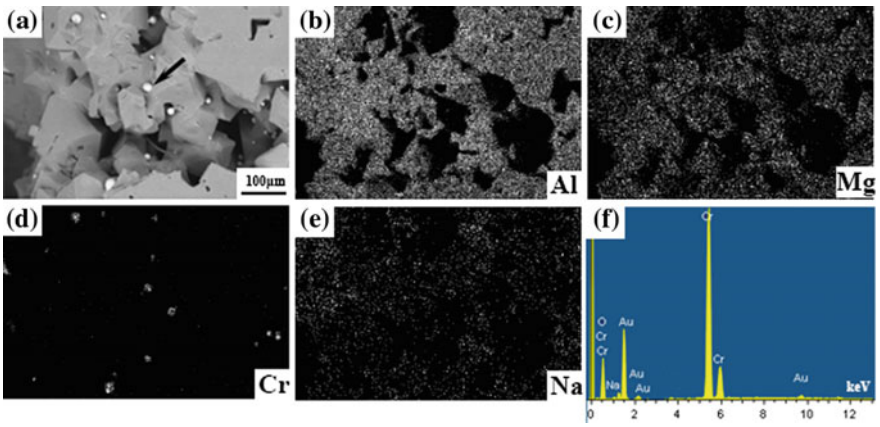

Fig. 5 Typical spinel morphology sample synthesized by chromium slag

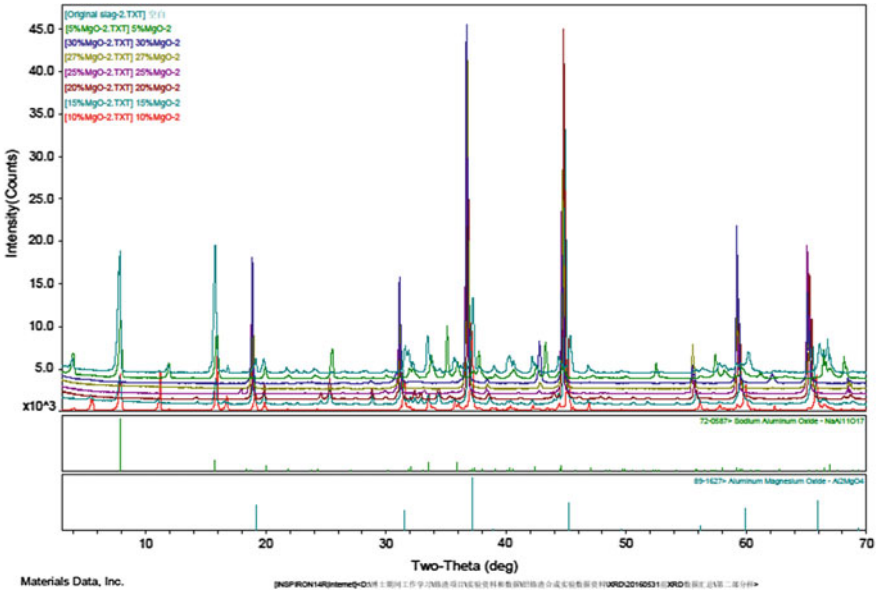

Fig. 6 XRD diagram of raw slag and synthetic samples

(4) Discussion on electric-melting method

Through the above experimental results can be known, electric-melting method can be used to synthesize dense $MgAl_2O_4$ spinel raw material, and to overcome the slag high alkali metal content. All these are required to strictly control the electro fusion process,and these processes include:

(a) To adopt shelling furnace, rather than using the pouring furnace, and when the capacity of the furnace is larger, it is more advantageous to the densification of the material.
(b) Along with the furnace cooling slowly get refractory raw material denser than quenching.
(c) Through the detection of the experimental results, the chromium slag added with magnesia fused spinel material has been synthesized.

Results of Performance Test

(1) Result of slag resistance test

First slag resistance experiment, the crucible after the slag erosion as shown in Fig. 7, which "MA" matrix using traditional $MgAl_2O_4$ spinel, "MAC" matrix with small-volume electric melting $MgAl_2O_4$ spinel; second experiment on slag resistance test, the crucible after the slag erosion as shown in Fig. 7, which "MA" matrix by traditional $MgAl_2O_4$ spinel, "MAC" matrix using large-volume electric melting $MgAl_2O_4$ spinel.

It can be seen from the experimental results that the slag resistance of the spinel prepared by chromium slag is equal to that of traditional $MgAl_2O_4$ spinel, so we can replace the traditional $MgAl_2O_4$ spinel in terms of slag resistance.

First thermal shock performance test results as shown in Fig. 8 and figure in "MA" matrix using traditional $MgAl_2O_4$ spinel, "MAC" matrix with small-volume electric melting $MgAl_2O_4$ spinel; diagram "MA" sample for heat shock after 8 times of real, "MAC" specimen for the thermal shock after 22 times real. The second thermal shock resistance test results as shown in Fig. 8 and figure in "MA" matrix using traditional $MgAl_2O_4$ spinel, "MAC" matrix with large-volume electric melting $MgAl_2O_4$ spinel; diagram "MA" sample for heat shock after 21 times of real, "MAC" specimen for the thermal shock after 30 times real.

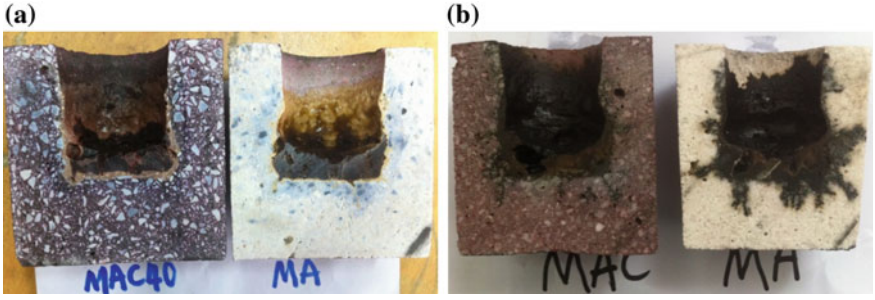

Fig. 7 Result of slag resistance test: **a** made of small batch $MgAl_2O_4$ spinel and traditional $MgAl_2O_4$ spinel; **b** made of large batch $MgAl_2O_4$ spinel and traditional $MgAl_2O_4$ spinel

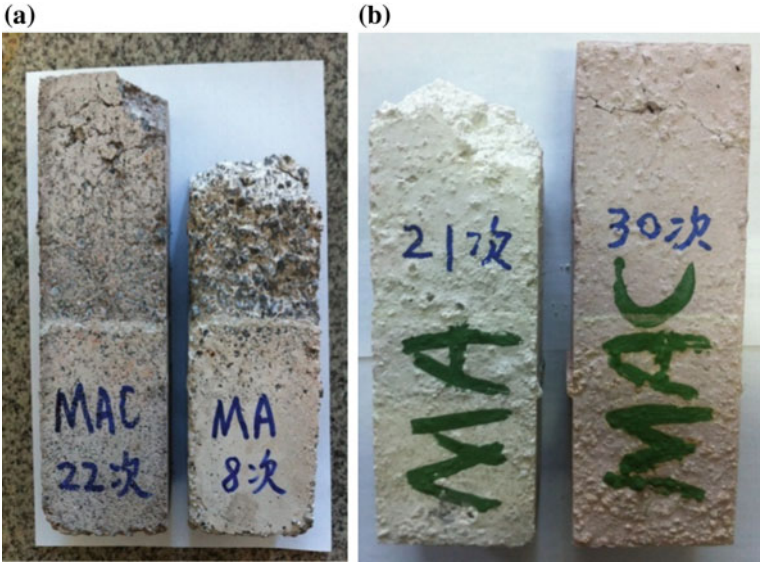

Fig. 8 Result of thermal shock resistance test: **a** made of small batch $MgAl_2O_4$ spinel and traditional $MgAl_2O_4$ spinel; **b** made of large batch $MgAl_2O_4$ spinel and traditional $MgAl_2O_4$ spinel

It can be seen from the results of the thermal shock experiment that our $MgAl_2O_4$ spinel is obviously better than the traditional $MgAl_2O_4$ spinel, so it can replace the traditional $MgAl_2O_4$ spinel from the aspect of thermal shock resistance.

To sum up, we have made use of chromium slag preparation of $MgAl_2O_4$ spinel materials in terms of physical properties, the use of performance, and so on, can replace the traditional $MgAl_2O_4$ spinel materials.

Discussions

(1) Discussion on sintering process: With chromium slag and light burning MgO powder, adding mineralizer or burning assistant by sintering method synthesis of $MgAl_2O_4$ spinel, much lower cost. It is also conducive to the two oxidation of chromium metal, but it will bring two problems: The first is the sintering raw material is hard to densification, although the sintering temperature to 1750 °C high temperature, burn out the raw material is still very loose; The second is the impurity in the chromium slag can't eliminate, especially Na_2O, still remain down.

Conclusions

This paper discusses chromium slag resource utilization, and chromium slag is produced chromium thermite byproduct. Through experimental research, we obtain the following conclusions:

(1) It is difficult to synthesize dense $MgAl_2O_4$ spinel by sintering method.
(2) By the method of electric melting, the $MgAl_2O_4$ spinel meets the requirement of the production of refractory materials.
(3) In the performance test, the slag resistance of the $MgAl_2O_4$ spinel prepared from chromium slag is equal to that of the traditional spinel, and the thermal shock resistance of the former is better than that of the latter.

References

1. Huang JL, Sun SY, Ko YC (1997) Investigation on high alumina spinel: effect of LiF and $CaCO_3$ addition. J Am Ceram Soc 80:3237–3241
2. Yamamura T, Hamazaki T, Kato H (1992) Alumina spinel castable refractories in steel teeming ladles. Taikabutsu Overseas 12:21–27
3. Sheehan JE, Sigalovsty J, Haggerty JS, Porter JR (1993) Mechanical properties of $MgAl_2O_4$ single crystal fibers. Ceram Eng Sci Proc 14(7/8):660–670
4. Tripathi HS, Mukherjee B, Das S, Haldar MK, Das SK, Ghosh A (2003) Synthesis and densification of magnesium aluminate spinel: effect of MgO reactivity. Ceram Int 29(8):915–918
5. Baudin G, Martinez R, Pena P (1995) High-temperature mechanical behavior of stoichiometric magnesium spinel. J Am Ceram Soc 78(7):1857–1862

Effect of Ferrosilicon on Reduction of Cr_2O_3 in Steelmaking Slags

Yue Yu, Jianli LI, Di Wang and Hangyu Zhu

Abstract The stainless steel slag as the by-product of steel-making plants contains 2–10 wt% Cr_2O_3, and the potential elution of hexavalent chromium impedes the utilization as a secondary resource. The reduction of chromium oxide in steel-making slag containing Cr_2O_3 by FeSi at 1550 °C was investigated in the laboratory. The experiments were performed in a carbon-tube furnace, and the samples collected during tests were analyzed using X Ray Fluorescence (XRF) and Scanning Electron Microscope (SEM) equipped Energy Dispersive Spectroscopy (EDS). The results show that the FeSi addition could efficiently enhance the reduction and recovery of chromium. When the amount of FeSi ranged from 2 upto 9 wt%, the recovery increased from 65.60% to 84.19%. The occurrence of residual chromium was metal particles, which dispersedly distributed in silicate phases owing to the size limitation. The sufficient FeSi could easily reduce chromium oxides into metal, but the critical factor of chromium recovery is the precipitation of suspending metal particles from the molten slag. Thus, some measures should be proposed in order to make sure that the suspending particles are adequate to aggregate into bigger ones.

Keywords Stainless steel slag · Cr_2O_3 · FeSi · Occurrence · Reduction Recovery rate

Introduction

The stainless steel slags containing 2–10 wt%Cr_2O_3 are the by-product of stainless steel-making process, and generated 150 kg/ton steel for Electric Arc Furnace (EAF) [1–3]. The possible leaching of chromium hinders the utilization as a kind of raw material [4, 5]. In terms of the leachability and generation of hexavalent chro-

Y. Yu · J. LI (✉) · D. Wang · H. Zhu
The State Key Laboratory of Refractories and Metallurgy,
Wuhan University of Science and Technology, Wuhan 430081, China
e-mail: jli@wust.edu.cn

Z. Sun et al. (eds.), *Energy Technology 2018*, The Minerals, Metals & Materials Series, https://doi.org/10.1007/978-3-319-72362-4_31

mium, there are a few references in the world. The treatment process of molten slags includes cooling, crushing, milling and magnetic separation. Besides the cooling procedure, the effect of milling and crushing on the formation and elution of hexavalent chromium could not be ignored. Glastonbury [6] reported that the shattering process of chromite coursed the transformation of chromium from trivalent, and the prolongation of treating time would enhance the Cr^{6+} amount. Beukes [7] found that the crushing and milling processes also promoted the Cr^{6+} generation in quantity. After milling for 10 min, the dissolution quality of chromium increased sharply from 0 upto 168.10 mg/kg for the steelmaking slag containing Cr_2O_3.

The generation of hexavalent chromium during the treatment processes is mainly on account of the existence of Cr_2O_3. Although some measures had been proposed to stabilize the chromium in silicates, such as the additions (Al_2O_3, MgO, SiO_2) to impel the formation of expected minerals [8, 9], they were hardly carried out due to the cost and operations. Therefore, the reduction and recovery of Cr_2O_3 from molten slags are the credible method to resolve the problem. So far, many researchers have focused the reduction of stainless steel slag by the different kind of reductants, for instance aluminum, graphite and silicon [10–12]. The content of chromium could be controlled to a fairly low grade, and the recovery rate of chromium was quite high upto 98.6% [13]. On basis of the present literatures, there are few ones that are associated with the occurrence of residual chromium and the relations between recovery rate and precipitation of metal particles in silicate melt.

In the present work, in order to further understand the reduction mechanism of stainless steel slags, the influence of FeSi Occurrence and Recovery of Chromium was investigated through a batch of experiments performed in a carbon-tube furnace.

Experiments

Materials

The raw materials include stainless steel slag collected from Electric Arc Furnace and FeSi (75.04 wt% Si and 24.00% Fe) taken as reductant. As shown in Table 1, the stainless steel slag consists of CaO, SiO_2, MgO and Cr_2O_3, etc. And the content of chromium oxide is upto 6.39 wt%. According to the XRD results, the major minerals of the slag are dicalcium silicate (Ca_2SiO_4), spinel ($MgCr_2O_4$) and tricalcium aluminate ($Ca_3Al_2O_6$). The slag microstructure acquired through SEM presents 4 different kinds of mineral phase. The Cr element mainly exists as the form of spinel phase and metal particle, while a few dissolved into silicate phase, such as Ca_2SiO_4

Table 1 Chemical composition of raw materials/wt%

CaO	MgO	Al_2O_3	SiO_2	FeO	MnO	Cr_2O_3	TiO_2
47.40	5.04	2.22	31.90	1.46	2.17	6.39	0.86

and matrix. Based on the assumption that Cr_2O_3, FeO and MnO containing in the slag could be reduced completely to corresponding metals, the accurate addition of FeSi is 3.30 wt%, calculated according to the thermodynamic data.

Experimental Procedure

Seen in Table 2, all the experiments were conducted in a carbon-tube furnace (25 kW) under the protecting atmosphere of argon. For the tests about reductant amount, the addition was divided into four different grades, 2.0, 3.3, 6.0 and 9.0 wt %, and the samples were heated for 10 min at 1550 °C. The weights of original slags are 400 g. All the samples were cooled in air, and collected into a desiccator.

Sample Analysis Methods

The treated slags were cut into two parts from the middle in order to prepare the samples for the following tests. Meanwhile, the metal containing reduced production and the residue slag were separated. The chemical composition of the slag were detected through X Ray Fluorescence, and the slag microstructural properties and the occurrence state of chromium were performed based on the scanning electron microscopy (SEM, Nova 400 Nano), equipped with a energy- dispersive spectrometer (EDS, Penta FET x-3 Si).

According to the chemical composition of slag samples and the assumption that the amount of CaO is a constant, the weight of treated slags (Ms) and the recovery rate of chromium (R_{Cr}) could be obtained, Eqs. (1) and (2).

$$M_s = \frac{\omega_0(CaO) \times w}{\omega(CaO)} \quad \text{(g)} \tag{1}$$

$$R_{Cr} = \frac{\omega_0(Cr_2O_3) \times w - \omega(Cr_2O_3) \times M_s}{\omega_0(Cr_2O_3) \times w} \times 100 \tag{2}$$

where, w is the weight of the original slags, $\omega_0(CaO)$ and $\omega_0(Cr_2O_3)$ refer to the contents of CaO and Cr_2O_3 in the original slags respectively, and $\omega(CaO)$ and

Table 2 The details of the experiments

No.	Slag weight,g	FeSi,wt%	T,°C	t,min
S1	400	2	1550	10
S2	400	3.3	1550	10
S3	400	6	1550	10
S4	400	9	1550	10

$\omega(Cr_2O_3)$ present the concentrations of CaO and Cr_2O_3 in the treated slags separately.

Results and Discussions

The reduction product of Cr_2O_3, FeO and MnO could form metal particles or briquettes with the iron contained in the FeSi, and might precipitate to the bottom of melts. The chemical composition of reduced slags and the recovery ratio of chromium are summarized in Table 3. Note that the element of chromium might exist as metal and metallic oxide in the treated slags, but is shown as Cr_2O_3 due to the limitation of XRF.

The experiments, the slags added 2, 3.3, 6.0 and 9 wt% FeSi, were conducted in a carbon-tube furnace at 1550 °C for 10 min, and the chemical composition and recovery ratio of chromium of reduced slags are shown in Table 3 and Fig. 1. The Table 3 reveals that the content of Cr_2O_3 in the slag phase decreases with the increase of FeSi addition. When the addition of FeSi varied from 2.0 upto 9.0 wt%, the content of Cr_2O_3 declined from 2.18 wt% down to 1.07%. MnO has the similar trend with Cr_2O_3. The Table 3 and Fig. 1 represent that the rise of FeSi addition promoted the recovery of chromium. When the usage of FeSi was 2.0 wt%, the recovery ratio of chromium was merely 65.60%. However, in terms of the sample with 9 wt% reductant, the ratio was enhanced upto 84.19%. According to the chemical reaction equilibrium of Eqs. (3) and (4), the rise of Si content in metal remarkably promotes the reduction of chromium oxide. Hence, the increase of FeSi amount effectively improved the reduction of chromium oxide and suppressed the content of Cr_2O_3 in the slag.

While in accordance with the theoretical arithmetic, the theoretical required amount of the reductant is just 3.3 wt% to completely reduce the metallic oxides (Cr_2O_3, MnO and FeO) in the original sample. Therefore, it is to be testified that whether the excess reductant could reduce the chromium oxide into metal completely and how the residual chromium existed in silicate phases.

The Fig. 2 presents the microstructure of S1 sample, observed through SEM. The four different mineral phases existed obviously, and were measured with SEM-eds. According to the chemical compositions of each phase, summarized in

Table 3 Chemical compositions (wt%) and recovery rate of chromium (%) of the reduced slags

No.	CaO	MgO	Al_2O_3	SiO_2	MnO	Cr_2O_3[a]	TiO_2	R_{Cr}
S1	47.00	4.96	4.54	40.00	1.00	2.18	0.89	65.60
S2	48.40	6.50	2.45	38.00	1.36	1.91	0.79	70.73
S3	46.10	5.01	4.58	38.30	1.04	1.42	0.61	77.15
S4	50.20	9.50	2.68	42.50	0.46	1.07	0.28	84.19

[a]All chromium element evaluated as Cr_2O_3

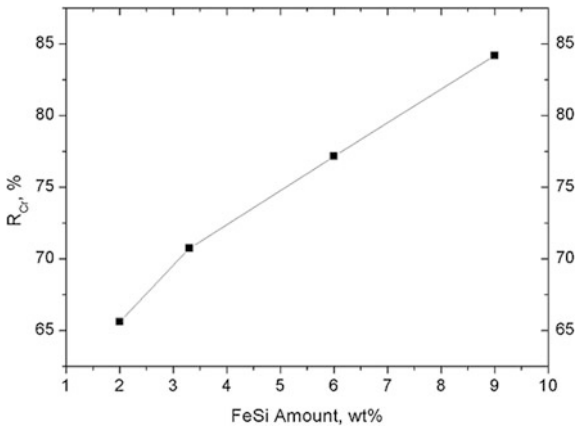

Fig. 1 Effect of FeSi amount on recovery rate of chromium

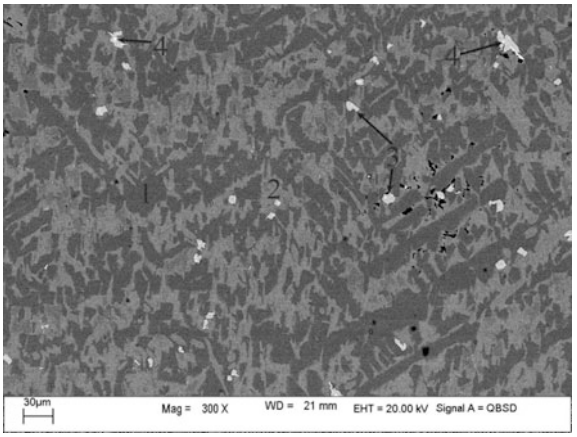

Fig. 2 The microstructure of S1 observed through SEM

Table 4, the gray sections include silicate matrix (phases "1") and dicalcium silicate (phase "2", a kind of solid solution), and the bright phases are spinel crystal (phase "3") and metal particle (phase "4"). The both phases always exist together, and distribute dispersedly. As shown in Table 4, the chromium element is the major component of metal particles, and the solid solution of C2S contains a few amount of chromium (0.67 wt%) besides silicon and calcium. The sizes of spinel particles are about 10 μm, and they mainly comprise chromium, manganese and magnesium. Therefore, the residual chromium after reduction has three different kinds of occurrence states in the slag. The portions of chromium contained in the dicalcium silicate and spinel reveal that the chromium and manganese oxides in S1sample added 2.0 wt% FeSi were not reduced completely. The part involved in the metal phase indicates that all the reduced product could not precipitate onto the bottom owing to the limitation of quite small size [14]. Hence, the incomplete reduction and the existence of metal caused the low recovery ratio of S1.

Table 4 The chemical composition of mineral phases marked in Fig. 2/wt%

No.	Phase	O	Mg	Al	Si	Ca	Ti	Cr	Mn	Fe
1	Matrix	35.06	4.83	8.09	18.42	32.41	–	–	1.18	–
2	C2S	33.84	1.45	0.81	19.39	42.64	–	0.67	0.7	–
3	spinel	20.14	8.79	4.34	0.84	1.33	2.81	50.06	11.64	–
4	metal	–	–	–	4.35	–	–	84.68	2.74	8.23

$$3[\mathrm{Si}] + 2(\mathrm{Cr_2O_3}) = 3(\mathrm{SiO_2}) + 4[\mathrm{Cr}] \tag{3}$$

$$\Delta G = \Delta G^{\theta} + RTln\frac{\alpha^4_{[Cr]} \cdot \alpha^3_{(SiO_2)}}{\alpha^3_{[Si]} \cdot \alpha^2_{(Cr_2O_3)}} \tag{4}$$

For the S2, S3 and S4 samples, the micro properties and the composition of mineral phases were summarized in Fig. 3 and Table 5, respectively. The 3 samples have the similar mineral components, consisting of dicalcium silicate, merwinite, matrix and metal particles. The differences among them are that the number of metal particles decreases and the size increases with the added amount of FeSi rising, which evidently illustrates the trend of chromium recovery ratio. On the basis of Table 5, there are few chromium existing in silicate phases due to the content lower than the limitation of detection devices, and the residual chromium presented mainly as metal. Moreover, the basic mineral phase in stainless steel slag, chromium spinel, was not detected in these samples. It elucidates that the chromium oxides are quite finite due to the addition of excess ferrosilicon. Therefore, the reduction of chromium oxides is simply and quite thorough with sufficient FeSi at 1550 °C, and the separation of metal particle by means of precipitation is the critical factor in the recovery rate of chromium.

And the difference of the surface tension between molten slag and liquid metal dominates the reduction product existing as metal droplets, which distribute dispersedly in liquid slag. There are three kinds of forces on the droplet, namely gravity, buoyancy and viscous resistance. On basis of the resultant force, the Stoke`s law is employed to describe the sedimentation velocity of a droplet (υ_m), as the Eq. 5 [15, 16].

$$\upsilon_m = \frac{(\rho_m - \rho_s)d^2}{18\mu} \cdot g \tag{5}$$

where ρ_m and ρ_s represent the density of metal droplet and molten slag respectively, μ is the viscosity of liquid slag, d is the diameter of the droplet, and g infers the acceleration of gravity. The Eq. (5) is suit for the separation of sphere droplet with the diameter less than 200 μm. It suggests that the precipitating velocity of droplets depends on the difference of density between slag and metal, droplet size, and the medium viscosity. The decline of slag viscosity and the increases of density difference and droplet size could observably enhance the separation speed.

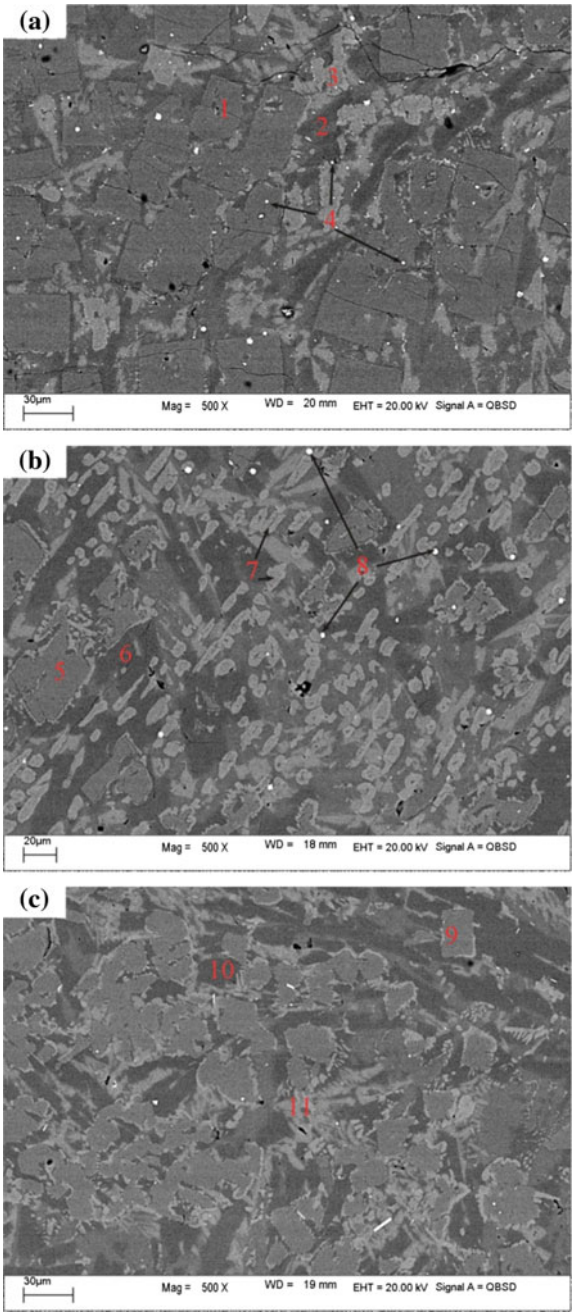

Fig. 3 The microstructures of reduced samples with different addition of ferrosilicon, **a** S2 with 3.3 wt %FeSi; **b** S3 with 6 wt% FeSi; **c** S4 with 9 wt%FeSi

Table 5 The chemical composition of mineral phases marked in Fig. 3/wt%

No.	Phase	O	Mg	Al	Si	Ca	Cr	Mn	Fe
1	Merwinite	33.20	7.70	0.49	19.46	38.48	–	0.68	–
2	Matrix	35.08	6.02	3.41	22.77	30.96	–	1.77	–
3	C2S	34.25	1.18	1.00	18.32	45.26	–	–	–
4	Metal	–	–	–	1.26	–	85.35	1.09	12.29
5	Merwinite	34.64	7.10	0.56	19.02	38.37	–	–	0.31
6	Matrix	35.36	7.43	3.05	23.26	30.90	–	–	–
7	C2S	33.23	3.56	0.35	18.95	43.91	–	–	–
8	Metal	–	–	–	16.21	–	64.05	5.90	13.84
9	Merwinite	33.43	7.66	0.77	19.57	38.57	–	–	–
10	Matrix	33.55	7.30	3.07	23.66	32.42	–	–	–
11	C2S	33.76	0.78	0.47	18.25	46.75	–	–	–

Furthermore, the size is more important than other factors. Therefore, the increase of droplet size is taken as the effective measure to promote the sedimentation of reduction product.

According to the minimization of Gibbs free energy, the molten slag containing a certain amount of metal droplets is unstable, and the droplets will aggregate spontaneously to form a bigger one [17]. For a certain system, the aggregation is critically controlled by the number of suspending particles and the time. Hence, this could be used to explain the influence of FeSi amount on the recovery of chromium. The increase of ferrosilicon addition not only insures the reduction of chromium oxide, but also raises the number of metal droplets due to the fusion of excess reductant, which make the distances among the suspending particles shrink. So the closer ones could combine together easily in a period of time. The growth of metal particles promotes the precipitation speed and enhances the rise of chromium recovery finally. Therefore, some measures should be proposed in order to make sure that the suspending particles are adequate to aggregate the reduction product.

Conclusion

The occurrence and recovery of chromium in the stainless steel slag reduced by ferrosilicon at 1550 °C for 10 min in a carbon-tube furnace were investigated, and the conclusions are obtained as follows. The increase of FeSi addition could efficiently promote the recovery of chromium. The recovery ratio rises from 65.60 upto 84.19% when the addition become from 2 to 9 wt%. And the excess reductant ensured that the content of chromium oxides dissolved into silicate minerals is lower than the detected limitation. The residual chromium distributed dispersedly among the silicates as the occurrence of metal particles, which could not precipitated into the crucible bottom in a certain time due to the limitation of size. Overall,

the sufficient FeSi could reduce chromium oxides thoroughly, while the precipitation of reduced production is the critical factor in the recovery of chromium.

Acknowledgements The research is supported by National Natural Science Foundation of China (No.51404173), Hubei Provincial Natural Science Foundation (No. 2016CFB579), China Postdoctoral Science Foundation (No.2014M562073), and State Key Laboratory of Refractories and Metallurgy (No.2014QN21).

References

1. Mostafaee S, Anderssona M, Jonsson P (2011) Petrographical study of microstructural evolution of EAF duplex stainless steelmaking slags. Ironmaking Steelmaking 38(2):90–100
2. Zhu R, Ma G, Cai Y et al (2016) Ceramic Tiles with black pigment made from stainless steel plant dust: physical properties and long-term leaching behavior of heavy metals. J Air Waste Manag Assoc 66(4):402–411
3. Tong Z, Ma G, Cai X et al (2016) Characterization and valorization of Kanbara reactor desulfurization waste slag of hot metal pretreatment. Waste Biomass Valoriz 7(1):1–8
4. Samada Y, Miki T, Hino M (2011) Prevention of chromium elution from stainless steel slag into seawater. ISIJ Int 51(5):728–732
5. Jianli LI, Anjun XU, Dongfeng HE et al (2013) Effect of FeO on the formation of spinel phases and chromium distribution in the $CaO\text{-}SiO_2\text{-}MgO\text{-}Al_2O_3\text{-}Cr_2O_3$ system. Int J Miner Metallurg Mater 20(3):253–258
6. Galstonbur R, Merwe W, Beukes J et al (2010) Cr(VI) generation during sample preparation of solid samples – A chromite ore case study. Water SA 36(1):105–109
7. Beukes J, Guest R (2001) Technical note: Cr(VI) generation during milling. Miner Eng 14 (4):423–426
8. Cabrera-Real H, Romero-Serrano A, Zeifert B et al (2012) Effect of MgO and CaO/SiO_2 on the immobilization of chromium in synthetic slags. J Mater Cycles Waste Manage 14(4):317–324
9. Garcia-Ramos E, Romero-Serrano A, Zeifert B et al (2008) Immobiliza- tion of chromium in slags using MgO and Al2O3. Steel Res Int 79(5):332–339
10. Shibata T, Egawa S, Nakamura T (2002) Reduction behavior of chromium oxide in molten slag using aluminum, ferrosilicon and graphite. ISIJ Int 42(6):609–613
11. Bostjan A, Tehovnik F (2007) The oxidation and reduction of chromium during the elaboration of stainless steels. Mater Technol 41(5):203–211
12. Gutierrez-Paredes J, Romero-Serrano A, Plascencia-Barrera G et al (2005) Chromium oxide reduction from slag by silicon and magnesium. Steel Res Int 76(11):764:768
13. Nakasuga T, Nakashima K, Mori K (2004) Recovery rate of chromium from stainless slag by iron melts. ISIJ Int 44(4):665–672
14. Iwamasa PK, Fruehan RJ (1996) Separation of metal droplets from slag. ISIJ Int 36 (11):1319–1327
15. Wang MY, Lou TP, Li Z et al (2008) Separation of iron droplets from titania bearing slag. J Iron Steel Res Int 15(1):45–48
16. Jang HS, Ryu JW, Sohn I (2015) FeMn metal droplet behavior in the $MnO\text{-}SiO_2\text{-}CaO$ slag system. Metallurg Mater Trans B 46(2):606–614
17. Zhang L, Zhang W, Li G (2016) Coalescence,growth and settling of metallic Fe droplets in molten Ti-bearing blast furnace slag under dynamic oxidation condition. Chin J Eng (12):1695–1701

Bacterial Degradation of Free Cyanide in Alkaline Medium Using *Bacillus Licheniformis* Strain

Amzy Tania Vallenas-Arévalo, Carlos Gonzalo Alvarez Rosario, Denise Crocce Romano Espinosa and Jorge Alberto Soares Tenório

Abstract Cyanide is a toxic chemical used in mining industry to recover gold and silver in leaching process. Effluents containing cyanide can be treated by bioremediation instead of physical and chemical processes which are often more expensive and less efficient. This study evaluated the capacity for free cyanide degradation of a *Bacillus licheniformis* strain previously isolated from an abandoned gold mine. First, bacterial growth in LB medium through OD_{600} was studied. Then, bacteria was adapted to grow on alkaline medium using CAPS buffer to keep pH10. Finally, cyanide degradation assays were performed using a 500 mgL^{-1} KCN pH10 50 mM CAPS solution. Free cyanide was measured using a polarographic method. Temperature influence was evaluated at 27, 32 and 37 °C. Results showed that *B. licheniformis* was able to degrade 99% of free cyanide after 5 days of incubation and works better at 32 °C showing the strain potential for cyanide biotreatment in mining industry.

Keywords Cyanide · Biodegradation · *Bacillus licheniformis* · Bacteria Gold mining

Introduction

Cyanide is a highly toxic chemical that can be present in the environment in high concentrations as a result of human activities including electroplating, fiber production, coal processing, cassava-processing and metallurgic processes [1–3]. Effluents containing cyanide represent a high risk for the environment because cyanide can be lethal for most living organisms as it inhibits the cytochrome-c oxidase, a key enzyme in the mitochondrial respiratory chain [4, 5]. In mining industry, it is used for gold and silver recovery in leaching processes [6].

A. T. Vallenas-Arévalo (✉) · C. G. A. Rosario · D. C. R. Espinosa · J. A. S. Tenório
Chemical Engineering Department, University of São Paulo (USP), Rua do Lago, 250, São Paulo, SP 05508-080, Brazil
e-mail: avallenas@usp.br

Z. Sun et al. (eds.), *Energy Technology 2018*, The Minerals, Metals & Materials Series, https://doi.org/10.1007/978-3-319-72362-4_32

Cyanidation is a widely used process for obtaining gold without using mercury since it has a lower environmental impact. However, cyanide is still and important environmental and occupational risk for operators [7].

There's a variety of methodologies for cyanide degradation including biological, chemical and physical processes. Thus, cyanide also suffers natural attenuation where cyanide is oxidized to more stable and less-toxic products [8]. However, complete cyanide destruction requires chemical processes despite the fact that part of residual cyanide is naturally degraded by sunlight or air oxidation [7]. Most common technologies for cyanide-treatment include oxidation using hydrogen peroxide and catalyzed by copper; oxidation with Caro's acid; sulfur dioxide process; and alkaline chlorination [6, 9]. Nevertheless, chemical and physical processes are often expensive and complex to operate [8]. In this context, biotreatment of cyanide-containing effluents represent a potential alternative to conventional processes.

It has been demonstrated that cyanide can be treated by bacteria in a viable process of cyanide-containing effluents [10]. Biological treatments represent economic advantages in operation costs. Commonly, *Pseudomonas sp.* and *Bacillus sp.* are used to treat cyanide-containing effluents [2, 3] but other bacteria, fungus and algae have also been reported [11]. This study aims to evaluate the ability for a *Bacillus licheniformis* strain, previously isolated from a gold mining tailing and identified, to treat free-cyanide in alkaline environments that minimize cyanide volatilization.

Methodology

A previous study isolated a cyanide-degrading bacteria from a gold mine tailing identified as *Bacillus licheniformis* [12]. However, bacterial isolation had been performed at physiological pH 7. Cyanide is known to be a highly volatile substance with pKa = 9.2. In order to minimize cyanhidric acid (HCN) formation, alkaline levels of pH have to be maintained during treatment processes. In order to achieve that, microorganisms used in cyanide treatment have to be able to grow in these kind of environments. Consequently, previously isolated bacteria was adapted to grow in alkaline medium prior to evaluation of cyanide degradation.

Adaptation to Alkaline Medium

Bacteria reproduce and mutate very fast; hence, they can adapt rapidly to hostile environments. Menawhile, in cyanide-containing effluents is important to keep high pH values to minimize HCN volatilization. Therefore, is important that microorganisms used are adapted to grown in these conditions. In order to achieve that, previously isolated and identified bacteria were activated in nutritive LB media

(15 gL^{-1} peptone, 5 gL^{-1} yeast extract, 10 gL^{-1} NaCl). Bacterial growth curves were calculated at pH 7, 8, 9 and 10. LB medium was prepared at different pH values using 50 mM Tris-HCl as buffer for LB medium at pH 7 and 8; and 50 mM CAPS-NaOH buffer for LB medium at pH 9 and 10. In all cases, mediums were sterilized by autoclaving.

Strain was grown in 250 mL Erlenmeyer flasks incubated at 190 RPM at 37 ºC with 50 mL of desire medium and a 100 µL inoculum of activated bacteria (1:500 proportion). Bacterial adaptation was measured using growth curves for each strain. Cellular growth was measured using OD_{600} absorbance.

Free-Cyanide Measurement

Free cyanide refers to the CN^- and HCN in aqueous solution, which are the most toxic forms of cyanide [9]. Free-cyanide concentration in aqueous solution was measured using a polarographic technique with a voltammetric analyzer (VA) Computrace Control 797, Metrohm. For this method an electrolyte solution with 0.2 M boric acid (H_3BO_3) and 0.17 M potassium hydroxide (KOH) was used. PH adjustment to 10.2 was done with a 0.01 M potassium hydroxide solution.

Cyanide Degrading Assays

To evaluate degrading efficiency a synthetic solution with a 500 mgL−1 of KCN concentration was prepared. First, bacteria adapted to pH 10 was grown in 50 mL sterile falcon tubes with 15 mL of LB medium incubated at 37 °C 190 RPM overnight; then an aliquot of 200 µL was transferred to an 250 mL Erlenmeyer flask containing 50 mL of LB 50 mM CAPS pH 10 NaOH medium and incubated to 190 RPM 37 °C until OD600 = 0.8. Bacterial solution with OD = 0.8 was transferred to sterile falcon tubes and centrifuged at 8000 rpm for 3 min. Supernatant was discarded and pellet was washed twice using buffer solution. Then, bacteria was re-suspended in 100 mL assay solution (500 mgL^{-1} CN^-, 50 mM CAPS pH 10 KOH), put into a 250 mL Erlenmeyer flask and incubated. Assay incubation lasted 5 days and were performed in triplicates together with a control with no bacteria inoculated. A 5 mL aliquot was taken from each flask to measure pH, cellular concentration, and free-cyanide each day.

Optimal conditions for degradation were tested with degradation assays at 27, 32 and 37 °C; and different rotation speed of 65 and 190 rpm. Cyanide degradation curves were elaborated with results obtained from free-cyanide measurements in % of cyanide concentration reduction according to Eq. 1.

$$\%[CN]d = \frac{[CN]_i - [CN]_f}{[CN]_i} \times 100\% \quad (1)$$

Where:
%[CN]: Percentage of free-cyanide concentration degraded
[CN]i: Initial concentration of free-cyanide in solution (mg/L)
[CN]f: Final concentration of free-cyanide in solution (mg/L)

Results and Discussion

Bacterial Adaptation to Alkaline Environments

Growth curves for *Bacillus licheniformis* strains are shown in Fig. 1. Strains was able to grow in increasing pH conditions. Cellular growth was measured during 26 h. In every case, B. licheniformis strains achieved stationary phase of growth in less than 24 h. Strain showed exponential growth between 6 and 22 h of incubation and reached OD = 0.8 after 13 h when viable cell concentration was $10^{6.4}$ CFU/mL. Strain achieve adaptation to alkaline environemts; however, increasing levels of pH resulted in a longer lag phase in bacterial growth. This shows the potential for bacteria to be used in the treatment of alkaline cyanide-containing effluents.

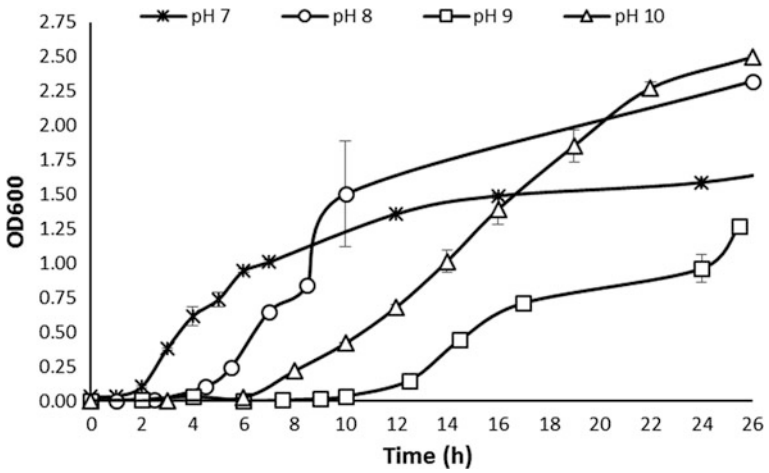

Fig. 1 *Bacillus licheniformis* growth in LB medium at pH 7, 8, 9 and 10 in orbital agitation at 37 °C 190 rpm. Assays were performed successively by increasing pH medium. Error bars show standard deviation between triplicates

Cyanide Degradation

Degradation assays at different temperatures were tested using *Bacillus licheniformis* strain. At all degradation assays, alkaline environments was kept by using 50 mM CAPS as buffer, and monitored daily to assure pH 10. Free-cyanide measurements during assays are show in Fig. 2. This showed that *B. licheniformis* degraded better free-cyanide solution at 32 °C obtaining a 98% degradation after 5 days of incubation.

Then, degrading assays at different rotations speed were performed. Results are shown in Fig. 3. Higher rotation speed resulted in better cyanide degradation rate. At 190 RPM rotation speed, *B. licheniformis* strain was able to degrade 79% of cyanide after 5 days of incubation whereas at 65 RPM speed, the degradation rate was 42% after the same period of time.

Rotation speed and temperature influence in natural degradation of free-cyanide as well, as these increase the amount of dissolve oxygen in water which can oxidize cyanide in synthetic solution. That is why is important to perform biodegradation assays together with a negative control that can identify the difference in the bacteria effect and degradation due to natural conditions. An assay using optimal conditions previously calculated compared with a negative control was performed, results are shown in Fig. 4. Compared to blank, *B. lciheniformis* strain was able to degrade more than 50% more than negative control showing a real bacterial degradation action to reduce cyanide concentrations in solution.

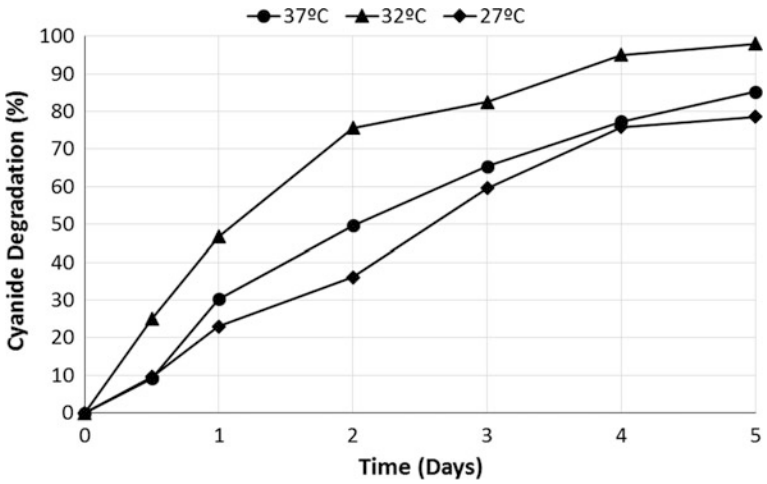

Fig. 2 Cyanide degradation using *Bacilus licheniformis* strain at 27, 32, and 37 °C 190 RPM

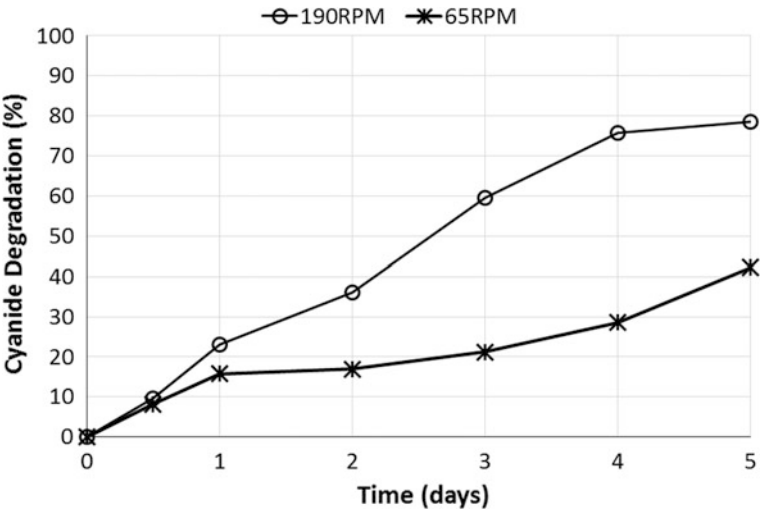

Fig. 3 Cyanide degradation using *Bacillus licheniformis* at 190 and 65 RPM, 27 °C

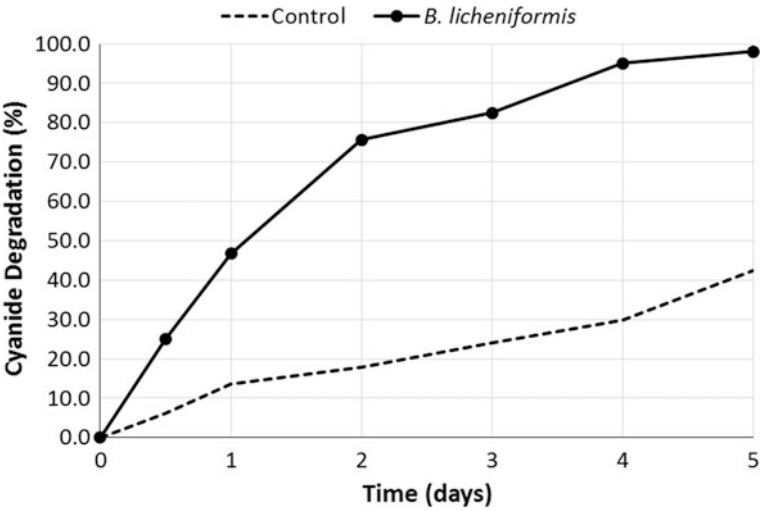

Fig. 4 Cyanide degradation using *Bacillus licheniformis* at optimal conditions (190 RPM, 32 °C) compared to control without bacteria

Conclusions

Cyanide-containing effluents must be treated before discharge to the environment as their toxicity represents a high risk for every living organisms. Normally, these effluents have high pH values to assure cyanide is contained in aqueous solution

and HCN formation is minimum. In this context, it's highly important for bacteria used in biodegradation to be adapted to alkaline environments and to be able to degrade cyanide in these conditions.

Bacillus licheniformis strain had previously been isolated and identified as a cyanide-degrading bacteria and adapted easily to nutritive medium at pH 10 showing its ability to grown in alkaline environments. Thus, *B. licheniformis* is able to degrade cyanide at these conditions. Cyanide degradation assays showed that strains degrades free-cyanide better at 32 °C and 190 RPM achieving up to 98% of cyanide degradation. This study shows that *B. licheniformis* isolated from mining wastes can degrade cyanide in alkaline environments and therefore, become a potential alternative in cyanide-containing effluents treatment.

References

1. Mudder T, Botz M (2004) Cyanide and society: a critical review. Tha Eur J Miner Process Environ Prot 4(1):62–74
2. Huertas MJ et al (2010) Alkaline cyanide degradation by Pseudomonas pseudoalcaligenes CECT5344 in a batch reactor. Influence of pH. J Hazard Mater 179(1–3):72–78
3. Luque Almagro VM et al (2005) Bacterial degradation of cyanide and its metal complexes under alkaline conditions. Appl Environ Microbiol 71(2):940–947
4. Gensemer RW, Deforest DK, Stenhouse AJ, Higgins CJ, Cardwell RD (2006) 14 aquatic toxicity of cyanide. In: Cyanide in water and soil, 2006
5. Maria C (2002) Toxicity of cyanide. In: Environmental sampling and analysis for metals, p 333
6. Mudder T, Botz MM, Smith A (1991) The chemistry and treatment of cyanidation wastes, p 373
7. Veiga M (1997) Introducing new technologies for abatement of global mercury pollution in Latin America
8. Akcil A (2003) Destruction of cyanide in gold mill effluents: biological versus chemical treatments. Biotechnol Adv 21(6):501–511
9. Botz MM, Mudder TI, Akcil AU (2016) Cyanide treatment: physical, chemical and biological processes. In: Adams M (ed) Gold ore processing, 2nd edn. Elsevier B.V., pp 619–645
10. Botz M (1999) Overview of cyanide treatment methods. Gold Inst (August):11
11. Dash RR, Gaur A, Balomajumder C (2009) Cyanide in industrial wastewaters and its removal: a review on biotreatment. J Hazard Mater 163(1):1–11
12. Monge C, Rosario CGA, Vallenas A, Coleti J, Justo S, Tenório JAS (2017) Isolation and characterization of cyanide degrading bacteria from artisanal gold mine tailings. In: The 32nd international conference on solid waste technology and management, 2017, pp 641–648

Determination of Limiting Current Density of a Solution with Copper, Zinc and EDTA from the Effluent of Brass Electrodeposition

K. S. Barros, J. A. S. Tenório and D. C. R. Espinosa

Abstract In the last decades, authors have been focused in the development of a cyanide-free bath for the electroplating industry of brass due to the risks that involves the use of cyanide and they have been evaluated the electrodialysis as an alternative method for the treatment of the effluent generated in this type of industry because of the limitations caused by the chemical precipitation. Hence, the present paper aimed to determine the limiting current density of the effluent generated in the free-cyanide electrodeposition of copper and zinc using EDTA as chelating agent for the treatment of the effluent by electrodialysis. The synthesized solutions were prepared with copper sulfate and zinc sulfate in different conditions of pH (10–12) and proportion of cupric ions (30%, 50%, 70%). According to the results, the increase of pH and the cupric ions proportion caused an increase in the limiting current density because of the larger amount of anionic species in solution and the consequent difficult to achieve the concentration polarization phenomenon.

Keywords Brass · EDTA · Electroplating industry · Limiting current Chronopotentiometry

Introduction

The electrodeposition of metal alloys coatings is usually used to produce materials with improved mechanical, decorative, electrochemical, magnetic or optical properties [1]. The electrodeposition of brass (copper + zinc), for example, was firstly tested in 1841 and has been widely used for decorative purposes, protection of steel and promotion of rubber adhesion to steel and other metals in many types of industries [2]. In general, cyanide is used in this process since it guarantees

K. S. Barros (✉) · J. A. S.Tenório · D. C. R. Espinosa
Department of Chemical Engineering, São Paulo University,
Avenida Professor Lineu Prestes, 580, Conjunto das Químicas,
Bloco 18, São Paulo, SP 05508-000, Brazil
e-mail: kayobarros.s@gmail.com

Z. Sun et al. (eds.), *Energy Technology 2018*, The Minerals, Metals & Materials Series, https://doi.org/10.1007/978-3-319-72362-4_33

high-quality deposits [3] due to the formation of a stronger complex of cyanide ions with Cu^{2+} compared to Zn^{2+}, bringing the reduction potentials of both metals closer together. However, it is widely known that cyanide is toxic and its use requires a rigorous maintenance and control of the pH of the solutions [4], which can make it unfeasible to be used. Hence, in the last years many authors have been tested alternative chelating agents to replace the cyanide, such as EDTA [5, 6], triethanolamine [7], glycine [8, 9], sorbitol [3, 10], tartrate [11], citrate [12], acetate [13], D-mannitol [14], pyrophosphate-oxalate [15] glucoheptonate [16] and gluconate-sulfate solutions [4]. Among the chelating agents, the use of EDTA is interesting since its properties are widely known, it does not cause risks for human health and it has already been tested as complexing agent in metals separation such as Ca and Cd [17], Ni and Co [18, 19], Ag, Zn and Cu [20], Na and Ca [21], Li e Co [22].

The most widely method used for the treatment of effluents generated in electroplating industry is chemical precipitation due to its simplicity, inexpensive equipment requirement and convenient and safe operations [23]. However, chemical precipitation requires a large amount of reagents and produces a huge volume of sludge which is difficult to be disposed and that requires further treatment. Hence, other methods have been evaluated and electrodialysis is one of the most considered options since it does not require additional reagents and allows the recovery and reutilization of water and the metals [24]. However, it is important to assess some properties of the membrane/solution system such as the limiting current density (LCD) to guarantee the viability of the electrodialysis use. The importance of the determination of LCD is related to the concentration polarization phenomenon, since if the current applied in electrodialysis is greater than the limiting one, the concentration of the cations at the membrane surface on the depleting solution side vanish, leading to a mass transfer limitation and high cell voltages [25]. For the determination of current limiting density, some electrochemical characterization methods can be used and among them, chronopotentiometry is a valuable method since it allows a direct access to the voltage contributions in different states of the solution–membrane system and the construction of current-voltage curves.

In view of the exposed, the present paper aimed the determination of limiting current densities of synthesized solutions from the effluent generated in the study of Almeida et al. [5, 6], which tested the non- cyanide brass electrodeposition on 1010 steel using EDTA as chelating agent. For the LCD determination, current-voltage curves (CVC) were constructed by chronopotentiometry with a system of three compartments and the anionic HDX 200 membrane. The synthesized solutions were prepared with copper sulfate and zinc sulfate in different conditions of pH (10–12) and proportion of cupric ions (30, 50 and 70%) to evaluate the influence of each metal and pH in the limiting current density of the solutions.

Experimental

Solutions

The synthesized solutions of brass electroplating effluent were prepared with copper sulfate pentahydrate, zinc sulfate heptahydrate, EDTA sodium salt and for the pH adjustment it was used NaOH since sodium is already present in EDTA molecule. The concentrations of the metals and EDTA were chosen based on the work made by Almeida et al. [5, 6], since the authors evaluated the deposition of brass using the proportion of cupric ions of 30, 50 and 70% with the total cationic concentration of Cu^{2+} and Zn^{2+} equal to 0.2 M, a fixed molar ratio of EDTA/Cu^{2+} equal to 2.5 and pH = 14. Hence, in the present paper the solutions were prepared by the dilution in 1% of the solutions tested by Almeida et al. As it was already verified by the software Hydra-Medusa [26] that both metals are complexed with EDTA in pH 10 and the membranes degrade under extreme pH values [27], the pH values evaluated in this paper were 10, 11 and 12. All the reagents employed were of analytical grade and the conditions tested are shown in Table 1.

Ion Exchange Membranes

The anion-exchange membrane evaluated in this work was HDX 200 (provided by Hydrodex®), which contains quaternary amine groups attached to its matrix. The cation-exchange membrane HDX 100 with sulfonic acid group was also used to compose the system. Both membranes are heterogeneous and have effective of 3.14 cm^2. Before the experiments, they were equilibrated in the working solutions for a period of 24 h. These membranes were chosen in this study since they were already tested in other papers in the field of chronopotentiometry and electrodialysis [28–31]. Table 2 presents the main characteristics of HDX 100 and HDX 200.

Table 1 Composition of the work solutions

Evaluation	ID	pH	Cu^{2+}proportion (%)	EDTA/Cu^{2+}	Concentration (mol/L)		
					Cu^{2+}	Zn^{2+}	EDTA
Cu^{2+}	I	10	30	2.5	0.0006	0.0014	0.0015
	II	10	50	2.5	0.0010	0.0010	0.0025
	III	10	70	2.5	0.0014	0.0006	0.0035
pH	IV	10	50	2.5	0.0010	0.0010	0.0025
	V	11	50	2.5	0.0010	0.0010	0.0025
	VI	12	50	2.5	0.0010	0.0010	0.0025

Table 2 Main characteristics of HDX 100 and HDX 200 membranes

Parameter	HDX 100	HDX 200	Unit
Ion group attached	$-SO_3^-$	$-NR_3^+$	–
Water content	35–50	30–45	%
Ion exchange capacity	≥ 2.0	≥ 1.8	$mol.kg^{-1}$ (dry)
Surface resistance (0.1 mol de NaCl)	≤ 20	≤ 20	$Ohm.cm^{-2}$
Permeselectivity (0.1 mol KCl/0.2 mol KCl)	≥ 90	≥ 89	%
Burst strengh	≥ 06	≥ 0.6	MPa
Dimensional change rate	≤ 2	≤ 2	%
Water permeability	≤ 0.1 (<0.2 MPa)	≤ 0.2 (<0.035 MPa)	$mL.h.cm^{-2}$

Electrochemical Cell and Chronopotentiometric Measurements

For the chronopotentiometric experiments it was used a three-compartment cell with a volume of 130 ml (each) and an anionic (HDX 200) and cationic membrane (HDX 100), which separated the central compartment from the anode and cathode, respectively. The potential drop through the anionic membrane was measured by two reference electrodes made by Ag/AgCl immersed in Luggin capillaries. The current applied was supplied by a potentiostat/galvanostat AUTOLAB and two graphite electrodes were disposed in the extremities of the cell to guarantee the current transport. The current-voltage curves were obtained from the steady-state polarization voltage corresponding to an applied current and as it was already detailed explained in the work published by Barros et al. [30], the CVC usually presents three regions. The first region is known as ohmic region since it shows a linear relation between the current density applied and the potential measured. The second region is known as a plateau zone and in this condition, there is no passage of ions through the membrane because of the achievement of the concentration polarization phenomenon. Hence, the limiting current density was determined in the present paper by the intersection of the tangents to the first and second regions. Finally, in the third region the current intensity increases again with the potential because of other mechanisms that promote ions transport such as the formation of water splitting products or electroconvection occurrence.

Results and Discussion

Evaluation of Copper Proportion

Current-voltage curves for solutions with 30, 50 and 70% of cupric ions (solutions I, II and III from Table 1) and pH = 10 were constructed and the limiting current densities were obtained. Figure 1 presents the curves for the solutions tested.

According to Fig. 1, the current-voltage curves obtained in the evaluation of the cupric ions proportion are typical for monopolar membranes and present the three regions clearly defined except for the solution with 30% of Cu^{2+}. It was also verified that the limiting current density increased with the copper proportion, even with the maintenance of the total cationic concentration of Cu^{2+} and Zn^{2+} equal to 0.002 mol/L. For the understanding of which species are responsible to the increase of the LCD, speciation diagrams for the three solutions were constructed by Hydra-Medusa and they are shown in Figs. 2, 3 and 4.

As can be seen in Figs. 2, 3 and 4, in pH = 10 the number of anionic species that passes through the anion-exchange membrane increases with the increase of copper proportion, which is responsible to the increase in the LCD. It can be verified, for example, three anionic species when the proportion of copper was 30%, while it was observed at least six anionic species when the proportion was 50 and 70%. Hence, as the LCD occurs in the moment of the ions scarcity in the membrane surface, its increase is related to the increase of the number of anionic species.

Evaluation of the PH

Current-voltage curves of solutions with Cu^{2+} proportion of 50% and pH of 10, 11 and 12 were constructed (solutions IV, V and VI) and the results are presented in Fig. 5.

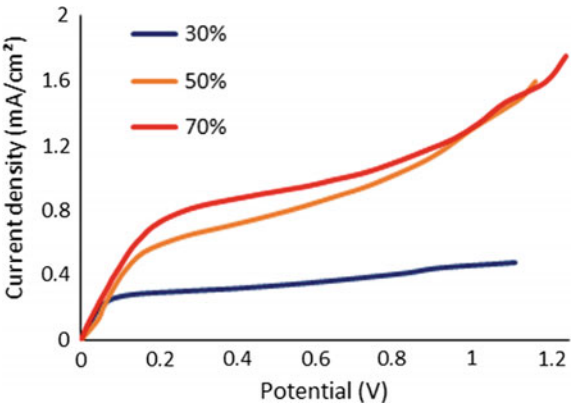

Fig. 1 CVC for solutions with 30, 50 and 70% of cupric ions

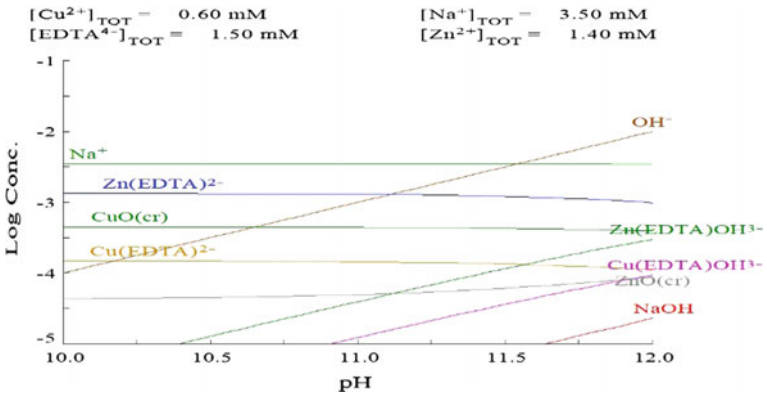

Fig. 2 Speciation diagrams for the solutions with cupric ions proportion of 30%

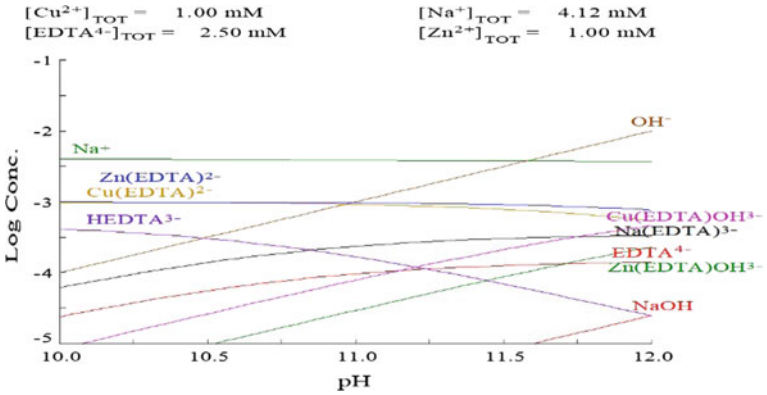

Fig. 3 Speciation diagrams for the solutions with cupric ions proportion of 50%

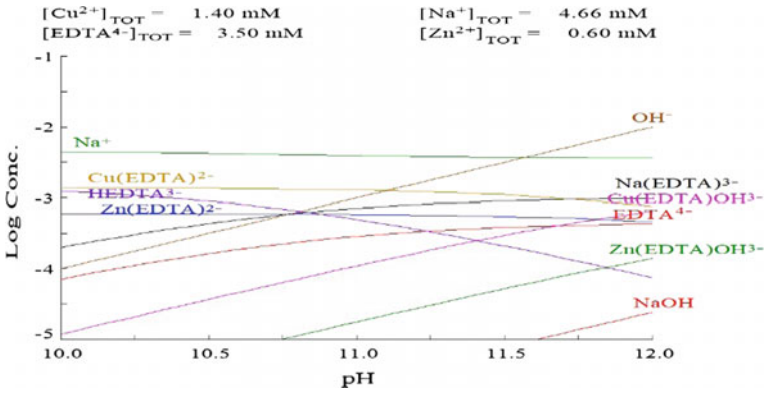

Fig. 4 Speciation diagrams for the solutions with cupric ions proportion of 70%

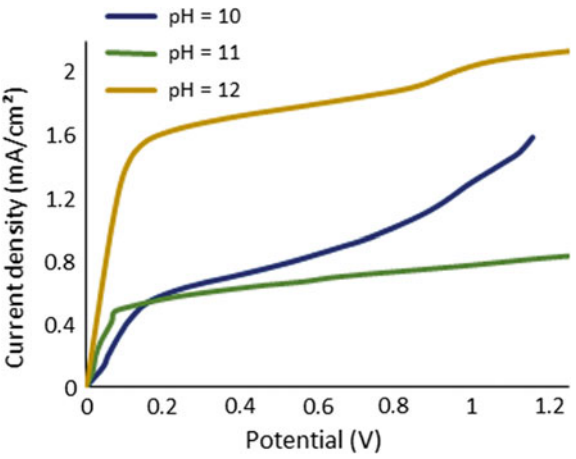

Fig. 5 CVC for solutions with 50% of cupric ions and pH 10, 11 and 12

According to Fig. 5, only the solution with pH 10 presented the three regions clearly defined since in the curves of the solutions with pH 11 and 12 it is not possible to identify the third region. However, the limiting current density could be effectively determined since it depends only on the first and second regions of the CVC. As it can be seen, there was no drastic change in the LCD from pH 10 to 11, while in pH 12 this property increased more than two times. It is also possible to verify in Fig. 2b that this difference in the behavior of the LCD may occurred because of the presence of chelates with copper and zinc, since these components are present in high concentration in pH 12 and in low concentration in pH equal to 10 and 11.

Conclusions

Current-voltage curves were effectively constructed by chronopotentiometry and limiting current densities were determined for solutions from the non-cyanide brass electroplating industry. According to the results, the LCD increases with the increase in copper proportion because of the larger amount of anionic species and the consequent increase in the difficult to achieve the depletion of ions in the membrane surface.

Finally, different pH values of the solution were evaluated and it was verified that when pH was increased from 10 to 11 there was no variation in the LCD since the ionic species in solution were almost the same. For pH equal to 12, it occurred an increase in the LCD due to the presence of chelates with copper and zinc, since these components are present in high concentration in this condition.

Acknowledgements The authors gratefully acknowledge the financial support given by funding agencies CNPq (Process 141346/2016-7) and FAPESP (Process 2012/51871-9).

References

1. Musa AY, Slaiman QJM, Kadhum AAH, Takriff MS (2008) Effects of agitation, current density and cyanide concentration on Cu-Zn alloy electroplating. Eur J Sci Res 22:517–524
2. Krishnan R, Muralidharan V, Natarajan S (1996) A non-cyanide brass plating bath. Bull Electrochem 12:274–277
3. Carlos LA, Almeida MRH (2004) Study of the influence of the polyalcohol sorbitol on the electrodeposition of copper-zinc films from a non-cyanide bath. J Electroanal Chem 562:153–159. https://doi.org/10.1016/j.jelechem.2003.08.028
4. Survila A, Mockus Z, Kanapeckaite S, Stalnionis G (2003) Kinetics of zinc and copper reduction in gluconate-sulfate solutions. Electrochim Acta 94:307–313. https://doi.org/10.1016/j.electacta.2013.01.157
5. Almeida MRH, Barbano EP, Zacarin MG, Brito MM, Tulio PC, Carlos IA (2016) Electrodeposition of CuZn films from free-of-cyanide alkaline baths containing EDTA as complexing agent. Surf Coat Technol 287:103–112. https://doi.org/10.1016/j.surfcoat.2015.12.079
6. Almeida MRH, Barbano EP, Carvalho MF, Carlos IA, Siqueira JLP, Barbosa LL (2011) Electrodeposition of copper-zinc from an alkaline bath based on EDTA. Surf Coat Technol 206:95–102. https://doi.org/10.1016/j.surfcoat.2011.06.050
7. Ramírez C, Calderón JA (2016) Study of the effect of Triethanolamine as a chelating agent in the simultaneous electrodeposition of copper and zinc from non-cyanide electrolytes. J Electroanal Chem 765:132–139. https://doi.org/10.1016/j.jelechem.2015.06.003
8. Ballesteros JC, Torres-Martínez LM, Juárez-Ramírez I, Trejo G, Meas Y (2014) Study of the electrochemical co-reduction of Cu2 + and Zn 2 + ions from an alkaline non-cyanide solution containing glycine. J Electroanal Chem 727:104–112. https://doi.org/10.1016/j.jelechem.2014.04.020
9. Rashwan SM (2017) Electrodeposition of Zn–Cu coatings from alkaline sulphate bath containing glycine. Trans IMF 85. https://doi.org/10.1179/174591907X216440
10. Almeida MRH, Barbano EP, Carvalho MF, Tulio PC, Carlos IA (2015) Copper-zinc electrodeposition in alkaline-sorbitol medium: electrochemical studies and structural, morphological and chemical composition characterization. Appl Surf Sci 333:13–22. https://doi.org/10.1016/j.apsusc.2015.02.005
11. Abd El Rehim SS, El Ayashy ME (1978) Effect of some plating variables on the electrodeposition of Cu-Zn alloys from alkaline tartrate baths. J Appl Electrochem 8:33–39. https://doi.org/10.1007/BF00615391
12. Assaf F, Rehim SSAE, Mohamed AS, Zaky AM (1995) Electroplating of brass from citrate-based alloy baths. Indian J Chem 2:147–152
13. Vreese P, Skoczylas A, Matthijs E, Fransaer J, Binnemans K (2013) Electrodeposition of copper-zinc alloys from an ionic liquid-likecholine acetate electrolyte. Electrochim Acta 108:788–794. https://doi.org/10.1016/j.electacta.2013.06.140
14. Juškenas R, Karpavičiene V, Pakštas V, Selskis A, Kapočius V (2007) Electrochemical and XRD studies of Cu-Zn coatings electrodeposited in solution with d-mannitol. J Electroanal Chem 602:237–244. https://doi.org/10.1016/j.jelechem.2007.01.004
15. Despić AR, Marinović V, Jović VD (1992) Kinetics of deposition and dissolution of brass from the pyrophosphate-oxalate bath. J Electroanal Chem 339:473–488. https://doi.org/10.1016/0022-0728(92)80468-J
16. Fujiwara Y, Enomoto H (1988) Characterization of Cu-Zn alloy deposits from glucoheptonate baths. Surf Coat Technol 35:113–124. https://doi.org/10.1016/0257-8972(88)90062-X

17. Kubal M, Machula T, Strnadová N (1998) Separation of calcium and cadmium by electrodialysis in the presence of ethylenediaminetetraacetic acid. Sep Sci Technol 33:1969–1980. https://doi.org/10.1080/01496399808545040
18. Chaudhary AJ, Donaldson JD, Grimes SM, Yasri NG (2000) Separation of nickel from cobalt using electrodialysis in the presence of EDTA. J Appl Electrochem 30:439–445. https://doi.org/10.1023/A:1003966132167
19. Labbe M, Fenyo JC, Selegny E (1975) Separation of nickel and cobalt by electrodialysis using ion-exchange membranes in the presence of EDTA. Sep Sci 10:307–322. https://doi.org/10.1080/00372367508058021
20. Cherif AT, Elmidaoui A, Gavach C (1993) Separation of Ag +, Zn2 + and Cu2 + ions by electrodialysis with monovalent cation specific membrane and EDTA. J Memb Sci 76:39–49. https://doi.org/10.1016/0376-7388(93)87003-T
21. Rozhkova MV, Shaposhnik VA, Strygina IP, Artemova LV (1996) Separation of cations with different charges in electrodialysis with the use of complex-formation. Russ J Electrochem 32:237–240
22. Iizuka A, Yamashita Y, Nagasawa H, Yamasaki A, Yanagisawa Y (2013) Separation of lithium and cobalt from waste lithium-ion batteries via bipolar membrane electrodialysis coupled with chelation. Sep Purif Technol 113:33–41. https://doi.org/10.1016/j.seppur.2013.04.014
23. Barakat MA (2011) New trends in removing heavy metals from industrial wastewater. Arab J Chem 4:361–377. https://doi.org/10.1016/j.arabjc.2010.07.019
24. Amado FDR, Rodrigues LF, Rodrigues MAS, Bernardes AM, Ferreira JZ, Ferreira CA (2005) Development of polyurethane/polyaniline membranes for zinc recovery through electrodialysis. Desalination 186:199–206. https://doi.org/10.1016/j.desal.2005.05.019
25. Martí-Calatayud MC, García-Gabaldón M, Pérez-Herranz V (2012) Study of the effects of the applied current regime and the concentration of chromic acid on the transport of Ni2+ ions through Nafion 117 membranes. J Memb Sci 392–393:137–149. https://doi.org/10.1016/j.memsci.2011.12.012
26. Puigdomench I (2001) Hydra Medusa—make equilibrium diagrams using sophisticated algorithms
27. Choi JH, Moon SH (2003) Structural change of ion-exchange membrane surfaces under high electric fields and its effects on membrane properties. J Colloid Interface Sci 265:93–100. https://doi.org/10.1016/S0021-9797(03)00136-X
28. Marder L, Bittencourt SD, Ferreira JZ, Bernardes AM (2016) Treatment of molybdate solutions by electrodialysis: the effect of pH and current density on ions transport behavior. Sep Purif Technol 167:32–36. https://doi.org/10.1016/j.seppur.2016.04.047
29. Martí-Calatayud MC, Buzzi DC, García-Gabaldón M, Ortega E, Bernardes AM, Tenório JAS, Pérez-Herranz V (2014) Sulfuric acid recovery from acid mine drainage by means of electrodialysis. Desalination 343:120–127. https://doi.org/10.1016/j.desal.2013.11.031
30. Barros KS, Tenório JAS, Espinosa DCR (2017) Chronopotentiometry applied to the determination of copper transport properties through a cation-exchange membrane. In: Energy technology 2017—carbon dioxide management other technologies. Springer International Publishing, Cham, pp 473– 481. https://doi.org/10.1007/978-3-319-52192-3_46
31. Martí-Calatayud MC, Buzzi DC, García-Gabaldón M, Bernardes AM, Tenório JAS, Pérez-Herranz V (2014) Ion transport through homogeneous and heterogeneous ion-exchange membranes in single salt and multicomponent electrolyte solutions. J Memb Sci 466:45–57. https://doi.org/10.1016/j.memsci.2014.04.033

Effect of the pH on the Recovery of Al^{3+}, Co^{2+}, Cr^{3+}, Cu^{2+}, Fe^{3+}, Mg^{2+}, Mn^{2+}, Ni^{2+} and Zn^{2+} by Purolite S950

Isadora Dias Perez, Mónica M. Jiménez Correa, Jorge A. Soares Tenório and Denise C. Romano Espinosa

Abstract The generation of mining waste has been the subject of environmental, economic and social concern. Alternative and sustainable methods of recycling metals technologies are desired. The present work focuses on the application of the ion exchange technique for the extraction of metals contained in a lateritic nickel mining effluent. The Purolite S950 chelating resin was used in the present work because it has the ability to adsorb transition metals present in an acidic solution. The experiments were carried out in a batch varying the pH in the range of 0.5–2.0. 1 g of resin was placed in contact with 50 mL of solution and stirred for 120 min at a speed of 200 rpm and temperature at 25 °C. The results demonstrated that the affinity of the resin varied with pH. The adsorbed metals were only copper, manganese, magnesium and zinc. The most extracted metal was copper, corresponding to 37%, when the solution was conditioned at pH 2.0.

Keywords Ion exchange · Transition metals · Chelating resin

Introduction

Lateritic nickel ore accounts for 60% of nickel reserves around the world, however, accounting for only 40% of world production [1]. This ore is processed according to its composition, emphasizing the pyrometallurgical and hydrometallurgical routes. As a consequence of the beneficiation via hydrometallurgical route, the leaching of the ores produces liquor. The leaching processes are rarely selective and the leach liquors contain impurities. On the other hand, the lateritic nickel ore processing generates liquor with solutions containing high concentrations of iron and manganese, traces of copper, nickel, cobalt, zinc and among others [2].

I. D. Perez (✉) · M. M. J. Correa · J. A. S. Tenório · D. C. R. Espinosa
Chemical Engineering Department, Polytechnic School, University of São Paulo, 158 Av. Prof. Luciano Gualberto, Trav. 3, São Paulo, SP 05424-970, Brazil
e-mail: dpisadora@gmail.com

Z. Sun et al. (eds.), *Energy Technology 2018*, The Minerals, Metals & Materials Series, https://doi.org/10.1007/978-3-319-72362-4_34

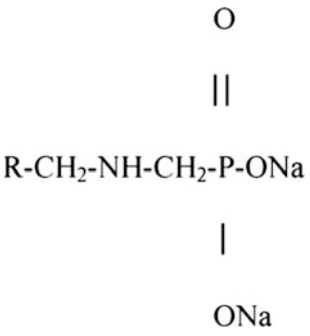

Fig. 1 The chemical structure of Purolite S950 [13]

Therefore, the metals present in the mining effluents could be separated by hydrometallurgical techniques. These techniques are able to purified and recovery of the desired metal [3]. Among the techniques used in the literature can be evidenced chemical precipitation, membranes, reverse osmosis, electrochemical precipitation, solvent extraction and ion exchange with resins [4–8]. These techniques provide the concentration of dilute solutions [3].

For the present work, the technique chosen to investigate the separation of the metals from the liquor was the chelating ion exchange resin, which has been used in several studies for the recovery of transition metals [9–11]. The leach liquor contains metals such as aluminum, cobalt, copper, chromium, iron, manganese, magnesium, nickel and zinc. Since the Purolite S950 chelating resin is capable of recovering transition metals, it has been chosen for its use.

Purolite S950 is characterized by aminophosphonic functional group. This chelating resin is bound in a macroporous polystyrene matrix [12]. Figure 1 shows the resin structure used in the study.

This paper focuses on the application of ion exchange technology for the recovery of metals from the mining effluent of lateritic nickel by chelating resin Purolite S950. The effect of pH was studied.

Materials and Methods

Material

For this research, the resin adopted was the chelating resin Purolite S950. Table 1 shows the resin characteristics.

Pretreatment of Resin

Prior to the batch studies, the resin was pretreated to remove impurities. The procedure was developed into a flask shaken and repeated 2 times to ensure that the

Table 1 Physical and chemical characteristics of commercial resin Purolite S950 [14]

Functional group	Aminophosphonic
Matrix	Macroporous styrene-divinylbenzene
Ionic form	Na^+
Moisture content (mass fraction)	60–68%
Particle size	0.3–1.2 mm
pH range (operation)	H^+ 2–6, Na^+ 6–11

resin was clean and ready for use. In the pretreatment, the resin was washed with deionized water and eluted with acid solution (4 M HCl) and base solution (2 M NaOH). Then, the resin was washed with deionized water at 60 °C.

The resin and solution separation was by filtration through a Millipore 20 µm filter paper. After filtration, the resin was dried in an oven at 60 °C for 120 min.

Preparation of Synthetic Solution

Analytical grade reagents $Al_2(SO_4)_3.17H_2O$, $CoSO_4.7H_2O$, $Cr_2(SO_4)_3.xH_2O$, $CuSO_4.5H_2O$, $Fe_2(SO_4)_3.xH_2O$, $MgSO_4.7H_2O$, $MnSO_4.H_2O$, $NiSO_4.6H_2O$, $ZnSO_4.7H_2O$ were used to prepare the synthetic solution. The concentrations of the metals are shown in the Table 2.

Batch Tests

For these tests, 1 g of chelating resin Purolite S950 was shaken with 50 mL of synthetic solution during 120 min. The shaking speed and the temperature were kept constant corresponding to 200 rpm and 25 °C, respectively. Figure 2 demonstrates how the experiments were developed. At the end of experiments, the resin was separated by filtration through a Millipore 20 µm filter paper. The remaining solution was chemically analyzed.

For the study of the effect of pH variation, the pH varied between 0.5–2.0. The choice of pH values was based on the precipitation of the metals present in the synthetic solution. According to the precipitation diagram (Fig. 3), ferric iron precipitates at pHs close to 2.

Table 2 Composition of the synthetic solution

Metal	Al^{3+}	Co^{2+}	Cr^{3+}	Cu^{2+}	Fe^{3+}	Mg^{2+}	Mn^{2+}	Ni^{2+}	Zn^{2+}
Concentration (mg/L)	4101.5	78.1	195.2	146.9	18713.5	7774.5	397.2	2434.2	36.7

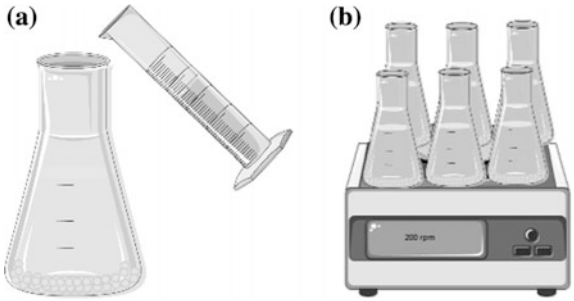

Fig. 2 Batch tests (**a**) contact of resin with synthetic solution (**b**) flask shaken during the experiments

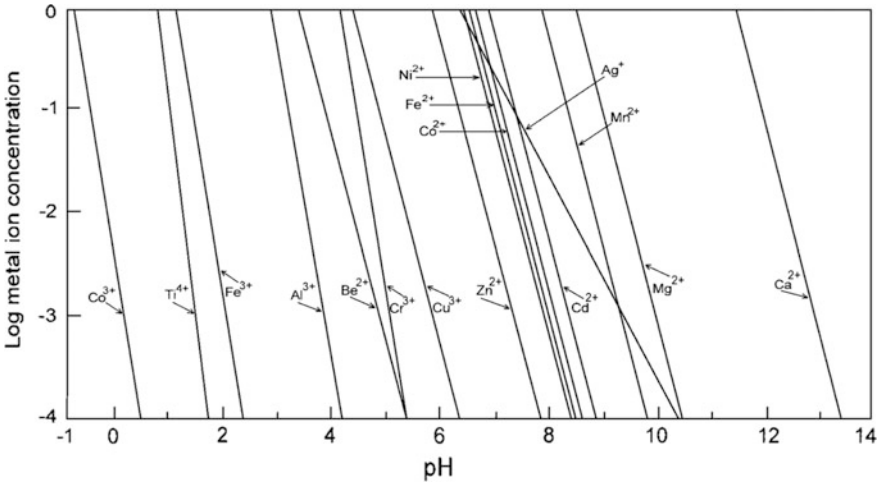

Fig. 3 Precipitation diagram of metal ions in the hydroxides form as a function of the pH variation in temperature of 25 °C [15]

Therefore, the analyzed pH values were 0.5, 1.0, 1.5 and 2.0. To adjust the pH value desired, 5 M H_2SO_4 or 2 M NaOH was used.

The adsorption capacity at equilibrium (q_e) was calculated by (1) [11]:

$$q_e = \frac{(C_o - C_e)}{M} \times V \tag{1}$$

Where q_e is the adsorption capacity at the equilibrium (mg/g), C_o and C_e is the initial and equilibrium metal concentration (mg/L), M is the amount of resin (g) and V is the volume (L) of metal solution used for sorption experiments, respectively [11].

The percentage removal of metal in equilibrium was calculated by (2) [16]:

$$\% = \frac{(C_o - C_e)}{C_o} \times 100 \quad (2)$$

Instrumentals

The chemical analysis of remaining metals in solution was obtained by Energy Dispersive X-ray Fluorescence Spectroscopy (EDX) *PANalytical Epsilon 3XL* equipment, identifying and quantifying of them. The *INFORS HT Multitron Pro* shaker was used by batch tests including adsorptions and temperature experiments. The pH meter chosen was *Hanna pH 21*.

Results

According to Diniz et al. [2], it is necessary to know the impact of pH variation during metal recovery processes. The solution pH is one of the parameters capable of controlling the resin adsorption process affecting the surface charge of adsorbent. In addition, pH change is responsible for the formation of specific chelates between the chelating agents and metal ions [11, 17].

Thus, the effect of pH variation on the adsorption capacity of the chelating resin with the metal ions present in the solution was studied. The solution was conditioned up to pH 2.0 in order to avoid the ferric iron precipitation and also the co-precipitation of other metals, such as copper [3, 15, 18].

The contact time was 120 min at 25 °C. The results are presented in Figs. 4 and 5 and they express the adsorption capacity and the percentage of each adsorbed metal, respectively.

Referring to Figs. 4 and 5, it may be assumed that the aluminum, cobalt, chromium, iron and nickel metals were not extracted by the Purolite S950. The adsorbed metals were only copper, manganese, magnesium and zinc.

For pH values 0.5, 1.0, 1.5 and 2.0, copper exchange capacity was 0.2, 1.6, 2.2 and 2.6 mg of copper/g of resin, respectively. The percentage of copper extracted increased from 1.8% (pH 0.5) to 37.2% (pH 2.0).

It was observed that the manganese showed a similar behavior to the copper, so when the pH increased from 0.5 to 2.0, exchange capacity changed from 1.7 mg of manganese/g of resin to 3.8 mg of manganese/g of resin. The maximum percentage removal of Mn^{2+} occurred at pH 2.0, corresponding to 11.5%.

As can be noticed in Figs. 4 and 5, the adsorption capacity of zinc was only 0.3 mg of zinc/g of resin at pH 2.0. However, the percentage extracted was 23.5%.

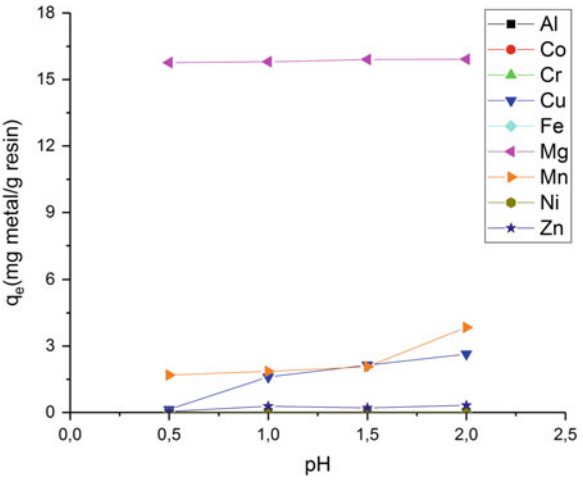

Fig. 4 Absorption capacity of metals in relation to the pH for the chelating resin Purolite S950. Experimental conditions: 1 g of resin; 50 mL of synthetic solution; 120 min; 25 °C

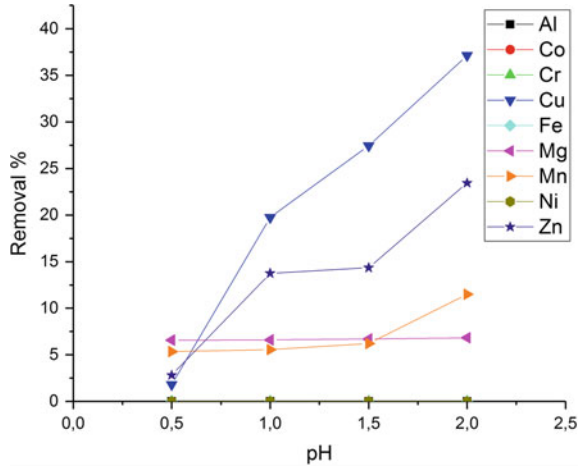

Fig. 5 Percentage of adsorption of metals in relation to the pH for Purolite S950 chelating resin. Experimental conditions: 1 g of resin; 50 mL of synthetic solution; 120 min; 25 °C

For magnesium, the adsorption was the highest among the metal ions studied, considering the mass adsorbed by the resin. The adsorption capacity of Mg^{2+} was 15.9 mg of magnesium/g of resin at pH 2.0. However, adsorption of magnesium is not only justified by its affinity with the resin, but also high magnesium concentration compared to the other metals. The concentration of Mg^{2+} is 53 times higher than the concentration of Cu^{2+}, 20 times greater than of Mn^{2+} and 212 times higher than of Zn^{2+}.

Analyzing the results for Cu^{2+}, Mn^{2+}, Mg^{2+} and Zn^{2+}, it was verified that the percentage of extraction of these metals increased progressively with the pH increase. This behavior has been extensively reported in literature. According to Bhatt and Shah [17], the sorption capacity of chelating resin is dependent on

solution pH. This situation is related to the charge of the functional group, which tends to become more electronegative as the pH increases, providing greater electrostatic attraction between the metal cations and the resin [17]. In addition, as the solution becomes more acidic, the concentration of H^+ increases. H^+ ions compete with the metal ions at the adsorption sites, reducing the exchange capacity of the resin [19].

It was also concluded that the metal most extracted by the resin was copper. This fact can be justified by the selectivity order of resin reported by some authors [20, 21]. According to Hamabe et al. [20], the selectivity of chelating resin Purolite S950 toward divalent metal ions at acidic pH is given by: $Ni^{2+} < Ca^{2+} < Mg^{2+} < Zn^{2+} < Cu^{2+} < Pb^{2+}$. Therefore, in the absence of Pb^{2+} in the working solution, Cu^{2+} is the metal that have the highest sorption affinity for Purolite S950. Copper has shown higher affinity for chelating resins with the aminophosphonic functional group than zinc, magnesium and manganese. In this way, copper is able to form chelates with an electron pair donor base (Lewis base) and be adsorbed by the resin even in situations where the solution is conditioned at pH <2.0 [22].

After evaluating the adsorption of zinc, this was the second metal most adsorbed by the resin. According to Hamabe et al. [20], the only commercial chelating resin capable of removing zinc ions from aqueous solution is the resin with the aminophosphonic functional group.

In theory, there are situations where the pH increases and the adsorption decreases. This is related to the formation of insoluble complexes composed of the hydroxides of the metallic ions present in the solution [17]. However, this situation was not verified in the present study, since the solution was conditioned up to pH 2.0, making it impossible to form complexes for the experimental conditions used.

Conclusions

The present work demonstrates that the chelating resin shows negligible higher selectivity for copper, magnesium, manganese and zinc. It was concluded that the aluminum, cobalt, chromium, iron and nickel metals were not extracted by the Purolite S950.

After the experiments, it can be concluded that the adsorbed percentage of the metals increased as the pH values ranged from 0.5 to 2.0. In addition, the adsorption capacity of the metals decreased as the solution became more acidic.

Through the batch tests was evaluated the effect of pH, the best performance for copper, magnesium, manganese and zinc occurred at pH 2.0, removing 37.2% Cu^{2+}, 6.8% Mg^{2+}, 11.5% Mn^{2+} and 23.5% Zn^{2+}.

Aknowledgements To the Counsel of Technological and Scientific Development (CNPq) for the financial support through doctorate grant.

To the Coordenação de Aperfeiçoamento de Pessoal de Nível Superior (CAPES) for the financial support through master grant.

To the Fundação de Amparo à Pesquisa do Estado de São Paulo (FAPESP) for financial support through the research Project 2012/51871-9.

To the Instituto Tecnológico Vale.

References

1. Bide T, Hetherington L, Gunn G, Minks A (2008) Nickel. British geological survey, pp 1–24
2. Diniz CV, Doyle FM, Ciminelli VST (2002) Effect of pH on the adsorption of selected heavy metal ions from concentrated chloride solutions by the chelating resin Dowex M-4195. Sep Sci Technol 37(14):3169–3185
3. Jackson E (1986) Hydrometallurgical extraction and reclamation. Ellis Horwood, Chichester
4. Fu F, Wang Q (2011) Removal of heavy metal ions from wastewaters: a review. J Environ Manage 92(3):407–418
5. Bessbousse H, Rhlalou T, Verchère JF, Lebrun L (2008) Removal of heavy metal ions from aqueous solutions by filtration with a novel complexing membrane containing poly (ethyleneimine) in a poly(vinyl alcohol) matrix. J Membr Sci 307(2):249–259
6. Cheng C, Boddy G, Zhang W, Godfrey M, Barnard K, Robinson D, Pranolo Y, Zhu Z, Zeng L, Wang W, Turner N, Shiers D, Hill T (2010) Separation of nickel and cobalt from manganese, magnesium and calcium by synergistic solvent extraction–from batch tests to pilot plant operation. In: XXV international mineral processing congress, pp 285–297
7. Chaudhari LB, Murthy ZVP (2010) Separation of Cd and Ni from multicomponent aqueous solutions by nanofiltration and characterization of membrane using IT model. J Hazard Mater 180(1–3):309–315
8. Guimarães AS, Da Silva PS, Mansur MB (2014) Purification of nickel from multicomponent aqueous sulfuric solutions by synergistic solvent extraction using Cyanex 272 and Versatic 10. Hydrometallurgy 150:173–177
9. Zainol Z, Nicol MJ (2009) Comparative study of chelating ion exchange resins for the recovery of nickel and cobalt from laterite leach tailings. Hydrometallurgy 96(4):283–287
10. Shaaban AF, Fadel DA, Mahmoud AA, Elkomy MA, Elbahy SM (2014) Synthesis of a new chelating resin bearing amidoxime group for adsorption of Cu(II), Ni(II) and Pb(II) by batch and fixed-bed column methods. J Environ Chem Eng 2(1):632–641
11. Kumar R, Kumar M, Ahmad R, Barakat MA (2013) L-Methionine modified Dowex-50 ion-exchanger of reduced size for the separation and removal of Cu(II) and Ni(II) from aqueous solution. Chem Eng J 218:32–38
12. Deepatana A, Tang JA, Valix M (2006) Comparative study of chelating ion exchange resins for metal recovery from bioleaching of nickel laterite ores. Miner Eng 19(12):1280–1289
13. Deepatana A, Valix M (2006) Recovery of nickel and cobalt from organic acid complexes: adsorption mechanisms of metal-organic complexes onto aminophosphonate chelating resin. J Hazard Mater 137(2):925–933
14. Kiefer R, Kalinitchev AI, Höll WH (2007) Column performance of ion exchange resins with aminophosphonate functional groups for elimination of heavy metals. React Funct Polym 67:1421–1432
15. Gupta CK (2003) Chemical metallurgy principles and practice. Wiley-VCH Verlag GmbH & Co. KGaA, Weinheim
16. Wang XS, Huang J, Hu HQ, Wang J, Qin Y (2007) Determination of kinetic and equilibrium parameters of the batch adsorption of Ni(II) from aqueous solutions by Na-mordenite. J Hazard Mater 142(1–2):468–476

17. Bhatt RR, Shah BA (2015) Sorption studies of heavy metal ions by salicylic acid-formaldehyde-catechol terpolymeric resin: Isotherm, kinetic and thermodynamics. Arab J Chem 8(3):414–426
18. Liebenberg CJ, Dorfling C, Bradshaw SM, Akdogan GA, Eksteen JJ (2013) The recovery of copper from a pregnant sulphuric acid bioleach solution with developmental resin Dow XUS43605. J South Afr Inst Min Metall 113(5):389–397
19. Shaaban AF, Fadel DA, Mahmoud AA, Elkomy MA, Elbahy SM (2013) Removal of Pb(II), Cd(II), Mn(II), and Zn(II) using iminodiacetate chelating resin by batch and fixed-bed column methods. Desalin Water Treat 51(28–30):5526–5536
20. Hamabe Y, Hirashima Y, Izumi J, Yamabe K, Jyo A (2009) Properties of a bifunctional chelating resin containing aminomethylphosphonate and sulfonate derived from poly(ώ-bromobutylstyrene-co-divinylbenzene) beads. React Funct Polym 69(11):828–835
21. Dabrowski A, Hubicki Z, Podkoscielny P, Robens E (2004) Selective removal of the heavy metal ions from waters and industrial wastewaters by ion-exchange method. Chemosphere 56 (2):91–106
22. Wołowicz A, Hubicki Z (2012) The use of the chelating resin of a new generation Lewatit MonoPlus TP-220 with the bis-picolylamine functional groups in the removal of selected metal ions from acidic solutions. Chem Eng J 197:493–508

Evaluation of the Occurrence of Fouling and Scaling on the Membrane HDX 200 for the Treatment of the Effluent of Brass Electrodeposition with EDTA as Complexing Agent

K. S. Barros, J. A. S. Tenório and D. C. R. Espinosa

Abstract Considering the risks involving the use of cyanide, other complexing agents have been evaluated for the treatment by electrodialysis of the effluent of brass electrodeposition and among them, EDTA is interesting since it has been already tested for many years to separate ions. The main objective of the present paper was to evaluate the occurrence of fouling and scaling on the surface of the anion-exchange membrane HDX 200 by the construction of chronopotentiometric curves and speciation diagrams in different conditions (pH between 10–12 and proportion of cupric ions of 30%, 50%, 70%). According to the results, the chronopotentiometric curves did not show additional inflexion points typical for the cases which occurs fouling and scaling for the pH values evaluated, which is in accordance with the speciation diagrams of the solutions constructed with the aid of Hydra-Medusa software. Hence, the pH and the proportion of cupric ions did not show influence on the curves behavior.

Keywords Brass · EDTA · Fouling · Scaling · Chronopotentiometry

Introduction

The electrodeposition of metals is widely present in different segments of industries since in general it is used for decorative purpose, protection of steel and promotion of rubber adhesion to steel or other metals [1]. Besides the deposition of pure metals is employed depending on the desired characteristics for the materials, the electrodeposition of alloys as brass (copper and zinc) is also used, for example,

K. S. Barros (✉) · J. A. S. Tenório · D. C. R. Espinosa
Department of Chemical Engineering, São Paulo University, Avenida Professor Lineu Prestes, 580, Conjunto Das Químicas, Bloco 18, São Paulo, SP 05508-000, Brazil
e-mail: kayobarros.s@gmail.com

Z. Sun et al. (eds.), *Energy Technology 2018*, The Minerals, Metals & Materials Series, https://doi.org/10.1007/978-3-319-72362-4_35

for corrosion protection and decorative purposes [2]. In the brass electroplating industry, cyanide is widely used as chelating agent since it is able to reduce the activity of Cu^{2+} ions in solution and produces high- quality deposits [3]. However, it is widely known that cyanide is highly toxic, requires a rigorous maintenance and the disposal and decomposition of its bath causes concerns to human health and the environmental [4]. Hence, in the last years efforts have been made to discover an alternative substance to the cyanide [1, 3–14] and among the chelating agents already evaluated, EDTA is promising since its properties are widely known, it is simple to be obtained and it does not cause risks for human health.

The wastewater from the electroplating industry are in general treated by hydroxide or sulfide precipitation because its relative simple and inexpensive to operate [15]. However, it requires a great amount of reagents and generates a large volume of relative low density sludge that causes dewatering and disposal problems [16]. To overcome these limitations, electrochemical processes have been tested to treat the effluent from the electroplating industry and among the options, electrodialysis is interesting since it does not require the addition of more reagents and allows the recovery and reutilization of water and the metals. However, for the technical viability of electrodialysis is essential to study the ions transport through the membrane and evaluate, for example, the species formed in solution and the occurrence of clogging of organic (fouling) or inorganic components (scaling) [17] since it can damage the membranes and enhance the resistance of the ions passage [18]. Some characterization electrochemical methods can be used in the study of precipitate formation and chronopotentiometry is usually used since it allows a direct access to the potential contributions in different states of the membrane/solution system and provides more information about the membrane behavior because the dynamic voltage response in time can be analyzed [19, 20].

In view of the exposed, the present paper aimed the evaluation of precipitates formation during the treatment by electrodialysis of the effluent from the free-cyanide brass electrodeposition using EDTA as chelating agent. The assessment was performed by chronopotentiometry since from the curves behavior obtained in this method it is possible to suggest the formation of a bipolar layer in the membrane caused by the precipitate formation. For the experiments, it was used a three-compartment cell, the membrane evaluated was the commercial HDX 200 and solutions in different cupric ions proportion (30, 50 and 70%) and pH (10–12) were evaluated. These conditions of solutions were chosen since Almeida et al. [6, 7] have studied the electrodeposition of brass on 1010 steel using EDTA as complexing agent and did not treated the effluent generated. For more detailed explanations about the species formed in the solution, speciation diagrams were constructed by the software Hydra-Medusa [21].

Experimental

Solutions

In the work developed by Almeida et al. [6, 7], the authors studied the influence of the metals concentration on the brass electrodeposition with solutions in pH 14, with cupric ions proportion of 30, 50 and 70% with a total cationic concentration of Cu^{2+} and Zn^{2+} equal to 0.2 M and a fixed EDTA/Cu^{2+} molar ratio of 2.5. Hence, the solutions evaluated in this paper were prepared by the dilution in 1% of those assessed by Almeida et al. to simulate the effluent generated in the brass electrodeposition industry using copper sulfate pentahydrate, zinc sulfate heptahydrate, EDTA sodium salt and NaOH for the pH adjustment. Firstly it was assessed the influence of the Cu^{2+} and Zn^{2+} ions by the solutions I, II and III from Table 1, which contains a proportion of cupric ions of 30, 50 and 70%, respectively. The solution pH was also evaluated by the solutions IV, V and VII. In this case, the pH values assessed were from 10 to 12 since it was verified by the software Hydra-Medusa [21] that both metals are already complexed with EDTA in pH 10 and the operation in pH higher than 12 can damage the membranes [22]. All the reagents employed were of analytical grade and their compositions are present in Table 1.

Ion Exchange Membranes

For the evaluation of precipitate formation and the clogging occurrence on the membrane surface, the commercial anion-exchange membrane HDX 200 (provided by Hydradex®) was used while the cation- exchange membrane was also used to compose the system. Both membranes are heterogeneous, have an effective circular area of 3.14 cm^2 and have similar properties, although HDX 200 has quaternary amine as fixed group and HDX 100 is charged with sulfonic acid [23]. The experiments were accomplished after a membrane equilibration period of 24 h

Table 1 Composition of the work solutions

Evaluation	ID	pH	Cu^{2+} proportion (%)	EDTA/Cu^{2+}	Concentration (mol/L)		
					Cu^{2+}	Zn^{2+}	EDTA
Cu^{2+}	I	10	30	2.5	0.0006	0.0014	0.0015
	II	10	50	2.5	0.0010	0.0010	0.0025
	III	10	70	2.5	0.0014	0.0006	0.0035
pH	IV	10	50	2.5	0.0010	0.0010	0.0025
	V	11	50	2.5	0.0010	0.0010	0.0025
	VI	12	50	2.5	0.0010	0.0010	0.0025

Table 2 Main characteristics of HDX 100 and HDX 200 membranes [24]

Parameter	HDX 100	HDX 200	Unit
Ion group attached	$-SO^{-}3$	$-NR^{+}3$	–
Water content	35–50	30–45	%
Ion exchange capacity	≥ 2.0	≥ 1.8	$mol.kg^{-1}$ (dry)
Surface resistance (0.1 mol de NaCl)	≤ 20	≤ 20	$Ohm.cm^{-2}$
Permeselectivity (0.1 mol KCl/ 0.2 mol KCl)	≥ 90	≥ 89	%
Burst strengh	≥ 06	≥ 0.6	MPa
Dimensional change rate	≤ 2	≤ 2	%
Water permeability	≤ 0.1 (< 0.2 MPa)	≤ 0.2 (< 0.035 MPa)	$mL.h.cm^{-2}$

using the same solution used in the experiments. Table 1 presents the main characteristics of the HDX membranes evaluated in the present paper (Table 2).

Electrochemical Cell and Chronopotentiometric Measurements

The experiments were accomplished in a system with three compartments with 130 mL (each), a cation-exchange membrane and anion-exchange membrane that separated the central compartment from the cathode and anode, respectively. As the complexed components have negative charge and consequently tended to pass from the central compartment to the anode, the potential drop through the HDX 200 was measured by two reference electrodes made by Ag/AgCl immersed in Luggin capillaries and disposed in each side of the membrane. Two graphite electrodes were disposed in the extremities of the cell to allow the current transport, which was provided by a potentiostat/galvanostat AUTOLAB. The chronopotentiometric curves were constructed after the application of some current densities applied below and above the limiting current density.

Results and Discussion

Evaluation of Copper Proportion

The copper proportion was evaluated by the construction of chronopotentiometric curves for solutions with 30, 50 and 70% of cupric ions in pH = 10 and for the better understanding of which species are present in solution and their influence on

the chronopotentiometric curves, speciation diagrams were constructed by the software Hydra-Medusa and the diagrams obtained are present in Figs. 1, 2 and 3.

According to Figs. 1, 2 and 3, it can be verified that the proportion of cupric ions caused significant alterations on the speciation diagrams. The formation of insoluble species, for example, occurred only when the proportion was 30% (Fig. 1). The curves of 50 and 70% did not present formation of precipitate and their behavior was similar.

The chronopotentiometric curves obtained for the solutions I, II and III of Table 1 are present in Fig. 4a–c.

According to Fig. 4 (a–c), for the solution with the cupric ions proportion from 50% to 70%, the chronopotentiometric curves were typical for a monopolar membrane since the curves for the current densities applied above the limiting current density showed a rapid increase and them the curves reached a steady state where the potential varied no more with time. In these cases, there was no suggestion of

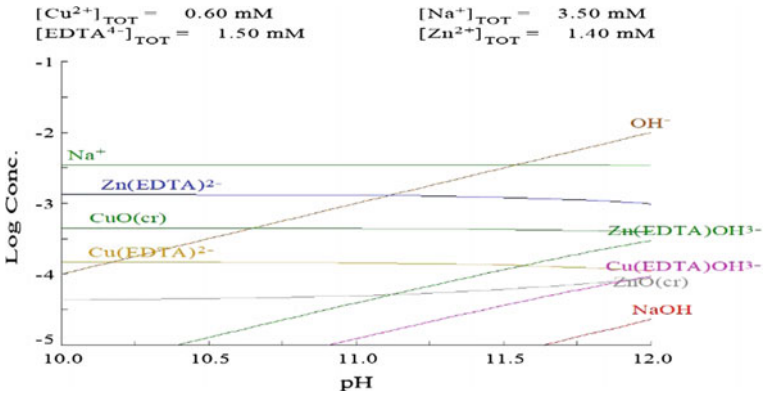

Fig. 1 Speciation diagrams for the solutions with cupric ions proportion of 30%

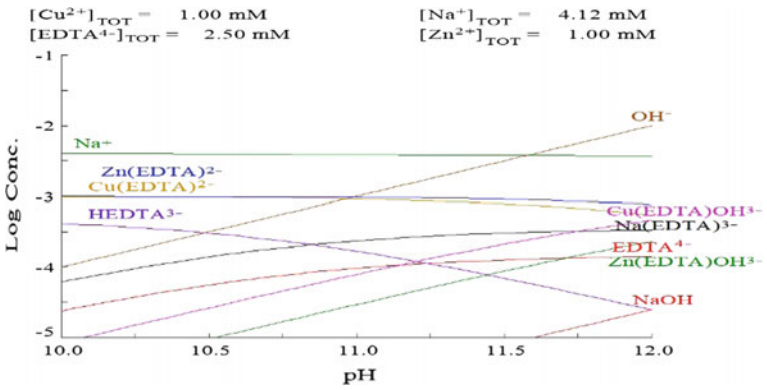

Fig. 2 Speciation diagrams for the solutions with cupric ions proportion of 50%

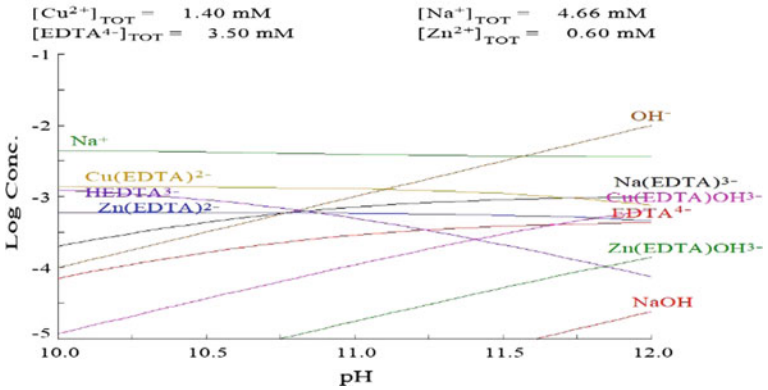

Fig. 3 Speciation diagrams for the solutions with cupric ions proportion of 70%

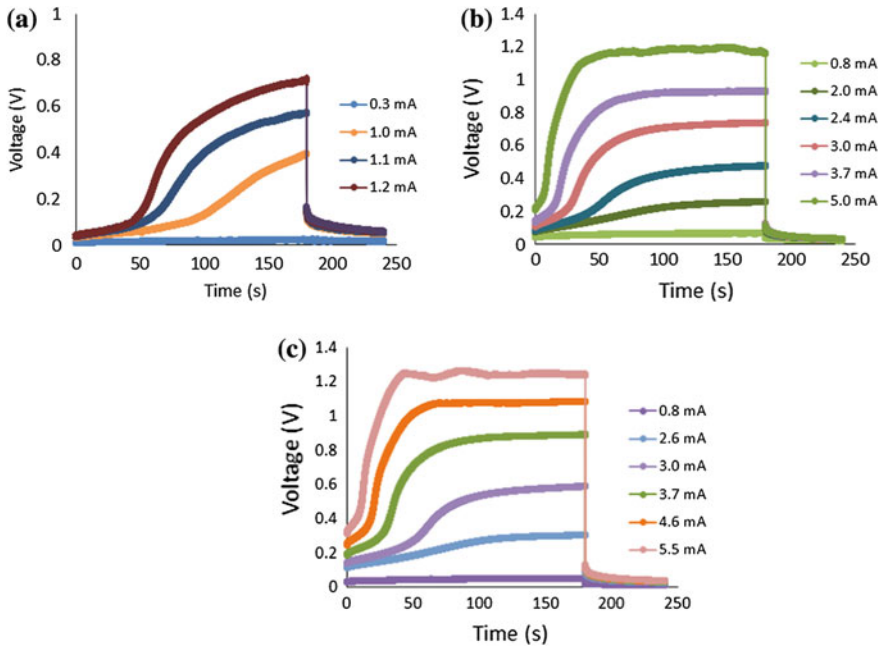

Fig. 4 Chronopotentiometric curves for solutions with cupric ions proportion of **a** 30%, **b** 50% and **c** 70%

precipitate formation by the behavior of the chronopotentiometric curves. According to the literature, when the voltage continues increasing even in a long time period for the experiments and the curves do not reach the constant value after a rapid voltage increase due to the scarcity of ions in the membrane surface at the moment of the

concentration polarization phenomenon, it occurs due to the formation of a precipitate since it can lead to an increase of the resistance and consequently to an enhance of the voltage. The absence of oscillations or additional inflexion points is confirmed by the Figs. 1, 2 and 3, since no precipitate is formed under pH 10. However, we suggest the application of higher current densities to confirm this behavior regarding the chronopotentiometric curves.

Evaluation of the PH of the Solution

The pH of the solution was also assessed and the chronopotentiometric curves obtained are presented in Fig. 5a–c.

According to Fig. 5 (a–c), typical chronopotentiometric curves were obtained for pH equal to 10, 11 and 12, since the curves showed a rapid increase in the potential due to the concentration polarization phenomenon and then they showed a constant potential behavior. Hence, we did not verify for any pH a non-expected additional increase in the potential in the moment of the stead steady. Additional inflexion points are typical for bipolar membranes but in monopolar membranes it can occur because of a bipolar layer formed by the recombination of the metals and hydroxide ions, since the pH in the surface of the anion-exchange membrane can achieve

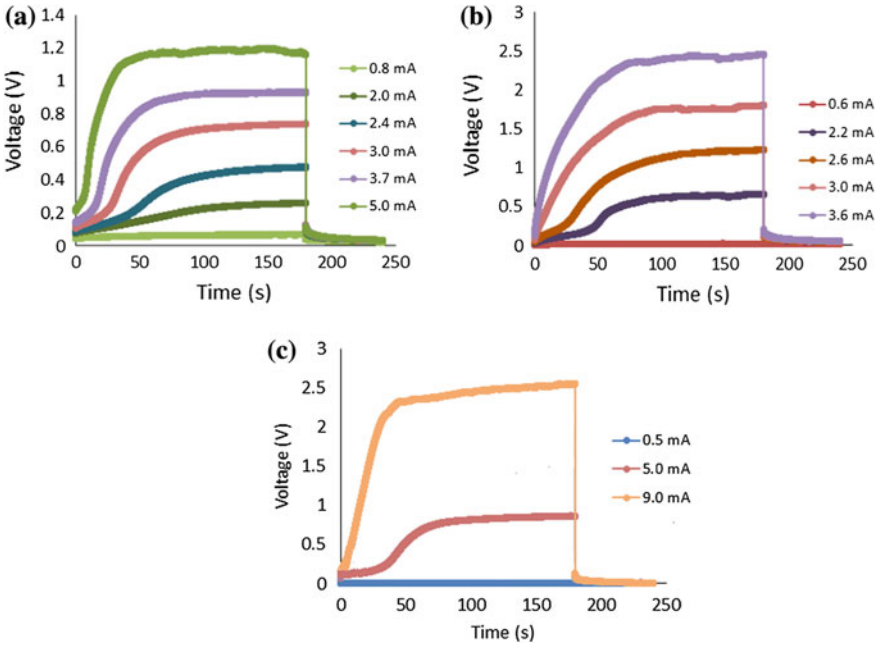

Fig. 5 Chronopotentiometric curves for solutions with pH equal to **a** 10, **b** 11 and **c** 12

extreme values because of the OH^- ions passage [24–26]. As it can be seen in the speciation diagram of Fig. 2, in pH 10, 11 or 12 it does not occur formation of an insoluble specie in the solution with cupric ions proportion of 50%.

Conclusions

Chronopotentiometric curves were effectively constructed and their behaviors were evaluated in function of the cupric ions proportion and pH of the solution. The curves obtained for 30%, 50% and 70% were typical for monopolar membranes and did not show an unexpected behavior. Hence, it was not verified the influence of the increase of cupric ions on the formation of a bipolar layer at the membrane surface.

Finally, the pH of the solution was evaluated and it was verified that typical chronopotentiometric curves for monopolar membranes were also obtained for pH 10, 11 and 12. Although the pH can achieve extreme values due to the rapid transport of hydroxyl ions, in this case it was not verified formation of an insoluble specie as a consequence of the recombination of the metals and hydroxide ions.

We suggest the application of higher current densities using the same solution composition to confirm the absence of precipitate formation, which can occur due to the smaller size of hydroxyl ions.

Acknowledgements The authors gratefully acknowledge the financial support given by funding agencies CNPq (Process 141346/2016-7) and FAPESP (Process 2012/51871-9).

References

1. Rashwan SM (2017) Electrodeposition of Zn–Cu coatings from alkaline sulphate bath containing glycine. Trans IMF 85. https://doi.org/10.1179/174591907X216440
2. Brenner A (1963) Electrodeposition of alloys. Academic Press, New York
3. Ramírez C, Calderón JA (2016) Study of the effect of Triethanolamine as a chelating agent in the simultaneous electrodeposition of copper and zinc from non-cyanide electrolytes. J Electroanal Chem 765:132–139. https://doi.org/10.1016/j.jelechem.2015.06.003
4. Ballesteros JC, Torres-Martínez LM, Juárez-Ramírez I, Trejo G, Meas Y (2014) Study of the electrochemical co-reduction of Cu^{2+} and Zn^{2+} ions from an alkaline non-cyanide solution containing glycine. J Electroanal Chem 727:104–112. https://doi.org/10.1016/j.jelechem.2014.04.020
5. Almeida MRH, Barbano EP, Carvalho MF, Tulio PC, Carlos IA (2015) Copper-zinc electrodeposition in alkaline-sorbitol medium: electrochemical studies and structural, morphological and chemical composition characterization. Appl Surf Sci 333:13–22. https://doi.org/10.1016/j.apsusc.2015.02.005
6. Almeida MRH, Barbano EP, Zacarin MG, Brito MM, Tulio PC, Carlos IA (2016) Electrodeposition of CuZn films from free-of-cyanide alkaline baths containing EDTA as complexing agent. Surf Coat Technol 287:103–112. https://doi.org/10.1016/j.surfcoat.2015.12.079

7. Almeida MRH, Barbano EP, Carvalho MF, Carlos IA, Siqueira JLP, Barbosa LL (2011) Electrodeposition of copper-zinc from an alkaline bath based on EDTA. Surf Coat Technol 206:95–102. https://doi.org/10.1016/j.surfcoat.2011.06.050
8. Assaf F, Rehim SSAE, Mohamed AS, Zaky AM (1995) Electroplating of brass from citrate-based alloy baths. Indian J Chem 2:147–152
9. Senna LF, Díaz SI, Sathler L (2003) Electrodeposition of copper-zinc alloys in pyrophosphate-based electrolytes. J Appl Electrochem 33:1155–1161. https://doi.org/10.1023/B:JACH.0000003756.11862.6e
10. Despić AR, Marinović V, Jović VD (1992) Kinetics of deposition and dissolution of brass from the pyrophosphate-oxalate bath. J Electroanal Chem 339:473–488. https://doi.org/10.1016/0022-0728(92)80468-J
11. Fujiwara Y, Enomoto H (1988) Characterization of Cu-Zn alloy deposits from glucoheptonate baths. Surf Coat Technol 35:113–124. https://doi.org/10.1016/0257-8972(88)90062-X
12. Krishnan R, Muralidharan V, Natarajan S (1996) A non-cyanide brass plating bath. Bull Electrochem 12:274–277
13. Rossi A (1992) A tartrate-based alloy bath for brass-plated steel wire production. J Appl Electrochem 22:64–72. https://doi.org/10.1007/BF01093013
14. Juškenas R, Karpavičiene V, Pakštas V, Selskis A, Kapočius V (2007) Electrochemical and XRD studies of Cu-Zn coatings electrodeposited in solution with d-mannitol. J Electroanal Chem 602:237–244. https://doi.org/10.1016/j.jelechem.2007.01.004
15. Ku Y, Jung IL (2001) Photocatalytic reduction of Cr(VI) in aqueous solutions by UV irradiation with the presence of titanium dioxide. Water Res 35:135–142. https://doi.org/10.1016/S0043-1354(00)00098-1
16. Fu F, Wang Q (2011) Removal of heavy metal ions from wastewaters: a review. J Environ Manage 92:407–418. https://doi.org/10.1016/j.jenvman.2010.11.011
17. Booster JL, Van Sandwijk A, Reuter MA (2004) Opposing scaling and fouling during electrodialysis of sodium fluoride solution in a membrane cell reactor. Hydrometallurgy 73:177–187. https://doi.org/10.1016/j.hydromet.2003.10.012
18. Ayala-Bribiesca E, Pourcelly G, Bazinet L (2007) Nature identification and morphology characterization of anion-exchange membrane fouling during conventional electrodialysis. J Colloid Interface Sci 308:182–190. https://doi.org/10.1016/j.jcis.2006.11.012
19. Marder L, Ortega Navarro EM, Perez-Herranz V, Bernardes AM, Ferreira JZ (2006) Evaluation of transition metals transport properties through a cation exchange membrane by chronopotentiometry. J. Memb Sci 284:267–275. https://doi.org/10.1016/j.memsci.2006.07.039
20. Pismenskaia N, Sistat P, Huguet P, Nikonenko V, Pourcelly G (2004) Chronopotentiometry applied to the study of ion transfer through anion exchange membranes. J Memb Sci 228:65–76. https://doi.org/10.1016/j.memsci.2003.09.012
21. Puigdomench I (2001) Hydra Medusa—make equilibrium diagrams using sophisticated algorithms
22. Choi JH, Moon SH (2003) Structural change of ion-exchange membrane surfaces under high electric fields and its effects on membrane properties. J Colloid Interface Sci 265:93–100. https://doi.org/10.1016/S0021-9797(03)00136-X
23. Barros KS, Tenório JAS, Espinosa DCR (2017) Chronopotentiometry applied to the determination of copper transport properties through a cation-exchange membrane. In: Energy technology 2017, carbon dioxide management and other technologies. Springer International Publishing, pp 473– 481. https://doi.org/10.1007/978-3-319-52192-3_46
24. Scarazato T, Buzzi DC, Bernardes AM, Tenório JAS, Espinosa DCR (2015) Current-Voltage curves for treating effluent containing HEDP: determination of the limiting current. Braz J Chem Eng 32:831–836
25. Marder L, Ortega Navarro EM, Pérez-Herranz V, Bernardes AM, Ferreira JZ (2009) Chronopotentiometric study on the effect of boric acid in the nickel transport properties through a cation-exchange membrane. Desalination 249:348–352. https://doi.org/10.1016/j.desal.2009.06.040

26. Marder L, Bittencourt SD, Zoppas Ferreira J, Bernardes AM (2016) Treatment of molybdate solutions by electrodialysis: the effect of pH and current density on ions transport behavior. Sep Purif Technol 167:32–36. https://doi.org/10.1016/j.seppur.2016.04.047
27. Wilhelm FG, Van der Vegt NFA, Wessling M, Strathmann H (2001) Chronopotentiometry for the advanced current-voltage characterisation of bipolar membranes. J Electroanal Chem 502:152–166. https://doi.org/10.1016/S0022-0728(01)00348-5

High Temperature Crystallization Kinetics of $MgSO_4 \cdot H_2O$

Kristine Bruce Wanderley, Denise Crocce Romano Espinosa and Jorge Alberto Soares Tenório

Abstract Magnesium is present in nickels leach liquor and it is often disposed in waste barriers. However, new technologies with the aim of recuperating magnesium and other metals in the liquor have proven that it is possible to reduce the amount of metal lost during nickel ore processing. In this context, high temperature crystallization removes magnesium, with a concentration of 8 g/L, as $MgSO_4 \cdot H_2O$ from the leach liquor. Kinetic studies of this process are needed to evaluate the thermodynamics of the growth of crystals. Thus, this work aims to study the crystallization kinetics of $MgSO_4 \cdot H_2O$. Temperatures of 230, 210 and 200 °C were investigated in a batch crystallization system in solutions with pH^2. Aliquots were taken at each hour up to 5 h of time residence and analysed by ion chromatography for magnesium concentration. The reaction mechanism as well as rate constant and activation energy for each reaction temperature were obtained.

Keywords Monohydrate · Leachate liquor · Avrami model

Introduction

Nickel is present in various materials and thus plays a major role in societies everyday life. However, mining of nickel ores to obtain nickel generates large volumes of waste which are carried to waste barriers. This waste consists of an aqueous solution with dissolved metals and is called liquor. A typical composition of the leach liquor consists of 5 g/L Ni^{2+}, 0,3 g/L Co^{2+}, 23 g/L Fe^{3+}, 6 g/L Al^{3+}, 1 g/L Cr^{3+}, 1 g/L Mn^{2+}, 8 g/L Mg^{2+} [1].

In order to minimize environmental impacts caused by waste barriers and also to reuse metal values both present and lost in the barrier, these metals must be recovered. To recover these metals values from solution, processes such as

K. B. Wanderley · D. C. R. Espinosa · J. A. S. Tenório (✉)
Chemical Engineering Dep., Polytechnic School, University of São Paulo, Rua Do Lago, 250, 2nd Floor, São Paulo, SP 05508-080, Brazil
e-mail: jtenorio@usp.br

Z. Sun et al. (eds.), *Energy Technology 2018*, The Minerals, Metals & Materials Series, https://doi.org/10.1007/978-3-319-72362-4_36

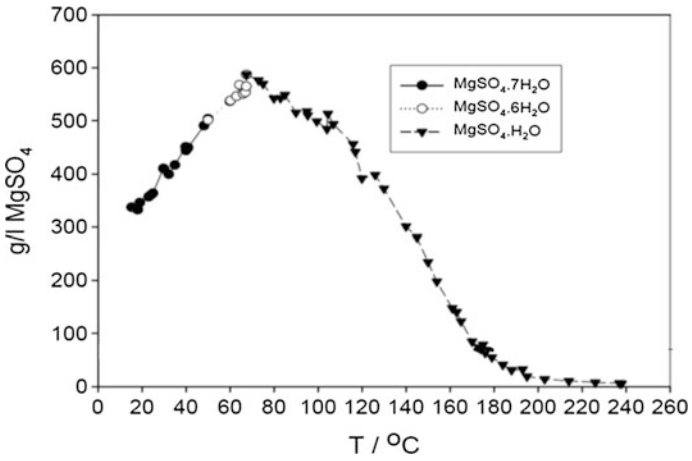

Fig. 1 Solubility curve of $MgSO_4$ [7]

precipitation/crystallization, solvent extraction and ion exchange may be carried out [2, 3]. Magnesium, which is present in the liquor as magnesium sulphate, may be removed from solution by crystallization.

The system $MgSO_4$-H_2O is very complex since temperature and humidity influence the transformation of the salt in different hydrated forms, each one being stable at a certain temperature and pressure [4, 5]. The three main stable forms are the heptahydrate (seven water molecules), which is stable at temperatures below 52 °C, hexahydrate (six water molecules), stable from 52 to 71 °C and monohydrate (one water molecule) which is stable at temperatures above 71 °C [6]. Therefore, as the temperature rises less hydrated forms are being formed.

The solubility curve for this salt begins with an increase in solubility with the increase in temperature. However, as the hydrated salt reaches one molecule of water, an inverse solubility is observed and the solubility decreases with the increase of temperature. Therefore, the monohydrate presents the lowest solubility at around 200 °C as can be seen from Fig. 1. Therefore, the present study aims to investigate the crystallization kinetics of the formation of $MgSO_4.H_2O$ at 230 °C at pH 2 at different time residences.

Johnson-Mehl-Avrami-Kolmogorov (JMAK) describes a kinetic model in which the extent of the crystallization of a material occurs as a function of time and temperature. The model describes the temporal dependence of the crystallized fraction (x) as follows [8]:

$$X = 1 - e^{-kt^n} \tag{1}$$

where,

X = Crystallized fraction;
K = Rate constant;

n = Index of reaction

Equation 1 may be written in the logarithmic form:

$$-\ln(1 - X) = kt^n \tag{2}$$

The index of reaction in the Avrami model corresponds to the sum of two constants that represent the mechanisms of crystallization in terms of steps in the process of crystallization and dimensionality of the growth process [9]. Table 1 shows how the value of n corresponds to the crystallization mechanism.

Values of k and *n* are evaluated by the logarithmic of Eq. 2 resulting in Eq. 3.

$$\ln[-\ln(1 - X) = \ln(k) + n\ \ln(t) \tag{3}$$

The plot of ln [- ln (1-X)] as a function of ln(t) results in a straight line having a slope of *n* and an intercept of ln k.

Materials and Methods

A solution with a concentration of 8 g/L of magnesium was prepared using magnesium sulphate heptahydrate and deionized water. This concentration corresponds to the concentration found in the leaching liquor of nickel limonite ore.

Batch experiments were carried out using a pressure reactor, shown in Fig. 2. The pH of the MgSO4 solution was adjusted to 2 with the addition of H_2SO_4 1 M. A volume of 200 mL of the solution was placed inside the reactor. Agitation speed was maintained at 1000 rpm throughout the residence time of 1, 2, 3, 4 and 5 h of operation at temperatures of 230, 210 and 200 °C.

The aliquots taken each hour were analyzed by ion chromatography to quantify residual magnesium in the solution. The crystals formed were analysed by DRX and MEV-EDS to evaluate the morphology and composition of the product. Product size distribution of the crystal was also carried out by sieve agitators.

Table 1 Values of *n* and the corresponding crystallization mechanism

Implied mechanism	*n*
Diffusion controlled	0.54–0.62
Phase boundary	1.07–1.11
Nucleation and growth	2.00, 3.00
Zero order	1.24
First order	1.00

Fig. 2 Pressure reactor used in the present study

Results and Discussion

Removal of Magnesium from Mother Liquor

The aliquots taken were analyzed by ion chromatography for magnesium concentration and indicate that the residence time of 5 h at 230 °C favored the removal of magnesium from solution and thus was the optimum time for crystallization amongst the investigated.

Figure 3 shows the percentage of magnesium removed from solution at temperatures of 230, 210 and 200 at 1 to 5 h of residence time.

Crystallization Kinetics

The values of magnesium crystallization at each temperature were applied to Eq. 3 and ln [− ln (1 − X)] as a function of ln(t) was plotted in Fig. 4.

Table 2 shows the values obtained from the straight line in Fig. 3 for n, k and R^2.

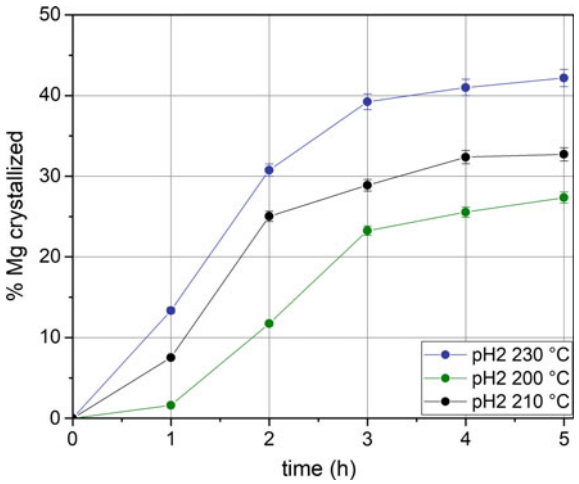

Fig. 3 Magnesium % removal at temperatures of 230, 210 and 200 at pH 2 °C as a function of time

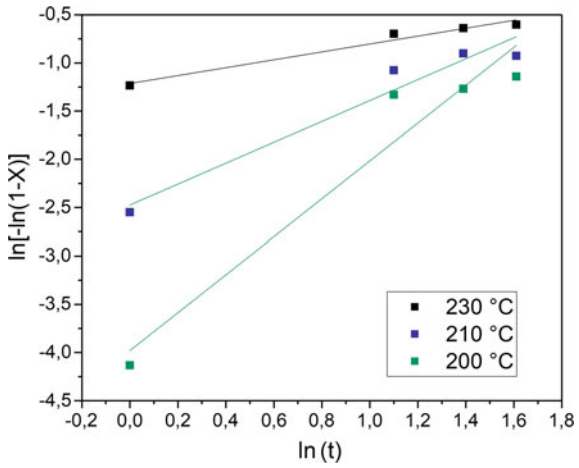

Fig. 4 Avrami model applied to the results of crystallization at temperatures of 230, 210 and 200 °C

Table 2 Values of n, k and R2 obtained from the Avrami model

T (°C)	n	k (1/h)	R^2
230	0,55	0,30	0,97
210	1,08	0,08	0,95
200	1,96	0,02	0,94

The distribution coefficient values (R^2) of 0.97, 0.95 and 0.94 for temperatures of 230, 210 and 200 °C, respectively, indicate that the study data follow the Avrami model.

Also, the index of reaction equal to 0,55 suggest that crystallization mechanism is controlled by diffusion at 230 °C. At 210 °C the mechanism is controlled by phase boundary and at 200 °C it is controlled by nucleation and growth.

The highest rate constant was for the temperature of 230 °C with a value of 0.30 h^{-1} and the lowest rate of 0.02 h^{-1} for the run performed at 200 ° C. This is due to the fact that the higher the temperature the more energy the molecules have, thus collision occurs and consequently a higher velocity rates are expected.

Activation Energy

Svante August Arrhenius in the late 1800 s suggested that the rate constant, k, varies with the system temperature according to Eq. 4 [8]. This equation, known as the Arrhenius equation, relates the reaction rate to temperature.

$$k = A * e^{-Ea/RT} \tag{4}$$

where,

k = rate constant (t^{-1});
A = frequency factor (m^{-1});
Ea = activation energy (kJ/mol);
R = gas constant (J/mol.K);
T = temperature (K)

The linearization of Eq. 4 results in Eq. 5:

$$lnk = lnA - \frac{Ea}{R} * \frac{1}{T} \tag{5}$$

The plot of ln k as a function of the inverse of the temperature results in a straight line having a slope of -Ea/R and an intercept of ln A, as shown in Fig. 5. The values o k and of temperature used are those shown in Table 2.

From the equation of the straight line, the activation energy is equal to 172 kJ/mol (41 kcal/mol) and ln A equal to 40,2

Product Characterization

Morphology

Samples of the crystals formed at 230 °C and at 5 h were analyzed by SEM-EDS, as shown in Fig. 6.

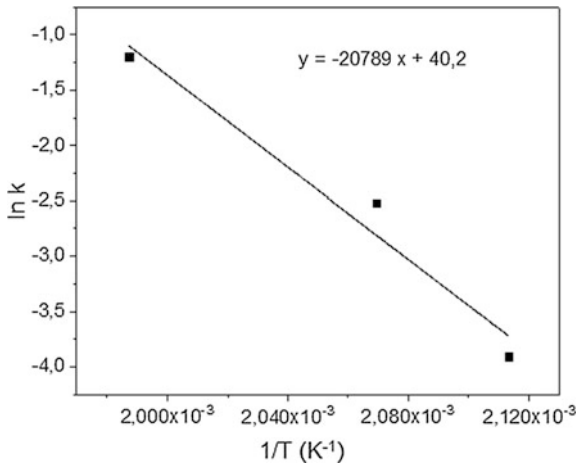

Fig. 5 Plot of ln k as a function of the inverse of the temperature

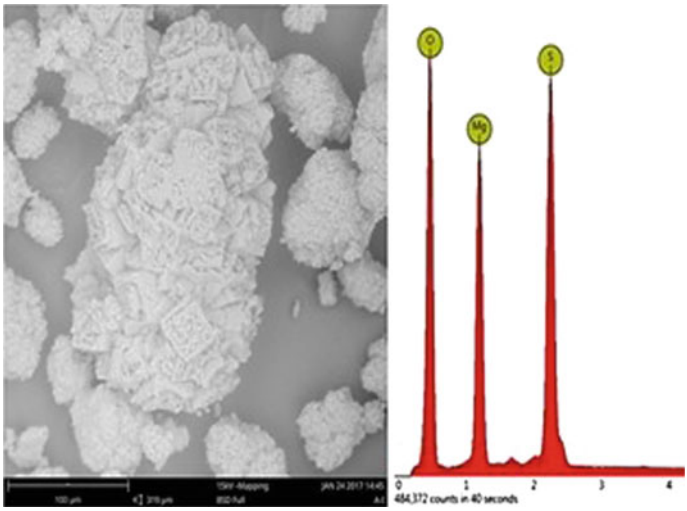

Fig. 6 SEM-EDS of crystals formed at 230 °C and at 5 h

Three peaks corresponding to O, Mg and S may be seen and the SEM image shows irregular shaped crystals surrounding an elongated crystal in the center.

Composition

DRX analysis of the product formed at each hour formed at 230 °C was carried out.

As can be seen from Fig. 7, the peaks shown in the diffractograms increase in intensity with increasing residence time. This represents a typical progression of

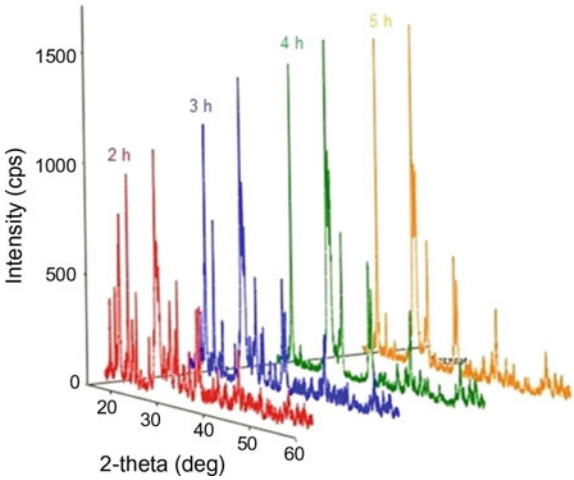

Fig. 7 X-ray diffraction (XRD) data for crystals formed at 230°C at each hour

crystallization as a function of residence time, as evaluated by XRD, since larger residence times allow greater crystalline growth and therefore more intense peaks are observed [10].

It is noteworthy that although peak intensities varied according to residence time, the composition of each peak was related to magnesium sulfate monohydrate.

Conclusion

Crystallization kinetics of magnesium sulphate monohydrate was studied at three different temperatures: 230, 210 and 200 °C with residence time varying from 1 to 5 h. Magnesium removal from solution increased with the increase in residence time and temperature of the system.

At 5 h of residence time and at 230 °C, the removal of from solution was favoured compared to the other temperatures.

The distribution coefficient values (R^2) of 0.97, 0.95 and 0.94 for temperatures of 230, 210 and 200 °C, respectively, indicate that the study data follow the Avrami model.

Applying experimental data to the Arrhenius equation it was possible to obtain a value of 172 kJ/mol (41 kcal/mol) for the activation energy.

MEV-EDS analysis showed a heterogeneous crystal growth and DRX analysis proved that the crystals formed were composed of magnesium sulphate monohydrate.

References

1. Agatzini-Leonardou S, Tsakiridis PE et al (2009) Hydrometallurgical process for the separation and recovery of nickel from sulphate heap leach liquor of nickeliferrous laterite ores. Miner Eng 22(14):1181–1192
2. Tsakiridis PE, Agatzini-Leonardou S (2005) Solvent extraction of aluminium in the presence of cobalt, nickel and magnesium from sulphate solutions by Cyanex 272. Hydrometallurgy 80 (1):90–97
3. Tsakiridis PE, Agatzini SL (2004) Simultaneous solvent extraction of cobalt and nickel in the presence of manganese and magnesium from sulfate solutions by Cyanex 301. Hydrometallurgy 72(3):269–278
4. Chipera SJ, Vaniman DT (2007) Experimental stability of magnesium sulfate hydrates that may be present on Mars. Geochim Cosmochim Acta 71(1):241–250
5. Himawan C, Kramer HJM et al (2006) Study on the recovery of purified MgSO4??7H2O crystals from industrial solution by eutectic freezing. Sep Purif Technol 50(2):240–248
6. Wang A, Freeman JJ et al (2009) Phase transition pathways of the hydrates of magnesium sulfate in the temperature range 50 to 5°C: Implication for sulfates on mars. J Geophys Res E: Planets 114(4):1–28
7. D'Ans J (1933) Aqueous salt systems of phase theoretical interest. American Chemical Society (ACS), pp 491–493
8. Zhi-jie YAN, Shu-e D et al (2008) Applicability of Johnson-Mehl-Avrami model to crystallization kinetics of Zr 60 Al 15 Ni 25 bulk amorphous alloy. Trans Nonferrous Metals Soc China 18(20051032):138–144
9. Gersten BL (2003) Growth of multicomponent perovskite oxide crystals: synthesis conditions for the hyrothermal growth of ferroelectric powders. In: Crystal growth technology, pp 299–333
10. Shalmani FM, Halladj R et al (2016) An investigation of the crystallization kinetics of zeotype SAPO-34 crystals synthesized by hydrothermal and sonochemical methods. Ultrasonics sonochemistry, vol 29, pp 354–362

Preparation of Glass-Ceramic from Titanium-Bearing Blast Furnace Slag by "Petrurgic" Method

Kuiyuan Chen, Yu Li, Long Meng, Yaodong Yi and Zhancheng Guo

Abstract Blast furnace slag is the main by-product discharged in the iron and steel industry and contains considerable waste heat at dischargeing temperature between 1450 and 1550 °C. To fully utilize waste heat and slag, this study directly converted high temperature liquid Ti-bearing blast furnace slag into glass-ceramics via the "Petrurgic" method. Samples at different crystallization temperature were prepared and its influence on crystal phases, pore structure, and compressive strength were investigated via SEM, XRD techniques, and compressive strength measurements. Results showed that all glass-ceramic samples contained main crystals of perovskite, diopside and gehlenite and had a qualified mechanical performance with compressive strength above 100 Mpa, which meets the requirement of Chinese national standard for natural granite stone. With increasing crystallization temperature, pore size decreased, while the size of the perovskite phase firstly decreased and then increased with decreasing crystallization temperature. Samples had an optimum crystallization temperature of 1215 °C, maximum grain size and a densified structure with minimal pore defect.

Keywords Ti-bearing blast furnace slag · "Petrurgic" method · Glass-ceramic Crystal temperature

K. Chen · Y. Li (✉) · L. Meng · Y. Yi · Z. Guo (✉)
State Key Laboratory of Advanced Metallurgy, University of Science and Technology Beijing, Beijing 100083, People's Republic of China
e-mail: leeuu00@sina.com

Z. Guo
e-mail: zcguo@ustb.edu.cn

K. Chen
e-mail: Chenkuiyuan_ustb@126.com

L. Meng
e-mail: longmeng0889@126.com

Y. Yi
e-mail: 1498327973@qq.com

Z. Sun et al. (eds.), *Energy Technology 2018*, The Minerals, Metals & Materials Series, https://doi.org/10.1007/978-3-319-72362-4_37

Introduction

Blast furnace (BF) slag is the main by-product of the iron and steel industry. Discharged between 1450 and 1550 °C, the slag contains considerable metallurgical waste heat. In 2014, China's crude steel output reached 823 million tons, resulting in about 274 million tons of BF slag [1], with a waste heat equivalent to 1590 tons of standard coal.

At present, the water quenching technique is the most effective disposal method for slag to obtain glass structure. However, it not only consumes excessive water, but also does not effectively utilize heat. To pursue the sustainable development of iron and steel industry and to meet the increasing demand for higher value added products, an efficient method of integrated recovery of waste heat and utilization of BF slag is urgently required. Therefore, an exploration of glass-ceramic prepared from BF slag using the "Petrurgic" method is meaningful.

The main components of BF slag are CaO, SiO_2, Al_2O_3, and MgO, which can be used to produce cement and glass ceramics [2]. In contrast to ceramics, glass-ceramics are fine-grained polycrystalline materials that are formed when glasses of suitable compositions are heat treated and thus undergo controlled crystallization to a lower energy, crystalline state [3, 4]. Heat treatment is critical for the attainment of an acceptable and reproducible product. Usually a glass-ceramic is not fully crystalline; typically the microstructure is 50–95 vol.% crystalline with the remainder being residual glass. One or more crystalline phases might form during heat treatment and since their composition normally differs from the parent glass, the composition of the residual glass also differs from the parent glass.

The conventional method for producing a glass-ceramic is to devitrify the glass via two-stage heat treatment (Fig. 1b). The first stage consists of a low temperature heat treatment at a temperature that provides a high nucleation rate (around T_N in Fig. 1a) thus forming a high nuclei density throughout the interior of the glass. A high nuclei density is important as it leads to the desirable microstructure consisting of a large number of small crystals. The second stage consists of a higher temperature heat treatment at around temperature T_G, which leads to growth of the nuclei at a reasonable rate. The parent glass may be shaped prior to the crystallization, employing any of the well-established and traditional glass shaping methods such as casting and forming [3–6] or more specialized methods such as extrusion [7–9]. Glass production and subsequent heat treatments are generally energy intensive and thus expensive.

The reason for such two-stage heat treatment of the glass is a consequence of the limited overlap between nucleation and growth rate curves (Fig. 1a). If an extensive overlap region of the rate curves exists, nucleation and growth can simultaneously take place during a single-stage heat treatment at temperature T_{NG} as indicated in Fig. 2. The rate curves, and the nucleation rate curve in particular, is sensitive to composition. Therefore, by optimizing the glass composition in some cases, such as for the nuclear reagent, the nucleation rate curve may be moved toward the overlap

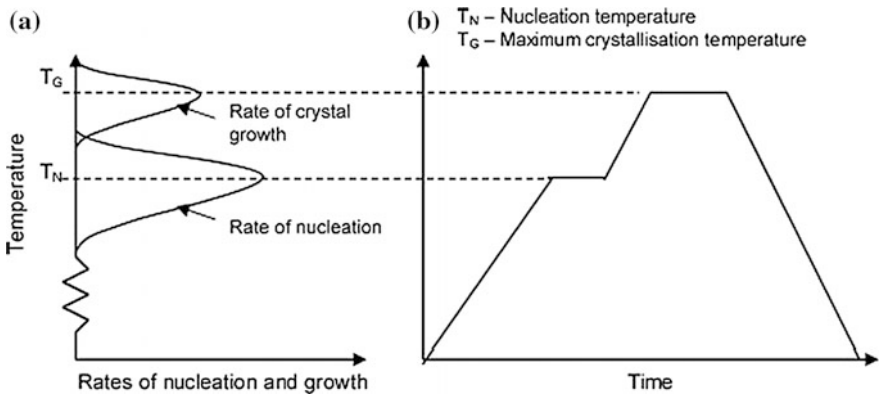

Fig. 1 Two-stage method. **a** Temperature dependence of the nucleation and growth rates with negligible overlap and **b** two-stage heat treatment

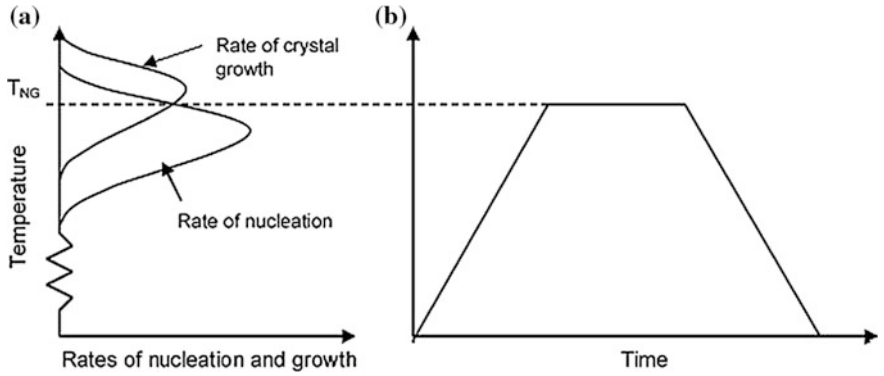

Fig. 2 One-stage method. **a** Temperature dependence of the nucleation and growth rates with significant overlap and **b** single-stage heat treatment

region with the growth rate curve. This is the first implementation of the glass ceramic system known as "Silceram" [10], which will be discussed below (Fig. 3).

It has been reported to make little difference whether the glass was heated up to T_{NG} from room temperature or whether the molten glass was cooled to T_{NG} [10]. Both results in the production of specific glass ceramics via controlled, usually very slow cooling from molten maternal glass, without a waiting period at an intermediate temperature. In the recent literature, this method is called the "petrurgic" method [11, 12], and can be used for nucleation and crystal growth during the cooling process. Traditional methods (single stage) and "petrurgic" methods are more economical than traditional methods (two-stage). However, the "petrurgic" method can directly use blast furnace slag, which saves a considerable energy compared to traditional methods. Therefore, the glass-ceramic produced with this

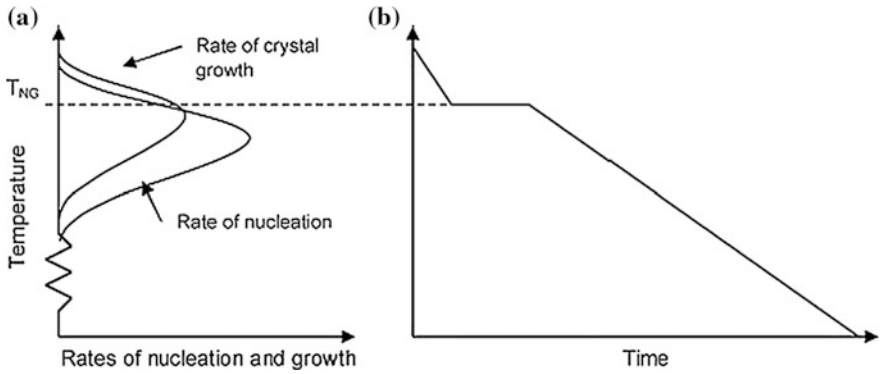

Fig. 3 Petrurgic method. **a** Temperature dependence of the nucleation and growth rates with significant overlap and **b** petrurgic treatment

method requires less energy consumption and produces less pollution, has a simpler process, and thus has great economic benefits. This article will introduce in detail, the glass-ceramic prepared via the "petrurgic" method from hot BF slag.

Experimental Procedure

Material

The BF slag (provided by the Panzhihua Iron and Steel Corporation of China) was pulverized via ball milling for about 1 h (arriving at a size below 74 μm). Then the slag was analyzed via X-ray fluoroscopy (SHIMADZU XRF-1800) to determine the content of slag, as indicated in Table 1. XRD measurements were performed to determine the original phase content of samples, as indicated in Fig. 4. The XRD patterns were obtained using a Rigaku XRD-D/max-1200 system with a scanning speed of 10° min^{-1}. Fig. 4 shows that the original phase of the slag was not amorphous. To conduct a DTA analysis on that slag, slag melting and water quenching were required. Then, 100 g slag powder was put into a graphite crucible (50 mm inner diameter and 80 mm height) and melted under an argon atmosphere at 1773 K (1500 °C) for 1 h in a $MoSi_2$ furnace to homogenize the slag. After melting, the slag was taken out for water quenching. Subsequently, the slag was pulverized via electromagnetic crushing for about 2 min (size below 74 μm), and the XRD test was conducted, as indicated in Fig. 5.

Table 1 Composition of titanium-bearing slag powder

Component	CaO	SiO_2	Al_2O_3	MgO	FeO	TiO_2	K_2O	NaO
Content/%	27.35	24.69	13.00	7.41	1.23	21.44	0.80	0.62

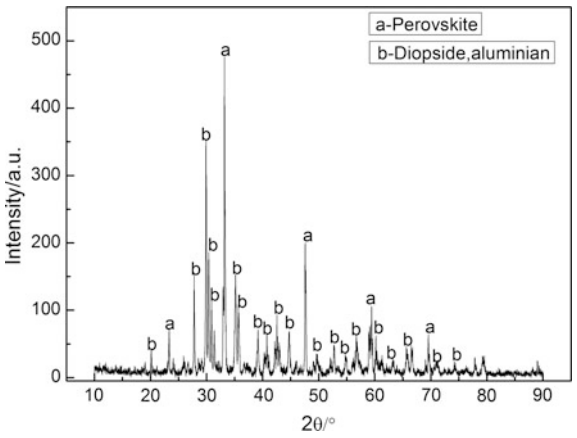

Fig. 4 XRD of original slag

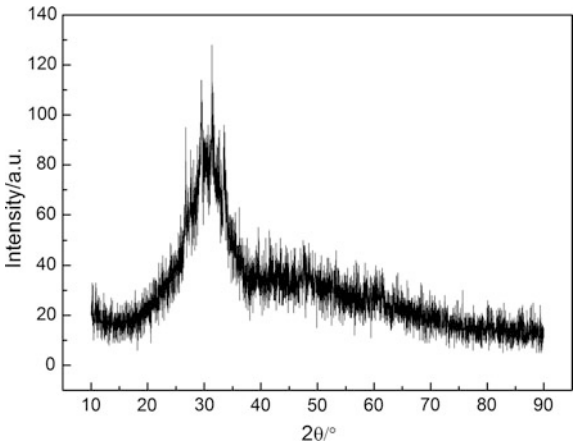

Fig. 5 XRD of water quenched slag

Differential Thermal Analysis (DTA)

A DAT instrument was applied to analyze the characteristic temperature of the blast furnace slag, including the glass transition temperature, crystallization peak temperature, and melt temperature with the temperature accuracy of ±0.05 °C. The sample was requested for 15 mg with 200 mesh powder. Sample analysis was conducted in argon atmosphere with a heating rate of 10 °C/min at a temperature range of 0–1200 °C, as indicated in Fig. 6.

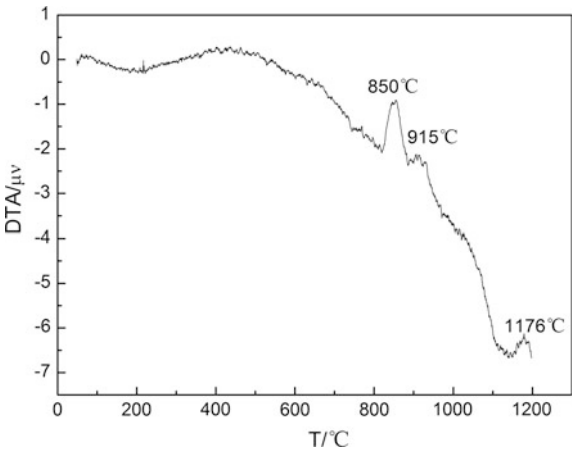

Fig. 6 Different thermal analysis of water quenched slag

Thermodynamic Calculation

The equilibrium phases of the normalized titanium-bearing slag (CaO-SiO_2-Al_2O_3-MgO-TiO_2 quinary system) at different temperatures were calculated via using FactSage 7.0, as shown in Fig. 7. It can be seen that the melting temperature of the slag was predicted to be 1440 °C. Perovskite is the primary phase crystal from the molten slag obtained during cooling. Titania spinel and $CaAl_2Si_2O_8$ are predicted to

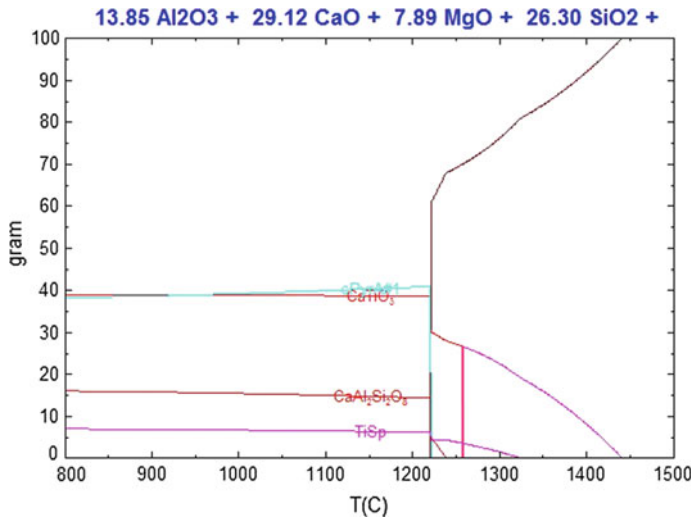

Fig. 7 Theoretical equilibrium phases of the normalized titanium-bearing slag at different temperatures (SLAGA, liquid slag; $CaTiO_3$, perovskite; cPyrA, clinopyroxene; TiSp, titania spinel)

crystallize at 1310 and 1235 °C, respectively. At the end of solidification, clinopyroxene is predicted to crystallize at 1215 °C. The perovskite phase provides the biggest percentage of phases above 1220 °C. The proportion of each phase is no longer changed below 1210 °C. Clinopyroxene and perovskite are similar in content with a content of about 40% and titanium spinel provides the smallest percentage with a content of about 8%.

Sample Preparation

According to Fig. 6, the crystallization peak temperatures were 850, 915, and 1176 °C. As clinopyroxene is predicted to crystallize at 1215 °C, to explore the equispaced temperature in higher temperature and one crystallization temperature upon 1200 °C, the following crystallization temperatures were selected 850, 915, 1015, 1115, and 1215 °C. Each sample consisted of 40 grams, and was heated to 1500 °C in a muffle furnace and insulated for 1 h, then cooled to 850, 915, 1015, 1115, and 1215 °C and retained at these temperatures for 1 h, respectively. Afterwards, the sample was cooled to for 650 °C and retained 1 h. The glass-ceramics sample was cleaned in an ultrasonic cleaning apparatus for 10 min. Samples were divided longitudinally, half of them were used to investigate the macro structure and were then polished for the SEM test, while the other half were broken in the electromagnetic for crusher about 2 min (below 74 μm), and were used for XRD analysis. The microstructure of the glass-ceramics was obtained via SEM (JSM-5310, JEOL) at an accelerating voltage of 15 kV. The samples were polished via SiC powder (2000 mesh) and chemically etched for 1 min in 5 mass% HF (0.5 mol/l). The other samples with parts that contained holes were horizontally cut off to test the compressive strength. The compression strength (plate-to-plate) was recorded with a Zwick Benchtop tensile/compression tester (Ulm, Germany) at a crosshead speed of 0.5 mm/min.

Results and Discussion

Macro Structure

The macro structures of samples with different crystallization temperatures were shown in Fig. 8. According to Fig. 8, the pores of all samples were in the upper part besides the sample with a crystallization temperature of 915 °C. The size of the pores in the samples were decreased with increasing crystallization temperature. The heat transfer schematic diagram in the crucible was shown in Fig. 9. The heat was focused on the slag surface, and then moved from the surface of the BF slag to the inside of the BF slag. Finally the heat radiation was transferred from the bottom

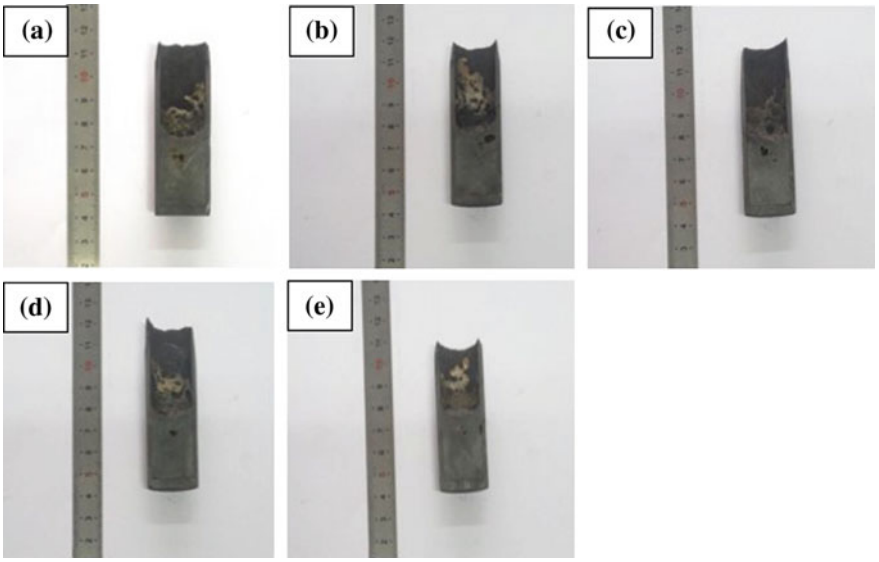

Fig. 8 Macro structures of samples with different crystallization temperatures: **a** 850 °C; **b** 915 °C; **c** 1015 °C; **d** 1115 °C; **e** 1215 °C

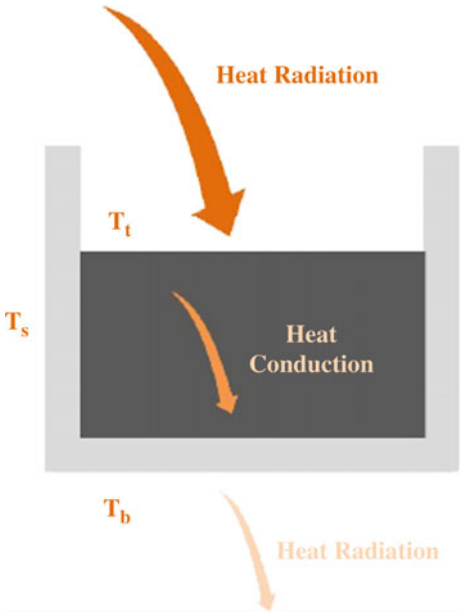

Fig. 9 Schematic diagram of heat transfer in slag sample

of the crucible. Liu et al. reported that the bottom temperature of the crucible was 71.3 K lower than the surface temperature of the slag, and the temperature of the crucible wall was lower [13]. During the continuous cooling process, the melt in the

crucible had a sufficient time for heat transfer in the crucible. The heat dissipation direction of the melt moved from introversion to outside through the wall of the crucible, leading to a decrease of temperature of the bottom and outer walls of the crucible. Therefore, the bottom and outer walls of the crucible priority solidified during the cooling process. The higher the crystal temperature, the lower the degree of supercooling was, the difference between the inside and the outside temperature and the viscosity were small and the inner and outer shrinkage was more consistent when the slag changed from the liquid phase to the solid phase, resulting in smaller pores.

Crystalline Phase

The XRD patterns of samples with different crystallization temperature are shown in Fig. 10. According to Fig. 8, the main phases of samples with different crystallization temperature were perovskite, diopside-alunimian and gehlenite. In general, a stronger peak results in greater crystallinity, while a weaker peak with greater width results in thinner grain [14]. The intensity and crystallinity of the diffraction peak had a specific relationship; however, this was not the only factor that determines the crystallinity. The lower base of the graph and higher intensity of the

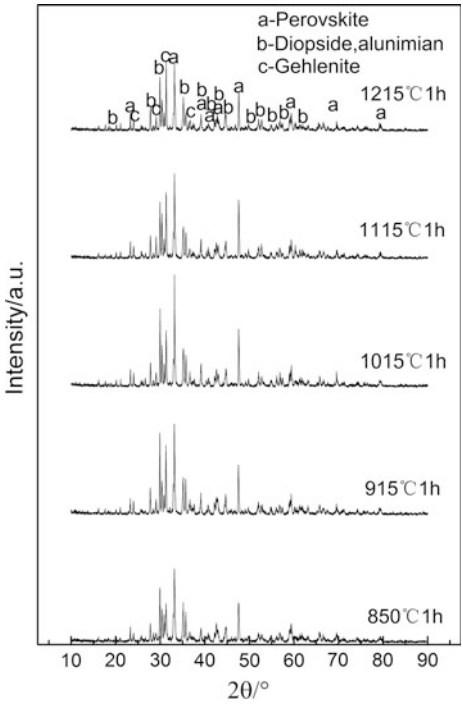

Fig. 10 XRD patterns of samples with different crystallization temperature

diffraction peak result in sharper diffraction peak and the better crystal quality. The test method was usually determined by the ratio between the area of the crystal peak and the total area; however, this was only a relative value.

According to Fig. 10, we knew all the peak types were sharp and the intensity of the peaks varied with temperature. A previous theory suggested that the crystal content (perovskite > diopside > gehlenite with a larger difference) was the least for a crystallization temperature of 850 °C, the crystal content (perovskite > diopside > gehlenite with a smaller difference) was the second largest but the relative content of diopside was the most for a crystallization temperature of 915 °C, the crystal content (perovskite > diopside > gehlenite with a larger difference) was the third largest but the relative content of perovskite was the most for a crystallization temperature of 1015 °C, the crystal content (perovskite > gehlenite > diopside with a small difference) was the fourth largest for a crystallization temperature of 1115 °C, the crystal content (gehlenite > perovskite > diopside with a small difference) was even smaller but the relative content of gehlenite was largest for a crystallization temperature of 1115 °C.

Microstructural Analysis

The SEM micrographs of relevant glass–ceramic microstructures are shown in Fig. 11. The EDS of the bright white area are shown in Fig. 12. Fig. 12 shows that the bright white area was perovskite. As a result, the dendrites observed were

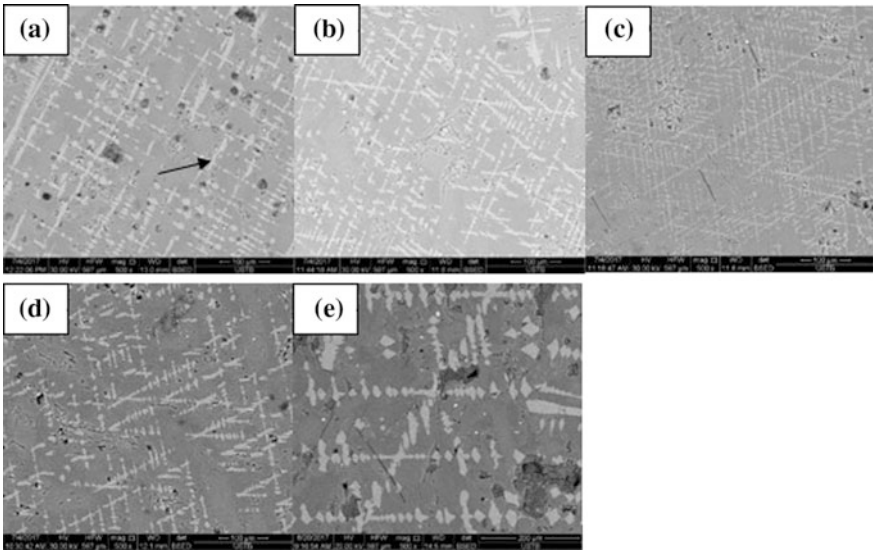

Fig. 11 The microstructure of samples with different crystallization temperatures at 500X magnification: **a** 850 °C; **b** 915 °C; **c** 1015 °C; **d** 1115 °C; **e** 1215 °C

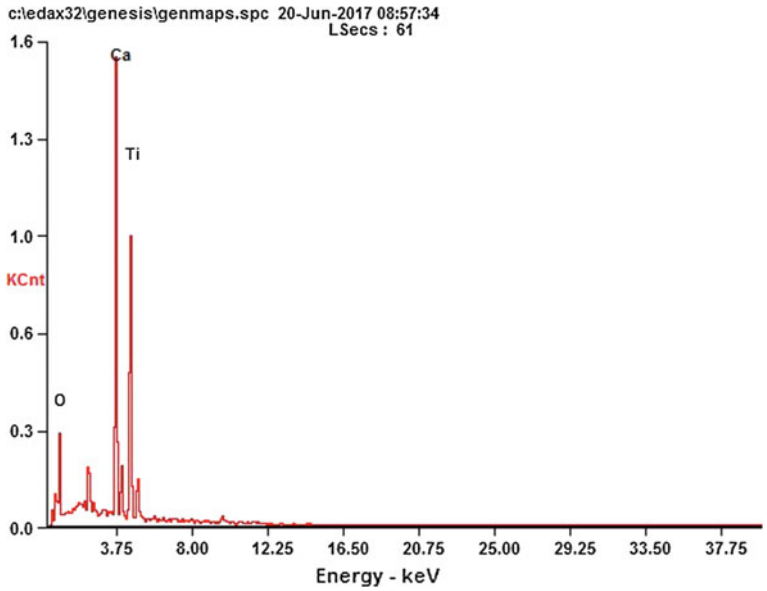

Fig. 12 EDS of bright white area

perovskite, while gehlenite and diopside were not observed probably because they had no clear specific crystal morphology within observable experimental temperature or because their size was too small to be detected.

According to Fig. 11, the grain size was decreased and then increased with decreasing crystallization temperature. The grain size reached a maximum at 1215 °C and a minimum at 1015 °C. Although the slag structure was complex, the solidification process of the perovskite still followed the theory of crystal precipitation [15]. The CaO - SiO_2 - TiO_2 - Al_2O_3 - MgO quinary system slag was formed via single ion (Ca^{2+}, Mg^{2+}, O^{2-}, Ti^{2+}, Ti^{3+}) and composite anion (SiO_4^{4-}, AlO_2^{1-}, TiO_3^{2-}) [16]. The perovskite phase consisted of Ca^{2+} and TiO_3^{2-}. The dendrite array grew toward the same direction where the primary dendrite trunks were parallel to each other. The secondary dendrite arms grew in the perpendicular direction with the primary truck and stopped growing when they encountered with each other. The concentration of Ca^{2+} and TiO_3^{2-} in the surrounding dendrites was lower as perovskite with high melting temperature precipitated. At high temperature, the viscosity was low and the resistance of the ion movement was small. Therefore, the size of perovskite particles was largest at 1215 °C. The viscosity increased with decreasing crystallization temperature, the resistance of ion movement enlarged, resulting in smaller and smaller grains until 1015 °C. When the crystallization temperature continued to decrease, the degree of supercooling became greater, the driving force of crystallization became greater. This also gave more time for the precipitation of perovskite. As a result, the crystals were getting bigger.

The crystal content was defined as the ratio between the crystal region and the whole field of vision. Therefore, the content of perovskite was maximal at 1015 °C, which was consistent with the results of the XRD analysis. The sample at 915 °C had almost no micro holes. The micro holes of the sample of 1215 °C treatment was larger while the micro holes of sample of 850 °C treatment were more numerous.

Mechanical Properties

Compressive strength was an important mechanical property of microcrystalline glass-ceramic especially in the application of building materials and decorative materials. The compression strength of samples is shown in Fig. 13. Fig. 13 shows that the compressive strength of all specimens were above 100 MPa, which met the requirements of natural stone (granite $\geq$ 100 MPa and marble $\geq$ 50 MPa). The compression strength of the 915 °C temperature sample was maximal while the compression strength of the 1215 °C temperature sample was minimal. The compression strength of 850 °C temperature sample was slightly larger than that of the 1215 °C temperature sample.

The compressive strength depended on both the amount and size of the crystal and the number of micro voids. In general, the more the crystal content was, the smaller and more homogeneous the grain size was, and the better the sample performance followed: In general, the priority order of good performance of minerals was diopside > perovskite > gehlenite. Furthermore, the better the density was, the less the hole was, the better the performance was. In the condition of 915 °C, and the highest proportion of diopside, the small and homogeneous distribution of the perovskite particles and the good density with few micro holes, the compressive strength was maximal. The compressive strength of sample of 1215 °C condition was minimal due to the highest proportion of gehlenite, the big perovskite particles

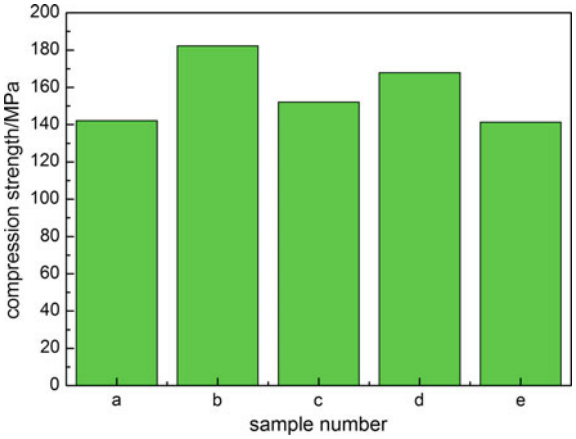

Fig. 13 Compression strength of samples **a** 850 °C; **b** 915 °C; **c** 1015 °C; **d** 1115 °C; **e** 1215 °C

and the poor density with larger micro holes. Since the sample in the condition of 850 °C had the least crystal content and poor density with many micro holes, the compressive strength was similar to that of the 1215 °C temperature sample.

These datas of the mechanical properties supplied the lower half of the samples, without considering the influence of macro holes. However, if the holes were considered, the samples with higher temperature heat treatment would have higher strength, while the mechanical performance of the large cavity will be much lower. Therefore, the best crystallization temperature was 1215 °C comprehensively considering the factors of compressive strength and holes.

Conclusion

In this paper, studies on converting titanium-bearing BF slag directly into glass ceramics have been conducted. Glass-ceramic prepared via titanium-bearing BF slag using the "Petrurgic" method is feasible. By this method, slag and its waste heat could be simultaneously reused with simpler process, lower cost, fewer environmental pollutions and higher economic benefits than those by the traditional method. From this research, the following main conclusions could be simultaneously:

(1) The size of pores defects in the samples simultaneously crystallization temperature, which was mainly caused by rapider solidification speed of outside liquid slag than that of inside liquid slag due to temperature difference between the inside and the outside temperature of the slag in crucible when it was undergoing a rapid cooling process.
(2) All glass-ceramic samples contained main crystals of perovskite, diopside, and gehlenite. Grain size of perovskite crystals firstly decreased and then increased as the crystallization temperature decreased, and reached a maximum at 1215 °C and reached a minimum at 1015 °C.
(3) The compressive strength of all specimens were above 100 MPa, which met the requirements of Chinese national standard for natural stone (granite and marble).

Acknowledgements The authors gratefully acknowledge the financial support of the National Key Research and Development Program of China (No. 2016YFB0601304).

References

1. Steel Statistical Yearbook 2015 (2015) World steel Committee on Economic Studies: Brussels, Belgium
2. Zhao L, Li Y, Zhang L et al (2017) Effects of CaO and Fe_2O_3 on the microstructure and mechanical properties of SiO_2-CaO-MgO-Fe_2O_3 ceramics from steel slag. ISIJ Int 57(1):15–22
3. Roberts JP (1979) Glass-ceramics, 2nd edn. "Non-Metallic Solids". Academic Press Inc. (London) Ltd., London

4. Holland W, Beall G (2002) Glass-ceramic technology. The American Ceramic Society, Westerville, OH
5. Strnad Z (1986) Glass-ceramic materials. Elsevier, Amsterdam
6. Pannhorst W (1997) J "Non-Cryst" Solids 219:198
7. Moisescu C, Jana C, Habelitz S, Carl G, Rüssel (1999) J Non-Cryst Solids 248:176
8. Atkinson DI, McMillan PW (1977) J Mater Sci 10; J Mater Sci:11 (1976):989; ibid 12 (1977):443
9. Yue Y, Keding R, Rüssel C (1999) J Mater Res 14:3983
10. Rawlings RD (1997) Glass-ceramic materials. Fundamentals and applications. In: Manfredini T, Pellacani GC, Rincon JM (eds) Mucchi Editore, Modena, Italy, p 115
11. Romero M, Rincón JM (1999) J Am Ceram Soc 82:1313
12. Francis AA, Rawlings RD, Boccaccini AR (2002) J Mater Sci Lett 21:975
13. Liu L, Hu M, Xu Y (2015) Structure, growth process, and growth mechanism of Perovskite in high-titanium-bearing blast furnace slag. Metallurg Mater Trans B 46B:1751–1758
14. Zhao W, Feng Y, Li J (2015) The main content of phases and elements in mineral products determined with X-ray diffraction method. Phys Test Chem Anal 51(4):523–526
15. Flemings MC (1974) Solidification processing. Mc-Graw-Hill Book Company, New York, p 152
16. Gu HX (1981) Principles of steel metallurgy. Metallurgical Industry Press, Beijing, p 78

Recovery of Copper from Nickel Laterite Leach Waste by Chemical Reduction Using Sodium Dithionite

A. B. Botelho Junior, I. A. Anes, M. A. Carvalho, D. C. R. Espinosa and J. A. S. Tenório

Abstract Recovery of metals from reserves with low grade and from waste with high presence of contamination is a challenge to be overcome. Metals like nickel, cobalt and copper could be recovery from nickel laterite leach waste by many different processes. Among recovery processes that could be applied are ion exchange, solvent extraction and precipitation. The aim of this work was recover copper from liquor of nickel laterite by precipitation using chemical reduction. Copper concentration in liquor was 146 mg L^{-1} and reducing agent used was sodium dithionite 1 mol L^{-1}. Influence of stirring speed was studied between 0–200 rpm. Results indicated a selective precipitation of copper on solution with others metals at 240 mV. The analyzes were conducted in SEM, energy-dispersive X-ray spectroscopy and XRD, that indicated presence of copper and sulfur.

Keywords Precipitation · Reducing process · Mining · Low grade ore

Introduction

There are two principal nickel ore types: sulfides and laterites. Laterites ores represent 72% of resources, but only 42% of primary nickel production. This occurs mainly because the difficulty of processing laterite ores compared to sulfides, that requires extensive and complex treatment, making it more expansive [1, 2]. Technologies has been developed in order to make the processing from laterite ores

The original version of this chapter was revised: Misspelt co-author name has been corrected. The erratum to this chapter is available at https://doi.org/10.1007/978-3-319-72362-4_57

A. B. Botelho Junior · M. A. Carvalho · D. C. R. Espinosa · J. A. S.Tenório (✉)
Chemical Engineering Department, Polythecnic School of University of Sao Paulo, Sao Paulo, Brazil
e-mail: tenorio@usp.br

I. A. Anes
Chemical Engineering, College of Chemistry of Faculdades Oswaldo Cruz, Sao Paulo, Brazil

Z. Sun et al. (eds.), *Energy Technology 2018*, The Minerals, Metals & Materials Series, https://doi.org/10.1007/978-3-319-72362-4_38

economically feasible. Among these technologies are high pressure acid leaching (HPAL) and atmospheric acid leaching (AL) using sulphuric acid as leaching agent [3, 4]. Besides nickel extraction, cobalt and copper could be also present in mineral and in solution obtained by leaching process [5–7].

In order to recover these metals from liquor generate in leaching step, there are ion exchange [8, 9], solvent extraction [10, 11] and precipitation [7, 12]. The problem of precipitation process is that, if use hydroxides to precipitate iron present in liquor at high concentration, it will precipitate with others metals like cobalt and copper, and further purification steps will be required [7]. Precipitation by reducing potential may be a solution to recover metals selectively.

Sodium dithionite is used to recover copper from solutions by reducing process. Chou et al. [13, 14] studied recovery process by chemical reduction using sodium dithionite on wastewater containing copper contaminated with ligands composts. Sodium dithionite could be applied as reducing agent in nickel laterite liquor, in order to reduce Fe(III) to Fe(II) [15].

The goal of this work was recovery copper from synthetic solution of nickel laterite, to simulate conditions of liquor obtained from leaching step using sulphuric acid. Influence of stirring speed was verified: 0, 45, 90, 150 and 200 rpm. Precipitate obtained by reducing process was analyzed at scanning electron microscope (SEM), energy-dispersive X-ray spectroscopy (EDX) and X-ray diffraction (XRD).

Materials and Methods

Sodium dithionite solution 1 mol L^{-1} was used in order to reduce potential of solution until 240 mV. Synthetic solution had follow composition: Al (4101 mg L^{-1}), Co (78 mg L^{-1}), Cu (147 mg L^{-1}), Cr (195 mg L^{-1}), Fe (18713 mg L^{-1}), Mg (7774 mg L^{-1}), Mn (387 mg L^{-1}), Ni (2434 mg L^{-1}) and Zn (37 mg L^{-1}). The synthetic solution was prepared in order to simulate real conditions of leach solution of nickel laterite waste. The pH was adjusted at 0.5 using sulphuric acid concentrated P.A. Experiments were realized at 25 °C during 120 min.

Potential was measured at t = 0 and at t = 120 min using an electrode Ag/AgCl (3 mol L^{-1}). Synthetic solution with reducing agent was analyzed at different stirring speeds: 0, 45, 90, 150 and 200 rpm. Metals concentration was analyzed at Energy-dispersive X-ray spectroscopy (EDX), and precipitate was analyzed at scanning electron microscope (SEM/EDS) and X-ray Diffraction (XRD).

Results and Discussion

Figure 1 presents percentage of copper removal by precipitation process using sodium dithionite as reducing agent for each stirring speed. Experiment realized without stirring speed (0 rpm), 94 ± 5% of copper present in solution precipitate.

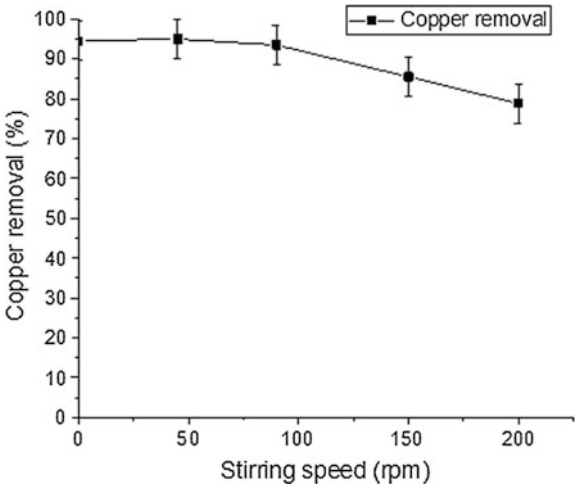

Fig. 1 Percentage of copper removal varying stirring speed

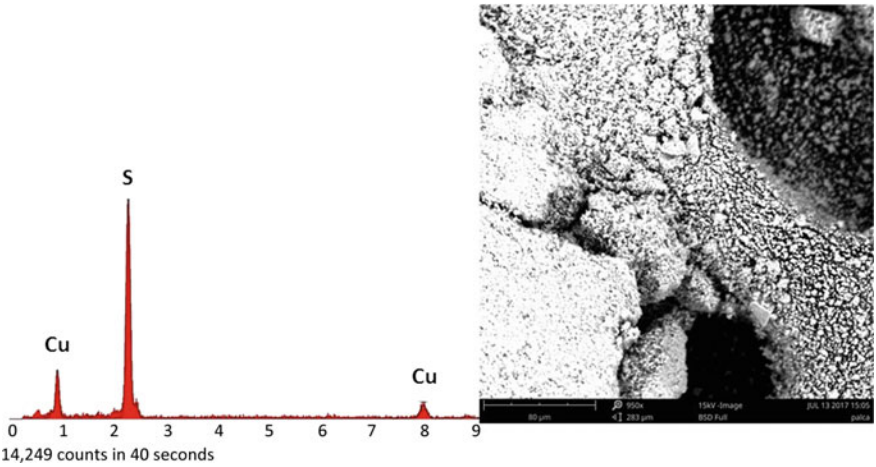

Fig. 2 EDS analyses and SEM of dried precipitate obtained after reducing process at pH 0.5 and 25 °C

This percentage of removal was observed also on 45 and 90 rpm. However, a different percent was observed on 150 and 200 rpm, that 85% ± 5% and 78% ± 5% of copper was removed, respectively. These results indicate that reducing process has efficiency decreased, while stirring speed increase.

When percentage of copper removal is compared with potential of solution after 120 min of time reaction, it was verified that potential at t = 0 increase while stirring speed increase, possibly due to solution aeration during experiment, in

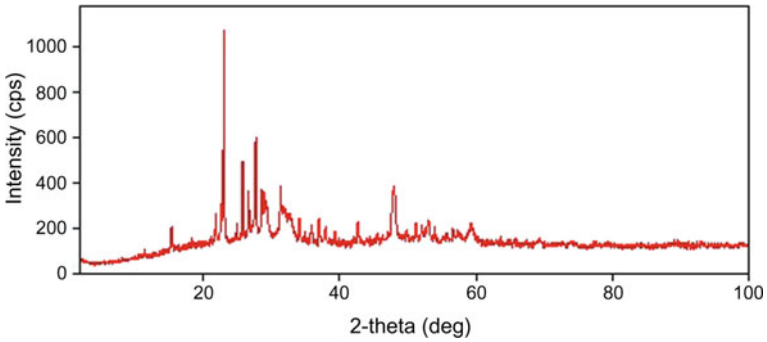

Fig. 3 XRD of dried precipitate obtained after reducing process at pH 0.5

Table 1 Composts obtained on precipitation by reducing process determined using XDR

	Formula	%
Chalcocite	Cu_2S	29
Djurleite	$Cu_{31}S_{16}$	48
Sulfur	S_8	23
Total		100
Cu_xS_y	77%	

which oxygen from air could have behave as oxidant agent in solution. On 45 rpm, potential at t = 120 was 410 mV, while on 150 rpm was 440 mV, that it has been enough to oxidize copper again to solution as Cu(II).

Precipitate obtained was analyzed in XRD and SEM/EDS. Figure 2 present result of EDS analyses and SEM of dried precipitate, that was verify presence of only copper and sulfur. Using XRD analyses (Fig. 3), it was determined that the precipitate's composition was 77 ± 5% Cu_xS_y.

Table 1 present composts of precipitate. Chalcocite and Djurleite are two copper sulfides obtained by process, that represent 77 ± 5% of solid. Sulfur, that represent 23 ± 5% of solid, could be form due to high quantity of sulphate present in solid in which the conditions of experiment was realized sulfur could precipitate, but also due to sodium dithionite decomposition [16].

Conclusion

Precipitation by reducing process demonstrated be efficient to separate selectively copper from liquor with presence of many metals different. Synthetic solution was prepared to simulate real conditions of real leach solution of nickel laterite waste. Results shows that working with potential, it is possible precipitate only one metal, where MEV/EDS analyses detected only copper and sulphur at precipitate obtained,

indicating a selective precipitation. This precipitate could be dissolved easily for any applications. The problem with other methods of metals separation by precipitation is co-precipitation, that will be necessary more steps of purification. By reducing process, it will be not necessary.

Acknowledgements To the São Paulo Research Foundation (Fundação de Amparo à Pesquisa do Estado de São Paulo—FAPESP), No 2016/05527-5 and 2012/51871-9, for the financial support.

References

1. Mudd GM (2010) Global trends and environmental issues in nickel mining: sulfides versus laterites. Ore Geol Rev 38:9–26. https://doi.org/10.1016/j.oregeorev.2010.05.003
2. Oxley A, Barcza N (2013) Hydro-pyro integration in the processing of nickel laterites. Miner Eng 54:2–13. https://doi.org/10.1016/j.mineng.2013.02.012
3. McDonald RG, Whittington BI (2008) Atmospheric acid leaching of nickel laterites review Part I Sulphuric acid technologies. Hydrometallurgy 91:56–69. https://doi.org/10.1016/j.hydromet.2007.11.010
4. Quast K, Connor JN, Skinner W, Robinson DJ, Li J, Addai-Mensah J (2014) Preconcentration strategies in the processing of nickel laterite ores Part 1: Literature review. Miner Eng 79:261–268. https://doi.org/10.1016/j.mineng.2015.03.016
5. Aliprandini P (2017) O uso da extração por solventes para tratamento de licor de lixiviação de minério limonítico de níquel, Universidade de São Paulo
6. Crundwell FK, Moats MS, Ramachandran V, Robinson TG, Davenport WG (2011) Extractive metallurgy of nickel, cobalt and platinum-group metals
7. Jiménez Correa MM, Aliprandini P, Tenório JAS, Espinosa DCR (2016) Precipitation of metals from liquor obtained in nickel mining, rewas. Towar Mater Resour Sustain 2016:333–338. https://doi.org/10.1007/978-3-319-48768-7_52
8. Jimenez Correa MM, Aliprandini P, Silvas FP, Abreu DO, Rosario CG, Tenorio JA, Espinosa DCR (2016) Adsorption of Nickel and Cobalt in the acid chelating resin amberlite Irc 748, In Proceedings of Fifth International Conference Industrial Hazard CRETE 2016, Waste Manag. Chania, 2016, p 8
9. Mendes FD, Martins AH (2005) Recovery of nickel and cobalt from acid leach pulp by ion exchange using chelating resin. Miner Eng 18:945–954. https://doi.org/10.1016/j.mineng.2004.12.009
10. Cheng CY, Urbani MD, Davies MG, Pranolo Y, Zhu Z (2015) Recovery of nickel and cobalt from leach solutions of nickel laterites using a synergistic system consisting of Versatic 10 and Acorga CLX 50. Miner Eng 77:17–24. https://doi.org/10.1016/j.mineng.2015.01.015
11. Hutton-Ashkenny M, Ibana D, Barnard KR (2015) Reagent selection for recovery of nickel and cobalt from nitric acid nickel laterite leach solutions by solvent extraction. Miner Eng 77:42–51. https://doi.org/10.1016/j.mineng.2015.02.010
12. Chang Y, Zhai X, Li B, Fu Y (2010) Removal of iron from acidic leach liquor of lateritic nickel ore by goethite precipitate. Hydrometallurgy 101:84–87. https://doi.org/10.1016/j.hydromet.2009.11.014
13. Chou Y-H, Yu J-H, Liang Y-M, Wang P-J, Li C-W, Chen S-S (2015) Recovery of Cu(II) by chemical reduction using sodium dithionite. Chemosphere 141:183–188. https://doi.org/10.1016/j.chemosphere.2015.07.016
14. Chou YH, Yu JH, Liang YM, Wang PJ, Li CW, Chen SS (2015) Recovery of Cu(II) by chemical reduction using sodium dithionite: Effect of pH and Ligands. Water Sci Technol 141:183–188. https://doi.org/10.1016/j.chemosphere.2015.07.016

15. Botelho Junior AB, Jiménez Correa MM, Espinosa DCR, Tenório JAS (2017) Chemical reduction of Fe(III) in nickel lateritic wastewater to recover metals by ion exchange. In Energy Technology 2017. Springer, Chalm, pp 467–472. doi:https://doi.org/10.1007/978-3-319-52192-3_45
16. Geoffroy N, Demopoulos GP (2009) Reductive precipitation of elemental selenium from selenious acidic solutions using sodium dithionite. Ind Eng Chem Res 48:10240–10246. https://doi.org/10.1021/ie9008502

Recovery of Nickel and Cobalt from a Waste Zone of Nickel Laterite Ore Using a Mixture of Extractants in Solvent Extraction Technique

Paula Aliprandini, Mónica M. Jiménez Correa, Jorge A. Soares Tenório and Denise Crocce Romano Espinosa

Abstract The surface zone of nickel laterite ore is generally considered as residue. However, because of the depletion of ore sources and the increase in demand, this previously discarded zone may now be processed economically for nickel and cobalt. After leaching and removal of the impurities, the solution contains cobalt, magnesium, manganese and nickel. Solvent extraction is a hydrometallurgical technique used in the separation of metals from aqueous solutions. Cyanex 272 and D2EHPA are extractants used to separate nickel from cobalt. The mixture of extractants can change the performance during the metals extraction. This work aims to evaluate the solvent extraction of nickel and cobalt when Cyanex 272 and D2EHPA are mixed. The results showed that the increased concentration of D2EHPA in the organic phase increased the extraction of nickel and magnesium. However, cobalt extraction was reduced and the manganese extraction was not altered.

Keywords Cobalt separation · Nickel separation · Cyanex 272 D2EPA · Hydrometallurgy

Introduction

Lateritic nickel ore is the major source of nickel. Approximately 60% of the world's nickel resources are found in laterites deposits [1]. The ore is divided into zones. The superficial zone is known as limonite, followed by saprolite zone [2]. Due to the different compositions, each zone is processed by a method.

Saprolite is the nickel-rich zone in the laterite ore [3]. For this reason, the zone is used to recover nickel. The high nickel concentration is usually linked to high

P. Aliprandini (✉) · M. M. Jiménez Correa · J. A. Soares Tenório · D. C. R. Espinosa
Chemical Engineering Department, Polytechnic School, University of São Paulo, R. Do Lago, 250, 05338-110 São Paulo, SP, Brazil
e-mail: paulaaliprandini@usp.br

Z. Sun et al. (eds.), *Energy Technology 2018*, The Minerals, Metals & Materials Series, https://doi.org/10.1007/978-3-319-72362-4_39

magnesium concentration [4]. Because of this, saprolite tend to be treated by pyrometallurgical process [5].

On the other hand, limonite is considered a low-grade resource of nickel. The limonite zone contains between 1 and 1.8% nickel [6]. In addition, this zone is a complex and heterogeneous mixture of metals [2, 7–10]. Other metals, such as iron and aluminum, make up more than 40% of the ore and are considered impurities [11, 12]. The low nickel concentration made the zone economically unviable and therefore, used to be discarded. However, as grades drop across the world because of the depletion of resources, limonite processing may become economical [13]. Besides nickel, cobalt can also be recovered from the limonite. Recovery of both metals is of great commercial interest [4].

Because of high iron concentration, the pyrometallurgical processes make metals recovery economical unattractive [5]. For this, hydrometallurgical techniques are used to treat limonite ore. Sulfuric acid is the most commonly used leaching agent. After leaching, several methods for metal separation and recovery are applied [2, 7]. The impurities are removed from leaching solution by precipitation processes before nickel and cobalt recovery [14].

Solvent extraction technique is applied to the metals recovery, including separation of nickel and cobalt [15–19]. This technique uses two immiscible solutions. One phase is aqueous from a leaching process which contains dissolved metals. The other phase is an organic solvent, which is composed of extractants and diluent [8, 17, 18, 20–22]. The extractants are capable of selectively extract metals from an aqueous phase. The diluent makes the organic phase easier to handle, without affecting the extraction process [8, 22]. The target metal ions are transferred from the aqueous phase to the organic phase when the phases are mixed. After extraction the aqueous phase is called the raffinate, while the organic phase is known as the loaded organic [8, 18, 21, 23].

Cyanex 272 is a commercial extractant. The active component is bis-(2, 4, 4-trimethylpentyl) phosphinic acid (Fig. 1). Cyanex 272 can be used to separate nickel and cobalt [2, 24, 25].

D2EHPA is another commercial extractant. D2EHPA is an acid extractant and the active component is the di-(2-ethylhexyl) phosphoric acid. Its structure is shown in Fig. 2 [25, 26].

According to Flet [25], the selectivity order for metals extraction with Cyanex 272 and D2EHPA follows the sequence:

$$\text{Cyanex 272}: \quad Fe^{+3} > Zn > Cu > Co > Mg > Ca > Ni$$

$$\text{D2EHPA}: \quad Fe^{+3} > Zn > Ca > Cu > Mg > Co > Ni$$

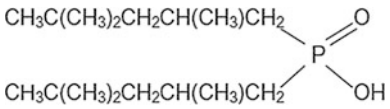

Fig. 1 Commercial extractant Cyanex 272 (bis (2, 4, 4-trimethylpentyl) phosphinic acid)

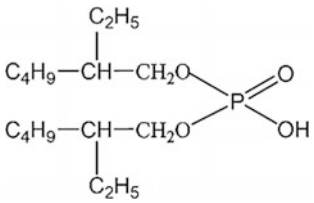

Fig. 2 The structure of D2EHPA (Di-(2-ethylhexyl) phosphoric acid)

It could be observed that both extractants can be used to separate cobalt from nickel. In addition, it is possible to extract magnesium before extract nickel.

This paper aims to study the solvent extraction behavior of cobalt, magnesium, manganese and nickel using a mixture of Cyanex 272 and D2EHPA in the organic phase. In theory, the metals extraction will increase with the mixture of extractants classified as acid [22, 27].

The mixture of Cyanex 272 and D2EHPA was studied for the separation of some metals. For Ahmadipour et al. [28] the mixture of the extractants increased the separation factor between zinc and manganese. At pH 5 with 15% Cyanex 272 and 5% D2EHPA in the organic phase compared to only one extractant.

For Darvishi et al. [29] the separation of cobalt and nickel during the solvent extraction was increased for a mixture of Cyanex 272 and D2EHPA at a concentration ratio 1/1, compared to only D2EHPA.

It is expected that the mixture of extractant can improve the separation of metals. For limonite ore, the separation of cobalt and nickel is focused on the beneficiation.

Experimental

For the study, a synthetic solution was prepared. The metals concentrations used are shown in Table 1. Analytical grade metal sulfates were dissolved in deionized water.

The synthetic solution was based on the leaching from limonite zone. Impurities such as iron, aluminum and zinc were previously considered to be removed from the leaching solution. Therefore, the metals remaining in the solution were cobalt, magnesium, manganese and nickel. The pH of the aqueous solution was adjusted to 5 using 1 M NaOH. The value of pH was chosen based on a previous study [30].

The organic phase was prepared using two extractants: Cyanex 272 and D2EHPA. They were mixed and the following relationships were used, as shown in Table 2. Kerosene was used as diluent.

Table 1 Metals concentrations in synthetic leach solution used for the study of solvent extraction

Metal	Co	Mg	Mn	Ni
Concentration (mg/L)	78	6350	360	2520

Table 2 Composition of the organic systems for different Cyanex 272 to D2EHPA ratios

Organic phases (v/v %)					
Cyanex 272	20	15	10	5	0
D2EHPA	0	5	10	15	20
Kerosene	80	80	80	80	80

Solvent extraction tests were carried out mixing equal volumes of aqueous and organic solutions (40 mL). The experiments were conducted at room temperature (25 ± 2 °C) with stirring for 20 min. The pH was maintained constant at 5 by adding 1 M NaOH. A separatory glass funnel was used to separate the two phases after extraction. The metals concentration in raffinate was determined by Energy-dispersive X-ray spectroscopy (EDX) and the metal concentrations in the loaded phase were calculated by mass balance.

The distribution ratio D (Eq. 1), the percentage of extraction %E (Eq. 2) and the separation factor S (Eq. 3) were calculated as follows [8, 21].

$$D = \frac{[X]_o}{[X]_a} \tag{1}$$

$$S = \frac{D_x}{D_y} \tag{2}$$

$$\%E = \frac{D * 100}{\frac{V_a}{V_o} + D} \tag{3}$$

where:

$[X]_o$ is the concentration of metal X in the organic phase;
$[X]_a$ is the concentration of metal X in the aqueous phase;
D_x is the distribution ratio of metal x;
D_y is the distribution ratio of metal y;
V_a is the volume of aqueous solution;
V_o is the volume of organic solution

Results

Figure 3 shows the percentage of metals extraction from the synthetic leach limonite solution using different organic systems. As can be seen in the figure, manganese extraction was almost achieved in all the performed experiments. In other words, Mn was not affected by changing the composition of the organic solution. The cobalt extraction decreased from 90 to 74% with increasing D2EHPA concentration in the organic phase. The extraction behavior of nickel and

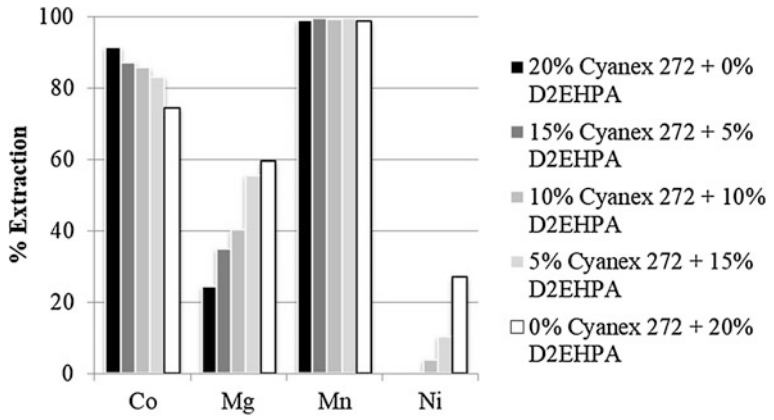

Fig. 3 Percentage of metals extracted from the synthetic leach solution with mixture of Cyanex 272 and D2EHPA in organic phase

magnesium changed when different organic phase composition were used. For both metals, increasing the concentration of D2EHPA, increased the metals extraction. Magnesium and nickel extraction were 59% and 27%, respectively, when organic phase composition was 0% Cyanex 272 and 20% D2EHPA.

Cyanex 272 confirmed the selectivity theory for cobalt over nickel.

The distribution ratio D is a comparative value. It is a measure of their extraction into the organic phase for each composition of the organic system. The higher the value of D means the greater tendency to transfer ions from the aqueous phase to the organic phase. Table 3 shows the values of D for the metals when the organic phase was changed.

The values of D for manganese showed that the metal had the greatest tendency to extract. However, the values of D for nickel showed the least tendency to extract, especially when the organic phase was formed only by Cyanex. For cobalt, the tendency to be extracted decreased with increasing of D2EHPA concentration. Magnesium showed the opposite behavior.

The separation factor S represents the process selectivity for separating one ion from another. Table 4 shows the S between cobalt and the other metals.

Table 3 Distribution ratio of metals after solvent extraction with different organic systems

Organic phase	D_{Co}	D_{Mg}	D_{Mn}	D_{Ni}
20% Cyanex 272 0% D2EHPA	12.31	0.37	134.45	0
15% Cyanex 272 5% D2EHPA	8.22	0.65	292.65	0
10% Cyanex 272 10% D2EHPA	7.65	0.87	208.82	0.05
5% Cyanex 272 15% D2EHPA	6.67	1.68	407.95	0.16
0% Cyanex 272 20% D2EHPA	4.01	2.03	105.57	0.51

Table 4 Separation factor between cobalt and the other metals using different organic systems

Organic phase	$S_{Co/Mg}$	$S_{Co/Mn}$	$S_{Co/Ni}$
20% Cyanex 272 0% D2EHPA	33.12	0.09	12309.39
15% Cyanex 272 5% D2EHPA	12.61	0.03	6023.65
10% Cyanex 272 10% D2EHPA	8.82	0.04	153.98
5% Cyanex 272 15% D2EHPA	3.98	0.02	42.84
0% Cyanex 272 20% D2EHPA	1.97	0.04	7.82

Based on Table 4, the best separation occurred between cobalt and nickel for all organic systems, especially when the organic phase was formed by 20% Cyanex 272 and 0% D2EHPA. For nickel and magnesium, better separation from cobalt were achieved with organic solution composed of only Cyanex 272. The worst separation values were between cobalt and manganese, where $S_{Co/Mn}$ values were less than 0.09 for all systems. This means that using Cyanex 272 alone or a combination of this extractant with D2EHPA made it difficult to separate cobalt from manganese.

The results presented showed that the combination of the extractants used in this study had an unfavorable performance during the separation of cobalt and/or nickel from magnesium and manganese impurities in leached limonite. The extraction of magnesium was improved by D2EHPA presence. However, the presence of D2EHPA also increased the nickel extraction. D2EHPA hindered the separation of cobalt and nickel from the impurities from leached limonite.

However, further complementary studies will be required to further develop this application.

Conclusions

The results from this study indicate that:

- Manganese extraction was almost complete in all the performed experiments. This metal was not affected by changing the composition of the organic solution.
- The cobalt extraction decreased from 90 to 74% with increasing D2EHPA concentration in the organic phase.
- Increasing the concentration of D2EHPA, increased the magnesium and nickel extraction. When organic phase composition was 0% Cyanex 272 and 20% D2EHPA, the extractions were 59% and 27%, respectively.
- For nickel and magnesium, better separation from cobalt were achieved with organic solution composed of only Cyanex 272.
- The worst separation values were between cobalt and manganese.
- The combination of the extractants Cyanex 272 and D2EHPA had an unfavorable performance during the separation of cobalt and nickel from magnesium and manganese impurities in leached limonite.

Acknowledgements To the Counsel of Technological and Scientific Development (CNPq), for financial support in the form of a doctorate grant.

To the Coordenação de Aperfeiçoamento de Pessoal de Nível Superior (CAPES) for financial support in the form of a doctorate grant.

To the Fundação de Amparo à Pesquisa do Estado de São Paulo (FAPESP) for financial support through research project 2012/51871-9.

To Ana Carolina Fadel Dalsin, for her technical assistance in the execution of testwork for this project.

References

1. U.S.Geological Survey (2016) Nickel. In: U.S.Geological Survey. Mineral Commodity Summaries 2017, Virginia, pp 114–115. doi:10.3133/70180197
2. Crundwell FK, Moats MS, Ramachandran V, Robinson TG, Davenport WG (2011) Extractive metallurgy of nickel, cobalt and platinum group metals. Elsevier, Oxford
3. Elias M (2002) Nickel laterite deposits—geological overview, resources and exploitation. In: Cooke DR, Pongratz J (ed) Giant ore deposits: characteristics, genesis and exploration; University of Tasmania, Tasmania, pp 205–220
4. Kyle J (2010) Nickel laterite processing technologies—where to next? Paper presented at ALTA 2010 Nickel/Cobalt/Copper Conference, Perth, Western Australia, 24–27 May 2010
5. Liu H, Reynolds GA (2012) Process for atmospheric leaching of laterite ores using hypersaline leach solution. US. Patent 8,268,039 B2. 18 September 2012
6. Neudorf D (2006) Method for nickel and cobalt recovery from laterite ores by reaction with concentrated acid and water leaching. US. Patent 11/166,125. 5 January 2006
7. Georgiou D, Papangelakis VG (1998) Sulphuric acid pressure leaching of a limonitic laterite: chemistry and kinetics. Hydrometallurgy 49(1–2):23–46
8. Gupta CK (2003) Chemical metallurgy principles and practice. Wiley-VCH, Weinheim
9. Kesler SE, Simon AC (2015) Mineral resources, economics and the environment. Cambridge University Press, Cambridge
10. Moskalyk RR, Alfantazi AM (2002) Nickel laterite processing and electrowinning practice. Miner Eng 15:593–605
11. Tang JA, Valix M (2006) Leaching of low grade limonite and nontronite ores by fungi metabolic acids. Miner Eng 19(12):1274–1279
12. Roche EG (2011) Iron Precipitation. US. Patent 12/991,985. 26 May 2011
13. McDonald RG, Whittington BI (2008) Atmospheric acid leaching of nickel laterites review Part I. Surphuric acid technologies. Hydrometallurgy 91(1–4):35–55
14. Büyükakinci E, Topkaya YA (2009) Extraction of nickel from lateritic ores at atmospheric pressure with agitation leaching. Hydrometallurgy 97(1–2):33–38
15. Dalvi AD, Bacon WG, Osborne RC (2004) The Past and the Future of Nickel Laterites. Paper presented at PDAC 2004 International Convention, Toronto, Canada, 7–10 March 2004
16. Flett DS (2004) Cobalt-Nickel separation in hydrometallurgy: a review. Chem Sustain Dev 12:81–91
17. de Morais CA, de Albuquerque RO, Ladeira ACQ (2014) Processos Físicos e Químicos Utilizados na Indústria Mineral. Cad Temáticos Química Nov na Esc 8:9–17
18. Vogel AI (1981) Análise química quantitativa. Editora Mestre Jou, São Paulo
19. Cheng CY, Urbani MD, Davies MG, Pranolo Y, Zhu Z (2015) Recovery of nickel and cobalt from leach solutions of nickel laterites using a synergistic system consisting of Versatic 10 and Acorga CLX 50. Miner Eng 77:17–24
20. Free M (2013) Hydrometallurgy: fundamentals and applications. Wiley, New Jersey

21. Habashi F (1970) Principles of extractive metallurgy –, vol 2. Gordon and Brach Science Publishers, New York
22. Kislik VS (2012) Solvent extraction: classical and novel approaches. Elsevier, Oxford
23. Ritcey GM, Ashbrook AW (1984) Solvent Extraction: principles and applications to process metallurgy –, vol 1. Elsevier, Oxford
24. Cytec (2008) CYANEX 272 Extractant. Cytec Industries Inc. http://www.cytec.com/sites/default/files/datasheets/CYANEX 272 Brochure.pdf. Accessed 21 February 2016
25. Flett DS (2005) Solvent extraction in hydrometallurgy: the role of organophosphorus extractants. J Organomet Chem 690(10):2426–2438
26. Zhang Y, Zhang T, Lv G, Zhang G, Liu Y, Zhang W (2016) Synergistic extraction of vanadium(IV) in sulfuric acid media using a mixture of D2EHPA and EHEHPA. Hydrometallurgy 166:87–93
27. Bart H-J, Stevens GW (2002) Reactive Solvent Extraction. In: Marcus Y, SenGupta AK, Marinsky JA (eds) Ion exchange and solvent extraction: a series of advances. Marcel Dekker, New York, pp 37–83
28. Ahmadipour M, Rashchi F, Ghafarizadeh B, Mostoufi N (2011) Synergistic effect of D2EHPA and Cyanex 272 on separation of Zinc and Manganese by solvent extraction. Sep Sci Technol 46:2305–2312
29. Darvishi D, Haghshenas DF, Keshavarz Alamdari E, Sadrnezhaad SK, Halali M (2005) Synergistic effect of Cyanex 272 and Cyanex 302 on separation of cobalt and nickel by D2EHPA. Hydrometallurgy 77:227–238
30. Aliprandini P (2017) O uso da extração por solventes para tratamento de licor de lixiviação de minério limonítico de níquel. Master's thesis, University of São Paulo

Mechanical Behavior of White Ordinary Portland Cement Paste with Iron Oxide Powders Containing Arsenic

Manuela Castañeda and Henry A. Colorado

Abstract This paper is about the use and stabilization of iron oxide based powders with arsenic contents coming from the purification of water. Cement paste samples with 0.0, 2.5, 10 and 20wt% of waste were fabricated by mixing mechanically all components. There are two main positive impacts of using this waste, first, this waste is produced in large amounts worldwide, and therefore the stabilization has a significant impact for the environment. Second, the waste can be used as an admixture and filler for cement, and therefore reduce the amount of cement in the concrete, which has a major impact in the CO_2 footprint since cement industry produces a lot of this gas. Compressive strength and density tests were tested after 28 days. Microstructure was analyzed with scanning electron microscopy and x-ray diffraction. Results show that compressive strengths greater than 20 MPa were obtained and the samples had calcite, portlandite and ettringite phases.

Keywords Arsenic · Water purification · Environmental · Cement

Introduction

Many countries experience an enormous issue with arsenic contaminating water sources, such as Bangladesh where it is a public health emergency [1] considered the largest poisoning of a population in history, and in many other nations worldwide [2, 3].

M. Castañeda · H. A. Colorado
CCComposites Laboratory, Universidad de Antioquia UdeA,
Calle 70 No. 52–21, Medellin, Colombia

H. A. Colorado (✉)
Facultad de Ingenieria, Universidad de Antioquia, Bloque 20,
Calle 67 No. 53–108, Medellin, Colombia
e-mail: henry.colorado@udea.edu.co

Z. Sun et al. (eds.), *Energy Technology 2018*, The Minerals, Metals & Materials Series, https://doi.org/10.1007/978-3-319-72362-4_40

Drinking water with arsenic for a long-term in can cause cancer in the skin, lungs, bladder and kidney. Arsenic has been associated with non-carcinogenic effects such as diabetes, peripheral neuropathy, and cardiovascular diseases as well [4].

Some countries like USA and Canada have understood clearly the risks and force the regulations to decrease the maximum allowable level from 50 to 10 μg/L [5]. On the contrary, some developing countries have a lack in the regulation or even no law of using arsenic in products such as pesticides and other massive consume products potentially affected with arsenic contamination [6].

Several techniques have been developed in order to remove arsenic (such as As (III) and As(IV)) from water or remediate a process with high arsenic contents: arsenic removal by oxidation techniques, by phytoremedation, by coagulation-flocculation, by electrocoagulation, adsorption, ion exchange, electrokinetics, and membranes [7]. Particularly adsorption uses iron based sorbents [8, 9] and can generate significant amount of ceramic powders (iron oxides based) difficult to dispose because its arsenic contents.

This investigation aims to understand the valorization and effective stabilization of iron oxide compounds containing arsenic in white ordinary Portland cement (WOPC) paste, coming from the remediation process of water containing arsenic. Previous research [10] presented the leachability and stabilization of arsenic-bearing iron wastes with cement, so this paper focus in the mechanical behavior in a similar mix.

Therefore, this paper looks for the understanding in the structure-property relation of the cement paste with the mentioned waste in order to be used in structural applications. Thus, compressive strength and density tests were conducted over diverse formulations and analyzed by scanning electron microscopy and x-ray diffraction. Other goal is to conduct investigation in arsenic contamination that can be applied in developing countries such as Colombia, where there are a lack in both the regulation in arsenic in food and agriculture [6, 11] and solutions for processing these type of wastes [12–14].

Experimental

White ordinary Portland cement (WOPC) was used in this research as a binder material for the fabrication of a composite cementitious material stabilizing hazardous waste. This waste is iron oxide containing arsenic. In all cases, water and cement were mixed first, then the waste was added to the mix. Thus, in all samples, water to cement ratio (W/C) was maintained 0.4. Samples with 0.0, 1.0, 2.5, 5.0, 10 and 20wt% of this iron oxide rust with arsenic contents. It was try to add up to 40wt% of waste but no successful samples were obtained, difficult to mix because its lack of water and difficult to handle was well. Samples have been cured in containers close to air contact and released at 28 days. A summary of the powders used in the samples formulations is in Table 1.

Table 1 Sample's composition fabricated in this investigation from WOPC and waste containing arsenic

Sample (wt%)	Waste (wt%)	WOPC (wt%)
0.0	0.0	100
1.0	1.0	99
2.5	2.5	97.5
5.0	5.0	95
10	10	90
20	20	80

Compression tests were conducted in a universal Shimadzu Autograhp machine, at a cross head speed of 1 mm/min, over at set of 6 samples per cement-waste formulation. Sample dimensions were 20 mm diameter and 24 mm height. X-ray diffraction (XRD) characterization was performed in a X'Pert PRO diffractometer with Cu Kα radiation of 1.5406 Å) for all fabricated samples and raw waste, over powdered samples. The XRD scanning was performed with 2θ between 5 and 70°, with a step size 0.02°. A JEOL JSM—6490 Scanning electron microscopy (SEM) was utilized to observe the microstructure of cured cement samples. Density tests were simply measured, over 6 samples, by weighting them and using their measured dimensions for this estimation. For both compressive strength and density the results were reported by the mean and its standard deviation.

Results and Analysis

Samples fabricated for compression and density tests are shown in Fig. 1. All these cylinders were carefully prepared as flat cylinders in order to obtain actual values.

The morphology of the waste powder is shown in Fig. 2 taken in the SEM. The powder is very fine in size, and have a complex shape mostly composed by many agglomerated particles, see Fig. 2a. At high magnification, see Fig. 2b, magnesium

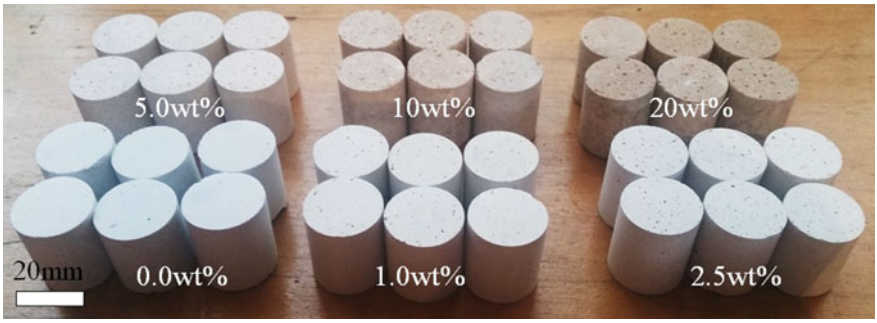

Fig. 1 Samples fabricated in this research with different waste contents for compression and other tests

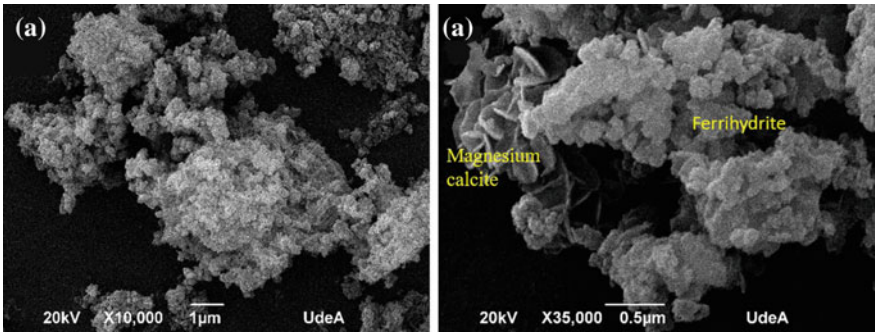

Fig. 2 Raw powder used as admixture for making cementitious samples at two different magnifications, **a** 10000X, **b** 35000X

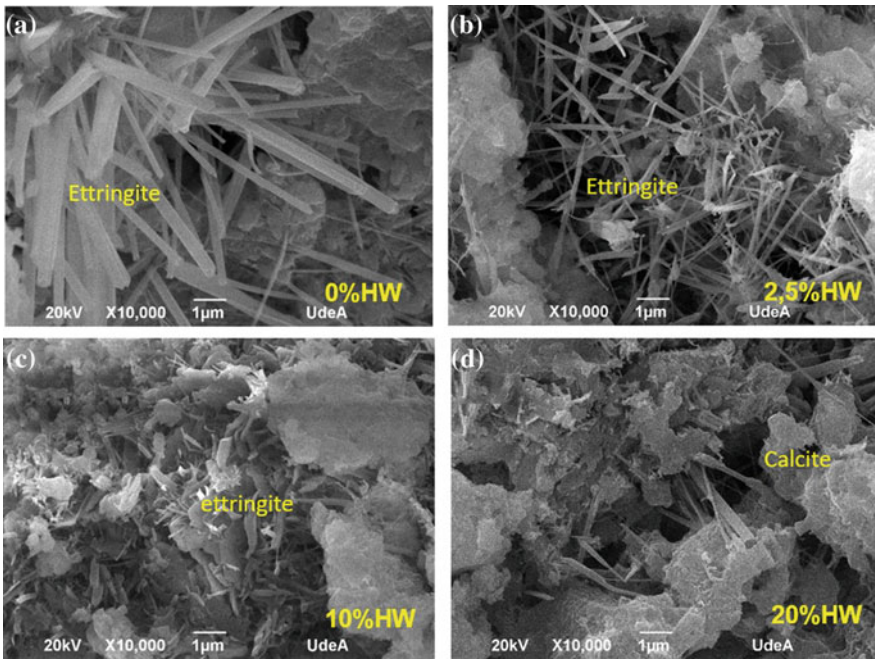

Fig. 3 SEM of samples fabricated with WOPC and iron oxide containing arsenic at different concentrations, **a** 0.0wt%, **b** 2.5wt%, **c** 10wt%, and **d** 20wt%

calcite and ferrihydrite phases appeared, which has been confirmed by the XRD evaluation later presented. The ferrihydrite exhibits an agglomerated particle like structure, with some of the individual particles going into the nanoscale. These particles have a rounded shape. On the other hand, magnesium calcite shows a complex branched structure, with some micro-plates consolidating a flower like structure.

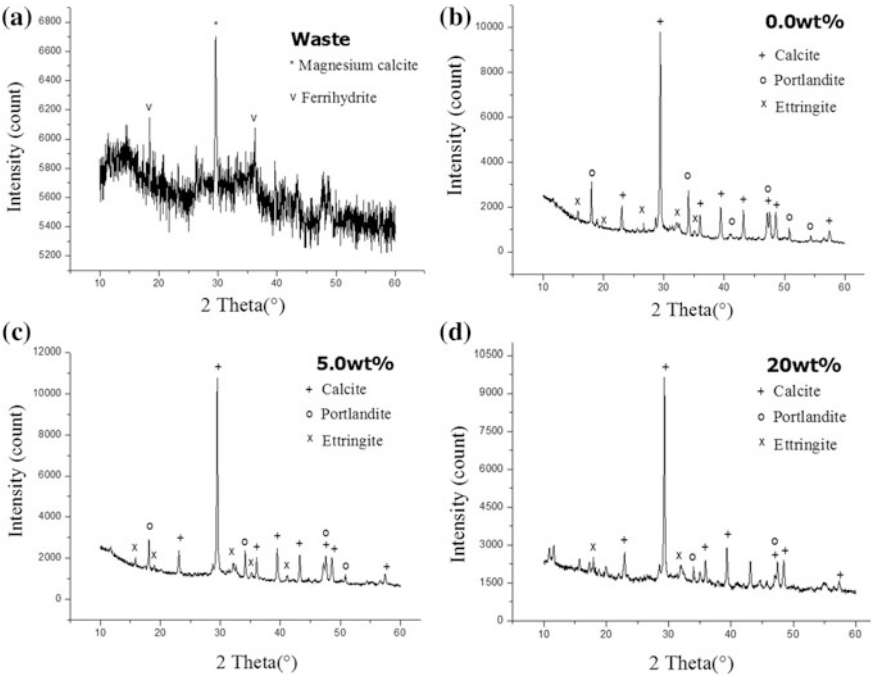

Fig. 4 XRD of **a** raw waste powder, **b** 0.0wt%, **c** 5wt%, **d** 20wt%

Figure 3 is a summary of SEM images for the WOPC with waste samples, after samples were released from molds close to air for 28 days. Images were collected over fractured surfaces and pores, which favored the nucleation of ettringite. This phase has been detected in all samples. Samples with 0.0 and 2.5wt% of waste, showed a lot of ettringite, see Fig. 3a, b. As the waste based on iron oxide with arsenic contents increased, the ettringite phase decreased as well, see Fig. 3c, d. The irregular shapes in these two last images are calcium silicate hydrate (C-S-H).

Figure 4 summarizes XRD data for the raw waste material and also for some of the fabricated samples. Figure 4a shows the XRD for the waste powder, an iron oxide based containing arsenic, showed magnesium calcite ($CaCO_3$) and ferrihydrite ($(Fe^{3+})_2O_3$•0.5H2O) phases. Figure 4b–d, show XRD spectra for WOPC with 0.0, 5.0 and 20wt% of waste. In all cases cement phases were found (calcite, portlandite, and ettringite). Only a reduction in ettringite was found as waste contents increased.

Finally, compression strength and density both had a trend of continuous decrease as the waste content increases, see Fig. 5a, b. This can be explained as lack of cement impregnation due to agglomeration of waste particles, which also leads to a greater porosity and as consequence a poor strength a low density. In terms of the compression tests, up to 2.5wt% of waste slightly increased the mean compressive strength, which typically mean the powdered waste is acting as filler of voids. Even

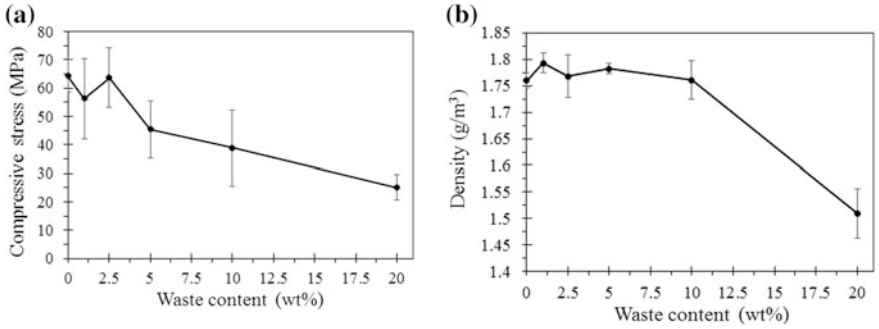

Fig. 5 **a** Compressive strength, and **b** density tests for WOPC with iron oxide containing arsenic at different concentrations

with 20wt% of waste the compressive values were acceptable for either non high strength applications such as sidewalks or decoration, or just as a hazardous waste stabilizer. Density did not experienced significant changes up to 10wt% of waste.

Conclusions

The addition of iron oxide base waste containing arsenic shows some positive results as an admixture or filler for cementitious materials. Even up to 20wt% the waste in the cement produced a composite material with acceptable values of strength, which is expected because the waste is based on iron oxide and it is very fine in size, which certainly can be not far from some of the components of typical cement. Thus, the stabilization of this waste in cement is a good solution for this problem that can be implemented in several countries that use this ceramics to filter the arsenic and other hazardous metals.

Acknowledgements Authors want to acknowledge Dr Susan Amrose from Mechanical Engineering Department at the Massachusetts Institute of Technology (MIT).

References

1. Smith AH, Lingas EO, Rahman M (2000) Contamination of drinking-water by arsenic in Bangladesh: a public health emergency. Bull World Health Organ 78(9):1093–1103
2. Gebel TW (1999) Arsenic and drinking water contamination. Science 283(5407):1455
3. Nordstrom DK (2002) Worldwide occurrences of arsenic in ground water. Science 296 (5576):2143–2145
4. Abernathy CO, Liu YP, Longfellow D, Aposhian HV, Beck B, Fowler B, Goyer R, Menzer R, Rossman T, Thompson C, Waalkes M (1999). Arsenic: health effects, mechanisms of actions, and research issues. Environ Health Perspect 107(7):593

5. Kapaj S, Peterson H, Liber K, Bhattacharya P (2006) Human health effects from chronic arsenic poisoning–a review. J Environ Sci Health Part A 41(10):2399–2428
6. Colombia carece de legislación sobre el uso de inmunizantes con arsénico, CCA. http://infomaderas.com/2013/04/05/colombia-carece-de-legislacion-sobre-el-uso-de-inmunizantes-con-arsenico-cca/. Accessed Sep 2017
7. Singh R, Singh S, Parihar P, Singh VP, Prasad SM (2015) Arsenic contamination, consequences and remediation techniques: a review. Ecotoxicol Environ Saf 112:247–270
8. Selvin N, Messham G, Simms J, Pearson I, Hall J (2000) The development of granular ferric media-arsenic removal and additional uses in water treatment. In: Proceedings of the AWWA water quality technology conference. Salt Lake City
9. Su C, Puls RW (2008) Arsenate and arsenite sorption on magnetite: relations to groundwater arsenic treatment using zerovalent iron and natural attenuation. Water Air Soil Pollut 193(1–4):65–78
10. Clancy TM, Snyder KV, Reddy R, Lanzirotti A, Amrose SE, Raskin L, Hayes KF (2015) Evaluating the cement stabilization of arsenic-bearing iron wastes from drinking water treatment. J Hazard Mater 300:522–529
11. Debe preocuparte el hecho de que haya arsénico en el arroz? http://www.wradio.com.co/noticias/salud/debe-preocuparte-el-hecho-de-que-haya-arsenico-en-el-arroz/20170214/nota/3383745.aspx. Accessed Sep 2017
12. Loaiza A, Cifuentes S, Colorado HA (2017) Asphalt modified with superfine electric arc furnace steel dust (EAF dust) with high zinc oxide content. Constr Build Mater 145:538–547
13. Colorado HA, Colorado SA (2016) Portland cement with battery waste contents. In: Rewas 2016. Springer International Publishing, pp 57–63
14. Colorado HA, Garcia E, Buchely MF (2016) White ordinary portland cement blended with superfine steel dust with high zinc oxide contents. Constr Build Mater 112:816–824

Part III
Solar Cell Silicon

Three-Dimensional Crystal-Plasticity Based Model for Intrinsic Stresses in Multi-junction Photovoltaic

Khaled H. Khafagy, Tarek M. Hatem and Salah M. Bedair

Abstract Our understanding for intrinsic stresses and defects evolution in photovoltaic devices has became an essential part of new developments. In particular, Multi-Junction Photovoltaic (MJ-PV) modules depend on multi-layer structures that may suffer high dislocation-densities as a result of high lattice and thermal expansion coefficient mismatch. These defects limit the performance, reliability, and lifetime of PV devices. In the current study, a three-dimensional multiple-slip crystal-plasticity model and specialized finite-element formulations are used to investigate *InGaN* growth on *Si* substrates. The formulation is based on accounting for thermal and intrinsic stresses as a result of different processing conditions and microstructures. Furthermore, the formulation was used to investigate a recently developed technique, Embedded Void Approach (EVA), which can be used to address both the high density of defects and the cracking/bowing of *InGaN* growth on *Si*. The current work lays the groundwork for more extensive use of silicon in MJ-PV devices.

Keywords Crystal plasticity · Solar cells · Multi-junction photovoltaic

K. H. Khafagy · T. M. Hatem (✉)
Centre for Simulation Innovation and Advanced Manufacturing,
The British University in Egypt, El-Sherouk City 11837, Cairo, Egypt
e-mail: tarek.hatem@bue.edu.eg

K. H. Khafagy
e-mail: khaled.khafagy@bue.edu.eg

S. M. Bedair
Department of Electrical and Computer Engineering, North Carolina State University,
Raleigh, NC 27695, USA

Z. Sun et al. (eds.), *Energy Technology 2018*, The Minerals, Metals & Materials Series, https://doi.org/10.1007/978-3-319-72362-4_41

Introduction

Over the last decade, the III-Nitride family has been identified as a commonly accepted semiconductor material after achieving a crucial development in several applications such as LED and Solar Cell applications. Furthermore, InGaN is a semiconductor that constitutes from GaN and InN that has a wide application in optical devices, especially in multi-junction photovoltaic (MJPV), as a result of its wide spectrum (from 0.7 to 3.4 eV). On the other hand, silicon is an optimum substrate to grow InGaN, and the rest of III-N family, in-terms of cost, efficiency, properties and available sizes. Although the growth of InGaN on silicon substrate offer good properties for solar devices, the deposition of InGaN layer on silicon is inherently difficult due to the chemical dissimilarities and the large thermal and lattice mismatches between both layers. The lattice and thermal expansion coefficient mismatch at the *InGaN/Si* interface leads to generate defects such as dislocations. Placing voids near to the interface could absorb the misfit dislocations therefore reducing the defects density at the top surface of the thin-film.

Therefore, the current study focuses on improving the efficiency of MJ-PV cells affected by dislocations generated from intrinsic stresses at the interface between different layers of MJPV cells. Furthermore, this research investigates a recently developed technique, Embedded Void Approach (**EVA**), which can be used to overcome high thermal expansion coefficient and lattice mismatch between different layers of MJ-PV device. The proposed technique reduces dislocation-densities as well as cracking/bowing that might result of the growth of Indium Gallium Nitride $In_{(x)}Ga_{(1-x)}N$ on Silicon *Si* substrates [1].

Voids are generated experimentally after the growth of III-nitride by etching the film using ICP-RIE plasma etching in order to produce III-nitride nanowires as shown in Fig. 1. Based on Bediar et al. [1], nanowires can be created using ICP-RIE plasma etching with no need for lithography processes. This mask-less etching technique is mainly based on the presence of dislocation in III-nitride at the beginning of the process. High etching rates occur at high dislocation sites producing nanowires with low defect density.

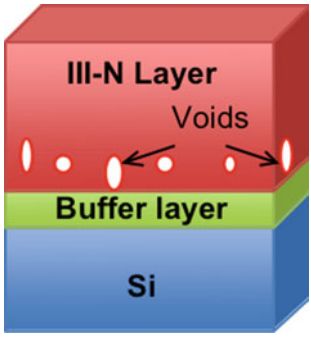

Fig. 1 Proposed MJ-PV structure with EVA [2]

This approach is experimentally validated to reduce dislocation-density on the surface of thin-film two orders of magnitude. In principle, due to the very high density of these voids and their lengths (a few microns), most of the misfit dislocations generated at the interface due to thermal expansion coefficient mismatch between the substrates and the epitaxial III-N films can be annihilated at the free surface of these voids.

A three-dimensional multiple-slip crystal plasticity model and specialized finite-element formulations are used to address *InGaN* growth on *Si* substrates. The formulation is based on accounting of thermal and intrinsic stresses as a result of different processing conditions and device structures. Commercial FE solver (ABAQUS) is used along with Düsseldorf Advanced Materials Simulation Kit (DAMASK) to model elastic and plastic behavior of *InGaN* growth on *Si* substrate, both with/without embedded voids. It is found that EVA considerably reduces the interface stresses leading to low stress at the thin film layer. Consequently, less dislocation-densities on the top surface leading to an increase in the diffusion length of the electron and overall efficiency the device.

Constitutive Model

A constitutive solution that couples deformation and stress is used to solve the value of continuum mechanical boundary problem [3–7]. This is carried out by calculating $\dot{\gamma}^{\alpha}$ is the plastic shear strain rate as function of the Second Piola–Kirchhoff Stress **S** tensor.

In that formulation, it has been assumed that the deformation gradient can be decomposed into elastic and inelastic components

$$\mathrm{D}_{ij} = \frac{1}{2}\left(\mathrm{V}_{i,j} + \mathrm{V}_{j,i}\right) \tag{1}$$

where, $\mathrm{D_{ij}}$: is the deformation rate tensor or stretching tensor and $\mathrm{W_{ij}}$ is the spin tensor or vorticity tensor,

$$\mathrm{W}_{ij} = \frac{1}{2}\left(\mathrm{V}_{i,j} - \mathrm{V}_{j,i}\right) \tag{2}$$

The total deformation-rate tensor, $\mathrm{D_{ij}}$, and the total spin tensor, $\mathrm{W_{ij}}$, are then each additively decomposed into elastic and plastic components as:

$$\mathrm{D}_{ij} = \mathrm{D}^{*}_{ij} + \mathrm{D}^{P}_{ij} \tag{3}$$

$$\mathrm{W}_{ij} = \mathrm{W}^{*}_{ij} + \mathrm{W}^{P}_{ij} \tag{4}$$

where, W_{ij} includes the rigid body spin. The inelastic parts are defined in terms of the crystallographic slip-rates as:

$$D_{ij}^{P} = P_{ij}^{(\alpha)} \dot{\gamma}^{(\alpha)} \tag{5}$$

$$W_{ij}^{p} = \omega_{j}^{(\alpha)} \dot{\gamma}^{(\alpha)} \tag{6}$$

where, α is summed over all slip-systems, and the tensors $P_{ij}^{(\alpha)}$ and $\omega_{ij}^{(\alpha)}$ are symmetric and skew-symmetric second-order tensors, and are defined in terms of the unit normal and the unit slip vectors as

$$P_{ij}^{(\alpha)} = \frac{1}{2}\left(S_{i}^{(\alpha)} n_{j}^{(\alpha)} + S_{j}^{(\alpha)} n_{i}^{(\alpha)}\right) \tag{7}$$

$$\omega_{ij}^{(\alpha)} = \frac{1}{2}\left(S_{i}^{(\alpha)} n_{j}^{(\alpha)} - S_{j}^{(\alpha)} n_{i}^{(\alpha)}\right) \tag{8}$$

where, $n_{i}^{(\alpha)}$ is the unit vector normal to the slip plane, and $s_{i}^{(\alpha)}$ is the unit vector in the slip direction. Material state is formulated as a function of total shear and shear rate as follows:

$$\dot{\gamma}^{\alpha} = \dot{\gamma}_{0} \left| \frac{\tau^{\alpha}}{\tau_{c}^{\alpha}} \right| \mathrm{sgn}(\tau^{\alpha}) \tag{9}$$

where, $\dot{\gamma}^{\alpha}$ is the shear rate for slip system α subjected to the resolved shear stress τ^{α} at a slip resistance τ_{c}^{α}; $\dot{\gamma}_{0}$ and m are material parameters that quantify the reference shear rate and the rate sensitivity of slip, respectively.

Then, the influence of any slip system β on the hardening behavior of slip system α is given by

$$\tau_{c}^{\alpha} = h_{\beta} \left| \dot{\gamma}^{\beta} \right| \tag{10}$$

$$h_{\alpha\beta} = q_{\alpha\beta} \left[h_{o} \left(1 - \frac{\tau_{c}^{\beta}}{\tau_{s}} \right)^{a} \right] \tag{11}$$

where, h_{o}, a, and τ_{s} are slip hardening parameters and $q_{\alpha\beta}$ is a hardening matrix.

Numerical Model

As shown in Fig. 2, the structure has 4 μm height and 2μ*rmm* ∗ 2μm square base area, as well it has two layers *InGaN* and *Si* that are shown in red and blue colors. A mesh convergence study has been conducted, where the mesh size of 0.2 μm has

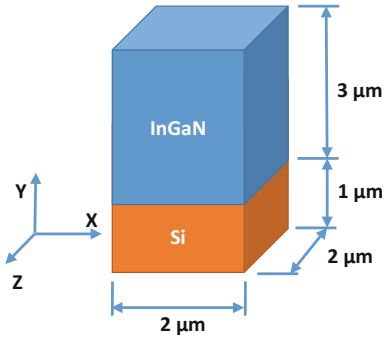

Fig. 2 InGaN/Si structure used in the current model, PBCs is introduced on both X and Z sides to account for an infinite extended structure in both directions

Table 1 Plastic and elastic model parameters of *InGaN* and *Si* [8–12]

Parameters	$In_{0.65}$ $Ga_{0.35}$ N	Si
$E(GPa)$	186.5	168.9
$v(Poisson\ ratio)$	0.3535	0.262
α (K^{-1})	$\alpha_a = 3.646 \times 10^{-6}$ $\alpha_c = 3.44 \times 10^{-6}$	2.6×10^{-6}
Initial dislocation density $(/m^2)$	10^8	10^7
Max. Dislocation density $(/m^2)$	10^{11}	$14 * 10^{10}$
Thermal Conductivity $(W/m°C)$	97.5	130
Thickness (µm)	3	1

been adapted for both *InGaN* and *Si* layers. However, lower mesh size is used around the void to account for high stress gradient around the void due to stress concentration. Plastic and elastic parameters of *InGaN* and *Si* are listed in Table 1. Periodic Boundary Conditions (PBCs) is used coupling the opposite sides (both in the X and Z directions) of the structure, while free boundary condition is assumed in both sides in the Y-direction.

In order to verify the numerical models developed here, the results of 2D and 3D elastic simulations have been compared to analytical results. The analytical results have been calculated as $\sigma = E.\varepsilon = E.\alpha.\Delta t$, where, σ is stresses due to thermal load (MPa), E is a Young's modulus (MPa), ε is a strain, α is the thermal expansion coefficient (K^{-1}), Δt is temperature change (K).

Model Parameters

Elastic and plastic parameters of *InGaN* and *Si* materials have been used with the proposed model to estimate the stresses, strains, and dislocation-densities of the structure.

Results

Results of the Structure Without Introducing Embedded Voids

As shown in Fig. 3 the two-dimensional elastic model shows that the theoretical calculation and numerical results match. Theoretical calculations showed that the maximum stress for 3μm height *InGaN* thin film layer was 476 MPa, and the minimum stress for 1μm height silicon substrate was 309.8 MPa , which match the results of the numerical analysis.

As shown in Fig. 4, because of the thermal mismatch in the interface of *InGaN* and *Si*, the maximum stress reveals at the interface reaches to around 1400 MPa. Further, higher stresses in the plastic results rather than elastic results are due to the effect of material plasticity parameters such as slipping.

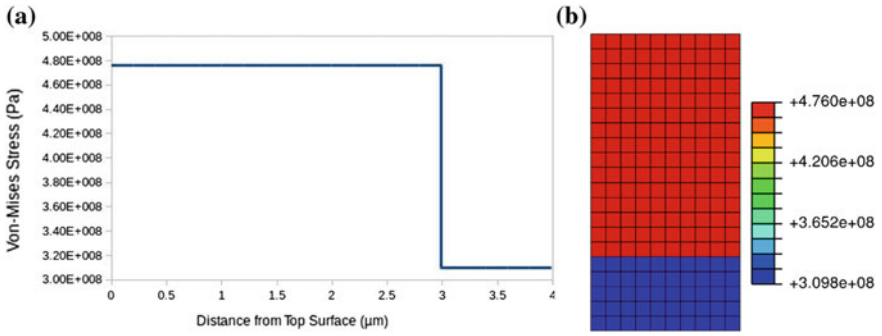

Fig. 3 Two-dimensional elastic model without voids used to validate the analytical results; **a** Von-Mises stresses along the thickness of the structure; **b** contour plot of Von-Mises stresses

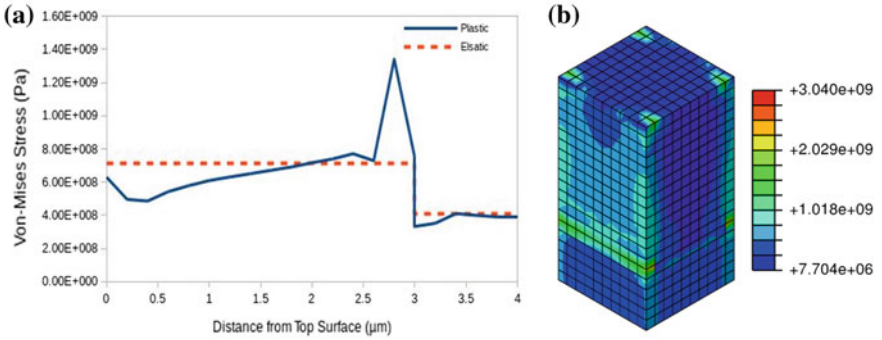

Fig. 4 Three-dimensional plastic model compared to elastic model without voids; **a** Von-Mises stresses along the thickness of the structure; **b** contour plot of Von-Mises stresses

Results After Introducing the Embedded Void

Introducing voids periodically to the presented structure resulted in slight increase from 710 to 748 MPa in Von-Mises stresses at the top surface. Similarly it led to slight increase in the stresses at the interface exactly from 710 to 748 MPa. Also, the void itself is considered as a stress concentration area, where a maximum stress of 1135 MPa is observed as shown in Fig. 5.

Figure 6 shows the plastic behavior of the void. The results of the plastic run showed further reduction in the interface stresses from that of the elastic run. At the top surface, stresses experienced no reduction. However, it experienced maximum increase at a distance of 0.5 by 520 MPa. Such significant increase in Von-Misses stresses occurred

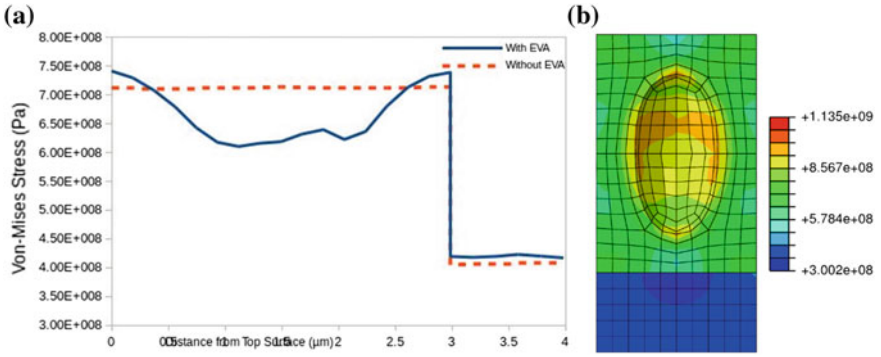

Fig. 5 Three-dimensional elastic model with embedded void (aspect ratio 1:1:2 and volume ratio 7%); **a** Von-Mises stresses along the thickness of the structure; **b** contour plot of Von-Mises stresses

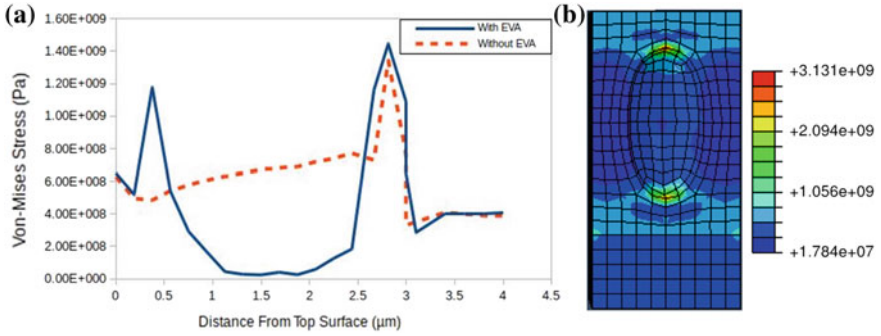

Fig. 6 Three-dimensional plastic model with embedded void (aspect ratio 1:1:2 and volume ratio 7%); **a** Von-Mises stresses along the thickness of the structure; **b** contour plot of Von-Mises stresses

near the void as a result of stress concentration due to geometrical discontinuity. Noticeable reduction occurred at a distance range from 0.5 to 2.8 μm with minimum and maximum stress reduction by 550 MPa and 667 MPa, respectively.

Conclusion

Numerical study of EVA that reduce defects and has potential to increase efficiency in MJ-PV cells has been introduced in the current work. Such an aim is achieved through investigating EVA effect in the reduction of stress and plastic strain to overcome thermal expansion coefficient and lattice mismatches between different MJ-PV layers. Analytical calculations for the analyzed system have been used to verify numerical results assuming elastic behavior. Results of CP-FEM simulations are compared to Elastic runs with/without embedded void approach.

Furthermore, numerical models was utilized to investigate the mentioned approach; the computational analysis encompasses addressing *InGaN* growth on *Si* substrate using three-dimensional multiple-slip crystal plasticity model and specialized commercial FE solver ABAQUS is integrated with crystal plasticity constitutive model implemented in DAMASK. Consequently, stress reduction will reduce the dislocation density at the top surface as voids act as a sink to interface generated dislocations.-

Acknowledgements The support from Young Investigators Research Grant (YIRG05) at the British University in Egypt is greatly appreciated.

References

1. Frajtag P et al (2011) Embedded voids approach for low defect density in epitaxial GaN films. Appl Phys Lett 98(2):2–4
2. Nikholas G et al (2012) Design of integrated III-nitride/non-III-nitride tandem photovoltaic devices. J Appl Phys 5:1–8
3. Hatem TM, Zikry MA (2011) A model for determining initial dislocation-densities associated with martensitic transformations. Mater Sci Technol 27(10):1570–1573
4. Hatem TM, Zikry MA (2010) Deformation and Failure in Single-Packet Microstructure of Martensitic Steels. Comput Mater Contin 17(2): 127–148)
5. Hatem TM, Zikry MA (2009) Dislocation-density crystalline plasticity modeling of lath martensitic microstructures in steel alloys. Phil Mag 89(33):3087–3109
6. Hatem TM, Zikry MA (2010) Dynamic shear-strain localization and inclusion effects in lath martensitic steels subjected to high pressure loads. J Mech Phys Solids 58(8) pp. 1057–1072
7. Hatem TM, Zikry MA (2009) Modeling of lath martensitic microstructure and failure evolution in steel alloys. J Eng Mater Technol ASME 131(041207):1–10
8. Maniatty AM, Karvani P. (2015) Constitutive relations for modeling single crystal gan at elevated temperatures. J Eng Mater Tech Trans ASME 137 (1)
9. Hadis M (2008) Handbook of nitride semiconductors and devices: materials properties physics and growth. Wiley-VCH Verlag GmbH & Co, KGaA, p 1

10. Horton Matthew K et al (2015) Segregation of Into dislocations in InGaN. Nano Lett 15(2):923–930
11. Łepkowski SP, Gorczyca I (2013) Elastic properties of InGaN and InAlN from first-principles calculations. In: Thomas Ihn, Clemens Rössler, Aleksey Kozikov (eds) AIP Conference proceedings, vol 1566, no 1. AIP
12. Salah SI et al (2017) Embedded void approach for nitride based multi-junction photovoltaic cells. 55th AIAA Aerospace sciences meeting

Review of Solar Silicon Recycling

York R. Smith and Pamela Bogust

Abstract Photovoltaic (PV) modules are becoming an ever increasingly larger part of our energy portfolio. As more and more PV modules are installed and come on-line, management of end-of-life (EOL) modules becomes an important issue. Currently, management of overburden EOL PV modules is not an issue, but is anticipated to be by 2030. Recovery and recycling of valuable metals in PV modules presents several environmental and economic advantages. In this brief review, we will describe processes for refurbishing and recycling of PV silicon. These processes involve some combination of mechanical, thermal, and chemical processing, all of which all have their oPV) modules have become wn respective challenges. Also, projections of PV module material streams are also highlighted.

Keywords Photovoltaic · Silicon · Recycling

Introduction

Photovoltaic (PV) modules have become a significant contributor to our current global power production in a short amount of time, with a production of only 40 GW in 2010 up to 227 GW in 2015 [1–3]. The growth rate of power production from PV's was 74% from 2006–2011 and 42% from 2010–2015, a significantly higher growth rate than any other renewable energy [2, 3]. The amount of power supplied by PV modules is expected to keep growing with an estimated cumulative installed capacity of 4,512 GW by 2050 [2, 3]. This dramatic increase in use of PV modules in a short time and the long life of PV modules (25–30 years) will result in a dramatic influx of PV module waste around 2030 [1, 4–6].

Y. R. Smith (✉) · P. Bogust
Metallurgical Engineering Department, University of Utah,
Salt Lake City, UT, USA
e-mail: york.smith@utah.edu

P. Bogust
e-mail: u1128127@utah.edu

Z. Sun et al. (eds.), *Energy Technology 2018*, The Minerals, Metals & Materials Series, https://doi.org/10.1007/978-3-319-72362-4_42

Currently, most EOL PV modules are being disposed of in landfills [4–6]. However, PV modules contain hazardous metals such as Pb and Cd, and leaching of these chemicals into water supplies from landfills would be harmful to the environment [6, 7]. The sale of some PV modules containing Cd are prohibited in China because of the high toxicity [7]. Recycling of PV modules can be even costlier then proper waste disposal, even in the case of hazardous waste disposal which, depending on the module type and applicable laws/regulations, may be required [4, 5, 7, 8]. Common recycling processes currently available focus on recycling the largest percent mass, and not on recovering valuable or hazardous materials [4, 5, 9]. This increases the environmental impact of PV use, making PV use less attractive [4, 5]. The cost of recycling is expected to decrease as the technology continues to develop, however [4, 5]. Disposal in landfills and as hazardous waste is expected to increase discouraging landfill use and encouraging recycling [4, 5].

The recycling of metals from PV modules would not only reduce the amount of waste but also preserve our limited supply of natural resources and reduce the amount of energy consumed to obtain and refine these resources [5, 6, 10]. There are currently studies investigating the need to recycle PV modules from an economic and environmental stand point. Many of these studies discuss the cost of recycling versus the cost of waste disposal [7, 8]. The low levels of valuable materials in the PV modules makes recycling currently not economical for crystalline Si modules and CdTe, while CIGS can be recycled for a profit [4, 8]. Commonly discussed alongside the economics of recycling is the responsibility of recycling. Studies of other electronic recycling regulations are compared to the PV market in an attempt to increase recycling of PV modules while not harming the PV market or detracting from PV use [4, 7].

Recoverable Materials and Projections

In crystalline Si modules, a p-n junction is installed on the front surface of the Si wafer and then coated with an anti-reflective layer [6]. An Al contact and a grid of Ag is screen printed on the back and front of the wafer, respectively to create cells [1, 11–13]. The cells are then connected by electrodes to make a module [6]. Ethylene vinyl acetate (EVA) is used to adhered the cells to the front glass and back sheet, commonly made of polyethylene terephthalate [14]. An aluminum frame is sometimes added to the modules for structural strength [14]. The general construction of a crystalline Si PV cell can be seen in Fig. 1. The crystalline Si wafers used in these modules accounts for about 4% of the panel by weight but the manufacturing of the high-purity Si wafer accounts for about 65% of the cost of the crystalline Si modules [6, 15, 16].

There are several common types of PV modules currently used; Copper indium gallium ($Cu(In_xGa_{1-x})Se_2$ (CIGS)), CdTe, monocrystalline Si and polycrystalline Si. CIGS make up about 4% of the current market and are expected to make up about 6.4% of the market by 2030 [1]. CdTe modules currently make up about 5% of the market and are expected decline to about to about 4.7% of the market by

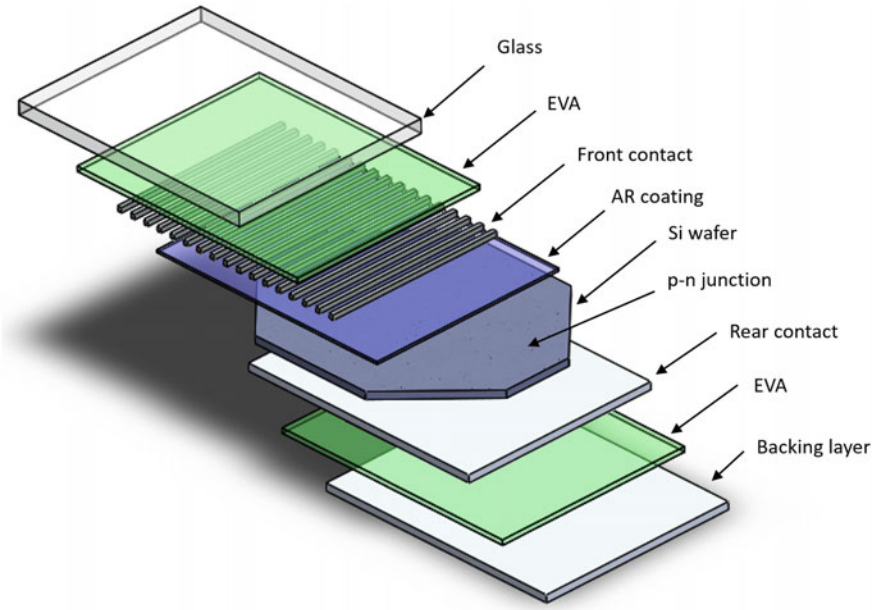

Fig. 1 Components of a crystalline Si PV cell

2030 [1]. About 92% of modules in use today are crystalline Si modules and they are projected to continue to dominate the market with 82% of market in 2020 [1, 6, 15]. Amorphous Si PV modules have recently been phased out due to their low efficiency and they contain the least value in metals and are therefore not considered in this analysis [1, 7].

Waste projections of PV modules were reported by International Energy Agency and International Renewable Energy Agency [1]. The production of each module type as well as the composition of the different modules was used for projections of waste categorized by material. The recovery rates of each material are from past reported studies, as seen in Table 1. A projection of the amount of valuable metals was estimated using the percentage of each metal by weight in each panel type and the amount of each panel manufactured as well as the expected recycling date of the panels, seen in Fig. 2. By mass, Si represents the second largest recoverable metal from PV modules.

Current Recycling Methods

In order to make recycling of PV modules economical, the cost of recycling must be reduced and the recovery of the valuable materials increased. A single recycling processes that could recycle all common types of PV modules would reduce the

Table 1 The weight percentage of the materials in each module type and their respective recovery rates

Component	Crystalline Si modules	CIGS modules	CdTe modules	Recovery rate
	Weight [%]	Weight [%]	Weight [%]	
Glass	71	88	96	0.9
Silcon	4	0	0	0.9
Aluminum	13	7	0	0.9
EVA	9	4	3	0
Copper	0.1	0.1	0.02	0.95
Silver	0.1	0	0	0.95
Indium	0	0.28	0	0.85
Gallium	0	0.1	0	0.85
Selenium	0	0.52	0	0.85
Nickel	0	0	0.1	0.85
Zinc	0	0	0.1	0.85
Tin	0	0	0.1	0.85
CdTe	0	0	0.12	0.85

Sources [1, 10–13, 17–20]

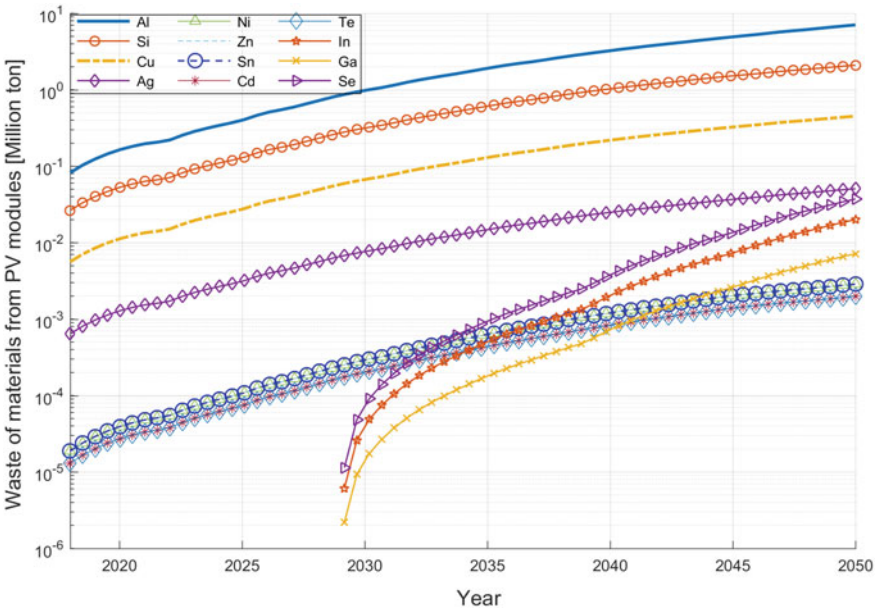

Fig. 2 The cumulative possible recovery of each metal from PV modules by year

costs of recycling [18, 21]. A recycling method that can allow for disposal of different PV module types is available, but this method does not recover the PV cell material. In this method, the frame and glass are manually removed for recycling and then the PV material is disposed of [4]. This method requires fewer treatments for recycling and reduces the amount of material to be disposed of in a landfill dramatically, making it a cheap waste treatment method [4]. While, this method allows for the processing of different PV module types, it does not extract the valuable or hazardous metals form the module [4].

Recycling Methods of Crystalline Si Modules

There are a few different focuses in current research on recycling and reuse of crystalline Si modules. These focuses are the reuse of PV cells and of Si wafers (remanufacturing), and the recovery and recycling of Si, Ag, and/or the largest percent of the panel [12]. A recent review by Tao and Yu [20] examines three types of recycling pathways from the perspectives of close-loop life cycle, which are manufacturing waste recycling, disposed module re-manufacturing, and recycling.

In order to reuse the PV cell or wafer they must not be damaged, if they are damaged they can be recycled and used as raw material [22]. The Si wafers used in crystalline Si modules are manufactured by melting Si and then solidifying it using a variety of techniques, such as Czochralski or directional solidification, to produce ingots [16, 20, 23]. The ingots are sliced using a multi-wire saw with an abrasive of ethylene glycol and silicon carbide to create the wafers [20, 24]. More than 40% of the Si ingot is lost in the slurry waste in the processes of manufacturing the wafer [16, 20, 23]. The loss of Si in manufacturing of the wafer as well as, the energy consumed in manufacturing processes makes the reuse of wafers desirable [20]. However, in the processes of etching the wafer to remove the p-n junctions part of the Si is lost leaving a thinner wafer [6, 24]. As much as 38% of the Si is lost in the etching processes performed by Wang et al. [24].

First Solar Inc. has developed a process for recovering crystalline Si cells, where the modules are lightly heated to remove the backing [4]. Then a thermal pyrolysis treatment is performed on the cells to decompose the EVA [4]. This leaves the crystalline Si cells to be recovered and reused [4]. The cells need to be intact to be reused and these reused cells have a slightly lower efficiency then new cells [4].

A recent study on the reuse of recovered Si wafers from crystalline Si modules was performed by Klugmann-Radziemska et al. [15]. The first step in recovering the Si wafer was heating the PV module in a SiO_2 bed. This process allowed for the separation of the cell from the PV module. The top Ag layer is first removed using aq.HNO_3 at 40 °C and then the Ag is recovered from the waste acid by electrolysis. The Al layer is removed next using KOH at 80 °C. The AR coating and p-n junction are removed last using a mixture of HNO_3, HF, CH_3COOH and Br_2 at temperatures ranging from 70 to 80 °C dependent on module type. The intact recovered Si wafers are then rinsed with deionized water and laser cut in

preparation to be reused for a new PV cell. In order to create a new cell, the wafer was texturized by etching with KOH and isopropyl alcohol for 30 min at 80 °C followed by HF for monocrystalline wafers and HF + HNO_3 + H_2O at 25 °C for polycrystalline. The wafers are then rinsed with deionized water again, before the p-n junction is formed. The p-n junction is formed through the process of diffusion with the liquid donor source, $POCl_3$, from 825 to 900 °C. The wafers are then covered by a phosphorus-silicate glass while a donor-doping layer is applied to the sides and edges. This is followed by chemical etching using HF + HNO_3 + H_2O to remove the parasitic junction. The wafer is then immersed in HF for 2 min to remove the phosphorus-silicate glaze. The wafer is then subject to a surface passivation process and then coated with a layer of SiO_2 by thermal oxidation. The electrical contacts are then printed on the wafer and annealed. These new cells had efficiencies of 12.7 and 15% without the AR layer. It was recognized that that the chemicals used in the etching process are toxic, reactive, and if released could be hazardous [15].

Another recent study to recover the Si wafer was performed by Shin et al. [25]. The modules were heated to 480 °C at a rate of 15 °C/min, separating the PV cells from the module. The unbroken wafers are then collected and immersed in HNO_3 then, KOH at 80 °C removing the Ag and Al. An etching paste containing phosphoric acid is then applied to the wafers and then the wafer are annealed with the applied paste. The wafers are then dipped in KOH, removing the top layer of the wafer and dissolving the AR coating. The new solar cells are then fabricated using the cleaned Si wafer, by first dipping the wafer in KOH to texturize the wafer. The n-doped layer is formed by thermal treatment with liquid source, $POCl_3$. Phosphosilicate glass is then removed using an HF solution. The AR coating is applied to the wafer by plasma-enhanced chemical vapor. This is followed by screen printing of the Al and Ag metal contacts to the wafer with an annealing step. Mini modules were then made using Pb free solder, 60SN-38Bi-2Ag, laminated using glass, EVA, and Tedlar. The modules had power conversion efficiencies of 15.0–16.0% compared to the initial module efficiencies of 16.5–17.0%. This process demonstrates that the Si wafer could be recovered without the use of harmful surfactants and the cell could be manufactured without the use of Pb [25].

Research on recovery of Si particles from crystalline Si modules was performed by Kang et al. [6]. The first step in the recycling processes was determining an organic solvent that would cause dissolution and swelling of the EVA resin. The module was immersed in toluene for 2 days at 90 °C, resulting in swollen and dissolved EVA that was separate from the tempered glass. The swollen EVA remained attached to the PV cell. The PV cell and EVA was heated to 600 °C and held there for 1 h under a flow of argon gas. This resulted in the complete removal of the EVA, but the metal electrodes, anti-reflective coating and the p-n junction layers remained on the PV cell. The PV cell particles were then put in a chemical etching solution made of HF, HNO_3, H_2SO_4, CH_3 COOH, distilled water and a surfactant of CMPMO- 2 for 20 min [6]. The metal impurities were oxidized, reduced and dissolved in the etching fluid, leaving Si of purity 99.999%. The recovery of the high purity Si was 86% using this method. In both recycling

methods performed by Kang et al. and Shin et al., the metals removed from the PV cell are not recovered while, Klugmann-Radziemska recovers Ag and not the Al from the etching processes [6, 13, 15].

Conclusion

Studies show that recycling technologies for EOL PV modules are explored and some are commercially available, although challenges still remain in process efficiency/continuous processing, reduction in process complexity, energy requirements, and use of chemicals. Environmental benefits and economic viability are also important to the establishment of feasible PV recycling systems, thereby improving the sustainability of PV. Studies suggest that EOL module recycling can have significant positive impacts on reducing environmental loads, required chemicals, scarce resources and energy for new modules are reduced. However, economic motivation to recycle is currently not favorable. The realization of PV recycling will depend on developing innovative processes and technologies capable of handling and separating large throughputs of PV material.

Acknowledgements Authors would like to acknowledge support provided by the U.S. Department of Energy, Office of Science, Energy Efficiency Renewable Energy, Sunshot Initiative. This publication was developed under an appointment to the Energy Efficiency and Renewable Energy (EERE) Research Participation Program, administered for the U.S. Department of Energy (DOE) by the Oak Ridge Institute for Science and Education (ORISE). ORISE is managed by ORAU under DOE contract number DESC0014664. This document has not been formally reviewed by DOE. The views and conclusions contained in this document are those of the authors and should not be interpreted as necessarily representing the official policies, either expressed or implied, of DOE, or ORAU/ORISE. DOE and ORAU/ORISE do not endorse any products or commercial services mentioned in this publication.

References

1. Energy Agency, Economic Co-operation, and Global Climate. End-Of-Life Management Solar Photovoltaic Panels
2. Ren21 (2012) Renewables 2012 Global Status Report 2012. Production, p 172
3. Sawin JL, Seyboth K, Sverrisson F (2016) Renewables 2016: Global Status Report
4. Fthenakis VM (2000) End-of-life management and recycling of PV modules. Energy Policy 28(14):1051–1058
5. Goe M, Gaustad G (2016) Estimating direct human health impacts of end-of-life solar recovery. In: Conference record of the IEEE photovoltaic specialists conference, 2016 November, pp 3606–3611
6. Kang S, Yoo S, Lee J, Boo B, Ryu H (2012) Experimental investigations for recycling of silicon and glass from waste photovoltaic modules. Renew Energy 47:152–159
7. McDonald NC, Pearce JM (2010) Producer responsibility and recycling solar photovoltaic modules. Energy Policy 38(11):7041–7047

8. Choi JK, Fthenakis V (2014) Crystalline silicon photovoltaic recycling planning: macro and micro perspectives. J Clean Prod 66:443–449
9. Müller A, Wambach K, Alsema E (2005) Life cycle analysis of solar module recycling process. MRS Proc 895(January 2011):03–07
10. Redlinger M, Eggert R, Woodhouse M (2015) Evaluating the availability of gallium, indium, and tellurium from recycled photovoltaic modules. Sol Energy Mater Sol Cells 138:58–71
11. Corcelli F, Ripa M, Leccisi E, Cigolotti V, Fiandra V, Graditi G, Sannino L, Tammaro M, Ulgiati S (2016) Sustainable urban electricity supply chain indicators of material recovery and energy savings from crystalline silicon photovoltaic panels. Ecol Indic
12. Dias P, Javimczik S, Benevit M, Veit H, Bernardes AM (2016) Recycling WEEE: extraction and concentration of silver from waste crystalline silicon photovoltaic modules. Waste Manag 57:220–225
13. Tammaro M, Rimauro J, Fiandra V, Salluzzo A (2015) Thermal treatment of waste photovoltaic module for recovery and recycling: experimental assessment of the presence of metals in the gas emissions and in the ashes. Renew Energy 81:103–112
14. Dias PR, Benevit MG, Veit HM (2016) Photovoltaic solar panels of crystalline silicon: characterization and separation. Waste Manag Res the J Int Solid Wastes Public Clean Assoc ISWA 34(3):235–45
15. Klugmann-Radziemska E, Ostrowski P, Drabczyk K, Panek P, Szkodo M (2010) Experimental validation of crystalline silicon solar cells recycling by thermal and chemical methods. Sol Energy Mater Sol Cells 94(12):2275–2282
16. Wang TY, Lin YC, Tai CY, Sivakumar R, Rai DK, Lan CW (2008) A novel approach for recycling of kerf loss silicon from cutting slurry waste for solar cell applications. J Cryst Growth 310(15):3403–3406
17. Berger W, Simon FG, Weimann K, Alsema EA (2010) A novel approach for the recycling of thin film photovoltaic modules. Resour Conserv Recycl 54(10):711–718
18. Granata G, Pagnanelli F, Moscardini E, Havlik T, Toro L (2014) Recycling of photovoltaic panels by physical operations. Sol Energy Mater Sol Cells 123(2014):239–248
19. Latunussa CEL, Ardente F, Blengini GA, Mancini L (2016) Life cycle assessment of an innovative recycling process for crystalline silicon photovoltaic panels. Sol Energy Mater Sol Cells 156:101–111
20. Tao J, Suiran Yu (2015) Review on feasible recycling pathways and technologies of solar photovoltaic modules. Sol Energy Mater Sol Cells 141:108–124
21. Rocchetti L, Beolchini F (2015) Recovery of valuable materials from end-of-life thin-film photovoltaic panels: Environmental impact assessment of different management options. J Clean Prod 89:59–64
22. Bohland JR, Anisimov II (1997) Possibility of recycling silicon PV modules. In: 26th photovoltaic specialists conference, pp 1173–1175
23. Kirk AP, Kirk AP (2015) Chap 5 resource demands and PV integration. Sol Photovolt Cells:71–83
24. Wang TY, Hsiao JC, Du CH (2012) Recycling of materials from silicon base solar cell module. In: Conference record of the IEEE photovoltaic specialists conference, pp 2355–2358
25. Shin J, Park J, Park N (2017) A method to recycle silicon wafer from end-of-life photovoltaic module and solar panels by using recycled silicon wafers. Sol Energy Mater Sol Cells 162(December 2016):1–6

Thermo-Calc of the Phase Diagram of the Fe–Si System

Shadia Ikhmayies

Abstract In this work Thermo-Calc software was used to calculate the phase diagram of the Fe–Si system. The deduced phase diagram includes twenty fields, where three fields represent pure phases; two solid solutions and a liquid phase. There are several fields of two co-existing phases; mixed solid phases, and mixed solid with liquid phases. A set of eutectic and eutectoid points were found, where transformation reactions and temperatures were identified. The results were compared with results in the literature and good agreements with some differences were found. This study is a step to understand the phase diagram of Ca–Fe-Si system for refining metallugical grade silicon (MG-Si).

Keywords Iron-silicon alloys · Phase diagrams · Fe–Si system
Ca–Fe-Si system · Silicon refining

Introduction

In order to understand and optimize the complex chemical reactions during refining of metallurgical grade silicon (MG-Si) and understand the evolution of Si alloy microstructure in various applications, knowledge of the phase diagram and thermodynamic properties of Si alloy is critical [1]. Phase diagrams and thermodynamic properties of impurity elements found in MG-Si is very important to understand the impurity behavior in Si-rich regions. In addition, thermodynamic parameters and phase diagrams are necessary to understand the reactivity with molten slag for slag-refining processes, and to understand impurity segregation between solid Si and liquid Si during solidification [1]. Typically, it is difficult to remove Fe molten Si during the slag-refining process; therefore, alternative acid-leaching processing routes were proposed to eliminate it [2]. In the acid-leaching process, the evolution of Fe intermetallic precipitates in solidified Si is important to determine the removal

S. Ikhmayies (✉)
Faculty of Science, Physics Department, Al Isra University, 11622 Amman, Jordan
e-mail: shadia_ikhmayies@yahoo.com

Z. Sun et al. (eds.), *Energy Technology 2018*, The Minerals, Metals & Materials Series, https://doi.org/10.1007/978-3-319-72362-4_43

rate of Fe. In the case of Fe removal by the acid-leaching process, Si–Ca-Fe ternary alloys can be considered. In order to maximize Fe removal, proper amounts of Ca can be intentionally added to Fe (Ca can also be dissolved from molten CaO-containing slag during the slag treatment). Studying the binary Fe–Si and Ca–Si systems are steps towards understanding the ternary Si–Ca-Fe system. On the other hand, Fe–Si alloy is used in steel industry and electrical-magnetic applications, and it is the most fundamental binary system for the ferrosilicon production. That is, impurity control in the liquid and solid Fe–Si alloys is important for the production and application of ferrosilicon alloy. Thus, the phase diagram of the Fe–Si system is of importance for the whole chain of the silicon steel and ferrosilicon alloy production and applications [3].

Unfortunately, little work was conducted to studying the phase diagram of Fe–Si binary system. Chart [4, 5] evaluated the thermodynamic properties related to the solid and liquid Fe–Si alloys, and reported a very early version of the calculated Fe–Si phase diagram. Kubaschewski [6] reported the most accepted version of the Fe–Si phase diagram based on the evaluation by Chart [5], and the experimental work by Schürmann and Hensgen [7]. In this work, Thermo-Calc software was used to deduce the phase diagram of Fe–Si system. A comparison between the results of this work and previous work was performed and discussed.

Methodology

The Thermo-Calc software is a sophisticated database and programming interface package used to perform thermodynamic calculations. It can calculate complex homogeneous and heterogeneous phase equilibria, and then plot the results as property diagrams and phase diagrams [8]. The software utilizes Gibbs free energy minimization procedure to calculate phase equilibria and thermodynamic properties of a chosen system [9]. For a given set of conditions, the computer determines the change in free energy for each possible combination of phases and phase compositions. Then, it selects the state that minimizes the total Gibbs free energy. Thermo-Calc is used in conjunction with different thermodynamic databases which contain the descriptions of the Gibbs free energies assessed using the CALPHAD approach. CALPHAD is a phase-based approach to model the underlying thermodynamics and phase equilibria of a system through a self consistent framework [10].

In this work, MAP calculations—a type of the calculations in the Thermo-Calc software—were used to calculate the equilibrium phase diagram of the Fe–Si system in the temperature range 0–1600 °C. The used database is the TCBIN: TC Binary Solutions v1.1 database and the mole fraction of silicon was varied from 0 to 1. The calculation type was chosen to be phase diagram.

Results and Discussion

Figure 1 shows the calculated phase diagram obtained in this work using Thermo-Calc software. The figure shows twenty (20) phase fields that include solid, liquid and mixed phases. Three (3) of them are single phase regions; the solid solution FCC-A1, the solid solution BCC-B2, and the liquid. There are seventeen (17) two phase co-existing fields; where five (5) of them contain a solid phase mixed with liquid, and twelve (12) fields contain two mixed solid phases. As the figure shows, the melting point of Fe is 1537.5 °C, which is very close to the known value 1538 °C [11]. While the melting temperature of Si is 1414.5 °C, which is also very close to the accepted value which is 1414.0 °C [12]. As Fig. 1 shows, pure Fe is ferrite (bcc) for T < 914.5 °C, but austenite (fcc) for 914.5 °C < T < 1392 °C. The ferrite (bcc) structure reappears at T > 1400 °C.

The solid solutions FCC-A1 and BCC-B2 are mostly Fe. FCC-A1 extends from 921.5 to 1885 °C, where the phase boundary varies in two directions with Si mole fraction; in the lower part, transition temperature increases, and in the upper part it decreases with Si mole fraction. That is, transformation temperature takes two values at each Si mole fraction in the range 0-0.033 due to the arc-shaped phase boundary. The field of the solid solution BCC-B2 extends from 0-0.3 Si mole fractions. In the region near the FCC-A1 field, the phase boundary takes the shape of an arc—as said before—which means the transition temperature also has two

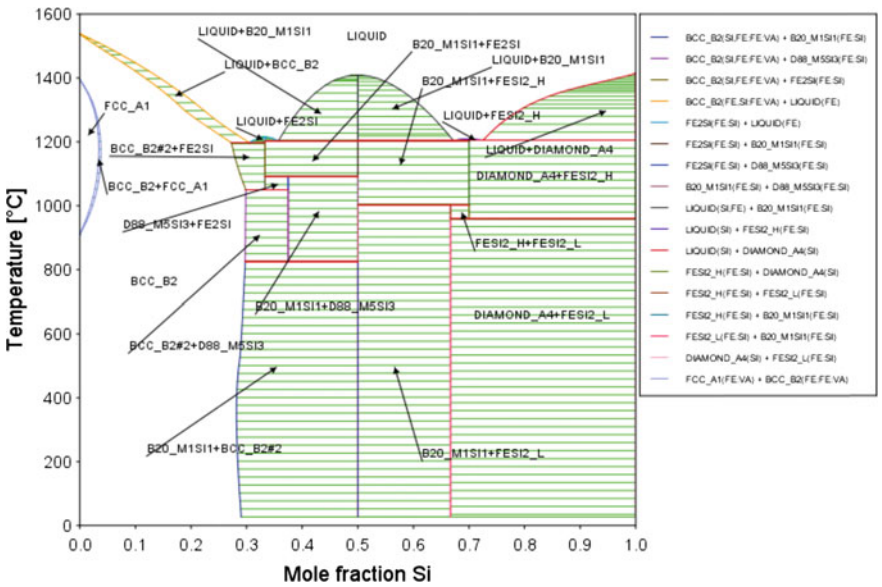

Fig. 1 Temperature- Si mole fraction percent phase diagram of the Fe–Si System

directions; increase and decrease with Si content, and it takes two values for each value of Si mole fraction. For Si mole fraction more than 0, transformation temperature drops with Si mole fraction until the point (0.27, 1197.4 °C), then it drops strongly until the point (0.30, 1050 °C) where it sharply drops to 21.3 °C. Pure liquid phase exists for T > 1202.5 °C, where the liquid consists of Fe and Si, and the ratio of Fe to Si decreases with Si mole fraction.

From the twelve (12) two solid phases co-existing fields, there are four (4) in which the BCC-B2 phase is stable. The first one is in the range 0.30–0.5 Si mole fraction between T = 26.5–825 °C and it contains the mixed phase FeSi + BCC-B2. The second field contains the mixed phase BCC-B2 + Fe_5Si_3 which is restricted in the ranges 0.3–0.37 Si mole fraction and 825–1050 °C. The third field contains the mixed phase BCC-B2 + Fe_2Si and extends in the temperature range 1050–1197.4 °C and 0.270–0.333 Si mole fraction, where the transformation temperature drops with the increase of Si content. The fourth field contains the mixed solid phase BCC + FCC and exists in a narrow arc-shaped strip that extends between 914.5 °C < T < 1400 °C and 0–0.038 Si mole fraction, where two directions of transformation temperature are found, in the lower part it increases with Si mole fraction and in the upper one it decreases with Si mole fraction.

The other eight (8) fields of two co-existing solid phases are FeSi + Fe_5Si_3 in the ranges 0. 0.375–0.50 Si mole fraction and 824.9–1091.3 °C, Fe_5Si_3 + Fe_2Si in the ranges 0.333–0.375 Si mole fraction and 1049.8–1091.3 °C, FeSi + Fe_2Si in the Si mole fraction range 0.333–0.5 and temperature range 1091.3–1202.5 °C, FeSi + $FeSi_2$-L in the region surrounded by the lines 0.5, 0.667 Si mole fractions and T = 26.9 °C, T = 1002.5 °C, $FeSi_2$-L + $FeSi_2$-H in the small region surrounded by 0.667, 0.700 Si mole fractions and T = 959.7 °C and 1002.5 °C, FeSi + $FeSi_2$-H in the region 0.50–0.7 Si mole fraction and 1002.5–1204 °C, Si-A4 + $FeSi_2$-L from 0.667–1.0 Si mole fraction and T = 26.9–959.7 °C, and $FeSi_2$-H + Si-A4 from 0.70–1.0 Si mole fraction and T = 959.7–1205.2 °C.

Figure 1 also shows five two co-existing phases where solid is mixed with liquid. The first of these phases is BCC-B2 +liquid, where this phase exists in the strip that starts at T = 0 and ends at T = 1197.5 °C in the Si mole fraction range 0.272–0.305. The second one is liquid + Fe_2Si which exists in the ranges 0.305–0.357 Si mole fraction and T = 1197.5–1214.8 °C. The third mixed phase of solid and liquid is liquid + FeSi which exists in the region 1202.6–1109.1 °C and 0.357–0.672 Si mole fraction. The fourth field of mixed solid and liquid phases contains $FeSi_2$-H + liquid, which is located in the ranges 1204.0–1207 °C and Si mole fraction 0.672–0.726. The fifth field of this set contains liquid + Si-A4 and it extends from 0.726–1.0 Si mole fraction and 1205.2–1414.6 °C. All of these phases are found for T $\geq$ 1197.4 °C, which is the minimum melting temperature, where no liquid can be found below it. It is noticed that this temperature is smaller than the melting points of pure Fe and Si. The composition at this temperature is restricted in the range 0.272–0.333 Si mole fraction.

BCC-B2 phase start to melt as a function of Si mole fraction starting from the melting temperature of Fe at Si mole fraction equals to 0.0. Then, the melting line drops with Si mole fraction to 1197.4 °C at Si mole fraction of 0.272. It continues melting at this temperature in the Si mole fraction range 0.333–0.357. The phase Fe_2Si starts to melt at the same temperature (1197.4 °C) in the range 0.357–0.672 of Si mole fraction. From 0.7–0.726 Si mole fraction, Si-A4 (diamond) starts to melt at 1205.2 °C, where the melting temperature is independent on Si content. From 0.726–1.0 Si mole fraction, the hexagonal $FeSi_2$-H phase starts to melt at T = 1205.2 °C, where the melting point is also independent on Si content. In the region 0.305–0.357 Si mole fraction the phase Fe_2Si melts completely, where the melting temperature which started at 1197.4 °C first increases with Si content and reaches maximum value of 1214.8 °C at 0.333 Si mole fractions, then decreases to 1197.4 °C with Si content until 0.357. The phase FeSi melts completely starting from T = 1214.8 °C at 0.333 Si mole fraction, then melting temperature increases with Si content, and reaches a maximum of 1409.2 °C at 0.5 Si mole fractions, then it decreases to 1204.0 °C at 0.672 Si mole fractions. Si (diamond) starts to melt at 1205.2 °C and Si mole fraction of 0.726, where melting temperature increases slowly with Si content and it reaches the melting point of pure silicon (1.0 Si mole fraction). $FeSi_2$-H phase melts completely in the ranges 0.672–0.70, where the melting temperature increases with Si content and reaches a maximum of 1208.8 °C, then decreases with Si content to reach 1205.2 at 0.726 Si mole fraction.

There are four eutectic points, where the eutectic transitions are as follows:

At 0.305 Si mole fraction and T = 1197.5 °C;

$$\text{Liquid} \leftrightharpoons BCC\_B2 + Fe_2\text{Si} \tag{1}$$

At 0.357 Si mole fraction and T = 1202.6 °C;

$$\text{Liquid} \leftrightharpoons FeSi + Fe_2\text{Si} \tag{2}$$

At 0.672 Si mole fraction and T = 1204.4 °C;

$$\text{Liquid} \leftrightharpoons FeSi + FeSi_2 \tag{3}$$

And at 0.726 Si mole fraction and T = 1205.1 °C there is an eutectic point where;

$$\text{Liquid} \leftrightharpoons FeSi_2 + Si \tag{4}$$

In addition, there are five eutectoid points, with the following transformations;

First, at about T = 825 °C and 0.298 Si mole fraction

$$BCC\_B2 \rightleftharpoons FeSi + Fe_5Si_3 \tag{5}$$

Second, at 0.299 Si mole percent and T = 1049.7 °C

$$BCC\_B2 \rightleftharpoons Fe_2Si + Fe_5Si_3 \tag{6}$$

Third, at 0.5 Si mole fraction and T = 825 °C

$$BCC\_B2 + Fe_5Si_3 \rightleftharpoons FeSi_2 \tag{7}$$

Fourth, at 0.667 Si mole fraction and T = 952.5 °C

$$FeSi \rightleftharpoons FeSi_2 - H + Si \tag{8}$$

Fifth, at 0.7 Si mole fraction and T = 1002.5 °C

$$FeSi + FeSi_2 - L \rightleftharpoons Si \tag{9}$$

Figure 2 shows the phase diagram of Fe-Si system taken from Cui S et al. [1]. Comparing Fig. 1 with Fig. 2, it is noticed that there is a good agreement between them, where most phases and temperatures were approximately the same. But there are small differences. In Fig. 1 the pure solid phases are FCC-A1 and BCC-B2, but in Fig. 2 there are three pure solid phases; FCC-A1, BCC-A2 and BCC-B2. In addition the phase Fe_3Si_7 was not observed in Fig. 1, but it exists in Fig. 2. The differences are due to differences in the experimental data used in each case.

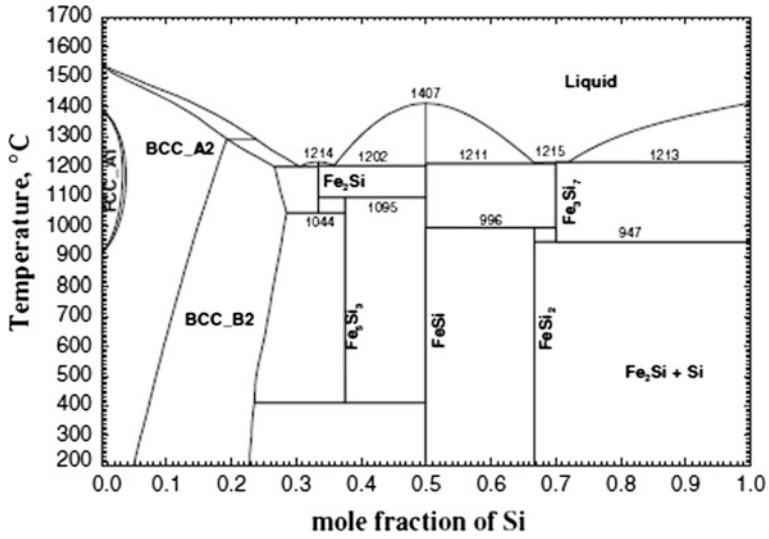

Fig. 2 Calculated phase diagram of the Fe-Si system. Reprinted after Cui S et al. [1]. Copyright © 2014. The Minerals, Metals and Materials Society and ASM International

Conclusions

Phase diagram of the Fe-Si system was calculated using thermo Calc-software. Two pure stable solid solutions were found, in addition to a pure stable liquid phase. A set of two co-existing solid phases were obtained in addition to mixed solid with liquid phases. The different phases were discussed and compared with the results obtained from the literature, and a good agreement was observed. The differences are related to differences in experimental data used in both cases to deduce the results.

References

1. Cui S, Paliwal M, Jung I-H (2014) Thermodynamic optimization of Ca-Fe-Si system and its applications to metallurgical Grade Si-refining Process. Metall Mater Trans E 1E: 68–79
2. Morita K, Miki T (2003) Thermodynamics of solar-grade-silicon refining. Intermetallics 11:1111–1117
3. Cui S, Jung I-H (2017) Critical reassessment of the Fe-Si system. Calphad 56:108–125
4. Chart TG (1970) Critical assessment of the thermodynamic properties of the system iron-silicon. High Temp High Press 2:461–470
5. Chart TG (1982) Critical assessment of thermodynamic data for the iron-silicon system. Natl Phys Lab Div Mater Appl. Teddingt, Uk 5–1:5–35
6. Kubaschewski O (1982) Iron–Binary Phase Diagrams. Springer, Berlin, pp 136–139
7. Schürmann E, Hensgen U (1980) Studies of the melting equilibria in the system iron-silicon. Arch Eisenhuettenwes 51:1–4
8. Introduction to Thermo-Calc (2017) Thermo-calc documentation set thermo-calc version 2017a, p 97. http://www.thermocalc.com/media/40962/thermo-calc-documentation-set.pdf. Accessed 26 Sept 2017
9. Boutwell BA,Thompson RG, Saunders N, Mannan SK, de Barbadillo JJ (1997) Phase formation modeling of an alloy casting using computational thermodynamics. Paper is presented at the 4th International Symposium on Superalloys and Derivatives, Pittsburgh, Pennsylvania, 15–18 June 1977
10. Introduction to Thermo-Calc (2016) http://www.thermocalc.com. Accessed 18 Sep 2016
11. Wikipedia (2017) Iron. https://en.wikipedia.org/wiki/Iron. Accessed 29 Sep 2017
12. Wikipedia (2017) Silicon https://en.wikipedia.org/wiki/Silicon. Accessed 29 Sep 2017

Crystal Growth Mechanism of Si in Hypereutectic Al–Si Melt During the Electromagnetic Directional Solidification

Jie Li, Wenzhou Yu and Xuewei Lv

Abstract An efficient enrichment of primary silicon from the Al–Si melt can be beneficial for the Si purification and the cost reduction of the solvent refining process. In this paper, an alternating magnetic field was used to enhance the mass transfer and promote the crystal growth of primary silicon during the directional solidification of hypereutectic Al–Si alloy. The results show that the growth rate and morphologies of Si crystals changed continuously along the directional solidification direction. With the decreasing of Si content in the melt and the weakness of the electromagnetic stirring, the crystal growth rate of primary silicon gradually decreased and the Si morphologies changed from plane to cellular, cellular dendrite, and columnar dendrite, respectively. This provides a deeper understanding of the Si crystal growth during the electromagnetic solidification, which will be good for achieving a high-efficiency enrichment of primary silicon in Al–Si melt.

Keywords Al–Si alloy · Electromagnetic directional solidification
Primary Si · Enrichment

Introduction

The rapid growth of photovoltaic (PV) industry has triggered a huge demand of solar-grade silicon (SOG-Si, Si purity: 99.9999%) in the past decade. Currently, SOG-Si is mainly manufactured by the modified Siemens technology, which is a high cost process along with high energy consumption and environmental impact. In order to reduce the production cost of SOG-Si, metallurgical technologies have been proposed for Si purification by removing the impurities from the metallurgical grade silicon (MG-Si, 98–99.9% purity). The traditional metallurgical methods

J. Li · W. Yu (✉) · X. Lv
College of Materials Science and Engineering, Chongqing University,
400045 Chongqing, China
e-mail: yuwenzhoucd@cqu.edu.cn

Z. Sun et al. (eds.), *Energy Technology 2018*, The Minerals, Metals & Materials Series, https://doi.org/10.1007/978-3-319-72362-4_44

usually include acid leaching [1], slag refining [2, 3], vacuum melting [4, 5], electro-beam melting [6] and directional solidification [7, 8].

Recently, a solvent refining using Al–Si melt has shown outstanding results in purifying Si more effectively and economically. Compared to traditional metallurgical routes, solvent refining with Al–Si melt can reduce costs because the refining temperatures are much lower than the Si melting point (1683 K). On the other hand, the segregation coefficient of impurities between solid Si and Al–Si melts is significantly smaller than that between solid and liquid Si, especially for B and P. Generally, the solvent refining process consists of three steps: (1) fusing the mixture of MG-Si and Al to obtain an Al–Si melt, (2) cooling the melt slowly to induce nucleation and growth of Si crystals, and (3) acid leaching to remove Al and other impurities for collecting Si crystals.

Owing to the similar densities of solid Si ($\sim$2300 kg/m^3) and Al–Si melt ($\sim$2400 kg/m^3) [9], the collection of Si crystals from the Al–Si melt is extremely difficult because the Si crystals always randomly distribute in the alloy. Acid leaching can remove Al solvent and collect Si crystals effectively; however, use of large amounts of acid will inevitably cause losses of Al and have negative impact on the environment. If the refined Si can be separated from the Al–Si melt and agglomerated at the end of the melt, the Si refining process will be more practical. Thus, to reduce the loss of Al and the amount of acid used, effective separation of primary silicon is necessary during the refining process. Recently, some researchers suggested that electromagnetic solidification could facilitate Si separation [9–11]. An electromagnetic force caused by the interaction of the magnetic field and the induced current may promote mass transfer and increase the growth rate of Si crystals. However, the continuous growth mechanism of Si crystals in the Al–Si melt under the condition of electromagnetic force has not yet been known. Thus, it is important to gain a deeper understanding of the Si crystal growth behavior; with this understanding, economical and efficient Al removal methods and Si purification technologies can be achieved.

In the present study, macro- and micro-growth behavior of Si crystals were studied to reveal the continuous growth mechanism. Additionally, the theory of constitutional supercooling was introduced to explain the growth morphologies of the Si crystals.

Experimental

30 g of hypereutectic Al-45 wt% Si alloy was prepared first by mixing of 16.5 grams high purity Al shot (99.999 wt%) and 13.5 g bulk MG-Si (99.9 wt%) in a graphite crucible. It was then placed in the middle of the induction coil of a 60 kW high frequency induction furnace for heating 30 min until the alloy melted completely. The electromagnetic directional solidification of the alloy was carried out by pulling the samples down from the induction coil at the velocity of 5 μm/s and the pulling distance is controlled at 10 cm below the initial position. During the

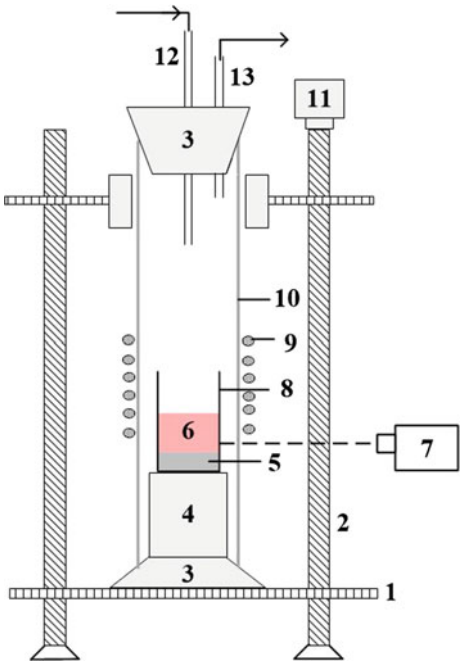

Fig. 1 Schematic of the experimental apparatus: 1. stainless steel plate, 2. ball screw, 3. silicon plug, 4. porous alumina holder, 5. primary silicon, 6.Al–Si melt, 7. infrared pyrometer, 8. graphite crucible, 9. induction coils, 10. quartz chamber, 11. stepping motor, 12. Ar inlet tube, 13. Ar outlet tube

process, the current intensity of coil was controlled at 10 A. High-purity argon gas was circulated through the system to prevent sample oxidation. The temperature of graphite crucible outer wall was determined by an infrared thermometer. A schematic diagram of the experimental setup is shown in Fig. 1.

After solidification the alloy samples were cut longitudinally to further reveal the crystal growth feature. The metallographic sections were ground using SiC paper and polished. The macrostructures and microstructures of solidified samples were respectively observed using a Sony digital camera and Olympus PME3 light optical microscope (LOM) along with a KAPA image analyzer. The mass fraction of primary Si in the enrichment zone was determined by an Image-Pro Plus image analysis software.

Results

Figure 2 shows the cross section of the Al-45 wt%Si alloy after electromagnetic directional solidification. It can be seen that the primary Si crystals are successfully enriched in the lower part of the sample and the separation interface appears clearly at the middle of the sample.

In order to further investigate the enrichment mechanism of primary Si, the microstructures at different positions in Fig. 2 are presented in Fig. 3. The distance

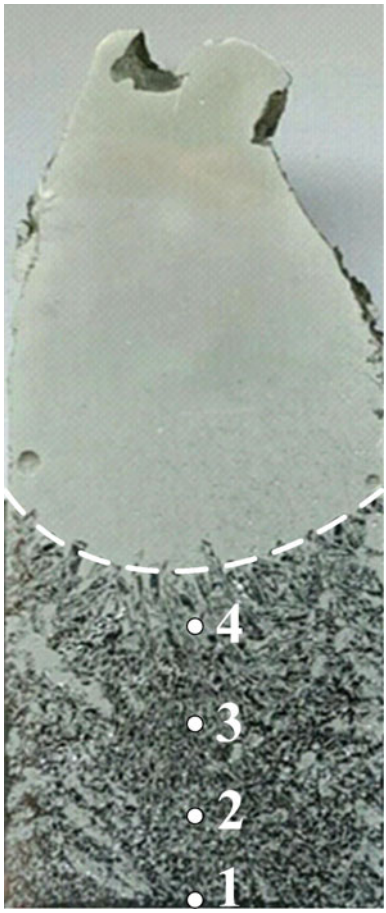

Fig. 2 Vertical section of Al-45 wt% Si alloy with a pulling rate of 5 μm/s

between two adjacent points in Fig. 2 (position 1 to position 2, position 2 to position 3 and position 3 to position 4) is 5 mm. It can be seen that the bulk Si with a thickness of about 1 mm formed at the bottom. The other positions show a gradual change from plane to cellular, cellular dendrite, and columnar dendrite, respectively, as shown in Fig. 3a–d. Additionally, the amounts of entrapped Al–Si alloy in the primary Si enrichment zone increased in the following order: Fig. 3a (position 1 in Fig. 2) < Fig. 3b (position 2 in Fig. 2) < Fig. 3c (position 3 in Fig. 2) < Fig. 3d (position 4 in Fig. 2).

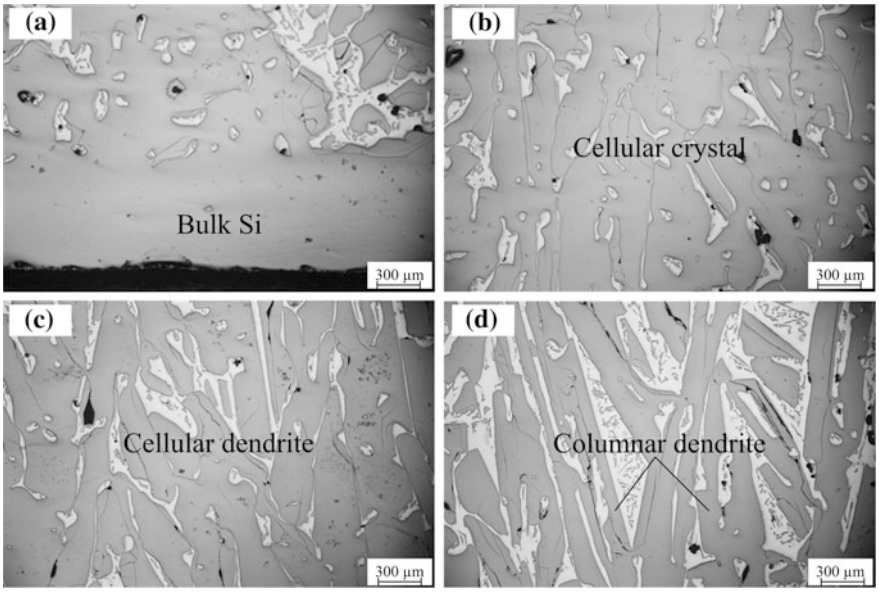

Fig. 3 Microstructures of different positions in Fig. 2: **a** position 1, **b** position 2, **c** position 3 and **d** position 4

Discussion

Enrichment Mechanism of Primary Si

The enrichment of primary Si from Al–Si alloy can be attributed to the combined effect of electromagnetic stirring and temperature gradient. Figure 4 shows a schematic diagram of the Si enrichment mechanism. In the process of electromagnetic directional solidification, the sample gradually leaves from the induction heating zone, which results in the temperature of Al–Si melt gradually decreases from the top to the bottom. As the temperature of Al–Si melt at the bottom

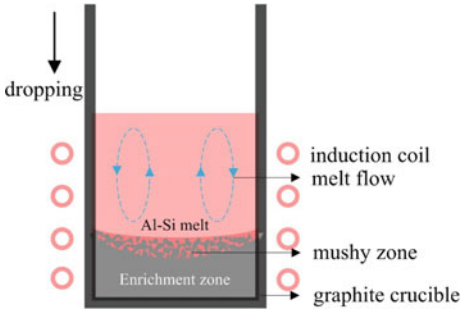

Fig. 4 Simulation diagram of Si enrichment mechanism

decreased to its liquidus temperature, the Si atom began to nucleate and grow. Simultaneously, a mushy zone formed at the front of the Si enrichment layer. With the continuous growth of primary Si, electromagnetic stirring plays an important role on the mass transfer. Under this condition, the melt flowing can be convective and the Si atoms would be homogeneous distributed in the whole melt. Thus, the concentration of Si atoms in the mushy zone is much higher than that without electromagnetic stirring. This helps to promote the continuous growth of primary Si. However, as the process continues, the concentration of Si atoms in the melt gradually decreases, which cause the Si morphology to change. Also, the Si enrichment efficiency changed. The crystal growth morphology of primary Si will be analyzed in the next section.

Crystal Growth of Primary Si

The concentration and temperature of the Al–Si melt are the two decisive factors for the growth of primary Si. Thus, it is necessary to calculate the Si atoms concentration and measure the temperature in the Al–Si melt during the solidification process.

According to the conservation of mass, the concentrate of Si atoms in the Al–Si melt expressed in Eq. (1):

$$C_{\text{Si in Al}-\text{Si melt}} = \frac{m_{\text{Si}} - m_{\text{solid Si}}}{m_{\text{Al}-\text{Si alloy}} - m_{\text{solid Si}}} \tag{1}$$

Where $C_{\text{Si in Al}-\text{Si melt}}$ is the concentration of Si atoms in Al–Si melt, m_{Si} is the initial mass of Si in Al–Si alloy, $m_{\text{solid Si}}$ is the mass of solid Si, $m_{\text{Al}-\text{Si alloy}}$ is the initial mass of Al–Si alloy. In these parameters, and $m_{\text{solid Si}}$ is the function of the height of the primary Si enrichment zone. Here, we define that the concentration of primary silicon is $f(x)$ when the height of enrichment zone is x, $m_{\text{solid Si}}$ can be represented as Eq. (2):

$$m_{\text{solid Si}} = \pi\rho r^2 \int_0^h f(x)dx \tag{2}$$

Where ρ is the density of solid Si, r is the radius of enrichment zone of primary Si, h is the height of primary Si enrichment zone, and x is the integral variable. In order to obtain the $f(x)$, the mass fraction of primary Si in the enrichment zone is measured at four different positions(as shown in Fig. 2).

Figure 5 shows the relationship between the mass fraction of primary Si and the height of enrichment zone. It is clearly seen that the mass fraction of primary Si in enrichment zone decreased with increasing height of enrichment zone. Figure 6 expresses the calculation results of mass fraction of Si atoms in Al–Si melt.

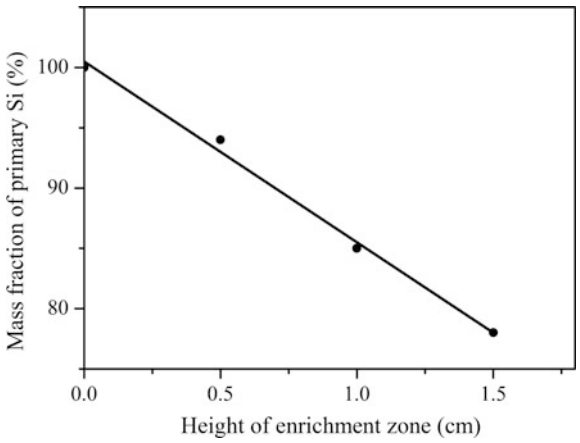

Fig. 5 Mass fraction of primary Si in enrichment zone dependence of enrichment zone height

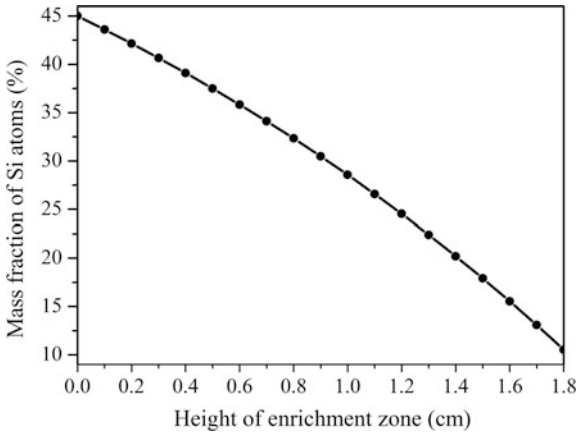

Fig. 6 Mass fraction of Si atoms in Al–Si melts dependence of enrichment zone height

The mass fraction of Si atoms in Al–Si melt decreased from 45% before solidification to 11.7% after solidification.

The melt temperature plays an important role in the enrichment of primary Si from Al–Si melt. According to the mass fraction of Si atoms in the Al–Si melt and Al–Si binary diagram [12], the liquid phase melting temperature gradient in the mushy zone can be represented as Eq. 3:

$$\frac{dT_L}{dx} = m_l \frac{dC_L}{dx} \tag{3}$$

Where T_L is the melt temperature, m_l is the liquidus slope and C_L is the mass fraction of Si atoms in melt.

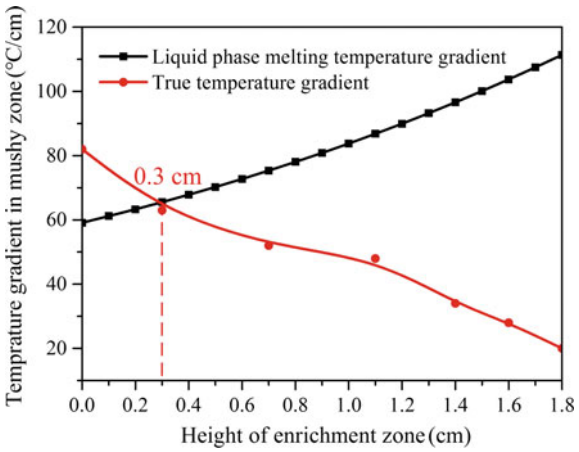

Fig. 7 Liquid phase melting temperature gradient and true temperature gradient in mushy zone under different height of enrichment zone

Figure 7 presents the calculated liquid phase melting temperature gradient and measured true temperature gradient in the mushy zone. It is surprising to see that there is an intersection point between the two curves, where the corresponding enrichment zone height is 0.3 cm. As the height of the enrichment zone is less than 0.3 cm, the liquid phase melting temperature gradients are less than the true temperature gradients in the mushy zone. Therefore, the true temperature of the melt at the front of the solid-liquid interface melt is higher than the crystallization temperature, which results in the absence of constitutional supercooling. Within this range, the morphology of the primary Si is bulk, as shown in Fig. 3a. However, the height of the bulk Si is only 0.1 cm, which is less than the theoretical height of 0.3 cm. This may be caused by a certain error between the outer wall of the crucible and the actual temperature of the melt. When the height of the enrichment zone is greater than 0.3 cm, the true temperature is lower than the crystallization temperature of melt. Therefore, the constitutional supercooling emerge at the front of the solid-liquid interface, which results in the Si morphology change from bulk to cellular, as shown in Fig. 3b. With the increasing of enrichment zone height, the degree of constitutional supercooling is more serious, by which the Si morphology changes from cellular and dendrite, as shown in Fig. 3c. The above analysis is consistent with the morphological change of primary Si in Fig. 3a–d.

Conclusions

In present work, the enrichment of primary Si was obtained from hypereutectic Al–Si alloy and the change of morphology of primary crystalline Si has been analyzed. The conclusions are summarized as follows:

(1) The enrichment of primary Si from Al–Si alloy is attributed to the temperature gradient and melt flowing.
(2) With the enrichment of primary Si, the morphology of primary Si gradual change from the plane to cellular, cellular dendrite, and columnar dendrite.

Acknowledgements This study was supported by The National Natural Science Foundation of China (No.51704053).

References

1. Dietl J (1983) Hydrometallurgical purification of metallurgical-grade silicon. Sol cells 10 (2):145–154
2. Teixeira LAV, Morita K (2009) Removal of boron from molten silicon using $CaO–SiO_2$ based slags. ISIJ Int 49(6):783–787
3. Johnston MD, Barati M (2011) Effect of slag basicity and oxygen potential on the distribution of boron and phosphorus between slag and silicon. J Non-Cryst Solids 357(3):970–975
4. Wei K, Ma W, Yang B, Liu D, Dai Y, Morita K (2011) Study on volatilization rate of silicon in multicrystalline silicon preparation from metallurgical grade silicon. Vacuum 85(7):749–754
5. Zheng S, Engh TA, Tangstad M, Luo X (2011) Numerical simulation of phosphorus removal from silicon by induction vacuum refining. Metall Mater Trans A 42(8):2214–2225
6. Yoshikawa T, Morita K (2012) An evolving method for solar-grade silicon production: solvent refining. JOM J Miner Met Mater Soc 1–6
7. Liu L, Nakano S, Kakimoto K (2008) Carbon concentration and particle precipitation during directional solidification of multicrystalline silicon for solar cells. J Cryst Growth 310 (7):2192–2197
8. Martorano MA, Neto JBF, Oliveira TS, Tsubaki TO (2011) Refining of metallurgical silicon by directional solidification. Mater Sci Eng B 176(3):217–226
9. Yoshikawa T, Morita K (2005) Refining of Si by the solidification of Si-Al melt with electromagnetic force. ISIJ Int 45(7):967–971
10. Yu W, Ma W, Lv G, Xue H, Li S, Dai Y (2014) Effect of electromagnetic stirring on the enrichment of primary silicon from Al–Si melt. J Cryst Growth 405:23–28
11. Jie J, Zou Q, Sun J, Lu Y, Wang T, Li T (2014) Separation mechanism of the primary Si phase from the hypereutectic Al–Si alloy using a rotating magnetic field during solidification. Acta Mater 72:57–66
12. Murray JL, McAlister AJ (1984) The Al-Si (aluminum-silicon) system. J Phase Equilibria 5 (1):74–84

Thermo-Calc of the Phase Diagram of Calcium Silicon (Ca–Si) System

Shadia Ikhmayies

Abstract Thermo-Calc software was used to investigate the phase diagram of the calcium silicon (Ca–Si) system for the range of Si mass percent 0–100, and temperature range T = 200–1800 K. The melting points of Ca and Si deduced from the phase diagram are very close to the values obtained experimentally. Three stable intermediate solid phases were found, which are Ca_2Si, CaSi, and $CaSi_2$, where the first one appeared in the Ca rich side of the phase diagram, and the third one in the Si rich side. In addition, three eutectic points were found at Si mass percents of 3.95, 33.00, 62, and temperatures T = 1048.7, 1519.14, 1308.5 K respectively. Atomic Si (Diamond structure) is found mixed with $CaSi_2$ intermediate phase for temperatures less than 1305 K, and mixed with a liquid CaSi for higher temperatures. These results are important for thermodynamic and metallurgic studies of these intermediate phases.

Keywords Phase diagrams · Binary systems · Calcium silicides Intermediate phases

Introduction

A great deal of research has been devoted to calcium silicides, due to the electronic and superconductive properties of some of these compounds, which make them potentially attractive in materials applications [1]. The Ca–Si system has been the object of several investigations [2–6] in order to obtain information concerning the possible existence of new calcium silicide phases and then to examine their properties as possible candidates to superconductivity [6]. Calcium silicon alloy is a compound alloy made up of elements silicon, calcium, and iron, is widely used to improve the quality, castability and machinability of steel. It is an ideal compound deoxidizer, and desulfurization agent in steel manufacturing.

S. Ikhmayies (✉)
Faculty of Science, Physics Department, Al Isra University, 11622 Amman, Jordan
e-mail: shadia_ikhmayies@yahoo.com

Z. Sun et al. (eds.), *Energy Technology 2018*, The Minerals, Metals & Materials Series, https://doi.org/10.1007/978-3-319-72362-4_45

On the whole, accurate studies on phase diagrams of the Ca-Si system are rather scarce. Manfrinetti et al. [6] experimentally investigated the Ca–Si phase diagram in the composition range 0–75 at.% Si. Wynnyckyj et al. in two papers [7, 8] reported on the measurement of calcium vapor pressure over a few calcium–silicon alloys mainly in the silicon rich side of the phase diagram (50–76at.% Si) and in the liquidus domain, and calculated the components activity. They confirmed the existence of five intermediate phases and characterized for the first time a new com pound, the Zintl-phase Ca_3Si_4. On the basis of phase diagram and thermodynamic information at the time available, Anglezio et al. [9] assessed the whole system by using the Calphad approach]. So, due to the incomplete knowledge of the phase diagram a correct attribution of vapor pressures to well define two-phase equilibria appears questionable [1], hence there is a need for more research on the phase diagrams of the Ca–Si system. The objective of this paper is to produce a phase diagram of this system using Thermo-Calc software, and to identify the intermediate in the temperature range 200–1800 K, then compare with experimental results. The three main solid silicides Ca_2Si, CaSi and $CaSi_2$ are identified and discussed in the light of experimental results found in the literature.

Methodology

Thermo-Calc software is a computational thermodynamic software that utilizes a Gibbs free energy minimization procedure to calculate phase equilibria and thermodynamic properties of a chosen system [10]. For a given set of conditions, the computer determines the free energy change for each possible combination of phases and phase compositions, and it selects the state that minimizes the total Gibbs free energy. Thermo-Calc is used in conjunction with different thermodynamic databases which contain the descriptions of the Gibbs free energies assessed using the CALPHAD approach. CALPHAD is a phase-based approach to model the underlying thermodynamics and phase equilibria of a system through a self consistent framework [11].

In this work, MAP calculations-a type of the calculations in the Thermo-Calc software–were used to calculate the equilibrium phase diagram of the Ca–Si system in the temperature range 200–1800 K. The used database is the TCBIN: TC Binary Solutions v1.1 database and the mass percent of silicon had varied from 0 to 100. The calculation type was chosen to be phase diagram.

Results and Discussion

Figure 1 displays the phase diagram of the Ca–Si system as obtained by the Thermo-Calc software, which represents the relationship between temperature and mass percent of Si in the temperature range 200–1800 K. From Fig. 1 the melting

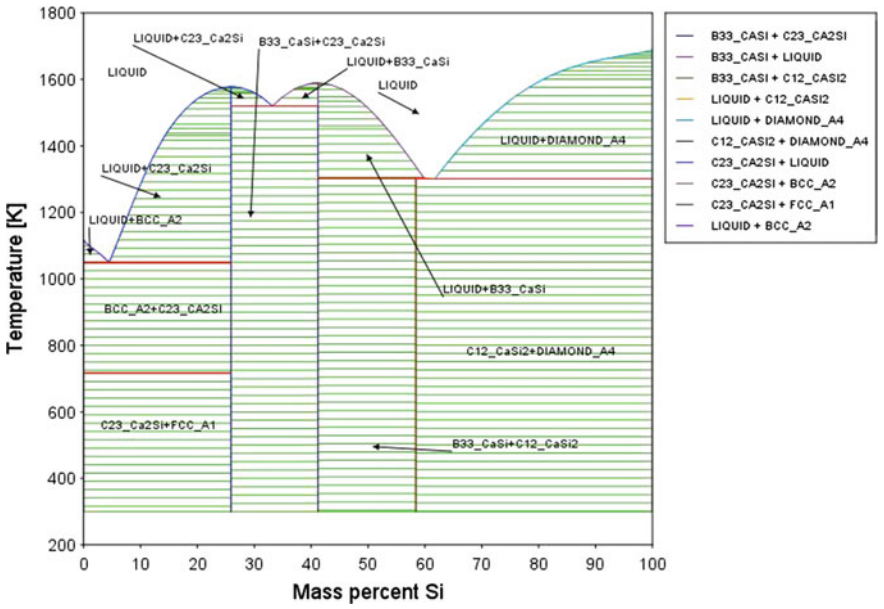

Fig. 1 Temperature against Si mass percent phase diagram of Ca–Si System

points of Ca and Si were deduced and found to be 1112.4 K (839.25 °C) for Ca, and 1683.64 K (1410.49 °C) for Si. These are very close to the accepted values ($T_{melting}$ (Ca) = 839 °C, and $T_{melting}$ (Si) = 1410 °C) [12], and to the values obtained by Manfrinetti et al. [6] who got $T_{melting}$ (Ca) = 842 °C, and $T_{melting}$ (Si) = 1414 °C as seen in Fig. 2. Also, Fig. 1 shows the presence of three intermediate stable solid phases, which are Ca_2Si ($PbCl_2$-type), CaSi (CrB type), and $CaSi_2$ ($CaSi_2$-type), where the first one appears in the Ca rich side of the phase diagram, and the third one appears in the Si rich side. But, the second phase appears mixed with the other two. Table 1 lists the crystallographic data for the intermediate phases of the Ca-Si System.

The Ca_2Si ($PbCl_2$-type) phase appears with increasing Si mass percent from 0-25 in the temperature ranges 300–725 K mixed with fcc Ca, 725–1100 K mixed with bcc Ca, and mixed with CaSi liquid for Si mass percent 4 to 25 and temperature range 1050–1560 K, where its concentration increases with temperature. This phase is also found in the Si mass percent 25–41 mixed with CaSi (CrB type) in the temperature range 300–1520 K, and mixed with liquid (CaSi) in the temperature range 1520–1560 and mass range 25–33%, where its concentration decreases with the increase of Si mass percent.

The phase CaSi (CrB type) appears first mixed with the phase Ca_2Si ($PbCl_2$-type) for Si mass percent 25–41 in the temperature range 300–1520 K-as mentioned in the previous paragraph, and mixed with (CaSi) liquid in the Si mass percent range 33–41, and T = 1514–1592 K. Then it is found first mixed with the $CaSi_2$

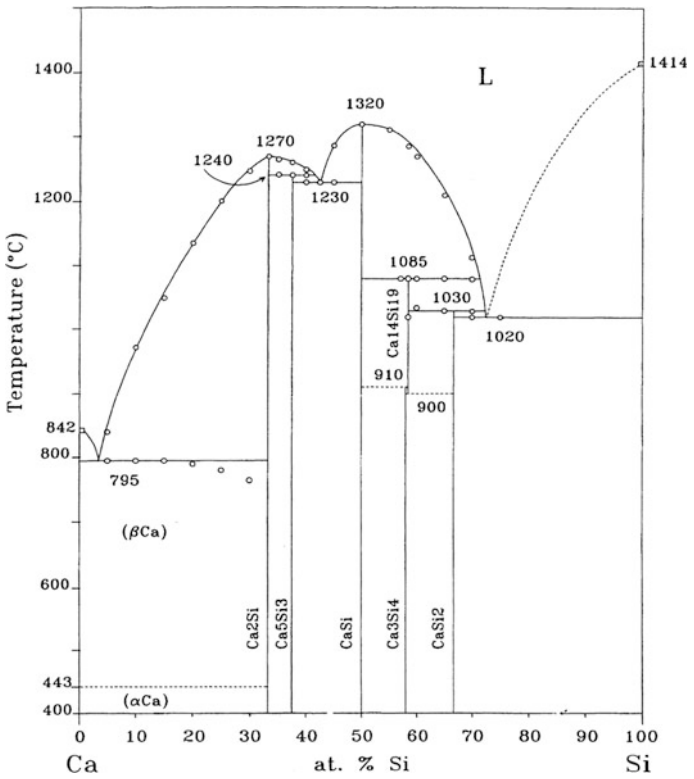

Fig. 2 Ca–Si phase diagram. Reprinted with permission from Manfrinetti et al. [6]. Copyright © 2000 Elsevier Science Ltd

Table 1 Crystallographic data for the intermediate phases of the Ca-Si System taken from reference [6]

Compound	At.% Si	Structure type	Lattice constants (pm)		
			a_0	b_0	c_0
$CaSi_2$	66.67	$CaSi_2$	386.3	–	3071.0
CaSi	50	CrB	456.1	1073.5	389.1
Ca–$_2$Si	33.33	(anti-$PbCl_2$-type)	769.1	481.6	903.5

($CaSi_2$-type) in the Si rich region 41–58 Si mass percent range and T = 300–1306 K, and second mixed with liquid CaSi in the Si mass percent range 41–60 and T = 1306–1592 K, where its concentration decreases with temperature.

The solid phase $CaSi_2$ ($CaSi_2$-type) appears in the Si rich region; first-as mentioned in the previous paragraph—mixed with CaSi (CrB type), in the Si mass percent range 41–58 and T = 300–1306 K, and second mixed with diamond Si in the Si mass percent range 58–100, and T = 300–1306 K. But as Si mass percent

increases from 62 to 100, and temperature increases from 1306 to 1691 K, the $CaSi_2$ ($CaSi_2$-type) phase disappears and a liquid of composition Si and Ca appears mixed with diamond Si, where its concentration increases with temperature until T = 1683.64 K at which Si melts.

There are six liquid domains, where the liquid phase is mixed with other solid phases as seen in Fig. 1. These domains extend in the Si mass percent range 0-100 and temperature range 1050-1691 K. The pure liquid phase- white regions in Fig. 1—is found in all Si mass percent amounts starting from the melting of Ca at 1050 K until the melting of Si at 1691 K, where all solid phases decompose to their constituents.

Comparing the phase diagram shown in Fig. 1 with that obtained experimentally by Manfrinetti et al. [6] and shown in Fig. 2, it is found that there is a good agreement between both of them. But, in this work just there are three intermediate phases, while Fig. 2 contains five intermediate phases. Manfrinetti et al. [6] got the additional phases: Ca_5Si_3, Ca_3Si_4, and $Ca_{14}Si_{19}$, where the first one is found in the Ca rich part, in the range 32–38 Si at.% and temperature range 400–1240 °C. The second one is found in the Si rich part of the phase diagram at 50–58 Si at.% and temperature range 400–910 °C. While the third one is found in the same Si atomic percent range, but for temperature range 910–1058 °C.

Three eutectics were found in the phase diagram hown in Fig. 1. The first one occurs as a result of the increase of Si mass percent that causes an eutectic reaction at Si mass percent of 3.95 and temperature 1048.7 K (775.55 °C). This is very close to the value obtained experimentally by Manfrinetti et al. [9] in this system: at about 3.5 at.% Si and 795 °C as seen in Fig. 2. The second eutectic reaction occurs at 1308.5 K (1035.35 C) and Si mass percent of 62%. While the same point in reference [6] occurs at 1020 °C and 72 at.% Si as seen in Fig. 2. The third eutectic reaction occurs at 33% Si mass percent and temperature 1519.14 K (1245.99 °C), which is comparable to that obtained by Manfrinetti et al. [6], which is 1230 °C and Si 42.5 at.%.

Conclusions

The phase diagram of the Ca-Si system was performed using thermo-Calc software in the silicon mass percent range 0–100%, and compared with an experimental one. The melting points of Ca and Si were deduced and found very close to accepted values. Three stable intermediate solid phases were found, which are; Ca_2Si, CaSi, and $CaSi_2$.Three eutectic points were found and they are comparable to those obtained experimentally. These results are important for thermodynamic and crystallographic characterization of intermediate phases of this system.

References

1. Brutti S, Ciccioli A, Balducci G, Gigli G, Manfrinetti P, Napoletano M (2001) Thermodynamic stabilities of intermediate phases in the Ca–Si system. J Alloys Comp 317–318:525–531
2. Hansen M, Anderko K (1958) Constitution of binary alloys, 2nd edn. New York: McGraw-Hill
3. Elliott RP (1969) Constitution of binary alloys (second supplement). McGraw-Hill, New York
4. Moffatt WG (1986) Handbook of binary phase diagrams, vol 2. Genium Publishing Corporation, Schenectady. New York
5. Massalski TB, Subramanian PR, Okamoto H, Kacprazak L (1990) Binary alloy phase diagrams, vol 1, 2nd edn. Materials Park, (OH) ASM International
6. Manfrinetti P, Fornasini ML, Palenzona A (2000) The phase diagram of the Ca–Si system. Intermetallics 8(3):223–228
7. Wynnyckyj JR (1972) Correlations between temperature/composition and pressure/temperature equilibrium diagrams. High Temp Sci 4:205–211
8. Wynnyckyj JR, Pidgeon LM (1971) Equilibria in the silicothermic reduction of calcined dolomite. Met Trans 2(4):979–986
9. Anglezio JC, Servant C, Ansara I (1994) Contribution to the experimental and thermodynamic assessment of the Al Ca Fe Si system-I. Al Ca Fe, Al Ca Si, Al Fe Si and Ca Fe Si systems. Calphad 18(3):273–309
10. Boutwell BA, Thompson RG, Saunders N, Mannan SK, de Barbadillo JJ (1997) Phase formation modeling of an alloy casting using computational thermodynamics. Paper is presented at the 4th International Symposium on Superalloys and Derivatives, Pittsburgh, Pennsylvania, 15–18, June 1997
11. Introduction to Thermo-Calc (2016) http://www.thermocalc.com. Accessed 18 Sep 2016
12. Bentor Y, Chemical Elements .com, Periodic Table: Melting point. http://www.chemicalelements.com/show/meltingpoint.html

Leaching of Indium from ITO Present in Amorphous Silicon Photovoltaic Modules

Pedro F. A. Prado, Jorge A. S. Tenório and Denise C. R. Espinosa

Abstract There is an increasing challenge of waste management regarding the growth of photovoltaic (PV) technology. Often overlooked by its environmental benefits of greenhouse gas emission reduction, PV technology contain metals that are highly hazardous for the environment. Amorphous silicon (a-Si) PV modules employ indium-tin-oxide as transparent conductive oxide and given the high price of indium its recovery could be advantageous from an economic perspective as well. Leaching of indium was predicted by comparing the Pourbaix diagram with the values of oxidoreduction potential and pH measured on a phosphoric acid solution. The a-Si panel was subjected to thermal treatment to remove the proprietary, protective coating and allow leaching to occur. Then, indium could be leached by phosphoric acid in a jacketed reactor, reaching a concentration of 55 ppm (67% leaching rate) with a 0.2 g/mL of a-Si panel to aqueous solution ratio. The leaching of indium with phosphoric acid is novel and could open doors for many other recycling routes for solar panels.

Keywords Indium · Leaching · Phosphoric

Introduction

Production of photovoltaic (PV) modules is growing at a fast rate, with panels reaching an amount of 50.6 GW generated in 2015 from 40 GW in 2014 [1]. However generation of solid waste by this technology is a concern projected for the

P. F. A. Prado (✉) · J. A. S. Tenório · D. C. R. Espinosa
LAREX—Department of Chemical Engineering, University of Sao Paulo,
Rua do Lago, 250, 2nd Floor, 05508-080 Sao Paulo, Brazil
e-mail: pfaprado@gmail.com

J. A. S. Tenório
e-mail: jtenorio@usp.br

D. C. R. Espinosa
e-mail: espinosa@usp.br

Z. Sun et al. (eds.), *Energy Technology 2018*, The Minerals, Metals & Materials Series, https://doi.org/10.1007/978-3-319-72362-4_46

next decades, since the lag time between production and disposal is longer when compared to other electrical and electronic equipment and the lifetime of the modules reaches 25 years. Toxic elements such as silver and indium could be released to the environment once PV waste is disposed negligently [2]. Since the ideal method for disposal is recycling, future research should encompass recycling methods for this recent new kind of electronic waste [3].

Amorphous silicon (a-Si) is a semiconductor employed in a wide range of electronics, particularly in calculators, watches and most recently, as stand-alone photovoltaic modules. The triple junction a-Si PV module is among those with highest efficiency in amorphous silicon technology, displaying three different p-i-n junctions (Fig. 1).

Each of these alloys of a-SiGe have different spectrum of light absorption. Above the triple junction, a fine coat (70 nm) of indium-tin-oxide (ITO), a transparent conducting oxide, is employed as an electrical contact to collect the electrons produced in the semiconductor material yet allowing most light to pass through [5]. Even though zinc oxide has less noble properties than ITO, it is employed as an inferior contact layer since there is no need for an optimal transparent conductor. Aluminum and zinc oxide are used to reflect photons which have not been absorbed by the semiconductor layers and avoiding diffusion of species into the

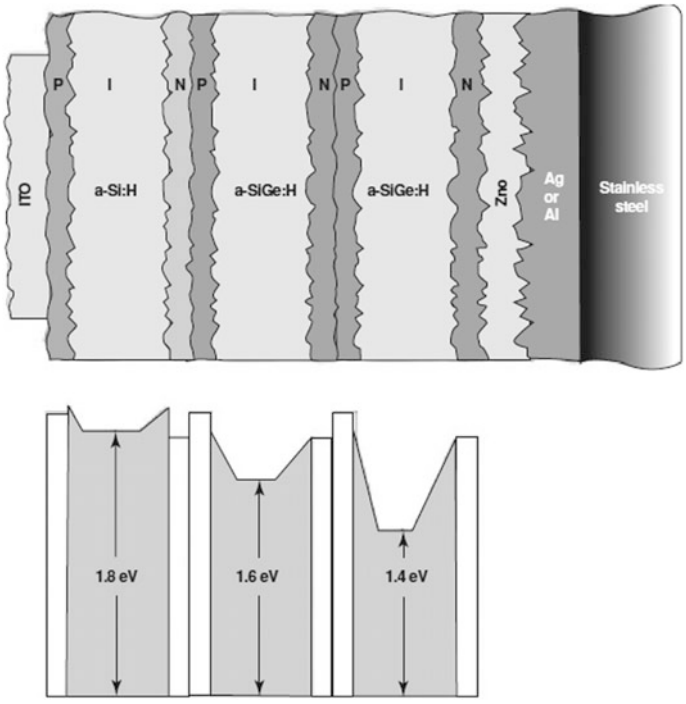

Fig. 1 Triple junction a-Si:H/a-SiGe:H/a-SiGe:H module and respective bandgaps to each semiconductor layer [4]

semiconductor. The backsheet is generally made of stainless steel, providing an unshatterable and flexible surface. A polymeric coating is generally applied to the surface of the resulting module, to protect against weathering [6].

Recovery of indium from ITO present in waste electrical and electronic equipment (WEEE) has only been reported for LCD panels, generally employing hot sulfuric acid as leaching agent [7]. Phosphoric acid is a cheaper acid and has a strong complexing effect [8]. Therefore its effectiveness for indium leaching was evaluated.

Materials and Methods

To evaluate whether phosphoric acid could be used as leaching agent for indium dissolution, the Pourbaix diagram for indium and sulfuric acid at 75 °C was built in the HSC 6.0 software with the equilibrium equations of oxidation and reduction reactions involving water (such as oxygen and hydrogen formation), phosphoric acid and indium. A 1 M phosphoric acid solution was prepared and the pH and oxidoreduction potential were measured. Comparing the values obtained with the Pourbaix diagram could indicate if the process was feasible thermodynamically.

Since a polymeric coating was located above the ITO layer, hindering the leaching of indium, it was removed by thermal treatment in an oven at 400 °C, according to [9]. The leaching solution of 1 M phosphoric acid was prepared and heated up to 75 °C in a jacketed reactor (Fig. 2).

Once the set temperature was reached and remained stable, samples of 25 cm^2 of the a-Si module were cut and fed into the reactor in a ratio of 0.2 g/mL of a-Si panel to phosphoric acid solution. A stirring rate of 800 rpm was necessary to maintain module samples fluidized. Aqueous samples were taken at every 5 min of experiment and then analyzed by inductively coupled plasma mass spectrometry (ICP-MS) in an Agilent 70 Series.

Results

The Pourbaix diagram for phosphoric acid and indium was built in the HSC 6.0 software and it is depicted in Fig. 3.

According to Fig. 3, indium is solid at very acidic (pH lower than 2) and reductive conditions (lower than—1.5 V). Some oxides are observed at pH higher than 10 and oxidative conditions (potential around 1.5 V). The conditions measured in a 1 M solution of phosphoric acid were 0.64 V oxidoreduction potential and pH 1.5. Therefore, the Pourbaix diagram supports that at these conditions indium might be leached by 1 M phosphoric acid at 75 °C. A leaching process however would only be commercially interesting once indium could be leached at a fast rate (kinetic factor).

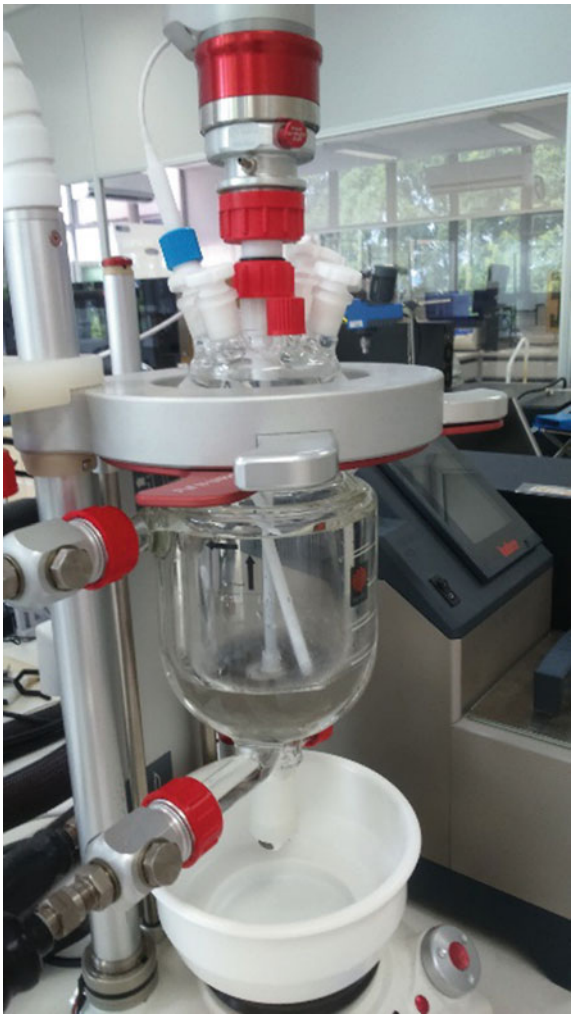

Fig. 2 Jacketed reactor used for leaching of indium from a-Si module

The leaching experiment revealed that indium could be leached with a stirring rate of 800 rpm. The a-Si module particles were effectively fluidized. A concentration of approximately 55 ppm was reached after 30 min, suggesting that 11 mg of indium was leached in 200 mL of solution (Fig. 4).

The reaction kinetics reached 20 ppm of indium by 5 min, with a leaching rate that decreased gradually up to reaching a plateau at 55 ppm. ITO layers of 70 nm are either sputtered or evaporated on a-Si cells [10] and since the density of ITO (which is 90% In_2O_3) is 7.14 g/cm^3 [11], it would be expected that 100% leaching would result in a concentration of 82 ppm under the solid-liquid ratio used. However, 55 ppm yields 67% of indium, revealing that further improvements in the experimental conditions should be targeted in the future.

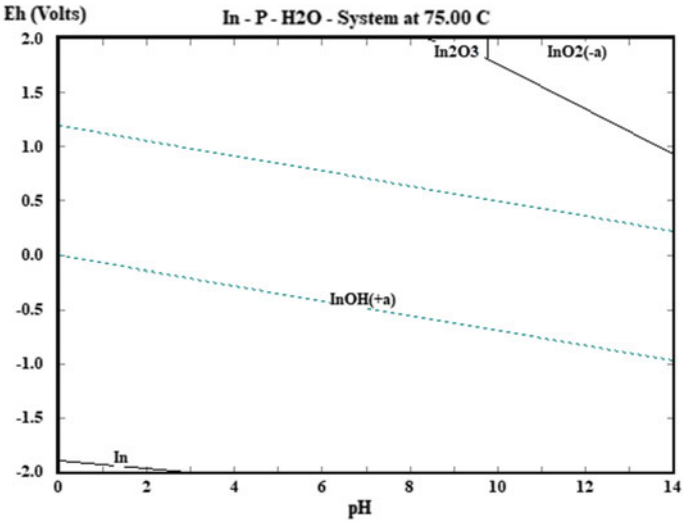

Fig. 3 Pourbaix diagram for indium in 1 M phosphoric acid at 75 °C. Dotted lines are reduction and oxidation of water. Continuous lines are equilibrium reactions involving indium and phosphoric acid

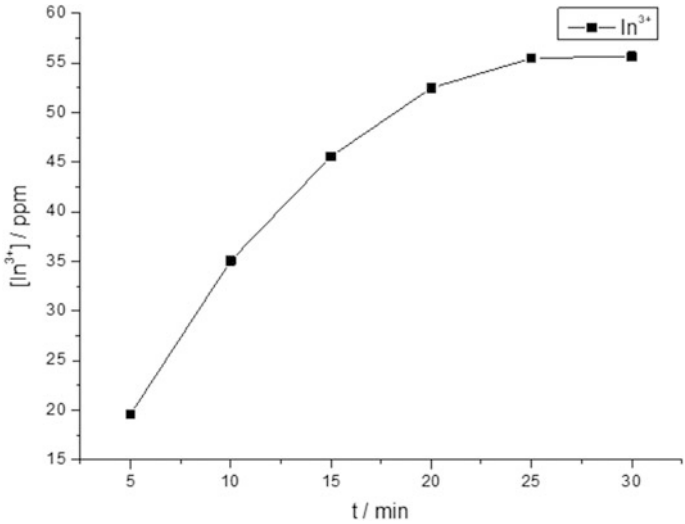

Fig. 4 Indium leaching kinetics for 1 M phosphoric acid at 75 °C and 0.2 g/mL solid-liquid ratio

Conclusion

The Pourbaix diagram revealed that was possible to leach indium with phosphoric acid, what was confirmed by the leaching results. A 1 M phosphoric acid solution at 75 °C and solid-liquid ratio of 0.2 g/mL leached indium up to a concentration of 55 ppm, representing a 67% leaching rate within 30 min.

Acknowledgements We acknowledge the support of CAPES and FAPESP (Projeto de Pesquisa 2012/51871-9).

References

1. SolarPower Europe (2015) Global market outlook 2016–2020. Accessed 25 Aug 2017
2. Kang HN, Lee Y, Kim JY, Kang S (2012) Experimental investigations for recy-cling of silicon and glass from waste photovoltaic modules. Renew Energy 47:152–159
3. Cucchiella F, D'Adamo Rosa P (2015) End-of-life of used photovoltaic modules: a financial analysis. Renew Sustain Energy Rev 47:552–561
4. Poortmans J, Arkhipov V (2006) Thin film solar cells: fabrication characterization and applications. Wiley, Amsterdam
5. Li Y, Liu Z, Li Q, Liu Z, Zeng L (2011) Recovery of indium from used indium–tin oxide (ITO) targets. Hydrometallurgy 105:207–212
6. Yan B, Yang J, Guha S (2012) Amorphous and nanocrystalline silicon thin film photovoltaic technology on flexible substrates. J Vac Sci Technol A 30:2012
7. Rocchetti L, Amato A, Beolchini F (2016) Recovery of indium from liquid crystal displays. J Clean Prod 116:299–305
8. Van der Bij HE, Cicmil D, Wang J, Meirer F, De Groot FMF, Weckhuysen BM (2014) Aluminum-phosphate binder formation in zeolites as probed with X-ray absorption microscopy. J Am Chem Soc 136:17774–17787
9. Prado PFA, Espinosa DCR (2017) Thermal treatment of flexible amorphous silicon photovoltaic modules. Int J Waste Resour 7:3
10. Xunming D, Schiff EA (2003) Amorphous silicon based solar cells. In: Luque A, Hegedus S (eds) Handbook of photovoltaic science and engineering. Wiley, Chichester, pp 505–565
11. Umicore (2017) In: Indium Tin Oxide (ITO) for deposition of transparent conductive oxide layers. http://www.thinfilmproducts.umicore.com/Products/TechnicalData/show_datenblatt_ito.pdf. Accessed 21 Sept 2017

Part IV
Materials for Energy Conversion and Storage

Direct Performance Simulation Based on the Microstructure of SOFC Electrodes: A Phase Field Approach

Yinkai Lei, Tian-Le Cheng and You-Hai Wen

Abstract A phase field model is developed to simulate the performance of SOFC electrodes. By solving the conduction equations on both the electrolyte and electrode phases, and incorporating the three-dimensional microstructure and reaction front at triple phase boundaries, the current-voltage relation of an electrode is directly simulated. By further coupling it to our recently developed coarsening model, we are able to investigate the effect of initial microstructure on the performance degradation in SOFC electrode. This model is applied to LSM-YSZ cathodes with different LSM volume fraction. The volume fraction effect on the electrode performance and its degradation rate has been analyzed and discussed.

Keywords SOFC · Coarsening · Phase field · Overpotential · Microstructure

Introduction

Solid oxide fuel cell (SOFC) is an electrochemical device with high fuel-to-electricity efficiency [1–3] and low pollutant emission [4]. It is considered as a promising candidate to achieve clean electricity generation. Operating at a relatively high temperature, e.g. 600–1000 °C [1], SOFC suffers from several degradation mechanisms

Y. Lei (✉) · T.-L. Cheng · Y.-H. Wen
U.S. DOE National Energy Technology Laboratory, Albany, OR 97321, USA
e-mail: yinkai.lei@netl.doe.gov

T.-L. Cheng
e-mail: tianle.cheng@netl.doe.gov

Y.-H. Wen
e-mail: youhai.wen@netl.doe.gov

Y. Lei
Oak Ridge Institute for Science and Education, Oak Ridge, TN 37831, USA

T.-L. Cheng
AECOM, Albany, OR 97321, USA

Z. Sun et al. (eds.), *Energy Technology 2018*, The Minerals, Metals & Materials Series, https://doi.org/10.1007/978-3-319-72362-4_47

including thermal coarsening [5], secondary phase formation [6], catalyst poisoning [7], etc. Understanding how those degradation mechanisms affect the performance of the SOFC electrode is important to improve the long term stability of SOFC.

Thermal coarsening is an important degradation mechanism in both SOFC anode and cathode which has been intensively investigated both in experiments and simulations [5, 6, 8–11]. Previous experiments show that the thermal coarsening in Ni-YSZ anode reduces the percolating volume fraction of Ni and triple phase boundary (TPB) density, which in turn increases the Ohmic and polarization resistance in anode [5, 7]. Previous phase field simulations show that both the specific surface area and TPB density decrease due to thermal coarsening, which is expected to increase the polarization resistance in cathode [10, 12]. In addition, our recent work shows that the degradation rate of the microstructure properties in SOFC electrode can be tuned by adjusting the attributes of the initial microstructure [11]. However, most of previous works on thermal coarsening are focused on the property degradation on the microstructure level, but failed to provide a direct link between the degradation of microstructure properties and the electrode performance.

There are several electrochemical models that can provide such a link between the degradation of microstructure properties and the electrode performance [9, 13–15]. The average effective microstructure properties were used as inputs in most of these electrochemical models. However, local change in microstructure is important to the degradation in SOFC electrode [16, 17], which is hard to be captured by using average effective properties. In addition, it is expected that the spatial distribution of microstructure properties would also affect the performance of SOFC electrodes. Therefore, an electrochemical model that can evaluate the electrode performance directly from its microstructure is essential to understand the link between the microstructure evolution and performance degradation in SOFC electrode.

In this work, we develop such an electrochemical model to simulate the electrode performance in SOFC. The performance of LSM-YSZ cathode with different volume fraction of LSM phase has been evaluated. Furthermore, we use our recently developed phase field model [10, 11] for coarsening to simulate the microstructure evolution, then evaluate the corresponding performance degradation in SOFC electrodes. The correlation between the microstructure property and the electrode performance has been analyzed and the effect of volume fraction on performance degradation rate has been investigated.

Methodology

Electrochemical Model

In this work, the SOFC electrode is represented by a model with an active layer in between an electrolyte layer and an electrode layer, as schemed in Fig. 1. The active layer is composed of three phases, i.e. electrolyte phase, electrode phase and pore

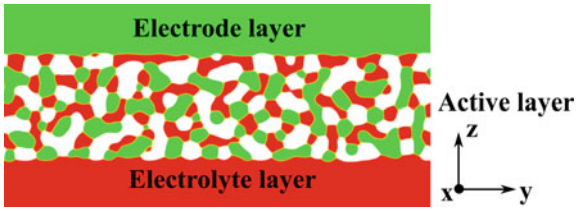

Fig. 1 The scheme of SOFC electrode in the electrochemical model

phase. The electrolyte phase is assumed to be ionic conductor while the electrode phase is assumed to be electronic conductor. The chemical reaction in the electrode is assumed to be happening on active TPB which is connected to both the electrode layer and electrolyte layer.

The transport of oxygen ions and electrons are described by the Poisson's equations, i.e.

$$\begin{aligned} \nabla \cdot [\sigma_O(\vec{r})\nabla\psi_O(\vec{r})] &= S_O(\vec{r}) \\ \nabla \cdot [\sigma_e(\vec{r})\nabla\psi_e(\vec{r})] &= S_e(\vec{r}) \end{aligned} \tag{1}$$

where $\sigma_O(\vec{r})$ and $\sigma_e(\vec{r})$ are the local conductivity of oxygen ion and electron respectively. The value of $\sigma_O(\vec{r})$ in the electrolyte phase is set to be the bulk ionic conductivity of electrolyte phase, while the value of $\sigma_e(\vec{r})$ in the electrode phase is set to be the bulk electronic conductivity of electrode phase. Both values are set to be zero elsewhere. $\psi_O(\vec{r})$ and $\psi_e(\vec{r})$ are the electrochemical potential of oxygen ion and electron respectively, i.e.

$$\begin{aligned} \psi_O(\vec{r}) &= -\frac{\mu_O(\vec{r})}{2F} + \phi(\vec{r}) \\ \psi_e(\vec{r}) &= -\frac{\mu_e(\vec{r})}{F} + \phi(\vec{r}) \end{aligned} \tag{2}$$

where $\mu_O(\vec{r})$ and $\mu_e(\vec{r})$ are the chemical potential of oxygen ion and electron respectively, and $\phi(\vec{r})$ is the electrostatic potential. The source of oxygen ion $S_O(\vec{r})$ and electron $S_e(\vec{r})$ in the active layer is non-zero only at active TPB. Their value is related to the chemical reaction at an active TPB segment by the Butler-Volmer equation, i.e.

$$S_O = -S_e \propto j_0^{TPB} l^{TPB} \left[\exp\left(\frac{\beta z F}{RT}\eta\right) - \exp\left(-\frac{(1-\beta) z F}{RT}\eta\right) \right] \tag{3}$$

where j_0^{TPB} is the exchange current per unit TPB length, l^{TPB} is the length of a TPB segment, z is the number of charge transfer in the chemical reaction at TPB, which is equal to 2 in LSM-YSZ cathode, β is the charge transfer coefficient, F and R are the Faraday constant and gas constant respectively, T is the temperature, and η is the overpotential at TPB, which is defined by [18]

$$\eta = (\psi_e^{TPB} - \psi_O^{TPB}) - \frac{\mu_O^0}{2F} - \frac{RT}{4F}\ln p_{O_2}^{Pore} \tag{4}$$

where ψ_O^{TPB} and ψ_e^{TPB} are the electrochemical potential of oxygen ion and electron at TPB respectively, μ_O^0 is the standard chemical potential of oxygen, and $p_{O_2}^{Pore}$ is the partial pressure of oxygen in pore. At the steady state, the overpotential is always negative. Therefore, we use the magnitude of overpotential in all the following discussion for convenience.

Equations (1), (3) and (4) are solved self-consistently. At iteration N, the overpotential at TPB is evaluated from $\psi_O^N(\vec{r})$ and $\psi_e^N(\vec{r})$ by Eq. (4), then the source of oxygen ion and electron is calculated by Eq. (3), which in turn are used to calculate $\psi'_O(\vec{r})$ and $\psi'_e(\vec{r})$ from Eq. (1). The $\psi_O^{N+1}(\vec{r})$ and $\psi_e^{N+1}(\vec{r})$ for the iteration $N+1$ are calculated by

$$\begin{aligned}\psi_O^{N+1}(\vec{r}) &= \lambda\psi'_O(\vec{r}) + (1-\lambda)\psi_O^N(\vec{r}) \\ \psi_e^{N+1}(\vec{r}) &= \lambda\psi'_e(\vec{r}) + (1-\lambda)\psi_e^N(\vec{r})\end{aligned} \tag{5}$$

where λ is the mixing constant that affects the convergence of the iterations. The simulation is stopped when the changes in $\psi_O(\vec{r})$ and $\psi_e(\vec{r})$ between two iterations are less than a predefined accuracy. Because the solution of Eq. (1) can be differing by an arbitrary constant field, it is essential to shift $\psi_O^{TPB}(\vec{r})$ and $\psi_e^{TPB}(\vec{r})$ at each step before evaluate the overpotential at TPB. In this work, the shift is determined by requiring the electrostatic potential difference between the electrode layer and electrolyte layer to be equal to IR_{ext}, where I is the total current in the electrode, and R_{ext} is a given external resistance. Using Eq. (2), this shift becomes

$$\psi_e^{electrode} = \psi_O^{electrolyte} + IR_{ext} - E^{Nernst} + \frac{\mu_O^0}{2F} + \frac{RT}{4F}\ln p_{O_2}^{Pore} \tag{6}$$

where E^{Nernst} is the Nernst potential between the electrode and electrolyte phase, which can be estimated from the equilibrium oxygen vacancy concentration in the electrode and electrolyte phase, i.e.

$$E^{Nernst} = \frac{\Delta\mu_V}{2F} + \frac{RT}{2F}\ln\frac{c_v^{electrolyte}}{c_v^{electrode}} \tag{7}$$

where $\Delta\mu_V$ is the difference between the chemical potential of oxygen vacancy in the electrolyte and electrode phase. The parameters used in this work are given in Table 1.

In this work, the microstructure is discretized on a cubic mesh with edge unit length of Δl. As a result, TPB is discretized into segments of length Δl. There are four unit cells surrounding a TPB segment. The average value of ψ_O over all electrolyte unit cells and ψ_e over all electrode unit cells surrounding a TPB segment

Table 1 The parameters used in electrochemical simulations

β	0.5
j_0^{TPB}(A/m) [19]	1.3×10^{-5}
μ_O^0(kJ/mol) [20]	−144.3
$p_{O_2}^{Pore}$(atm)	0.2
$c_v^{electrolyte}$(8%YSZ)	0.08
$c_v^{electrode}$(LSM) [21]	5×10^{-9}
$\Delta\mu_V$(kJ/mol) [22]	−7.7
T (°C)	1000
σ_O^{YSZ}(S/m) [23]	11.54
σ_e^{LSM}(S/m) [24]	8000

are used to calculate the local difference between ψ_O^{TPB} and ψ_e^{TPB}. The source terms S_O and S_e are assigned to the unit cells surrounding the TPB segments with a strength of

$$S = \frac{j_0^{TPB}}{n(\Delta l)^2}\left[\exp\left(\frac{\beta zF}{RT}\eta\right) - \exp\left(-\frac{(1-\beta)zF}{RT}\eta\right)\right] \tag{8}$$

where n is the number of electrode or electrolyte unit cells surrounding the TPB segment. To keep the electrode charge neutral, a uniform drain of oxygen ion and electron has been added to the boundary of electrolyte and electrode layer respectively with the total strength equal to that of the TPB sources but with opposite sign. The whole electrode is modeled on a mesh with 128 × 128 × 136 mesh points, in which the size of the electrolyte, electrode and active layer is 128 × 128 × 4, 128 × 128 × 4, and 128 × 128 × 128 respectively. The edge length Δl is set to 0.1 μm. The iterative solver developed by Eyre and Milton [25] is implemented to solve Eq. (1), which is efficient in current work given the huge conductivity contrast between LSM and YSZ/Pore. A vacuum layer of size 128 × 128 × 136 points is added on top of the simulation cell to satisfy the periodic boundary condition required to apply this solver.

Phase Field Simulation

Our recently developed phase field model is used to simulate the microstructure evolution in the active layer [10, 11]. In this model, the three-phase active layer is described by two types of order parameters, i.e. the composition order parameter (COP) C_i and grain order parameter (GOP) η_j^i. The COP represents the phase fraction of each phase, and the GOP represents the grains in the solid phases. The free energy of the system is assumed to be a functional of COPs and GOPs, i.e.

$$F(\{C_i\},\{\eta_j^i\}) = \int \left[f_0(\{C_i\},\{\eta_j^i\}) + \sum_{i=1}^{2}\sum_{j=1}^{M_i} \frac{\kappa_\eta^{ij}}{2}(\nabla\eta_j^i)^2 + \sum_{i=1}^{2}\sum_{j=i}^{2} \frac{\kappa_C^{ij}}{2}(\nabla C_i \cdot \nabla C_j)^2 \right] d\boldsymbol{v} \tag{9}$$

where κ_η^{ij} and κ_C^{ij} are the gradient energy coefficients. The bulk free energy density $f_0\left(\{C_i\},\left\{\eta_j^i\right\}\right)$ is defined as

$$\begin{aligned} f_0(\{C_i\},\{\eta_j^i\}) = &\sum_{i=1}^{2}\rho_i f_1(C_i) + \rho_{12} f_1(C_1+C_2) + \sum_{i=1}^{2}\chi_i\left[f_2(C_i) + \sum_{j=1}^{M_i} f_3(C_i,\eta_j^i)\right] \\ &+ \sum_{i=1}^{2}\sum_{j=1}^{M_i}\sum_{k=j+1}^{M_i} \varepsilon_{jk}^i f_4(\eta_j^i,\eta_k^i) \end{aligned} \tag{10}$$

where

$$\begin{aligned} f_1(C) &= C^2(1-C)^2 \\ f_2(C) &= \frac{1}{4}C^4 \\ f_3(C,\eta) &= -\frac{1}{2}C^2(2\eta^3-\eta^4) + \frac{1}{4}\eta^4 \\ f_4(\eta_j,\eta_k) &= \frac{1}{2}(\eta_j)^2(\eta_k)^2 \end{aligned} \tag{11}$$

These functions are chosen so that $f_0(\{C_i\},\{\eta_j^i\})$ has three degenerate local minima which correspond to three phases in the SOFC electrode. The value of the energetic parameters ρ_i, ρ_{12}, χ_i and ε_{jk}^i, and the gradient energy coefficient κ_η^{ij} and κ_C^{ij} are tuned to match the interfacial energy of the LSM-YSZ material system.

The governing equations of the evolution of COPs and GOPs are the Cahn-Hilliard equation and the time-dependent Ginzburg-Landau equation respectively, i.e.

$$\frac{\partial C_i}{\partial t} = \nabla\cdot\left[M_C^i\nabla\left(\frac{\partial f_0}{\partial C_i} - \sum_{j=1}^{2}\kappa_C^{ij}\nabla^2 C_j\right)\right] \tag{12}$$

$$\frac{\partial \eta_j^i}{\partial t} = -M_\eta^{ij}\left(\frac{\partial f_0}{\partial \eta_j^i} - \kappa_\eta^{ij}\nabla^2\eta_j^i\right) \tag{13}$$

where M_C^i and M_η^{ij} are the mobility of COPs and GOPs respectively. M_C^i is related to the atomic diffusivity, and M_η^{ij} is related to the grain boundary (GB) mobility in one

phase. In this work, M_C^i and M_η^{ij} are set to match the bulk diffusivity of Mn ion and the GB mobility in LSM phase at 1000 °C respectively [10]. A detailed discussion on energetic parameters and the mobility has been given in Ref. [10].

DREAM.3D [26] is used in this work to generate initial microstructure of the active layer in LSM-YSZ cathode. The initial average grain size and standard deviation of grain size in the active layer are set to 0.53 μm and 0.13 μm respectively for all phases. To investigate the effect of LSM volume fraction, we create three cathode models with the volume fraction of LSM (YSZ) to be 25% (45%), 35% (35%) and 45% (25%) while keeping the porosity to be 30%. The microstructure evolution in the active layer is simulated up to 150 h.

Results

Performance Degradation in the Cathode with 35%LSM

The microstructures in the cathode with 35% LSM at 0 and 150 h are given in Fig. 2a. The increase in the grain size of LSM can be seen clearly. The current-voltage and power density curve of the corresponding cathode at different time step are given in Fig. 2b. It shows that the electrode performance consistently degrades with time. The overpotential at current density 1 A/cm^2 increases from 0.42 to 0.44 V while the maximum power density decreases from 0.96 to 0.88 W/cm^2 after 150 h, as shown in Fig. 3a.

The time evolution of the overpotential at current density 1 A/cm^2 and the maximum power density of the cathode is given in Fig. 3a. It shows that the degradation is fastest in the first 50 h then it gradually slows down. This is consistent with the time evolution of the average LSM grain radius which increases by 1.37 μm in the first 50 h but only by 0.86 μm in the last 100 h. The correlation between the TPB density in the cathode and its performance is given in Fig. 3b.

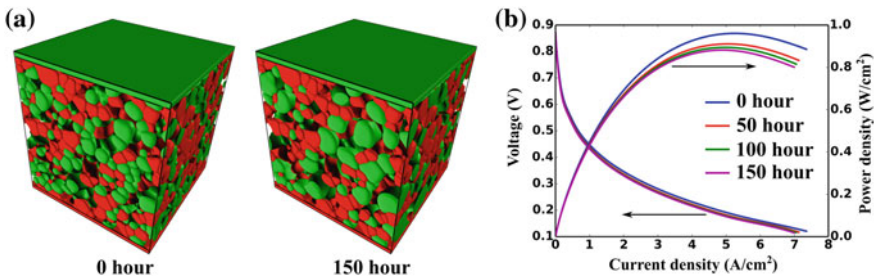

Fig. 2 **a** The microstructure of the cathode with 35% LSM at 0 and 150 h. The red and green phases are YSZ and LSM respectively. **b** The current-voltage and power density curve at different time step

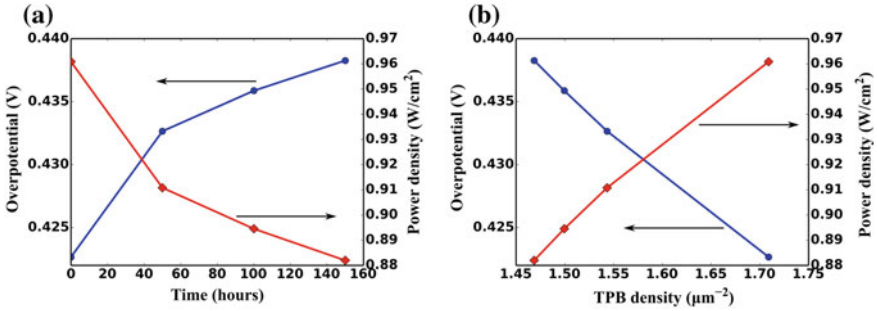

Fig. 3 **a** The time evolution of overpotential at 1 A/cm2 and maximum power density. **b** The correlation between TPB density and the cathode performance

A very good linear correlation can be seen, which suggests that the reduction of TPB density is responsible for the performance degradation in cathode.

Volume Fraction Effect

The current-voltage and power density curve for the cathodes with 3 different LSM volume fraction at 0 h are given in Fig. 4a. It shows that the electrode performance worsens as the volume fraction of LSM increases. The maximum power density of the cathode decreases by 0.55 W/cm^2 and the overpotential at current density 1 A/cm^2 increases by 0.06 V as the volume fraction of LSM increases from 25 to 45%. Similar trend has been observed at 50, 100 and 150 h as well. To further understand this effect of LSM volume fraction, the activation and resistance overpotential of the cathode are given in Fig. 4b. The activation overpotential of the cathode is calculated by Eq. (4), whereas ψ_e^{TPB} and ψ_O^{TPB} are the average electrochemical

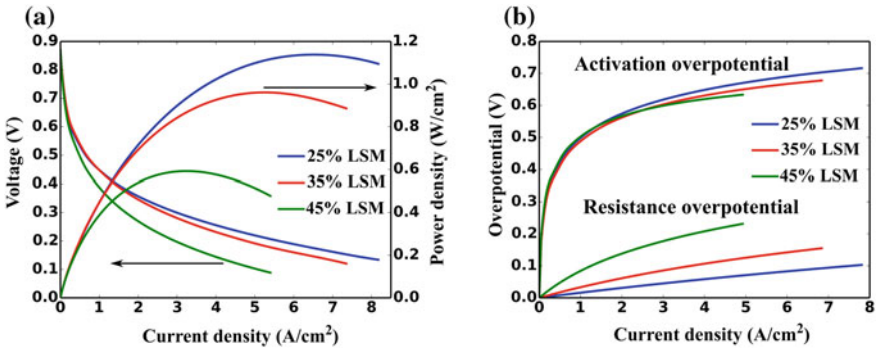

Fig. 4 **a** The current-voltage and power density curve, and **b** the activation and resistance overpotential for the cathode with 25% LSM, 35% LSM and 45% LSM at 0 h

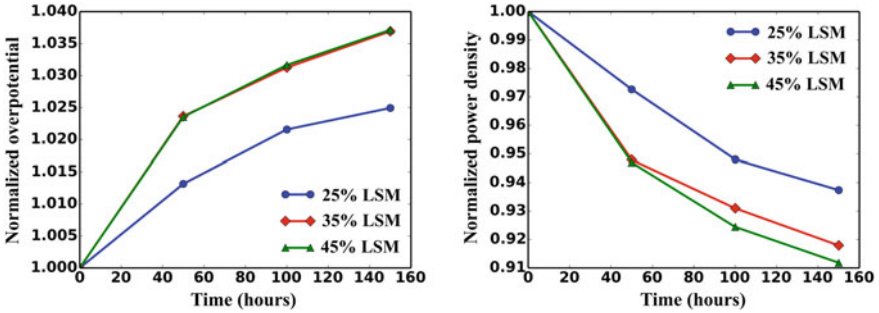

Fig. 5 The time evolution of the normalized overpotential at current density 1 A/cm^2 (left) and the normalized maximum power density (right) in the cathode with 25% LSM, 35% LSM and 45% LSM

potential of electron and oxygen over all TPBs. The resistance overpotential of the cathode is calculated by the summation of the resistance overpotential in both YSZ and LSM phase, which are in turn determined by the difference between the average ψ_e and ψ_O at TPBs and electrolyte/electrode layer in the YSZ and LSM phase respectively. Figure 4b shows that the activation overpotential in all three cathodes are similar while the resistance overpotential significantly increases as the LSM volume fraction increases. Since the resistance overpotential is mainly contributed by the YSZ phase due to its relatively small conductivity comparing to LSM phase, Fig. 4b clearly demonstrates that the slow ionic transport in YSZ has an important role in determining the electrode performance.

The time evolution of the overpotential at current density 1 A/cm^2 and the maximum power density in the cathodes with three different LSM volume fractions are given in Fig. 5. In order to compare the degradation rate in all three cathodes, both the overpotential and maximum power density are normalized by the corresponding property at 0 h. Interestingly, Fig. 5 shows that the LSM volume fraction has significant effect on the degradation rate of cathode performance only when it is less than a certain critical volume fraction, e.g. 35%. Below such critical volume fraction, the degradation rate of the cathode performance reduces as the volume fraction of LSM decreases. But increasing the LSM volume fraction over the critical volume fraction would not significantly increase the degradation rate of cathode performance.

Conclusions

In this work, we developed an electrochemical model that evaluates the electrode performance directly from the three dimensional microstructure of SOFC electrode. We applied this model to three cathode with 25% LSM, 35% LSM and 45% LSM respectively and found that the performance of the cathode improves as the LSM

volume fraction decreases. Furthermore, we coupled this electrochemical model to our recently developed phase field model to simulate the performance degradation in LSM-YSZ cathode. We found that the performance degradation in cathode is well correlated with the TPB density reduction due to coarsening and the LSM volume fraction has significant effect on the degradation rate of cathode only when it is below a critical volume fraction.

Acknowledgements The authors are grateful to Drs. Kirk Gerdes, Gregory Hackett, Harry Abernathy, Thomas Kalapos, William Epting, Jerry Mason and Jason Vielma (NETL) for valuable discussions. This project is supported in part by an appointment to the Internship/Research Participation Program at the National Energy Technology Laboratory, U.S. Department of Energy, administered by the Oak Ridge Institute for Science and Education.

References

1. Ding D, Li X, Lai SY, Gerdes K, Liu M (2014) Energy Environ Sci 7:552–575
2. Singhal SC (2014) Wiley interdisciplinary reviews: energy and environment. Energy Environ 3:179–194
3. Mahato N, Banerjee A, Gupta A, Omar S, Balani K (2015) Prog Mater Sci 72:141–337
4. Choudhury A, Chandra H, Arora A (2013) Renew Sustainable Energy Rev 20:430–442
5. Holzer L, Iwanschitz B, Hocker Th, Munch B, Prestat M, Wiedenmann D, Vogt U, Holtappels P, Sfeir J, Mai A, Graule Th (2011) J Power Sources 196:1279–1294
6. Liu Y, Thyden K, Chen M, Hagen A (2012) Solid State Ionics 206:97–103
7. Yokokawa H, Tu H, Iwanschitz B, Mai A (2008) J Power Sources 182:400–412
8. Kennouche D, Chen-Wiegart Y-CK, Riscoe C, Wang J, Barnett SA (2016) J Power Sources 307:604–612
9. Abdeljawad F, Volker B, Davis R, McMeeking RM, Haataja M (2014) J Power Sources 250:319–331
10. Lei Y, Cheng T-L, Wen Y-H (2017) J Power Sources 345:275–289
11. Lei Y, Cheng T-L, Wen Y-H (2017) J Electrochem Soc 164:F3073–F3082
12. Li Q, Liang L, Gerdes K, Chen L-Q (2012) Appl Phys Lett 101:033909
13. Kim YT, Jiao Z, Shikazono N (2017) J Power Sources 342:787–795
14. Mason J, Celik I, Lee S, Abernathy H, Hackett G (2017) ECS Trans 78:2323–2336
15. Hsu T, Mahbub R, Epting WK, Abernathy H, Hackett GA, Rollett AD, Lister S, Salvador PA (2017) ECS Trans 78:2711–2722
16. Liu YL, Hagen A, Barfod R, Chen M, Wang HJ, Poulsen FW, Hendriksen PV (2009) Solid State Ionics 180:1298–1304
17. Wang S, Cruse TA, Krumpelt M, Ingram BJ, Salvador PA (2011) J Electrochem Soc 158: B152–B158

18. Matsuzaki K, Shikazono N, Kasagi N (2011) J Power Sources 196:3073–3082
19. Miyoshi K, Miyamae T, Iwai H, Saito M, Kishimoto M, Yoshida H (2016) J Power Sources 315:63–69
20. M.W. Chase Jr., NIST-JANAF Themochemical Tables, Fourth Edition, *J. Phys. Chem. Ref. Data, Monograph*, **9**, 1–1951 (1998)
21. Gong M, Gemmen RS, Liu X (2012) J Power Sources 201:204–218
22. Hong L, Hu J-M, Gerdes K, Chen L-Q (2015) J Power Sources 287:396–400
23. Badwal SPS (1984) J Mater Sci 19:1767–1776
24. McCarthy B, Pederson L, Chou Y, Zhou X-D, Surdoval W, Wilson L (2008) J Power Sources 180:294–300
25. Eyre DJ, Milton GW (1999) Euro Phys J Appl Phys 6:41–47
26. Groeber MA, Jackson MA (2014) Integrating Mater Manufacturing Innovation 3:1–17

Effect of Sonication Power on Al_2O_3 Coated $LiNi_{0.5}Mn_{0.3}Co_{0.2}O_2$ Cathode Material for LIB

Dila Sivlin and Ozgul Keles

Abstract Lithium ion batteries are potential energy source of next generation electric vehicles (EVs). However, some problems such as safety, durability, low capacity, cycle life etc. restrict their use in EVs. These problems mostly related with cathode materials, an improvement in cathode materials may cause significant changes in battery performance. In this work, to overcome cycle life problem Al_2O_3 coating on $LiNi_{0.5}Mn_{0.3}Co_{0.2}O_2$ cathode material produced by sol—gel method. The surface modification of $LiNi_{0.5}Mn_{0.3}Co_{0.2}O_2$ was started by adding $LiNi_{0.5}Mn_{0.3}Co_{0.2}O_2$ powders into alumina sol. Then, sonication was started and two different sonication powers were tested (45, 100%). After the second gel is obtained, last heat treatment for Al_2O_3 crystallization was done at 600 °C for 4 h. X—ray diffraction (XRD) measurements showed that the material had a well—ordered layered structure and Al was not in the $LiNi_{0.5}Mn_{0.3}Co_{0.2}O_2$. Al_2O_3 coated materials show better cycling performance compared to the pristine material. It is believed that, this improvement is caused by the fact that Al_2O_3 layer prevents direct contact between active material and electrolyte and reducing decomposition reactions.

Keywords Surface modification · NMC cathode materials · Al_2O_3 coating Lithium ion batteries

Introduction

With the increasing demand for clean energies, the high efficient, high capacity and long life energy storage devices are broadly needed and investigated [1]. Compared to other energy storage devices lithium ion batteries are the most preferred devices in terms of storage higher energy in per unit weigh and volume and design flexibility [2, 3]. Due to these properties lithium ion batteries are widely used in electronic

D. Sivlin · O. Keles (✉)
Department of Metallurgical and Materials Engineering,
Istanbul Technical University, 34469 Maslak, Istanbul, Turkey
e-mail: ozgulkeles@itu.edu.tr

Z. Sun et al. (eds.), *Energy Technology 2018*, The Minerals, Metals & Materials Series, https://doi.org/10.1007/978-3-319-72362-4_48

applications such as smart phones, laptops etc. [4]. However, some problems restrict their usage in high energy applications such as hybrid electric vehicles (HEVs) and electric vehicles (EVs), these are safety, cost, capacity fading and cycle life [5]. To overcome these problems cathode materials which are key component of the batteries and determine its quality are extensively investigated [6]. $LiCoO_2$ one of the layered structure cathode material has been widely used as cathode materials in commercial applications [9]. However; this cathode material can not meet the requirements for high energy applications since, although its theoretical capacity is 274 mAh/g, the practical capacity in applications approximately 150 mAh/g by charging up to 4.2 V [9, 10]. When charge cut-off voltage increases more than 4.2 V crystal structure deteriorated because of phase transformation and the battery shows weak electrochemical performance results from microcracks formed by [24]. Among all cathode materials NMC's ($LiNi_{1-x-y}Mn_xCo_yO_2$) are mostly studied materials due to their high discharge capacity, high rate capability and good structural stability [7]. However, despite these promising advantages, NMC cathodes have several drawbacks that restrict their usage in high energy required applications [8]. One of these restrictions is that NMC cathode materials show undesireable irreversible capacity loss during first charge—discharge [11]. Lu et al. claimed that this irreversible capacity loss is related with the loss of oxygen from the crystal lattice [12]. Also, Choi et al. claimed that owing to an overlap of the metal: 3d band with the top of the oxygen:2p band, layered oxide cathode materials tend to loose oxygen from the lattice at deep charge and result in a huge capacity loss [16]. Another restriction is that when $LiPF_6$ which is the key component of electrolyte decomposes in the existence of moisture, one of the product is HF that leads to transition metal dissolution in electrolytes resulting surface corrosion of cathode material [13]. In addition, Ni^{4+} ion is easily dissolved into the electrolyte at high voltages. The reactions between cathode materials and electrolytes decreases capacity and cyclic performance of the battery [10]. To overcome these problems, one of the approaches is coating of active material surface with electrochemically inactive metal oxides, phosphates and fluorides [14]. Surface modification can prevent the reactions between electrolytes and cathode materials and can reduce the oxygen activity of the cathode at high voltages [10, 15]. Among the surface modifiers metal oxides are the most preferred materials in order to provide better protection than the others [17]. Various coatings, such as ZrO_2, ZnO, TiO_2, $LiAlO_2$ and Al_2O_3 have been applied on several cathodes however; Al_2O_3 stands forward among the other metal oxides, due to its abundance, low cost and the ease of coating [18, 19]. In addition, it is reported that Al_2O_3 coating reduces capacity difference between first charge and discharge and cathode surface corrosion [20]. When all these advantages are taken into consideration Al_2O_3 is chosen as a surface modifier for this study.

In this work, $LiNi_{0.5}Mn_{0.3}Co_{0.2}O_2$ cathode material was produced by sol—gel method and Al_2O_3 coating was applied by dispersing the alumina source in the water using ultrasonic stirrer with 45% (NMC-45) and 100% (NMC-100) sonication power. The aim of the study is investigating the effect of sonication power on alumina distribution on the $LiNi_{0.5}Mn_{0.3}Co_{0.2}O_2$ cathode materials and investigating cathode performance.

Experimental

Layered $LiNi_{0.5}Mn_{0.3}Co_{0.2}O_2$ was synthesized by sol—gel method using citric acid as a chelating agent. Stoichiometric amounts of lithium acetate (Alfa Aesar), nickel acetate (Alfa Aesar), manganese acetate (Alfa Aesar) and cobalt acetate (Alfa Aesar) were dissolved in distilled water and mixed with citric acid. Metal/acid ratio was kept at 1/2. The pH value was adjusted to 8–9 by addition of 30% ammonia solution. The solution was stirred at 80 °C for 4 h to obtain green viscous gel. The gel was dried at 120 °C for 24 h. The dried powder was precalcined at 500 °C for 7 h to eliminate the organic substances then, the powder calcined at 900 °C for 12 h to obtain crystalline $LiNi_{0.5}Mn_{0.3}Co_{0.2}O_2$ cathode material.

To produce Al_2O_3 coating on $LiNi_{0.5}Mn_{0.3}Co_{0.2}O_2$ powders, $Al(NO_3).9H_2O$ (Alfa Aesar) was dissolved in distilled water and stirred by ultrasonic stirrer (Hielscher–UP200Ht) 5 min (water and the $Al(NO_3).9H_2O$ with the weight ratio was kept at 200:1). Then, active material was slowly added into the solutions with the $Al(NO_3).9H_2O$ content of 0.5 wt% and stirred 5 min with the sonication power of 45 and 100%. X-ray diffraction patterns for the sample was recorded using Rigaku with Cu K_α radiation. It was operated at 40 kV in the 2θ range of 10–80° in the continuous scan mode 0.02 with step size $3^o\ min^{-1}$. Scanning electron microscope (FESEM; JSM 7000 F, JEOL Ltd.) was used to observe particle morphology of the powders.

The electrodes were fabricated from 80:10:10 (wt%) mixture of active material, polyvinylidene difluoride (PVDF) as binder and carbon black as conductor. The PVDF was dissolved in N-methylpyrrolidione (NMP) and conductor added and stirred 45 min then active material was added and stirred 12 h. Obtained slurry was coated on aluminum foil which is used as a current collector and dried overnight at 120 °C.

Standard 2032 coin cells were assembled in an argon filled glove box ($O_2 < 0.\ 01$ ppm, $H_2O < 0.\ 01$ ppm) in order to test the electrochemical properties of the cathode material. Lithium foil was used as a reference electrode, 1 M $LiPF_6$ in EC: DMC (1:1 in volume) used as electrolyte, and a polypropylene micro-porous film (Cellgard 2300) as a separator. The galvanostatic tests were performed between 3.0–4.5 V on the Neware battery test system.

Results and Discussion

Figure 1 shows the XRD patterns of the pristine $LiNi_{0.5}Mn_{0.3}Co_{0.2}O_2$ pristine NMC, NMC-45 and NMC-100, respectively. It is observed that all samples have a layered structure. Also, all the peaks can be identified clearly indicating that the samples are well crystallized. No impurity peak observed in the XRD patterns of the coated materials. This shows that Al_2O_3 coating do not change the crystal structure of the cathode material [10]. The intesity ratio of (003) and (104) planes shows the

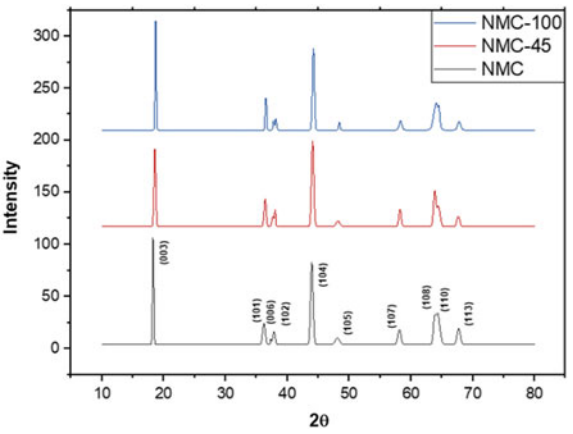

Fig. 1 XRD patterns of the samples

degree of cation mixing which is the results of partial occupation of Ni^{2+} lattice sites by Li^{+} ions [21, 22]. When this ratio is higher than 1.2, the degree of cation mixing is lower and materials show better electrochemical performances [23]. I_{003}/I_{104} intesity ratio calculated for the NMC, NMC-45 and NMC-100 are 1.324, 1.325 and 1.333, respectively. Also, R factor ($R = (I_{006} + I_{102})/I_{101}$) that is, the intesity ratio of the doublet peaks which show the hexagonal characteristic of the material, is calculated for all samples and the values are found to be 0.4782, 0.4596 and 0.444 for NMC, NMC-45 and NMC-100, respectively. When this ratio is higher than 0.5, it is expected that materials could show weak electrochemical performance [10, 25].

The SEM images of the samples are given in Fig. 2. All particles are 200–300 nm in size and have cornes. Particles with and without surface modification have similar morphologies. With the help of EDS analyses, the stoichiometric ratios are given in Table 1. It is clear that all samples are produced in expected ratios. A slight difference is observed in aluminum content in Table 1. NMC-100 sample contains more Al than the other sample.

Galvanostatic performances of the cathode materials with and without surface modification are given in Fig. 3. First discharge capacities of the samples are calculated as 178.28, 130.22 and 141.34 mAh/g for pristine NMC, NMC-45 and

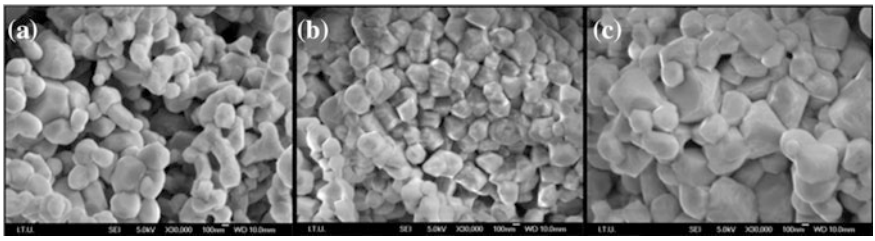

Fig. 2 SEM images of the Samples **a** NMC **b** NMC-45 **c** NMC-100

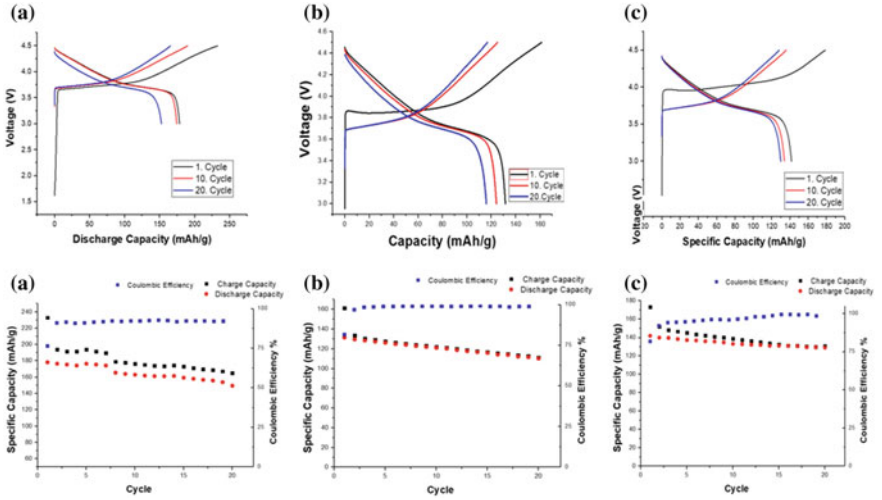

Fig. 3 Specific capacity and cycle profiles of the samples **a** Pristine **b** NMC-45 **c** NMC-100

Table 1 EDS analysis of the samples

	Ni	Mn	Co	Al	O
NMC	0.504	0.286	0.197	–	1.941
NMC-45	0.506	0.308	0.214	0.408	1.945
NMC-100	0.516	0.328	0.208	0.541	1.949

NMC-100, respectively. The discharge capacity difference among samples can be explained with Al_2O_3 modification assumed to be on the surface of the particle which may lead to change Li diffusion during lithiation. Chen et al. [10] claimed that Al_2O_3 coating layer acts as a barrier for Li^+ ions diffusion and prevent intercalation/deintercalation of Li^+ ions from the active material. NMC-45 sample shows the lowest discharge capacity and this could be a result of non- uniform alumina on the cathode material. On the other hand, NMC-100 sample shows slightly better first discharge capacity. This difference between coated samples could result from the sonication power. When the solution stirred fast, the alumina could be distributed more homogeneously resulting thinner protective layer on the cathode surface. After 20 cycles the discharge capacities of the samples are calculated to be 149.50, 110.24 and 129.17 and the capacity retentions 83.83%, 84.65% and 91.38% for pristine NMC, NMC-45 and NMC-100, respectively. It is clear that even though first discharge capacities are lower than pristine material, the surface modified samples show better capacity retention. Kim et al. [9] found that Al_2O_3 coated material shows lower discharge capacity than the pristine material. The surface modified sample has 89.1% capacity retention and 93.9% coulombic efficiency. After 20 cycles coulombic efficiencies of the samples are found to be 91.95, 99.01 and 99.56% for pristine, NMC-45 and NMC-100. The first charge and

Table 2 First discharge and charge capacities of the samples

Sample code	First charge capacity (mAh/g)	First discharge capacity (mAh/g)	Difference (mAh/g)
NMC	232.9	178.28	54.62
NMC-45	161.16	130.22	30.94
NMC-100	173.33	141.34	31.99

discharge capacities of the samples are given in Table 2. The pristine sample has the highest first charge and discharge capacity difference. On the other hand, surface modified samples show rather small differences in first discharge and charge capacities. This could be a result of surface modification. Liu et al. [26] claimed that Al_2O_3 layer may prevent the oxygen loss from the crystal structure also prevents side reactions and makes the structure more stable.

Conclusions

In this work, $LiNi_{0.5}Mn_{0.3}Co_{0.2}O_2$ cathode material was produced by sol—gel method. Al_2O_3 was chosen as a surface modifier and coated on $LiNi_{0.5}Mn_{0.3}Co_{0.2}O_2$ cathode material by using ultrasonic stirrer. No impurity phase observed. The particles are 200–300 nm size and have corners. NMC-100 sample contains more Al and this could result from the sonication power. The first discharge capacities of the samples are 178.28, 130.22 and 141.34 and coulombic efficiencies are found to be 91.95, 99.01 and 99.56% for pristine, NMC-45 and NMC-100 samples respectively. Surface modification increases coulombic efficiency. Also, the first charge and discharge capacities differences of the samples are calculated as 54.62, 30.94 and 31.99 for pristine, NMC-45 and NMC-100 respectively. We think that slight difference between the first charge and discharge capacities is resulted from surface modification. Coating reduces the oxygen loss from the crystal structure and make the structure more stable.

Acknowledgements The authors thank Prof. Dr. Sebahattin Gürmen and Prof. Dr. Gültekin Göller for their contributions to the study; Barış Yavaş, Şerzat Safaltın and Hüseyin Sezer for their help in accomplishing the SEM, XRD and EDS analyses.

References

1. Wang Q, Tian N, Xu K, Han L, Zhang J, Zhang W, Guo S, You C (2016) A facile method of improving the high rate cycling performance of LiNi1/3Co1/3Mn1/3O2 cathode material. J Alloys Compd 686:267–272
2. Manthiram A (2011) Materials challenges and opportunities of lithium ion batteries. J Phys Chem Lett 2(3):176–184

3. Tarascon JM, Armand M (2001) Issues and challenges facing rechargeable lithium batteries. Nature 414:359–367
4. Hu SK, Cheng GH, Cheng MY, Hwang BJ, Santhanam R (2009) Cycle life improvement of ZrO2-coated spherical LiNi1/3Co1/3Mn1/3O2 cathode. J Power Sources 188(2):564–569
5. Huang Y, Chen J, Ni J, Zhou H, Zhang X (2009) A modified ZrO2-coating process to improve electrochemical performance of Li(Ni1/3Co1/3Mn1/3)O2. J Power Sources 188 (2):538–545
6. Yan J, Liu X, Li B (2014) Recent progress in Li-rich layered oxides as cathode materials for Li-ion batteries. RSC Adv 4:63268–63284
7. Li D, Kato Y, Kobayakawa K, Noguchi H, Sato Y (2006) Preparation and electrochemical characteristics of LiNi1/3Mn1/3Co1/3O2 coated with metal oxides coating. J Power Sources 160(2):1342–1348
8. Croy JR, Gallagher KG, Balasubramanian M, Long BR, Thackeray MM (2014) Quantifying Hysteresis and Voltage Fade in xLi2MnO3•(1-x)LiMn0.5Ni0.5O2 Electrodes as a Function of Li2MnO3 Content. J Electro chem Soc 161(3):A318–A325
9. Kim Y, Kim HS, Martin SW (2006) Synthesis and electrochemical characteristics of Al2O3-coated LiNi1/3Co1/3Mn1/3O2 cathode materials for lithium ion batteries. Electrochim Acta 52(3):1316–1322
10. Chen Y, Zhang Y, Wang F, Wang Z, Zhang Q (2014) Improve the structure and electrochemical performance of LiNiCoMnO2 cathode material by nano Al2O3 ultrasonic coating. J Alloys Compd 611:135–141
11. Wu Y, Manthiram A (2006) High capacity, surface-modified layered LiLi, 1 − x…/3Mn, 2 − x…/3Nix/3Cox/3O2 cathodes with low irreversible capacity loss. Electrochem Solid State Lett 9(5):A221–A224
12. Lu Z, Dahn JR (2002) Understanding the anomalous capacity of $Li[Ni_xLi_{(1/3-2X/3)}Mn_{(2/3-x/3)}O_2$ cells using in situ X-ray diffraction and electrochemical studies. J Electrochem Soc 147(7): A815–A822
13. Chen Z, Qin Y, Amine K, Sun YK (2010) Role of surface coating on cathode materials for lithium-ion batteries. J Mater Chem 20:7606–7612
14. Hao S, Wolverton C (2013) lithium transport in amorphous Al2O3 and AlF3 for discovery of battery coatings. J Phys Chem C 117(16):8009–8013
15. Huang Y, Chen J, Cheng F, Wan W, Liu W, Zhou H, Zhang X (2010) A modified Al2O3 coating process to enhance the electrochemical performance of Li(Ni1/3Co1/3Mn1/3)O2 and its comparison with traditional Al2O3 coating process. J Power Sources 195(24):8267–8274
16. Choi J, Manthiram A (2005) Investigation of the irreversible capacity loss in the layered LiNi1/3Mn1/3Co1/3O2 cathodes. Electrochem Solid State Lett 8(8), C102–C105
17. Bhuvaneswari D, Babu G, Kalaiselvi N (2013) Effect of surface modifiers in improving the electrochemical behavior of LiNi0.4Mn0.4Co0.2O2 cathode. Electrochim Acta 109:684–693
18. Riley LA, Atta SV, Cavanagh AS, Yan Y, George SM, Liu P, Dillon AC, Lee SH (2011) Electrochemical effects of ALD surface modification on combustion synthesized LiNi1/ 3Mn1/3Co1/3O2 as a layered-cathode material. J Power Sources 196(6):3317–3324
19. Yuan X, Xu QJ, Liu X, Liu H, Min Y, Xia Y (2016) Layered cathode material with improved cycle performance and capacity by surface anchoring of TiO2 nanoparticles for Li-ion batteries. Electrochim Acta 213:648–654
20. Wu Y, Manthiram A (2007) Effect of Al3+ and F− doping on the irreversible oxygen loss from layered Li[Li0.17Mn0.58Ni0.25]O2 Cathodes. Electrochem Solid- State Lett 10(8), A151–A154
21. Choi YM, Pyun S, Moon SI (1996) Effects of cation mixing on the electrochemical lithium ktercalation reaction into porous $Li_{1-\delta}Ni_{1-}yCo_yO_2$ electrodes. Solid State Ionics 89(1–2): 43–52
22. Shim JH, Kim CY, Cho SW, Missiul A, Kim JK, Ahn YJ, Lee S (2014) Effects of heat-treatment atmosphere on electrochemical performances of Ni-rich mixed-metal oxide (LiNi0.80Co0.15Mn0.05O2) as a cathode material for lithium ion battery. Electrochim Acta 138:15–21

23. Wang T, Liu ZH, Fan L, Han Y, Tang X (2008) Synthesis optimization of Li1 + x[Mn0.45Co0.40Ni0.15]O2 with different spherical sizes via co-precipitation. Powder Technol 187(2):124–129
24. Kim Y, Kim HS, Martin SW (2006) Synthesis and electrochemical characteristics of Al2O3-coated LiNi1/3Co1/3Mn1/3O2 cathode materials for lithium ion batteries. Electrochim Acta 52(3):1316–1322
25. Kong JZ, Zhai HF, Ren C, Gao MY, Zhang X, Li H, Li JX, Tang Z, Zhou F (2013) Synthesis and electrochemical performance of macroporous LiNi0.5Co0.2Mn0.3O2 by a modified sol–gel method. J Alloys Compd 577:507–510
26. Liu J, Manthiram A (2009) Functional surface modifications of a high capacity layered Li $[Li_{0.2}Mn_{0.54}Ni_{0.13}Co_{0.13}]O_2$ cathode. J Matem Chem 20:3961–3967

Effect of Nano-Graphite Dispersion on the Thermal Solar Selective Absorbance of Polymeric-Based Coating Material

Iman S. El-Mahallawi, Ahmed A. Abdel-Rehim, N. Khattab, Nadia H. Rafat and Hussein Badr

Abstract The basic part of solar water heaters is the collector and the main functional part of the collector is the absorber layer. In this work, a commercial locally available black painting (PACEN code 10382 colour 890), used for swimming pools solar heating, was modified by adding nano-graphite dispersion. The effect of nano-graphite particles percentage on the spectral absorbance of the material was examined on samples containing two values of 1.5 and 2.5% nano-graphite particles by weight. Fourier transform spectroscopy (FTIR) analysis was also used to identify the functional groups in the developed material. A simple experimental setup was designed to evaluate the performance of the developed nanodispersed selective coating polymeric based material, by measuring the increase in temperature of circulating water. It was shown that adding 1.5–2.5% nano-graphite particles to a polymer based black coating causes an increase in the optical absorptance, and an increase in the circulating water temperature.

Keywords Solar heaters · Selective absorber · Nano-graphite particles Polyurethanes composites · Polymer coating

I. S. El-Mahallawi (✉) · N. H. Rafat · H. Badr
Faculty of Engineering, Department of Metallurgical Engineering, Cairo University, Giza 12316, Egypt
e-mail: ielmahallawi@bue.edu.eg

N. H. Rafat
e-mail: nhrafat@hotmail.com

H. Badr
e-mail: husseinbadr93@gmail.com

I. S. El-Mahallawi · A. A. Abdel-Rehim
Centre for Renewable Energy, British University in Egypt, Cairo 11837, Egypt
e-mail: Ahmed.Azim@bue.edu.eg

A. A. Abdel-Rehim
Shoubra Faculty of Engineering, Benha University, Cairo 11629, Egypt

N. Khattab
National Research Centre NRC, Cairo 12622, Egypt
e-mail: nag_khb@yahoo.com

Z. Sun et al. (eds.), *Energy Technology 2018*, The Minerals, Metals & Materials Series, https://doi.org/10.1007/978-3-319-72362-4_49

Impact Statement

Adding 1.5–2.5% nano-graphite particles to a polymer based black coating causes an increase in the optical absorptance, providing an economic alternative for selective solar coatings

Introduction

Solar water heaters are widely used in the domestic sector where the demand temperature is low, for provision of hot water to residents. A solar thermal system consists of many components: a collector, a heat storage unit, pumps, sensors and control instruments. The basic part of the system is the collector and the main functional part of the collector is the absorber layer, which is protected by a transparent cover. The absorber converts short-wave radiation into thermal energy (photo-thermal conversion) and it must be temperature resistant (up to 200 ºC). The most important material requirement for selecting the absorber layer is based on its surface emission ε, absorbance *a*, and transmittance, which are functions of the wavelength of the radiation, as well as the recipient material.

Selective surfaces combine a high absorptance for radiation with a low emittance for the temperature range in which the surface emits radiation. This combination of surface characteristics is possible because 98% of the energy in incoming solar radiation is contained within wavelengths below 3 μm, whereas 99% of the radiation emitted by black or gray surfaces at 400 K is at wavelengths longer than 3 μm. Almost all black selective surfaces are generally applied on a metal base (copper or aluminium), which provides low emittance for thermal radiation and simultaneously good heat transfer characteristics for photo thermal applications [2, 3]. Previous studies showed that the performance of solar thermal absorber can be improved by change of absorber materials and coating thickness [2–4].

The efficiency of any solar absorber depends on its ability to transform incident solar radiation into thermal energy. Materials used for thermal solar panels must be capable of absorbing, storing and transmitting energy from the sun to a transport medium (generally water or water-based fluid coolant) with minimum thermal losses. Consequently, for this application, one must use materials of high absorptivity ($\alpha > 0.95$) and low emissivity ($\varepsilon < 0.10$). In addition, as thermal transmission is usually by conduction, good thermal conductivity for such materials is necessary. Selective coatings take advantage of the differing wavelengths of incident high irradiance solar radiation and the infrared emissive radiation. In some low-temperature flat-plate collectors, black coating may be simply used as the absorber material. Black coatings are mostly prepared by liquid phase deposition or vapor phase deposition. Black nickel and black chromium are the most important electrodeposited materials whereas the films elaborated by vapor phase deposition include mainly titanium alloys and carbon based materials.

The ideal spectrally selective surface should be of low-cost, easy to manufacture and chemically and thermally stable in air at the operational temperatures. By means of a special mixture of coating as well as the surface structure, heat radiation can be reduced. The absorbance of the collector surface for shortwave solar radiation depends on the nature and color of the coating and on the incident angle [5].

Interest is growing on developing spectrally selective paint coatings which are regarded as a cheap alternative to currently available sophisticated surface treatments. Earlier attempts have been made to replace the expensive oxide selective absorber coatings by cheaper lightweight collector surfaces made by polymers [6, 7]. It has been shown [7] that using cheap thermoplastic materials for selective absorber coated with dispersions of inorganic colorant particles retain considerable radiation selectivity, though the actual composition of the materials was kept confidential. Compared to metals, polymers are known to possess low thermal conductivity (0.17–0.23 $Wm^{-1}\ K^{-1}$) and relatively high specific heat capacity (polyethylene 1800 $J\ kg^{-1}\ K^{-1}$). Those properties, combined with lightweight and low cost, have persuaded solar water heater designers to use polymers as low-cost alternative materials for solar thermal conversion applications [6–10]. However, the low thermal conductivity is a crucial drawback of polymers. It has been shown by previous work that photo-thermal and electrical properties of materials are changed by adding gold and platinum nanoparticles [11–17].

Though, the nanocarbon group (nano-graphite, nanotubes, etc.) are known for high thermal conductivity [18, 19], no previous work is found in literature to show the effect of adding nano sized carbon based particles (nano-graphite or carbon nanotubes) to polymers to enhance their spectral selective properties. Previous work by the authors [13] has illustrated the effect of adding carbon multi-walled nanotubes to a host matrix of polyvinyl alcohol, at different testing conditions, where a gain in temperature of the circulated water between 8 and 15 °C was achieved. Carbon nanotubes possess attractive thermal conductivity properties (an average thermal conductivity of 6600 $Wm^{-1}\ K^{-1}$ was reported [20]) compared to 1900 $Wm^{-1}\ K^{-1}$ for graphite [21]. The structure of a nanotube is similar to that of graphite, with the difference that the sheets are closed to form a tube or a cylinder with a small diameter tending to have a polygonal cross section as the diameter increases [20].

This idea of this work is to enhance the thermal conductivity of commercial economic polymer based black coating material (initially developed to be used for heating swimming pools) by introducing nano-graphite particles to the slurry. Nano-graphite is selected in this work because it possesses high conductivity combined with its economy and ease of preparation. At this stage, proof of concept on the laboratory scale was targetted, which will open the door for improved collector efficiencies and more economic products. The effect of nano graphite on both the emittance and water heating capacity during summer and winter will be examined in this work.

Materials and Methods

In this work a polymer based selective absorber coating was prepared by adding 1% nano-graphite particles to a commercial black coating (PACEN code 10382 colour 890) used for thermal solar absorptance in Egyptian market. Material and performance characterization are carried out. A prototype thermal solar collector was built (Fig. 1) to evaluate the performance of the developed selective absorber coating, where the copper serpentine was coated with the new material, the thickness of the coating was about 100 μm.

The effect of nano-graphite particles percentage on the spectral absorbance of the material was examined on samples containing two values of 1.5 and 2.5% nano-graphite particles by weight. The commercial coating is manufactured by a local manufacturer in Egypt (Paints and Chemical Industries) and is coded as PACEN code 10382 color 890. The nano-graphite particles were purchased in micro scale, and they were ground to the nanosize at the Central Metallurgical Research and Development Institute (CMRDI) [22]. The size of particles was in the average range (50-70) nm. The nano-graphite particles used have properties of 2.27 g/cm^3 mass density, 960 MPa ultimate tensile strength, 3500 °C melting temperature and 150 GPa Young's modulus.

A V-570 Spectrophotometer from Jasco Company Japan was used to record the intensity of the transmitted light resulting from three samples without and with 1.5 and 2.5% nano-grpahite dispersion in the commercial black coating. A hydrogen lamp generated light with wavelength of 220–2000 nm and a silicon photodiode was used to record the transmitted light. Fourier transform spectroscopy (FTIR) analysis was also used to identify the functional groups in the developed material. Hydrogen Magnetic Resonance Test (HNMR) was also made.

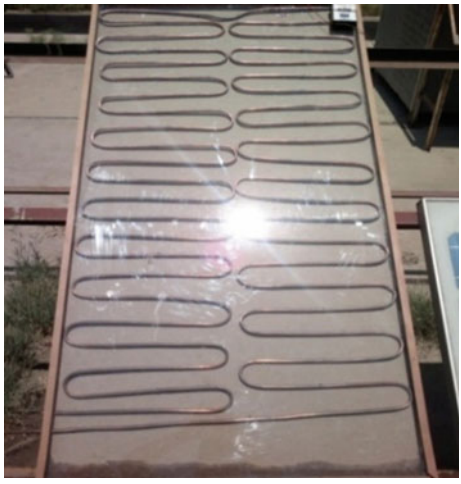

Fig. 1 Proto-type Cu serpentine collector

The test was designed to simply rely on measuring the difference in temperature of inlet and outlet water, using T type thermocouples. The water flow rates were selected to be in the range of 0.4–1.0 L/min. The tests were done at the National Research Centre, Giza, Egypt during June 2012 and Feb 2014 between. The tests were run twice daily on two days, first between 11:45 AM and 12:45 PM, and then between 12:45 and 01:45 PM. It is worth mentioning that both inlet and outlet water temperatures were measured initially at the start of the test, simultaneously, after the water was forced into the system.

Results and Discussion

The results obtained from the spectrophotometry test are shown in Fig. 2, from which it is seen that the material with 2.5% nano-graphite has the highest absorbance. This effect is attributed to the beneficial effect of the nano-graphite particles on enhancing the absorbance of the polymer black paint. Addition of fine inorganic metal powders in heat absorbing coatings was shown to enhance the temperature rise in a given interval of time [7, 11], and was attributed to rendering the coating more optically selective and to enhancing its absorbance efficiency, thus, enhancing the solar to thermal conversion efficiency. The specific effect of nano-graphite is attributed to its high thermal conductivity due to strong C–C covalent bonds and phonon scattering, its black color that allows solar energy absorbance over a broad range of solar spectrum, as well as the high surface area to volume ratio [19].

FTIR of purchased commercial polymer is shown in Fig. 3. the absorption peak observed at 3443.28 cm^{-1} is characteristic of N-H stretching vibration. The second peak observed at 2927.41 cm^{-1} is due to symmetric stretching vibration of CH_2 group. Another important peaks of 1726.26 cm^{-1} and 1652.7 cm^{-1} is observed to originate the presence of stretching vibrations of hydrogen bonded carbonyl group (−C = O) in a urethane group. The other peak observed at 1952.7 cm^{-1} is also characteristic of stretching vibrations of carbonyl group but may originating the usage of amides as chain extender for polyurethane. These amides chain extenders are used for polyurethane thermal and environmental properties enhancement. These functional groups originating that the commercial polymer is amid chain extender polyurethane. The addition of nano-garphite particles introduces no further different bonds to the fabricated composite as it is inherent material to its hosting matrix.

Figure 4 shows a sample of the measured temperatures for the three systems tested at the National Research Centre: bare Copper tubes, black coated copper tubes, and black coated with nano-graphite copper tubes. The first three figures (a, b and c) show the results obtained during summer 2012, whereas the figure (d) shows the results for winter 2014. It can be seen from Fig. 4a (wind speed 12 km/hr) that the inlet temperature is 33 °C at the beginning and reaches the maximum of 39 °C at 12:15 PM during the first hour between 11:45 AM to 12:45 PM with flow rate 0.47 L/min. It is also noted that the outlet temperature was 39 °C at the beginning

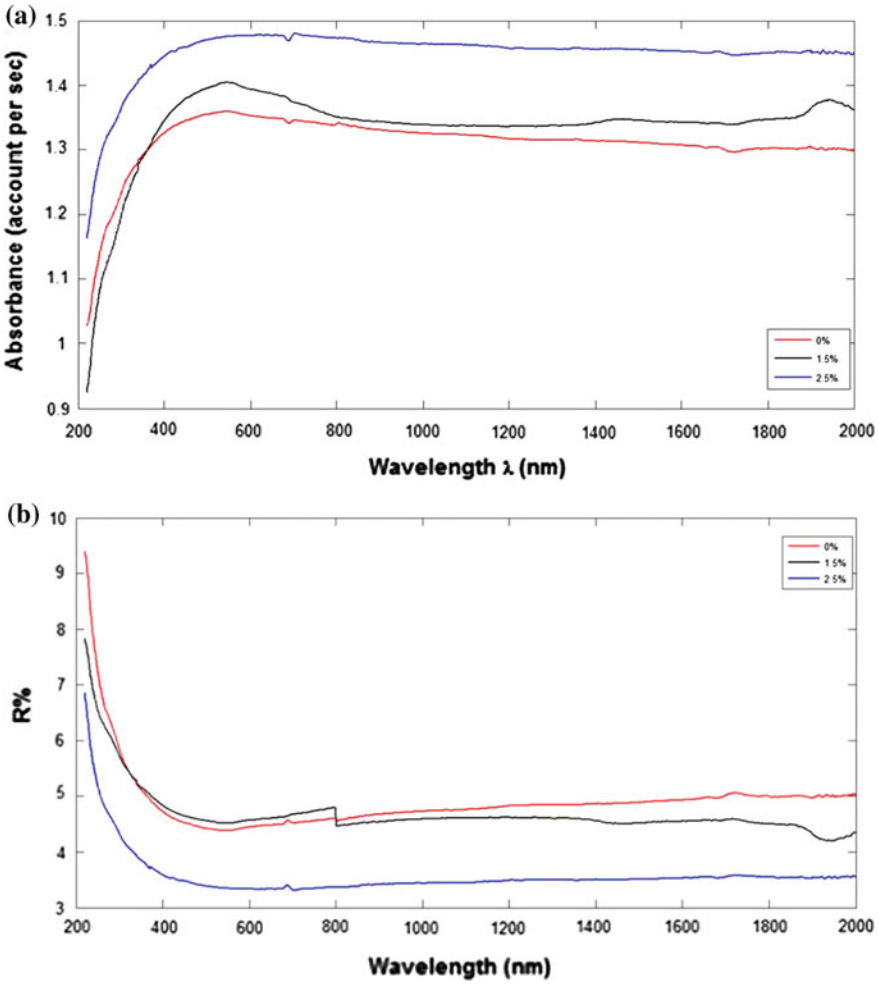

Fig. 2 Absorbance (**a**) and reflectance (**b**) spectral characteristics of the 0, 1.5 and 2.5% nano-graphite

of the test and reached its maximum temperature of 44 °C at 12:15PM. The temperature gain was 4.8 °C, while the intensity at the first hour reached its maximum value of 951 W/m^2 at 12:00 PM and it decreased gradually during that hour to a minimal and final value of 800 W/m^2 at 12:45 PM. Figure 4b (wind speed 11 km/hr) shows the measured temperatures for the case of black coated copper tubes. During the first hour with flow rate of 0.4 L/min, it is shown that the inlet temperature was 38 °C, and at the end of the hour there was a slight increase to 41 °C. The inlet temperature reached a maximum of 42 °C at 12:05 PM. The outlet temperature was 44 °C at the start and end of the test, while it reached the maximum of 49 °C at 12:05 PM and at 12:35 PM. The temperature gained was 6.5°C.

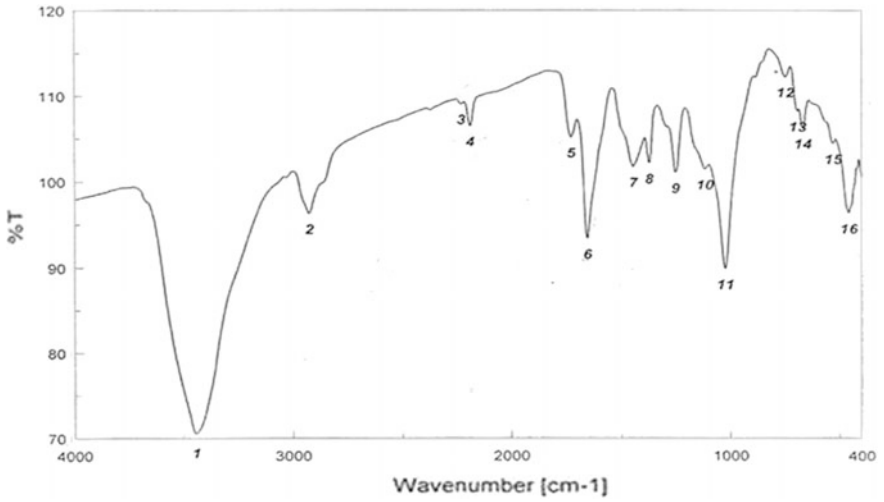

Fig. 3 FTIR of the developed material

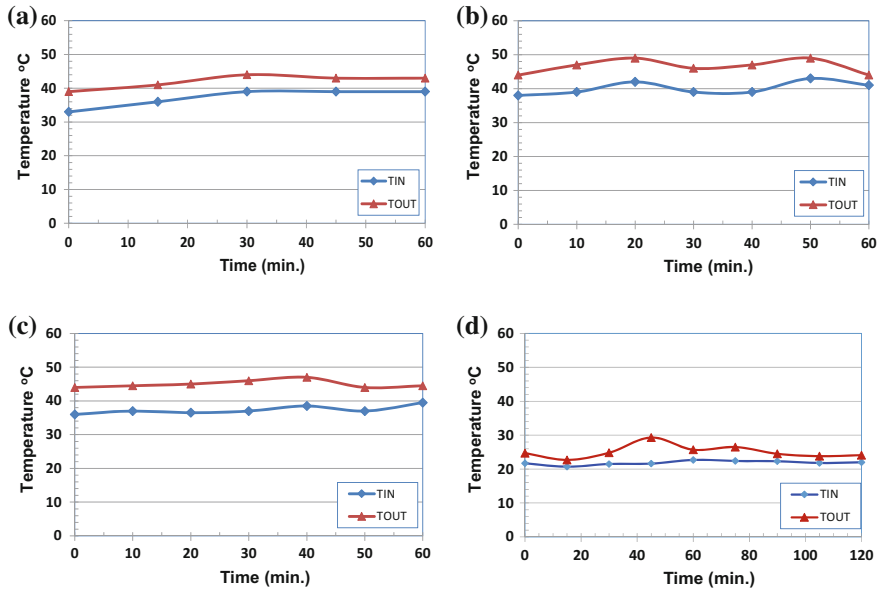

Fig. 4 Inlet and outlet temperature verses time. **a** for (bare Cu) flow rate = 0.47 L/min and wind speed 12 km/hr, solar radiation intensity 800–950 W/m2. **b** (Cu-Black coating) for flow rate = 0.41 L/min and wind speed 11 km/hr, solar radiation intensity 810–900 W/m2. **c** (Cu-Black coating with nano graphite) flow rate = 0.46 L/min and wind speed 13 km/hr, solar radiation intensity 850–950 W/m2. **d** Cu-Black coating with nano- graphite flow rate = 0.4 L/min and wind speed 24 km/hr, day time temperature 230C, solar radiation intensity 100–325 W/m2

The solar intensity readings decreased from a maximum of 905 W/m^2 at 12:00 PM to a minimum value of 800 W/m^2 at 12:45 PM. Figure 4c (wind speed 13 km/hr) shows the measured temperatures for the third case of black coating with nano-graphite. During the first hour with flow rate of 0.47 L/min, the figure illustrates that the lowest temperature of 36 °C was recorded at the beginning, while the maximum value of 39.5 °C was reached at the end of that hour. The outlet temperature reached the maximum of 47 °C at 12:25 PM. The temperature gained was 7.2 °C. As for the solar intensity, the maximum value was 950 W/m^2 at 11:55 AM and the minimum value was 850 W/m^2 recorded at 12:05 PM, which then increased gradually until the end of that hour till it reached 875 W/m^2. Figure 4d shows the black coated Cu tubes with nano-graphite dispersion during February 2014, between 10.00 and 12.00 AM, wind speed 24 km/hr and water flow rate 0.4 l/min. It is shown from Fig. 4d that during the first hour the lowest temperature of 22.7 °C was recorded at the beginning of the test, while the maximum value of 29.3 °C was reached after 45 min. The outlet temperature reached the maximum of 29.7 °C at 10:40 PM. The temperature gained was 7.7 °C. As for the solar intensity, the maximum value was 325 W/m^2 at 10.00 AM and the minimum value was 200 W/m^2 recorded towards the end of the testing time.

Figure 5 shows a comparison of the circulating water temperature gain versus the incident solar radiation intensity for the three tested systems at water flow rate (0.4–0.47 L/min). It can be seen that generally as the incident solar intensity increases the temperature gain in circulating water also increases. For most of the intensities range, the temperature gain for the nanodispersed black coating system is the highest followed by the plain black coating then the pure copper.

According to the above results, it can be seen that there are great options for enhancing the efficiency of thermal solar collectors through the development of new materials, which have appropriate selective absorbing properties. The results obtained from the prototype experimental setup showed that: in the case of pure copper the gain in temperature was only 4.5 °C, after applying the black matt coating the gain in temperature increased to 6 °C, which means 25.7% increase in water temperature. The use of black coating loaded with nano-graphite particles caused the temperature to increase to 7.7 °C, which means 51.7% increase in water

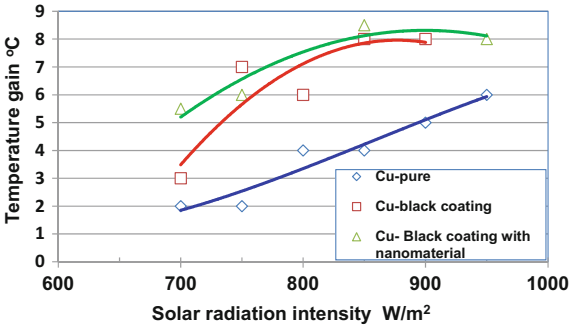

Fig. 5 The gain in temperature vs incident solar radiation intensity for the three systems tested

temperature, which indicates enhancement in the selective absorptive properties of the absorber. It has been shown [7] that dispersions of suitable inorganic colorant particles in a polymer matrix result films with an infra-red (IR) radiation characteristic that is of high opacity in the visible wavelength and low absorptivity (and therefore emissivity) in the IR region. Understanding the role of nanoparticles has been revealed by a recent study [16], which showed that nanoparticles influence the emission spectra of the multilayered structures. The study has also stated that wavelength selectivity can be altered and controlled by size and/or volume fraction of the nanoparticles. It has been also shown that the presence of nanoparticles in a host material gives rise to an appearance of new emission peaks and a shift in the existing peaks in the emission spectra.

The previous study by the authors [23] has shown that the differences in calculated efficiencies of different absorber coating materials become smaller at low temperature differences, where the FPSC are used for low temperature applications (50 °C < T < 100 °C), thus it is more convenient to use less expensive coatings at that temperature range without affecting the collector`s performance. The study has highlighted that both the design and the absorber material play a crucial role in determining the efficiency of FPSCs. This study has shown that there are significant options for developing new economic ideas for solar water heating based on development of new materials.

Conclusions

1. In this work it was demonstrated that coating copper tubes with the commercial polymer based black solar coating (PACEN code 10382 colour 890) dispersed with graphite nanoparticles results an enhancement in its heating capacity represented by an increase in the water temperature circulating through these pipes compared to the temperature increase for the monolithic material. The use of black coating loaded with nano-graphite particles caused an increase of 7.7 °C in water temperature, compared to 6.5 °C for the black coating without nanoparticles and 4.8 °C for the bare copper without coating, This finding opens options for manufacturing simple economic low temperature (<100 °C) thermal solar systems by combining simple materials and a nano-graphite dispersed commercial polymer based black coating.
2. It was also shown that adding 1.5 and 2.5% nano-graphite particles to the polymer based black coating causes an increase in the optical absorbance and a decrease in the emittance, where the highest absorptance and lowest emittance were obtained for 2.5% addition.
3. The commercial polymer base coatings carrier used as a solar selective absorber consists of polyurethane based mixtures with some additions (such as amides chain extenders) for thermal and environmental stability enhancement.

Acknowledgements The authors are grateful to the Final Year students (Cohort July 2012 and July 2014) working on this project at both Cairo University and the British University in Egypt whom without their efforts and enthusiasm this work wouldn't have come to light. The authors are also grateful to the national Research Centre in Egypt for providing its testing facilities. Finally, the authors thank Dr Amr Mohsen and Dr. Samah Mohamed for providing the raw material used for developing the selective absorber coating used in the experimental part of this work.

References

1. Martin K, Wolfgang S, Andreas W (2007) Renewable energy: technology, economics and environment. Springer, Heidelberg
2. Madhukeshwara N, Prakash ES (2012). An investigation on the performance characteristics of solar flat plate collector with different selective surface coatings. Int J Energy Environ, 3 (1):99–108
3. Selvakumar N, Barshilia HC (2012) Review of physical vapor deposited (PVD) spectrally selective coatings for mid- and high-temperature solar thermal applications. Sol Energy Mater Sol Cells 98:1–23
4. Kennedy CE (2002) Review of mid- to high-temperature solar selective absorber materials. Natl Renew Energy Lab
5. Kalogirou SA (2004) Solar thermal collectors and applications. Prog Energy Combustion Sci 30:231–295
6. Tsilingiris PT (2000) Heat transfer analysis of low thermal conductivity solar energy absorbers. Appl Thermal Eng 20:1297–1314
7. Highgate DJ, Probert SD (1996) Cheap effective thermal solar-energy collectors. Appl Energy 53:349–363
8. Köhl M, Meir MG, Papillon P, Wallner GM, Saile S (eds) (2012) Polymeric materials for solar thermal applications. Wiley
9. Alghoul MA, Sulaiman MY, Azmi BZ, Abd. Wahab M (2005) Review of materials for solar thermal collectors. Anti-Corrosion Methods Mater, 52(4):199–206
10. Tsilingiris PT (1999) Towards making solar water heating technology feasible-the polymer solar collector approach. Energy Convers Manag 40:1237–1250
11. Selvaraj K (2011) Increase in efficiency of solar water heaters using fine metal powders mixed in heat absorbing coatings and their applications in electrical engineering. Int J Res Rev Comput Sci 2:61–64
12. Van Koppen CWJ, Thomas JPS, and Veltkamp WB (1979) The actual benefits of thermally stratified storage in small—and medium—size storage system. In: Elmsford, NY (ed) Proceedings of the Silver Jubilee Congress Sun II, vol 1, (A80-33401 13-44), Pergamon Press Inc., pp 576–580
13. El-Mahallawi IS, Rafat NH, Khattab N, Nabil MA, Abdel-Rehim AA, Akl S, Amr M (2014) Economic technical solutions for enhancing the efficiency of thermal solar systems. In: International Conference on Industry—Academia Collaboration, Fairmont Helipolis Hotel Cairo Egypt, IAC 3–5 March
14. Han Dongxiao, Meng Zhaoguo, Daxiong Wu, Zhang Canying, Zhu Haitao (2011) Thermal properties of carbon black aqueous nanofluids for solar absorptance. Nanoscale Res Lett Springer Open 6(457):1–7
15. Talghader JJ, Gawarikar AS, Shea RP (2012) Spectral selectivity in infrared thermal detection. Light Sci Appl, 1:e24. https://doi.org/10.1038/lsa.2012.24
16. Ghanekar A, Lin L, Su J, Sun H, Zheng Y (2015) Role of nanoparticles in wavelength selectivity of multilayered structures in the far-field and near-field regimes. Optical Soc Am 23(19): A1129–A1139. https://doi.org/10.1364/OE.23.0A1129

17. Chang C-C, Huang C-L, Chang C-L (2013) Poly(urethane)-based solar absorber coating containing nanogold. Sol Energy 91:350–357
18. Kakani SL, Kakani A (2004) Material Science. New Age International Publishers, New Delhi
19. Singh V et al (2011) Graphene based materials: past, present and future. Prog Mater Sci 56:1178–1271
20. Lehman J, Terrones M, Mansfield M, Hurst K, Meunier V (2011) Evaluating the characteristics of multiwall carbon Nanotubes. Carbon 49:2581–2602
21. Shinde SL, Goela J (2006) High thermal conductivity materials. Springer Science and Business Media, The United States of America
22. Mohamed SS (2010) Mechanical and tribological characteristices of polymeric matrix composite, PhD Thesis, Benha University- Shoubra Faculty of Engineering
23. Yahia N, El-Mahallawi IS, Abdel-Rehim AA, Hatem T, Khattab N (2015) Modelling and experimentation of thermal flat plate solar collector design parameters. In Conference Proceedings, SusTEM, Newcastle, UK, 7–8 July, 2015

Synthesis of MoAlB Particulates and Their Porous Derivatives by Selective Deintercalation of Al from MoAlB

S. Gupta and M. Fuka

Abstract This paper reports for the first time the synthesis of deintercalated MoAlB particulates which belongs to a family of novel ternary borides called MAB phases by selected etching of Al from these particulates by treating them with a solution of LiF and HCl. The FESEM analysis showed that these particulates had a stacked 2D-particles like morphology reminiscent of multilayered MXenes, but unlike MXenes, the 2D layers were interconnected with anisotropic porosity between them with an average length and width of pores being 257 ± 126 nm and 35 ± 10 nm, respectively. The EDS analysis of particulates showed that a typical particulate had a chemistry of $(Mo_{0.67}Al_{0.33})B\{O_{0.19}F_{0.02}\}$ which indicate partial deintercalation of Al from the particulates. These novel particulates were also referred to as MABenes due to their microstructural similarity with multilayered MXenes.

Keywords MAB phases · MABenes · Particulate design · MXenes

Introduction

By now, it is well established that 2D materials have unusual electronic, mechanical, and optical properties which have led to their extensive study in the past decade for diverse applications [1–9]. Several types of novel 2D materials, for example, single-element 2D materials like graphene [1–3], silicone [4], germanene [5], and phosphorene [6]; two elements like dichalcogenides and oxides or more elements like clays [3, 7, 8] have been studied. For further tuning the properties, it is critical to design novel chemistries where these complex layers can contain more than one element which can offer novel properties as they provide different compositional variable for tuning the specific properties [9, 10].

S. Gupta (✉) · M. Fuka
Department of Mechanical Engineering, University of North Dakota, Grand Forks, ND 58201, USA
e-mail: surojit.gupta@engr.und.edu

Z. Sun et al. (eds.), *Energy Technology 2018*, The Minerals, Metals & Materials Series, https://doi.org/10.1007/978-3-319-72362-4_50

MXenes are a promising addition to the novel 2D materials as they can be synthesized in different types of chemistry [9, 10]. More particularly, MXenes can be fabricated by selective etching of A group element from MAX phases [9, 10]. As a background, $M_{n+1}AX_n$ (MAX) phases (over 70+ phases), where n = 1, 2, 3; M is an Early Transitional Metal, A is a Group A element (mostly groups 13 and 14); and X is C and/or N, are novel ternary carbides and nitrides (space group *P6₃/mmc*) [11–14]. In these solids, the selective etching of A-element from the layers are possible as the M–A bonds are more chemically active than the stronger M–X bonds [9]. Neguib et al. [10] reported for the first time that 2D nanosheets, composed of a few Ti_3C_2 layers and conical scrolls, can be produced by exfoliating Ti_3AlC_2 in hydrofluoric acid. Later, Ghidiu et al. [15] demonstrated that MXene can be synthesized by etching in HCl–LiF solution where HCl and LiF react to form HF in situ, which then selectively etches the A atom from MAX phases. MXenes have also been derived from non-MAX-phase precursors, for example, Mo_2CT_x is fabricated by etching Ga layers from Mo_2Ga_2C [16]. These fundamental research has showed that 2D solids can potentially derived from complex ternary phases.

Ternary transition metal borides where boride sub-lattice is interleaved by one or two Al layers in M_2AlB_2-type (space group *Cmmm*) and MAlB-type (space group *Cmcm*) are promising candidates for exfoliation because of above mentioned reasons [17, 18]. Ade et al. [19] noted the similarity of these phases to MAX Phases and referred to these ternary solids as "MAB-phases". In a recent paper, Kota et al. [20] reported dense and predominantly single-phase MoAlB by using a reactive hot pressing method. In this proceeding paper, we will present a preliminary study to explore the etching behavior of MoAlB particulates.

Experimental

Initially, MoAlB powder was fabricated by mixing powders of MoB (Part number 12563 (99% pure), Alfa Aesar, Haverhill, MA) and Al powder (Part number 11067 (99.5% pure), Alfa Aesar, Haverhill, MA) in the molar ratio of 1:1.2 by dry ball milling (8000 M mixer Mill, SPEX SamplePrep, Metuchen, NJ) for 5 min. Thereafter, the powders were cold pressed, and annealed at 750 °C for 2 h at a ramp rate of 10 °C/min. The annealed samples were then heat treated at a ramp rate of 5 °C/min to 1550 °C for 120 min in a tube furnace under flowing Ar. XRD analysis was performed to confirm whether the reacted powders were single phase (Fig. 1a). Predominantly single phase MoAlB powder was then ball milled and sieved until −325 mesh by using a sieve shaker.

MoAlB particulates were etched by treating the particulates with ∼40 ml of 12 M HCl (ACS reagent 37%, Sigma Aldrich, St. Louis, MO) and 1 g (∼1 M) LiF (BioUltra, ≥99.0%, Sigma Aldrich, St. Louis, MO). Initially, 1 M LiF was dissolved in 40 ml of 12 M HCl by stirring in a plastic container on a heated plated by Teflon coated magnetic stirrer at ∼40 °C for ∼15 min. Thereafter, 1 g (∼0.2 M) of MoAlB was added to the stirring solution. The resulting suspension was stirred

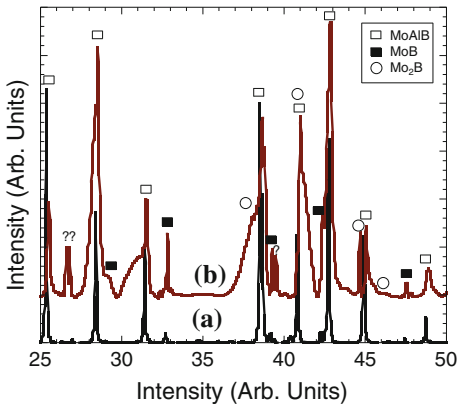

Fig. 1 XRD plot of, **a** MoAlB, and **b** etched MoAlB particulates

for ~40 h at ~40 °C. The resulting suspension was then centrifuged at ~3,000 rpm for 5 min. The resulting filtrate was drained, and fresh DI (distilled) water was added to the residue. The suspension was centrifuged again for 5 min. This cycle was continued for 6 cycles until the pH was 6. The resulting suspension was sonicated. Few drops were collected for microscopy analysis and rest of the suspension was then dried in oven at ~100 °C. XRD analysis was then performed on the dried and etched particulates. In future, the authors plan to perform centrifugation after the sonication step to compare the results with current study.

Rigaku Diffractometer (SmartLab, Rigaku, Japan) was used for all XRD measurements at a scan rate of 0.05 °/min from 20 to 50°. JEOL JSM-6490LV Scanning Electron Microscope (JEOL USA, Inc., Peabody, Massachusetts.) was used to obtain Secondary electron (SE) and Backscattered Electrons (BSE) images of the synthesized MoAlB particulates. X-ray information was obtained via a Thermo Nanotrace Energy Dispersive X-ray detector with NSS-300e acquisition engine. All the other images were taken by Field Emission Scanning Electron Microscope (FESEM) in SE (Secondary) and BSE (Backscattered Electron) mode by a JEOL JSM-7600F scanning electron microscope (JEOL USA, Inc., Peabody, MA). Energy-dispersive spectroscopy information was acquired by using an UltraDry silicon drift X-ray detector and NSS-212e NORAN System 7 X-ray Microanalysis System (Thermo Fisher Scientific, Madison, Wisconsin). Please note, it is very difficult to detect B by EDS, hence the result presented here is very qualitative. More studies are needed to understand the exact chemistry. In addition, an average of 3 results is presented for each experimental reading.

For qualitative comparison, the length (l) and width (w) of pores in the etched grain was measured by Image J software [21]. An average of 10 pores is reported for a sample.

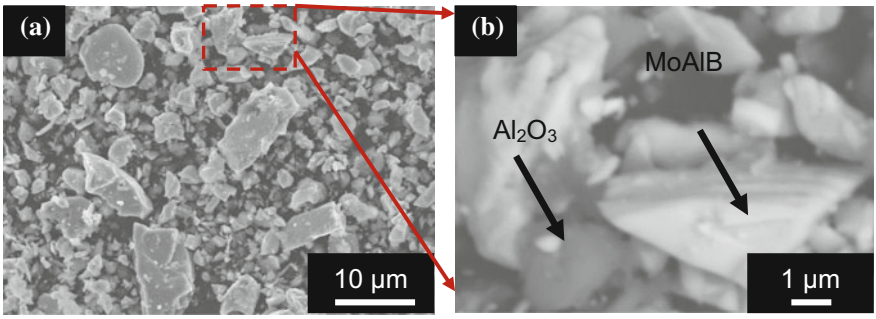

Fig. 2 SEM SE micrograph of as-synthesized MoAlB particulates at, **a** lower, and **b** BSE image at higher magnifications. The average of composition of MoAlB particulate was $Mo_{0.48}Al_{0.52}O_{0.33}B$

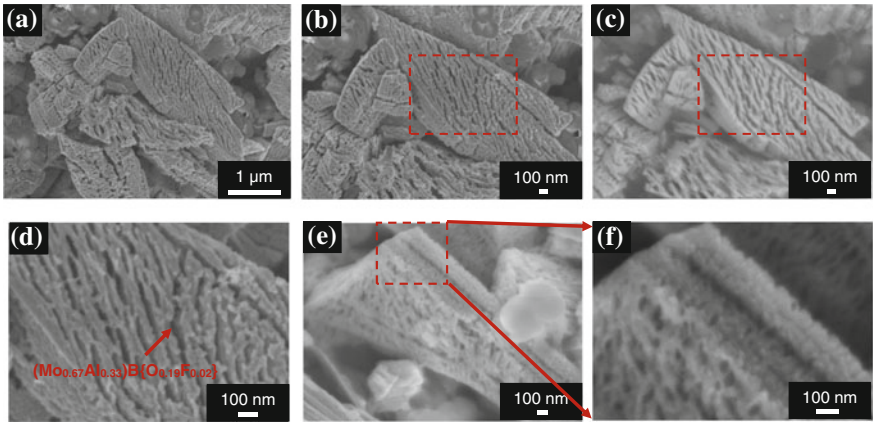

Fig. 3 FESEM SE micrographs of, **a** etched MoAlB particulates, **b** top surface of etched MoAlB particulate at higher magnification, **c** BSE of the same region, **d** higher magnification of the marked region in (**b**), **e** side view of a etched particulate, and **f** higher magnification of the same region

Results and Discussion

XRD pattern shows that MoAlB is the predominant phase in the pattern (Fig. 1). Figure 2 show morphology of MoAlB particulates. However, at higher magnification, micron sized Al_2O_3 particles were also detected. Based on the XRD and SEM results (Figs. 1 and 2), it can construed that the MoAlB formed during the synthesis process is predominantly single phase although EDS analysis showed that there is some O signal in MoAlB particulate which may also be due to the presence of neighboring Al_2O_3 particles. Currently, the authors have no tools to differentiate this and detailed studies are recommended to further explore the chemistry of MoAlB particulates. (Fig. 2b).

Figure 3 shows the morphology of different particulates after the chemical treatment. Figure 3a shows an overview of etched surface of different particulates. Several particulates are observed with etched surfaces. On a closer inspection of the top surface of a single particulate (Fig. 3b–d), it seemed that several interconnected 2D layers within a single particulate are present. In addition, the pores between the layers are linear and highly anisotropic, for example, on average—the length of the interlaminar pores was 257 ± 126 nm, and the width of the pores was 35 ± 10 nm. The EDS analysis of the particulate showed the composition of a region is $(Mo_{0.67}Al_{0.33})B\{O_{0.19}F_{0.02}\}$. The reaction of HCl and LiF resulted in the in situ formation of HF [16]. The HF formed by in situ reaction reacts with the MoAlB particulates, and the Al is then selectively etched from the particulates. XRD of the etched MoAlB particulates showed that the MoAlB peaks are broadened as compared to the as-synthesized MoAlB which further support the formation of Al-deficient MoAlB (Fig. 1). Figures 3e–f shows the morphology of edge of a etched particulate. Several pores (<100 nm) were observed on the surface. Detailed TEM studies are needed to document the crystal structure of these etched phases. The XRD pattern also detected the presence of Mo_2B and MoB which indicate that some of the particulates have converted fully to binary borides. Based on the oxidation results, Kota et al. [20] also reported that MoAlB can exist with a deficiency of Al, thus MoAlB phase can be a potential candidate for particulate design.

The chemistry of etched particulates ($(Mo_{0.67}Al_{0.33})B\{O_{0.19}F_{0.02}\}$) is very similar to MXenes which have a general formula of $M_{n+1}X_nT_x$, where T represents the surface terminations which is a combination of –OH, –O and –F groups [9]. This study shows that novel particulates can be designed by partial selective etching of Al from MoAlB (MAB Phases). The stacked layers are reminiscent of multilayered MXenes (Fig. 2 in Ref. 9), but the multilayers are connected in this case (Fig. 3d). Due to structural similarity to multilayered MXenes, these novel particulates can be referred as MABenes as the Al is not completely deintercalated from the MoAlB particulate. Authors accept the fact that more detailed studies are needed to understand the composition of filtrate as it may possible that residual AlF_3 is trapped inside the porous structures. As mentioned the experiment section, the authors plan to perform centrifugation after the sonication step to compare the results with current study. In an excellent review article, Anasori et al. [9] summarized that etching rate of Al-containing MAX phases is dependent on the atomic number of M, for example M with larger atomic number requires a longer and stronger etching. In addition, MXenes with larger n in $M_{n+1}C_nT_x$ require stronger etching and/or a longer etching time. For example, $Mo_2Ti_2AlC_3$ ($n = 3$) requires an etching time that is twice as long as its $n = 2$ counterpart (that is, Mo_2TiAlC_2) under the same etching conditions [9]. Based on these findings, it can be further hypothesized that by optimizing the etching conditions, it will be possible to generate MXene like MBene phases which will offer scientists more flexibility in materials design for energy applications.

Interestingly, there has not been significant study on the design of particulates by partial etching of MAX phases. It is also hypothesized that MAXenes particulates can be fabricated by the partial etching of MAX Phases.

Conclusions

Novel porous particulates were designed by deintercalation of MoAlB particulates by treating them with a solution of LiF and HCl. These particulates showed a unique stacked 2D-particles like morphology and were riddled with pores of dimensions 257 ± 126 nm and 35 ± 10 nm, respectively. The EDS analysis showed that particulates had a chemistry of $(Mo_{0.67}Al_{0.33})B\{O_{0.19}F_{0.02}\}$ due to partial deintercalation of Al from MoAlB.

Acknowledgements One of the authors (SG) would like to acknowledge the University of North Dakota start up funding, SSAC, ND Venture Grant, and NSF EPSCoR for support. NDSU Electron Microscopy Center core facility is also acknowledged for the microscopy. This material is also based upon work supported by the National Science Foundation under Grant No. 0619098, and 1229417. Any opinions, findings, and conclusions or recommendations expressed in this material are those of the author(s) and do not necessarily reflect the views of the National Science Foundation.

References

1. Koppens F et al (2014) Photodetectors based on graphene, other two-dimensional materials and hybrid systems. Natl Nanotechnol 9:780–793
2. Bhimanapati et al (2015) Recent Advances in Two-Dimensional Materials beyond Graphene, ACS Nano, 9, pp 11509–11539 (2015)
3. Nicolosi V, Chhowalla M, Kanatzidis MG, Strano MS, Coleman JN (2013) Liquid exfoliation of layered materials. Science 340, 1226419
4. Lalmi B, Oughaddou H, Enriquez H, Kara A, Vizzini S, Ealet B, Aufray B (2010) Epitaxial growth of a silicene sheet. Appl Phys Lett 97, 223109 (2010)
5. Dávila ME, Xian L, Cahangirov S, Rubio A, Le Lay G (2014) Germanene: a novel two-dimensional germanium allotrope akin to graphene and silicone. New J Phys 16, 095002
6. Han Liu AT, Neal Z, Zhu Z, Luo X, Xu D (2014) Phosphorene: an unexplored 2D semiconductor with a high hole mobility. In Tomanek, Ye PD (eds), ACS Nano, 8, 4033–4041
7. Chaoliang T, Hua Z (2015)Two-dimensional transition metal dichalcogenide nanosheet-based composites", Chem Soc Rev 44, 2713
8. Ataca C, Sahin H, Ciraci S (2012) Stable, single-layer MX_2 transition-metal oxides and dichalcogenides in a honeycomb-like structure. J Phys Chem C 116, 8983–8999
9. Anasori B, Lukatskaya MR, Gogotsi Y 2D metal carbides and nitrides (MXenes) for energy storage. Nature Rev, vol 2, 16098
10. Naguib M et al (2011) Two-dimensional nanocrystals produced by exfoliation of Ti_3AlC_2. Adv Mater 23:4248–4253
11. Barsoum MW (2013) MAX phases: properties of machinable ternary carbides and nitrides. Wiley

12. Barsoum MW, Radovic M (2011) Elastic and Mechanical Properties of the MAX Phases. Annu. Rev. Mater. Res. 41, 195–227
13. Barsoum MW, El-Raghy T (1996) Synthesis and characterization of a remarkable ceramic: Ti_3SiC_2. J. Am. Ceram. Soc. 79, 1953–1956
14. Barsoum MW (2000) The $M_{n+1}AX_n$ phases: a new class of solids; thermodynamically stable nanolaminates. Prog Solid State Chem 28, 201–281
15. Ghidiu M, Lukatskaya MR, Zhao MQ, Gogotsi Y, Barsoum MW (2014) Conductive two dimensional titanium carbide 'clay' with high volumetric capacitance. Nature 516, 78–81
16. Meshkian et al R (2015) Synthesis of two-dimensional molybdenum carbide, Mo_2C, from the gallium based atomic laminate Mo_2Ga_2C. Scripta Mater 108, 147–150 (2015)
17. Jeitschko W (1966) Die Kristallstruktur von MoAlB. Monatshefte für Chemie und verwandte Teile anderer Wissenschaften 97, 1472–147
18. Jeitschko W (1969) The crystal structure of Fe_2AlB_2. Acta Crystallogr Sect B Struct Crystallogr Cryst Chem 25, 163–165 (1969)
19. Ade M, Hillebrecht H (2015) Ternary borides Cr_2AlB_2, Cr_3AlB_4, and Cr_4AlB_6: the first members of the series $(CrB_2)_nCrAl$ with n = 1,2, 3 and a unifying concept for ternary borides as MAB-Phases. Inorg Chem 54, 6122–6135 (2015)
20. Kota S, Zapata-Solvas E, Ly A, Lu J, Elkassabany O, Huon A, Lee WE, Hultman L, May SJ, Barsoum MW Synthesis and Characterization of an Alumina Forming Nanolaminated Boride: MoAlB, Scientific Reports, 6, 26475. https://doi.org/10.1038/srep26475
21. Schneider CA, Rasband WS, Eliceiri KW (2012) NIH Image to ImageJ: 25 years of image analysis. Nat Method, 9, 671–675

A New Economical Method for Fabricating High-Purity Bi_2O_3 via Extraction-Precipitation Stripping and Post Annealing

C. Jun and Z. Jing

Abstract High-purity Bi_2O_3 was prepared via extraction-preparation stripping method use $BiCl_3$ leaching solution. Parameters such as oxalic acid concentration, phase ration, aging duration, feeding duration, were examined for their effect on the size and morphology of precipitate. The precipitate was characterized by X-ray diffraction (XRD), scanning electron microscopy (SEM), particle size analysis, differential scanning calorimetry and thermal gravity analysis (DSC-TGA) and infrared spectroscopy analysis (FT-IR). Bi_2O_3 was characterized by elements analysis, particle size analysis and scanning electron microscopy (SEM). Bi_2O_3 product of 680 nm was obtained using 15 g/L oxalic acid, 1/1 phase ration, 0 min aging duration, 0 min feeding duration and calcinating at 500 °C for 2 h.

Keywords Bi_2O_3 · Oxalic acid · Bismuth oxalate · Particle size Morphology

Bismuth oxide is an environmental and friendly material [1–4], it has been widely used in gas sensors, solid oxide fuel cells, optical coating, ceramic glass manufacturing, due to its excellent physical and chemical properties [5–8]. Usually, Bi_2O_3 was prepared via various methods as follows: oxidative metal vapor transport deposition [9], chemical bath decomposition [7, 8, 10, 11], solvothermal method [12], hydrothermal method [13, 14], aqueous crystallization method [15], anodization method [16], chemical vapor deposition method [17] from analytical grade bismuth material or high-purity bismuth. Such as Lu et al. prepared Bi_2O_3 by aqueous crystallization strategy use bismuth nitrate [15]. Faisal et al. synthesized Bi_2O_3 nanosheets via hydrothermal processes use bismuth nitrate [13]. But, all the above methods were comparatively complicated with high material cost.

C. Jun · Z. Jing (✉)
School of Metallurgy and Environment, Central South University, Changsha 410083, People's Republic of China
e-mail: zhanjing2001@hotmail.com

C. Jun
e-mail: Cj_csu@163.com

Z. Sun et al. (eds.), *Energy Technology 2018*, The Minerals, Metals & Materials Series, https://doi.org/10.1007/978-3-319-72362-4_51

What's more, few researchers have been reported on prepared high-purity Bi_2O_3 from leaching solution of copper smelter converter dust or bismuth ore. Generally, the preparation of Bi_2O_3 from leach solution consist of hydrolysis and dechlorination transformation. Ha et al. [2] prepared Bi_2O_3 through hydrometallurgy process use leaching solution, the process for preparation of bismuth oxide was carried out in three stages: SO_2 reduction; hydrolysis; conversion of BiOCl to Bi_2O_3. However, the drawback of this method was the product of high chlorine due to it difficult to be dechlorinated. Herein, we are seeking for a new economical method for production of Bi_2O_3 from leaching solution.

It was well know that, the rare earths were recovered from leaching solution by solvent extraction and finally precipitated from the strip solution as rare oxalates [18–21]. Chen et al. fabricated nanoscaled yttrium oxide by citrate precipitation method from YCl_3 solution [22]. Mei et al. nano-size ceria by stripping precipitation using oxalic acid as a precipitating agent from cerium nitrate solution [23]. However, there was no reported that high-purity Bi_2O_3 was synthesized via extraction-precipitation stripping and calcination. Herein, we will synthesized Bi_2O_3 via extraction-precipitation stripping and calcination use $BiCl_3$ leaching solution, and, we have reported the extraction mechanism of Bi by TBP from hydrochloric acid medium [24]. So, this paper aims at investigating the effects of oxalic concentration, aging duration, phase ration, and feeding duration on the size and morphology of precursor.

Experimental

Materials and Reagents

Tributyl phosphate(TBP), hydrochloric acid, oxalic acid, ammonium hydroxide, sulfonated kerosene (0.8 g/mL) and ethanol were provided by XiLong Chemical Co., Ltd., China. All the chemicals used in this study were of analytical grade without further purification. The contents of $BiCl_3$ solution was listed in Table 1.

Preparation of Bi_2O_3

(1) The $BiCl_3$ solution was prepared through this method [4], and followed by hydrolysis purified. In the solvent extraction tests the procedure followed was as follows: a measured amount of $BiCl_3$ solution and extraction agents were put

Table 1 Contents of $BiCl_3$ solution

Elements	Bi	Fe	Cu	Mn	Pb
Concentration (g/L)	19.0566	4.3939	0.0896	0.9009	0.6114

into the separatory funnel and shook rapidly. The shaking speed which gave sufficient mixing was kept constant in all the experiments. At the end of solvent extraction duration, organic-aqueous phases were separated by separatory funnel.

(2) In the stripped tests the procedure followed was as follows: a measured amount of loaded organic and oxalic acid was put into the separatory funnel and shook rapidly. The shaking speed which gave sufficient mixing was kept constant in all the experiments. At the end of stripped duration, organic-aqueous-precursor phases separation by that separatory funnel. The organic phase was used to extract again after washing.

(3) The precursor was washed with ethanol for removing organic matter which was subsequently heated at various temperatures to get the Bi_2O_3 powder. The decomposition behavior was listed in Eqs. (1) and (2).

$$Bi_2(C_2O_4)_3 \bullet 7H_2O \rightarrow Bi_2O_2CO_3 + Bi_2O_3 + CO_2 \ + \ H_2O \quad (1)$$

$$Bi_2O_2CO_3 \rightarrow Bi_2O_3 \ + \ CO_2 \quad (2)$$

Characterizations

X-ray diffraction (XRD, D8 Advance) pattern of the samples were obtained for phase identification. Scanning electron microscopy (SEM, JSM-6490LV) operated at 20 kV to observe morphologies and particle size. Differential scanning calorimetry and thermal gravity analysis (DSC-TGA, SDTQ600) were employed to investigate the decomposition behavior of the precipitates. The particle size distribution of Bi_2O_3 was analysed by particle size laser analyzer (Masterssizer 2000). The functional group of precursor were obtained from the absorption peaks of fourier transform infrared spectroscopy (FT-IR, WQF-510A).

Results and Discussion

Extraction of Bi

The optimum extracting conditions of Bi were obtained at a temperature of 25 °C for a extracting duration of 5 min with 60%TBP-sulfonated kerosene system and using a aqueous-organic ration 1/1 mL/mL. Under these optimized conditions, the extracting rate of Bi (III) was about 82% through 1 stage. The loaded organic phase contents showed in Table 2.

Table 2 Contents of loaded organic

Elements	Bi	Fe	Cu	Mn	Pb
Concentration (g/L)	15.6264	3.6029	0.0428	0.0964	0.0288

Precipitation Stripping of Bi

The purpose of stripped experiments were to investigated the effect of oxalic acid concentration, phase ration (Vo/Va), aging time, feeding duration on the size and morphology of precursor. The stripped experiments were carried out at 25 °C.

Influence of Oxalic Acid Concentration

Concentration of oxalic acid has an important impact on the size and morphology of precursor. Bi was stripped by varying the concentration of oxalic acid from 12 to 20 g/L. Other parameters was listed in the notes of Fig. 1. The average particle diameter was increased as the concentration of oxalic acid increase, and the size distribution was shown in Fig. 1. The distribution of the particle size become narrower for higher concentration of oxalic acid. The concentration of oxalic from 12 to 15 g/L, morphologies of precursor could be changed from sphere-like to block-shape (Fig. S1). By reason that when concentration of oxalic acid was increased gradually, crystal nucleation rate becomes faster, the crystal grows up in a regimental way [25].

Influence of Phase Ratio (Vo/Va)

Phase ratio has a remarkable effect on the size and morphology of precursor. Ratio of organic phase to aqueous phase was changed from 1:2 to 2:1. Other parameters was listed in the notes of Fig. 2. The particle size of precursor was increased as the

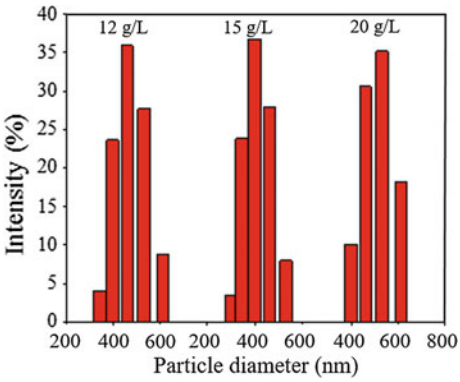

Fig. 1 Effect of oxalate acid concentration on the size distribution of precursor. Phase ration: 1:1, feeding duration: 0 min, aging time: 0 min

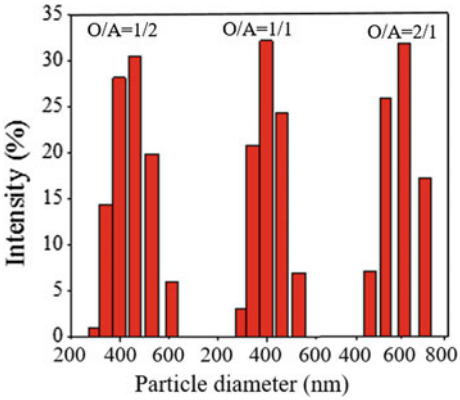

Fig. 2 Effect of phase ration on the size distribution of precursor. Oxalic acid concentration:15 g/L, aging duration:0 min, feeding duration: 0 min

ratio increases. The size distribution was shown in Fig. 2, and it can be seen that the distribution of the particle size become narrower for higher phase ration. As the phase ration increase, the effect of phase ration on the morphology of precursor is similar to that the effect of oxalic acid concentration on it (Fig. S2). By reason that the phase ratio from 1:2 to 2:1, the mixed phase from W/O microemulsion region to O/W microemulsion [17], the major growth mechanism of precursor was Ostwald ripening, this was similar to that of CuO nanoplates reported by Li et al. [26].

Influence of Aging Duration

Aging duration has a little influence on the size and morphology of precursor, it was ranging from 0 to 30 min. Other parameters was listed in the notes of Fig. 3. The particle size of precursor was decreased as the aging duration increase and the size distribution was shown in Fig. 3, it was apparent that the distribution of particle size become wider for a higher phase ration. With the extension of aging time, the size of the sheet-like precursor becomes smaller as the aging time was prolonged (Fig. S3). By reason that extract and stripped of Bi were commutative caused by extending the aging duration, as the contact between the precursor and organic phase becomes larger, so that part of the precursor redissolved, causing the precursor particle size distribution was not uniform.

Influence of Feeding Duration

The effect of feeding duration on the size and morphology of precursor was obvious as shown in Fig. 4. Feeding duration was varying from 0 to 30 min. Other parameters was listed in the notes of Fig. 4. The particle size of precursor was decreased as the feeding duration increase. As it was observed from the Fig. 4, the distribution of the particle size become wider for a longer aging duration. When

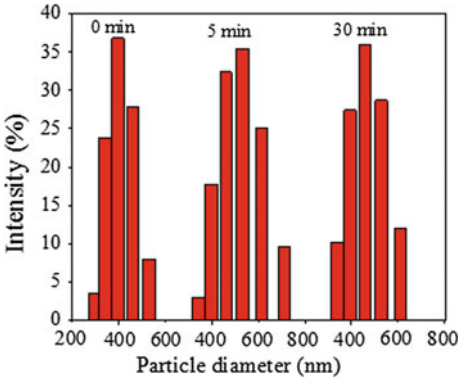

Fig. 3 Effect of aging duration on the size distribution of precursor. Oxalic acid concentration:15 g/L, phase ration:1:1, feeding duration: 0 min

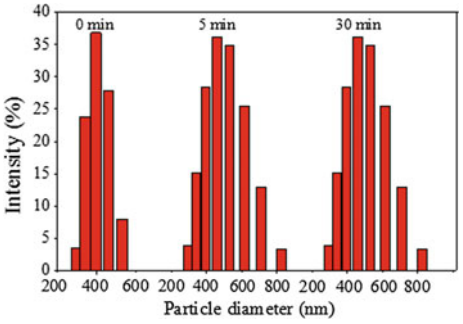

Fig. 4 Effect of feeding duration on the size distribution of precursor. Oxalic acid concentration:15 g/L, aging duration:0 min, phase ration:1:1

lowering the feeding rate, the degree of agglomeration of the precursor was exacerbated (Fig. S4). The reason may be that newly generated precipitates will be overlapped on the original precipitate [27], and part of the precursor was redissolved.

Characterization of Precursor

Figure 5 was FT-IR spectra of bismuth oxalate. The precursors $Bi_2(C_2O_4)_3.7H_2O$ showed a wide absorption band at 3444 cm^{-1}, corresponding to the stretching and bending modes of dissociative hydrocarbon chain, indicating a large amount of crystal-water inside. The peaks at 1585 cm^{-1} was ascribed to the stretching vibration of the C = O.

The corresponding XRD pattern of bismuth oxalate powder was shown in Fig. 6. The peaks at 15.883° and 18.819° of XRD patterns can be indexed as a triclinic lattice of $Bi_2(C_2O_4)_3 \blacksquare 7H_2O$ with crystal cell constants $a \neq b \neq c$, and a = 9.43 Å, b = 9.18 Å, c = 11.17 Å, $\alpha = 78.3°$, $\beta = 101.0°$, $\gamma = 73.7°$,which are

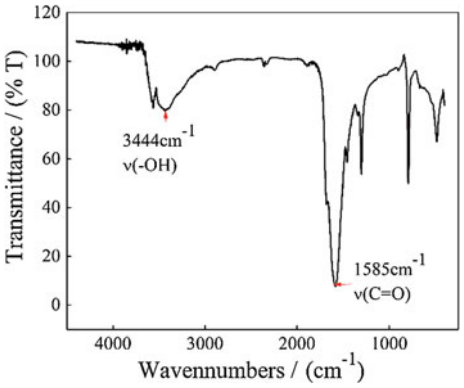

Fig. 5 FT-IR spectra of bismuth oxalate

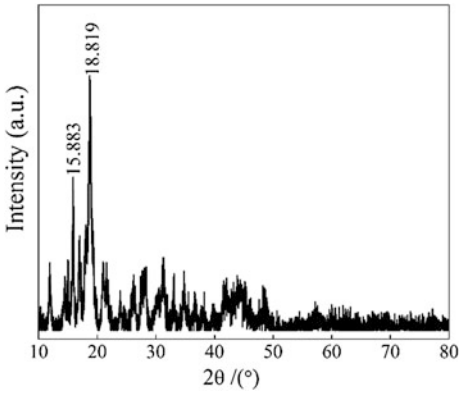

Fig. 6 XRD pattern of bismuth oxalate

close to the JCPDS file data (PDF no. 38-0548). The sharpness of the peaks suggested that the precursor was well crystallized.

To understand the decomposition behavior of bismuth oxalate, DSC-TGA curves were shown in Fig. 7. Decomposition processed in a two-step process: at first, a weight loss of 5.80% was noted from 25 to 245 °C, the second sharp weight loss of 28.82% was noted from 245 to 285 °C. The total weight loss (34.43%) was lower than in the earlier reports assigned for $Bi_2(C_2O_4)_3$■$7H_2O$ decomposition (42.20%) [28], indicating that some organic residues were wrapped into precursor. The flat roof appeared when the temperature was higher than 300 °C, implying no weightlessness at high temperature. TGA study showed one exothermic peak at 270 °C and three endothermic peaks at 180, 480, and 720 °C, respectively. The first one was due to the decomposition of organic residues, the second one could be attributed to the decomposition of bismuth oxalate, the last two were ascribed to the β-Bi_2O_3 → α-Bi_2O_3 and α-Bi_2O_3 → δ-Bi_2O_3, respectively. And this behavior was consistent with the earlier reports assigned for bismuth oxalate transformation into Bi_2O_3 [16, 29].

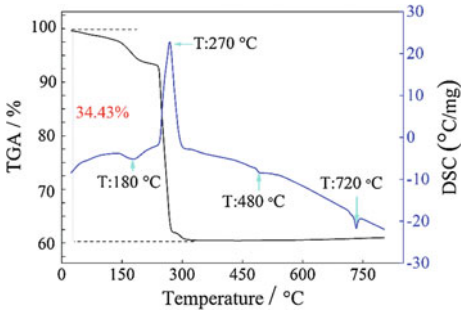

Fig. 7 DSC-TGA curves of bismuth oxalate

Characterization of Bi_2O_3

The corresponding XRD pattern of the thermally decomposed products from bismuth oxalates with different calcination temperature were shown in Fig. 8. It was clear that Bi_2O_3 can be changed from beta phase to delta phase as the calcination temperature increased from 260 to 730 °C. In Fig. 8b all the diffraction peaks of XRD pattern can be indexed to tetragonal crystal structure of the β-Bi_2O_3 phase with lattice parameters of a = b = 7.741 Å, c = 5.634 Å, and α = β = γ = 90°(PDF no. 78-1793). In Fig. 8d, the XRD pattern show that the synthesized α-Bi_2O_3 belongs to monoclinic system with lattice parameters of a = 5.8486 Å, b = 8.1661 Å, c = 7.509 Å, and α = β = γ = 113.0°(PDF no. 41-1499). In Fig. 8e all the diffraction peaks of XRD pattern can be indexed to monoclinic crystal structure of the δ-Bi_2O_3 phase and the corresponding lattice parameters were: a = 5.84 Å, b = 8.16 Å, c = 7.49 Å, α = 90°, β = 67.07°, γ = 90°(PDF no. 65-2366). In the XRD pattern of Bi_2O_3, the sharp peaks indicated that all the samples were highly crystallized, and the phase transition was consistent with the DSC-TGA curves

The chemical analysis of Bi_2O_3 was presented in Table 3. The main impurity elements as follows: Ca, Fe and Pb, the content (w%) was 132×10^{-6} %,

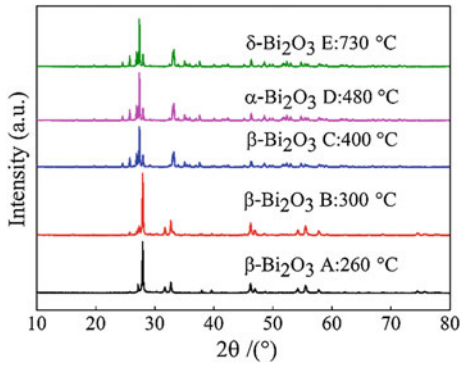

Fig. 8 XRD of Bi_2O_3 with different calcination temperature

Table 3 Elements contents of Bi_2O_3

Element	Na	Al	K	Ca	Fe	Cu	Zn	Mo	W	Pb	Bi_2O_3
Unit(wt%)	82.9 $\times 10^{-6}$	13.6 $\times 10^{-6}$	19 $\times 10^{-6}$	132 $\times 10^{-6}$	99 $\times 10^{-6}$	12.8 $\times 10^{-6}$	63.1 $\times 10^{-6}$	11.7 $\times 10^{-6}$	28.1 $\times 10^{-6}$	245 $\times 10^{-6}$	99.929

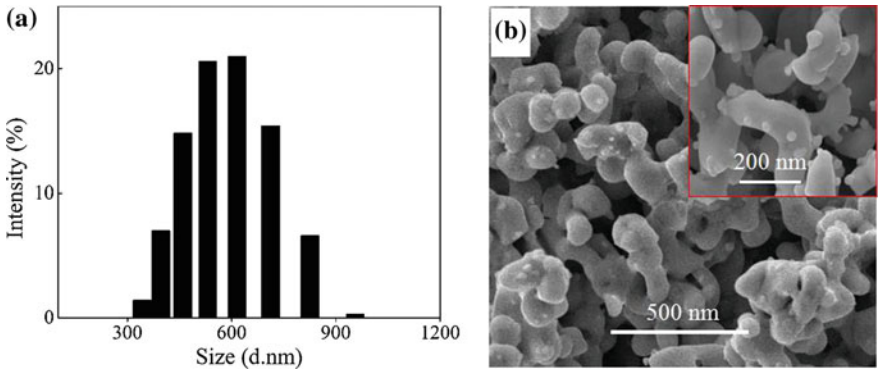

Fig. 9 Size distribution (**a**) and SEM (**b**) photos of Bi_2O_3

99 $\times 10^{-6}$ %, 245 $\times 10^{-6}$ %, respectively. The purity of Bi_2O_3 was 99.929%, achieved the demand of high-purity Bi_2O_3.

To characterize the prepared Bi_2O_3 powder, size distribution of Bi_2O_3 are given in Fig. 9a and their SEM pictures are revealed in Fig. 9b on the scales of 200 and 500 nm. In this study, the conditions for synthesizing precursor precipitates from loaded organic phase were 15 g/L oxalic acid, 1/1 phase ration, 0 min aging duration and feeding duration of 0 min. Then, the precursor precipitates was calcined at 500 °C for 2 h. As shown was Fig. 9a, the size distribution was relatively narrow, about 400–800 nm. As for the morphologies of Bi_2O_3 powders, SEM pictures shown in Fig. 9b reveal that the product was hovenia aceerba-like and size distribution around 680 nm. Fine particles were sized between 100 and 2500 nm, and coarse particles cover a range between 2500 and 10000 nm [30, 31].

Conclusions

A economical process has been developed to extract Bi as Bi_2O_3 from leaching solution. Bi_2O_3 powders were prepared by oxalic precipitation method in this study. The results indicated that concentration of oxalic acid and aging duration made a full impact on the precursor morphologies, while the aging and feeding duration have an obvious influence on the size of precursor. Bi_2O_3 product of 680 nm was obtained using 15 g/L oxalic acid, 1/1 phase ration, 0 min aging duration, 0 min feeding duration and calcinating at 500 °C for 2 h. Using this method, Bi_2O_3 product of 99.929%, purity was achieved.

References

1. Wang L, Cui ZL, Zhang ZK (2007) Bi nanoparticles and Bi_2O_3 nanorods formed by thermal plasma and heat treatment. Surf Coat Tech 201:5330
2. Ha TK, Kwon BH, Park KS, Mohapatra D (2015) Selective leaching and recovery of bismuth as Bi_2O_3 from copper smelter converter dust. Sep Purif Technol 142:122
3. Song NZ, Li WJ, Jia Q (2013) Solvent extraction of bismuth with 2-ethylhexylphosphonic acid mono-(2-ethylhexyl) ester and 2,20-bipyridyl. Sep Purif Technol 104:64
4. Ding FH, Zhan J, Wang ZJ, Chai LY, Zhang CF (2016) Simultaneous leaching of low grade bismuthinite and pyrolusite ores in hydrochloric acid medium. Hydrometallurgy 166:279
5. Zheng FL, Li GR, Ou YN, Wang ZL, Su CY, Tong YX (2010) Synthesis of hierarchical rippled Bi_2O_3 nanobelts for supercapacitor applications. Chem Commun 46:5021
6. Fan HT, Teng XM, Pan SS, Ye C, Li GH, Zhang LD (2005) Optical properties of δ-Bi_2O_3 thin films grown by reactive sputtering. Appl Phys Lett 87:231916
7. Bhande SS, Mane RS, Ghule AV, Han SH (1084) A bismuth oxide nanoplate-based carbon dioxide gas sensor. Scripta Mater 2011:65
8. Shaikh SMF, Rahman G, Mane RS, Joo OS (2013) Bismuth oxide nanoplates-based efficient DSSCs: influence of ZnO surface passivation layer. Electrochim Acta 111:593
9. Qiu YF, Liu DF, Yang JH, Yang SH (2006) Controlled synthesis of bismuth oxide nanowires by an oxidative metal vapor transport deposition technique. Adv Mater 18:2604
10. Gujar TP, Shinde VR, Lokhande CD, Mane RS, Han SH (2005) Bismuth oxide thin films prepared by chemical bath deposition (CBD) method: annealing effect. Appl Surf Sci 250:161
11. Wang Y, Jiang LX, Tang D, Liu FY, Lai YQ (2015) Characterization of porous bismuth oxide (Bi_2O_3) nanoplates prepared by chemical bath deposition and post annealing. RSC Adv 5:65591
12. Qin F, Zhao HP, Li GF, Yang H, Li J, Wang RM, Liu YL, Hu JC, Sun HZ, Chen R (2014) Size-tunable fabrication of multifunctional Bi_2O_3 porous nanospheres for photocatalysis, bacteria inactivation and template-synthesis. Nanoscale 6:5402
13. Faisal M, Ibrahim AA, Bouzid H, Al-Sayari SA, Al-Assiri MS, Ismail AA (2014) Hydrothermal synthesis of Sr-doped α-Bi_2O_3 nanosheets as highly efficient photocatalysts under visible light. J Mol Catal A Chem 387:69
14. Lu HB, Wang SM, Zhao L, Dong BH, Xu ZX, Li JL (2012) Surfactant-assisted hydrothermal synthesis of Bi_2O_3 nano/microstructures with tunable size. RSC Adv 2:3374
15. Lu Y, Zhao Y, Zhao JZ, Song YH, Huang ZF, Gao FF, Li N, Li YW (1031) Induced aqueous synthesis of metastable β-Bi_2O_3 microcrystals for visible-light photocatalyst study. Cryst Growth Des 2015:15
16. Lv XW, Zhao JL, Wang XX, Xu XR, Bai LY, Wang BX (2013) Novel Bi_2O_3 nanoporous film fabricated by anodic oxidation and its photoelectrochemical performance. J Solid State Electr 17:1215
17. Takeyama T, Takahashi N, Nakamura T, Itoh S (2006) Heteroepitaxial growth of d-Bi_2O_3 thin films on CaF_2 (111) by chemical vapour deposition under atmospheric pressure. Mater Res Bull 41:1690
18. Combes E, Sella C, Bauer D, Sabot JL (1997) Precipitation-stripping of yttrium oxalate powders from yttrium-loaded HDEHP organic solutions using an ultrasonic stirrer. Hydrometallurgy 46:1
19. Zielinski S, Buca M, Famulski M (1998) Precipitation-stripping processes for heavy metals. Hydrometallurgy 48:253
20. Konishi Y, Noda Y, Asai S (1998) Precipitation stripping of yttrium oxalate powders from yttrium-loaded carboxylate solutions with aqueous oxalic acid solutions. Ind Eng Chem Res 37:2093
21. Konishi Y, Noda Y (2001) Precipitation stripping of rare-earth carbonate powders from rare-earth-loaded carboxylate solutions using carbon dioxide and water. Ind Eng Chem Res 40:1793

22. Chen JQ, Huang B, Huang C, Sun XQ (2017) Preparation of nanoscaled yttrium oxide by citrate precipitation method. J Rare Earth 35:79
23. Mei Y, Wang W, Sun H, Nie ZR (2012) Preparation and morphology of nano-size ceria by a stripping precipitationusing oxalic acid as a precipitating agent. J Rare Earth 30:1265
24. Wang ZJ, Ding FH, Zhan J, Zhang CF (2016) Solvent extraction mechanism and precipitation stripping of bismuth (III) in hydrochloric acid medium by tributyl phosphate. J Cent South Univ 23:3085
25. Soare LC, Bowen P, Lemaitre J, Hofmann H (2006) Precipitation of nanostructured copper oxalate: substructure and growth mechanism. J Phys Chem B 110:17763
26. Li YG, Tan B, Wu YY (2007) Ammonia-evaporation-induced synthetic method for metal (Cu, Zn, Cd, Ni) hydroxide/oxide nanostructures. Chem Mater 20:567
27. Zhu CQ, Panzer MJ (2014) Seed layer-assisted chemical bath deposition of CuO films on ITO-Coated glass substrates with tunable crystallinity and morphology. Chem Mater 26:2960
28. Monnereau O, Tortet L, Llewellyn P, Rouquerol F, Vacquier G (2003) Synthesis of Bi_2O_3 by controlled transformation rate thermal analysis: a new route for this oxide? Solid State Ionics 157:163
29. Rivenet M, Roussel P, Abraham F (2008) One-dimensional inorganic arrangement in the bismuth oxalate hydroxide $Bi(C_2O_4)OH$. J Solid State Chem 181:2586
30. Buzea C, Pacheco II, Robbie K (2007) Nanomaterials and nanoparticles: sources and toxicity. Biointerphases 2:MR17
31. Taylor R, Coulombes S, Otanicar T, Phelan P (2013) Small particles, big impacts: a review of the diverse applications of nanofluids. J App Phy 113:011301

Part V
Stored Renewable Energy in Coal

Aluminum-Silicon Alloys Prepared from High-Aluminum Fly Ash to Extract Magnesium from Serpentine

Huimin Lu, Guangzhi Wu and Neale R. Neelameggham

Abstract In China's Inner Mongolia Tuquan County, 1.4 billion tons of reserves of serpentine deposits were found. Because serpentine belongs to magnesium silicate, there is no good reducing agent to reduce magnesium. In the local there is also a large reserves of high-aluminum bituminous coal for thermal power, power plants each year produce a large number of high-aluminum fly ash. The aluminum-silicon alloys obtained from this high-aluminum fly ash as the raw material by carbothermal reduction method can reduce the magnesium from the serpentine. In this paper, first, the feasibility of producing aluminum-silicon alloys by carbothermal reduction of high-alumina fly ash was studied, the hypereutectic aluminum-silicon alloys were obtained; and then the investigation on aluminum-silicon alloy as a reducing agent to reduce of metal magnesium from serpentine was carried out. According to the previous investigation, the optimized technical process for the extraction of metal magnesium from serpentine was proposed.

Keywords Carbothermal reduction · High-aluminum bearing coal fly ash Aluminum-silicon alloy · Serpentine · Magnesium

H. Lu (✉)
School of Materials Science and Engineering, Beihang University,
37 Xueyuan Road, Beijing 100191, China
e-mail: lhm0862002@aliyun.com

G. Wu
Inner Mongolia Xintai Construction and Installation Group Co, Ltd,
Huafeng Street, Tuquan County, Xintai 137599, Inner Mongolia, China
e-mail: 13910518379@126.com

N. R. Neelameggham
IND LLC, 9859 Dream Circle, South Jordan, South Jordan, UT 84095, USA
e-mail: neelameggham@gmail.com

Z. Sun et al. (eds.), *Energy Technology 2018*, The Minerals, Metals & Materials Series, https://doi.org/10.1007/978-3-319-72362-4_52

Introduction

Magnesium is the lightest metal of all the commonly utilized metal and applied in as structural material, such as construction material, in the automotive industry, medical industry and other industries [1]. In 2016 the global production of magnesium reached 900 thousand tons. The production of magnesium is based on Pidgeon process and electrolytic process, and more than 90% production of magnesium was produced by Pidgeon process from China.

Magnesium production in the world is currently dominated by the Pidgeon process which uses silicon, in the form of ferrosilicon, to reduce magnesia from calcined dolomite under vacuum. The overall reaction of the process can be written as follows [2]:

$$2\mathrm{MgO(s)} + 2\mathrm{CaO(s)} + (\mathrm{xFe})\mathrm{Si(s)} = 2\mathrm{Mg(g)} + \mathrm{Ca_2SiO_4(s)} + \mathrm{xFe(s)} \quad (1)$$

The reaction is performed in batch mode within steel retorts that operate around 1200 °C and a vacuum of 10–20 Pa to produce approximately 20 kg of Mg over an eight to ten hour period. The process suffers from high energy usage and low productivity.

In China's Inner Mongolia Tuquan County, 1.4 billion tons of reserves of serpentine deposits were found. Because serpentine belongs to magnesium silicate, there is no good reducing agent to reduce magnesium. Magnesium production in the laboratory is carried on by the Pidgeon process which uses aluminum-silicon alloy, to reduce magnesium silicate from serpentine under vacuum. The overall reaction of the process can be written as follows:

$$\begin{aligned} &54\mathrm{CaO(s)} + 14[2\mathrm{MgO} \bullet \mathrm{SiO_2(s)}] + 7[\mathrm{MgO} \bullet \mathrm{SiO_2(s)}] + 14\mathrm{Al(s)} + 7\mathrm{Si} \\ &\quad = 12\mathrm{CaO} \bullet 7\mathrm{Al_2O_3(s)} + 14[2\mathrm{CaO} \bullet \mathrm{SiO_2(s)}] + 35[\mathrm{Mg}](\mathrm{g}) + 14[\mathrm{CaO(s)} \bullet \mathrm{SiO_2(s)}] \end{aligned} \quad (2)$$

At present the Al–Si alloys are produced from silicon and aluminum separately, alloying while aluminum is melted for subsequent casting. Primary aluminum is generally produced from bauxite using molten salt electrolysis which is an extremely costly process. Silicon is generally produced in an electric arc furnace from pure quartz and extremely pure coal and coke. Each of these processes requires considerable amounts of energy and places high demands on the raw materials. It is therefore of great interest to be able to produce aluminum-silicon alloys directly from the high-aluminum bearing minerals, such as andalusite, cyanite, kaolinite, sillimanite and so on [3, 4]. The energy consumption in such a process will be considerably lower. This process also has many other advantages such as short production time, small investments for equipment, high production and energy utilization rates [5, 6]. Some countries, mainly Russia and Ukraine, have been conducting industrial trails on a large scale, where attempts have been made to recover aluminum-silicon alloys from various aluminum-silicon minerals

carbo-thermically in an electric arc furnace. In this case the mineral and carbon powder are mixed and formed into briquettes. After heat-treatment, the briquettes are charged into an electric arc furnace. The authors also produced aluminum-silicon alloys directly from andalusite by carbothermal reduction method in laboratory [7].

In the local there is also a large reserves of high-aluminum bituminous coal for thermal power, power plants each year produce a large number of high-aluminum fly ash. The aluminum-silicon alloys obtained from this high-aluminum fly ash as the raw material by carbothermal reduction method can reduce the magnesium from the serpentine. In this paper, first, the feasibility of producing aluminum-silicon alloys by carbothermal reduction of high-alumina fly ash was studied, the hyper-eutectic aluminum-silicon alloys were obtained; and then the investigation on aluminum-silicon alloy as a reducing agent to reduce of metal magnesium from serpentine was carried out. According to the previous investigation, the optimized technical process for the extraction of metal magnesium from serpentine was proposed.

Experimental Procedure

Laboratory experiments for producing aluminum-silicon alloys were conducted in a 100kVA DC submerged arc furnace, as pictured in Fig. 1. Process conditions were as follows: electrode diameter ϕ150 mm; furnace crucible diameter ϕ300 mm; depth of furnace 380 mm; transformer primary voltage 380 V, three-phase bridge rectifier DC voltages divided into four levels 22 V, 25 V, 28 V, 32 V; ratio of current to voltage 4; maximum current 4000 A when voltage at 1000 V. The electrodes used in the furnace were graphite electrodes.

Laboratory experiments for producing magnesium were conducted in a 120 kW serpentine continuous reduction of magnesium test furnace, as pictured in Fig. 2. Process conditions were as follows: the reaction is performed in semi-continuous feeding charge 30 kg each within magnesium test furnace that operate around 1200 °C and a vacuum of 10–20 Pa over an two to four hour period.

Fig. 1 100kVA DC submerged arc furnace

Fig. 2 120 kW serpentine continuous reduction of magnesium test furnace

Raw Materials

High-aluminum bearing coal fly ash. High-aluminum bearing coal fly ash (HACFA) was taken from Hequ Second Power Co. Ltd.; its sizes were smaller than 120 μm. The main composition in HACFA is 88.16 mass% ash content, 2.66 mass % volatile content, 1.54 mass% moisture content, 5.91 mass% solid carbon content. The chemical compositions of the ash content are as follows: 38.05 mass% Al_2O_3, 41.12 mass% SiO_2, 4.66 mass% Fe_2O_3, 4.07 mass% CaO, 0.34 mass%MgO, $Na_2O{\cdot}K_2O$0.32 mass% and 11.44 mass% ablation.

Bitumenite. Bitumenite (BT) was from Shanxi Datong Washing Coal Plant. Prior to use it was ground to <0.5 mm. Its composition was 12.64 mass% ash content, 28.92 mass% volatile content, 3.70 mass% moisture content, 54.74 mass% solid carbon content. The chemical compositions of the ash content are as follows: 19.52 mass% Al_2O_3, 49.84 mass% SiO_2, 6.52 mass% Fe_2O_3, and 11.72 mass% CaO.

Petroleum coke. Petroleum coke (PC) was from Tianjin Dagang Petroleum Chemical Industrial Company. Before experiments it was ground to <0.5 mm. Its composition was 0.28 mass% ash content, 8.04 mass% volatile content, 0.39 mass % moisture content, 91.29 mass% solid carbon content.

Charcoal. Charcoal (CL) used in experiments was purchased from market, its sizes were smaller than 0.5 mm. Its composition was 1.03 mass% ash content, 2.99 mass % volatile content, 3.94 mass% moisture content, 92.04 mass% solid carbon content.

Adhesive paper industry wastewater. Adhesive paper industry wastewater was from Jizhou Paper Mill. Its composition was 27.04 mass% ash content, 46.74 mass% volatile content, 5.26 mass% moisture content, 20.96 mass% solid carbon content.

Iron oxide powder. Iron oxide powder was from Tangshan Iron and Steel Plant. Its composition was 54.12 mass% Fe_2O_3, 12.74 mass% CaO, 14.02 mass% MgO, 6.11 mass%Al_2O_3 and 9.01 mass%SiO_2.

Table 1 Analysis of serpentine ore used in this work/mass%

MgO	Al_2O_3	CaO	Fe_2O_3	FeO	SiO_2	Na_2O
35.54	0.64	3.36	5.23	1.47	37.17	0.0097
K_2O	Mn	Ni	Cr	H_2O	P	S
0.055	0.048	0.22	0.12	0.48	0.0022	0.0009

Serpentine. Serpentine ore powder was taken from Inner Mongolia Xintai Construction and Installation Group Co., Ltd, the size was smaller than 0.5 mm. The main minerals in the serpentine ore are 96 mass% serpentine, and with a small amount of olivine, chrome spinel, and metal minerals including magnetite, hematite, chromite, nickel pyrite and chalcopyrite. The assay of the serpentine ore is shown in Table 1.

Test Methods

The raw materials for producing aluminum-silicon alloys were mixed uniformly in the given proportions in a stirring machine, briquetted into ovals with the major axis 60 mm and the minor axis 40 mm, and dried in the electrothermal drying box at 150 °C for 2 h until the moisture content was lower than 1%. The average density of briquettes was 1.12–1.36 g/cm^3, the porosity was 40–44%. The dried briquettes were charged into the 100 kVA DC submerged arc furnace with temperature 2000–2200 °C and time 4 h. The Al–Si alloy was discharged. The samples were analyzed by XRD, XRF analysis, SEM analysis and chemical analysis.

The raw materials for producing magnesium were mixed uniformly in the given proportions in a stirring machine, dry pressure briquetted into ovals with the major axis 40 mm and the minor axis 20 mm. The average density of briquettes was 1.62–1.66 g/cm^3, the porosity was 44–47%. The briquettes were charged into the 120 kW serpentine continuous reduction of magnesium test furnace with temperature 1150–1200 °C, vacuum of 10–20 Pa and time 2–4 h. The Mg was discharged. The samples were analysed by XRD, SEM analysis and chemical analysis.

Results and Discussion

Comprehensive Experiment for Producing Al–Si Alloys

The content of the furnace charge is 65 mass% HACFA in which the impurities are quartz, calcium oxide and magnesia etc. and the total impurities amount is not in excess of 20 mass%; 22 mass% reducing agent (bitumenite and petroleum coke, mixing ratio of bitumenite and petroleum coke 70:30) 7 mass%iron oxide powder

Table 2 The results of chemical analysis for the Al–Si alloys (mass%)

Al	Si	Fe	Cu	Ti	Mg
35.00	48.06	16.31	0.022	0.011	0.021
Zn	Mn	Ni	Ca		
0.13	0.13	0.023	0.35		

and 6 mass% adhesive paper industry wastewater. First, all the raw materials are mixed uniformly, briquetted and dried, then the carbothermal reduction experiments are conducted in the 100kVA DC submerged arc furnace with reducing temperature 2200 °C and reducing time 4 h, the aluminum-silicon alloys containing 35.00 mass % aluminum, 48.06 mass% silicon and 17% mass%iron are obtained with aluminum recovery rate 80% and silicon 70%. Table 2 lists the results of chemical analysis for the Al–Si alloys.

The analysis results of the slag by element fluorescence analysis were as follows (mass%): Al 18.13, Si 20.50, O 21.88, Ca4.54, Fe 2.53, Mg 1.03, Cr 0.05, S 0.04, K 0.02, Co 0.02, Zr 0.01, Ni0.01and C 31.24. The slag can be used as a deoxydizing or dephosphorizing agent in steel smelting. Therefore, no waste accumulates when using high-aluminum bearing coal fly ash as raw material for carbothermal Al–Si alloy production.

The analysis of the smoke from the experiments were as follows: N_2 78 vol.%, O_2 19 vol.%, $CO_2$1.5 vol.%, $SO_2$140 mg/Nm^3, solid particales 0.6 g/Nm^3; Al_2O_3 50 mass% of solid particles, SiO_2 26 mass% of solid particles. Al–Si fine powder collected from the off-gas could be used as the raw material for smelting Al–Si alloy again.

Comprehensive Experiment for Producing Magnesium

According to the condition test parameters, the comprehensive experiment was carried out on a 120 kW new serpentine semi-continuous magnesium reduction furnace. Each filling 35.8 kg, of which dry serpentine 20 kg, lime 12 kg, Al–Si alloy 3 kg, fluorite 0.8 kg, mixed even dry powder ball into the furnace, keeping vacuum 10 Pa, temperature 1200 °C, to maintain the reduction time 3 h. Comprehensive experimental raw materials and products taken from the serpentine semi-continuous magnesium reduction furnace were pictured in Fig. 3. The recoveries of magnesium extracted from serpentine by Al - Si alloy can reach 85%. The chemical analysis results of the crude magnesium obtained in the test is shown in Table 3. Visible, as crude magnesium, its quality is very good. Further refined, high quality Mg products can be obtained. The reduction slag can be used as a cement raw material due to the transformation of calcium dichromate crystal in form of expansion and self-crushing loose white powder, the size smaller than 50 μm, the chemical analysis results were as follows: 61.69 mass%CaO, 13.45 mass% Fe_2O_3, 17.44 mass%SiO_2, 4.39 mass% Al_2O_3, and 3.03 mass%MgO. The obtained residue was subjected to magnetic

Fig. 3 Comprehensive experimental raw materials and products. (Left upper: pellet; left lower: crystalline magnesium; Right upper: nickel-iron alloy; right lower: slag)

Table 3 The chemical analysis results of the crude magnesium (mass%)

Si	Cr	Ni	Cu	Zn	Ca	Fe	Al	Mg
0.001	0.002	0.002	0.002	0.002	0.003	0.005	0.002	99.58

separation to obtain a nickel iron block. The chemical analysis results were as follows: 2.32 mass%Ni, 97.68 mass% Fe. Nickel iron recovery rate was about 85%.

Conclusions

1. It is feasible to produce aluminum-silicon alloys by carbothermal reduction of high-aluminum bearing coal fly ash. The optimum mixing ratio of furnace charge was determined to be 65% high-aluminum bearing coal fly ash; 22% bitumenite and petroleum coke as reducing agent, the mix proportion of bitumenite and petroleum coke should be in the range of 8:2–6:4; with 6% binder calcium lignosulphonate and 7 mass% iron oxide powder. All these raw materials are mixed uniformly, briquetted and dried, the carbothermal reduction experiments are conducted in a 100kVA DC submerged arc furnace with

reducing temperature 2000–2200 °C and reducing time 4 h, the aluminum-silicon alloys containing 35 mass% aluminum, 45 mass% silicon and 17 mass% Fe can be obtained with aluminium recovery rate 80% and silicon 75%.

2. The process of extracting magnesium from the aluminum-silicon alloy heat-reducing serpentine is reasonable. The Al–Si alloy and the calcium oxide can extract the metallic magnesium from the serpentine at 10–20 Pa of vacuum and from 1100 to 1200 °C. In the process of magnesium extraction, at the same time these nickel-iron alloy and dicalcium silicate and aluminum silicate slag used as raw materials for the preparation of cement can be obtained.
3. Laboratory scale of comprehensive experimental studies has shown that serpentine extraction of magnesium metal is feasible, and magnesium recovery rate reaches 80%. This is a cleaning process with no carbon dioxide emissions.
4. Laboratory semi-continuous reduction furnace improves magnesium production efficiency and reduces costs, it is worth further study, and it has a bright future. Raw materials for production of Al–Si alloy are obtained easily, such as coal gangue, fly ash and so on. Semi-continuous process with aluminum-silicon alloy from the serpentine extraction of metal magnesium is simple, clean production, and low cost.

References

1. Eliezer D et al (1998) Magnesium Science, Technology and Applications. Adv Perform Mater 5:201–212
2. Halmann M et al (2008) Magnesium production by pidgeon process involving dolomite calcinations and MgO silicothermic reduction: thermodynamic and environmental analyses. Ind Eng Chem Res 47:2146–2154
3. Striplin Jr. MM et al (1949) Production of silicon aluminum alloys.US Patent 2488568, 22 Nov 1949
4. King K (1987) Aluminum and its alloys. Ellis Horwood Limited, England
5. He Chongping, Wang Enhui (1994) The production technology of aluminum-silicon alloy by electrothermal method. Science and Technology Press, Beijing
6. Zhang Feng, Li Mengji (2003) Technology of producing Aluminum–Silicon Alloys (Al50%). Ferro-Alloys 171(4):17–21
7. Yuan S, Lu H, Wang P (2017) Study on producing solar grade silicon by carbothermal reduction of andalusite Ore. In: Energy technology. The minerals, metals & materials society, carbon dioxide management and other technologies, pp 325–332

Organic Agriculture Using Natural Material Coal

Neale R. Neelameggham and Brian R. Davis

Abstract Organic agriculture is using natural materials such as degrading plant matter to replenish soils. This includes use of naturally degraded plant components such as peat, humus and weathered brown coals. Another important natural organic matter which has not been applied in agriculture thus far has been the black coal, Here we show that reversing the coal formation reaction by combined hydro-oxidation principles of biochemical engineering in natural conversion methods in an accelerated fashion. The modified coal soil additive can convert arid lands into farm lands for the future to sustain the population growth. In addition, the development of this new use of black coal will revive economically deprived areas from phasing out coal in the USA and Europe. This will show how the Stored energy in coal can be made renewable in helping plant growth under the soil to facilitate above ground photosynthesis.

Keywords Organic agriculture · Soil organic carbon · Humates
Coal · Bituminous · Lignite · Hydro-oxidation · Arid land greening

Introduction

Using natural materials such as degrading plant matter to replenish the soils is termed as organic agriculture. This includes use of naturally degraded plant components such as peat, humus and weathered brown coals called leonardite. Another important natural organic matter which has not been applied in agriculture thus far has been black coal containing considerable organic elements of carbon, hydrogen, oxygen and nitrogen. With the advent of alternate energy resources for nonfood items it becomes feasible to use this coal in agriculture. There is a need for

N. R. Neelameggham (✉)
IND LLC, UT, South Jordan, UT, USA
e-mail: neelameggham@outlook.com

B. R. Davis
Brian Davis Consultants Associates, Manvel, TX, USA

Z. Sun et al. (eds.), *Energy Technology 2018*, The Minerals, Metals & Materials Series, https://doi.org/10.1007/978-3-319-72362-4_53

replenishing organic matter in soils which have become weak in organic matter. Increasing population and the projected increase in population during the next several decades indicates the need for increased water as well as food resources. The increased need for food supplies means increased agricultural growth. This can only happen by improving nonagricultural lands including arid lands.

Soil Organic Carbon

The land types are classified by their soil organic carbon amounts. [1, 2]. Naturally available 'peat' material such as sphagnum act as the effective organic matter and in retaining water, help initiate sprouting from seeds, and root growth. Peat becomes lignite or brown coal during the long-term natural decay of plant matter. The reversal of the process on lignite–called weathering recreates leonardite containing humates used in organic gardening. The short-term decay of plant matter is called Compost—which also contains humates applied by household organic gardening [3]. It should be noted that although decay of plant matter in the short term is called 'composts' for partial decaying and long term conversion to more complete decay is termed conversion to 'brown and black coals'. Understanding of the chemical phenomenon can facilitate 21st century methods of carrying out both the forward decay of plants which had 'life' and the reverse revival back from black to brown coal—humates—peat and to higher moisture laden matter capable of self-propagation. The forward or the reverse process can be accelerated to shorter time periods.

Soils rich in organic carbon is usually dubbed as topsoil, and is considered a matter of commerce, similar to sphagnum peat, soil amendments from leonardite, and natural humus which are essentially 'coal in the making'. Freeman Dyson had noted that "replenishing topsoil world-wide in its efficient use of products of energy component release in the air as follows—"Good topsoil contains about ten percent biomass, [Schlesinger, 1977], so a hundredth of an inch of biomass growth means about a tenth of an inch of topsoil. Changes in farming practices such as no-till farming, avoiding the use of the plow, cause biomass to grow at least as fast as this. If we plant crops without plowing the soil, more of the biomass goes into roots which stay in the soil, and less returns to the atmosphere…'\" [4].

Humates

The study of humates presented by Robert E Petitt, Texas A and M, discusses the importance of organic matter in healthy and fertile soils. Pettit shows that "the oxidative degradation of some humic substances produces aliphatic, phenolic, and benzenecarboxylic acids in addition to n alkanes and n fatty acids. The major phenolic acids released contain approximately 3 hydroxyl (OH) groups and

between 1 and 5 carboxyl (COOH) groups [5]. Petitt also notes the importance of the humic components to keep the soil fertile for several centuries.

One of the volumes of UNESCO books–Encyclopedia of Life support systems ELOSS discusses the structure of different types of coal—notes parts of the phenolic groups present in humates. [5]. The differences between the hydrophobic and hydrophyllic nature of different ranks of coal—black (hydrophobic) and brown (hydrophyllic) have also been noted during the clean coal production by froth flotation. The difference is due to the variation of the phenolic and carboxylic groups of the coal. Students of organic chemistry know the methods of carboxylation or carbonylation of phenolic groups to carboxylic group [6]. Such methods are also parts of weathering reactions can be stimulated in an organic fashion in the soil. These are evidenced by the changes in the soil carbon content and water holding capacity in the revegetated coal mines which takes place within a short period of 10 to 12 years [7].

Flora Friendliness of Coal

The Flora friendliness of coal—and its organic matter utilization is evidenced in plants growing among coal spills as shown in Fig. 1 taken near an abandoned coal mine in Utah.

The natural manures—which are animal digested vegetation—when dried becomes energy fuel and are combustible similar to longer term deoxygenated and dehydrated plant matter which is coal. Humates are also naturally decayed vegetation and are used as fuel matter where necessary similar to bio-fuels from wood burning [still younger decaying wood] or charcoals. While full conversion reactions to carbon dioxide and water vapor make these energy maerial. The partial soil

Fig. 1 Indian paint brush plant growing on coal spills

reactions make the core of organic agriculture providing energy for consumption in the form of agricultural products. This is the basis for organic energy conversions.

It is to be noted that most of the coals formed from plant matter decay still contain mineral nutrients [ash formers when combusted] besides the basic plant life producing major elements of carbon, hydrogen, oxygen, nitrogen with minor [interim quantities] elements of phosphorous, potassium and sulfur.

Organic Agricoal

We have been developing the manufacturing of an organic agricultural matter from coals. These methods include

[a] use of accelerated natural conversion of black coals in providing increase in soil carbon
[b] use of accelerated natural conversion of black coals in facilitating organic agriculture of arid lands as well as promoting fertile land in depleted soils
[c] quantify organic gardening methods of natural conversion of black coals in providing the fundamental reactions by laboratory measurements of functional soil chemistry.

We have the fundamentals for developing manufacturing methods for large scale natural conversion of the coals into agricultural products of commerce. The conversions can be monitored using proven techniques of FTIR methods used in the studies of humates [8–11].

Arid Lands Worldwide

There are vast areas of the world which were made arid several centuries ago—which are known as Deserts of the world. In addition, the human population growth has created 'drought prone' areas and arid lands—due to the trials and errors of anthropogenic misjudgments. Allan Savory [12] had expressed that such follies as getting rid of 'elephant population' in Africa and how it caused desertification of grass-lands. Similar events of lowering cattle population in other parts of Africa—causing lowering of soil carbon, nitrogen and other nutrients which cattle were recyling back to the grass lands from their solid and liquid excretions, leading to desertification. Cattle or animal excreta are full of the basic elements CHON with minor P and K and other micro elements from their plant matter fodder digestion. Deforesting is another of our follies to cause an imbalance in photosynthesis of our 'soul vapor re-incarnation'. City scaping making soil impervious by asphalt roads [without sufficient permeable soils] leading to lack of ground water replenishments

is another 'error' even in high rain area cities lacking drinking water. This is in addition to urban heat islands.

Allan Savory's holistic approach to reverse desertification is impressive, but we need a larger scale rapid conversion of global arid lands to help provide water and food for the human population increases in the coming decades. Material balances would show that it would require a large quantitative replenishment of soil carbon in a short time. We can accomplish such conversions with the plentiful coal in the world by judicious applications in the arid lands of the world providing the resurrection of the land—by resurrecting the valuable elements in coal, lignite and the like by reversing coalification. This is a method of extracting the stored energy in the renewable energy matter—COAL.

Conclusion

Arid lands lack soil organic carbon to facilitate plant growth. Our initial studies have indicated the use of naturally available organics such as modified coal—can act as soil amendment for organic 'agriCoalture', usable in providing the organic carbon required for plant growth. Organic carbon alone cannot sustain plant growth —the soil amendment should be made in a manner to maintain soil moisture for the growth of the plants. The modified coal should also preferably be augmented by other basic minor and macro nutrients of 'life of plants' besides the essential CHON major matter in the arid soils. Proprietary techniques are being developed to show enhancing water retention properties along with needed carbon in the arid soils to facilitate root system buildup for efficient plant growth.

We are considering demonstrations of this in arid areas of the US—around Mojave Desert as well as in the Horn of Africa arid lands in Ethiopia, Somalia and Kenya,

References

1. Burbingh P (1984) Organic carbon in soils of the world. In: Woodwell GM (ed) The role of terrestrial vegetation in the global carbon cycle: measurement by remote sensing SCOPE, Wiley, pp 91–110
2. Scharlemann JPW, Tanner EVJ, Hiederer R, Kapos V (2014) Global soil carbon: understanding and managing the largest terrestrial carbon pool. Carbon Manag 5(1):81–91. https://doi.org/10.4155/cmt.13.77
3. Moore R (2017) Caring and sharing organic gardening–compost, equipment, ideas and training, http://www.thesoilguy.com/SG/HumicAcid. [seen 15 Jan 2017]
4. Dyson F (2016) Heretical thoughts about science and society. https://www.edge.org/conversation/freeman_dyson-heretical-thoughts-about-science-and-society. [seen 23 July 2016]
5. Pettit RE (2017) http://www.humates.com/pdf/ORGANICMATTERPettit.pdf. [seen 15 Jan 2017]

6. Kechang X (2009) Coal geology and geochemistry. In: Jinsheng G (ed) Coal, oil shale, natural bitumen, heavy oil and peat—Encyclopedia of life support systems, vol I, UNESCO publication, pp 40–75
7. Singh RS, Tripathi N, Chaulya SK (2012) Ecological study of revegetated coal mine spoil of an Indian dry tropical ecosystem along an age gradient. Biodegradation 23:837. https://doi.org/10.1007/s10532-012-9573-6
8. Ye Y, Jin R, Miller JD (1988) The hydrophobic character of pretreated coal surfaces. In: Proceedings of the surface chemistry of coal, 196th american chemical society national meeting, Los Angeles, California, 25–30 September 1988, pp 811–818
9. Wang J, He Yaqun, Yang Y (2017) Research on quantifying the hydrophilicity of leached coals by FTIR spectroscopy. Physicochem Prol Miner Process 53(1):227–239
10. Enev V, Pospíšilová L, Klučáková M, Liptaj T, Doskočil L (2014) Spectral characterization of selected humic substances. Soil Water Res 9:9–17
11. Bleasa M, Miranda JL, Moliner R (2003) Micro-FTIR study of the blend of humates with calcium hydroxide used to prepare smokeless fuel briquettes. Vib Spectrosc 33:31–35
12. Allan Savory Talk—video, https://www.ted.com/talks/allan_savory_how_to_green_the_world_s_deserts_and_reverse_climate_change. [seen May 2017]

Extraction and Production of Rare Earth Elements from Coal-Seam Bedrock and Caprock

John Gordon

Abstract Rare earth elements (REE) required in modern technological products are found in shale rocks above and below coal seams. Often during the process of mining coal, shale rock adjacent to the seam inadvertently is removed then diverted to landfill sites. Ecologically sound and potentially economic methods of extracting the REEs from these landfills are proposed. Methods include utilizing geomemembrane barrier beneath the landfill site, ion exchanging with moderate pH, slightly acidic, sodium chloride solutions. Sodium hydroxide is utilized to precipitate the REE-hydroxides subsequently converted to REE-chlorides with suitable amount of hydrochloric acid. All acid and base streams are co-produced with efficient membrane/electrolysis technology. Concentrated-REE chlorides are transported to centralized solvent extraction facilities for isolation and purification. Solvent extraction processes also employ the methodology of using co-produced acid/base streams. This paper details minimization of environmental impacts and maximizing economics to produce valuable REEs while increasing the economics of coal mining.

Keywords Rare earth elements · Coal byproducts · Ion exchange
Solvent extraction

Background

Rare earth elements such as light rare earth elements (LREE) Sc, La, Ce, Pr, Nd, Eu, Sm, Gd and heavy rare earth elements (HREE) Y, Tb, Dy, Ho, Er, Tm, Yb, Lu are produced nearly exclusively in China but are strategic to modern technology used in permanent magnets, phosphors, lasers, automotive catalytic converters, fiber optics/superconductors, electronic device, cell phone displays, advanced batteries, and wind generation turbines. Developing additional supplies of these elements as a

J. Gordon (✉)
JG Novel Solutions LLC, Salt Lake City, US
e-mail: johnhowardgordon555@gmail.com

Z. Sun et al. (eds.), *Energy Technology 2018*, The Minerals, Metals & Materials Series, https://doi.org/10.1007/978-3-319-72362-4_54

byproduct to existing operations in other industries would work toward stabilizing supply and prices. One of the problems which occurred in both the US in the past and in China currently is negative environmental impact due to strong acids utilized in extraction of the REE's. REE's can be found in the bedrock and caprock surrounding coal seams. For example, S. Miskovic in "Extraction of REE from Coal, Univ. Of Utah—REE recovery from Western Coals", January 2015 [1], reported REE content between 200—over 600 ppm in the inorganic content of coal samples in the Western United States [1]. Ion exchange is a technique which has been utilized to pull REE's from REE bearing clays and rock in some cases.

Goals

A goal is to develop a methodology for extracting REE's from the waste rock of coal mining operations which are destined for landfill where the methodology is cost effective and environmentally sensitive.

A second goal is to expand the methodology to reduce environmental impact from the REE separation and purification required for saleable products.

We propose to focus on coal byproduct resources rich in clay type material suitable for ion-exchange.

Typically physical separation/mineral processing methods are used to concentrate REE minerals. According to Papangelakis and Moldoveanu, many REE bearing minerals require harsh leaching conditions: concentrated sulfuric or hydrochloric acid and sometimes high temperature with concentrated sulfuric or 70% sodium hydroxide. At the same time, "in spite of their low grade, ion-adsorption clays account for –35% of the China's total REE production …" [2] While pursuing the high concentration minerals would provide higher yield, the methods used may not be appropriate for extracting REE's from low grade sources such as coal byproducts because of high process expense and also because of the risk of leaving behind undesirable acidic or basic waste streams.

Hower et al. report "rare earths have been found in interesting concentrations in the strata above and below certain coal seams" [3]. Finkelman estimated that not more than 10% of the total REE' in the lignite had an organic association, the remaining 90% of the REE were associated with REE-bearing minerals [4]. Hower reports Finkelman and Palmer presented in unpublished U.S. Geological Survey data, the distribution of light and heavy REE's vary in distribution from association with clays, phosphates, and carbonates. REE's associated with clays require the least aggressive conditions to extract, and at the same time result in lower uptake in non-REE's such as alumina and silica in the process [3]. Looking at 36 samples of coal byproducts in the Western U.S. from 7 states, Sanja Miskovic of the University of Utah reported REE content in the inorganic portion of a variety of samples ranging from less than 100 ppm to over 600 ppm total REE with about half in the 200–450 ppm range [1]. Among these, the distribution of REE's includes a sizable portion of scandium, one of the most valuable REE's. Miskovic found no benefit

from physical methods of concentration such as particle classification density separation, flotation, and wet magnetic separation in concentrating the REE's content. In part to confirm Miskovic's findings, samples were obtained from two veins of a in the mine near Price, Utah and another coal mine near Salina, Utah. These were rock samples. Analysis of REE's in the roof rock of these veins, verified the presence of REE's and significant amounts of scandium. Analysis of volcanic ash based rock obtained from a source in Emery, Utah, located between the two coal mines was rich in REE's and about 50 ppm scandium. This finding is consistent with Hower reporting:

Some Kentucky, Utah, and Wyoming REY occurrences are largely the result of volcanic ash falls. Crowley et al. noted three enrichment mechanisms:

(1) Leaching of volcanic ash with subsequent concentration by organic matter;
(2) Leaching of volcanic ash with subsequent incorporation into secondary minerals; and
(3) Incorporation of volcanic minerals into the peat [3].

We propose to use mildly acidic sodium chloride lixiviant and concentrate the REE with hydroxide precipitation in mildly basic pH

Papangelakis and Moldoveanu report, while aggressive conditions in terms of acid or base concentrations and temperatures are required to extract REE's from many minerals such as the bastnasite, monazite, xenotime, breaking down mineral matrixes, *with clays ion exchange at room temperature is possible*. "A simple leach using monovalent sulphate or chloride salt solutions at ambient temperature can produce a high-grade REO product."… "…under atmospheric conditions, the leaching power of monovalent ions for REE extraction depends on the hydration energy of the exchange ion, following the order Cs^{+}>$NH4^{+}$>Na^{+}>Li^{+}, in both sulphate and chloride. Batch leaching studies also revealed that the ion exchange process achieved equilibrium in as little as 5 min, regardless of the experimental conditions; ambient temperatures and moderately acidic acid pH values (4–5) represent optimum conditions for maximum REE recovery."…"REE occur as soluble free cations/hydrated cations or part positively-charged complexes in solution adsorbed species on clays [2]. These species account for 60−90% of total content of rare earths in ores and can be recovered by ion-exchange leaching with monovalent salts."

The standard ion exchange process utilizes ammonium sulfate solution contacted with the REE bearing clays. Ammonium ion exchanges for the REE cations solubilizing the REE:

$$2\,\text{Clay-REE} + 3(NH_4)_2SO_{4_{(aq)}} \rightarrow 2\,\text{Clay-}(NH_4)_3 + REE_2(SO_4)_{3_{(aq)}}$$

The next step is utilized to concentrate the REE from the dilute solution. Oxalic acid is used to precipitate the REEs:

$$REE_2(SO_4)_3 + 3\,H_2C_2O_4 + 10\,H_2O \rightarrow REE_2(C_2O_4)_3{\cdot}10H_2O + 3H_2SO_4$$

Following precipitation, REE-oxalate is roasted to convert to REE-oxide, releasing carbon monoxide and carbon dioxide as part of the process.

Earlier, in what Papangelakis and Moldoveanu call "first generation leaching technology," in the early 1970s, NaCl was used instead of ammonium sulfate [2]. NaCl is less expensive and less harmful ultimately to streams if leakage were to occur. The reason NaCl was less preferred was that Na-oxalate co-precipitated with the REE-oxalate resulting in low purity and poor utilization of the oxalate.

We propose precipitation with mild pH sodium hydroxide—it is lower in cost than oxalic acid and avoids a roasting step

Fortunately, Clifford Meloche and Frederick Vratny reported on the formation of REE- hydrous hydroxides and their solubility's as a function of pH. Essentially all the REE's form hydroxides and precipitate by pH 9 as the pH is increased. Even with varying temperature, the solubility of the REE-hydroxide is very low once pH 9 is reached [5]. Thus, addition of sodium hydroxide can be utilized to precipitate REE's and separate them from dilute chloride solutions. In this way the expense of purchasing oxalic acid with associated roasting and CO_2 emissions can be avoided.

We propose utilizing less expensive and environmentally preferred NaCl, nearly as effective as NH_4^+ for exchanging with REE^{+++}, over ammonium sulfate. NaCl is lower in cost, we will exchange with a higher concentration, say 1M NaCl versus 0.3 M ammonium sulfate. Thus the proposed scheme is the following:

- Reactions

$$\text{Clay-REE} + 3\text{NaCl}_{(aq)} \rightarrow \text{Clay-Na}_3 + \text{REE(Cl)}_{3(aq)} \qquad \text{Ion - Exchange}$$

$$\text{REE(Cl)}_{3(aq)} + 3\text{NaOH}_{(aq)} \rightarrow \text{REE(OH)}_{3(s)} + 3\text{NaCl}_{(aq)} \qquad \text{Precipitation}$$

$$\text{Clay-REE} + 3\text{NaOH} \rightarrow \text{REE(OH)}_{3(s)} + \text{Clay}-\text{Na}_3 \qquad \text{Overall}$$

Maintaining overall process neutrality

Simply converting REE's to REE-hydroxides creates an acid/base imbalance. If a goal is to have an overall neutral process, after crashing out REE-hydroxides, the hydroxides can be converted to chlorides with the co-generated HCl.

$$\text{REE(OH)}_3 + 3\text{HCl} \rightarrow \text{REE - Cl}_3 + 3\text{H}_2\text{O}$$

Once dried the REE-chlorides mixture can be ship to a central processing site for further processing, separating the REEs, after crashing out REE-hydroxides, the hydroxides can be converted to ch

Producing all the acid and base on-demand with inexpensive NaCl feedstock

Figure 1 shows a schematic 4 chamber electrochemical cell which can be utilized for taking inexpensive NaCl (the same material to be used as a lixiviant) and

produce all the acid and base necessary for adjusting the pH of the lixiviant to the desired level (pH 3–5 likely), to raise the pH of the pregnant leach solution to pH9 to produce REE-hydroxides, then to neutralize the hydroxides back to chlorides desirable for shipping and subsequent separation and purification processing. Sodium chloride solution enters the second chamber. Under a potential gradient, sodium ion passes through a cation exchange membrane to the first (left) chamber where hydroxyl ion is formed at the cathode, and hydrogen is evolved—thus sodium hydroxide is produced in the first chamber. Concurrently, chloride ion passes from the second chamber through an anion exchange membrane to the third chamber. In the fourth chamber, protons are formed at the anode, evolving oxygen. Those protons pass through a cation exchange membrane from the fourth to the third chamber. The reason for dividing the third and fourth chamber is to avoid the possibility of chlorine evolution at the anode. Thus hydrochloric acid is produced in the third chamber at the same rate as sodium hydroxide in the first chamber. The overall acid/base production and requirements are balanced. The same type of cell is used later in the separation and purification processing. The hydrogen and oxygen gases from the anode and cathode reactions can be reacted back to water or used for some other purpose.

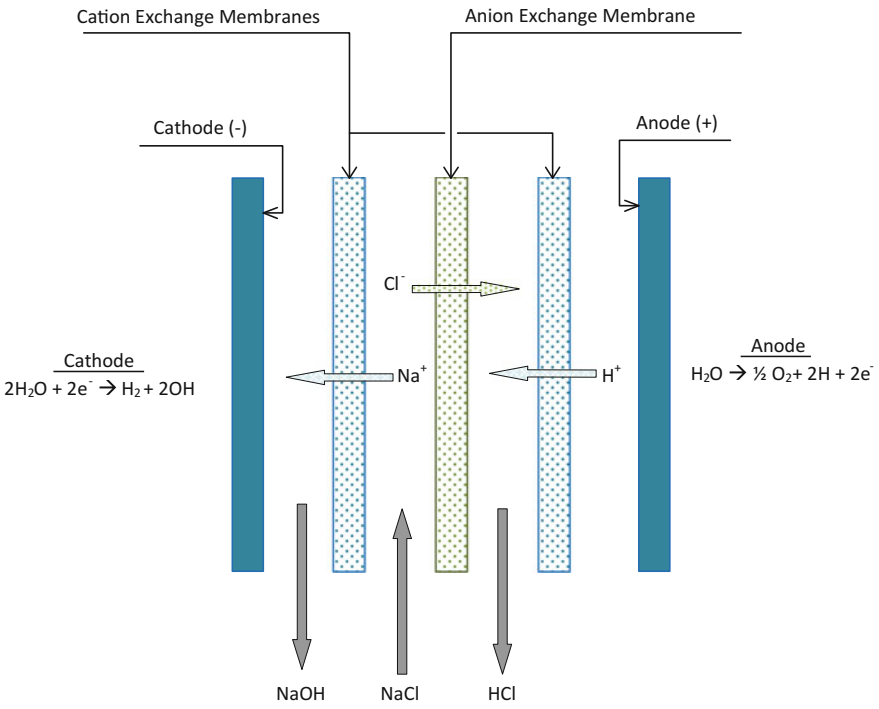

Fig. 1 Schematic of electrochemical cell and process

Assuming average REE atomic weight of 139, REE concentration of 300 ppm (based on weighted averages of the REE distribution found by Miskovic and typical REE concentrations reported), and 40% overall yield, and $100/ton for the NaCl cost, the cost for NaCl will amount to about $0.30/kg REE-oxide.

For the electrolysis the standard open circuit potential is about 2.06 V. Assuming 4 V operating, $0.10/kWh, average REE atomic weight of 139, REE concentration of 300 ppm, and 40% overall yield, the power cost will amount to about $0.49/kg-REE-oxide.

This overall scheme thus far is shown schematically in Figs. 2 and 3.

The method by which the ion-extraction can be executed may vary. For example, crushed rock may be placed in tanks then exposed to lixiviant. Tanks may be far easier to execute quickly since permitting process would be more easily obtained. But possibly the lowest cost approach may involve heap leaching. At some mines,

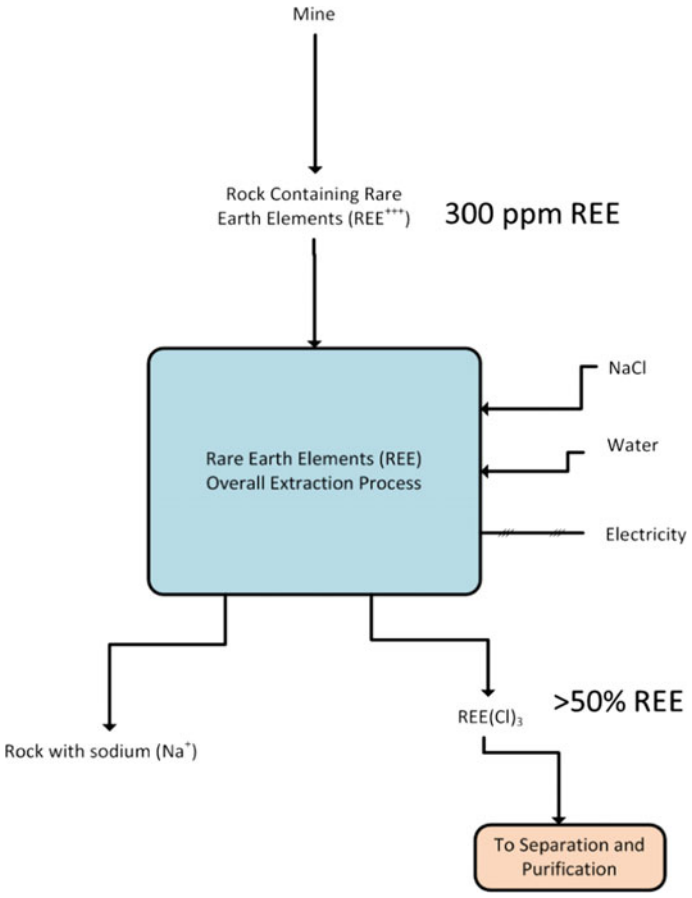

Fig. 2 Overall schematic of ion extraction procession-extraction process

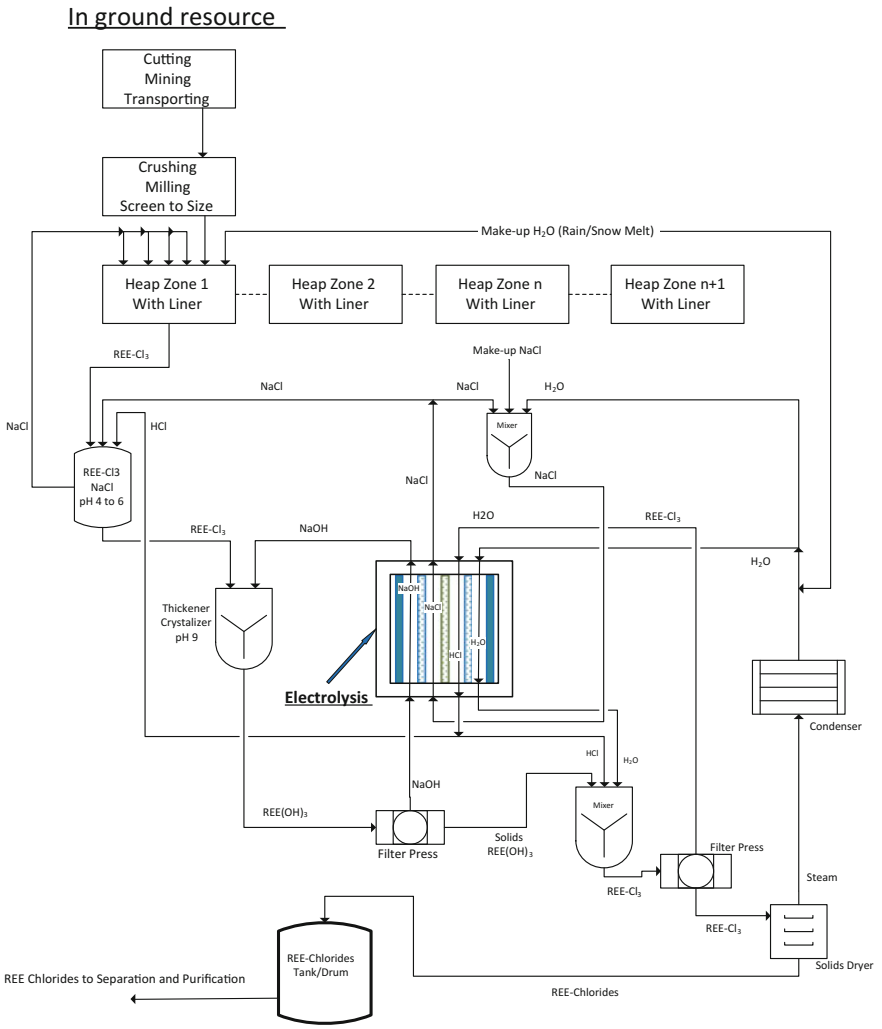

Fig. 3 Schematic ion-extraction process

for example, the waste rock is transported into a cavity in the terrain where it fills in, is packed, then eventually covered with soil for land reclamation. As an alternative, the process could be altered where a geomembrane is first placed at the bottom of the cavity and a liquid collection system. After the rock is place, pipes for distributing lixiviant could be place on the top and a leaching cycle could begin. Once the lixiviant is pregnant with REE with REE a leaching cycle could begin. Once the lixiviant is pregnant with REE with REEREEembrane is first placed at the bottom of the cavity atation waste rock to the cavity are already born by the standard coal mining process. The incremental change is the addition of the geomembrane.

The simplicity of the process and the lack of expensive equipment makes the process economic for metals such as gold and copper. In the case of gold ore leaching the process is performed on ores that contain only 1–2 parts per million gold in the host rock matrix. In the case of rare earth elements, the concentrations are much higher, but the values are lower. However the process is also performed commercially for relatively low cost copper with concentration levels of around 2500 ppm. Thus, with the concentration of rare earth elements of around 300 ppm with average values of recovered elements that are much higher than copper, it is clear that this approach for metal extraction and recovery of rare earth elements could be economically viable and provide additional income to coal mining companies, and in some cases may have sufficient value to justify rare earth element production without coal production.

Extraction Technology

Low concentration resources such as those found for rare earth elements in coal necessitate low-cost methods of extraction in order to make the extraction economically viable. The lowest cost, practical chemical extraction method for extraction of metals from host rock ore particles such as coal or minerals adjacent to coal seams is heap leaching. Heap leaching begins after the metal-bearing minerals are crushed to an appropriate size. Ideally, the size is fine enough for excellent penetration and extraction, but coarse enough that piles of material have excellent mechanical stability [6]. The mechanical stability of the heaps is necessary to eliminate legacy issues such as tailings failures that have been problematic in some closed coal processing facilities. The process of heap leaching can be easily modeled by appropriate methods [Michael L. Free, Proceedings of Copper 2016, Nov. 15, 2016, Kobe, Japan] [7].

For heap leaching, Smith and Parra reviewed the pad costs for 28 installations over the world and normalized the costs to 2014 dollars [8]. They report an average of \$36/m^2 for earthworks costs and \$9/m^2 for the geomembrane liner system for a total of \$45/m^2. Cost in the US were 35% less than average and conventional pads were about 40% less than valley leach pads, but in the interest of being conservative we assumed the overall average cost; although, it can be argued much of the expense of earthworks is already part of the current coal mining expense. Heap leach depths typically are 100 to 200 feet and as high as 500 feet. Assuming 200 foot depth of the heap (61 m), and assuming waste rock specific gravity of 2.65 g/cc and overall effective density of 1.17 g/cc the earthworks and geomembrane, assuming average REE atomic weight of 139, REE concentration of 300 ppm, and 40% overall yield and no credit for current waste rock disposal costs, the heap leaching structure and membrane cost amounts to \$2.67/kg yielded REE-oxide.

Figure 4 depicts a modular extraction skid housing tanks, pumps, electrolysis module, filter and solids dryer coupled to a heap leach pad with three zones (not to scale).

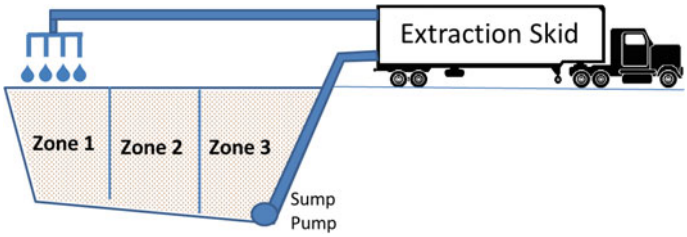

Fig. 4 Cartoon of a modular extraction skid coupled with 3 heap leach zones

We propose using nearly standard solvent extraction with the exception that the acid/base cell developed for ion-extraction is also used for pH adjustments and to finally concentrate the purified REE's

Chemical Separation Technology

Effective separations of rare earth elements require appropriate use of separation technologies such as solvent extraction or liquid-liquid extraction. In solvent extraction loading, an organic solvent containing selective organic extractant molecules is mixed in a mixer (see Fig. 4) with an aqueous solution containing metal that was dissolved during an extraction step such as heap leaching as discussed previously. As the selective organic extractant molecules in the solvent contact the metal-bearing aqueous phase, the metal binds to the extractant molecules and is dissolved in the mixture of organic solvent and organic extractant that form an organic phase. After the metal has been transferred from the aqueous phase to the organic phase, the organic phase is allowed to separate from the aqueous phase in a settler. The organic phase is then transferred to a stripping unit that has a mixer and settler that utilize an aqueous phase that contains a high acid concentration that replaces the dissolved metal in the organic phase, thereby transferring the metal into a more concentrated and acidic solution than in the previous loading stage [9].

Solvent extraction is typically performed using multiple loading stages in a counter-current flow pattern The number of stages is determined using a McCabe-Thiele diagram. The McCabe-Thiele diagram is based on equilibrium measurements for the aqueous and organic phases at different metal ion concentrations as well as a mass balance for the aqueous and organic flows in the system. Several authors detail the specifics of solvent extraction purification including Feng Xie et al., C. K. Gupta and N. Krishnamurthy. W. Wang and C. Y. Cheng specifically provide details for scandium separation and purification which is of particular importance to us because of the large presence observed in coal-byproducts and very high market price [10–12].

In general, if we assume the we will primarily utilize REE-chlorides as feed to the aqueous phase, and organophosphate acids like Di-(2-ethylhexyl)phosphoric acid (D2EHPA, DEHPA, HDEHP) in the organic phase, there is a certain amount of acid and base required to maintain optimal loading and stripping. For example, raffinate from solvent extraction separation is acidic due to the protons released from the organophosphoric acid as it loads up with REE, we want to neutralize the raffinate with base before feeding to the next separation stage. On the other hand, aqueous chloride solution feed to the scrub section is acidified to about pH4 to

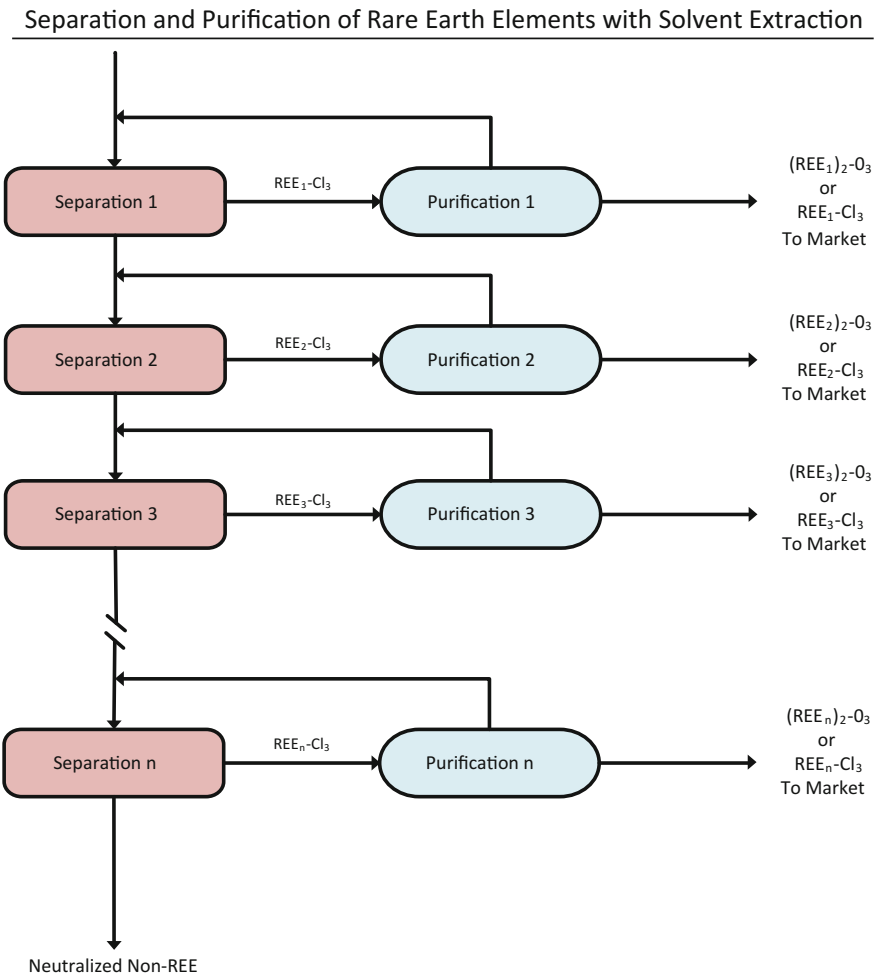

Fig. 5 Schematic of overall Solvent Extraction separation and purification

promote uptake of protons from the organophosphoric acid so it unloads the REE and likewise, for the Purification solvent extraction train for the same purpose. These acids and bases can be generated by the same type of cell shown in Fig. 4. Exiting the purification train scrub exit, we will use the same methodology as at the ion-exchange site, where we add sodium hydroxide bringing the pH to about 9 to

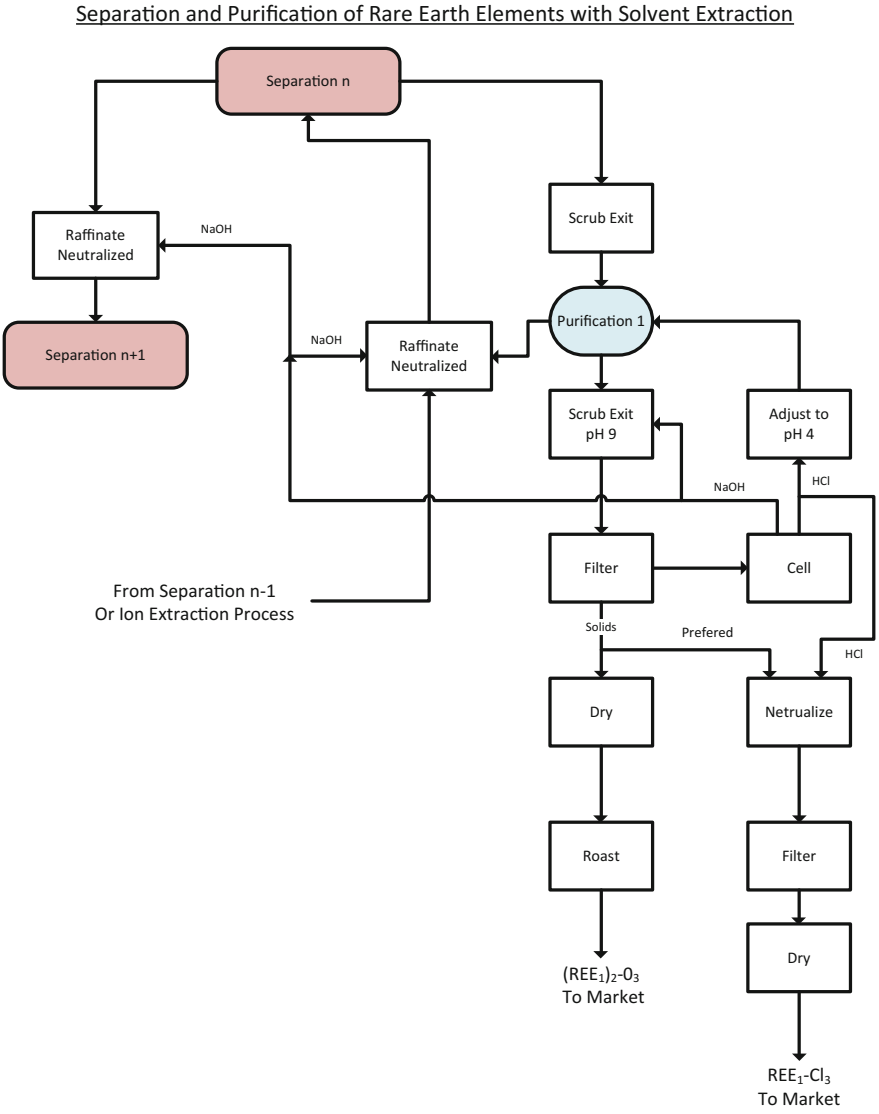

Fig. 6 Detailed schematic flow chart of separation/purification Solvent Extraction Process

precipitate purified REE-hydroxide which is filtered from the solution. Following filtration, the REE-hydroxide will either be dried and roasted to for an oxide form product or neutralized with hydrochloric acid to form purified REE-chloride which may be sent to electrowinning (conversion to metal) depending on market demand. Ideally the REE is converted to the chloride form so our acid and base production evenly matches. Otherwise acid and base may be purchase or sold to provide overall balance. Again, the electricity cost for the acid/base production, assuming 40% yield is $0.49/kg REE-oxide.

Figure 5 is a simplified schematic of the separation/purification process with solvent extraction.

Figure 6 is another schematic process flow diagram with more detail.

Partial Summary of Preliminary Costs

Table 1 provides a summary of the estimated extraction and purification costs estimated so far. These costs are rolled into the costs shown in Table 1.

The estimates are based on 40% yield. Some REE-oxides are below $3.95 today in the market place such as La, Ce, and Sm, but the rest are valued higher and some much higher, especially scandium oxide valued at $4200/kg. Thus if the scandium is only 5% of the REE mass, the process could cost $210 per kg justified by the scandium alone, well above $3.95 per kg. The known costs are less than 2% of the value of the scandium alone.

Also, scandium is one of the very first REE's expected to be separated from the solvent extraction process while the others follow, it would be possible to discard the raffinate after scandium but at that point, the incremental cost is just $0.49/kg for the power to produce acid/base. All of the REE-oxides are valued above that value, so it would make sense to proceed separating and purifying them.

Table 1 Process cost estimates

Process	Item	$/kg REE-oxide
Ion extraction	Heap leach preparation and membrane	2.67
Ion extraction	Sodium chloride	0.30
Ion extraction	Acid base power cost	0.49
Solvent extraction	Acid base power cost	0.49
Total		3.95

Summary of advantages of proposed technology approach

(1) Suitable for low grade feedstock
(2) Lowest cost inputs (only need NaCl, water, electricity)
(3) Mild pH range of process—4 to 9
(4) On-demand co-generation production of acid & base needed
(5) No waste streams other than neutral non-REE extracted
(6) Known process costs are less than 2% of expected salable product value when 40% yield was assumed

Description of Laboratory Work to Date

Numerous samples of waste rock were collected from the a coal mine near Salina, UT and from two seams in the a mine near Price, UT. Also samples were collected of volcanic ash origin rock near Emery, UT close to the Emery coal mine. The lab work to date focuses on roof rock from the 3 sources and the volcanic ash rock. All could be broken without much effort in mortar and pestle. These 4 samples were all analyzed for 8 REE's (to minimize cost). They all had REE's, not quite at the level reported by Miskovic but at attractive levels. The volcanic ash rock was higher than in Miskovic's report. All of the coal mine samples had around 20 ppm scandium and the volcanic ash rock was about 50 ppm scandium. Based on the scandium alone, these feedstocks all appear viable.

Block Flow Diagram Identifying Steps

See Fig. 2: Overall schematic of ion extraction process,
Fig. 3: Schematic ion-extraction process,
Fig. 5: Schematic of Overall Solvent Extraction Separation and Purification
Fig. 6: Detailed schematic flow chart of Separation/Purification Solvent Extraction Process,
and Fig. 7: Block flow diagram of overall process.

Our concept is to provide an "Extraction module" at multiple mine locations which could be anywhere in the USA. From there, REE-chlorides which are >50% REE are transported to a central facility for separation and purification steps which would be in the form of chloride, or oxide. Select REE-chlorides may be reduce to metals but not part of the immediate program [13].

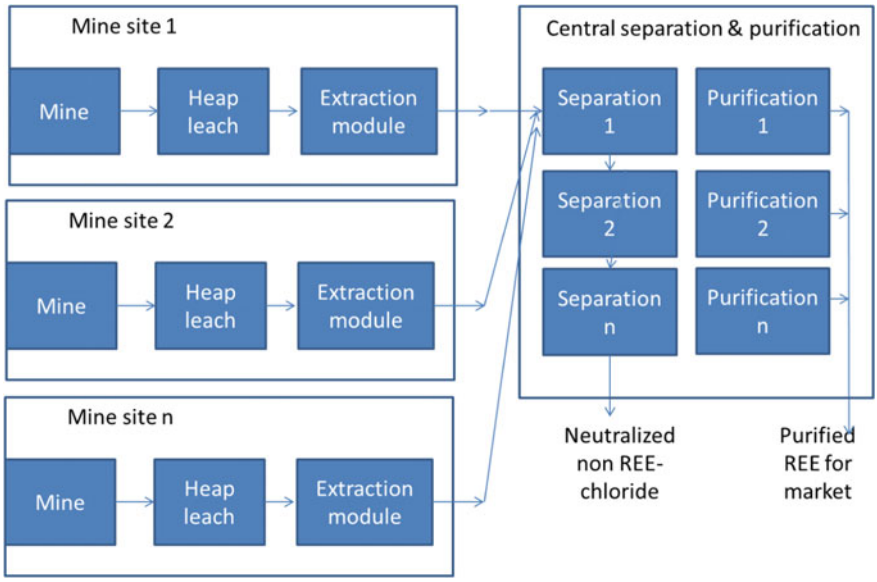

Fig. 7 Block flow diagram of overall process

How the Technology Would Be Scaled up?

This technology is very scalable. The extraction skids will be portable. Power for electrolysis is only about 1000 Watts requiring very little energy. The potential for scale-up is enormous. If every coal mine in the US closed today, there would be the waste rock from the decades of mining in the past that could be processed with this technology. Individuals at mines currently operating were receptive to this technology because it opens the door to additional revenue. The limiting factor will be obtaining permitting for leaching operation but the mild nature of the lixiviant should provide the best scenario for obtaining permits.

Preliminary Economics

Preliminary cost estimates were made for capital costs for the extraction units, solvent extraction and the respective operating costs. A business model was developed which showed favorable economics through the sale of the REE's.

Summary

A first look at extraction of REE's from coal mine waste rock using environmentally benign methods looks economically attractive.

Samples of caprock from sources in Utah confirmed that REE's indeed exist in rock currently removed in day to day coal mining operations which are sent to landfill.

Developing a process to extract the REE's from these wastes would provide an additional revenue stream to coal mining operations and increase the supply of REE's.

References

1. Miskovic S (2015) Extraction of REE from Coal—S203-UTA-PPM4002 Mod 01—University of Utah—REE recovery from Western Coals. U.S. DOE Prime Awaed DE-F0004002, 2015
2. Papangelakis VG, Moldoveanu G (2014) Recovery of rare earth elements from clay mineral. In: 1st European rare earth resources conference
3. Hower JC et al (2016) Notes on contributions to the science of rare earth element enrichment in coal and coal combustion byproducts. Minerals
4. Finkelman RB (1981) The origin, occurance, and distribution of the inorganic constituents in low-rank coals. In: Proceedings of the basic coal science workshop
5. Meloche C, Vratny F (1959) Solubility product relations in the rare earth hydrous hydroxides. Anal Chim Acta
6. Breitenbach AJ Heap leach pad design and construction practices in the 21st century
7. Michael L (2016) Free. In: Proceedings of copper 2016, Kobe, Japan, 15 Nov 2016
8. Smith M, Parra D (2014) Leach pad cost benchmarking. In: Proceedings of heap leach solutions
9. Michael L (2013) Free, hydrometallurgy fundamentals and applications. Wiley
10. Xie F et al (2014) A critical review on solvent extraction of rare earths from aqueous solutions. Miner Eng
11. Gupta CK Krishnamurthy N (2005) Extractive metallurgy of rare earths. CRC Press
12. Wang W, Cheng CY (2011) Separation and purification of scandium by solvent extraction and related technologies: a review. J Chem Technol Biotechnol
13. Yamamura T et al (2004) Electrochemcial processing of rare-earth and rare metals by using molten salts. Chem Sustain Dev

Extraction and Thermal Dissolution of Low-Rank Coal by N-Methyl-2-Pyrrolidinone

Jun Zhao, Haibin Zuo, Siyang Long, Jingsong Wang and Qingguo Xue

Abstract In order to effectively use of low rank coal, the thermally dissolve coal (TDC) was extracted from four kinds of low-rank coals by N-2-methyl-2-purrolidinone(NMP) at high temperature and high pressure. The structures of thermally dissolve coal and residues were characterized by element analysis, FT-IR spectra. The effects of temperatures, coal rank, solid-liquid ratio and extraction time on the extraction yields of TDC were studied, respectively. Moreover, the extraction mechanism of TDC at mild conditions is proposed. The results show that the ash contents of TDCs from four raw coals are significantly lower than that of raw coals, and the volatile contents and H/C are significantly improved. For KL coal, with the increase of temperature, the extraction yield of KL-TDC is improved evidently from 33.75% to 56.25% and the ash content is decreased from 0.57% to 0.49% at 350 °C.

Keywords Low-rank coal · Extraction yield · Reaction mechanism

J. Zhao (✉) · H. Zuo · S. Long · J. Wang · Q. Xue
State Key Laboratory of Advanced Metallurgy, University of Science and Technology Beijing, Beijing 100083, People's Republic of China
e-mail: zjwithcian@163.com

H. Zuo
e-mail: zuohaibin@ustb.edu.cn

S. Long
e-mail: longsiyang@163.com

J. Wang
e-mail: wangjingsong@ustb.edu.cn

Q. Xue
e-mail: xueqingguo@ustb.edu.cn

Z. Sun et al. (eds.), *Energy Technology 2018*, The Minerals, Metals & Materials Series, https://doi.org/10.1007/978-3-319-72362-4_55

Introduction

Coal is one of the most important energy sources in our society, and there has been increasing environment concern toward coal utilization [1]. The combustion of coal emits a great deal of carbon dioxide and forms the ash deposition, causing some serious problems, such as erosion and corrosion of turbine blade and fouling when used in coal-fired power. Therefore more efficient coal utilization is required to minimize the ash content of coal [2]. Thermal dissolution (TD) with organic solvents can produce low-ash coal, as reported by some researches [3–5]. The ash content of thermally dissolve coal (TDC) can be approximately reduced by 90%. TDC can be produced from a wide range of low-rank coals, such as sub-bituminous coals and lignite coals, and this thermal dissolution process can convert these low-rank coals to caking coals. Therefore, the development and utilization of TDC is the key to reduce the environment population of coal industry.

The extraction yield of coal is one of most important factors in the TDC production process. In order to have a better knowledge of the extraction behavior of TDC, some of research methods were proposed one after another. The research methods of extraction behavior are classified into the following types: acid extraction [6], organic solvent extraction [7] and oxidant extraction [8]. Masaki K [6] investigated that the extraction yield of low-rank coal by carbonic acid at high temperature, it was found that the thermal extraction yields of 52% and 45% for WY (sub-bituminous) and ND (lignite) coal at 360 °C, respectively. Iino M [9] researched the effect of coal rank on the extraction behavior by CS_2-NMP at room temperature, it was discussed that high yields of 30-66% were obtained for bituminous coal (C% 76.9–90.6% daf). Pan [8] studied the oxidative depolymerization of shenfu sub-bituminous coal at 320 °C, the results revealed that the conversion of TDI at 60 °C in 20% H_2O_2 was 41.8%. According to the researches of coal extraction, it is of great potent for its characters of high extraction yield, environmental protection and saving energy in extraction coal by NMP [10]. Consequently, it is needed to study the extraction behavior of coal in NMP.

In this study, the extraction behavior of four kinds of low-rank coals by NMP were investigated. The effects of coal type, temperature, solid-liquid ratio, and extraction time on the extraction yield were preliminary determined. The structures of thermally dissolve coals and residues were characterized by elemental-analysis and FT-IR spectra and the reaction mechanism of TDC by NMP was proposed. This study aims to providing theoretical guidance for its industrial application.

Experimental

Materials

Two sub-bituminous coals (KL, GD) and two lignite coals (XB, ZS) were used in this study. The coal samples were dried at 80 °C for 12 h in vacuum and ground

Table 1 Proximate and ultimate analysis of coal samples

Samples	Proximate analysis (wt% on dry basis)			Ultimate analysis (wt% on dry basis)					Atomic ratio	
	V	A	FC	N	C	S	H	O	H/C	O/C
KL	32.20	10.37	57.43	1.59	73.38	0.96	4.73	7.48	0.77	0.08
GD	14.31	9.14	76.55	1.23	80.19	1.22	3.78	3.65	0.57	0.03
XB	31.81	9.87	58.33	0.65	63.83	0.89	3.89	8.95	0.73	0.11
ZS	29.11	11.42	59.47	0.61	61.75	0.25	3.68	9.46	0.71	0.11

V, volatile matters; A, ash; FC, fixed carbon

into less than 200 mesh (74 μm), then deposited in sealed bags carefully for succeeding experiments. NMP (AR, >99.0%) was purchased from Shanghai Aladdin bio-chem technology co. LTD. All solvents used are commercial pure chemical reagent without further purification. The proximate and ultimate analyses of the coal samples are given in Table 1.

Thermal Dissolution

The coal thermal dissolution was performed following a published procedure [5]. The TD of four coal samples was conducted using an apparatus for thermal dissolution, as shown in Fig. 1. Approximate 8 g of coal sample and 400 mL NMP was charged into a stain steel tuber cell. High purity nitrogen was introduced into the autoclave reactor with a flow of 400 mL/min for 15 min to ensure inert atmosphere. The cell was heated to required temperature at a rate of −10 °C/min, and held at that temperature for 60 min. the cell was then cooled to room temperature for 2–3 h. about 200 mL ethanol was put into the cell to wash the residue, and the filtrate was also collected into round-bottom flask, the residual solid was recovered, washed with ethanol, and dried at 80 °C for 12 h in vacuum. The filtrate was added to a rotary evaporator to recovery organic solvent and precipitate soluble constituents The soluble constituents were flushed repeatedly by ethanol, and then the TSCs were dried at 80 °C for 12 h in vacuum. The thermal soluble constituents from four kinds of coals were named KL-TSC,GD-TSC,XB-TSC and ZS-TSC respectively. The yield of soluble constituents was calculated according to Eq. (1):

$$\mathrm{Y},\% = \frac{\mathrm{Mr} - \mathrm{Mc}}{Mr \times (1 - Ad)} \times 100\% \tag{1}$$

Where Mr (g), Mc (g) and A_d (%) were the initial mass of the coal, the mass of the residue, and the ash content of the initial coal, respectively.

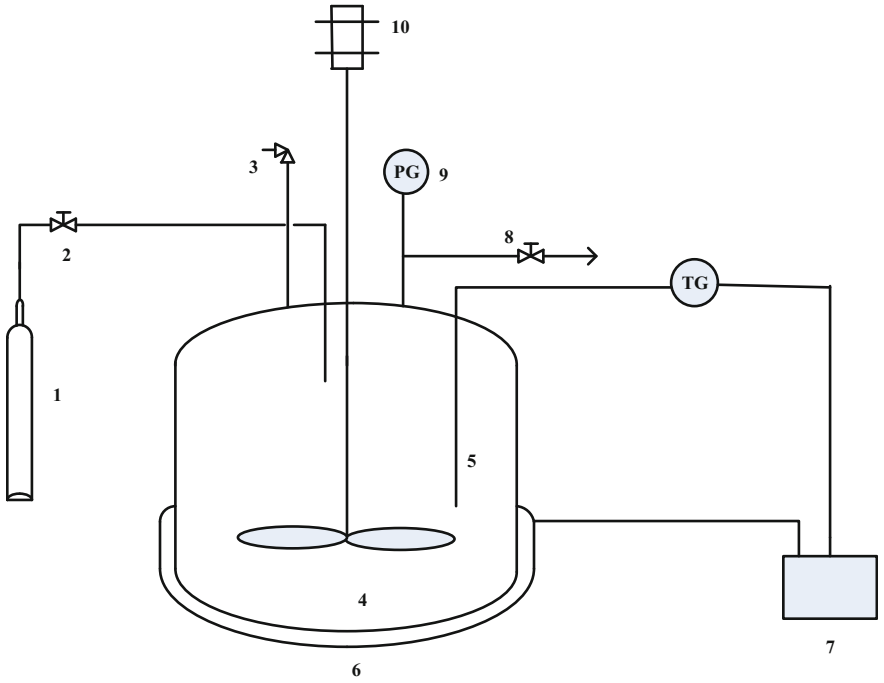

Fig. 1 Schematic diagram of apparatus for thermal dissolution

1. Gas cylinder
2. Gas inlet
3. Pressure relieve valve
4. High-pressure reactor
5. Thermocouple
6. Heating jacket
7. Temperature control unit
8. Gas outlet
9. Pressure gauge
10. Mechanical agitator.

Results and Discussion

Ultimate and Proximate Analyses of TDCs

The properties of four kinds of TDCs were shown in Table 2. The ash contents of TDCs were all less than their raw coals. It was confirmed that most of ash in coal could be removed by thermal dissolution process.

Table 2 ultimate and proximate analyses of four kinds of TDCs

Samples	Proximate analysis (wt % on dry basis)			Ultimate analysis (wt% on dry basis)					Atomic ratio	
	V	A	FC	N	C	S	H	O	H/C	O/C
KL-TDC	49.91	0.49	50.00	4.14	79.13	0.53	5.27	6.85	0.80	0.06
GD-TDC	29.00	0.68	70.32	3.25	83.34	1.20	4.70	6.46	0.68	0.06
XB-TDC	47.02	1.26	51.72	3.08	80.84	0.27	4.60	8.65	0.68	0.08
ZS-TDC	44.77	0.90	54.34	2.75	77.97	0.26	5.66	10.85	0.87	0.10

V, volatile matters; A, ash; FC, fixed carbon

The carbon contents and volatile contents of TDCs were far higher than their raw coals, indicating that the structure of coal was interrupted by the solvent and thermal, and substantial amounts of hydrocarbons were dissolved in the solvent. The H/C ratio of KL-TDC, GD-TDC and ZS-TDC was much higher than the raw coals, it implied that the enrichment of aliphatic in these TDCs. However, the produced TDC from XB showed lower H/C than its raw coal, this was probably due to the extraction temperature was much higher than its softening temperature, the light hydrocarbon components were reassembled to form the heavy aromatic hydrocarbon components. The sulfur content showed significantly decreased in the TDCs compared to raw coals. But ZS coal had less change of sulfur content since the sulfur content in ZS raw coal was low. The inorganic sulfur in TDCs was completely removed by the thermal dissolution process, and only some organic sulfur remained. A significant amount of nitrogen was contained in TDCs might be the result of forming the nitrogen-containing-compounds between the NMP and the light components during the thermal dissolution process. The O/C ratio showed slightly decreased in the TDCs compared with raw coals. while GD coal expressed opposite result owning to the low oxygen content in its raw coal.

Effect of Coal Rank on the Extraction Yield

Figure 2 shown variations of extraction yield by coal type. The extraction yields using NMP were 12–57%, and the highest yield was found in KL coal. GD gave the lowest extraction yield (12.57%), it might be ascribed to the higher degree of coalification and C/H ratio than other coals, leading to the lower content of aliphatic and higher heat-stability for GD coal. Accordingly, the structure of GD coal was little effected by thermal and solvent. While XB coal and ZS coal as a low-rank coal, the softening temperature was far lower than KL and GD. When the extraction temperature exceeding its softening temperature, the light hydrocarbon components were reassembled to form the heavy aromatic hydrocarbon components, which were hardly extracted by NMP.

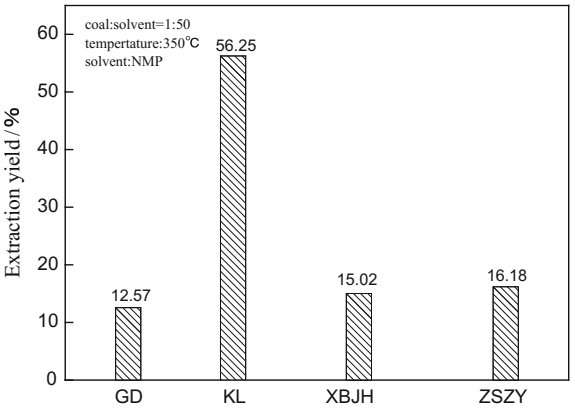

Fig. 2 Effect of coal type on extraction yield

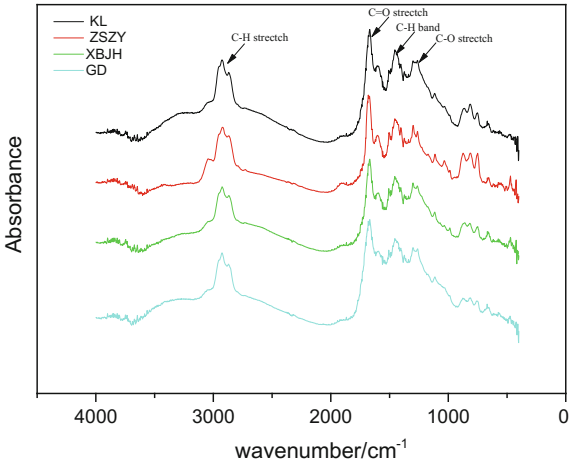

Fig. 3 FT-IR spectra for four TDCs obtained by NMP extraction at 350 °C

Figure 3 shown FT-IR spectra for four TDCs from the extraction of NMP at 350 °C. For all TDCs, the absorbance at 1669, 1262, 1192 cm^{-1} were stronger and almost no absorbance due to hydroxyl groups around 3640 and 3300 cm^{-1} could be obtained, indicating that oxygen-containing groups in raw coals were converted to -$COOCH_3$ by thermal dissolution. The absences of aliphatic groups at 2920 and 2858 cm^{-1} in TDCs were remarkably stronger than aromatic groups (3050 cm^{-1}), suggesting that the light hydrocarbon components were extracted in TDCs. the magnitude ordering of absences for oxygen-containing groups and aliphatic groups as follows: KL-TDC > ZS-TDC > XB-TDC > GD-TDC. This was fortunately consistent with the results of extraction yield, it indicated that the extraction yields of TDCs were affected by the light hydrocarbon components and oxygen-containing groups in raw coals and the softening temperature.

As shown in previous results, KL coal had performed better in terms of extraction yield. Therefore, it was decided to study the effects of temperature, charge ratio and thermal dissolution time on the extraction yield utilizing the KL coal.

Effect of Temperature on Extraction Yield and Ash Content

Figure 4 shown the extraction yield of KL coal in NMP at different temperatures. the extraction yield increased rapidly with the raising of thermal dissolution temperature and the maximum yield (56.25%) was obtained at 350 °C. Further raising the temperature to 380 °C, the extraction yield decreased to 45.28%. NMP was a polar solvent, the high extraction yield of KL coal by NMP might be attributed to the result of heat-induced and solvent-induced structural relaxation followed by dissolution of coal micromolecular components in the NMP. The decreased extraction yield above 360 °C was caused by the promoted polymerization of micromolecular components to form heavy aromatic components which was hardly extracted by NMP at high temperature. With an increasing of temperature, the ash content of KL-TDC slightly decreased.

Figure 5 shown FT-IR spectra for KL raw coal (RAW), the residue (RE) and the KL-TDC obtained by NMP extraction at 300–380 °C. For the spectra of TDCs at different temperature, the peaks assigned to mineral matter (500–600 cm^{-1}, 1000–1100 cm^{-1}, 3600–3700 cm^{-1}) almost disappeared compared to those of raw coal and residue. These results were consistent with the ash content of KL-TDC was lower than its raw coal. It indicated that the thermal dissolution process could be used to improve the quality of the low-rank coal. With an increasing of temperature, the peaks assigned to aliphatic hydrocarbon (2920 and 2858 cm^{-1}) and oxygen-containing compounds (1669, 1262 and 1192 cm^{-1}) remarkably increased. it was reported that polar solvent such as NMP are strongly absorbed on -OH and aliphatic hydrocarbon by forming rather strong hydrogen bonds with the released

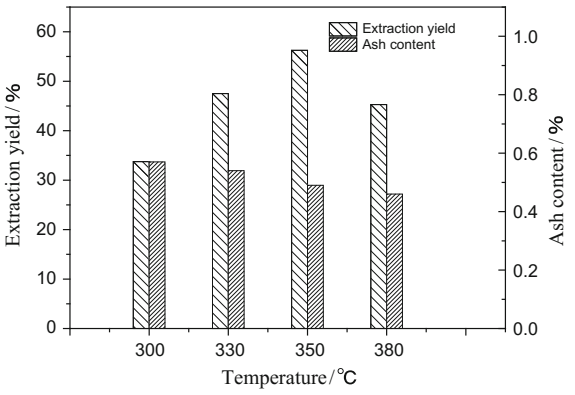

Fig. 4 Effect of temperature on extraction yield and ash content

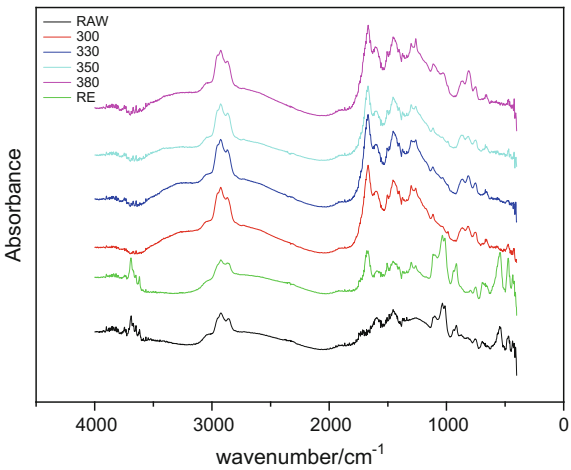

Fig. 5 FT-IR spectra for KL raw coal (RAW), the residue (RE) and the KL-TDC obtained by NMP extraction at 300–380 °C

OH groups and aliphatic hydrocarbon [11], as a nucleophilic atom in NMP, nitrogen could attack and cleave the C-H and C-O by hydrogen bond force. Therefore, it can be concluded that NMP released nitrogen in KL coal and formed rather strong hydrogen bonds with the released OH groups. This would give an additional solvent-induced relaxation of coal structure, resulting in much higher extraction yield and peak intensity. When the temperature above 350 °C, the peaks gradually decreased. This was owing to the high temperature induced poly-condensation reaction between the NMP and the light aliphatic hydrocarbon and oxygen-containing groups. It produced a great deal of gas, such as CO_2 and H_2O, leading to the extraction yield decreased.

Effect of NMP/Coal Ratio on the Extraction Yield and Ash Content

In order to reduce the amount of NMP used and improved the economy of the thermal dissolution of KL coal, effects of the NMP/coal ratio on the extraction yield and ash content of KL coal were studied and the results were shown in Fig. 6. The thermal dissolution was carried out at 350 °C for 1 h with 400 mL NMP and a varied amount of KL coal. It can be found that the extraction yield and ash content of KL coal reached to 56.25% and 0.49% respectively, during the ratio of NMP/coal was 400/8. With an increasing of NMP/coal ratio, the extraction yield of KL coal decreased, the ash content of KL-TDC slightly decreased. This was because the extraction efficiency of NMP reached maximum value at 400/8, continuing to increase the ratio of NMP/coal, the light hydrocarbon components were difficultly extracted by NMP and reassembled to form the heavy aromatic components, these

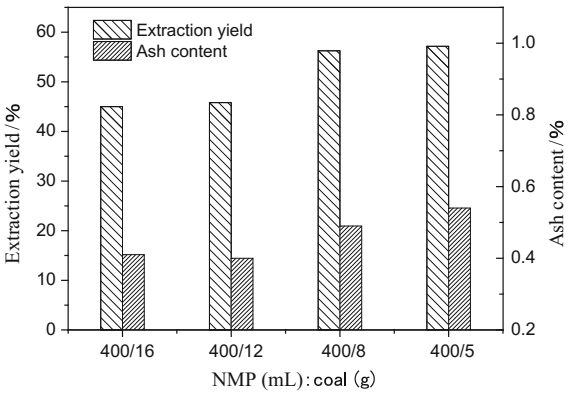

Fig. 6 Effect of NMP/coal ratio on the extraction yield and ash content

would seriously affect the ability that NMP dissolved and permeated in the carbon skeletal structure of coal.

Effect of Thermal Dissolution Time on the Extraction Yield and Ash Content

As shown in Fig. 7. It can be found that the thermal dissolution time insignificantly affected the extraction yield and ash content. When the thermal dissolution time is 30 min, the extraction yield and ash content reached about 45 and 0.52%. While continuing to increase the time, the extraction yield and ash content were basically maintained at about 56 and 0.45%. Thus, it can be concluded that thermal dissolution time played an inessential role in extraction process.

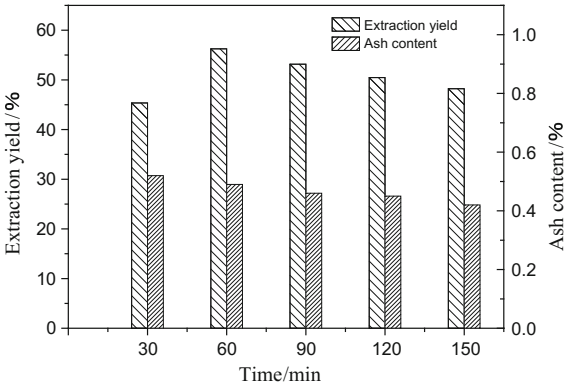

Fig. 7 Effect of thermal dissolution time on the extraction yield and ash content

In conclusion, the optimized process conditions were: thermal dissolution temperature 350 °C, thermal dissolution time 1 h, charge ratio of 400 mL:8 g (NMP/KL coal).

Determination of the Reaction Mechanism for Thermally Dissolve Coal

According to the above results, the proposed mechanism of coal extraction by NMP was as follows:

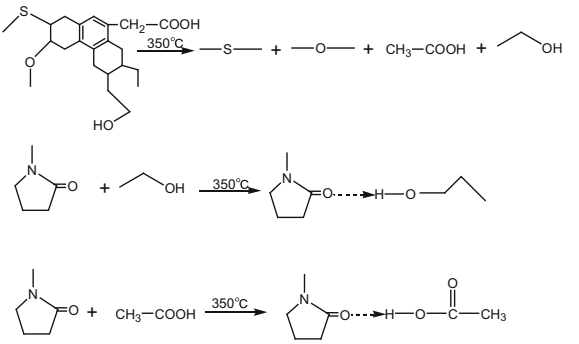

The process of coal extraction was inferred to begin with the structure of coal interrupting by thermal, some light aliphatic hydrocarbon components and oxygen-containing groups to be released since the NMP dissolved and permeated in the carbon skeletal structure of coal. Then, some hydrogen bonds were formed between NMP and light aliphatic hydrocarbon and oxygen-containing groups. Meanwhile, with a substantial amount of micromolecular components releasing, polymerization reaction was produced by itself, and a great deal of gas to be formed, such as CO_2 and H_2O. The release of these interactions should increase the extraction yield of subbituminous coal.

Conclusions

1. The ash content and sulfur content can be significantly reduced by the thermal dissolution process, and the combustion property of TDC can be effectively improved based on the increasing of volatile.
2. KL coal has a good reaction activity with NMP compared with other coals. the extraction yield of KL coal and ash content of KL-TDC reached to 56.25% and 0.49% at 350 °C for one hour with the NMP/coal ratio equal to 400 mL/8 g, respectively.

3. During the thermal dissolution process, coal rank and temperature played the main role on the effect of extraction yield and ash content compared with other factors.
4. The proposed mechanism of coal extraction by NMP was deduced, the main reaction was the formation of hydrogen bonds between NMP and light micro-molecular components.

Acknowledgements This work was financially supported by the 'National Natural Science Foundation of China (NO. 51574023) and National Key Research and Development Program (2016YFB0600701).

References

1. Xiong G, Li Y, Jin L et al (2015) In situ FT-IR spectroscopic studies on thermal decomposition of the weak covalent bonds of brown coal. J Anal Appl Pyrol 115:262–267
2. Kashimura N, Takanohashi T, Saito I (2006) Upgrading the solvent used for the thermal extraction of sub-bituminous coa. Enegy Fuel 20:2063–2066
3. Shui H, Zhao W, Shan C et al (2014) Caking and coking properties of the thermal dissolution soluble fraction of a fat coal. Fuel Process Technol 118:64–68
4. Takanohashi T, Shishido T, Saito I (2008) Effects of hypercoal addition on coke strength and thermoplasticity of coal blends. Enegy Fuel 22:1779–1783
5. Rahman M, Samanta A, Gupta R (2013) Production and characterization of ash-free coal from low-rank Canadian coal by solvent extraction. Fuel Process Technol 115:88–98
6. Masaki K, Kashimura N, Takanohashi T et al (2005) Effect of pretreatment with carbonic acid on "HyperCoal" (ash-free coal) production from low-rank coals. Enegy Fuel 19:2021–2025
7. Wang YN, Wei XY, Li ZK et al (2017) Extraction and thermal dissolution of Piliqing subbituminous coal. Fuel 200:282–289
8. Pan CX, Liu HL, Liu Q et al (2017) Oxidative depolymerization of Shenfu subbituminous coal and its thermal dissolution insoluble fraction. Fuel Process Technol 155:168–173
9. Iino M, Takanohashi T, Ohsuga H et al (1988) Extraction of coals with CS2-N-methyl-2-pyrrolidinone mixed solvent at room temperature: effect of coal rank and synergism of the mixed solvent. Fuel 67:1639–1647
10. Do Kim S, Woo KJ, Jeong SK et al (2008) Production of low ash coal by thermal extraction with N-methyl-2-pyrrolidinone. Korean J Chem Eng 25:758–763
11. Shui H, Zhou Y, Li H et al (2013) Thermal dissolution of Shenfu coal in different solvents. Fuel 108:385–390

Enhancement of Coal Nanostructure and Investigation of Its Novel Properties

B. Manoj

Abstract Coal is a mineral and is extensively used as a solid fuel in developing nations and has a sizeable share in the global fossil fuel reserve. Utilization of this resource generates excess spoil and large volume of low grade waste to the environment. In recent years there have been serious research on enhancing its value and exploring the utility of this carbonaceous material to novel carbon materials.

Keywords Nano carbon · Low grade coal · Crystalline carbon
Fungal leaching

Fungal Solubilisation of Coal

Coal is extensively used as a solid fuel in developing nations and has a sizeable share in the global fossil fuel reserve [1–5]. Utilization of this resource generates excess spoil and large volume of low grade waste to the environment. Being inherently low quality due to the mineral matter and ash, leaching of coal is need before any application. Generally mineral acids or alkalis are used for the complete demineralization of coal, although froth flotation can reduce the ash content of coal close to 2% from about 10 or 12% Even though mineral matter could be removed, the disposal of the used chemical in safe manner is a serious concern. These chemicals generally corrode the environment and generates serious environmental pollution. In this scenario, a facile, ecofriendly demineralization technique of coal is worthwhile problem to be investigated. Microorganisms have the ability to breakdown while beneficiating the low grade coal. For commercial utility of coal bio-demineralization, fungal leaching is an ideal eco-friendly method. These fungus secretes mild organic acids which partially removes the minerals in coal without much modification to the organic structure [6, 7].

B. Manoj (✉)
Department of Physics, Christ University, Bangalore 560029, Karnataka, India
e-mail: manoj.b@christuniversity.in

Z. Sun et al. (eds.), *Energy Technology 2018*, The Minerals, Metals & Materials Series, https://doi.org/10.1007/978-3-319-72362-4_56

Solubilization of minerals in coal has the potential to elevate this inherently dirty solid fuel to a value-added products like graphene, graphene quantum dots or carbon nanotubes [1–5]. Carbon structure in coal has short domain characteristics and is an ideal precursor for nano carbon dots and diamonds. Graphene is sp^2 hybridized form of carbon, appears in many forms like graphite, nanotubes or fullerenes [4, 5]. Nano domain in coal consists of about 3–4 stacked carbon layers, with lateral dimension and interlayer spacing of 3 nm and $\sim$0.35 nm respectively. The amorphous realms constituted of polycyclic aromatic compounds, which are graphene sheets having irregular onion-like arrangement along with other organic constituents.

In the present work, efficacy of the fungus *Aspergillus niger* in leaching coal and its effect on nano carbon layer stacking is discussed. It is a green extraction of preformed carbon structure from low rank coal. Changes in the stacking structure, nature of defect, degree of graphitization and change surface morphology with bioleaching is also highlighted. The mechanism of demineralization with carboxylic acid secreted by *Aspergillus niger* was elaborated in our earlier work and studies carried out by other groups [8–12].

Coal biodegradation is a naturally complex process, which appears to be driven by extracellular enzymes in the presence of various chelators released by different fungi. Under favourable conditions, microorganism secretes organic acids which have the ability to degrade the coal minerals in an eco-friendly manner [13–17]. The present research work is focused on laboratory scale screening methodologies to investigate both the microorganisms and mechanism involved.

Indian coal of different rank are biosolubilzed with various fungi and the obtained product are charcterized by various techniques. Proximate analysis and elemental composition of raw coal and its biosolubilized products are presented in Tables 1 and 2. The carbon content was incremented by 20%, accompanied by a reduction in oxygen, which clearly indicates that, overt oxidation in the solid portion did not occur during bioleaching. The ash content was lowered from 12.87 to 0.55 wt%, owing to the removal of all minerals by *A. niger*. It was observed for the first time that, *Aspergillus* leaching could reduce the traces of ash to less than 0.6 wt%.

The mixed culture (GM) and *Pencillium* leaching (GP) could also reduce the ash to 1.21% and 3.05 wt% respectively. The mechanism for demineralization by fungi is discussed in our earlier reported studies [8, 13].

When the sample (GX) was treated with *A. niger* (GA) alone, the sulphur content was decreased from 0.46 to 0.09 wt%, because of the reaction with bassanite (Table 2). Other elements such as carbon and nitrogen were increased, but oxygen content was decreased from 31.11 to 19.14 wt%. The proximate analysis confirmed maximum removal of ash *A. niger* leaching (95.7%), followed by mixed culture leaching (90.6%), by eliminating Al and Si minerals. The ash content of various leached coal samples are shown in Fig. 1.

When the raw coal was treated with *A. niger*, the carbon content was enhanced to 72.05 wt% from an initial value of 60.12 wt%, while hydrogen decreased from 6.84 to 2.98 wt%. On inoculating coal with *A. flavus*, the oxygen content was furher

Table 1 Proximate analysis of coal after bio-demineralization

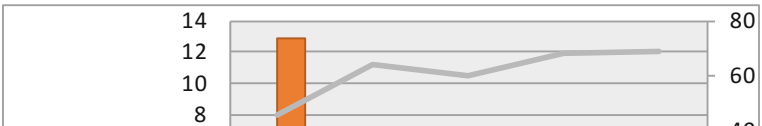

	GX	GA	GF	GP	GM
Moisture	4.57	3.7	3.66	3.68	3.5
Ash	12.87	0.55	4.12	3.05	1.21
Fixed carbon	45.66	64.09	60.12	68.01	68.55
VM	36.9	31.66	32.1	25.26	26.68

Table 2 Ultimate analysis of coal after bio-demineralization

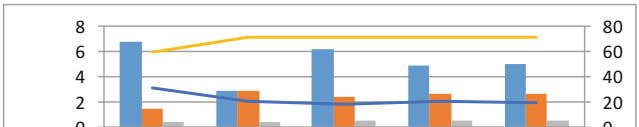

	GX	GA	GP	GF	GM
H	6.84	2.98	6.23	4.96	5.02
N	1.47	2.98	2.49	2.66	2.64
S	0.46	0.49	0.59	0.55	0.57
C	60.12	72.05	71.56	71.22	71.5
O	31.11	21.5	19.14	20.62	20.27

(GX- Virgin sample, GA -leached with Aspergillus niger, GP-Leached with Penicillium spp. GF- Leached with Aspergillus Flavus, GM- Leached in mixed culture of all three)

diminished to 19.14 wt%, while carbon was increased to 71.56 wt%. When the sample was treated with a mixed culture of *A. niger* and *Penicillium spp* (GM), no further enhancement in carbon was observed. Proximate analysis of the sample reported an increase of fixed carbon content for about 51% after *Pencillium spp* leaching. The percentage of volatile matter remained constant, at ~25 wt%. The calorific value of sub-bituminous coal (GX), after demineralization with different fungal leachants on ash free basis, was also calculated. The leaching process with *A. niger* (GA) reportd a rise in calorific value of coal by 26.6%, while on leaching with *Penicillium spp* (GP) and mixed culture (*A. niger* and *Penicillium spp*-GM) the calorific value was raised by 23.7 and 27% respectively.

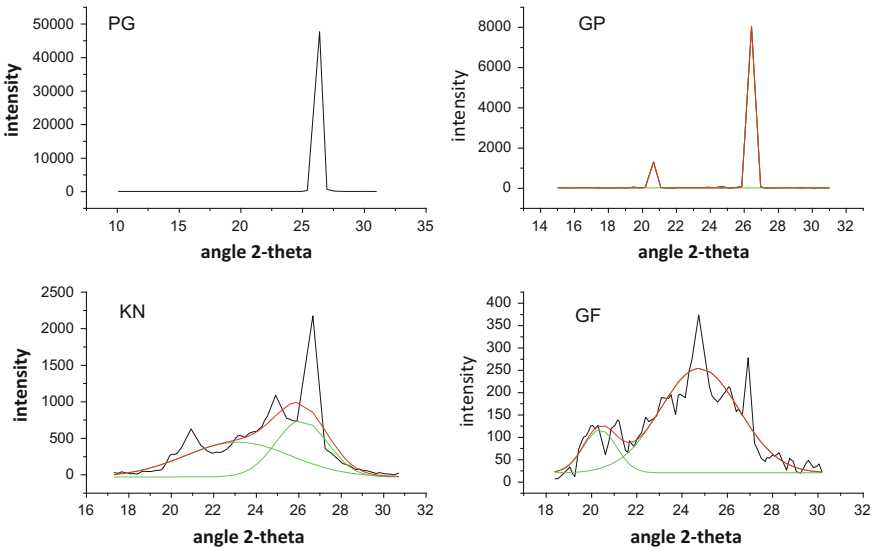

Fig. 1 X-ray spectrum of biosolubilized coal samples with A. Niger (PG-Pure graphite, GP-Penicillium sp. Leached sub-bituminous coal, KN-Aspergillus niger leached bituminous coal, GF-Sub-bituminous coal leached with Aspergilllus flavus)

The existence of crystallites in the bio-solubilized coal structure was identified by the (002) and (110) reflections in the XRD spectrum [4, 5]. It is notice that the crystallites in all coal samples possess intermediate structures between graphite and amorphous state, the so called turbostratic or random layer lattice structure [4, 5]. *Penicillium spp* treated sample (GP) exhibited only two defined peaks at 26.40° (π-band) and 20.57° (γ-band) and has more of graphitic or ordered structure.

The intensity ratio (I_{20}/I_{26}) of γ to π-band is a measure of imperfection in amorphous carbon [13]. The lower the ratio, higher the ordering of carbon layers in coal sample and it approaches graphitic nature. For *Penicillium* leached coal samples, the values of (I_{20}/I_{26}) and aromaticity were evaluated as 0.19 and 0.86 respectively. The lateral size along the *c*-axis (L_c) was found to be varied from 22.32 to 2.25 nm, while L_a from 343.64 to 1.50 Å. The calculated structural parameters are presented in Table 3.

The X-ray diffraction studies could confirm the removal of minerals more efficiently in *A. niger* leaching than *A. flavus*, *Penicillum spp* and mixed culture. On *Penicillium spp* leaching, the carbon atoms were reorganized to graphite like structure.

Table 3 Structural parameters of coal samples treated with various fungi

Sample	I_{20}/I_{26}	f_a	L_a (nm)	L_c (nm)	d_{002} (Å)
GP	0.19	0.86	34.36	22.32	0.337
GA	0.61	0.44	39.77	3.22	0.343
GF	0.41	0.86	0.15	2.25	0.360
PG	0.00	1.00	30.58	15.53	0.335

Coal as a Source of Novel Nanocarbon Materials

The nanostructure and graphene layers present in coals of different rank was determined from demineralized coal after chemical leaching. The structural parameters of the samples were elucidated by the modified Scherer formula as reported earlier by same research group [4]. The X-ray profile analysis of samples shows two peaks at 2θ–18.29° and 24.85° originated from the γ-band and the π-band (Fig. 2). The π-band being for the aromatic ring while the γ-band is due to the aliphatic content. The diffraction profile shows broadening of peak in the (20–26°) region mainly due to the existence of carbon nano crystallites as reported earlier [1–5].

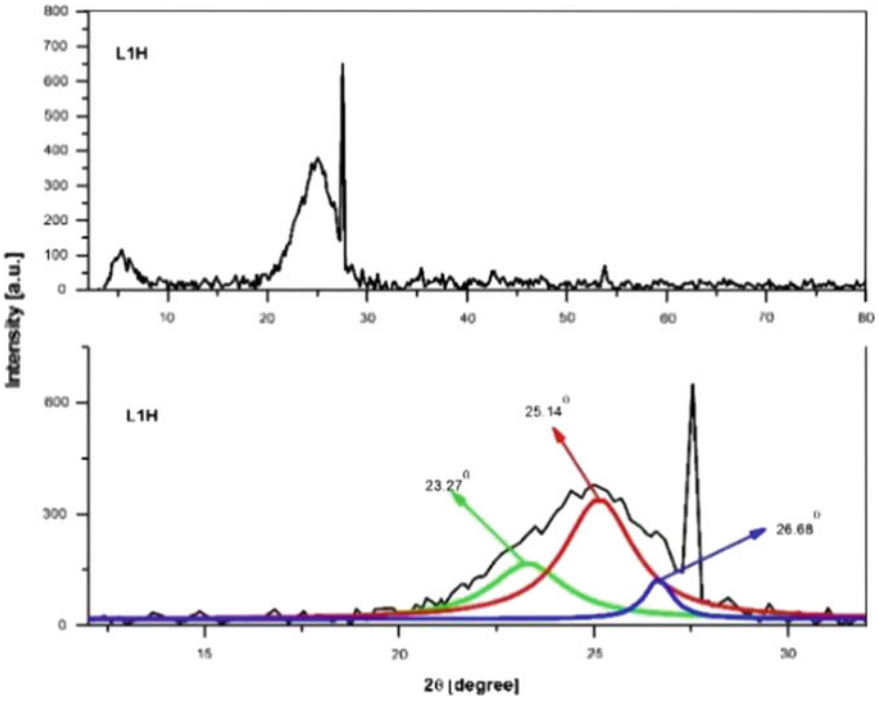

Fig. 2 XRD spectrum of nanostructure obtained from Lignite (L1H)

The X-ray analysis confirms the formation of stacked graphene layers in coal. The stacking height increases with decrease in coal rank or and the number aromatic lamellae shows a reverse trend with increase in rank. With the chemical synthesis, the high rank coals are converted to few layer graphene oxide while lignite shows the structure of graphite with wrinkles.

Raman spectra of the nanocarbon from coal is presented in Fig. 3. Raman spectrum of graphite comprises of strong peaks at 1580 and 2700 cm^{-1} named as G band and 2D band (a second order of D band) respectively. The G band arises due to the in plane optical phonon modes. G mode has E_{2g} symmetry which does not require the presence of six fold rings and hence it occurs at all sp^2 sites [1, 2, 18–20]. The 2D band originates from the double resonance process and hence appears to be dispersing in nature. In addition to these bands, a D band is noticed at 1350 cm^{-1} which arises due to the proximity of The sp^3 carbon network show characteristic Raman features prominently at 1148 cm^{-1}, secondary peaks at 1274 and 1307 cm^{-1} (ta-C) for sub-bituminous coal. Earlier studies assigned this band to hexagonal diamond, nanocrystalline diamond or sp^3 rich carbon structures. There are also studies which have designated the origin of this band to be sp^2–sp^3 mixed structure [9].

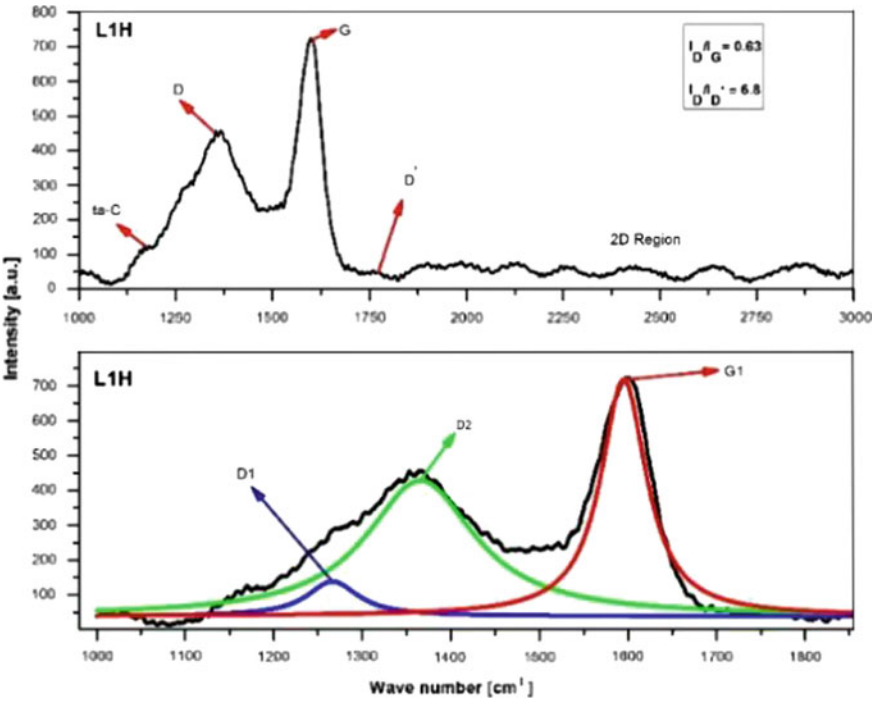

Fig. 3 Raman spectrum of nanostructure obtained from Lignite (L1H)

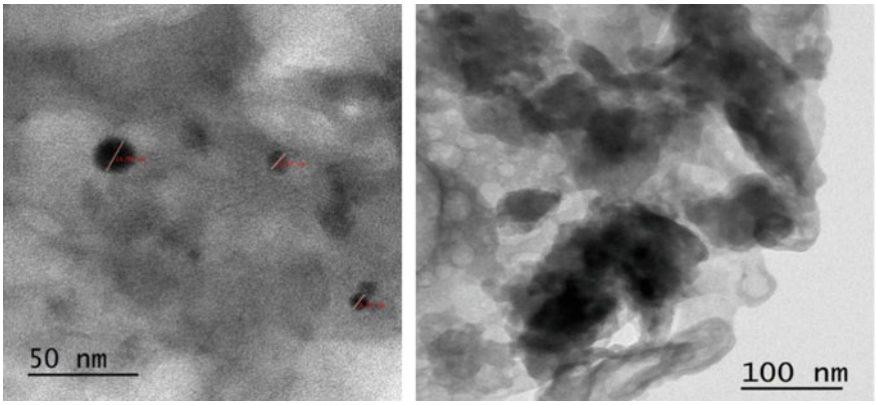

Fig. 4 TEM micrograph of nanostructure obtained from bituminous coal and sub-bituminous coal

Other than the G and 2D peaks, D and D' peaks are also observed in the spectrum and are attributed to defect-induced Raman features which are inactive in highly crystalline carbon. The intensity ratio (I_D/I_G) of the D and G band is widely used for characterizing the defect quantity in graphitic materials and was found to be 0.54 for sub-bituminous coal, 0.58 for bituminous coal (spectra not shown) and 0.63 for lignite. This reveals the presence of graphitic nano carbon with fewer defects. The intensity ratio ($I_D/I_D^{'}$) gives the information about the nature and concentration of defects. D' peak have generally low intensity compared to D peak (which generally appear as a small shoulder to G peak). This ratio was found to be 3.40 for sub-bituminous coal due to boundary like defects, 3.16 for bituminous coal indicating boundary like defects and 6.8 for lignite attributed to vacancy—like defects [9, 20].

The TEM image of the carbon nano dots formed in the bituminous coal (B1H) is presented in Fig. 4. Spherical carbon nano dots of the size 14 to 4.8 nm are observed in the micrograph.

Conclusions

The mineral content in coal samples was completely removed by leaching with *A. niger* and its mixed cultures. The concentration of ash was decreased by 98.5% (*A. niger* leaching) and 90% (mixed culture leaching). The intensity ratio (I_{20}/I_{26}), a measure of disorder in amorphous carbon, was found to be 0.19 for *Penicillium spp* leached coal samples. *A. niger* was able to remove minerals efficiently, than *A. flavus*, as evident from the XRD studies. The interlayer spacing of *Pencillium spp* leached sample was computed to be 3.37 Å, which is near to ordered graphite (3.35 Å). Therefore, it is concluded that, the fungal stains: *A. niger, A. flavus* and

Penicillium spp could significantly affect the structure of carbon layers of coal samples upon leaching.

Different types of coal are investigated for the production of mixed phase graphene like nanostructures by simple oxidation followed by sonication. They have the unique structure and are ideal precursor for the synthesis of graphene quantum dots, nano diamonds, graphene layers, carbon dots and mixed phase graphene structure. The properties of the carbon structure, its shape and size is highly dependent on the rank of the coal used. It could be concluded that Sub-bituminous, Bituminous and Lignite coal serve as efficient precursors for the production of carbon nanostructures at low cost by exploiting the simple acidic oxidation method. The preformed nanostructure are mixed phase in nature.

References

1. Dong Y, Jianpeng L, Chen Y, Fengfu F, Yuwu C, Chen G (2014) Graphene quantum dots, graphene oxide, carbon quantum dots and graphite nanocrystals in coals. Nanscale 6:7410–7415
2. Ye R, Xiang C, Lin J, Peng Z, Huang K, Torr J (2013) Coal as an abundant source of graphene quantum dots. Nat Commun 4:2943–2947
3. Xiao J, Liu P, Yang W (2015) Nanodiamonds from coal under ambient conditions. Nanoscale 7:6114–6125
4. Manoj B (2014) Investigation of nano-crystalline structure in selected carbonaceous materials. Int J Miner Mater Metall 21(9):940–946
5. Manoj B, Kunjomana AG (2014) Systematic Investigations of graphene layers in sub-bituminous coal. Russ J Appl Chem 87(11):1726–1733
6. Båsaran Y, Denizli A, Sakintuna B (2003) Bio-liquefaction/ Solubilization of low-rank lignite. Energy Fuel 17:1068–1074
7. Celin A, Sukla LB, Misra VN (2005) Biological elimination of sulphur from high sulphur coal by Aspergillus-like fungi. Fuel 84:1597–1600
8. Elcey CD, Manoj B (2013) Demineralization of sub-bituminous coal by fungal leaching: structural characterization by X-ray and FTIR analysis. Res J Chem Environ 17(8):11–15
9. Elcey CD, Manoj B (2016) Graphitization of coal by bio-solubilization: structure probe by Raman spectroscopy. Asian J Chem 28(7):1557–1560
10. Ghorbani Y, Oliazadeh M, Shavedi A, Roohi R, Pirayehgar A (2007) Use of some isolated fungi in biological leaching of aluminium from low grade bauxite. Afr J Biotechnol 6(11): 1284–1288
11. Jaklitsch WM, Kubicek CP, Scrutten MC (1991) Intracellular location of enzymes involved in citrate production by Aspergillus niger. Can J Microbiol 37:823–827
12. Kubicek CP, Scherferl KG, Wöhres W (1988) Evidence for a cytoplasmic pathway of oxalate biosynthesis in Aspergillus niger. Appl Environ Microbiol 54(3):633–637
13. Manoj B (2013) Bio-demineralization of Indian bituminous coal by Aspergillus niger and characterization of the products. Res J Biotechnol 8:39–54
14. Ramachandran S, Pierre F, Pandey A (2006) Gluconic acid: properties, applications and microbial production. Food Technol Biotechnol 44(2):185–195
15. Sharma DK, Wadhwa G (1997) Demineralization of coal by stepwise bioleaching: a comparative study of three Indian coals by Fourier transform infrared and X-ray diffraction techniques. World J Microbiol Biotechnol 13(1):29–36

16. Volesky B (2001) Detoxification of metal-bearing effluents: biosorption for the next century. Hydrometallurgy 59:203–216
17. Wang J, Chen C (2006) Biosorption of heavy metals by Saccharomyces cerevisiac: a review. Biotechnol Adv 4:417–451
18. Ferrari AC, Robertson J (2001) Resonant Raman spectroscopy of disordered, amorphous and diamond like carbon. Phys Rev B 64:075414-1–075414
19. Manoj B (2016) A comprehensive analysis of various structural parameters of Indian coals with the aid of advanced analytical tools. Int J Coal Sci Technol 3(2):123–132
20. Eckmann A, Felten A, Mishchenko A, Britnell L, Krupke R, Novoselov KS, Casiraghi C (2012) Probing the nature of defects in graphene by Raman spectroscopy. Nano Lett 12(8): 3925–3930

Erratum to: Recovery of Copper from Nickel Laterite Leach Waste by Chemical Reduction Using Sodium Dithionite

A. B. Botelho Junior, I. A. Anes, M. A. Carvalho, D. C. R. Espinosa and J. A. S. Tenório

Erratum to:
Chapter "Recovery of Copper from Nickel Laterite Leach Waste by Chemical Reduction Using Sodium Dithionite" in: Z. Sun et al. (eds.), *Energy Technology 2018*, The Minerals, Metals & Materials Series, https://doi.org/10.1007/978-3-319-72362-4_38

In the original version of the book, the misspelt co-author name "M. A. Caralho" has been corrected as "M. A. Carvalho" in chapter "Recovery of Copper from Nickel Laterite Leach Waste by Chemical Reduction Using Sodium Dithionite", front matter (Table of Content) and Author Index. The erratum book has been updated with the change.

The updated online version of this chapter is can be found at https://doi.org/10.1007/978-3-319-72362-4_38

Z. Sun et al. (eds.), *Energy Technology 2018*, The Minerals, Metals & Materials Series, https://doi.org/10.1007/978-3-319-72362-4_57

Author Index

Z. Sun et al. (eds.), *Energy Technology 2018*, The Minerals, Metals & Materials Series, https://doi.org/10.1007/978-3-319-72362-4

Subject Index

Z. Sun et al. (eds.), *Energy Technology 2018*, The Minerals, Metals & Materials Series, https://doi.org/10.1007/978-3-319-72362-4